UNIVERSITY OF CALIFORNIA
SANTA CRUZ

DESIGN AND SYNTHESIS OF NANOSTRUCTURED CATALYSTS FOR EFFICIENT ENERGY CONVERSION: INSIGHTS INTO STRUCTURAL ENGINEERING

A dissertation submitted in partial satisfaction
of the requirements for the degree of

DOCTOR OF PHILOSOPHY

in

CHEMISTRY

by

Qiming Liu

September 2023

This Dissertation of Qiming Liu is approved:

Professor Shaowei Chen, Chair

Professor Scott Oliver

Professor Xiao Wang

Peter Biehl
Vice Provost and Dean of Graduate Studies

TABLE OF CONTENTS

LIST OF FIGURES

Chapter 1

(c) ORR polarization curves of HP-FeN_4, FeN_4 and NC catalysts in O_2-saturated 0.5 M H_2SO_4 and 20% Pt/C in 0.1 M $HClO_4$ at the rotating rate of 1600 rpm.

Figure 11. (a) Dark-field STEM image of the NCAC-Zn/Fe aerogel. Red circles indicate single Fe atoms. Inset is a TEM image of the NCAC-Zn/Fe aerogel, and the scale bar is 30 nm. (b) AFM images of NCAC-Zn/Fe aerogels: adhesion force image. (c) Side/top view and simulated STM image (at a bias of -1.0 V) of normal FeN_4 and FeN_4 SW-doped graphene sheets. (d) Density of state (DOS) of normal FeN_4 and FeN_4 SW-doped graphene sheets. (e) ORR polarization curves of CAC, CAC/Fe, NCAC/Fe, and NCAC-Zn/Fe, as well as the Pt/C at 1600 rpm in 0.1M KOH at the potential sweep rate of 5mV s^{-1}.

Figure 12. (a) Scheme of the formation of isolated copper sites (Cu ISAS/N-C) catalyst. (b) Free energy diagram for ORR process on these three models at the equilibrium potential (U = +0.40 V vs. NHE or U = +1.23 V vs RHE) at pH=14. (c) Linear sweep voltammetry (LSV) curves of NC, Cu ISAS/NC and Pt/C catalysts in 0.1 M KOH solution at the sweep rate of 10 mV s^{-1} and rotation rate of 1600 rpm.

Figure 13. (a) Preparation of (Fe,Co)/N-C. (b) Energies of intermediates and transition states in mechanism of ORR at (Fe,Co)/N-C from DFT. (c) RDE polarization curves of Pt/C, Co SAs/N-C, Fe SAs/N-C, and (Fe,Co)/N-C in O2-saturated 0.1 M HClO4 with sweep rate 10mV s−1 and rotation rate 1600 rpm. Inset:E_{onset} of different catalysts.

Figure 14. Ultrafast thermal shock. (a) Digital photographs of the Joule heating device before and during heat treatment. (b) Processed temperature values for the spectra along with the intensity on the 858 nm channel. (c) Schematic illustration of the ultrafast, in

situ transformation of minerals to catalyst nanoparticles. (d) Schematic diagram of the preparation of dislocation-rich Pt nanoparticles by thermal shock. (e) HRTEM image of the Dr-Pt nanoparticle, (f) corresponding inverse fast Fourier transform (IFFT) of (110) plane, and (g) strain distribution related to (110) plane. (h) HER activity and (i) durability evaluation of Dr-Pt. (j) Miscibility of Cu with other metals. (k) Elemental mappings of $Cu_{0.9}Ni_{0.1}$ and (l) $Cu_{0.9}Ag_{0.1}$. (m) Faraday efficiency of pure Cu and different $Cu_{0.9}X_{0.1}$ bimetallic catalysts at -0.70 ± 0.01 V vs. RHE towards COR.

Figure 15. Catalysts prepared by Flash joule heating. (a) Circuit diagram of the FJH setup. (b) Photograph of the FJH reaction box. (c) Current vs time profile during the FJH process. (d) Atomic structure of the 2H and 1T phases and corresponding 2H MoS_2 precursors and FJH-prepared 1T MoS_2. (e) HER polarization curves of FJH-prepared 1T MoS_2.

Figure 16. Laser ablation in liquid and pyrolysis. (a) A schematic illustration of the LAL synthesis and structure of L-Ag NPs. PC, perfect crystal; SC, stacking fault crystal. (b, c, d) representative TEM images of L-Ag NPs. The yellow arrows denote stacking faults. (e) HER polarization curves of L-Ag, S-Ag, T-Ag, and Pt/C in 0.5 M H_2SO_4 at a scan rate of 5 mV s^{-1}. Inset shows the corresponding polarization curves at higher current densities.

Figure 17. Schematics of various ultrafast synthetic methods. (a) Flame synthesis of Co-doped TiO_2. (b) Electrosynthesis of high entropy glass nanoparticles. Current transient corresponds to the collision of a single nanodroplet onto a carbon fiber UME, where nanodroplet contents are fully (>98%) reduced within 100 ms, facilitating

on the initial feed of palladium. (c) Pore size distribution profiles of HNC and Pd-HNC_{10}.

Figure 2. Pd-HNC_{10} before and after thermal refluxing. The resulting supernatant demonstrates a similar yellowish color, indicating that the HNC is saturated with Pd centers.

Figure 3. Cumulative pore volume as a function of pore width of the HNC and Pd-HNC_{10} samples.

Figure 4. Comparison of the ORR performance of HNC and solid N-doped carbon (NC) at the rotation rate of 1600 rpm in oxygen-saturated 0.1 M KOH.

Figure 5. (a-c) Representative TEM images of Pd-HNC_{10} at varied magnifications. (d) HAADF-STEM image of Pd-HNC_{10} and the corresponding elemental maps of carbon, nitrogen, oxygen, palladium, and overlap.

Figure 6. TEM images of (a) Pd-HNC_1, (b) Pd-HNC_2, and (c) Pd-HNC_5. Red circles in panels (b) and (c) highlight the few palladium nanoparticles.

Figure 7. (a-c) TEM images of PdNP/HNC at varied magnifications. Inset to panel (c) is the corresponding Fast Fourier Transform (FFT) pattern of the Pd nanoparticles in the white square.

Figure 8. HAADF-STEM images of the edge side (without apparent particles) of Pd-HNC_{10} and the corresponding elemental maps of carbon, nitrogen, oxygen, palladium, and overlap.

Figure 9. XRD patterns of PdNP/HNC, Pd-HNC_{10}, Pd-HNC_2, and HNC. Dashed lines indicate the expected 2θ position of the (111) diffractions of *fcc* Pd (JCPDS no. 96-101-1105).

Figure 10. XPS survey spectra of PdNP/HNC, Pd-HNC_{10}, Pd-HNC_5, Pd-HNC_2, Pd-HNC_1, and HNC.

Figure 11. (a) High-resolution XPS spectra of the Pd 3d electrons of the Pd-HNC series and PdNP/HNC. (b) High-resolution XPS spectra of the C 1s (upper) and N 1s (bottom) electrons of HNC. (c) High-resolution XPS spectra of O 1s electrons of HNC and Pd-HNC_{10}.

Figure 12. High-resolution XPS spectra of the (left panels) O 1s and (right panels) N 1s electrons of (a, b) PdNP/HNC, (c, d) Pd-HNC_{10}, (e, f) Pd-HNC_5, (g, h) Pd-HNC_2, and (i, j) Pd-HNC_1.

Figure 13. (a) Pd K-edge normalized XANES profiles of Pd-HNC_{10}, Pd-HNC_2, and Pd foil. Fourier transform EXAFS spectra of (b) Pd-HNC_{10}, (c) Pd-HNC_2, and (d) Pd foil.

Figure 14. ORR performance of the Pd-HNC series in oxygen-saturated 0.1 M KOH. (a) Linear sweep voltammograms (LSVs) of Pd-HNC nanocomposites and control samples of HNC, PdNP/HNC, and Pt/C at the rotation rate of 1600 rpm. (b) The corresponding electron-transfer number (n, solid), yield of H_2O_2 (%), and (c) Tafel plots with the slopes shown in mV dec^{-1}. (d) Poisoning test of Pd-HNC_{10} with EDTA and KSCN treatments. (e) Stability test of Pd-HNC_{10} under 5000 cycles in N_2 saturated 0.1 M KOH.

Chapter 4

(d) X-ray absorption near edge spectra (XANES) and (e) the corresponding Fourier transformed extended X-ray absorption spectra (FT-EXAFS) of Ru-200, Ru-300, Ru-400, and Ru-600.

Figure 11. Ru 3p XPS spectra of Ru-300-S, Ru-300, and Ru-300-L.

Figure 12. C 1s and Ru 3d spectra of (a) Ru-200, Ru-300, Ru-400, and Ru-600, (b) Ru-300-S, Ru-300, and Ru-300-L.

Figure 13. Cl 2p XPS spectra of Ru-300-S, Ru-300, and Ru-300-L.

Figure 14. O 1s spectra of (a) Ru-200, Ru-300, Ru-400, and Ru-600, (b) Ru-300-S, Ru-300, and Ru-300-L.

Figure 15. EXAFS fittings of Ru-200, Ru-300, Ru-400, Ru-600, Ru-300-S, and Ru-300-L.

Figure 16. (a) X-ray absorption near edge spectra (XANES) and (b) the corresponding Fourier transformed extended X-ray absorption spectra (FT-EXAFS) of Ru-300-S, Ru-300, Ru-300-L.

Figure 17. CV scans of Ru-200, Ru-300, Ru-400, and Ru-600 at a scan rate of 50 mV s^{-1} in N_2 saturated 0.5 M H_2SO_4.

Figure 18. (a) Linear scanning voltammetry (LSV) curves and (b) the corresponding Tafel plots of Ru-200A, Ru-300, Ru-400, Ru-600, and $RuCl_3$ in 0.5 M H_2SO_4. (c) LSV curves of Ru-200, Ru-300, Ru-400, Ru-600, and $RuCl_3$ in 1 M KOH and (d). Stability test of Ru-300 in (e) 0.5 M H_2SO_4 and (f) 1 M KOH. XPS spectra of the (g) Ru 2p and (h) Cl 2p electrons of Ru-300 after stability test in acidic and alkaline media.

Chapter 5

(c) Nyquist plots of Co-NC-200, Co-NC-400, and Co-NC-600 at the overpotential of +300 mV. (d) Stability tests by i-t measurements of Co-NC-200, Co-NC-400, Co-NC-600, and RuO_2 at their respective h_{20} for 20 h. (e) OER polarization curves of Co-NC-200, Co-NC-400, Co-NC-600, and RuO_2 acquired at different time points during the stability tests.

Figure 19. Comparisons of OER overpotentials at 10 and 200 mA cm^{-2} amongst the samples.

Figure 20. OER Polarization curves of Co-NC-400 before and after acid leaching in 1 M KOH at a scan rate of 10 mV s^{-1}.

Figure 21. Representative TEM images of Co-NC-400 after leaching in 0.5 M H_2SO_4. Scale bars are both 50 nm.

Figure 22. XPS spectra of (a) Co 2p, (b) O 1s, and (c) N 1s spectra for Co-NC-400 before (top curves) and after (bottom curves) acid leaching.

Figure 23. Co 2p spectra of Co-NC-200, Co-NC-300, Co-NC-400, Co-NC-500, and Co-NC-600 after 10 scans of OER polarization curves.

Figure 24. XPS spectra of the O 1s electrons of Co-NC-200, Co-NC-400, and Co-NC-600 after 10 scans of OER polarization curves.

Figure 25. The contents (at%) of Co, OOH, and OH after 10 scans of OER polarization curves for Co-NC-200, Co-NC-400, and Co-NC-600.

Figure 26. XPS spectra of the N 1s electrons of Co-NC-200, Co-NC-400, and Co-NC-600 after 10 scans of OER polarization curves.

showing the morphology of FeNiO-250-4. (b) Atomic-resolution HAADF-STEM image and an enlarged image (inset) corresponding to the boxed region in a) acquired along the <111> zone axis. (c) High-resolution energy-dispersive spectroscopy (EDS)-based elemental maps of Fe and Ni in a FeNiO-250-4 particle. (d) High-resolution TEM (HRTEM) image of nanospindles in FeNiO-250-4. (e-f) HAADF-STEM images of nanospindles on the edge of FeNiO-250-4 (low-contrast regions). (g) EDS mapping images of the interface between nanospindles and nanoparticles in FeNiO-250-4. (h) HAADF-STEM images and (i) EDS mapping images of FeNiONC-250-4. (j) HAADF-STEM and (k) EDS mapping image of FeNiO-250-16.

Figure 3. Crystal structure of Fe-Ni oxide spinel, where blue, pink and red indicate Fe, Ni and O atoms, respectively.

Figure 4. HAADF-STEM images of Fe-Ni oxide spinel in FeNiO-250-4 along the [112] zone axis.

Figure 5. HAADF-STEM images of Fe-Ni oxide spinel in FeNiO-250-4 along the [100] zone axis.

Figure 6. HAADF-STEM images of Fe-Ni oxide spinel in FeNiO-250-4 along the [103] zone axis.

Figure 7. TEM and electron diffraction studies. (a,c) TEM images and (b,d) selected area electron diffraction patterns of nanospindle crystals around the Fe3-xNixO4 particles of FeNiO-250-4.

Figure 8. EDS-based elemental mapping analysis. (a-c) EDS mapping studies of FeNiO-250-4.

Figure 17. Electrochemical activities. (a) LSV curves and (b) the corresponding Tafel plots of FeNiO-250-4, FeNiO-250-4-NC, FeNiO-250-16 and 20% Ru/C in 1 M KOH. (c) Polarization curves of FeNiO-250-4 in the first scan, after 10 h's stability tests at 1.53 V.

Figure 18. LSV curves of FeNiO-250-4 in 1 M KOH at different levels of iR compensation.

Figure 19. CV curves at difference scan rates for (a) FeNiO-250-4, (b) $FeNiO_{NC}$-250-4, and (c) FeNiO-250-16. (d) Corresponding ECSA calculations.

Figure 20. (a) LSV curves normalized by ECSA. (b) TOF curves of FeNiO-250-4, $FeNiO_{NC}$-250-4, and FeNiO-250-16.

Figure 21. Optimization of OER performance of FeNiO samples. OER polarization curves of (a) FeNiO-X-4 at X = 100, 150, 200, 250, 300, 400, and 600 A, (b) FeNiO-250-4 but at different initial feed ratios of Ni:Fe (1:0, 20:1, 10:1, 5:1, 3:1, 1:1, 1:3, and 0:1), and (c) FeNiO-250-Y at Y = 2, 4, 8, and 16 s.

Figure 22. XPS studies of FeNiO-250-4 after stability test.

Figure 23. SEM studies of FeNiO-250-4 after stability test.

Figure 24. Computational studies of OER energetics. Structural models of (a) $Ni(OH)Fe_2O_4(Cl)$, (b) $Ni(OH)Fe_2O_4$, (c) $Fe(OH)Fe_2O_4(Cl)$, (d) $Fe(OH)Fe_2O_4$, (e) Ni(OH)NiO(Cl), and (f) Ni(OH)NiO.

Figure 25. Charge density difference and evolution of bond lengths of two-site models. (a-d) Charge density difference isosurface with a value of 0.01. Light blue corresponds to negative and yellow to positive; (e-h). Evolution of bond distances of HO*—#O

species: (a,e) Fe(OH)Fe2O4, (b,f) Fe(OH)Fe2O4(Cl), (c,g) Ni(OH)Fe2O4 and (d,h) Ni(OH)Fe2O4(Cl).

Figure 26. PDOS of the Fe1 atom. (a-d) $Fe(OH)Fe_2O_4$, (e-h) $Fe(OH)Fe_2O_4(Cl)$, (i-l) $Ni(OH)Fe_2O_4$ and (m-p) $Ni(OH)Fe_2O_4$ (Cl).

Figure 27. Additional materials prepared by MIHRQ. XRD patterns of (a) Ni_3S_2, (b) TiO_2, (c) Ir, and (d) Pt produced on nickel foam. Photographs of (e) carbon nitride (C_3N_4), (f) nickel foam before (right piece) and after (left piece) induction heating in air, and (g) 10 heating setups for larger-scale synthesis or for the preparation of a diverse range of materials.

Chapter 7

Scheme 1. Schematic illustration of the synthetic procedure of Ir nanoparticles capped with varied organic ligands.

Figure 1. TEM images of (a,b) Ir nanoparticles and (c) the corresponding core size histogram.

Figure 2. (a) UV-vis absorption and (b) photoluminescence emission spectra of the varied organically capped Ir nanoparticles.

Figure 3. FTIR spectra of EPA, DBSA and EPT monomeric ligands and the corresponding organically capped Ir nanoparticles.

Figure 4. Interfacial charge transfer characterizations. (a) High-resolution XPS profiles of the Ir 4f electrons of Ir-C≡, Ir=N, and Ir-S nanoparticles, and (b) the corresponding spectra of valence band maximum (VBM). (c) (top panels) Optimized structures of Ir-

C≡, Ir=N, and Ir-S slabs and (bottom panels) the corresponding interfacial charge density distributions.

Figure 5. Optimized structures of Ir-C≡ with (a) one, (b) two, or three ligands per slab and the corresponding interfacial charge density distribution.

Figure 6. Bifunctional electrocatalytic performance towards HER and OER in 1.0 M KOH. (a) HER polarization curves of the series of electrocatalysts, and (b) the corresponding Tafel plots. (c) OER polarization curves of the series of electrocatalysts, and (d) the corresponding Tafel plots. (e) Current-voltage profiles of overall water splitting with Ir-C≡ and commercial Ir/C as bifunctional electrocatalysts in 1.0 M KOH, and (f) the corresponding activity retention tests by chronoamperometric measurements at the respective initial E_{10}.

Figure 7. Comparison of the bifunctional catalytic performance in alkaline media. (a) HER current densities of the varied Ir nanoparticles at the potential of -50 mV in 1.0 M KOH. (b) OER current densities of the varied Ir nanoparticles at the potential of +1.55 V in 1.0 M KOH.

Figure 8. Nyquist plots at the potential of (a) -50 mV (HER) and (b) 1.55 V (OER) in 1 M KOH. Inset is the Randle equivalent circuit: R_{ct} is the charge transfer resistance, C_{dl} is the double layer capacitance, and R_s is the series resistance.

Figure 9. Current-voltage profiles of overall water splitting with Ir-C≡ and commercial Ir/C as bifunctional electrocatalysts in 1.0 M KOH before and after the constant-potential stability test.

Figure 10. Bifunctional electrocatalytic performance towards HER and OER in 0.5 M H_2SO_4. (a) HER polarization curves of the series of electrocatalysts, and (b) the corresponding Tafel plots. (c) OER polarization curves of the series of electrocatalysts, and (d) the corresponding Tafel plots. (e) Current-voltage curves of overall water splitting using Ir-C≡ and commercial Ir/C as the bifunctional catalysts in 0.5 M H_2SO_4, and (f) the corresponding activity retention test by chronoamperometric measurements at the respective initial E_{10}.

Figure 11. Comparison of the bifunctional catalytic performance in acidic media. (a) HER current densities of the various Ir nanoparticles at the potential of -50 mV in 0.5 M H_2SO_4. (b) OER current densities of the various Ir nanoparticles at the potential of +1.55 V in 0.5 M H_2SO_4.

Figure 12. Nyquist plots at the potential of (a) -100 mV (HER) and (b) 1.50 V (OER) in 0.5 M H_2SO_4.

Figure 13. Current-voltage profiles of overall water splitting with Ir-C≡ and commercial Ir/C as bifunctional electrocatalysts in 1.0 M KOH before and after the constant-potential durability test.

Figure 14. DFT calculation results of HER. (a) Averaged Gibbs free energy of H* adsorption (ΔG_{H^*}) on ligand-anchoring Ir atoms (solid spheres) and the neighboring Ir atoms (hollow spheres) in different organically modified Ir(111) slabs and bare Ir(111) slab. Error bars reflect variations among similar sites. Inset shows the relaxed Ir-C≡ structure and the ligand-anchoring Ir atoms circled in red. (b) Structural configuration of the relaxed Ir-C≡ model. (c) PDOS and d band center (E_d) of ligand-anchoring Ir and

Figure 3. Control sample that is prepared in the same manner except for the addition of any organic ligands.

Figure 4. Control sample that is prepared in the same manner but without the addition of $NaHSO_3$.

Figure 5. Control sample that is prepared in the same manner but with the addition of 0.5 M H_2SO_4 instead of 0.5 M KOH.

Figure 6. Control sample that is prepared in the same manner but without the addition of 0.5 M KOH.

Figure 7. Control sample that is prepared in the same manner but with the addition of 5 M KOH. Photographs of the final product (a) in solution and (b) on a silicon wafer.

Figure 8. Stability of CuOH-EPA dispersed in ethanol for up to 24 hours with the addition of different concentrations of H_2SO_4 or KOH.

Figure 9. XPS results of CuOH-EPA in water after 24 hours. High-resolution scans of (a) Cu 2p, (b) O 1s, and (c) C 1s spectra.

Figure 10. XPS results of CuOH-EPA in 0.01 M KOH after 24 hours. High-resolution scans of (a) Cu 2p, (b) O 1s, and (c) C 1s spectra.

Figure 11. XPS results of CuOH-EPA in 0.1 M KOH after 24 hours. High-resolution scans of (a) Cu 2p, (b) O 1s, and (c) C 1s spectra.

Figure 12. XPS results of CuOH-EPA in 1 M KOH after 24 hours. High-resolution scans of (a) Cu 2p, (b) O 1s, and (c) C 1s spectra.

Figure 13. Representative TEM images of the organically capped CuOH samples: (a, d, g) CuOH-EPA, (b, e, h) CuOH-HC16, (c, f, i) CuOH-EPT. Scale bars are (a-c) 200

nm, (d-f) 20 nm, and (g-i) 5 nm. (j) AFM topograph of CuOH-EPA and (k) the corresponding height profile along the red line in panel (j). (l) XRD patterns of CuOH-EPA, simulated CuOH-EPA, traditional Cu-alkyne polymer (CCDC-242490), CuOH (cuprice), and Cu_2O. (m and n) Simulated CuOH-EPA structure. (o) FTIR spectra of CuOH-EPA, CuOH-HC16, and CuOH-EPT nanostructures, and the corresponding ligand monomers (light-colored curves).

Figure 14. Control sample that is prepared in the same manner but with the addition of a 5× initial feed of Cu(OAc) salts.

Figure 15. Representative AFM topograph of CuOH-EPA.

Figure 16. (a, b) Representative AFM topographs of CuOH-HC16.

Figure 17. Representative AFM topographs of CuOH-EPT.

Figure 18. (a-c) SEM images of CuOH-EPA and (d) the corresponding EDX-based elemental maps of Cu, C, and O.

Figure 19. (a-c) SEM images of CuOH-HC16 and (d) the corresponding EDX-based elemental maps of Cu, C, and O.

Figure 20. (a-c) SEM images of CuOH-EPA and (d) the corresponding EDX-based elemental maps of Cu, C, O, and S.

Figure 21. Electron images and corresponding EDS mappings of Cu, O of CuOH-EPA.

Figure 22. Electron images and corresponding EDS mappings of Cu, O of CuOH-HC16.

Figure 23. Electron images and corresponding EDS mappings of Cu, O, S of CuOH-EPT.

Figure 35. (a) Bulk CuOH-HC4 showing the layered structure, H-bonding between layers. (b) PBE calculated band structure and DOS of CuOH.

Figure 36. (a) Bulk CuOH-EPT showing the layered structure, H-bonding between layers. (b) PBE calculated band structure and DOS of CuOH.

Figure 37. Optimized structure of (a) CuOH-EPA and EPA ligand, (c) CuOH-HC4 and HC4, (e) CuOH-EPT and EPT with corresponding bond distances (black) and Bader charges in |e| (blue). Charge density difference isosurfaces of (b) CuOH-EPA, (d) CuOH-HC4, and (f) CuOH-EPT (±0.0016|e|).

Figure 38. Photographs of different organically capped CuOH nanostructures (a) in ambient light (dispersed in DCM) and under 365 nm photoirradiation (b) when dispersed in DCM and (c) as solid films). The colors of the CuOH-EPA, CuOH-HC16 and CuOH-EPT dispersions in DCM are all yellowish, while the photoluminescence is red, yellow, and orange, respectively when dispersed in DCM or solid films. (d, f, h) UV-vis and photoluminescence spectra of the ligands-functionalized CuOH nanostructures at the excitation at 395 nm and (e, g, i) the excitation-dependent PL profiles: (d,e) CuOH-EPA, (f,g) CuOH-HC16, and (h,i) CuOH-EPT.

Figure 39. Calculated density of states (DOS) for CuOH-EPA, CuOH-HC4, and CuOH-EPT.

Figure 40. (a) Projected local density of states of CuOH-EPA (top) and CuOH-HC4 (bottom). (b) Proposed PL mechanism. (c) TDDFT-based UV-vis spectrum of CuOH-EPA, "*" means the experimental values. (d) Natural transition orbitals (NTO) analysis of CuOH-EPA.

LIST OF TABLES

Chapter 2

Chapter 3

Chapter 4

Chapter 5

ABSTRACT

DESIGN AND SYNTHESIS OF NANOSTRUCTURED CATALYSTS FOR EFFICIENT ENERGY CONVERSION: INSIGHTS INTO STRUCTURAL ENGINEERING

Qiming Liu

The growing demand for efficient energy conversion technologies has compelled researchers to explore novel approaches for catalytic systems that can address the pressing global challenges associated with energy sustainability. The unique properties exhibited by nanomaterials, such as their unique electronic structure, high surface area, tailored morphology, and tunable surface chemistry, offer tremendous opportunities for optimizing their catalytic activity. Herein, my dissertation presents a comprehensive exploration of the design and synthesis of nanostructured catalysts, focusing on the principles of structural engineering to manipulate the composition, morphology, and surface properties of materials. Structural engineering plays a pivotal role in tailoring the properties of nanostructured catalysts, enabling the precise control of their electrochemical behavior, and enhancing their performance in energy conversion processes. By carefully designing the structure at the atomic and nanoscale levels, it becomes possible to optimize the catalysts' activity, stability, and selectivity, ultimately advancing the field of energy conversion and enabling the development of high-performance catalyst materials.

Specifically, this dissertation will delve into the atomic structure of metal-nitrogen-carbon materials (**Chapter 2 and 3**), ultrafast synthesis of catalysts with non-

equilibrium structures (**Chapter 4-6**), and the surface functionalization of nanoparticles/nanostructures by using conjugated alkyne ligands (**Chapter 7 and 8**):

Chapter 1 serves as an introductory chapter, providing a comprehensive overview of the fundamental ideas and principles in energy conversion, including the importance of electrocatalysis and the role of nanostructured catalysts. It sets the stage for the subsequent chapters, highlighting the significance of structural engineering for achieving high-performance catalysts. Meanwhile, some background review of metal-nitrogen-carbon nanomaterials, ultrafast synthesis, and the surface functionalization of materials are provided. **Chapter 2** investigates the fabrication of metal-nitrogen-carbon (MNC) nanocomposites using a wet-impregnation procedure. The obtained Pd-HNC nanocomposites demonstrate superior ORR activity compared to metallic Pd nanoparticles and even outperform commercial Pt/C and relevant Pd-based catalysts. This highlights the effectiveness of atomic dispersion and surface enrichment of palladium in a carbon matrix. In **Chapter 3**, carbon nanocomposites based on transition-metal oxides are explored for the ORR. The introduction of dual metals (Ru and Fe) and nitrogen doping results in RuFe-NC nanocomposites with excellent ORR activity, rivaling commercial Pt/C benchmarks. The use of a trinuclear complex facilitates atomic dispersion of ruthenium within iron oxide nanoparticles, leading to enhanced ORR performance. Introducing dopants is also a very effective structural engineering method in improving the electrocatalytic activity of nanomaterials. **Chapter 4** focuses on the use of ruthenium nanoparticles supported on carbon paper for the hydrogen evolution reaction (HER). The metallic Ru nanoparticles prepared

using a novel magnetic induction heating (MIH) method exhibit remarkable HER activity, comparable to commercial Pt/C benchmarks. The surface metal-Cl species, which are hard to preserve in conventional heating methods, play a critical role in enhancing electrocatalytic activity. **Chapter 5** explores the ultrafast preparation of cobalt/carbon nanocomposites using MIH. The resulting nanocomposites exhibit excellent oxygen evolution reaction (OER) performance, surpassing commercial RuO_2. Charge transfer between the carbon scaffold and metal nanoparticles contributes to their superior catalytic activity. Operando x-ray absorption spectra (XAS) was employed to reveal the electrocatalytic mechanism that metallic Co nanoparticle would transform into CoO_x species to act as active sites for OER. In **Chapter 6**, carbon-FeNi spinel oxide nanocomposites are synthesized using MIH-quenching, resulting in high-performance catalysts for the OER. The rapid heating and quenching process prevents phase segregation and produces a Cl-rich surface, contributing to the exceptional catalytic activity, confirmed both experimentally and theoretically. **Chapter 7** investigates the design of bifunctional catalysts using 4-ethylphenylacetylene-functionalized iridium nanoparticles. The Ir-C≡ nanoparticles exhibit enhanced electrocatalytic activity for both HER and OER, surpassing commercial Ir/C and Pt/C benchmarks. The formation of Ir-C≡C- conjugated interfacial linkage enhances the electron density and interactions with reaction intermediates, leading to improved performance in electrochemical water splitting. In **Chapter 8**, a facile wet-chemistry procedure is reported for the preparation of stable CuOH nanostructures through deliberate functionalization with select organic ligands. The resulting CuOH

nanostructures exhibit a nanoribbon morphology with embedded nanocrystals within an amorphous nanosheet-like scaffold. The functionalization with acetylene and mercapto derivatives forms Cu-C≡ and Cu-S- interfacial bonds, respectively, leading to effective electronic coupling at the ligand-core interface in the former case. The acetylene-capped CuOH nanostructures demonstrate enhanced photodynamic activity in inhibiting bacterial growth, attributed to reduced material bandgap and effective photocatalytic generation of reactive oxygen species.

DEDICATION

To My parents, Liangqian & Xia.

&

To My wife, Qianhui.

ACKNOWLEDGEMENTS

Life is but a dream. It feels so unreal for me to receive my Ph.D. degree after five years in the United States, after encountering a horrible pandemic, a notorious wildfire, and countless power outages, after witnessing breathtaking sunsets and starry skies of the Central Coast, ceaseless ebbs and flows of the waves in Monterey Bay, and the inspiring grandeur of the Sierra Nevada's rolling mountains and towering redwoods, and especially, after days and nights of experiments and paper writing in PSB 190 of the Science Hill. Here, I would like to express my gratitude to all those who have supported me during my journey towards my Ph.D. degree.

First and foremost, I am sincerely grateful to my advisor, Prof. Shaowei Chen, for his exceptional guidance and support over the past five years. Under his mentorship, I have gained extensive knowledge in various experiments, characterization techniques, data analysis, scientific writing skills, and research mindsets. In the field of chemistry and materials, Prof. Chen is remarkably insightful and incisive, consistently inspiring me with constructive ideas during our one-on-one and group meetings. His passion for research is significant, as he is always available to discuss research ideas and address problems, even during late nights, weekends, and holidays. His flexibility and dedication in creating a great research atmosphere have allowed us to explore novel and challenging ideas together. Moreover, his patience and caring nature have been invaluable, as he has tolerated my procrastination on every project while motivating me to overcome every challenge. Additionally, Prof. Chen has provided me with

invaluable advice on my life, career, and future. I am truly grateful for his mentorship, which has significantly influenced my academic and professional growth.

I would like to thank Prof. Bud Bridges for introducing me to XAS with data collection and analysis and guiding me on in-situ experiments. Despite being in his 80s and a professor emeritus, he continues to actively engage in research even on a daily basis, which is both astonishing and inspiring to me. It is remarkable and unforgettable to witness his dedication as he took XAS shifts at the beamline 4-1 in SLAC for over 24 hours without sleep. Every time we discuss projects, I am motivated by his immense curiosity of science. I would also like to thank him for being my outside committee member for my qualification exam and several recommendation letters when applying fellowships and jobs.

I would like to express my gratitude to Prof. Yuan Ping, who opened the gate of DFT calculations for me. She taught me how to integrate theory with experiments and various methods of calculations on different materials, offering me multiple resources of supercomputers. Meanwhile, she served as my committee member for over four years and provided several recommendation letters for me.

I want to thank my committee professor, Prof. Scott Oliver, for his great support throughout my grad school, including the second-year seminar, qualifying exam, and annual year reviews. Also, my committee professor, Prof. Xiao Wang, for generously offering his time as my dissertation reading committee member.

I would like to thank Dr. Peter Weiss and Dr. Randa Roland for instructing me as teaching assistants for general chemistry classes. Thank you, Prof. Ilan Benjamin,

Prof. Jin Z. Zhang, and Prof. Yat Li, for teaching graduate-level courses. I also thank Ms. Karen Meece, Ms. Katie Cramton, and Ms. Alissa Nolan for their great work as graduate coordinators in the chemistry department.

I would like to thank our lab members, students, and visiting scholars for their help and support in my research and life throughout the years. Especially, I thank Dr. Yi Peng, who taught me synthesis, electrochemical experiments, data analysis, and guided me in the design of projects. He encouraged me to be patient and persistent in research and also taught me how to maintain a work-life balance. We were roommates for one year, and he cooked many great dishes and took us out of the lab for the Grand Circle Road Trip. I thank Dr. Bingzhang Lu for his help on several projects. We came up with the idea of magnetic induction heating and made many efforts to succeed in ultrafast synthesis. He taught me how to use Quantum Espresso for theoretical calculations. We had so much fun over two years, both inside and outside of the lab. I thank Dr. Forrest Nichols for his company over the years and for helping with TEM and BET experiments. We used to carpool together to LBL numerous times, took beamline shifts in SLAC, and had lunch together every day. Thank you, Dr. Gustavo Chata, for your company in the lab. Thank you, Gabby Lu, for your help in research and life. Thank you, Dr. Rene Mercado, for your XPS measurements and for teaching me some Spanish words. Thank you, Ms. Carolin Wahl, for your encouragement when I was in my first year of Ph.D. Moreover, thank you, Dr. John Diniz, Dr. Samantha Sweeney, Ms. Warisha Naseeb, for your help. I would also like to thank visiting scholars, Prof. Ting He, Prof. Yulin Zhang, and Prof. Hongbo Zhou, for their wonderful

collaboration on several projects. I would also like to thank some newer members of the Chen lab, including Mr. Bingzhe Yu, Mr. Dingjie Pan, Ms. Davida Dubois, Mr. John Tressel, Mr. Tianchen Cui, Mr. Colton Jones, and Mr. Xingjian Song, for their helpful discussion and company. Besides, I would like to thank my undergraduate students, Amrinder Bhuller, Gabriel Flannery, Natalie Martin, Marcus Hawley, and Isaiah Torres for being my mentees and working hard on several projects.

In addition, I would like to thank my friends from other labs. I thank Dr. Dun Lin for being my roommate and having fun with me for years. I thank Mr. Kejun Li for his great help in DFT calculations and his company. Thank you, Mr. Chunhao Guo, for your guidance in bouldering and outdoor activities. I also thank Mr. Jiahao Luo for road trips, food, and wine. Thank you, Dr. Junqing Xu, Dr. Tianyi Kou, Dr. Shanwen Wang, Dr. Mingpeng Chen, Dr. Bin Yao, Dr. Ke Xu. I thank many friends from Group C of the GPP program. I would like to thank my friends for life including Changhan Ge, Ziyi Xiao, Xiaowei Ge, Kexin Wang, and Xuhong Ling.

I would also like to thank Prof. Glenn Millhauser, Dr. Tufa Assafa, and Dr. Kevin Singewald for EPR measurements. Thank you, Mr. Jeremy Barnett, for XRD measurements. Thank you, Dr. Brian Dreyer, for ICP measurements. Thank you, Dr. Tom Yuzvinsky and Dr. Brandon Cheney, for SEM measurements.

I would also like to thank some collaborators outside UCSC. Especially, I want to thank Prof. Qingfeng Ge from Southern Illinois University for his help with DFT calculations on multiple projects. And his student, Dr. Zaheer Masood, did many computational works and was very patient with many urgent requests. Without them,

our paper could not be published in top journals. I would like to thank Prof. Peng Zhang and his student, Mr. David Morris, from Dalhousie University for XAS measurements. I would like to thank Prof. Jennifer Q. Lu and her student, Mr. Han-Lin Kuo, from UC Merced for providing TEM and EDS measurements. I would like to thank Dr. Virginia Altoe, Mr. Chengyu Song, Dr. Emory Chan, Dr. Paul Ashby from the Lawrence Berkeley National Laboratory for their help and supervision in using various equipment.

Last but not least, I would like to thank my parents and family who have always supported and encouraged me to pursue my dream. Also, I would express sincere gratitude to my wife Qianhui Shi for coming across 10201.11 kilometers to meet and marry me, for bringing endless happiness now and in the future.

♦ ♦ ♦

I acknowledge the following funding sources and awards for my research: UCSC dissertation year fellowship, Natural Science Foundation, Sigma Xi, the Joseph W. Richards Summer Fellowship from the Electrochemical Society, IPMI student award from the International Precious Metals Institute, Chinese Government Award for Outstanding Self-Financed Students Abroad, UCSC Lux supercomputer, Stampede2 supercomputer of TACC by XSEDE, Lawrence Berkeley National Lab, and SLAC National Accelerator Laboratory.

♦ ♦ ♦

The text of this dissertation includes reprints of the following previously published material:

- Yi Peng#, Qiming Liu#, Shaowei Chen, “Structural Engineering of Semiconductor Nanoparticles by Conjugated Interfacial Bonds”, The Chem. Rec., 2020, 20, 41.
- Qiming Liu, Qiaoxia Li, Shaowei Chen, “Metal-Nitrogen Coordination Moieties in Carbon for Effective Electrocatalytic Reduction of Oxygen”, Curr. Opin. Electrochem., 2020, 21, 46.
- Qiming Liu, Yi Peng, Qiaoxia Li, Ting He, David Morris, Forrest Nichols, Rene Mercado, Peng Zhang, Shaowei Chen, “Atomic Dispersion and Surface Enrichment of Palladium in Nitrogen-Doped Porous Carbon Cages Leads to High-Performance Electrocatalytic Reduction of Oxygen”, ACS Appl. Mater. Interfaces, 2020, 12, 17641.
- Yi Peng#, Qiming Liu#, Bingzhang Lu#, Ting He, Forrest Nichols, Xiao Hu, Tiffanie Huang, Grace Huang, Lizette Guzman, Yuan Ping, Shaowei Chen, “Organically Capped Iridium Nanoparticles as High-Performance Bifunctional Electrocatalysts for Full Water Splitting in Both Acidic and Alkaline Media: Impacts of Metal-Ligand Interfacial Interactions”, ACS Catal., 2021, 11, 1179.
- Qiming Liu, Hong Bo Zhou, Forrest Nichols, Han-Lin Kuo, Rene Mercado, Bingzhang Lu, Weiya Zhu, Yashu Liu, Jennifer Q. Lu, Frank Bridges, Shaowei Chen, “Oxygen reduction reaction catalyzed by carbon composites with ruthenium-doped iron oxide nanoparticles”, Mater. Adv., 2022, 3, 4556.
- Bingzhang Lu#, Qiming Liu#, Chunyang Wang, Zaheer Masood, David J. Morris, Forrest Nichols, Rene Mercado, Peng Zhang, Qingfeng Ge, Huolin L.

Xin and Shaowei Chen, “Ultrafast Preparation of Non-Equilibrium Fe-Ni Spinels by Magnetic Induction Heating for Unprecedented Oxygen Evolution Electrocatalysis”, Research, 2022, 2022, 9756983.

- Qiming Liu, Bingzhang Lu, Forrest Nichols, Jeffrey Ko, Rene Mercado, Frank Bridges, Shaowei Chen, “Rapid preparation of carbon-supported ruthenium nanoparticles by magnetic induction heating for efficient hydrogen evolution reaction in both acidic and alkaline media”, SusMat, 2022, 2, 335.
- Qiming Liu, Shaowei Chen, “Ultrafast synthesis of electrocatalysts”, Trends Chem., 2022, 4, 918-934.
- Qiming Liu,# Yi Peng,# Zaheer Masood,# Davida DuBois, John Tressel, Paul Ashby, Forrest Nichols, Rene Mercado, Han-Lin Kuo, Jennifer Q. Lu, Tufa Assafa, Dingjie Pan, Frank Bridges, Glenn Millhauser, Qingfeng Ge, Shaowei Chen, “Stable Cuprous Hydroxide Nanostructures by Organic Ligand Functionalization”, Adv. Mater. 2023, 35, 2208665.
- Qiming Liu, Samuel McNair, Forrest Nichols, Bingzhang Lu, Bingzhe Yu, Dingjie Pan, Jamie Ko, Amrinder Bhuller, Frank Bridges, Shaowei Chen, “Ultrafast synthesis of cobalt/carbon nanocomposites by magnetic induction heating for oxygen evolution reaction”, Adv. Sens. Energy Mater. 2023, 2, 100046.

The corresponding author, Professor Shaowei Chen, listed in the publications, directed, and supervised the research which forms the basis for the dissertation.

Chapter 1 Introduction

1.1 Energy Conversion Reactions in Sustainable Technologies

1.1.1 Oxygen reduction reaction

Proton exchange membrane fuel cells (PEMFC) and metal-air batteries represent two leading technologies for next-generation sustainable and clean energy conversion (Figure 1).[1-4] In these electrochemical systems, oxygen reduction reaction (ORR) at the cathode plays a critical role in determining the device performance, primarily because of the sluggish electron transfer kinetics and complex pathways of ORR. Platinum-based nanoparticles have been the catalysts of choice for ORR; yet the high cost and low natural abundance has severely hampered the wide-spread applications of the technologies.[1,3-5] Therefore, extensive research efforts have been devoted to the development of viable catalysts that are of low cost and high activity.

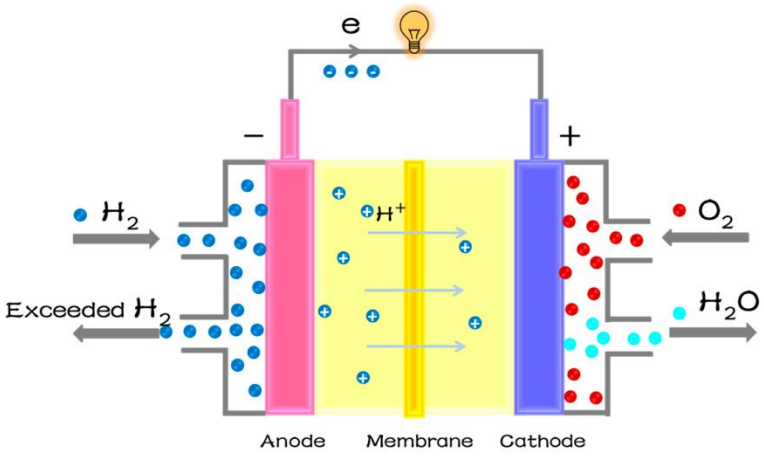

Figure 1. Schematic diagram of the proton exchange membrane fuel cells (PEMFC). Reprinted with permission from ref.[6] © 2020, Open access under the terms of the CC-BY license.

During ORR, the reduction of O_2 into H_2O may follow two mechanisms:

Associative mechanism:

$$* + O_2 + H^+ + e^- \rightarrow OOH* \quad (1)$$

$$OOH* + H^+ + e^- \rightarrow O* + H_2O \quad (2)$$

$$O* + H^+ + e^- \rightarrow OH* \quad (3)$$

$$OH* + H^+ + e^- \rightarrow H_2O + * \quad (4)$$

Dissociative mechanism:

$$O_2 + 2* \rightarrow 2\ O* \quad (5)$$

$$2O* + 2H^+ + 2e^- \rightarrow 2OH* \quad (6)$$

$$2OH* + 2H^+ + 2e^- \rightarrow 2\ H_2O + 2* \quad (7)$$

in which * denotes the active sites of catalysts on the anode, and O*, OH*, OOH* represents adsorbed intermediates. Meanwhile, it is found that the O binding energy (ΔE_O) on metals shows a volcano relationship to their activities (Figure 2). Amongst these, Pt is located on the top of the volcano with the most optimal binding energy for O. When metals possess a strong affinity for oxygen, their activity is restricted by the transfer of protons and electrons to O* or OH*. Conversely, when metals exhibit a weak affinity for oxygen, the activity is limited by the transfer of protons and electrons to O_2* (an associative mechanism) or the cleavage of the O-O bond in O_2 (a dissociative mechanism). It should be noted that the binding energies of the O species can be significantly affected by the electronic structure of the active sites on the catalysts. Therefore, the structural engineering on the catalysts may efficiently vary their binding energies to the O species during the reaction. For example, extensive research has shown that ΔE_O can be tuned by changing the atomic coordination environment of single atom catalysts, where their electron distribution would change across the Fermi

level, affecting the bonding between the d orbitals of metal center and the p orbitals of O species.

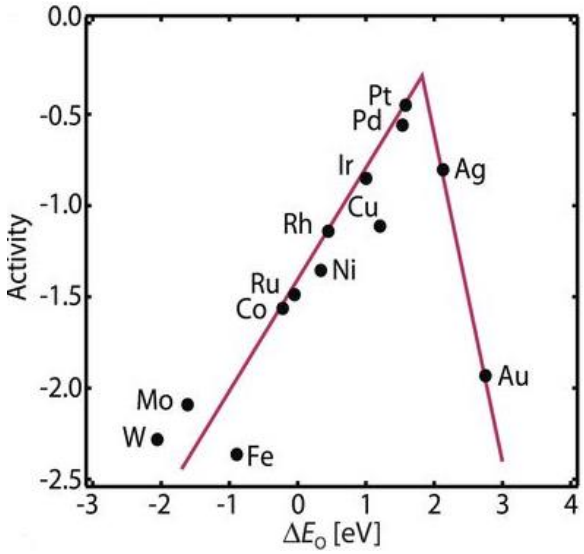

Figure 2. ORR volcano plot for metals. Reprinted with permission from ref.[7] © 2017, American Association for the Advancement of Science.

Besides the four-electron pathway of ORR for fuel cell application. The O_2 gas can be electrochemically reduced to H_2O_2 instead of H_2O, through a two-electron pathway. By varying the adsorption of OOH* species, the selectivity of ORR can be tuned between either the four-electron or two-electron pathways. The mechanism shows as follows:

$$OOH^* + (H^+ + e^-) \rightarrow O^* + H_2O \qquad (8)$$

$$OOH^* + (H^+ + e^-) \rightarrow H_2O_2 + * \qquad (9)$$

One can see from Figure 3, the key point of selectivity is the step after the adsorption of OOH* species. If the O-O bond of OOH* breaks, the reaction will take the four-electron pathway, instead of converting to H_2O_2. This suggests that all catalysts with strong binding energies of O are not suitable for the two-electron pathway, due to the favorable formation of O* by breaking OOH* (Figure 3).[8] This guidance is very useful

in designing ORR catalysts for different purposes. For example, one can see that Pt has the most suitable ΔE_O for four-electron ORR. But when alloyed with Hg into PtHg,[9] the alloy has an optimal ΔG_{OOH*}, weaker than the that of Pt alone, meaning the OOH* on the active sites (*) is less likely to break into O* and favorable for the two-electron ORR.

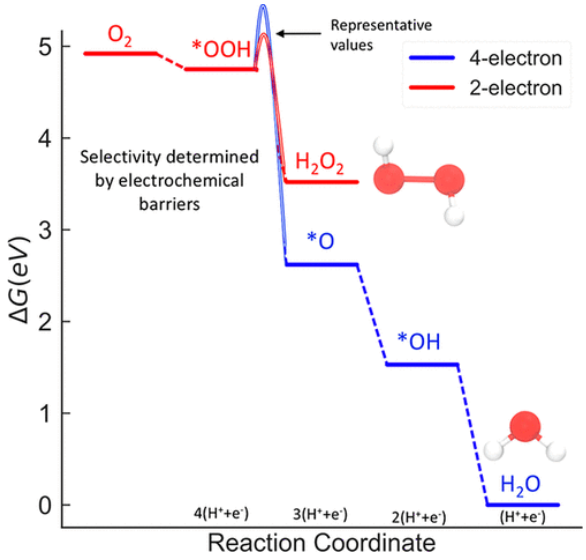

Figure 3. Free energy diagram for the four- and two-electron oxygen reduction in blue and red, respectively, on Au(111). Reprinted with permission from ref.[8] © 2018, American Chemical Society.

By utilizing this two-electron pathway of ORR, it is possible to electrochemically produce H_2O_2, through a PEM electrolyzer, but not using the traditional anthraquinone process, which leads to environmental issues because of its complicated synthesis steps and byproduct generation (Figure 4).[10,11]

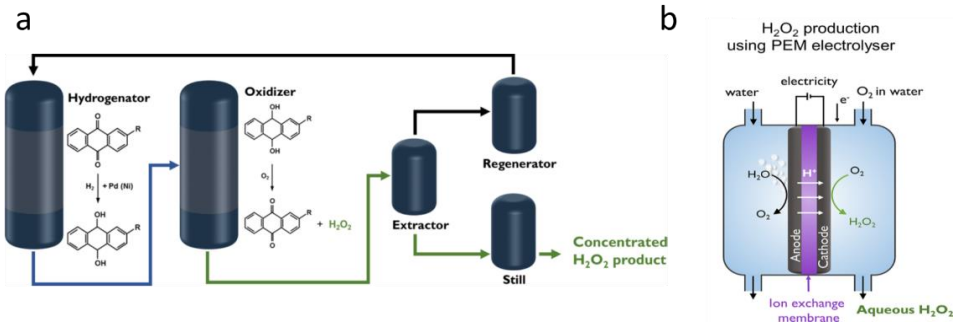

Figure 4. (a) Schematic of the anthraquinone process. (b) Electrolytic H_2O_2 production using a proton-exchange membrane (PEM) electrolyzer. Reprinted with permission from ref.[11] © 2018, American Chemical Society.

1.1.2 Hydrogen evolution reaction

Due to the growing demand for energy and the rapid depletion of traditional fossil fuels, hydrogen gas (H_2) is being recognized as a highly promising renewable energy resource. However, the current predominant method of H_2 production involves steam-methane reforming at high temperatures (700~1000 °C), which is both energy-intensive and costly. An alternative approach is electrochemical water splitting, also known as water electrolysis, which offers an effective solution. In this process, H_2 is generated in a water electrolyzer using electricity from sustainable sources such as wind, sunlight, and hydraulics. An electrolyzer consists of hydrogen evolution reaction (HER) on the cathode and oxygen evolution reaction (OER) on the anode (Figure 5). Ideally, the voltage of the electrolyzer is 1.23 V, which is much higher in practice due to the overpotentials generated on both electrodes.

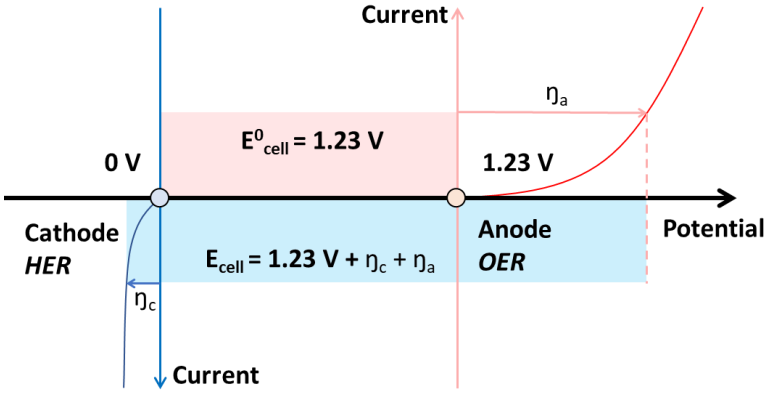

Figure 5. Schematic illustration of electrochemical water splitting.

For HER, as a two-electron transfer reaction, its mechanism is much simpler than these four-electron transfer reactions like ORR or OER (vide infra), which normally consists of equations as follows:

$$\text{Vomer step: } H^+ + e^- + * \rightarrow H^* \qquad (8)$$

$$\text{Heyrovsky step: } H^* + H^+ + e^{-+} \rightarrow H_2 + * \qquad (9)$$

$$\text{Tafel step: } 2H^* \rightarrow H_2 + 2^* \qquad (10)$$

in which * denotes the active sites of catalysts on the cathode, and H* means the H atom adsorbed on catalysts, as the only catalytic one intermediate in the reaction. The HER may occur through either the Volmer-Heyrovsky or the Volmer-Tafel mechanism (Figure 6).[12]

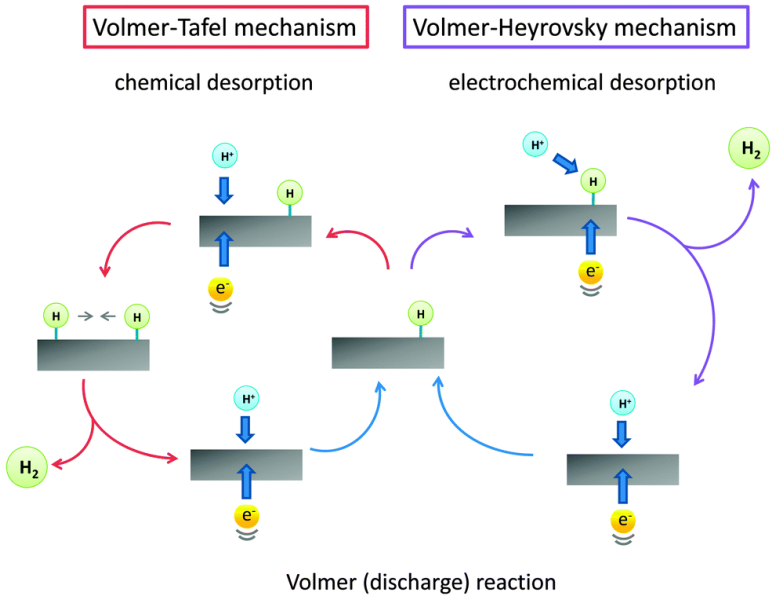

Figure 6. Mechanism of hydrogen evolution on the surface of an electrode in acidic solutions. Reprinted with permission from ref.[12] © 2014, Royal Society of Chemistry.

Therefore, H adsorption is very critical for the overall reaction, which cannot be too weak or too strong, affecting either the adsorption step or the desorption step. In theoretical calculation, the free energy of hydrogen adsorption ΔG_{H^*} has been used as a common descriptor, which has a volcano like relationship to the activity of metals as shown in Figure 7, so called HER volcano plot. One can find that a suitable catalyst for HER could provide active sites with an optimal $\Delta G_{H^*} \approx 0$ eV, where platinum and some noble metals appear on the summit of the volcano plot with best activity. Up to now, catalysts based on platinum nanoparticles have been favored for HER in the practical application, but their high cost and limited natural abundance have hindered their widespread application.[13,14] The development of cost-effective alternatives with high performance is of great importance from both a fundamental and technological standpoint.[15,16]

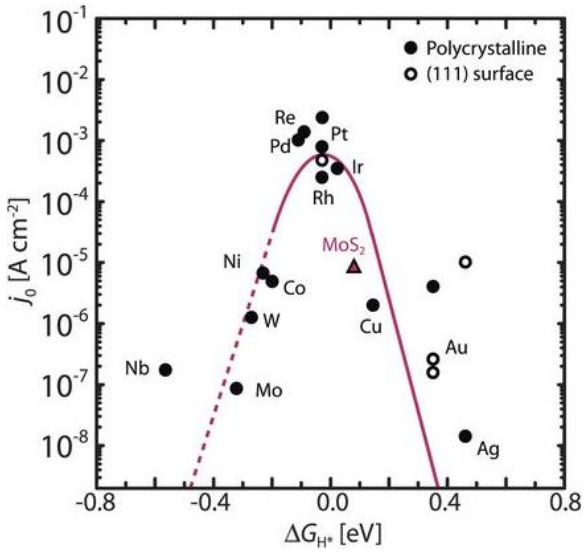

Figure 7. HER volcano plot for metals and MoS_2. Reprinted with permission from ref.[7] © 2017, American Association for the Advancement of Science.

It should also be noted that the HER discussed above is based on the acidic environment. In alkaline electrolyte (e.g., KOH), the H adsorption is not a direct reaction due to the lack of protons. Instead, H atoms are generated by the dissociation of H_2O molecules. Therefore, a good HER catalyst in acidic media does not guarantee its performance in alkaline condition. For instance, as shown in Figure 8, despite Pt has a perfect ΔG_{H^*}, the water dissociation barrier (ΔG_B) is much larger than Ru_{fcc}, resulting inferior HER activity in alkaline media, in comparison to that of Ru_{fcc}.[17] Also note that Ru_{hcp} possesses a big ΔG_B, making it difficult for HER in alkaline.

Therefore, structural engineering can be critical for HER in different pH conditions as the mechanism gets complicated, which is not solely dictated by the adsorption of H alone.

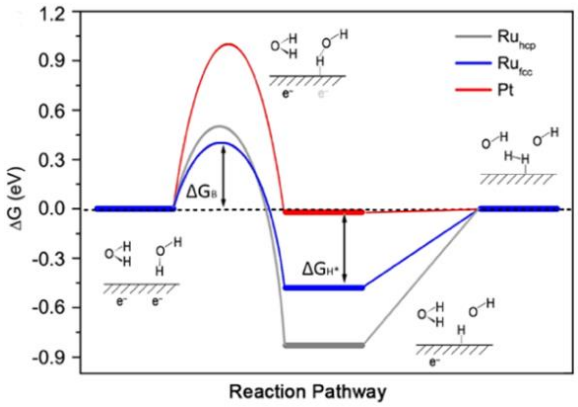

Figure 8. Gibbs free energy diagram of HER on different surfaces including reactant initial state, intermediate state, final state, and an additional transition state representing water dissociation. ΔG_{H^*} indicates hydrogen adsorption free energy, and ΔG_B indicates water dissociation free energy barrier. Reprinted with permission from ref.[17] © 2016, American Chemical Society

1.1.3 Oxygen evolution reaction

During OER, the generation of only one O_2 molecule involves charge transfer of $4e^-$ and several reaction steps of other intermediates. The mechanism and intermediates are much more complex than HER. Several reaction paths are shown in the following equations:

I. Oxide path:

$$H_2O + * \rightarrow OH^* + H^+ + e^- \quad (11)$$

$$2OH^* \rightarrow {}^*O + * + H_2O \quad (12)$$

$$2O^* \rightarrow 2* + O_2 \quad (13)$$

II. Electrochemical oxide path:

$$H_2O + * \rightarrow OH^* + H^+ + e^- \quad (14)$$

$$OH^* \rightarrow O^* + H^+ + e^- \quad (15)$$

$$2O^* \rightarrow 2^* + O_2 \quad (16)$$

III. Electrochemical metal peroxide path:

$$H_2O + * \rightarrow OH^* + H^+ + e^- \quad (17)$$

$$2OH^* \rightarrow O^* + * + H_2O \quad (18)$$

$$O^* + H_2O \rightarrow OOH^* + H^+ + e^- \quad (19)$$

$$2OOH^* \rightarrow O^* + H_2O + O_2 + * \quad (20)$$

IV. DFT-predicted peroxide path:

$$H_2O + * \rightarrow OH^* + H^+ + e^- \quad (21)$$

$$OH^* \rightarrow O^* + H^+ + e^- \quad (22)$$

$$O^* + H_2O \rightarrow OOH^* + H^+ + e^- \quad (23)$$

$$OOH^* \rightarrow O_2 + * + H^+ + e^- \quad (24)$$

Amongst mechanisms above, mechanism IV is the most prevalent mechanism for DFT studies, in which * denotes the active sites of catalysts on the anode, and O*, OH*, OOH* represents adsorbed intermediates, which will greatly influence the overpotential of OER. And in theory, as OOH* has a constant difference of energy level with OH*, ΔG_{O^*}-ΔG_{OH^*} has been the universal descriptor of OER to determine the activity of a catalyst in the Sabatier volcano plot as shown in Figure 9. Therefore, a highly active OER catalyst should have optimal adsorption of O* and OH*. One can see from Figure 9a, different metal oxides will have various ΔG_{O^*}-ΔG_{OH^*}, which alternate their overpotential for OER. However, one complicated factor for OER is that structural rearrangement will happen on these materials. Take NiO as one example, the intrinsic activity of NiO is located at the summit of the volcano plot amongst various

metal oxides in theory. However, the transformation of NiO into NiOOH will happen in alkaline media due to the high electrochemical potentials of OER, the adsorption energies of those intermediates will vary accordingly, leading to a larger overpotential gap as shown in Figure 2b. Therefore, to narrow the gap, two pathways can be adopted. On the one hand, by doping other metal atoms into NiOOH, the adsorption of intermediates on the Ni sites of NiMOOH may get improvement owing to the interaction between the metal and Ni (Figure 9b). On the other hand, those doped metal atoms can act as more optimal adsorption sites than Ni to enhance the OER activity (Figure 9c). A similar strategy can be adopted on the design of high-performance OER catalysts.

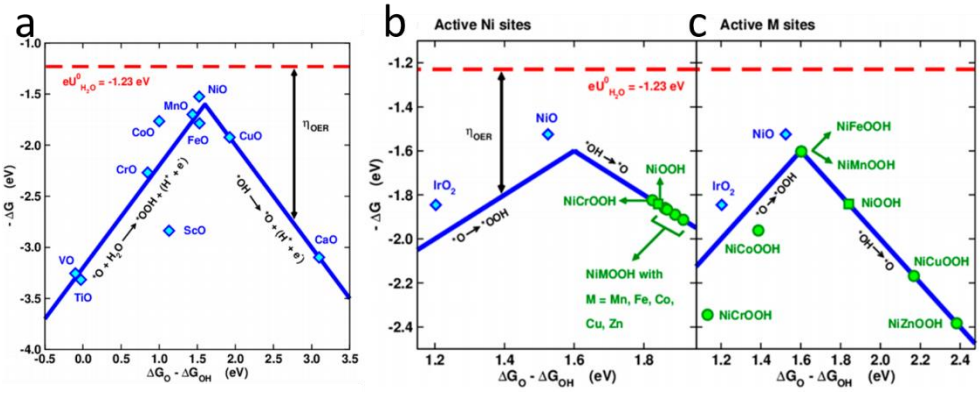

Figure 9. Theoretical Sabatier-type volcano plot for (a) the pristine (001) surfaces of the monoxides, (b) Ni sites of the pristine or metal-doped NiOOH, (c) metal sites of metal-doped NiOOH. Reprinted with permission from ref.[18] © 2015, American Chemical Society.

Overall, one can tell that OER is much more complicated than other electrochemical reactions due to various possible mechanisms (besides the equations above). For example, lattice oxygen evolution reaction may happen, that the lattice oxygen of the

catalyst can involve in the reaction coordinates, even affecting the stability of the catalyst.[19] In another example like Fe-doped NiOOH,[20] both Fe and Ni may contribute together for different O intermediates. Therefore, in recent years, operando/in-situ characterization techniques are developing to understand the structural change of the catalysts during the OER reaction, combining with traditional ex-situ characterizations and computational studies.[21] This is also critical for designing the OER catalyst, elucidating the real and effective structure for the reaction.

1.2 Metal-Nitrogen-Carbon for Electrocatalytic Reduction of Oxygen

Single (metal) atom catalysts (SACs) have been attracting special attention, where the high atom utilization and maximal interactions with the supporting substrate render it possible to fundamentally optimize the catalytic efficiency and concurrently minimize the cost of the catalysts [2,22]. Among the various transition metals, SACs of Fe, Co, and Cu have shown remarkable ORR activity [2,4,22], which are mostly embedded within carbon matrices by taking advantage of carbon's low cost, high electrical conductivity, and ready manipulation of the electronic structures by deliberate doping with select heteroatoms. For instance, nitrogen is a commonly used dopant and can serve as effective binding sites to immobilize metal atoms forming M-N bonds [23]. In general, ORR occurs via two possible pathways, the direct pathway whereby oxygen undergoes four-electron reduction to water, and the sequential pathway which involves the formation of hydrogen peroxide as an intermediate before the production of water [2,22]. Oxygen adsorption on SACs is in general argued to be the rate-determining step (RDS), where a moderate adsorption is preferred for high-efficiency ORR [2]. Herein, we

introduce recent progress of SACs involving Fe, Co, and Cu towards ORR, within the context of MN_x coordination configuration [24-27], nitrogen dopants [28-30], and carbon defects [31-35], and conclude with a perspective of the promises and challenges of SAC nanocomposites in ORR electrocatalysis.

1.2.1 Fe-N-C coordination moieties

Fe,N-codoped carbon SACs have been found to exhibit apparent activity toward ORR and can outperform state-of-art Pt/C in alkaline media [29,30,36-41]. This is mostly ascribed to the formation of FeN_x moiety, where the activity has been argued to be dependent on the x value. For example, in one recent study [24], Li et al. prepared three FeN_xC_{4-x} samples (x = 1, 3, 4) by pyrolysis of N-doped carbon with Fe salts at increasing temperature and observed that the ORR activity decreased in the order of FeN_4 > FeN_3C > FeN_1C_3 both in acid and alkaline electrolytes, in good agreement with results from DFT calculations where the order of ORR activity was found to be FeN_4 > FeN_3C > FeN_2C_2 > FeN_1C_3 > FeN_5. In fact, FeN_4 has been argued to be the ORR active sites in a large number of studies [28,29,42-44]. Yet in another study [25], Shen et al. argued that FeN_2C_2 was more beneficial for ORR than FeN_4 both experimentally and theoretically, where, due to the solvation effect, the DFT model of FeN_2C_2 was reconfigured with an additional dangling hydroxy ligand that was connected to the Fe center. Zhu et al. [26] also observed that FeN_2-type catalysts exhibited a competitive ORR performance with a half-wave potential ($E_{1/2}$) of +0.927 V vs. RHE in alkaline media, and the catalysts even resisted the poisoning of SCN^- due to the high affinity to O_2, in contrast to leading results in the literature. The fact that the ORR activity was accounted for by different

FeN_x coordination structures in these studies suggests that other structural factors have to be included in the mechanistic discussion.

Several important questions arise. Will the activity vary when the metal center is coordinated to pyrrolic N and pyridinic N? In addition to the metal center, are the adjacent C and N atomic sites also active in ORR electrocatalysis? In one earlier study [29], Lu et al. pyrolyzing tellurium nanowire@melamine formaldehyde polymer impregnated with Fe salts and observed that the obtained Fe-N-C materials exhibited an ORR activity comparable to that of Pt/C in 0.1 M KOH. DFT calculations of two types of FeN_4 (normal pyridine-type and Stone-Wales pyrrole-type FeN_4), showed that the Fe center of either FeN_4 was the predominant active site for ORR rather than the coordinated N atoms, and the C sites in the Stone-Wales FeN_4 could also contribute to the ORR activity, whereas in metal-free N-doped carbon the ORR activity was relatively low, due to weak binding of oxygen species to the N and C sites. Yang et al. [42] reached a similar conclusion that the ORR activity originated from the synergistic interactions between the carbon sites and Fe center of the pyrrole type Fe-N moieties. Taken together, these results suggest that in SACs, both the metal centers and adjacent N and C sites need to be considered in ORR electrocatalysis.

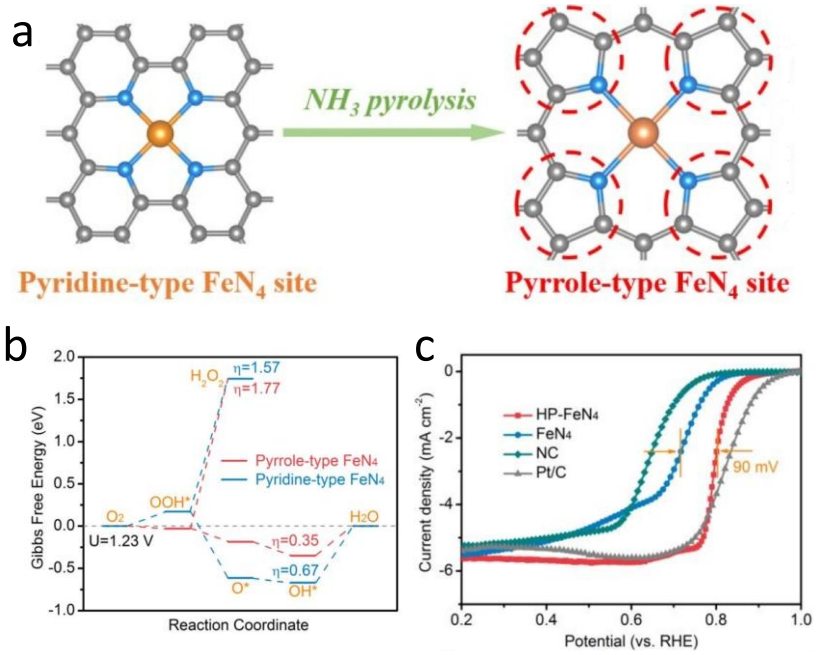

Figure 10. (a) Preparation process of high-purity pyrrole-type FeN_4 structure. The balls in grey, blue and orange represent C, N and Fe atoms, respectively. (b) Free energy diagram of the oxygen reduction reaction on pyrrole-type FeN_4 and pyridine-type FeN_4. (c) ORR polarization curves of HP-FeN_4, FeN_4 and NC catalysts in O_2-saturated 0.5 M H_2SO_4 and 20% Pt/C in 0.1 M $HClO_4$ at the rotating rate of 1600 rpm. Reprinted with permission from Ref.[28] © 2020, Royal Society of Chemistry.

In a more recent study [28], Zhang et al. used a polyaniline precursor to prepare pyridine-type FeN_4 which was then converted into pyrrole-type FeN_4 by a pyrolytic treatment with ammonia (Figure 10a), as manifested in soft X-ray absorption spectroscopy (XAS) measurements of the N K-edge and X-ray photoelectron spectroscopy (XPS) measurements of the N 1s electrons. Such a configurational transformation led to a significant enhancement of the ORR activity, with $E_{1/2}$ increased to +0.80 V from +0.71 V in 0.5 M H_2SO_4 (Figure 10c). Moreover, results from theoretical study (Figure 10b) showed that the pyrrole-type FeN_4 exhibited a lower overpotential (0.35 eV) from the

initial O_2 to H_2O than that of the pyridine-type FeN_4 (0.67 eV) and suppressed the two-electron pathway of H_2O_2. In fact, pyrrole-type FeN_4 exhibited preferred oxygen adsorption with a lower overpotential from O_2 to OOH^* than that for the pyridine-type. This argument was further supported in studies with covalent organic frameworks (COF) derived carbon that contained much better-defined coordination of FeN_4, in contrast to traditional pyrolysis that typically generates random configurations of FeN_x. For instance, without any pyrolysis treatment, Peng et al. [5,45] prepared a π-conjugated COF to in-situ capture Fe ions forming uniform pyrrole-type FeN_4, used these directly for ORR electrocatalysis, and observed a high $E_{1/2}$ of +0.910 V and enhanced performance as the cathode catalyst for a zinc-air battery, in comparison with commercial Pt/C.

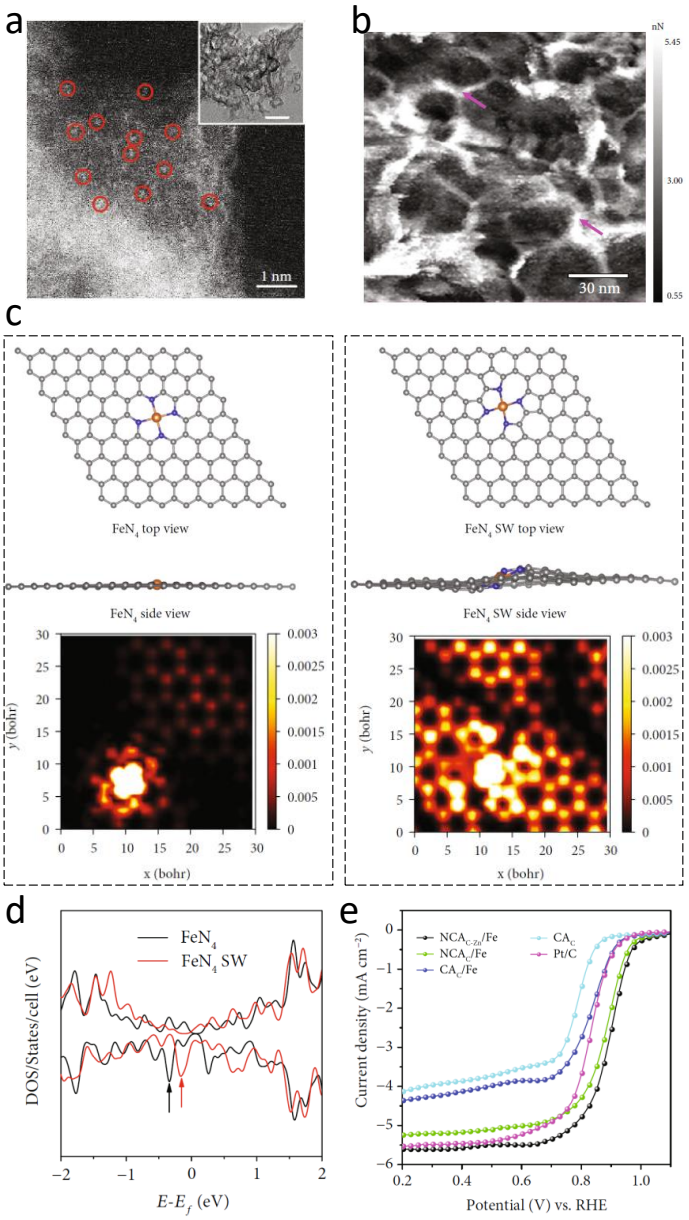

Figure 11. (a) Dark-field STEM image of the NCAC-Zn/Fe aerogel. Red circles indicate single Fe atoms. Inset is a TEM image of the NCAC-Zn/Fe aerogel, and the scale bar is 30 nm. (b) AFM images of NCAC-Zn/Fe aerogels: adhesion force image. (c) Side/top view and simulated STM image (at a bias of -1.0 V) of normal FeN_4 and FeN_4 SW-doped graphene sheets. (d) Density of state (DOS) of normal FeN_4 and FeN_4 SW-doped graphene sheets. (e) ORR polarization curves of CAC, CAC/Fe, NCAC/Fe,

and NCAC-Zn/Fe, as well as the Pt/C at 1600 rpm in 0.1M KOH at the potential sweep rate of 5mV s^{-1}. Reprinted with permission from Ref.[30] © 2019, Open access under the terms of the CC-BY license.

It should be noted that in recent earlier studies, a two-dimensional planar atomic model is generally assumed for FeN_x, although topological defects are common in pyrolytic carbon. In a latest study [30], He et al. prepared nanowrinkled carbon aerogels (NCA_{C-Zn}/Fe) embedded with abundant FeN_x moieties by controlled pyrolysis of biomass-derived hydrogels mixed with Fe and Zn compounds. From Figure 11a, the atomic scale wrinkled structures (Stone-Wales FeN_4) can be readily identified in the TEM images. Additionally, adhesion force measurements (Figure 11b) showed that the winkled structure exhibited a high adhesion force, corresponding to a hydrophilic domain. Fast force mapping measurements suggest that the FeN_4 wrinkled regions also displayed a high electrical conductance. From the simulated STM images (Figure 11c), one can see that the wrinkled Stone-Wales FeN_4 moiety indeed showed a distorted non-planar structure, in contrast to the normal counterpart. Meanwhile, Figure 11d displays the total density of state (DOS) of normal and Stone-Wales FeN_4, where the Fe centers can be found to dominate the contribution to the DOS near the Fermi level and the marked state of Stone-Wales FeN_4 can be seen to lie closer to the Fermi level than the normal pyridine-type FeN_4, suggesting faster electron-transfer of oxygen reduction. This is clearly manifested in electrochemical measurements (Figure 11e).

Results from these studies suggest that non-planar/distorted carbon skeletons may lead to additional, unique manipulation of the electronic structure and facilitate mass

transfer and accessibility of the ORR active sites. In other words, both the coordination chemistry and carbon topology are important factors in the rational design and engineering of ORR catalysts.

1.2.2 Co-N-C and Cu-N-C coordination moieties

Cobalt and nitrogen-codoped carbon nanocomposites have also been found to be highly active towards ORR [46-49]. For instance, Yin et al. [47] prepared carbon-supported Co single atom catalysts by controlled pyrolysis of zeolitic imidazolate frameworks (ZIFs) at different temperatures, and found that CoN_2 exhibited a better ORR activity ($E_{1/2}$ = +0.881 V) than CoN_4 ($E_{1/2}$ = +0.863 V). DFT calculations showed that CoN_2 was more favorable for the four-electron reduction pathway. However, similar to the iron and nitrogen-codoped carbon nanocomposites, in most studies CoN_4 is the leading coordination structure proposed to be the ORR active sites. For instance, Wan et al. [50] prepared a cobalt and nitrogen-codoped carbon nanocomposite by pyrolysis of a cobalt complex, and ascribed the high ORR activity ($E_{1/2}$ = +0.85 V) and anti-poisoning ability in alkaline but not in acidic media to the formation of CoN_4 configurations in the final product (CoNC). They argued that the pyridinic N sites neighboring the Co center served as the main active sites when SCN^- was bound to Co in alkaline media, but not in acid. Cheng et al. [49] also found that CoN_4 exhibited better resistance against SCN^- poisoning than FeN_4, consistent with results from DFT calculations that O_2 increased the stability of CoN_4 but not for FeN_4. It should be noted that whereas CoN_4 has been recognized as the ORR active moiety in most studies, further research is desired to

unravel the mechanistic correlation of the CoN_x atomic configuration with the ORR activity.

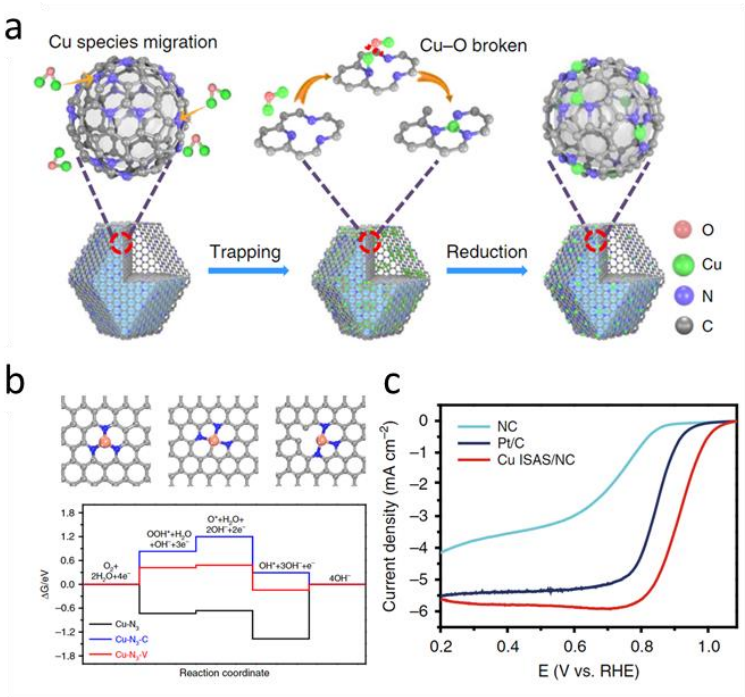

Figure 12. (a) Scheme of the formation of isolated copper sites (Cu ISAS/N-C) catalyst. (b) Free energy diagram for ORR process on these three models at the equilibrium potential (U = +0.40 V vs. NHE or U = +1.23 V vs RHE) at pH=14. (c) Linear sweep voltammetry (LSV) curves of NC, Cu ISAS/NC and Pt/C catalysts in 0.1 M KOH solution at the sweep rate of 10 mV s^{-1} and rotation rate of 1600 rpm. Reprinted with permission from Ref.[35] © 2019, Macmillan Publishers Limited.

Copper and nitrogen-codoped carbon nanocomposites have also emerged recently as promising ORR catalysts in alkaline media, with a performance comparable to that of state-of-the art FeN_x [27,35,51-53]. For instance, Li et al. [27] synthesized a CuN_x single atom catalyst via the pyrolysis and acid leaching method, which outperformed Pt/C in alkaline media towards ORR with an $E_{1/2}$ of +0.865 V. XAS fitting analysis showed a

mixed structure of CuN_4 and CuN_2 (without C coordination), and the latter exhibited a more favorable adsorption affinity to O_2 and OOH than the former. The conclusion is consistent with results from a former study by Wu et al. [51] that CuN_2 ($E_{1/2}$ = +0.80 V in alkaline media) was the apex amongst the series of CuN_x configurations. Another study by Yang et al. [35] suggested that defected structures like CuN_3-V (vacancy, without C coordination, Figure 12e) might account for the remarkable ORR activity as well. As shown in Figure 12d, when Cu(I)O was evaporated onto the defect-rich carbon skeleton derived pyrolytically from ZIF 8, the obtained CuN_x nanocomposites reached a record high $E_{1/2}$ of +0.92 V in alkaline media (Figure 12f). Theoretical calculations in Figure 12e showed that the formation of OOH^* was the RDS of the CuN_3-V and CuN_3-C structures and the removal of OH^* is the RDS of CuN_3. Moreover, the vacancy defect of CuN_3-V was argued to decrease the theoretical ORR overpotential (0.42 eV), much lower than that of CuN_3-C (0.83 eV) and CuN_3 (1.37 eV). With N-doped graphene or carbon nanotubes, neither of the Cu single atoms exhibited good ORR activity. This suggests that the introduction of structural defects (vacancies) into the CuN_x moiety may be a promising way to manipulate and enhance the ORR activity.

1.2.3 Other Metal-N-C coordination moieties

Besides Fe, Co, and Cu, other metal and nitrogen-codoped carbon nanocomposites have also been prepared and shown apparent ORR activity, such as Ni [54], Zn [55,56], and Cr [57]. For example, Li et al. [55] slowly annealed ZIF 8 powers (at the heating rate of 1°C min^{-1}) to produce carbon embedded with ZnN_4 which exhibited an ultrahigh loading of 9.33 wt% Zn and an $E_{1/2}$ of +0.873 V towards ORR in 0.1 M KOH. The performance

was slightly subpar as compared to the FeN_x counterparts prepared in the same fashion, and DFT calculations showed that ZnN_4 was more stable than FeN_4 and hence less active in binding oxygen intermediates. In another study [57], Luo et al. pyrolyzed Cr^{3+}-soaked ZIF 8 and successfully prepared CrN_4-doped carbon which exhibited an $E_{1/2}$ of +0.773 V in acid. In comparison with FeN_4, CrN_4 showed superb durability of ORR activity, showing only a 15 mV decrease of $E_{1/2}$ after 20,000 cyclic voltammetric cycles. It should be noted that most metal and nitrogen-codoped carbon hybrids demonstrate remarkable ORR activity in alkaline media, but the activity deteriorates markedly in acid. In a recent study [58], Dong et al. demonstrated that the assistance of a neighboring metal site led to a significant improvement of the ORR activity in acid. This suggests that structural engineering of dinuclear moieties ($M_1M_2N_x$) may be an effective strategy to extend the applications of carbon-based SACs to ORR in acid. For instance, Wang et al. [59] used a host-guest strategy (Figure 13a) to construct Fe-Co coupling sites in N-doped carbon, and the resulting dinuclear catalyst showed an $E_{1/2}$ of +0.863 V in 0.1 M $HClO_4$, a performance much better than those of FeN_x and CoN_x (Figure 4c). DFT calculations of the N_3-Fe-Co-N_3 model (Figure 13b) showed that the dissociation barrier of O_2, OOH on Fe-Co dual sites was much lower than those with FeN_x and CoN_x alone. In addition, the calculations showed that the bridge-like adsorption of O_2 molecules was facilitated on the Fe-Co dinuclear sites, which led to enhanced dissociation of the O atoms and the four-electron reduction pathway.

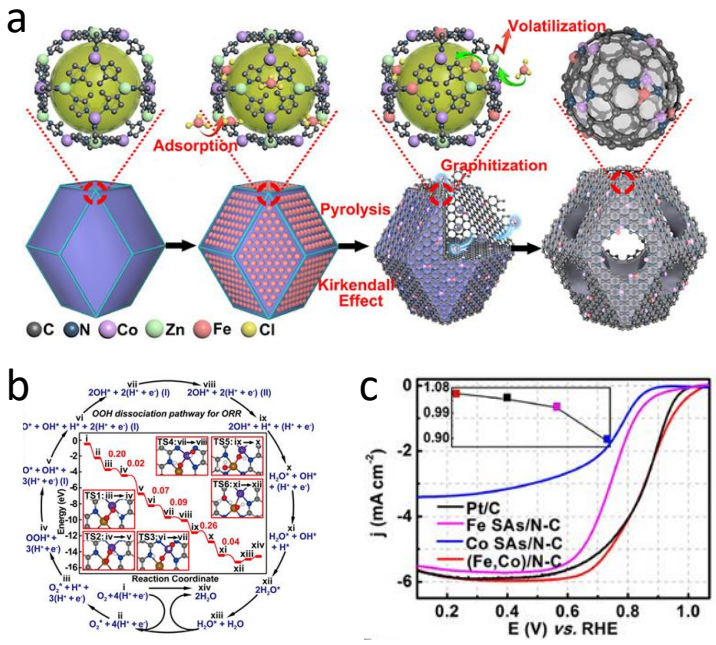

Figure 13. (a) Preparation of (Fe,Co)/N-C. (b) Energies of intermediates and transition states in mechanism of ORR at (Fe,Co)/N-C from DFT. (c) RDE polarization curves of Pt/C, Co SAs/N-C, Fe SAs/N-C, and (Fe,Co)/N-C in O2-saturated 0.1 M HClO4 with sweep rate 10mV s−1 and rotation rate 1600 rpm. Inset:Eonset of different catalysts. Reprinted with permission from Ref.[59] © 2017, American Chemical Society.

Alkaline ORR electrocatalysis can also be enhanced with a dinuclear configuration by taking advantage of the electronic coupling between the metal centers, analogous to that in alloy nanoparticles [36,39,60-63]. There are several critical challenges in these studies. The first is to develop effective synthetic protocols to prepare dinuclear atom catalysts. Second, it is critical to quantify the atomic configurations of the metal centers, in particular, the electronic interactions between the two metal sites. In addition to XAS, other techniques, such as sub-angstrom EELS mapping and in-situ Raman spectroscopy, are highly desired to resolve the fine structures of the dinuclear $M_1M_2N_xC_y$ moiety. In conjunction with DFT studies, the mechanistic insights can then be unraveled, an

important step towards rational design and engineering of ORR catalysts in both acidic and alkaline media.

In summary, recently there has been substantial progress in the design and engineering of metal-nitrogen coordination moieties in carbon for ORR electrocatalysis. Mechanistically, the incorporation of select metal centers within the carbon scaffolds in the form of M-N bonds leads to activation of multiple atomic sites in the proximity, which collectively contribute to the ORR activity. Thus, the exact atomic configuration is found to play a key role in determining the adsorption of critical reaction intermediates and the eventual catalytic performance. Furthermore, recent studies have shown that the carbon topological defects are another important variable that can be exploited for further enhancement of the electrocatalytic activity, in particular, to develop SACs that are selective for the four-electron oxygen reduction pathway.

It should be recognized that despite the progress, it remains challenging to unify the mechanistic accounts for the ORR activity. In fact, one can see that there exists an apparent discrepancy among leading studies in literature. This is primarily because most carbon SACs are prepared pyrolytically and exhibit structural complexity, and the nonuniformity within even the same batch of sample further compounds the issue, whereas in theoretical modeling, the structures are highly simplified and short-ranged. This inevitably creates a gap between the theoretical model and the actual structure, raising questions about the validity of the identification of the ORR active sites by a correlation between the experimental work and theoretical modeling and simulations. An immediate question arises. Is it possible to develop *de novo* bottom-up approaches

to the fabrication of carbon-based SACs? It will no doubt be a daunting undertaking. Yet the well-defined structures will allow for a reliable correlation between experiment and theory. Furthermore, extensive progress in organometallic chemistry can be exploited to extend the study to a wide range of coordination chemistry, within the context of metal centers, coordinating ligands, metal-ligand charge transfer, metal-metal chare transfer, etc. Furthermore, to aid in the unraveling of the fundamental mechanisms of catalytic reactions, development of effective tools for in-situ spectroscopic/microscopic measurements is equally important. Some of these are being pursued now.

1.3 Ultrafast Synthesis of Non-equilibrium and Meta-stable Nanomaterials

Design and engineering of low-cost, high-performance electrocatalysts represents a critical first step in the advancement of important electrochemical energy technologies, such as fuel cells, water electrolyzers, and metal-air batteries, thanks largely to the complex reaction pathways and sluggish electron-transfer kinetics of the cathode and anode reactions [64]. Whereas precious metal-based materials are the catalysts of choice for these reactions, carbon-based nanocomposites have recently emerged as viable alternatives with their reduced costs and competitive performances. These composites are generally prepared by thermal treatment of select precursors at elevated temperatures, such as controlled pyrolysis and hydro/solvothermal procedures, which are time- and energy-intensive [65]. Recently, effective techniques have been developed for the ultrafast synthesis (see Glossary) of such functional nanocomposites [66,67], based on carbothermal shock, flash Joule heating [68-70], microwave irradiation [71-73], laser

ablation [74], magnetic induction heating [75,76], flame synthesis [77-79], plasma sputtering [80,81], and electrosynthesis [82], among others. In these ultrafast procedures, the samples can be prepared within milliseconds (ms) to seconds, and the materials structures may exbibit a clear deviation from the thermodynamic equilibrium that is manifested in the traditional time-temperature-transformation (TTT) diagram, in sharp contrast to those derived from conventional synthesis [70,83]. In fact, immiscibility of metals can be overcome by allowing the formation of unprecedented alloys. Additionally, because of the short heating duration, mobility and aggregation of atomic species is significantly impeded [75,82], leading to the formation of rampant structural defects, such as stacking faults, twin boundaries, dislocations, Schottky defects, and Frenkel defects [84-88]. Such nonequilibrium features may play a critical role in dictating the interactions with key reaction intermediates and the eventual electrocatalytic activity. Herein, we introduce some representative ultrafast synthetic techniques.

1.3.1 Thermal shock

Carbothermal shock can be exploited to heat conductive samples up to thousands of kelvins at high direct currents (DC) within milliseconds (Joule's law), leading to a drastic transformation of the materials structures. For instance, microparticles of Al, Si, Sn, Au, and Pd supported on reduced graphene oxide (rGO) can be readily converted to nanoparticles of ca. 10 nm by applying a high DC for 2 ms (Figure 14a,b), due to thermal shock (ca. 1700 K) that melted the starting particles into smaller ones [89]. The procedure was also used to convert Ni microparticles on rGO into Ni nanoparticles of ca. 75 nm encapsulated by thin carbon layers [90], which exhibited a remarkable

electrocatalytic activity towards the electrooxidation of H_2O_2 (602 mA cm^{-2} at +0.2 V vs. Ag/AgCl), a performance 150 times higher than that of the original Ni microparticles. In a similar fashion, metal chalcogenide (e.g., FeS_2) nanoparticles were produced on rGO by thermal shock of micron-sized precursors at ca. 2470 K followed by quenching to room temperature within 12 ms (Figure 14c) [91]. The obtained FeS_2/rGO composites exhibited an excellent electrocatalytic activity towards the hydrogen evolution reaction (HER) in acidic media, with an overpotential ($\eta_{HER,10}$) of -139 mV to reach the current density of 10 mA cm^{-2}, much lower than that of the micro-sized ones (-260 mV), due to the manipulation of the chemical composition and structure of the nanoparticles and their interactions with the rGO substrate. When thermal shock was applied to carbon nanofibers (CNF) coated with $PdCl_2$ and $NiCl_2$ at 1550 K for 1 s, the salts were decomposed into PdNi nanoparticles with abundant twin boundaries and stacking faults [88]. Such unique structural features were difficult to produce in traditional synthetic methods, resulting in an excellent activity towards HER ($\eta_{HER,10}$ = -86.3 mV) and H_2O_2 electrooxidation. Excellent HER activities in alkaline media were also observed with thermal shock-derived IrNi nanoalloy and Pt nanoparticles (Figure 14d) [92,93].

Thermal shock even enables localized high-temperature (ca. 1400 K) synthesis under extreme conditions, such as in liquid nitrogen (ca. 77 K, Figure 14d), where the fast quenching facilitates the formation of strains within the nanoparticles. In fact, Pt nanoparticles synthesized in liquid nitrogen (Dr-Pt) possessed abundant dislocations (Figure 14e,f), and the strong strain effects (Figure 14g) impacted the adsorption of H*

species. In contrast, Pt particles synthesized in ambient Ar (Dp-Pt) did not exhibit many dislocations, and the HER activity was markedly lower (Figure 14h). The Dr-Pt nanoparticles also displayed excellent stability (Figure 14i). Similarly, thermal shock has been used to synthesize NiO with O vacancies [94] and Pd nanoparticles with twin boundaries [95] for the electrocatalytic oxidation of methanol, ethylene glycol, and ethanol.

Thermal shock can also be exploited to overcome the thermodynamic immiscibility between metal elements [70,96]. For instance, Cu is immiscible with most transition metals, and phase segregation typically occurs in bimetallic systems (Figure 14j). Yet, it has been demonstrated that thermal shock of a mixture of Cu-X salts (X = Ag, Ni, Sn, In, Pd) on CNF at 1300 °C for 0.2 s produced Cu-X nanoalloys (ca. 16 nm) with a homogenous phase (Figure 14k,l) [96]. For comparison, phase segregation was observed for particles prepared at 1000 °C with a conventional furnace, and the size was much larger at 100-500 nm. Monte Carlo simulations showed that the nonequilibrium bimetallic mixture was kinetically stable at room temperature. The obtained Cu-X nanoalloys could effectively catalyze the electroreduction of CO into multicarbon products (Figure 14m), and $Cu_{0.9}Ni_{0.1}$ showed the highest Faradic efficiency of ca. 76% at a current density of ca. 93 mA cm^{-2}, much higher than that of Cu alone. *In situ* attenuated total reflection surface-enhanced infrared absorption spectroscopy (ATR-SEIRAS) measurements showed that Ni alloying strengthened the adsorption of CO on the active sites.

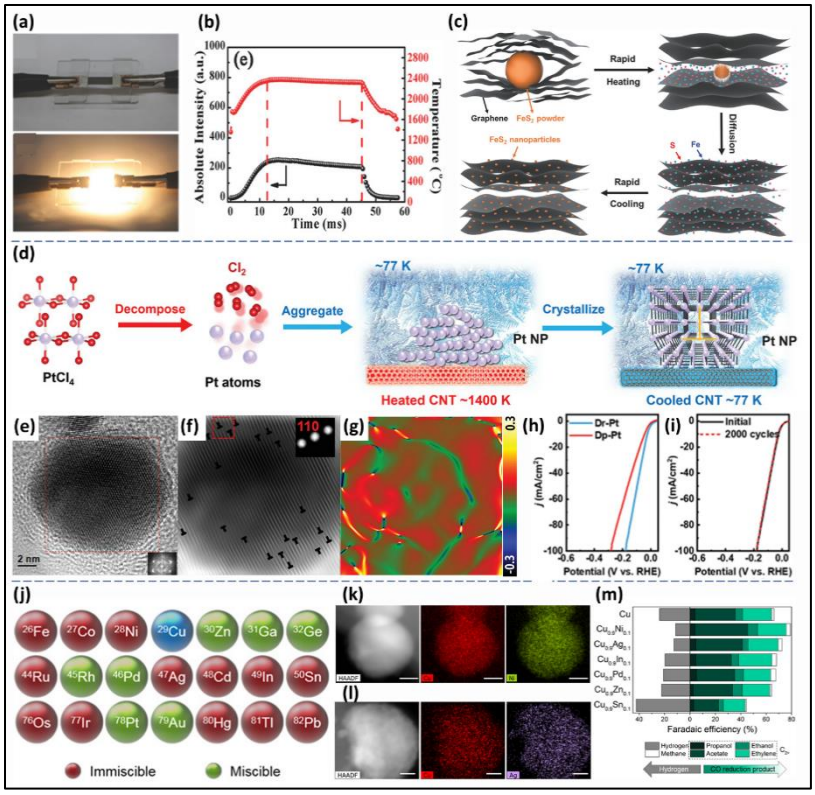

Figure 14. Ultrafast thermal shock. (a) Digital photographs of the Joule heating device before and during heat treatment. (b) Processed temperature values for the spectra along with the intensity on the 858 nm channel. Reproduced with permission from Ref.[90] © 2017, WILEY-VCH Verlag GmbH & Co. KGaA, Weinheim. (c) Schematic illustration of the ultrafast, in situ transformation of minerals to catalyst nanoparticles. Reproduced with permission from Ref.[91] © 2017, WILEY-VCH Verlag GmbH & Co. KGaA, Weinheim. (d) Schematic diagram of the preparation of dislocation-rich Pt nanoparticles by thermal shock. (e) HRTEM image of the Dr-Pt nanoparticle, (f) corresponding inverse fast Fourier transform (IFFT) of (110) plane, and (g) strain distribution related to (110) plane. (h) HER activity and (i) durability evaluation of Dr-Pt. Reproduced with permission from Ref.[92] © 2021, Wiley-VCH GmbH. (j) Miscibility of Cu with other metals. (k) Elemental mappings of $Cu_{0.9}Ni_{0.1}$ and (l) $Cu_{0.9}Ag_{0.1}$. (m) Faraday efficiency of pure Cu and different $Cu_{0.9}X_{0.1}$ bimetallic

catalysts at −0.70 ± 0.01 V vs. RHE towards COR. Reproduced with permission from Ref.[96] © 2020, Open access under the terms of the CC-BY-NC license.

High-entropy nanoalloys [97], oxides [98,99], sulfides [100], and phosphates [101] have also been readily prepared by thermal shock, exhibiting breaking of the linear scaling correlation between the electronic properties and electrocatalytic activities [83,102] that is key to the enhancement and optimization of the electrocatalytic performance, in sharp contrast to samples prepared by traditional methods.

Thermal shock is indeed a powerful tool in the high-throughput preparation and screening of electrocatalysts, which can be aided by data-driven calculations and machine learning. Further research is desired to explore the application of thermal shock in a controlled atmosphere (e.g., H_2 or CO_2) or in a liquid medium for more deliberate manipulation of the materials structures.

1.3.2 Flash Joule heating

Flash Joule heating (FJH) is another ultrafast heating technique based on high-voltage electric discharge that can be powered with a capacitor bank and generate a temperature over 3000 K under 100 ms (Joule's law), along with an ultrafast cooling rate up to 10^4 K s^{-1}. Such rapid heating and quenching is almost impossible to attain in conventional methods (Figure 15a,b) [69], and can be exploited for the efficient preparation of metastable materials. In one study [103], a simple FJH treatment at a current of 1350 A for hundreds of milliseconds in a mild vacuum transformed commercial bulk 2H-phase MoS_2 and WS_2 into the metallic 1T-phase (Figure 15c,d), which is metastable, thermally unfavorable and difficult to prepare directly by traditional methods [104,105].

This was ascribed to the formation of S vacancies that accumulated excessive negative charges and made the 1T phase kinetically preferred. The obtained 1T phase exhibited a much-enhanced HER activity ($\eta_{HER,10}$ = -221 mV), as compared to the pristine 2H MoS_2 (-491 mV) (Figure 15e).

Metal/covalent carbides have also been prepared by FJH [106]. For instance, phase-pure and defective MoC_{1-x} could be readily obtained at select voltages, such as hexagonal β-Mo_2C (30 V), metastable cubic α-MoC_{1-x} (60 V) and hexagonal η-MoC_{1-x} (120 V). The topotactic transition of β-Mo_2C to either α-MoC_{1-x} or η-MoC_{1-x} was mainly driven by the formation of abundant C vacancies. Electrochemically, β-Mo_2C exhibited a much-enhanced HER activity in 0.5 M H_2SO_4 ($\eta_{HER,10}$ = -220 mV), as compared to α-MoC_{1-x} (-310 mV) and η-MoC_{1-x} (-510 mV), along with excellent stability.

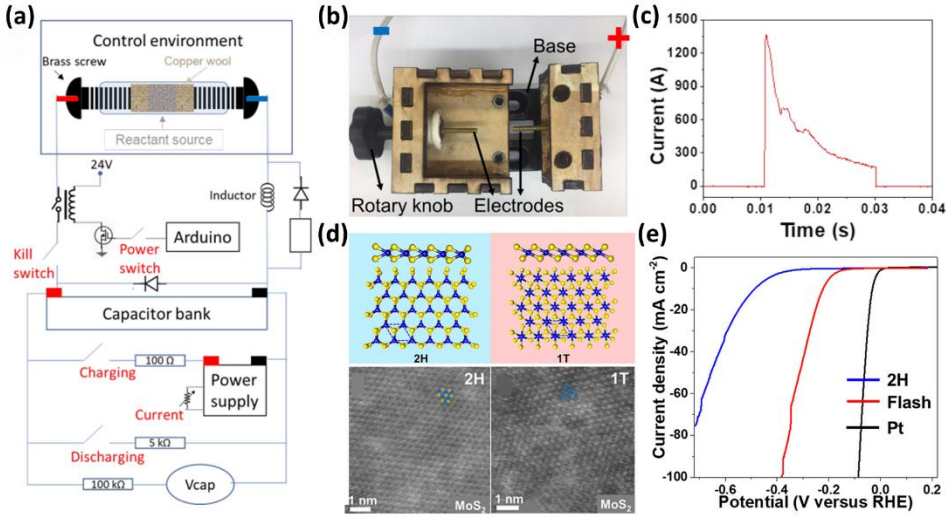

Figure 15. Catalysts prepared by Flash joule heating. (a) Circuit diagram of the FJH setup. (b) Photograph of the FJH reaction box. (c) Current vs time profile during the FJH process. (d) Atomic structure of the 2H and 1T phases and corresponding 2H MoS_2 precursors and FJH-prepared 1T MoS_2. (e) HER polarization curves of FJH-prepared

1T MoS_2. Reproduced with permission from Ref.[103] © 2021, American Chemical Society.

FJH is also a viable tool to synthesize carbon-based composites [107,108]. Recently, FJH was used as a solvent- and catalyst-free process to prepare heteroatom-doped (i.e., B, N, O, P, and S) flash graphene (FG) within 100-200 ms at ca. 3000 K [68]. Notably, the S-doped FG showed a high electrocatalytic activity towards ORR in the 4-e pathway in alkaline media, with a half-wave potential ($E_{1/2}$) of ca. +0.77 V vs reversible hydrogen electrode (RHE), whereas the 2-e pathway and hence H_2O_2 production was preferred with N-doped FG. Notably, the synthesis could be scaled up to one ton per day.

Overall, while still at an early stage for catalyst preparation, FJH is a low-cost and powerful method to produce novel electrocatalysts, even on a large scale. Nevertheless, the FJH operation is rather complex, which requires interdisciplinary knowledge of both electrical engineering and chemistry. Meanwhile, FJH requires the addition of conductive materials (e.g., graphene and metals) into the precursors, which may lead to the formation of byproducts and/or impurities.

1.3.3 Laser ablation

Laser ablation, based on a nanosecond/picosecond pulse laser, has been used to prepare a range of materials, with a heating/cooling rate up to 10^9 K s^{-1} [109], such as nanoalloys [86,87,110,111], metal oxides [112,113], hydroxides [85,114,115], carbides [116-118], nitrides [119], and chalcogenides [84,120]. In these studies, unique material structures can be produced. For instance, as shown in Figure 16a, dense stacking faults were observed with Ag

nanoparticles (L-Ag) prepared by laser ablation in liquid (LAL) by shining a pulsed Nd:YAG laser (pulse width 7 ns) on a bulk Ag target in deionized water, where quenching by the surrounding cool water facilitated the formation of abundant vacancies on Ag (111) facets and stacking faults (Figure 16b,c,d).[87] The obtained L-Ag nanoparticles displayed an $\eta_{HER,10}$ of only -32 mV in 0.5 M H_2SO_4 (Figure 16e), significantly lower than that for samples synthesized by conventional wet chemistry (-450 mV), and even slightly better than that of commercial Pt/C (-35 mV). This was because the stacking faults of L-Ag lowered the Ag coordination number from 12 to 8 and enhanced H adsorption. LAL was also performed on a bulk Ru target in a Au salt solution to produce Au single atom alloys of Ru, which exhibited an $\eta_{HER,10}$ of only -24 mV in alkaline media [111], due to fast-quenching by the solvent that helped freeze the mobile atoms and create a metasTable tructure. Note that Ru and Au are immiscible, and it is challenging to synthesize RuAu alloys in traditional methods [121]. Laser ablation of other targets, such as bulk MoS_2 [122] and $CoNi_2P$ [123], have also yielded high-performance electrocatalysts for water splitting.

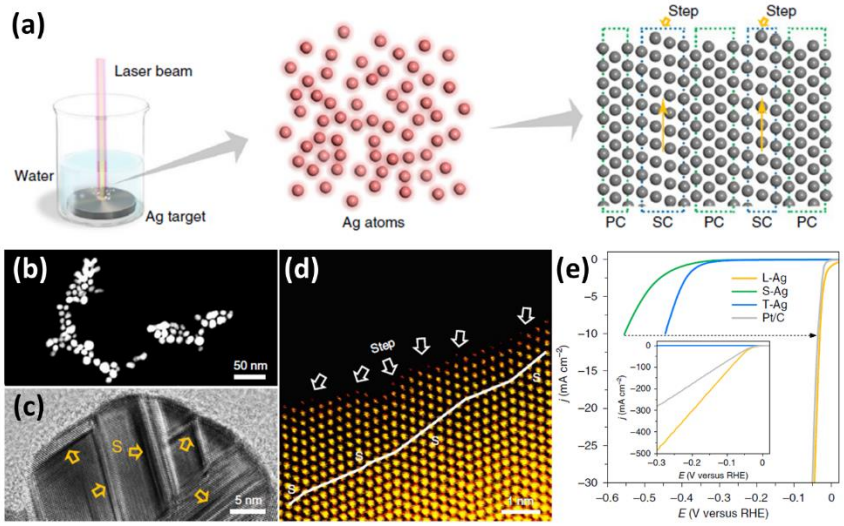

Figure 16. Laser ablation in liquid and pyrolysis. (a) A schematic illustration of the LAL synthesis and structure of L-Ag NPs. PC, perfect crystal; SC, stacking fault crystal. (b, c, d) representative TEM images of L-Ag NPs. The yellow arrows denote stacking faults. (e) HER polarization curves of L-Ag, S-Ag, T-Ag, and Pt/C in 0.5 M H_2SO_4 at a scan rate of 5 mV s^{-1}. Inset shows the corresponding polarization curves at higher current densities. Reproduced with permission from Ref.[87] © 2019, Springer Nature Limited.

Indeed, laser ablation has been used extensively to produce effective electrocatalysts. Because of the high energy and fast quenching rate, it provides a promising route to synthesize metastable electrocatalysts. Nevertheless, laser ablation requires rather expensive apparatus, and the sample productivity is relatively low.

1.3.4 Microwave irradiation

Microwave irradiation can generate an oscillating electric field, electrical dipole, and/or charge, and induce molecular frictions and collisions in target materials, where the kinetic energies can be converted into heat producing a temperature up to 1000 K [71,73]. The heating rate of microwave ranges from tens to even thousands of K s^{-1}, which

depends on several parameters, such as the microwave power and reaction pressure of the machine, as well as target materials morphology, size, loss factor, conductivity, and even structural defects [71,73,124,125]. Microwave-assisted synthesis was first reported in 1986 for organic synthesis [126], and has ever since been extended to the rapid synthesis of a range of materials, such as carbon derivatives [73,127-131], metal/alloy nanoparticles [124,125,132,133], high-entropy alloys/oxides [134,135], metal oxides/hydroxides/nitrides [135-138], metal chalcogenides [139-142], and even single atom catalysts (SACs) [72,143-145].

For example, graphene-supported SACs were successfully prepared by microwave irradiation of a mixture containing amine-modified graphene oxide (AGO), $CoCl_2$, and trace graphene (as a catalyst) at 1000 W for only 5 s [72]. Bright flashes were observed, signifying the production of a high (though unknown) temperature, which facilitated the reduction of AGO and N doping into the graphene nanosheets forming N-doped graphene (NG). Meanwhile, the diffusion of metal atoms was impeded by the structural defects and carbon vacancies generated during the heating, leading to immobilization of the metal species and formation of abundant Co single atoms on NG. The Co single atoms were found to possess a relatively low oxidation state and a distorted symmetry of D_{4h}, and surrounded by defective graphene, a clear deviation from the atomic configuration of perfect CoN_4C_4 or Co(II)Pc (cobalt(II) phthalocynine). The obtained Co-NG composites exhibited a relatively low $\eta_{HER,10}$ of -175 mV in 0.5 M H_2SO_4 and a high turnover frequency (TOF) of 0.385 s^{-1}, whereas Co SACs prepared by prolonged heating in a conventional furnace consisted of CoN_4 moieties and exhibited a much lower TOF of only 0.104 s^{-1} [146].

In summary, microwave irradiation can reduce the sample preparation time and yield unconventional structures. As microwave irradiation is readily accessible and low-cost, it may be integrated into other traditional methods, such as ball milling and hydrothermal treatment, as well as be combined with other ultrafast methods like laser or Joule heating, for further control of the materials structure and activity. Yet, control of heating temperature is challenging, and the heating rate is relatively low.

1.3.5 Other methods

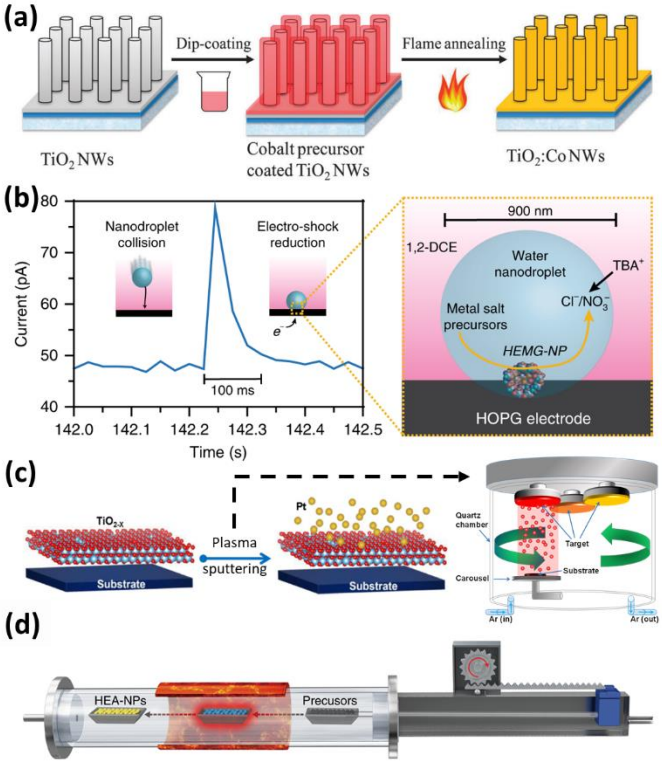

Figure 17. Schematics of various ultrafast synthetic methods. (a) Flame synthesis of Co-doped TiO_2. Reproduced with permission from Ref.[79] (b) Electrosynthesis of high entropy glass nanoparticles. Current transient corresponds to the collision of a single nanodroplet onto a carbon fiber UME, where nanodroplet contents are fully (>98%) reduced within 100 ms, facilitating disordered co-deposition of various metal

precursors. Reproduced with permission from Ref.[82] (c) Synthesis of Pt single atoms on TiO_{2-x} by rapid plasma sputtering. Reproduced with permission from Ref.[147] © 2021 Elsevier Ltd. (d) Setup of the fast-moving bed for the pyrolytic synthesis of HEA-NPs. Reproduced with permission from Ref.[148] © 2020, Open access under the terms of the CC-BY-NC license.

Ultrafast synthesis of electrocatalysts has also been explored by using other energy sources such as flame, electricity, and plasma. For instance, flame has been used to synthesize various OER and HER catalysts, such as Co-doped WS_2 [78], copper ferrite [77], and Co-doped TiO_2 [79] (Figure 17a). The synthesis typically took minutes and could generate unique features like core-shell structures, defects, and meta-1T phases that might be beneficial to electrocatalysis. Glasscott and colleagues [82] used an electro-shock method (Figure 17b) to synthesize high-entropy metallic glass nanoparticles (HEMG-NPs, from unary to even octonary) on the surface of carbon fiber ultramicroelectrodes directly for a duration of ca. 100 ms, where the stoichiometric ratios of CoFeLaNiPt HEMG-NPs could be precisely controlled, leading to tunable activity towards electrochemical water splitting. Plasma has also been used to assist rapid synthesis of electrocatalysts [80]. Select materials, such as metal nitrides and single atoms (Figure 17c) that are difficult to synthesize with traditional methods, can be feasibly produced by plasma synthesis within tens of seconds [81,147]. Furthermore, it is worth noting that traditional furnaces can be equipped with a moving bed/reciprocal device (Figure 17d), such that samples can be moved into and out of the high-temperature region at select time points for a precise control of heating and quenching

of the samples. This has indeed been demonstrated in the synthesis of high-entropy nanoalloys and SACs towards effective HER and CO_2 reduction [148,149].

Recently, we used Magnetic induction heating (MIH) to prepare high-performance OER and HER electrocatalysts for water splitting [75,76]. MIH, a traditional metallurgical tool, is a new addition to the ultrafast synthesis of functional materials. Upon the application of a magnetic field, an Eddy current can be generated onto the metal surface, thus almost instantly heating the surface to a very high temperature within seconds, due to the Joule heating[150]. MIH has been used for heat management in the thermal catalytic synthesis of graphene [151,152]. We will introduce more details of catalysts prepared MIH in Chapter 4-6.

1.4 Structural Engineering of Nanoparticles by Conjugated Interfacial Bonds

1.4.1 Metal Nanoparticles

A variety of organic derivatives with thiols (-SH), amines ($-NH_2$), carboxyl (-COOH), and phosphine/phosphonyl ($-PR_3$/$-PO(OR)_2$) are popular choices of anchoring ligands, which can form M-S, M-N, or M-O-C/P interfacial bonds.[153-155] However, one issue raised here is that all ligands listed above can only create nonconjugated bonds with the particle core, leading to inefficient interfacial charge transfer and blocking of active sites, which would be detrimental to their applications like photo/electro-catalysis.[156] In fact, extensive research has shown that d orbitals of metal can hybridize with π bonds of carbon, triggering strong intraparticle charge transfer. This has been evidenced on various noble metal nanoparticles such as Ru, Rh, Pd, Ag, Ir, Pt, and Au.[157-166] For instance, as shown in Figure 18, ruthenium nanoparticles could readily form Ru-

vinylidene (Ru=C=CH-R) interfaces with alkyne derivatives or form Ru=carbene π bonds with ferrocenyl moieties, which exhibited interesting electrochemical and optical properties.[160,167,168]

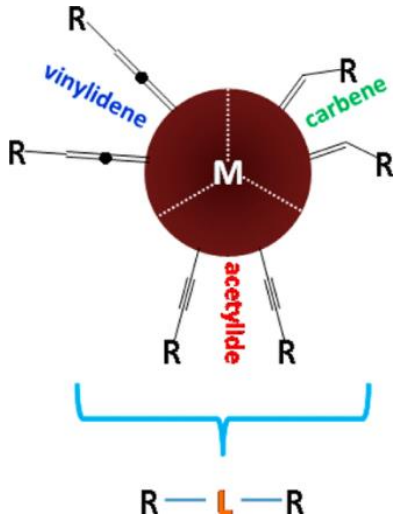

Figure 18. Metal nanoparticles are functionalized by conjugated ligands including vinylidene, carbene, or acetylide. Reprinted with permission from Ref.[169] © 2016, American Chemical Society.

In another study (Chapter 7), we demonstrated that acetylene derivatives could form iridium-alkyne (Ir-C≡C-) dπ bonds with iridium nanoparticles,[163] withdrawing electrons from the core, confirmed by both experimental and theoretical results. Such a unique anchoring point can significantly cause the redistribution of d electrons of the Ir atom, thereby enhancing its electrocatalytic activity. In contrast, a mercapto-capped (Ir-S-) interface revealed limited charge redistribution, serving only to block and reduce the number of active sites. Moreover, alkynyl-protection has been an effective strategy to synthesize atomically precise metal (Au, Ag, or AuAg alloy) nanoclusters for various

catalytic applications like semi-hydrogenation of alkynes, electrochemical CO_2 reduction, hydrogen evolution, and fuel oxidation.[170-174]

1.4.2 Semiconductor Nanoparticles

Silicon is a remarkable semiconductor and has been widely used in electronics, optics, and photovoltaics.[175-179] For nanosized silicon, it shows novel, tunable optical and electronic properties, where surface functionalization plays a critical role. Early studies[180,181] have shown that porous silicon can be readily functionalized with alkenes/alkynes through ethylaluminum dichloride ($EtAlCl_2$) mediated hydrosilylation. Similar surface chemistry has also been employed to stabilize and functionalize silicon nanoparticles by the formation of Si-C, Si-C=,[181-189] and Si-C≡[190] interfacial bonds, in addition to other covalent linkages, such as Si-O,[191] Si-N,[192,193] and Si-halide[194].

Experimentally, to covalently functionalize silicon (including Si nanoparticles, silicene quantum dots, etc), the silicon surface is in general activated by chemical etching to produce silicon-hydride moieties (Si-H). When the hydrogenated Si surface is exposed to olefin and acetylene derivatives, surface hydrosilylation occurs under relatively mild conditions, such as UV photoirradiation, heat, microwave or metallic/organometallic catalysts, leading to the formation of Si-CH_2-CH_2- or Si-CH=CH- interfacial linkages.[182,184,195,196] The former involves saturated interfacial bonds, whereas the latter exhibit conjugated characters.

Such surface modification is schematically depicted in Figure 19a. For instance, for alkenyl-capped silicon nanoparticles prepared with acetylene derivatives (e.g., 1-ethynyl-3-flurobenzene, 3-ethynylthiophene, phenylacetylene),[182] the conjugated

characteristics of the interfacial linkage is found to lead to diminishment and a slight red shift of the photoluminescence emission (Figure 19a), as compared to the alkyl-capped counterparts, due to enhanced interfacial conductivity and the formation of a deep trap in the nanoparticle.[184] These observations suggest a ready control of the nanoparticle electronic property (bandgap) simply by the disparity of surface functionalization.

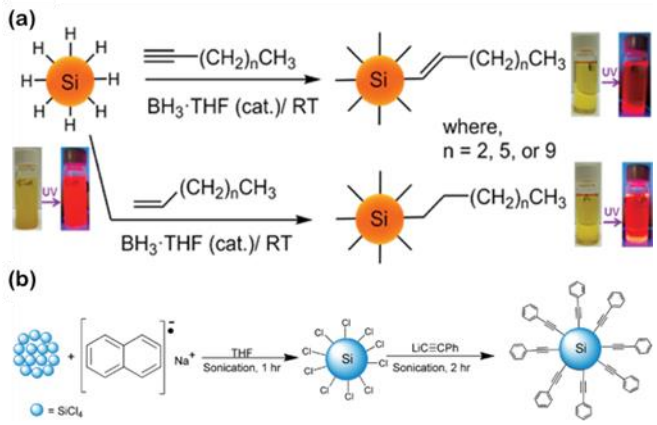

Figure 19. (a) Borane-catalyzed functionalization of hydride-terminated silicon nanoparticles with olefin and acetylene derivatives to yield an alkyl/alkenyl surface capping layer. Reprinted with permission from ref.[182] © 2014, American Chemical Society. (b) Synthesis of phenylacetylene-capped silicon nanoparticles. Reprinted with permission from ref.[190] © 2014, The Royal Society of Chemistry.

Notably, for alkyl-passivated Si nanoparticles, the core bandgap is also found to diminish, albeit slightly, as compared to that of the hydrogenated precursor. This has been demonstrated in *ab initio* calculations by Reboredo and Galli.[197] Interestingly, they observed an apparent shift of the relative energy (with respect to the vacuum) of the LUMO and the HOMO with the carbon chain length, which led to a decrease of the ionization potentials and electron affinities of the silicon cores, in comparison with the

hydride-terminated counterparts. In addition, calculations based on time-dependent density functional theory (TD-DFT)[198] also showed that in excitation spectral measurements within the energy window of zero to three times the bandgap, the absorption of silicon nanoparticles capped with methyl/hexyl groups could increase by up to 45%.

Modification of Si surfaces with acetylene derivatives can also be achieved by nucleophilic substitution of halide-terminated surfaces with organolithium reagents.[190] As shown in Figure 19b, Ashby et al.[190] prepared phenylacetylene-capped Si nanoparticles using lithium phenylacetylide. They found that the Si-C≡C- conjugated linkage further improved the conductivity of the Si nanoparticles and the thermoelectric activity, as compared to other silicon-based materials. This was accounted for by a higher Seebeck coefficient due to a higher concentration of charge carriers introduced by conjugated capping ligands. Nevertheless, studies have been scarce focusing on the charge transfer property of Si-C≡C- modified Si nanoparticles.

Metal oxides represent a large family of semiconductor materials, and carboxylic acids have been widely used as surface capping ligands for metal oxide nanoparticles,[199-214] where several structural models have been proposed to account for the interfacial bonding interactions between –COOH and metal oxide surface, such as monodentate ester, bidentate chelating, bidentate bridging, H-bonded, etc. Yet, the chemical nature of the interfacial linkage has remained under active debate.[153] Although electron transfer can occur across the carboxylic-oxide interface, the electronic coupling

between the nanoparticles and surface ligands remains relatively weak, limiting the efficiency of interfacial charge transfer.[199-201,207]

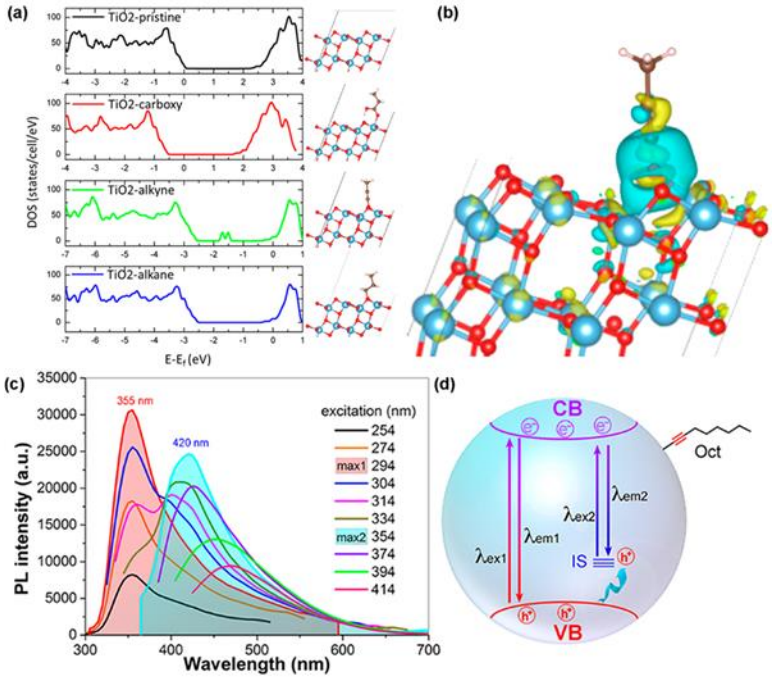

Figure 20. (a) Total density of states (TDOS) and interfacial configurations of a pristine TiO_2 slab (black curve) and slabs functionalized by carboxyl (-COOH, red curve), alkynyl (-C≡C-, green curve) and alkanyl (-CH_2-CH_2-, blue curve) ligands. (b) Bader charge transfer between alkynyl ligand and TiO_2 slab, where the cyan area indicates electron loss and yellow area indicates electron gain. The isosurface value is 0.003 e au^{-3}. (c) Photoluminescence spectra of TiO_2-HC8 at various excitation wavelengths. The shadowed ones represent maximal emissions at select excitation wavelengths. (d) Schematic illustration of the TiO_2-HC8 band structure based on the photoluminescence results. Reprinted with permission from ref.[215] © 2018, American Chemical Society.

It should be noted that in these earlier studies, the ligand-oxide interfacial bonds are mostly nonconjugated in nature. In another study,[215] our group demonstrated that metal oxide nanoparticle could also be functionalized with conjugated interfacial linkages by

using acetylene derivatives as the capping ligands. The resulting nanoparticles exhibited markedly different optical and electronic properties, as compared to those capped with conventional ligands like carboxylic acids. Experimentally, TiO_2 nanoparticles were used as the illustrating example, because of their applications in diverse areas. The nanoparticles were prepared and capped with acetylene by a two-phase synthetic approach.[215,216] Experimental studies, in conjunction with DFT calculations, were carried out to investigate the chemical and electronic structure of the interface. Firstly, DFT calculations suggested that energetically the most stable interfacial linkage was Ti-O-C≡C- which resulted in the shortening of the C-O bond and elongation of the C≡C bond, as compared to their pristine counterparts, due to partial charge transfer from the p-electrons in C≡C to TiO_2. Figure 20a depicts the density of state (DOS) plots of a TiO_2 slab with and without surface ligands. Clearly, the DOS profiles of TiO_2 slabs functionalized by acetate or ethyl ligands are similar to that of a pristine TiO_2 slab with a band gap of 2.2 eV. However, for the TiO_2 slab functionalized with acetylenyl ligands, a new state emerged between the valance band (VB) and conduction band (CB), which was denoted as the interfacial state (IS, about 0.5 eV higher than the VB). Further calculations of the Bader charge (Figure 20b) showed that about 1.2 electrons were transferred to the TiO_2 slab per ligand. Experimentally, the photoluminescence emission (Figure 20c) of octyne-capped TiO_2 (TiO_2-HC8) nanoparticles indeed suggested the formation of a new interfacial state, with two emission peaks observed at ca. 355 nm and 420 nm under the excitation of 294 nm and 354 nm, respectively. The first one contributed to band edge emission,

while the second one to CB-IS transition, consistent with results from DFT calculations. This is summarized in Figure 20d. That is, a new interfacial state is formed as the result of the interaction between the C≡CH anchor and TiO_2. This may be exploited for a deliberate manipulation of the nanoparticle optical and electronic properties and applications.

It should be noted that, in one recent study,[217] we present a simple and efficient wet-chemistry method for synthesizing stable CuOH nanostructures. The key approach involves the deliberate modification of the nanostructures with specific organic ligands, such as acetylene and mercapto derivatives. The resulting nanostructures display a nanoribbon shape, comprising of small nanocrystals embedded within a predominantly amorphous nanosheet-like framework. The acetylene derivatives interact with CuOH through Cu-C≡ linkages, while the mercapto ligands form Cu-S- interfacial bonds. Spectroscopic measurements and theoretical studies based on first principles calculations reveal that the acetylene derivatives establish effective electronic coupling at the ligand-core interface, whereas the interfacial bonds formed with the mercapto ligands are mostly non-conjugated. More details will be presented in Chapter 8.

In summary, breakthroughs from recent studies have shown that intraparticle charge transfer of semiconductor nanoparticles can be enhanced with conjugated core-ligand interfacial linkages, akin to the metal counterparts. This can be achieved by using olefin and acetylene derivatives as the capping ligands, where the reduced interfacial impedance facilitates electronic coupling between the organic ligands and nanoparticle cores. Such unique interfacial chemistry can be exploited as an effective addition to the

toolbox for nanoparticle surface functionalization and structural engineering, a critical step towards their diverse applications.

This raises an immediate, interesting question. Will the same chemistry be applicable to other semiconductor nanoparticles, such as metal chalcogenides, nitrides, and carbides? Note that these semiconductor nanoparticles have also found a wide range of applications, where a fundamental understanding of the mechanistic control of their optical and electronic properties plays an indispensable role.[218,219] Development of effective chemistries for the deliberate surface functionalization represents a key strategy. At the meantime, there are still several things need to be done. For instance, for metal nanoparticles researchers revealed that the density of organic ligands can affect the properties of the capped nanoparticles. While for the semiconducting nanoparticle, this hasn't been explored yet. Also, since the unique interfacial state is ascribed to charge transfer from organic ligands to nanoparticle cores, will the density of ligands affect the electronic structure and the density of the interfacial state of the final material? Answering these questions will give us more guidelines for the design of ligands for specific applications such as dye-sensitized solar cell, dye-sensitized photocatalyst, electrode material for water splitting, photovoltaic, light-emitting diode, etc. This will be the focus of future studies.

1.5 Reference

1. Z. W. Seh, J. Kibsgaard, C. F. Dickens, I. B. Chorkendorff, J. K. Norskov, T. F. Jaramillo. *Science* **2017**, *355*, eaad4998.

2. Y. Peng, B. Z. Lu, S. W. Chen. *Adv Mater* **2018**, *30*, 1801995.

3. Y. Xiong, Y. Yang, F. J. DiSalvo, H. D. Abruna. *J Am Chem Soc* **2019**, *141*, 10744-10750.

4. H. Ren, Y. Wang, Y. Yang, X. Tang, Y. Q. Peng, H. Q. Peng, L. Xiao, J. T. Lu, H. D. Abruna, L. Zhuang. *Acs Catal* **2017**, *7*, 6485-6492.

5. Y. Peng, B. Z. Lu, N. Wang, J. E. Lu, C. H. Li, Y. Ping, S. W. Chen. *Acs Appl Mater Inter* **2019**, *11*, 24707-24714.

6. M. X. Song, Y. H. Song, W. B. Sha, B. S. Xu, J. J. Guo, Y. C. Wu. *Catalysts* **2020**, *10*.

7. Z. W. Seh, J. Kibsgaard, C. F. Dickens, I. B. Chorkendorff, J. K. Norskov, T. F. Jaramillo. *Science* **2017**, *355*.

8. A. Kulkarni, S. Siahrostami, A. Patel, J. K. Norskov. *Chem Rev* **2018**, *118*, 2302-2312.

9. S. Siahrostami, A. Verdaguer-Casadevall, M. Karamad, D. Deiana, P. Malacrida, B. Wickman, M. Escudero-Escribano, E. A. Paoli, R. Frydendal, T. W. Hansen, I. Chorkendorff, I. E. L. Stephens, J. Rossmeisl. *Nat Mater* **2013**, *12*, 1137-1143.

10. J. M. Campos-Martin, G. Blanco-Brieva, J. L. G. Fierro. *Angew Chem Int Edit* **2006**, *45*, 6962-6984.

11. S. Yang, A. Verdaguer-Casadevall, L. Arnarson, L. Silvio, V. Colic, R. Frydendal, J. Rossmeisl, I. Chorkendorff, I. E. L. Stephens. *Acs Catal* **2018**, *8*, 4064-4081.

12. C. G. Morales-Guio, L. A. Stern, X. L. Hu. *Chem Soc Rev* **2014**, *43*, 6555-6569.

13. Y. X. Wang, H. Y. Su, Y. H. He, L. G. Li, S. Q. Zhu, H. Shen, P. F. Xie, X. B. Fu, G. Y. Zhou, C. Feng, D. K. Zhao, F. Xiao, X. J. Zhu, Y. C. Zeng, M. H. Shao, S. W. Chen, G. Wu, J. Zeng, C. Wang. *Chem Rev* **2020**, *120*, 12217-12314.

14. W. Song, M. Li, C. Wang, X. Lu. *Carbon Energy* **2021**, *3*, 101-128.

15. J. Wang, F. Xu, H. Y. Jin, Y. Q. Chen, Y. Wang. *Adv Mater* **2017**, *29*, 1605838.

16. X. X. Zou, Y. Zhang. *Chem Soc Rev* **2015**, *44*, 5148-5180.

17. Y. Zheng, Y. Jiao, Y. H. Zhu, L. H. Li, Y. Han, Y. Chen, M. Jaroniec, S. Z. Qiao. *J Am Chem Soc* **2016**, *138*, 16174-16181.

18. O. Diaz-Morales, I. Ledezma-Yanez, M. T. M. Koper, F. Calle-Vallejo. *Acs Catal* **2015**, *5*, 5380-5387.

19. X. H. Xie, L. Du, L. T. Yon, S. Y. Park, Y. Qiu, J. Sokolowski, W. Wang, Y. Y. Shao. *Adv Funct Mater* **2022**, *32*.

20. H. Shin, H. Xiao, W. A. Goddard. *J Am Chem Soc* **2018**, *140*, 6745-6748.

21. A. Lim, M. F. Tesch, I. Spanos. *Curr Opin Electroche* **2023**, *39*.

22. M. M. Liu, L. L. Wang, K. N. Zhao, S. S. Shi, Q. S. Shao, L. Zhang, X. L. Sun, Y. F. Zhao, J. J. Zhang. *Energ Environ Sci* **2019**, *12*, 2890-2923.

23. J. Deng, P. J. Ren, D. H. Deng, X. H. Bao. *Angew Chem Int Edit* **2015**, *54*, 2100-2104.

24. Y. Li, X. Liu, L. Zheng, J.-X. Shang, X. Wan, R. Hu, X. Guo, S. Hong, J. Shui. *Journal of Materials Chemistry A* **2019**, *7*, 26147-26153.

25. H. J. Shen, E. Gracia-Espino, J. Y. Ma, H. D. Tang, X. Mamat, T. Wagberg, G. Z. Hu, S. J. Guo. *Nano Energy* **2017**, *35*, 9-16.

26. C. Z. Zhu, Q. R. Shi, B. Z. Xu, S. F. Fu, G. Wan, C. Yang, S. Y. Yao, J. H. Song, H. Zhou, D. Du, S. P. Beckman, D. Su, Y. H. Lin. *Adv Energy Mater* **2018**, *8*, 1801956.

27. F. Li, G. F. Han, H. J. Noh, S. J. Kim, Y. L. Lu, H. Y. Jeong, Z. P. Fu, J. B. Baek. *Energ Environ Sci* **2018**, *11*, 2263-2269.

28. N. Zhang, T. Zhou, M. Chen, H. Feng, R. Yuan, W. Yan, Y.-C. Tian, X. Wu, W. Chu, C. Wu. *Energ Environ Sci* **2020**, https://doi.org/10.1039/C9EE03027A.

29. B. Z. Lu, T. J. Smart, D. D. Qin, J. E. Lu, N. Wang, L. M. Chen, Y. Peng, Y. Ping, S. W. Chen. *Chem Mater* **2017**, *29*, 5617-5628.

30. T. He, B. Lu, Y. Chen, Y. Wang, Y. Zhang, J. L. Davenport, A. P. Chen, C.-W. Pao, M. Liu, Z. Sun, A. Stram, A. Mordaunt, J. Velasco Jr., Y. Ping, Y. Zhang, S. Chen. *Research* **2019**, https://spj.sciencemag.org/research/aip/6813585/

31. X. G. Fu, N. Li, B. H. Ren, G. P. Jiang, Y. R. Liu, F. M. Hassan, D. Su, J. B. Zhu, L. Yang, Z. Y. Bai, Z. P. Cano, A. P. Yu, Z. W. Chen. *Adv Energy Mater* **2019**, *9*, 1803737.

32. R. Jiang, L. Li, T. Sheng, G. F. Hu, Y. G. Chen, L. Y. Wang. *J Am Chem Soc* **2018**, *140*, 11594-11598.

33. M. J. Workman, A. Serov, L. K. Tsui, P. Atanassov, K. Artyushkova. *Acs Energy Lett* **2017**, *2*, 1489-1493.

34. S. H. Lee, J. Kim, D. Y. Chung, J. M. Yoo, H. S. Lee, M. J. Kim, B. S. Mun, S. G. Kwon, Y. E. Sung, T. Hyeon. *J Am Chem Soc* **2019**, *141*, 2035-2045.

35. Z. K. Yang, B. X. Chen, W. X. Chen, Y. T. Qu, F. Y. Zhou, C. M. Zhao, Q. Xu, Q. H. Zhang, X. Z. Duan, Y. Wu. *Nat Commun* **2019**, *10*, 3734.

36. K. Jiang, S. Back, A. J. Akey, C. Xia, Y. F. Hu, W. T. Liang, D. Schaak, E. Stavitski, J. K. Norskov, S. Siahrostami, H. T. Wang. *Nat Commun* **2019**, *10*, 3997.

37. N. R. Sahraie, U. I. Kramm, J. Steinberg, Y. J. Zhang, A. Thomas, T. Reier, J. P. Paraknowitsch, P. Strasser. *Nat Commun* **2015**, *6*, 8618.

38. Y. Mun, S. Lee, K. Kim, S. Kim, S. Lee, J. W. Han, J. Lee. *J Am Chem Soc* **2019**, *141*, 6254-6262.

39. K. Qi, X. Q. Cui, L. Gu, S. S. Yu, X. F. Fan, M. C. Luo, S. Xu, N. B. Li, L. R. Zheng, Q. H. Zhang, J. Y. Ma, Y. Gong, F. Lv, K. Wang, H. H. Huang, W. Zhang, S. J. Guo, W. T. Zheng, P. Liu. *Nat Commun* **2019**, *10*, 5231.

40. Y. J. Sa, S. O. Park, G. Y. Jung, T. J. Shin, H. Y. Jeong, S. K. Kwak, S. H. Joo. *Acs Catal* **2019**, *9*, 83-97.

41. H. B. Zhang, L. Yu, T. Chen, W. Zhou, X. W. Lou. *Adv Funct Mater* **2018**, *28*, 1807086.

42. L. Yang, D. J. Cheng, X. F. Zeng, X. Wan, J. L. Shui, Z. H. Xiang, D. P. Cao. *P Natl Acad Sci USA* **2018**, *115*, 6626-6631.

43. Y. J. Chen, S. F. Ji, Y. G. Wang, J. C. Dong, W. X. Chen, Z. Li, R. A. Shen, L. R. Zheng, Z. B. Zhuang, D. S. Wang, Y. D. Li. *Angew Chem Int Edit* **2017**, *56*, 6937-6941.

44. T. He, Y. Q. Zhang, Y. Chen, Z. Z. Zhang, H. Y. Wang, Y. F. Hu, M. Liu, C. W. Pao, J. L. Chen, L. Y. Chang, Z. F. Sun, J. Xiang, Y. Zhang, S. W. Chen. *Journal of Materials Chemistry A* **2019**, *7*, 20840-20846.

45. P. Peng, L. Shi, F. Huo, C. X. Mi, X. H. Wu, S. J. Zhang, Z. H. Xiang. *Sci Adv* **2019**, *5*, eaaw2322.

46. Y. H. Han, Y. G. Wang, W. X. Chen, R. R. Xu, L. R. Zheng, J. Zhang, J. Luo, R. A. Shen, Y. Q. Zhu, W. C. Cheong, C. Chen, Q. Peng, D. S. Wang, Y. D. Li. *J Am Chem Soc* **2017**, *139*, 17269-17272.

47. P. Q. Yin, T. Yao, Y. Wu, L. R. Zheng, Y. Lin, W. Liu, H. X. Ju, J. F. Zhu, X. Hong, Z. X. Deng, G. Zhou, S. Q. Wei, Y. D. Li. *Angew Chem Int Edit* **2016**, *55*, 10800-10805.

48. T. T. Sun, S. Zhao, W. X. Chen, D. Zhai, J. C. Dong, Y. Wang, S. L. Zhang, A. J. Han, L. Gu, R. Yu, X. D. Wen, H. L. Ren, L. B. Xu, C. Chen, Q. Peng, D. S. Wang, Y. D. Li. *P Natl Acad Sci USA* **2018**, *115*, 12692-12697.

49. Q. Q. Cheng, L. J. Yang, L. L. Zou, Z. Q. Zou, C. Chen, Z. Hu, H. Yang. *Acs Catal* **2017**, *7*, 6864-6871.

50. G. Wan, P. F. Yu, H. R. Chen, J. G. Wen, C. J. Sun, H. Zhou, N. Zhang, Q. R. Li, W. P. Zhao, B. Xie, T. Li, J. L. Shi. *Small* **2018**, *14*, 1704319.

51. H. H. Wu, H. B. Li, X. F. Zhao, Q. F. Liu, J. Wang, J. P. Xiao, S. H. Xie, R. Si, F. Yang, S. Miao, X. G. Guo, G. X. Wang, X. H. Bao. *Energ Environ Sci* **2016**, *9*, 3736-3745.

52. D. H. Wang, C. C. Ao, X. K. Liu, S. Fang, Y. Lin, W. Liu, W. Zhang, X. S. Zheng, L. D. Zhang, T. Yao. *ACS Appl Energ Mater* **2019**, *2*, 6497-6504.

53. Y. T. Qu, Z. J. Li, W. X. Chen, Y. Lin, T. W. Yuan, Z. K. Yang, C. M. Zhao, J. Wang, C. Zhao, X. Wang, F. Y. Zhou, Z. B. Zhuang, Y. Wu, Y. D. Li. *Nat Catal* **2018**, *1*, 781-786.

54. H. L. Fei, J. C. Dong, Y. X. Feng, C. S. Allen, C. Z. Wan, B. Volosskiy, M. F. Li, Z. P. Zhao, Y. L. Wang, H. T. Sun, P. F. An, W. X. Chen, Z. Y. Guo, C. Lee, D. L. Chen, I. Shakir, M. J. Liu, T. D. Hu, Y. D. Li, A. I. Kirkland, X. F. Duan, Y. Huang. *Nat Catal* **2018**, *1*, 63-72.

55. J. Li, S. G. Chen, N. Yang, M. M. Deng, S. Ibraheem, J. H. Deng, J. Li, L. Li, Z. D. Wei. *Angew Chem Int Edit* **2019**, *58*, 7035-7039.

56. P. Song, M. Luo, X. Z. Liu, W. Xing, W. L. Xu, Z. Jiang, L. Gu. *Adv Funct Mater* **2017**, *27*, 1700802.

57. E. G. Luo, H. Zhang, X. Wang, L. Q. Gao, L. Y. Gong, T. Zhao, Z. Jin, J. J. Ge, Z. Jiang, C. P. Liu, W. Xing. *Angew Chem Int Edit* **2019**, *58*, 12469-12475.

58. J. C. Dong, X. G. Zhang, V. Briega-Martos, X. Jin, J. Yang, S. Chen, Z. L. Yang, D. Y. Wu, J. M. Feliu, C. T. Williams, Z. Q. Tian, J. F. Li. *Nat Energy* **2019**, *4*, 60-67.

59. J. Wang, Z. Q. Huang, W. Liu, C. R. Chang, H. L. Tang, Z. J. Li, W. X. Chen, C. J. Jia, T. Yao, S. Q. Wei, Y. Wu, Y. D. Lie. *J Am Chem Soc* **2017**, *139*, 17281-17284.

60. D. Y. Zhang, W. X. Chen, Z. Li, Y. J. Chen, L. R. Zheng, Y. Gong, Q. H. Li, R. A. Shen, Y. H. Han, W. C. Cheong, L. Gu, Y. D. Li. *Chem Commun* **2018**, *54*, 4882-4882.

61. S. P. Gong, C. L. Wang, P. Jiang, L. Hu, H. Lei, Q. W. Chen. *Journal of Materials Chemistry A* **2018**, *6*, 13254-13262.

62. L. Z. Zhang, J. M. T. A. Fischer, Y. Jia, X. C. Yan, W. Xu, X. Y. Wang, J. Chen, D. J. Yang, H. W. Liu, L. Z. Zhuang, M. Hanke, D. J. Searles, K. K. Huang, S. H. Feng, C. L. Brown, X. D. Yao. *J Am Chem Soc* **2018**, *140*, 10757-10763.

63. Z. Y. Lu, B. F. Wang, Y. F. Hu, W. Liu, Y. F. Zhao, R. O. Yang, Z. P. Li, J. Luo, B. Chi, Z. Jiang, M. S. Li, S. C. Mu, S. J. Liao, J. J. Zhang, X. L. Sun. *Angew Chem Int Edit* **2019**, *58*, 2622-2626.

64. K. I. Ozoemena, S. Chen, Nanomaterials for Fuel Cell Catalysis. In *Nanostructure Science and Technology*, 1st ed.; Springer International Publishing: Cham, 2016; pp 1 online resource (VIII, 583 pages 248 illustrations, 177 illustrations in color.

65. J. Greeley, T. F. Jaramillo, J. Bonde, I. B. Chorkendorff, J. K. Norskov. *Nat Mater* **2006**, *5*, 909-913.

66. R. Jiang, Y. M. Da, X. P. Han, Y. A. Chen, Y. D. Deng, W. B. Hu. *Cell Rep Phys Sci* **2021**, *2*, 100302.

67. K. M. Wyss, D. X. Luong, J. M. Tour. *Adv Mater* **2022**, *34*, 2106970.

68. W. Chen, C. Ge, J. T. Li, J. L. Beckham, Z. Yuan, K. M. Wyss, P. A. Advincula, L. Eddy, C. Kittrell, J. Chen, D. X. Luong, R. A. Carter, J. M. Tour. *ACS Nano* **2022**, *16*, 6646-6656.

69. D. X. Luong, K. V. Bets, W. A. Algozeeb, M. G. Stanford, C. Kittrell, W. Chen, R. V. Salvatierra, M. Q. Ren, E. A. McHugh, P. A. Advincula, Z. Wang, M. Bhatt, H. Guo, V. Mancevski, R. Shahsavari, B. I. Yakobson, J. M. Tour. *Nature* **2020**, *577*, 647-651.

70. Y. G. Yao, Z. N. Huang, P. F. Xie, S. D. Lacey, R. J. Jacob, H. Xie, F. J. Chen, A. M. Nie, T. C. Pu, M. Rehwoldt, D. W. Yu, M. R. Zachariah, C. Wang, R. Shahbazian-Yassar, J. Li, L. B. Hu. *Science* **2018**, *359*, 1489-1494.

71. M. B. Gawande, S. N. Shelke, R. Zboril, R. S. Varma. *Accounts Chem Res* **2014**, *47*, 1338-1348.

72. H. L. Fei, J. C. Dong, C. Z. Wan, Z. P. Zhao, X. Xu, Z. Y. Lin, Y. L. Wang, H. T. Liu, K. T. Zang, J. Luo, S. L. Zhao, W. Hu, W. S. Yan, I. Shakir, Y. Huang, X. F. Duan. *Adv Mater* **2018**, *30*, 1802146.

73. A. M. Schwenke, S. Hoeppener, U. S. Schubert. *Adv Mater* **2015**, *27*, 4113-4141.

74. D. S. Zhang, B. Goekce, S. Barcikowski. *Chem Rev* **2017**, *117*, 3990-4103.

75. B. Lu, Q. Liu, C. Wang, Z. Masood, D. Morris, F. Nichols, R. Mercado, P. Zhang, Q. Ge, H. Xin, S. Chen. *Research*, https://spj.sciencemag.org/journals/research/aip/9756983/.

76. Q. Liu, B. Lu, F. Nichols, J. Ko, R. Mercado, F. Bridges, S. Chen. *SusMat*, https://doi.org/10.1002/sus2.66.

77. S. Park, J. H. Baek, L. Zhang, J. M. Lee, K. H. Stone, I. S. Cho, J. H. Guo, H. S. Jung, X. L. Zheng. *Acs Sustain Chem Eng* **2019**, *7*, 5867-5874.

78. X. J. Shi, M. Fields, J. Park, J. M. McEnaney, H. P. Yan, Y. R. Zhang, C. Tsai, T. F. Jaramillo, R. Sinclair, J. K. Norskov, X. L. Zheng. *Energ Environ Sci* **2018**, *11*, 2270-2277.

79. L. L. Cai, I. S. Cho, M. Logar, A. Mehta, J. J. He, C. H. Lee, P. M. Rao, Y. Z. Feng, J. Wilcox, F. B. Prinz, X. L. Zheng. *Phys Chem Chem Phys* **2014**, *16*, 12299-12306.

80. S. Dou, L. Tao, R. L. Wang, S. El Hankari, R. Chen, S. Y. Wang. *Adv Mater* **2018**, *30*, 1705850.

81. Y. X. Tian, L. L. Yu, C. Q. Zhuang, G. Z. Zhang, S. R. Sun. *Mater Today Energy* **2021**, *22*, 100877.

82. M. W. Glasscott, A. D. Pendergast, S. Goines, A. R. Bishop, A. T. Hoang, C. Renault, J. E. Dick. *Nat Commun* **2019**, *10*, 2650.

83. Y. Yao, Q. Dong, A. Brozena, J. Luo, J. Miao, M. Chi, C. Wang, I. G. Kevrekidis, Z. J. Ren, J. Greeley, G. Wang, A. Anapolsky, L. Hu. *Science* **2022**, *376*, eabn3103.

84. C. Meng, M. C. Lin, X. W. Du, Y. Zhou. *Acs Sustain Chem Eng* **2019**, *7*, 6999-7003.

85. C. Meng, M. C. Lin, X. C. Sun, X. D. Chen, X. M. Chen, X. W. Du, Y. Zhou. *Chem Commun* **2019**, *55*, 2904-2907.

86. H. B. Wang, J. Q. Wang, N. Mintcheva, M. Wang, S. Li, J. Mao, H. Liu, C. K. Dong, S. A. Kulinich, X. W. Du. *Materials* **2019**, *12*, 3028.

87. Z. Li, J. Y. Fu, Y. Feng, C. K. Dong, H. Liu, X. W. Du. *Nat Catal* **2019**, *2*, 1107-1114.

88. F. J. Chen, Y. G. Yao, A. M. Nie, S. M. Xu, J. Q. Dai, E. Hitz, Y. J. Li, A. J. Lu, Z. N. Huang, T. Y. Li, R. Shahbazian-Yassar, L. B. Hu. *Adv Energy Mater* **2018**, *8*, 1800466.

89. Y. N. Chen, G. C. Egan, J. Y. Wan, S. Z. Zhu, R. J. Jacob, W. B. Zhou, J. Q. Dai, Y. B. Wang, V. A. Danner, Y. G. Yao, K. Fu, Y. B. Wang, W. Z. Bao, T. Li, M. R. Zachariah, L. B. Hu. *Nat Commun* **2016**, *7*, 12332.

90. Y. J. Li, Y. N. Chen, A. M. Nie, A. J. Lu, R. J. Jacob, T. T. Gao, J. W. Song, J. Q. Dai, J. Y. Wan, G. Pastel, M. R. Zachariah, R. S. Yassar, L. B. Hu. *Adv Energy Mater* **2017**, *7*, 1601783.

91. Y. N. Chen, S. M. Xu, Y. C. Li, R. J. Jacob, Y. D. Kuang, B. Y. Liu, Y. L. Wang, G. Pastel, L. G. Salamanca-Riba, M. R. Zachariah, L. B. Hu. *Adv Energy Mater* **2017**, *7*, 1700482.

92. S. L. Liu, Y. Shen, Y. Zhang, B. H. Cui, S. B. Xi, J. F. Zhang, L. Y. Xu, S. Z. Zhu, Y. A. Chen, Y. D. Deng, W. B. Hu. *Adv Mater* **2022**, *34*, 2106973.

93. S. L. Liu, Z. Hu, Y. Z. Wu, J. F. Zhang, Y. Zhang, B. H. Cui, C. Liu, S. Hu, N. Q. Zhao, X. P. Han, A. Y. Cao, Y. N. Chen, Y. D. Deng, W. B. Hu. *Adv Mater* **2020**, *32*, 2006034.

94. C. Liu, W. Zhou, J. F. Zhang, Z. L. Chen, S. L. Liu, Y. Zhang, J. X. Yang, L. Y. Xu, W. B. Hu, Y. N. Chen, Y. D. Deng. *Adv Energy Mater* **2020**, *10*, 2001397.

95. C. Liu, Y. Shen, J. F. Zhang, G. Li, X. R. Zheng, X. P. Han, L. Y. Xu, S. Z. Zhu, Y. A. Chen, Y. D. Deng, W. B. Hu. *Adv Energy Mater* **2022**, *12*, 2103505.

96. C. P. Yang, B. H. Ko, S. Hwang, Z. Y. Liu, Y. G. Yao, W. Luc, M. J. Cui, A. S. Malkani, T. Y. Li, X. Z. Wang, J. Q. Dai, B. J. Xu, G. F. Wang, D. Su, F. Jiao, L. B. Hu. *Sci Adv* **2020**, *6*, eaaz6844.

97. Y. G. Yao, Z. N. Huang, L. A. Hughes, J. L. Gao, T. Y. Li, D. Morris, S. E. Zeltmann, B. H. Savitzky, C. Ophus, Y. Z. Finfrock, Q. Dong, M. L. Jiao, Y. M. Mao, M. F. Chi, P. Zhang, J. Li, A. M. Minor, R. Shahbazian-Yassar, L. B. Hu. *Matter-Us* **2021**, *4*, 2340-2353.

98. T. Y. Li, Y. G. Yao, B. H. Ko, Z. N. Huang, Q. Dong, J. L. Gao, W. Chen, J. G. Li, S. K. Li, X. Z. Wang, R. Shahbazian-Yassar, F. Jiao, L. B. Hu. *Adv Funct Mater* **2021**, *31*, 2010561.

99. Q. Dong, M. Hong, J. L. Gao, T. Y. Li, M. J. Cui, S. K. Li, H. Y. Qiao, A. H. Brozena, Y. G. Yao, X. Z. Wang, G. Chen, J. Luo, L. B. Hu. *Small* **2022**, *18*, 2104761.

100. M. J. Cui, C. P. Yang, B. Y. Li, Q. Dong, M. L. Wu, S. Hwang, H. Xie, X. Z. Wang, G. F. Wang, L. B. Hu. *Adv Energy Mater* **2021**, *11*, 2002887.

101. H. Y. Qiao, X. Z. Wang, Q. Dong, H. K. Zheng, G. Chen, M. Hong, C. P. Yang, M. L. Wu, K. He, L. B. Hu. *Nano Energy* **2021**, *86*, 106029.

102. J. Perez-Ramirez, N. Lopez. *Nat Catal* **2019**, *2*, 971-976.

103. W. Y. Chen, Z. Wang, K. V. Bets, D. X. Luong, M. Q. Ren, M. G. Stanford, E. A. McHugh, W. A. Algozeeb, H. Guo, G. H. Gao, B. Deng, J. H. Chen, J. T. Li, W. T. Carsten, B. I. Yakobson, J. M. Tour. *ACS Nano* **2021**, *15*, 1282-1290.

104. G. Eda, T. Fujita, H. Yamaguchi, D. Voiry, M. W. Chen, M. Chhowalla. *ACS Nano* **2012**, *6*, 7311-7317.

105. Y. S. Guo, D. Z. Sun, B. Ouyang, A. Raja, J. Song, T. F. Heinz, L. E. Brus. *Nano Lett* **2015**, *15*, 5081-5088.

106. B. Deng, Z. Wang, W. Y. Chen, J. T. C. Li, D. X. Luong, R. A. Carter, G. H. Gao, B. I. Yakobson, Y. F. Zhao, J. M. Tour. *Nat Commun* **2022**, *13*, 262.

107. M. G. Stanford, K. V. Bets, D. X. Luong, P. A. Advincula, W. Y. Chen, J. T. Li, Z. Wang, E. A. McHugh, W. A. Algozeeb, B. I. Yakobson, J. M. Tour. *ACS Nano* **2020**, *14*, 13691-13699.

108. W. A. Algozeeb, P. E. Savas, D. X. Luong, W. Y. Chen, C. Kittrell, M. Bhat, R. Shahsavari, J. M. Tour. *ACS Nano* **2020**, *14*, 15595-15604.

109. K. Habiba, V. I. Makarov, B. R. Weiner, G. Morell, Fabrication of nanomaterials by pulsed laser synthesis. In *Manufacturing nanostructures*, A, W.; N, A., Eds. One central press (OCN): UK, 2014; pp 263-292.

110. J. Johny, Y. Li, M. Kamp, O. Prymak, S. X. Liang, T. Krekeler, M. Ritter, L. Kienle, C. Rehbock, S. Barcikowski, S. Reichenberger. *Nano Res* **2021**, https://doi.org/10.1007/s12274-021-3804-2.

111. C. H. Chen, D. Y. Wu, Z. Li, R. Zhang, C. G. Kuai, X. R. Zhao, C. K. Dong, S. Z. Qiao, H. Liu, X. W. Du. *Adv Energy Mater* **2019**, *9*, 1803913.

112. Y. Feng, Z. Li, C. Q. Cheng, W. J. Kang, J. Mao, G. R. Shen, J. Yang, C. K. Dong, H. Liu, X. W. Du. *Appl Catal B-Environ* **2021**, *299*, 120658.

113. F. F. Zhang, C. Q. Cheng, J. Q. Wang, L. Shang, Y. Feng, Y. Zhang, J. Mao, Q. J. Guo, Y. M. Xie, C. K. Dong, Y. H. Cheng, H. Liu, X. W. Du. *Acs Energy Lett* **2021**, *6*, 1588-1595.

114. K. Y. Niu, F. Lin, S. Jung, L. Fang, D. Nordlund, C. C. L. McCrory, T. C. Weng, P. Ercius, M. M. Doeff, H. M. Zheng. *Nano Lett* **2015**, *15*, 2498-2503.

115. G. Y. He, Y. T. Wang, X. M. Chen, Y. Zhou, C. Meng, F. T. Li. *Electrochim Acta* **2022**, *411*, 140074.

116. Y. S. Wu, Z. Huang, H. Q. Jiang, C. Wang, Y. Zhou, W. Shen, H. L. Xu, H. X. Deng. *Acs Appl Mater Inter* **2019**, *11*, 44573-44581.

117. X. N. Zang, C. Y. Jian, T. S. Zhu, Z. Fan, W. L. Wang, M. S. Wei, B. X. Li, M. F. Diaz, P. Ashby, Z. M. Lu, Y. Chu, Z. Z. Wang, X. R. Ding, Y. X. Xie, J. H. Chen, J. N. Hohman, M. Sanghadasa, J. C. Grossman, L. W. Lin. *Nat Commun* **2019**, *10*, 3112.

118. D. S. Zhang, C. Zhang, J. Liu, Q. Chen, X. G. Zhu, C. H. Liang. *Acs Appl Nano Mater* **2019**, *2*, 28-39.

119. I. V. Zelepukin, A. A. Popov, V. O. Shipunova, G. V. Tikhonowski, A. B. Mirkasymov, E. A. Popova-Kuznetsova, S. M. Klimentov, A. V. Kabashin, S. M. Deyev. *Mat Sci Eng C-Mater* **2021**, *120*, 111717.

120. M. Mahjouri-Samani, M. Tian, K. Wang, A. Boulesbaa, C. M. Rouleau, A. A. Puretzky, M. A. McGuire, B. R. Srijanto, K. Xiao, G. Eres, G. Duscher, D. B. Geohegan. *ACS Nano* **2014**, *8*, 11567-11575.

121. I. A. Pasti, E. Fako, A. S. Dobrota, N. Lopez, N. V. Skorodumova, S. V. Mentus. *Acs Catal* **2019**, *9*, 3467-3481.

122. G. Ou, P. X. Fan, X. X. Ke, Y. S. Xu, K. Huang, H. H. Wei, W. Yu, H. J. Zhang, M. L. Zhong, H. Wu, Y. D. Li. *Nano Res* **2018**, *11*, 751-761.

123. X. C. Sun, J. Q. Wang, Y. H. Yin, H. B. Wang, S. Li, H. Liu, J. Mao, X. W. Du. *Chem-Eur J* **2020**, *26*, 2793-2797.

124. S. M. Xu, G. Zhong, C. J. Chen, M. Zhou, D. J. Kline, R. J. Jacob, H. Xie, S. M. He, Z. N. Huang, J. Q. Dai, A. H. Brozena, R. Shahbazian-Yassar, M. R. Zachariah, S. M. Anlage, L. B. Hu. *Matter-Us* **2019**, *1*, 759-769.

125. G. Zhong, S. M. Xu, M. J. Cui, Q. Dong, X. Z. Wang, Q. Q. Xia, J. L. Gao, Y. Pei, Y. Qiao, G. Pastel, T. Sunaoshi, B. Yang, L. B. Hu. *Small* **2019**, *15*, 1904881.

126. R. Gedye, F. Smith, K. Westaway, H. Ali, L. Baldisera, L. Laberge, J. Rousell. *Tetrahedron Lett* **1986**, *27*, 279-282.

127. D. Voiry, J. Yang, J. Kupferberg, R. Fullon, C. Lee, H. Y. Jeong, H. S. Shin, M. Chhowalla. *Science* **2016**, *353*, 1413-1416.

128. W. F. Chen, L. F. Yan, P. R. Bangal. *Carbon* **2010**, *48*, 1146-1152.

129. H. W. Huang, S. Zhou, C. Yu, H. L. Huang, J. J. Zhao, L. M. Dai, J. S. Qiu. *Energ Environ Sci* **2020**, *13*, 545-553.

130. H. W. Huang, C. Yu, H. L. Huang, W. Guo, M. D. Zhang, X. T. Han, Q. B. Wei, S. Cui, X. Y. Tan, J. S. Qiu. *Small Methods* **2019**, *3*, 1900259.

131. B. K. Barman, K. K. Nanda. *Acs Sustain Chem Eng* **2018**, *6*, 4037-4045.

132. T. T. Gao, X. Q. Li, X. J. Chen, C. X. Zhou, Q. Yue, H. Y. Yuan, D. Xiao. *Chem Eng J* **2021**, *424*, 130416.

133. H. Zhao, Y. Y. Yuan, D. Zhang, Y. N. Qin, Y. Han, H. D. Li, Z. C. Wang, S. X. Li, J. P. Lai, L. Wang. *Acs Appl Nano Mater* **2021**, *4*, 11221-11230.

134. H. Y. Qiao, M. T. Saray, X. Z. Wang, S. M. Xu, G. Chen, Z. N. Huang, C. J. Chen, G. Zhong, Q. Dong, M. Hong, H. Xie, R. Shahbazian-Yassar, L. B. Hu. *ACS Nano* **2021**, *15*, 14928-14937.

135. M. Kheradmandfard, H. Minouei, N. Tsvetkov, A. K. Vayghan, S. F. Kashani-Bozorg, G. Kim, S. I. Hong, D. E. Kim. *Mater Chem Phys* **2021**, *262*, 124265.

136. Y. Choi, T. Chen, D. Kim, S. G. Ji, H. Hong, L. Lyu, M. Jang, Y. Piao. *Appl Mater Today* **2021**, *24*, 101093.

137. J. M. Barforoush, D. T. Jantz, T. E. Seuferling, K. R. Song, L. C. Cummings, K. C. Leonard. *Journal of Materials Chemistry A* **2017**, *5*, 11661-11670.

138. K. L. Yan, M. L. Sheng, X. D. Sun, C. Song, Z. Cao, Y. J. Sun. *ACS Appl Energ Mater* **2019**, *2*, 1961-1968.

139. S. Sarwar, A. Nautiyal, J. Cook, Y. F. Yuan, J. H. Li, S. Uprety, R. Shahbazian-Yassar, R. G. Wang, M. Park, M. J. Bozack, X. Y. Zhang. *Sci China Mater* **2020**, *63*, 62-74.

140. R. Souleymen, Z. T. Wang, C. Qiao, M. Naveed, C. B. Cao. *Journal of Materials Chemistry A* **2018**, *6*, 7592-7607.

141. D. H. Youn, C. Jo, J. Y. Kim, J. Lee, J. S. Lee. *J Power Sources* **2015**, *295*, 228-234.

142. A. Morozan, H. Johnson, C. Roiron, G. Genay, D. Aldakov, A. Ghedjatti, C. T. Nguyen, P. D. Tran, S. Kinge, V. Artero. *Acs Catal* **2020**, *10*, 14336-14348.

143. B. Wang, J. Tang, X. H. Zhang, M. Hong, H. K. Yang, X. Guo, S. Xue, C. C. Du, Z. X. Liu, J. H. Chen. *Chem Eng J* **2022**, *437*, 135295.

144. Y. Cheng, S. Y. Zhao, H. B. Li, S. He, J. P. Veder, B. Johannessen, J. P. Xiao, S. F. Lu, J. Pan, M. F. Chisholm, S. Z. Yang, C. Liu, J. G. Chen, S. P. Jiang. *Appl Catal B-Environ* **2019**, *243*, 294-303.

145. B. Z. Lu, Q. M. Liu, S. W. Chen. *Acs Catal* **2020**, *10*, 7584-7618.

146. H. L. Fei, J. C. Dong, M. J. Arellano-Jimenez, G. L. Ye, N. D. Kim, E. L. G. Samuel, Z. W. Peng, Z. Zhu, F. Qin, J. M. Bao, M. J. Yacaman, P. M. Ajayan, D. L. Chen, J. M. Tour. *Nat Commun* **2015**, *6*, 8668.

147. Y. Q. Zhang, B. Ouyang, J. Xu, G. C. Jia, S. Chen, R. S. Rawat, H. J. Fan. *Angew Chem Int Edit* **2016**, *55*, 8670-8674.

148. S. J. Gao, S. Y. Hao, Z. N. Huang, Y. F. Yuan, S. Han, L. C. Lei, X. W. Zhang, R. Shahbazian-Yassar, J. Lu. *Nat Commun* **2020**, *11*, 2016.

149. Y. B. Guo, S. Yao, Y. Y. Xue, X. Hu, H. J. Cui, Z. Zhou. *Appl Catal B-Environ* **2022**, *304*, 120997.

150. O. Lucia, P. Maussion, E. J. Dede, J. M. Burdio. *Ieee T Ind Electron* **2014**, *61*, 2509-2520.

151. W. Wang, G. Tuci, D. V. Cuong, Y. F. Liu, A. Rossin, L. Luconi, J. M. Nhut, N. D. Lam, P. H. Cuong, G. Giambastiani. *Acs Catal* **2019**, *9*, 7921-7935.

152. T. Zhao, C. Xu, W. Ma, Z. B. Liu, T. Y. Zhou, Z. Liu, S. Feng, M. J. Zhu, N. Kang, D. M. Sun, H. M. Cheng, W. C. Ren. *Nat Commun* **2019**, *10*, 4854.

153. E. Galoppini. *Coordin Chem Rev* **2004**, *248*, 1283-1297.

154. A. Heuer-Jungemann, N. Feliu, I. Bakaimi, M. Hamaly, A. Alkilany, I. Chakraborty, A. Masood, M. F. Casula, A. Kostopoulou, E. Oh, K. Susumu, M. H. Stewart, I. L. Medintz, E. Stratakis, W. J. Parak, A. G. Kanaras. *Chem Rev* **2019**, *119*, 4819-4880.

155. V. Jain, S. Roy, P. Roy, P. P. Pillai. *Chem Mater* **2022**, *34*, 7579-7597.

156. L. F. Lu, S. H. Zou, B. Z. Fang. *Acs Catal* **2021**, *11*, 6020-6058.

157. G. Li, R. C. Jin. *J Am Chem Soc* **2014**, *136*, 11347-11354.

158. F. Q. Zhang, J. J. Fang, L. Huang, W. M. Sun, Z. Lin, Z. Q. Shi, X. W. Kang, S. W. Chen. *Acs Catal* **2019**, *9*, 98-104.

159. W. Chen, N. B. Zuckerman, X. W. Kang, D. Ghosh, J. P. Konopelski, S. W. Chen. *J Phys Chem C* **2010**, *114*, 18146-18152.

160. X. W. Kang, N. B. Zuckerman, J. P. Konopelski, S. W. Chen. *Angew Chem Int Edit* **2010**, *49*, 9496-9499.

161. X. W. Kang, N. B. Zuckerman, J. P. Konopelski, S. W. Chen. *J Am Chem Soc* **2012**, *134*, 1412-1415.

162. G. Q. He, Y. Song, X. W. Kang, S. W. Chen. *Electrochim Acta* **2013**, *94*, 98-103.

163. Y. Peng, Q. M. Liu, B. Z. Lu, T. He, F. Nichols, X. Hu, T. Huang, G. Huang, L. Guzman, Y. Ping, S. W. Chen. *Acs Catal* **2021**, *11*, 1179-1188.

164. P. G. Hu, Y. Song, L. M. Chen, S. W. Chen. *Nanoscale* **2015**, *7*, 9627-9636.

165. D. C. Kennedy, C. S. Mckay, L. L. Tay, Y. Rouleau, J. P. Pezacki. *Chem Commun* **2011**, *47*, 3156-3158.

166. Y. Peng, E. Y. Hirata, W. Z. Pan, L. M. Chen, J. E. Lu, S. W. Chen. *Chinese J Chem Phys* **2018**, *31*, 433-438.

167. P. G. Hu, L. M. Chen, C. P. Deming, L. W. Bonny, H. W. Lee, S. W. Chen. *Chem Commun* **2016**, *52*, 11631-11633.

168. X. W. Kang, W. Chen, N. B. Zuckerman, J. P. Konopelski, S. W. Chen. *Langmuir* **2011**, *27*, 12636-12641.

169. P. G. Hu, L. M. Chen, X. W. Kang, S. W. Chen. *Accounts Chem Res* **2016**, *49*, 2251-2260.

170. X. K. Wan, Z. J. Guan, Q. M. Wang. *Angew Chem Int Edit* **2017**, *56*, 11494-11497.

171. Z. J. Guan, F. Hu, J. J. Li, Z. R. Wen, Y. M. Lin, Q. M. Wang. *J Am Chem Soc* **2020**, *142*, 2995-3001.

172. X. S. Ma, Y. Tang, G. Y. Ma, L. B. Qin, Z. H. Tang. *Nanoscale* **2021**, *13*, 602-614.

173. Y. Wang, X. K. Wan, L. T. Ren, H. F. Su, G. Li, S. Malola, S. C. Lin, Z. C. Tang, H. Hakkinen, B. K. Teo, Q. M. Wang, N. F. Zheng. *J Am Chem Soc* **2016**, *138*, 3278-3281.

174. L. B. Qin, F. Sun, X. S. Ma, G. Y. Ma, Y. Tang, L. K. Wang, Q. Tang, R. C. Jin, Z. H. Tang. *Angew Chem Int Edit* **2021**, *60*, 26136-26141.

175. E. C. Cho, S. Park, X. J. Hao, D. Y. Song, G. Conibeer, S. C. Park, M. A. Green. *Nanotechnology* **2008**, *19*, 245201.

176. N. M. Park, T. S. Kim, S. J. Park. *Appl Phys Lett* **2001**, *78*, 2575-2577.

177. R. Ban, F. F. Zheng, J. R. Zhang. *Anal Methods-Uk* **2015**, *7*, 1732-1737.

178. Z. H. Kang, C. H. A. Tsang, N. B. Wong, Z. D. Zhang, S. T. Lee. *J. Am. Chem. Soc.* **2007**, *129*, 12090-12091.

179. F. Priolo, T. Gregorkiewicz, M. Galli, T. F. Krauss. *Nat Nanotechnol* **2014**, *9*, 19-32.

180. J. M. Buriak, M. J. Allen. *J. Am. Chem. Soc.* **1998**, *120*, 1339-1340.

181. J. M. Buriak, M. P. Stewart, T. W. Geders, M. J. Allen, H. C. Choi, J. Smith, D. Raftery, L. T. Canham. *J. Am. Chem. Soc.* **1999**, *121*, 11491-11502.

182. T. K. Purkait, M. Iqbal, M. H. Wahl, K. Gottschling, C. M. Gonzalez, M. A. Islam, J. G. Veinot. *J. Am. Chem. Soc.* **2014**, *136*, 17914-7.

183. M. A. Islam, T. K. Purkait, M. H. Mobarok, I. M. D. Hoehlein, R. Sinelnikov, M. Iqbal, D. Azulay, I. Balberg, O. Millo, B. Rieger, J. G. C. Veinot. *Angew. Chem. Int. Ed.* **2016**, *55*, 7393-7397.

184. J. A. Kelly, J. G. C. Veinot. *ACS Nano* **2010**, *4*, 4645-4656.

185. M. Dasog, J. Kehrle, B. Rieger, J. G. C. Veinot. *Angew. Chem. Int. Ed.* **2016**, *55*, 2322-2339.

186. A. Gupta, M. T. Swihart, H. Wiggers. *Adv. Funct. Mater.* **2009**, *19*, 696-703.

187. C. S. Yang, R. A. Bley, S. M. Kauzlarich, H. W. H. Lee, G. R. Delgado. *J. Am. Chem. Soc.* **1999**, *121*, 5191-5195.

188. F. J. Hua, M. T. Swihart, E. Ruckenstein. *Langmuir* **2005**, *21*, 6054-6062.

189. M. Rosso-Vasic, E. Spruijt, B. van Lagen, L. De Cola, H. Zuilhof. *Small* **2008**, *4*, 1835-41.

190. S. P. Ashby, J. A. Thomas, J. Garcia-Canadas, G. Min, J. Corps, A. V. Powell, H. L. Xu, W. Shen, Y. M. Chao. *Faraday Discuss* **2014**, *176*, 349-361.

191. B. Sweryda-Krawiec, T. Cassagneau, J. H. Fendler. *J Phys Chem B* **1999**, *103*, 9524-9529.

192. Q. Li, T. Y. Luo, M. Zhou, H. Abroshan, J. C. Huang, H. J. Kim, N. L. Rosi, Z. Z. Shao, R. C. Jin. *ACS Nano* **2016**, *10*, 8385-8393.

193. E. Rogozhina, G. Belomoin, A. Smith, L. Abuhassan, N. Barry, O. Akcakir, P. V. Braun, M. H. Nayfeh. *Appl Phys Lett* **2001**, *78*, 3711-3713.

194. M. Dasog, K. Bader, J. G. C. Veinot. *Chem. Mater.* **2015**, *27*, 1153-1156.

195. R. K. Baldwin, K. A. Pettigrew, J. C. Garno, P. P. Power, G. Y. Liu, S. M. Kauzlarich. *J. Am. Chem. Soc.* **2002**, *124*, 1150-1151.

196. R. D. Tilley, J. H. Warner, K. Yamamoto, I. Matsui, H. Fujimori. *Chem. Commun.* **2005**, 1833-5.

197. F. A. Reboredo, G. Galli. *J Phys Chem B* **2005**, *109*, 1072-1078.

198. A. Gali, M. Voros, D. Rocca, G. T. Zimanyi, G. Galli. *Nano Lett* **2009**, *9*, 3780-3785.

199. M. I. Asghar, K. Miettunen, J. Halme, P. Vahermaa, M. Toivola, K. Aitola, P. Lund. *Energ Environ Sci* **2010**, *3*, 418-426.

200. A. Hagfeldt, G. Boschloo, L. C. Sun, L. Kloo, H. Pettersson. *Chem Rev* **2010**, *110*, 6595-6663.

201. P. T. Nguyen, A. R. Andersen, E. M. Skou, T. Lund. *Sol Energ Mat Sol C* **2010**, *94*, 1582-1590.

202. K. Sodeyama, M. Sumita, C. O'Rourke, U. Terranova, A. Islam, L. Han, D. R. Bowler, Y. Tateyama. *J Phys Chem Lett* **2012**, *3*, 472-7.

203. D. L. Ashford, W. Song, J. J. Concepcion, C. R. Glasson, M. K. Brennaman, M. R. Norris, Z. Fang, J. L. Templeton, T. J. Meyer. *J Am Chem Soc* **2012**, *134*, 19189-98.

204. K. Hu, K. C. D. Robson, P. G. Johansson, C. P. Berlinguette, G. J. Meyer. *J Am Chem Soc* **2012**, *134*, 8352-8355.

205. H. Y. Chen, S. Ardo. *Nat Chem* **2018**, *10*, 17-23.

206. S. Ye, A. Kathiravan, H. Hayashi, Y. J. Tong, Y. Infahsaeng, P. Chabera, T. Pascher, A. P. Yartsev, S. Isoda, H. Imahori, V. Sundstrom. *J Phys Chem C* **2013**, *117*, 6066-6080.

207. R. Long, D. Casanova, W. H. Fang, O. V. Prezhdo. *J Am Soc Chem* **2017**, *139*, 2619-2629.

208. B. Fritzinger, R. K. Capek, K. Lambert, J. C. Martins, Z. Hens. *J Am Chem Soc* **2010**, *132*, 10195-10201.

209. S. M. Harrell, J. R. McBride, S. J. Rosenthal. *Chem Mater* **2013**, *25*, 1199-1210.

210. Z. Y. Huang, Z. H. Xu, M. Mahboub, X. Li, J. W. Taylor, W. H. Harman, T. Q. Lian, M. L. Tang. *Angew Chem Int Edit* **2017**, *56*, 16583-16587.

211. X. Li, V. M. Nichols, D. P. Zhou, C. Lim, G. S. H. Pau, C. J. Bardeen, M. L. Tang. *Nano Lett* **2014**, *14*, 3382-3387.

212. L. R. Hou, Q. Zhang, L. T. Ling, C. X. Li, L. Chen, S. Chen. *J Am Chem Soc* **2013**, *135*, 10618-10621.

213. D. Zherebetskyy, M. Scheele, Y. J. Zhang, N. Bronstein, C. Thompson, D. Britt, M. Salmeron, P. Alivisatos, L. W. Wang. *Science* **2014**, *344*, 1380-1384.

214. M. Puri, V. E. Ferry. *Acs Nano* **2017**, *11*, 12240-12246.

215. Y. Peng, B. Lu, F. Wu, F. Zhang, J.-E. Lu, X. Kang, Y. Ping, S. Chen. *J. Am. Chem. Soc.* **2018**, *140*, 15290-15299.

216. Y. Peng, J. E. Lu, C. P. Deming, L. M. Chen, N. Wang, E. Y. Hirata, S. W. Chen. *Electrochim. Acta* **2016**, *211*, 704-710.

217. Q. M. Liu, Y. Peng, Z. Masood, D. DuBois, J. Tressel, F. Nichols, P. Ashby, R. Mercado, T. Assafa, D. J. Pan, H. L. Kuo, J. Q. Lu, F. Bridges, G. Millhauser, Q. F. Ge, S. W. Chen. *Adv Mater* **2023**, *35*.

218. A. Fernando, K. L. Dimuthu, M. Weerawardene, N. V. Karimova, C. M. Aikens. *Chem Rev* **2015**, *115*, 6112-6216.

219. J. R. Xiao, S. H. Yang, F. Feng, H. G. Xue, S. P. Guo. *Coordin Chem Rev* **2017**, *347*, 23-47.

Chapter 2 Atomic Dispersion and Surface Enrichment of Palladium in Nitrogen-Doped Porous Carbon Cages Leads to High-Performance Electrocatalytic Reduction of Oxygen

Reproduced with the permission from:

Qiming Liu, Yi Peng, Qiaoxia Li, Ting He, David Morris, Forrest Nichols, Rene Mercado, Peng Zhang, Shaowei Chen, "Atomic Dispersion and Surface Enrichment of Palladium in Nitrogen-Doped Porous Carbon Cages Leads to High-Performance Electrocatalytic Reduction of Oxygen", ACS Appl. Mater. Interfaces, 2020, 12, 1764.

2.1 Abstract

Metal-nitrogen-carbon (MNC) nanocomposites have been hailed as promising, efficient electrocatalysts toward oxygen reduction reaction (ORR) due to the formation of MN_x coordination moieties. However, MNC hybrids are mostly prepared by pyrolysis of organic precursors along with select metal salts, where part of the MN_x sites are inevitably buried in the carbon matrix. This limited accessibility compromises the electrocatalytic performance. Herein, we describe a wet-impregnation procedure by facile thermal refluxing whereby palladium is atomically dispersed and enriched onto the surface of hollow, nitrogen-doped carbon (HNC) forming Pd-N coordination bonds. The obtained Pd-HNC nanocomposites exhibited an ORR activity in alkaline media markedly higher than that of metallic Pd nanoparticles, and the best sample even outperforms commercial Pt/C and relevant Pd-based catalysts reported in the literature. The results suggest that atomic dispersion and surface enrichment of palladium in a carbon matrix may serve as an effective strategy in the fabrication of high-performance ORR electrocatalysts.

2.2 Introduction

Oxygen reduction reaction (ORR) is a critical process at the cathodes of fuel cells and metal-air batteries, where the sluggish electron-transfer kinetics has been recognized as a major bottleneck that limits the device performance.[1-3] Platinum-based nanoparticles have been used as the catalysts of choice toward ORR.[4-7] Palladium also exhibits apparent ORR activity. In the well-known "volcano plot", bulk palladium shows a moderate oxygen adsorption energy; yet it remains too strong, as compared to

that of platinum.[2,8] Therefore, a range of structural variables have been examined to manipulate the electronic structure of Pd so as to further enhance the ORR activity, such as nanoparticle size and shape,[9-12] alloying,[13,14] and interfacial interactions with substrate supports/capping ligands.[15-18] Atomic dispersion of Pd into a nitrogen-doped carbon matrix forming PdN_x moieties represents a new strategy to reach the apex of the "volcano plot".[15,19] In such single atom catalysts (SACs),[20,21] the catalytic activity, durability, and selectivity can be enhanced by the unique metal-support interfacial interactions, as compared to their corresponding nanoparticle or bulk counterparts.[22-31] SACs are prepared predominantly by pyrolysis. For instance, Zhou et al.[32] prepared Pd single atoms by pyrolysis of N-doped graphene with Pd salts at 800 °C. The obtained sample showed a 93.5% selectivity in the semi-hydrogenation of acetylene to ethylene, a performance superior to that (56%) with Pd nanoparticles. A similar behavior was also observed by Wei et al.,[33] where Pd nanoparticles encapsulated by zeolitic-imidazole frameworks 8 (ZIF-8) were transformed into Pd single atoms by pyrolysis at 900 °C, and the resultant sample showed a better catalytic selectivity (93.4%) than Pd nanoparticles (71.8%). In these studies, the catalytic activity was ascribed to the formation of PdN_x structures. However, high-temperature pyrolysis inevitably renders part of the resulting PdN_x moieties to be buried within the carbon matrix and become inaccessible, which compromises the overall catalytic performance.[23,24,34,35] This issue can be effectively mitigated by wet impregnation whereby metal centers are immobilized mostly onto the surface of the substrate support and the surface enrichment facilitates accessibility of the catalytic centers. For instance, Podyacheva et

al.[36] used N-doped carbon nanotubes to capture Pd single atoms (0.2-0.5 wt%) in acetone, followed by H_2 reduction. The PdN_x active sites exhibited a higher turnover frequency (TOF, 0.081 s^{-1}) than Pd particles (~ 0.06 s^{-1}) toward formic acid decomposition at 125 °C. Bulushev et al.[37] soaked N-doped mesoporous carbon into a palladium salt solution to produce single Pd active sites (~1 wt%). The sample that consisted of isolated Pd(II) cations demonstrated a TOF over 3 times higher than that of commercial Pd powders toward hydrogen production from formic acid. Nevertheless, in these earlier studies, only a small number of PdN_x active sites were formed because of the low concentration of N dopants in the carbon matrices, which limited the eventual catalytic performance.

It should be noted that studies of palladium SACs for ORR have been scarce, although atomic palladium species are known to exhibit more optimal binding for oxygen intermediates than the bulk metal of palladium, and drastically enhanced mass activity.[19,38-40] For instance, Passaponti et al.[38] deposited N-coordinated Pd(II) macrocyclic complexes on carbon nanotubes and observed apparent ORR activity with an onset potential (E_{onset}) of +0.95 V vs. RHE and a half-wave potential ($E_{1/2}$) of +0.86 V, markedly better than that of a polycrystalline Pt electrode (E_{onset} = +0.91 V, and $E_{1/2}$ = +0.82 V). Xiang et al.[39] reported that Pd single atoms supported on manganese(IV) oxide-carbon nanotube (MnO_2-CNT) nanocomposites exhibited an optimized binding strength to ORR intermediates, with a much higher Pd mass activity (484 A g^{-1} at +0.90 V) than that of commercial Pd/C (20 A g^{-1}). Arrigo et al.[19] also observed that PdN_x in Pd-doped carbon nanotubes improved the ORR activity with an E_{onset} of +0.88 V, in

comparison to only +0.75 V with metallic Pd nanoparticles. Yet, the ORR performance of these palladium-based catalysts remains subpar, as compared to that of state-of-the-art Pt/C.

Herein, we describe a wet-impregnation procedure based on facile thermal refluxing[41,42] to embed Pd metal centers onto the surface of N-doped porous carbon cages (HNC) that were prepared *a prior* pyrolytically from ZIF-8. The resulting Pd-HNC nanocomposites were found to exhibit abundant micro-/meso-/macropores decorated with pyridinic/pyrrolic nitrogen dopants, which facilitated the chelation of metal ions.[43,44] Since the Pd centers resided mostly on the carbon surface, the electrochemical accessibility was maximal, a critical feature for the optimization of the electrocatalytic (mass) activity. Experimentally, we observe that whereas a small number of Pd nanoparticles were also produced in the samples, the Pd SACs in Pd-HNC played a dominant role in ORR electrocatalysis, and the sample with a saturated Pd loading even outperformed commercial 20% Pt/C with an $E_{1/2}$ that was 40 mV more positive.

2.3 Experimental Section

Chemicals

2-Methylimidazole ($CH_3C_3H_2N_2H$, 99%, Acros Organics), tannic Acid ($C_{76}H_{52}O_{46}$, certified ACS, Electron Microscopy Sciences), ethylenediamine tetraacetic acid disodium salt dihydrate (EDTA, ACS, Calbiochem), zinc nitrate hexahydrate ($Zn(NO_3)_2 \cdot 6H_2O$, certified ACS, Fisher Chemicals), palladium(II) acetate ($Pd(OAc)_2$, 99.98%, Alfa Aesar), potassium hydroxide (KOH, certified ACS, Fisher Chemicals),

potassium thiocyanate (KSCN, Spectrum Chemicals), and Pt/C (20 wt%, Alfa Aesar) were used as received without further purification. Water was supplied from a Barnstead Nanopure Water System (18.3 MΩ·cm).

Synthesis of ZIF-8

In a typical synthesis,[45] 1.116 g of $Zn(NO_3)_2 \cdot 6H_2O$ was dissolved in 30 mL of methanol in a vial, and 1.232 g of 2-methylimidazole in 30 mL methanol in another vial. These two solutions were then mixed under sonication for 10 min to form a milky-white solution. The solution was transferred to a 100 mL Teflon-lined stainless-steel autoclave and heated at 120 °C for 2 h, producing a milky precipitate that was collected via centrifugation at 6000 rpm for 5 min, rinsed three times with methanol, and dried under vacuum at 50 °C for 12 h. The obtained product was the ZIF-8 crystals.

Synthesis of Hollow ZIF-8

80 mg of the as-prepared ZIF-8 crystals was dispersed in 3 mL of Nanopure water under sonication for 20 min, into which was then injected 7 mL of a tannic acid solution (5 mg mL^{-1} in water) under magnetic stirring for 10 min to form an orange solution. After centrifugation, the precipitates were rinsed three times with water and then dried under vacuum at 50 °C, affording hollow ZIF-8.

Synthesis of HNC

HNC was prepared by pyrolysis of hollow ZIF-8. Experimentally, the hollow ZIF-8 powders prepared above were transferred into a ceramic boat, which was then placed into a tube furnace, and heated to 900 °C at a ramp rate of 5 °C min^{-1} and kept at 900

°C for 3 h under a nitrogen atmosphere. The pyrolyzed sample was cooled down naturally, which was denoted as HNC.

Synthesis of Pd-HNC

Under sonication for 20 min, 20 mg of HNC was dispersed in 30 mL of acetonitrile in a flask, along with the addition of a certain amount of $Pd(OAc)_2$ (i.e., 1 mg, 2 mg, 5 mg, or 10 mg). The mixture was refluxed at 70 °C for 10 h in an oil bath, before the precipitates were collected by centrifugation and dried under vacuum at 50 °C for 12 h. The resulting samples were referred to as Pd-HNC_1, Pd-HNC_2, Pd-HNC_5, and Pd-HNC_{10}, respectively.

A control sample PdNP/HNC was prepared by $NaBH_4$ reduction of $Pd(OAc)_2$ in the presence of HNC, where Pd nanoparticles were deposited on the HNC surface. Briefly, 20 mg of HNC was dispersed in 15 mL of acetonitrile with 1.5 mg of $Pd(OAc)_2$ (0.1 mg mL^{-1}) in an ice bath, into which was then injected 250 μL of a freshly prepared $NaBH_4$ solution (7 mg mL^{-1}). The resulting precipitates were centrifuged and dried under vacuum at 50 °C for 12 h.

Characterizations

Transmission electron microscopic (TEM) measurements were performed with a JEOL JEM-2100F electron microscope. X-ray photoelectron spectra (XPS) were acquired with a PHI-5400/XPS instrument with an Al K_α source operated at 350 W and 10^{-9} Torr. X-ray diffraction (XRD) patterns were collected with a Bruker D8 Advance diffractometer with Cu K_α radiation ($\lambda = 0.15418$ nm). The specific surface areas of the samples were measured by using Langmuir and Brunauer-Emmett-Teller (BET)

methods on an Micromeritics ASAP 2020 porosimetry system at 77.3 K. The adsorption branches of the isotherms were used to obtain the pore width distribution curves by using non-local density functional theory (NLDFT). Contents of metal elements in the catalysts were quantified by using inductively coupled plasma-optical emission spectrometric (ICP-OES) on a PerkinElmer Optima instrument. UV-vis absorption spectra were acquired with a PerkinElmer Lambda 35 UV-vis spectrometer.

X-ray absorption spectroscopy (XAS)

Pd K-edge XAS data was collected at the CLS@APS (Sector 20-BM) beamline at the Advanced Photon Source (7.0 GeV) in Argonne National Laboratory, Chicago, IL, USA. Powdered samples were measured in fluorescence mode simultaneously with a Pd foil reference. All measurements were conducted at room temperature and ambient pressure. Extended X-ray absorption fine structure (EXAFS) data was transformed and normalized into k- and R-space using the Athena program following conventional procedures.[46] A k weighting of 2 was used to obtain all FT-EXAFS spectra. A k-range of 3.5 to 11.0 $Å^{-1}$ and a R-range of 1.0 to 3.3 Å was used. Self-consistent multiple-scattering calculations were performed using the FEFF6 program to obtain the scattering amplitudes and phase-shift functions used to fit various scattering paths with the Artemis program. In the fitting of all samples, the E_0 values were correlated together to minimize the number of independent values, allowing reliable fitting results to be obtained.

Electrochemistry

All electrochemical tests were carried out with a CHI 710 electrochemical workstation in a conventional three-electrode cell, using a Ag/AgCl (1 M KCl) electrode as the reference electrode, a graphite rod as the counter electrode, and a polished rotating ring (gold)-disk (glassy carbon) electrode (RRDE, from Pine Instrument) as the working electrode. The Ag/AgCl electrode was calibrated against a reversible hydrogen electrode (RHE), and all potentials in the present study were referenced to this RHE. During the ORR tests, the ring potential was set at +1.5 V vs. RHE. To prepare the catalyst inks, 2 mg of the samples obtained above was added into 1 mL of an isopropanol/water (3:1 v/v) mixture and 10 μL of a 20 wt.% Nafion solution. The suspension was sonicated to form a homogeneous ink. 20 μL of the ink was then dropcast onto the glassy carbon disk electrode (surface area 0.246 cm^2), dried at room temperature and coated with 5 μL of a Nafion solution, corresponding to a catalyst loading of 0.162 mg cm^{-2}.

2.4 Results and Discussion

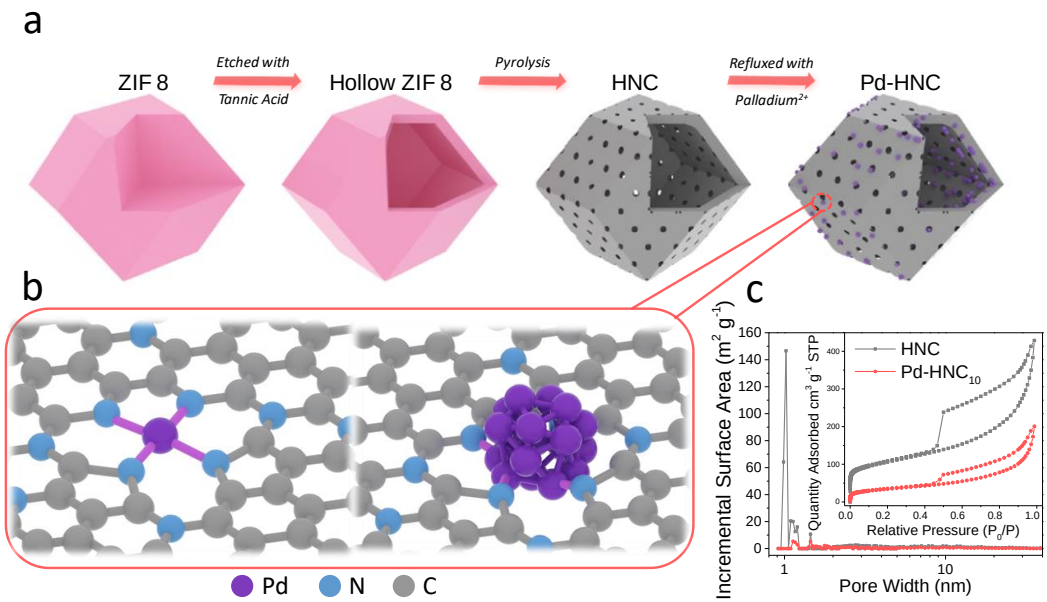

Figure 1. Schematic illustrations of (a) the preparation of Pd-HNC, where (b) both atomically dispersed PdN_x sites and palladium nanoclusters may be formed depending on the initial feed of palladium. (c) Pore size distribution profiles of HNC and Pd-HNC_{10}. Inset is the corresponding nitrogen sorption isotherms.

The synthetic procedure of the Pd-HNC samples entails four major steps. As illustrated in Figure 1a, the first step is hydrothermal synthesis of ZIF-8 powders from zinc(II) nitrate and 2-methylimidazole.[47] Tannic acid is then used to etch the inner part of ZIF-8 resulting in the formation of a hollow structure.[48-50] Notably, in comparison to other template-based methods to produce hollow nanostructures,[25,51] chemical etching by tannic acid can not only facilely remove the ZIF-8 inner cores, but also retain the pristine shape.[47,52] Subsequent pyrolysis at 900 °C leads to effective carbonization of the hollow ZIF-8 precursor into HNC with abundant nitrogen dopants.[43] During pyrolysis, the volatilization of the zinc compounds within the hollow ZIF-8 leads to the

formation of extensive porosity in the carbon matrix. Palladium species are then impregnated onto the HNC surface by thermal refluxing of HNC and palladium(II) acetate, most likely by virtue of the formation of Pd-N bonds, leading to atomic dispersion and surface enrichment of the Pd centers (Figure 1b). Note that a small number of Pd nanoclusters can also be formed at high palladium feeding ratios.

Four Pd-HNC samples (Pd-HNC_1, Pd-HNC_2, Pd-HNC_5, and Pd-HNC_{10}) were prepared with the addition of 1, 2, 5, and 10 mg of $Pd(OAc)_2$ to 20 mg of HNC, respectively. Note that for the Pd-HNC_{10} sample, the color of the supernatant remained virtually unchanged before and after thermal refluxing, suggesting saturated loading of Pd into the HNC matrix (Figure 2). The exact Pd contents in the samples were then quantitatively assessed by ICP-OES measurements (Table 1), 0.87 wt% for Pd-HNC_1, 1.75 wt% for Pd-HNC_2, 4.36 wt% for Pd-HNC_5, and 7.77 wt% for Pd-HNC_{10}. For the control sample PdNP/HNC where Pd nanoparticles were deposited onto the HNC surface by $NaBH_4$ reduction of $Pd(OAc)_2$, the palladium content was estimated to be 2.61 wt%.

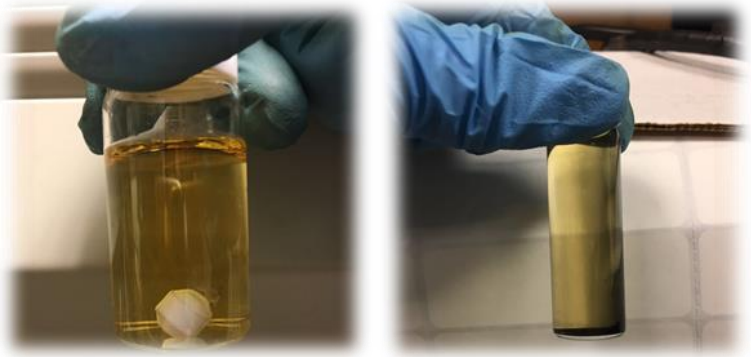

Figure 2. Pd-HNC_{10} before and after thermal refluxing. The resulting supernatant demonstrates a similar yellowish color, indicating that the HNC is saturated with Pd centers.

Table 1. Pd contents in the series of samples as determined by ICP-OES and XPS measurements.

Samples	Pd-HNC_1	Pd-HNC_2	Pd-HNC_5	Pd-HNC_{10}	PdNP/HNC
Pd (wt%) calculated from ICP-OES	0.87	1.75	4.36	7.77	2.61
Pd(II) (wt%) calculated from XPS	0.74	1.43	3.39	5.42	1.14

The loading of Pd into the HNC matrix led to a marked change of the sample porosity. Figure 1c inset shows the N_2 sorption isotherms of HNC and Pd-HNC_{10}. For the HNC sample, one can see a sharp increase of the adsorbed N_2 quantity at low relative pressures, suggesting a substantial number of micropores. In fact, NLDFT fitting shows that the HNC sample was dominated with micropores (~ 1 nm), as evidenced in the pore-size distribution diagram (Figure 1c). Furthermore, in contrast to the porous carbon derived pyrolytically from solid ZIF-8 powders (without tannic acid etching) reported in the literature,[50] the HNC sample demonstrated a huge adsorption-desorption hysteresis loop and a range of mesopores between 2 and 10 nm. This suggests that HNC

consisted of a hierarchical structure with mesopores and micropores (Figure 3), a unique feature conducive to enhanced accessibility of the catalytic active sites on the carbon matrix and electrochemical mass transfer, as compared to solid nitrogen-doped carbon (Figure 4).[23] Interestingly, after thermal refluxing with $Pd(OAc)_2$, the specific surface area, based on the BET method, was found to decrease markedly by about 80% from 410.21 $m^2 g^{-1}$ for HNC to only 85.39 $m^2 g^{-1}$ for Pd-HNC_{10}. In fact, from Figure 1c, one can see that micropores (~ 1 nm) disappeared almost completely from the pore size distribution plot, consistent with the impregnation of Pd species into the HNC matrix most likely by the N dopant/defect sites; and the fact that the hysteresis loop remained in the N_2 adsorption-desorption isotherm indicates that the Pd-HNC_{10} sample mainly contained mesopores (Figure 3).

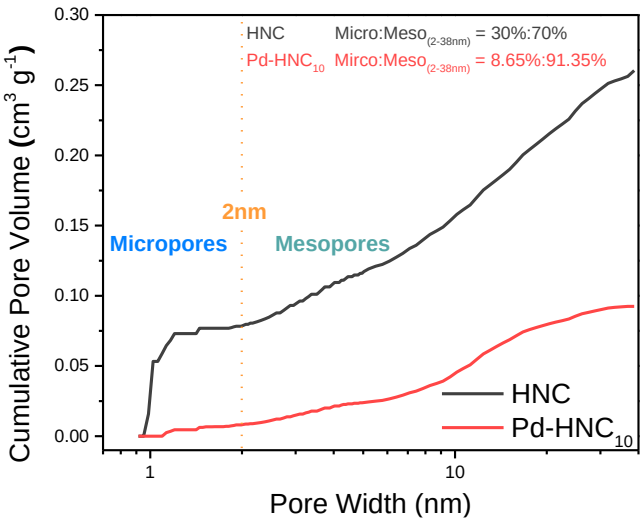

Figure 3. Cumulative pore volume as a function of pore width of the HNC and Pd-HNC_{10} samples.

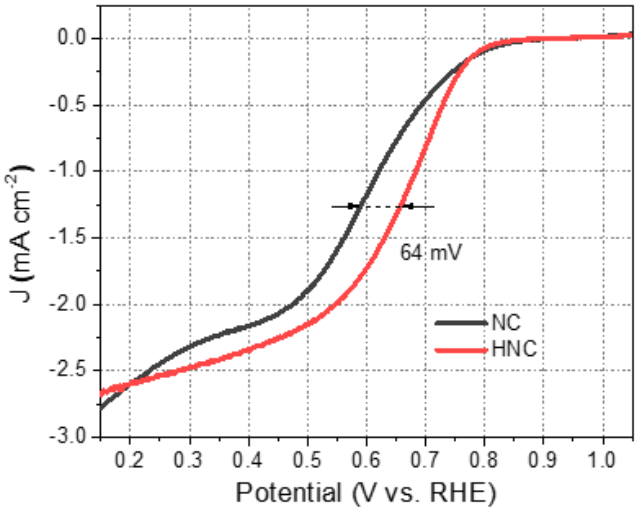

Figure 4. Comparison of the ORR performance of HNC and solid N-doped carbon (NC) at the rotation rate of 1600 rpm in oxygen-saturated 0.1 M KOH. Following the same procedure but without the etching process, we directly pyrolyzed ZIF-8 precursors into solid N-doped carbon (NC). The corresponding ORR polarization curves are shown in Figure 4. One can see that HNC clearly outperformed the NC sample, with an $E_{1/2}$ that is 64 mV more positive. Meanwhile, the diffusion-limited current of HNC was also larger than that of NC, suggesting that the hollow structure is indeed conducive to the ORR electrocatalysis.

The morphology of the Pd-HNC samples was then characterized by TEM measurements. From Figure 5a, the Pd-HNC_{10} sample can be seen to display a cage-like structure with a diameter of around 200 nm and a shell thickness of ca. 20 nm. Similar hollow structures are produced with other Pd-HNC samples (Figure 6), and extensive mesoporosity can be seen in all samples. At higher magnifications (Figure 5b,c), one can see that the sample surface was also decorated with a few nanoparticles of ca. 3 nm in diameter, and the number of nanoparticles diminishes with decreasing loading of $Pd(OAC)_2$ in thermal refluxing — none can be found with Pd-HNC_1 (Figure

6a). The nanoparticles display well-defined lattice fringes with a d spacing of 0.23 nm that can be ascribed to the (111) planes of *fcc* palladium;[53,54] and these Pd nanoparticles[55-57] can be seen to be partly encapsulated within a carbon shell. By contrast, no carbon encapsulation was observed for the palladium nanoparticles in PdNP/HNC (also ca. 3 nm in diameter), which clustered onto the HNC surface (Figure 7), with the {111} facets clearly identified in the Fast Fourier Transform (FFT) patterns.

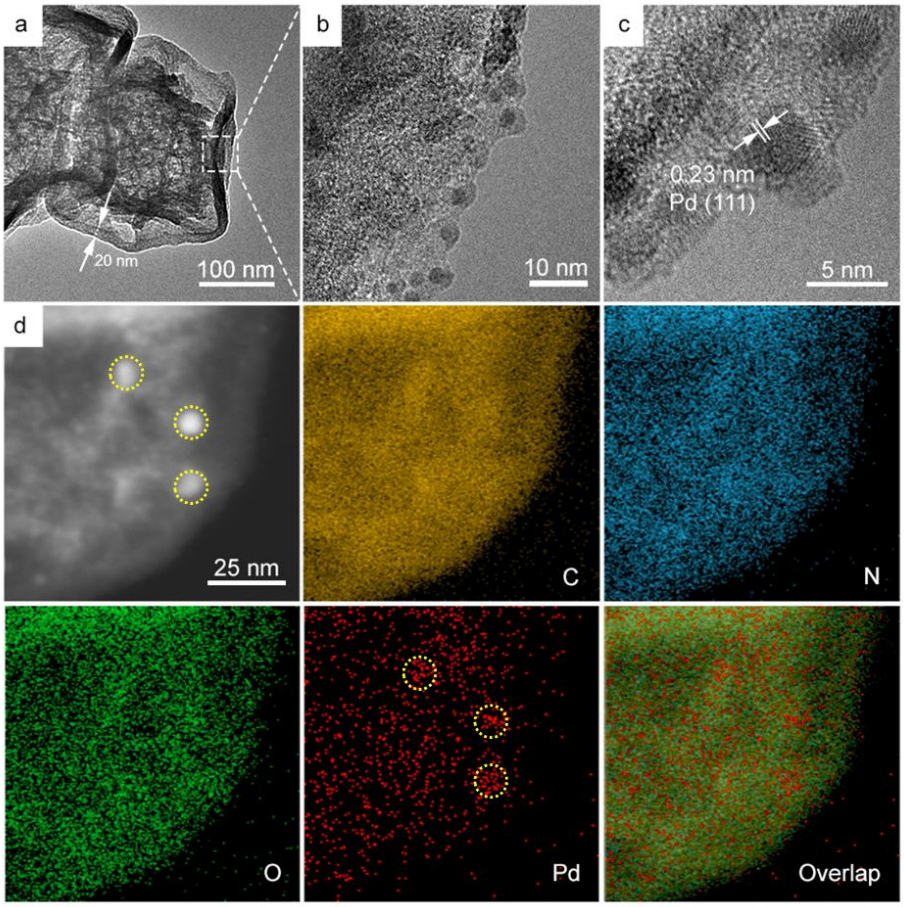

Figure 5. (a-c) Representative TEM images of Pd-HNC$_{10}$ at varied magnifications. (d) HAADF-STEM image of Pd-HNC$_{10}$ and the corresponding elemental maps of carbon, nitrogen, oxygen, palladium, and overlap. The few Pd nanoparticles are highlighted in dotted yellow circles.

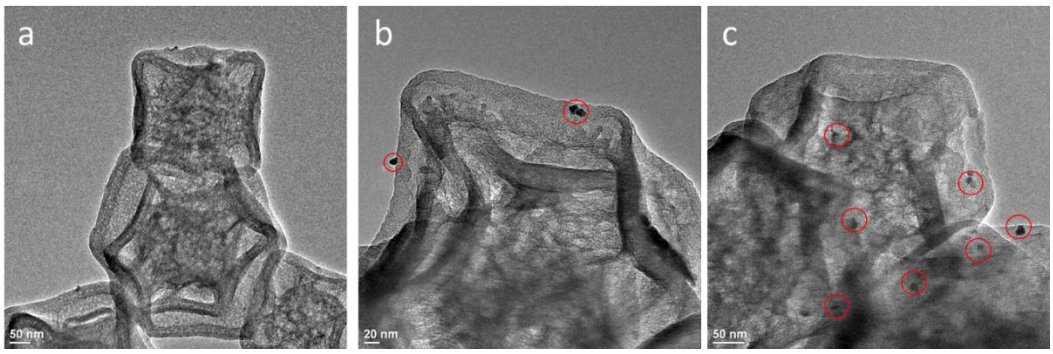

Figure 6. TEM images of (a) Pd-HNC$_1$, (b) Pd-HNC$_2$, and (c) Pd-HNC$_5$. Red circles in panels (b) and (c) highlight the few palladium nanoparticles.

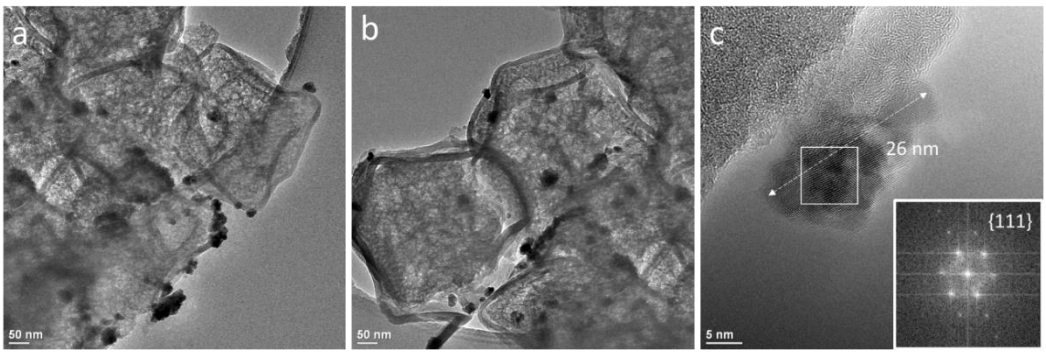

Figure 7. (a-c) TEM images of PdNP/HNC at varied magnifications. Inset to panel (c) is the corresponding Fast Fourier Transform (FFT) pattern of the Pd nanoparticles in the white square.

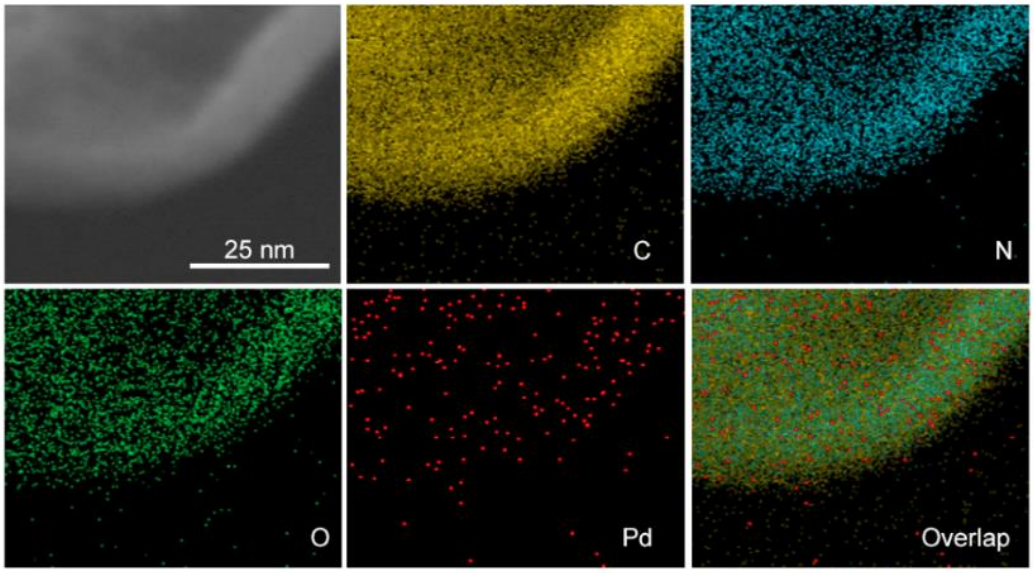

Figure 8. HAADF-STEM images of the edge side (without apparent particles) of Pd-HNC$_{10}$ and the corresponding elemental maps of carbon, nitrogen, oxygen, palladium, and overlap.

Further structural details were obtained from high angle annular dark field-scanning TEM (HAADF-STEM) measurements and the corresponding elemental mapping studies based on energy-dispersive X-ray (EDX) analysis (Figure 5). One can see that (a) nitrogen (and oxygen) is distributed rather evenly over the entire carbon matrix, confirming successful nitrogen doping of the carbon skeletons; and (b) in addition to the few Pd nanoparticles (dotted yellow circles), a large number of palladium atomic species can also be seen to be homogeneously dispersed within the HNC matrix (Figure 5 and 8).

Consistent results were obtained in XRD measurements. From Figure 9, both PdNP/HNC and Pd-HNC$_{10}$ samples can be seen to exhibit only a broad diffraction peak at $2\theta = 39.5^{o}$, which can be ascribed to the (111) crystalline planes of *fcc* palladium

(JCPDS no. 96-101-1105).[58] This diffraction feature was not observed with HNC alone or other Pd-HNC samples prepared at reduced Pd loadings, consistent with the results from TEM measurements (Figure 5 and 6).

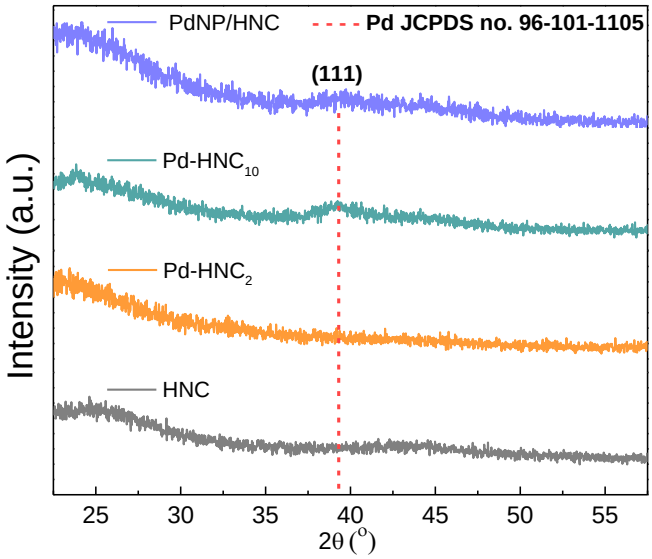

Figure 9. XRD patterns of PdNP/HNC, Pd-HNC$_{10}$, Pd-HNC$_2$, and HNC. Dashed lines indicate the expected 2θ position of the (111) diffractions of *fcc* Pd (JCPDS no. 96-101-1105). Note that Pd-HNC$_{10}$ contained more metallic palladium than PdNP/HNC based on results from XPS measurements.

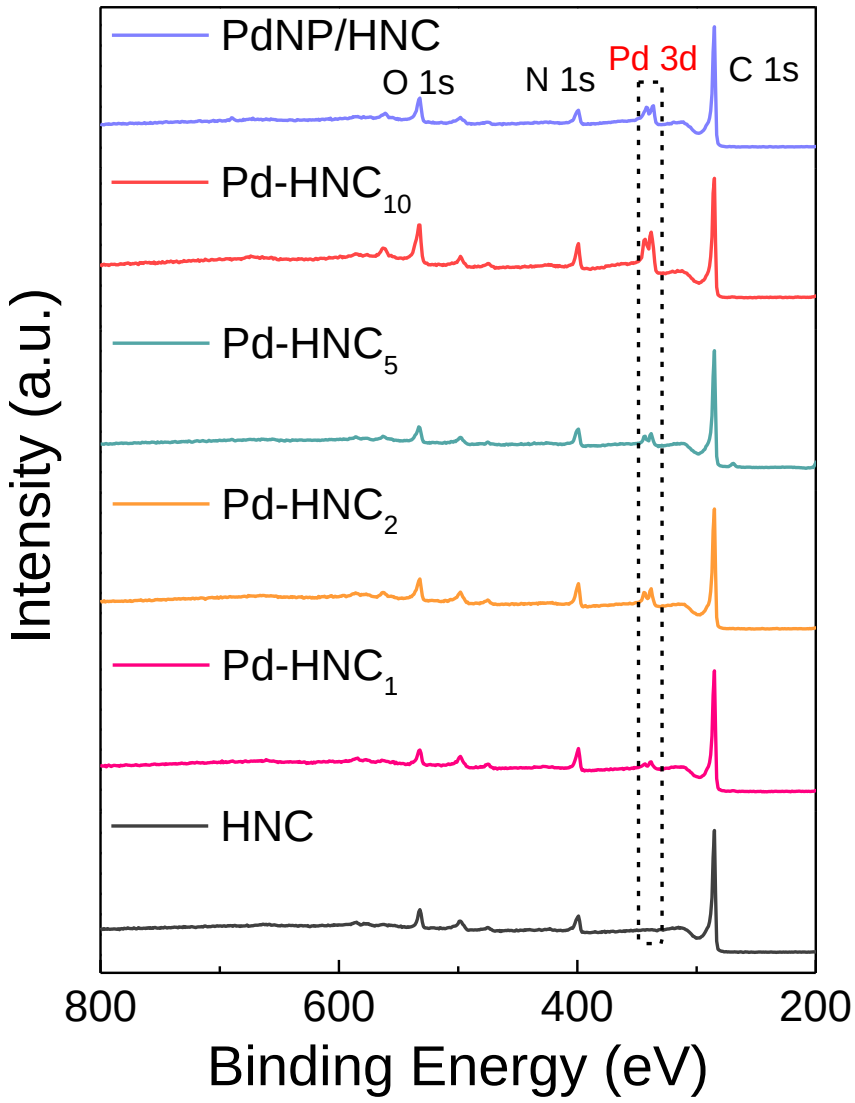

Figure 10. XPS survey spectra of PdNP/HNC, Pd-HNC$_{10}$, Pd-HNC$_5$, Pd-HNC$_2$, Pd-HNC$_1$, and HNC.

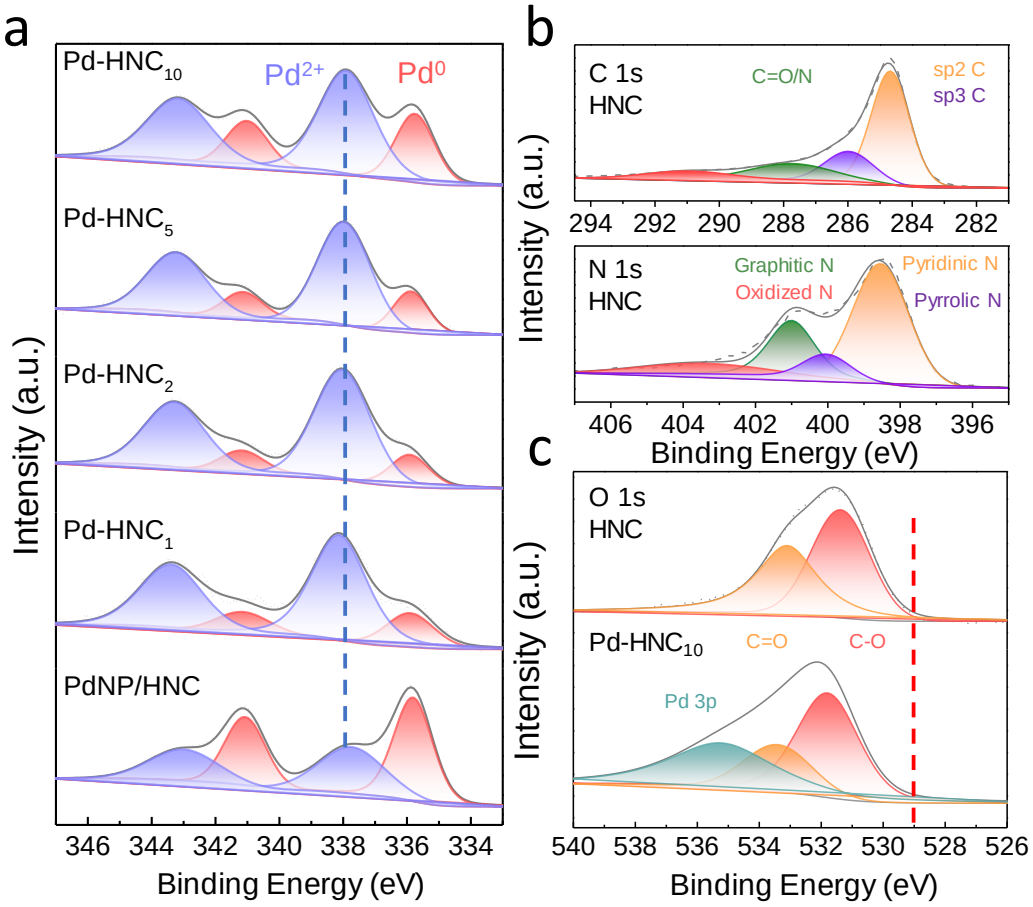

Figure 11. (a) High-resolution XPS spectra of the Pd 3d electrons of the Pd-HNC series and PdNP/HNC. (b) High-resolution XPS spectra of the C 1s (upper) and N 1s (bottom) electrons of HNC. (c) High-resolution XPS spectra of O 1s electrons of HNC and Pd-HNC_{10}. Red dashed line indicates the binding energy of the O 1s electrons in Pd-O. Solid curves are experimental data and shaded peaks are deconvolution fits.

XPS measurements were then carried out to examine the elemental composition and valence states of the samples. From the survey spectra in Figure 10, the elements of C, Pd, N, and O can be readily identified at 284, 356, 400, and 531 eV, respectively, for all Pd-HNC and PdNP/HNC samples, from which the Pd content was found to increase with the increasing feed ratio of $Pd(OAc)_2$, 3.55 wt% for Pd-HNC_1, 7.74 wt% for Pd-

HNC_2, 6.58 wt% for Pd-HNC_5, and 17.48 wt% for Pd-HNC_{10}, in comparison to 9.88 wt% for PdNP/HNC (Table 2). One may note that these concentrations are markedly higher than those obtained by ICP-OES measurements (Table 1), suggesting that Pd was indeed predominantly situated and enriched on the HNC surface, as XPS probes only the surface layers of the samples. The high-resolution scans of the Pd 3d electrons are depicted in Figure 11a, where deconvolution can be seen to yield two doublets. The first pair (red peaks) at 335.8 and 341.1 eV can be attributed to the $3d_{3/2}$ and $3d_{5/2}$ electrons of metallic palladium, most likely due to the few nanoparticles observed in TEM measurements (Figure 5).[19,37,59,60] The other pair (purple peaks) appear at higher binding energies of 337.9 and 343.2 eV, comparable to those of Pd(II) species,[61,62] consistent with results from HAADF-STEM measurements (Figure 5d) which clearly showed atomic dispersion of Pd(II) species within the HNC matrix. It should be noted that the binding energies of Pd(II) in Pd-HNC are much higher than those of PdO (ca. 336.5 and 341.8 eV) but lower than those of $Pd(OAC)_2$ (ca. 338.5 and 343.8 eV),[19,61,63-65] suggesting that the Pd(II) species in Pd-HNC were unlikely due to the surface oxidation of Pd nanoparticles or excessive metal precursors. Moreover, based on the integrated peak areas, the atomic ratio of Pd(II):Pd(0) in the samples can be seen to increase with decreasing $Pd(OAC)_2$ feed, at 5.6 for Pd-HNC_1, 4.5 for Pd-HNC_2, 3.5 for Pd-HNC_5, and 2.3 for Pd-HNC_{10} (Table 2). That is, for the Pd-HNC series, the dominant species is Pd(II) atomically dispersed within the HNC matrix. For comparison, the Pd(II):Pd(0) ratio is only 0.77 in PdNP/HNC, suggesting that nanoparticles are the major product together with a small number of atomic Pd species.

Furthermore, in conjunction with the total Pd content obtained from ICP-OES measurements (Table 1), one can see that Pd-HNC_{10} possessed the highest loading of atomic Pd(II) species (5.42 wt%), which is drastically higher than those of Pd SACs reported in the literature (Table 3).

Table 2. Pd 3d binding energies and concentrations in the series of sample as determined by XPS measurements.

Samples	Pd^0 (eV)		Pd^{2+} (eV)		Pd^{2+}:Pd^0	Pd at%	Pd wt%	Pd:N
PdNP/HNC	335.805	341.065	337.736	342.996	0.77	1.27	9.88	1:6.7
Pd-HNC_{10}	335.74	341.00	337.897	343.157	2.3	2.45	17.48	1:4.6
Pd-HNC_5	335.875	341.135	337.961	343.221	3.5	0.81	6.58	1:11.2
Pd-HNC_2	335.913	341.173	338.014	343.274	4.5	0.97	7.74	1:11.6
Pd-HNC_1	335.595	340.855	338.040	343.300	5.6	0.43	3.55	1:26.1

Table 3. Comparison of the content of atomic Pd species between Pd-HNC_{10} and relevant Pd SACs in the literature.

Samples	Atomic Pd content (wt%)	Reference
Pd-HNC_{10}	5.42	This work
Pd-SAs	0.16	[33]
Pd_1/C_3N_4	0.5	[66]
Pd/N-CNTs	0.5	[36]
[Pd]mpg-C_3N_4	0.5	[67]
RGO@AC/Pd SACs	0.4	[68]

Pd1%NCNT	0.9	19

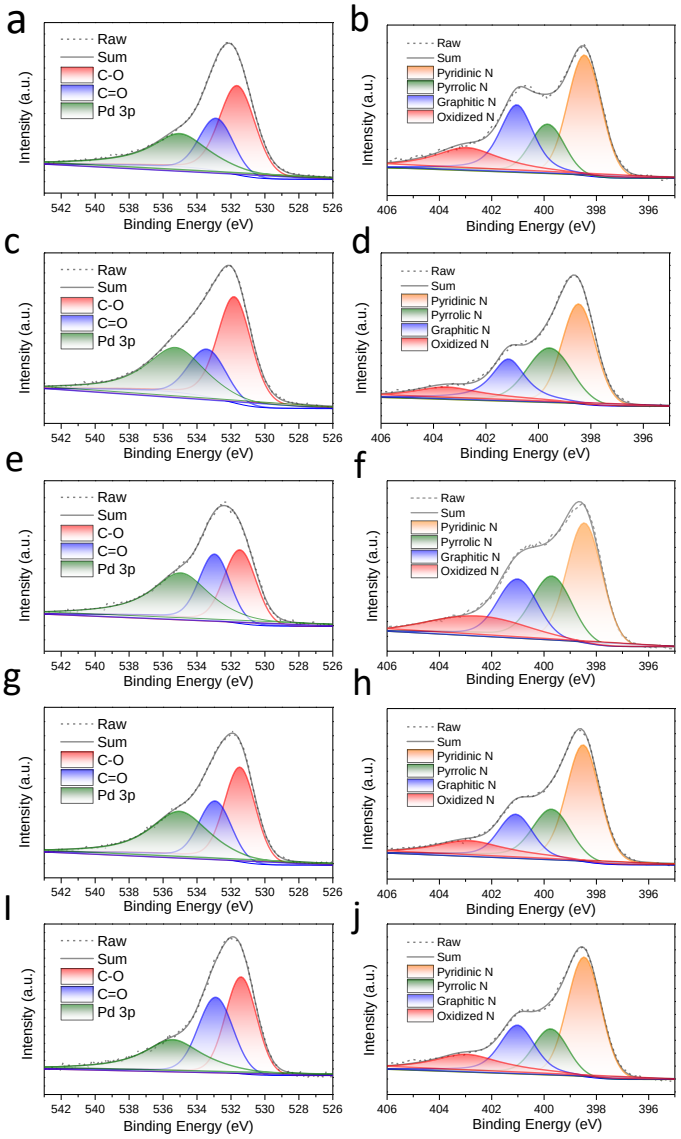

Figure 12. High-resolution XPS spectra of the (left panels) O 1s and (right panels) N 1s electrons of (a, b) PdNP/HNC, (c, d) Pd-HNC$_{10}$, (e, f) Pd-HNC$_5$, (g, h) Pd-HNC$_2$, and (i, j) Pd-HNC$_1$.

The C 1s and N 1s spectra of the HNC sample are shown in Figure 11b. In the C 1s spectrum, the major component is sp^2-hybridized C, which accounts for ca. 77 at% of the sample, indicating effective carbonization of the ZIF-8 precursor by pyrolysis. In the N 1s spectrum, deconvolution yields four peaks at 398.5 eV for pyridinic N, 400.0 eV for pyrrolic N, 401.0 eV for graphitic N, and 402.8 eV for oxidized N; and their contents are 4.63 at%, 1.49 at%, 1.58 at%, and 1.40 at%, respectively, corresponding to a total nitrogen dopant concentration of *ca*. 9.1 at%. In the Pd-HNC samples, the Pd(II) species is most likely coordinated to the pyrrolic/pyridinic N. This argument is supported, in part, by the observation that no Pd-O peak (529 eV, red dashed line) can be resolved in the O 1s spectra (Figure 11c and 12). However, it is difficult to resolve Pd-N in the N 1s spectra because the binding energy is close to those of pyrrolic/pyridinic N.[22]

Such structural details can be resolved in XAS measurements. Figure 13a depicts the Pd K-edge X-ray absorption near-edge structure (XANES) spectra of Pd-HNC_{10} and Pd-HNC_2, with a Pd foil as the reference. One can see that Pd-HNC_{10} and Pd-HNC_2 display very similar XANES profiles, suggesting similar Pd electronic environments. Yet the absorption edge can be seen to appear at a higher energy than that of the Pd foil, along with a higher peak intensity for the first peak following the edge, consistent with the existence of positively charged Pd species in the Pd-HNC samples, which was evidenced in TEM and XPS measurements (Figure 5 and 11). Furthermore, the flat post-edge feature of Pd-HNC_{10} and Pd-HNC_2 within the range of 24370 to 24385 eV can be attributed to the combined contributions of Pd atomic species (which display a

peak-like feature) and Pd nanoparticles (which display a valley-like feature).[33,69] Moreover, the post-edge intensity of Pd-HNC$_{10}$ (red curve) is slightly higher than that of Pd-HNC$_2$ (blue curve), in good agreement with the higher concentration of Pd(II) species in Pd-HNC$_{10}$, as determined by XPS measurements (Table 2).

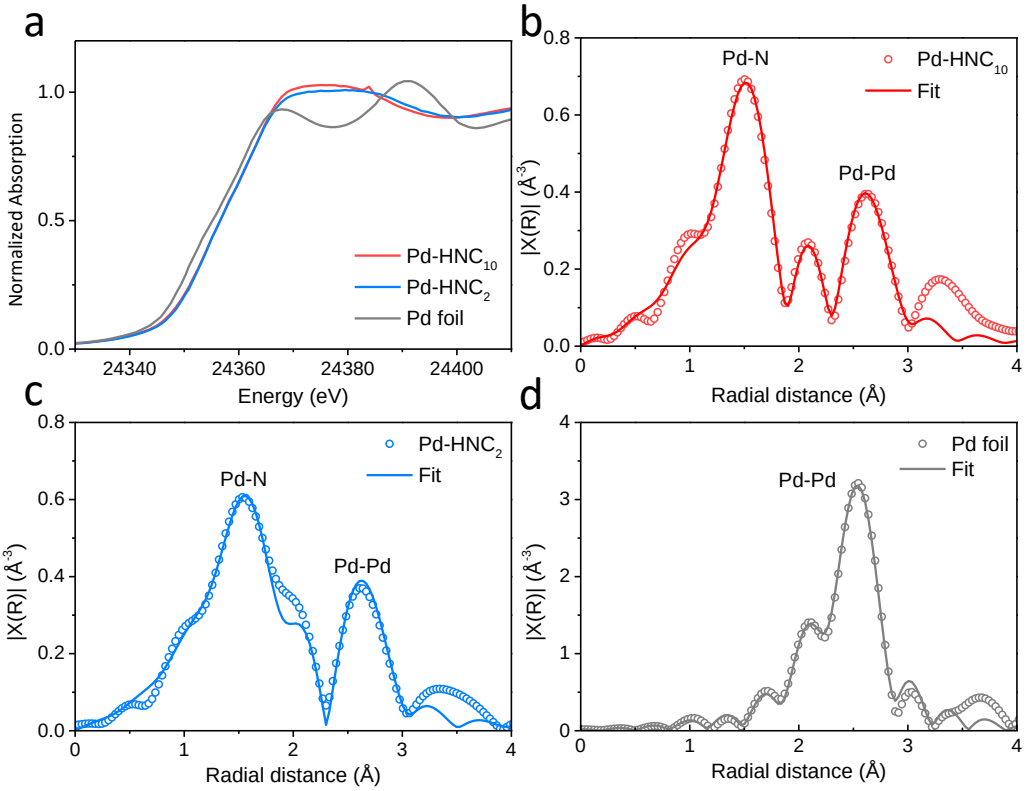

Figure 13. (a) Pd K-edge normalized XANES profiles of Pd-HNC$_{10}$, Pd-HNC$_2$, and Pd foil. Fourier transform EXAFS spectra of (b) Pd-HNC$_{10}$, (c) Pd-HNC$_2$, and (d) Pd foil. Symbols are experimental data and solid curves are the fits.

Table 4. Summary of the fitting results of the EXAFS spectra of Pd-HNC$_{10}$, Pd-HNC$_2$, and Pd foil. Note: CN, coordination number; R, interatomic distance; σ^2, Debye-Waller factor; and E_0, edge energy shift. The R factor is used to value the goodness of the fitting.

Samples	bond	CN	R (Å)	σ^2 (Å) x 10^{-3}	E_0 (eV)	R factor

Pd Foil	Pd-Pd	12 (Fixed)	2.741(2)	5.2(3)	1.4(4)	0.0048
Pd-HNC_{10}	Pd-Pd	2.2(4)	2.797(6)	7(1)	2.9(7)	0.0029
	Pd-N	3.4(3)	2.004(5)	4(1)	2.9(7)	
Pd-HNC_2	Pd-Pd	2.1(8)	2.80(2)	7(3)	6(2)	0.0213
	Pd-N	5(1)	2.07(2)	10(3)	6(2)	

Further structural insights were obtained from analysis of the EXAFS spectra. From the Fourier transform EXAFS spectra in Figure 4b-d, one can see that the Pd foil displays a major peak at 2.54 Å arising from the Pd-Pd bond.[70] This peak is also visible in both Pd-HNC_{10} and Pd-HNC_2, consistent with the formation of Pd nanoparticles in the samples; however, a more prominent peak can be identified below 2 Å that most likely arose from Pd-O and/or Pd-N bonds with the carbon support.[71] Yet, as mentioned earlier, in the XPS measurements of the Pd 3d and O 1s electrons of Pd-HNC_{10} and Pd-HNC_2 (Figure 11a, 11c and 12), no Pd-O species was found, indicating that this peak most likely arose from a Pd-N bonding interaction. Consistent results were obtained in EXAFS measurements where no Pd-Pd bonds from Pd-O-Pd at ca. 3.0 Å can be resolved,[33,72] indicating the absence of PdO_x nanoclusters in the samples. From fitting of the spectral data (Figure 13b-d), the bond length can be calculated to be 2.004 Å for Pd-N, and 2.797 Å for Pd-Pd in Pd-HNC_{10} (note that the peak positions may deviate from the true bond lengths due to the Fourier transform process, and EXAFS fitting allows for the actual bond lengths in the samples to be calculated). The latter is slightly longer than that (2.741 Å) of the Pd foil. Yet the corresponding coordination numbers (CN) were found to be 3.4 for Pd-N and 2.2 for Pd-Pd in Pd-HNC_{10}. One can see that the latter is markedly smaller than that (12) of the Pd foil. This is because Pd single

atoms are the predominant species in the Pd-HNC_{10} sample.[56] Similar CN and bond lengths (Table 4) were obtained for Pd-HNC_2, suggesting a very similar bonding configuration of atomic Pd in the Pd-HNC samples, which is most likely in the form of $PdN_{3\sim4}$.

The ORR activity of the obtained samples was then assessed and compared by RRDE measurements in O_2-saturated 0.1 M KOH at the rotation rate of 1600 rpm and potential sweep rate of 10 mV s^{-1}. From the linear sweep voltammograms (LSV) in Figure 14a, all Pd-HNC samples can be seen to exhibit apparently enhanced electrocatalytic activity towards ORR, as compared to HNC alone, and the performance increases with increasing Pd loading in the sample. That is, Pd-HNC_{10} stood out as the best ORR catalysts among the series, within the present experimental context. For instance, Pd-HNC_1 exhibited E_{onset} = +0.946 V and $E_{1/2}$ = +0.808 V, over 100 mV better than HNC alone; and both E_{onset} and $E_{1/2}$ further increased to +0.958 V and +0.846 V for Pd-HNC_2, +0.994 V and +0.889 V for Pd-HNC_5, and +1.00 V and +0.898 V for Pd-HNC_{10}. For comparison, the E_{onset} and $E_{1/2}$ of the PdNP/HNC sample can be identified at +0.975 and +0.853 V, respectively, comparable to the performance of Pd-HNC_2 despite a higher Pd content (Table 1), suggesting that atomic Pd species in the Pd-HNC samples made dominant contributions to the ORR activity, with minor contributions from the nanoparticles. Notably, one can see that the Pd-HNC_{10} even outperformed commercial 20 wt% Pt/C (E_{onset} = +0.996 V, $E_{1/2}$ = +0.857 V), and is also superior to leading Pd-based ORR catalysts reported recently in the literature (Table 5).

Table 5. Comparison of the ORR activity between Pd-HNC and relevant Pd-based catalysts in the literature in 0.1 M KOH

Samples	$Catalyst_{metal}$ Loading (μg cm^{-2})	$E_{1/2}$ (V vs. RHE)	n	J_k (A/mg)	References (Year)
$Pd\text{-}HNC_{10}$	12.58	0.898	3.97	0.30 @ +0.85 V	This Work
$Pd\text{-}HNC_5$	7.09	0.889	3.95	0.49 @ +0.85 V	This Work
$Pd\text{-}HNC_2$	2.84	0.846	3.94	0.65 @ +0.85 V	This Work
Au-O-PdZn	40	~0.9	3.96	0.105 @ +0.90 V	[73] (2019)
Pd HBNDs	50	0.863	~4	/	[74] (2019)
fct-PdFe@Pd@NG	/	0.83	~3.9	/	[75] (2018)
$Pd/TiO_2\text{-}V_o$	~15.12	~0.82	3.8	/	[76] (2018)
$Au@Pd_{0.5}$	10.2	~0.9	3.8	0.5 @ +0.85 V	[77] (2018)
Pd nanocubes @Mo/C	20.4	0.837	~3.9	0.11 @ +0.85 V	[78] (2018)
Pd/3D-GNS-L90	~66	~0.8	~3.9	/	[79] (2018)
Pd-Net	16.9	0.84	3.98	0.62 @ +0.85 V	[80] (2018)
PdNPs	22.6	0.78	3.45	0.15 @ +0.85 V	[80] (2018)
Pd-N/3D-GNS	~40	~0.82	~4.0	/	[81] (2017)

To further analyze the ORR kinetics, the number of electron transfer (n) was estimated by $n = \frac{4i_D}{i_D + i_R/N}$, where i_R and i_D are the ring current and disk current, respectively, and N is the collection efficiency of the ring electrode (0.40, Figure 15). From Figure 14b,

one can see that the n number of the Pd-HNC$_{10}$ sample is over 3.97 at +0.85 V, even higher than that of Pt/C (3.84), indicating high selectivity toward the four-electron pathway of oxygen reduction. The Pd-HNC$_{10}$ also showed a very low H_2O_2% yield of 1.1% at +0.85 V, which was calculated by $H_2O_2\% = \frac{200i_R/N}{i_D+i_R/N}$, much lower than that of Pt/C (7.6%). In the Tafel plots (Figure 14c), Pd-HNC$_{10}$ exhibited the smallest slope of 65.3 mV dec^{-1}, in comparison to 76.9 mV dec^{-1} for PdNP/HNC, 83.5 mV dec^{-1} for Pd-HNC$_2$, and 82.4 mV dec^{-1} for Pt/C, implying efficient electron transfer to O_2 and splitting of the O-O bonds.[82]

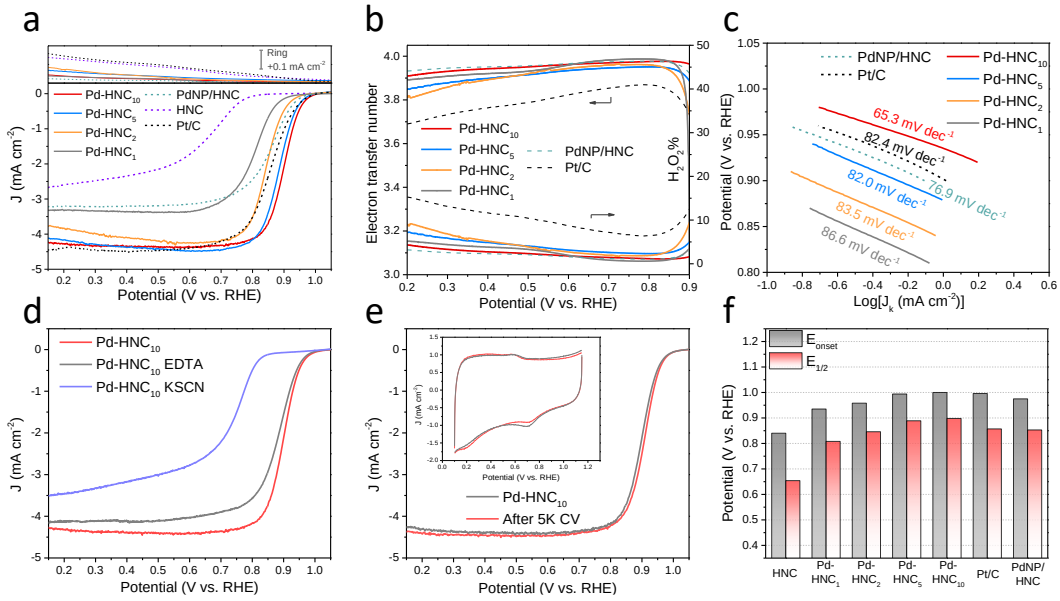

Figure 14. ORR performance of the Pd-HNC series in oxygen-saturated 0.1 M KOH. (a) Linear sweep voltammograms (LSVs) of Pd-HNC nanocomposites and control samples of HNC, PdNP/HNC, and Pt/C at the rotation rate of 1600 rpm. (b) The corresponding electron-transfer number (n, solid), yield of H_2O_2 (%), and (c) Tafel plots with the slopes shown in mV dec^{-1}. (d) Poisoning test of Pd-HNC$_{10}$ with EDTA and KSCN treatments. (e) Stability test of Pd-HNC$_{10}$ under 5000 cycles in N_2 saturated 0.1 M KOH. Inset is the corresponding cyclic voltammograms at the scan rate of 50 mV s^{-}

[1] before and after the stability test. (f) Comparison of E_{onset} and $E_{1/2}$ of the Pd-HNC series with those of HNC, PdNP/HNC and Pt/C.

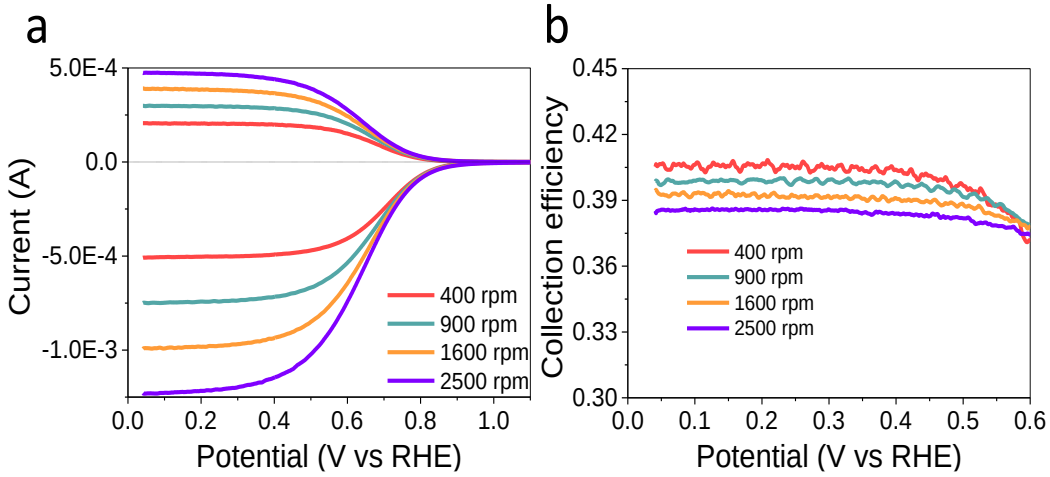

Figure 15. (a) Collection experiments by RRDE voltammetry at the rotation rates of 400 to 2500 rpm in 0.1 M KOH with 10 mM $K_3Fe(CN)_6$. The ring electrode potentia is set at +0.2 V (b) Collection efficiency (N) calculated from the ring and disk currents at varied electrode potentials. The procedure to determine the collection efficiency (N) of the ring electrode was adopted from ref. [83]. The electrolyte was 0.1 M KOH with 10 mM $K_3Fe(CN)_6$. RRDE voltammograms was acquired at the rotation rates of 400 to 2500 rpm (Figure 15a). On the disk electrode, ferricyanide was reduced into ferrocyanide, $Fe(CN)_6^{3-} + e^- \rightarrow Fe(CN)_6^{4-}$, part of which diffused to the ring electrode and was oxidized back into ferricyanide, $Fe(CN)_6^{4-} \rightarrow Fe(CN)_6^{3-} + e^-$. The disk and ring limiting currents were then used to calculate the empirical collection efficiency (N, Figure 15b), $N = |\frac{i_{Ring}}{i_{Disk}}\frac{n_D}{n_R}|$, where n_D and n_R are the numbers of electron transfer of the disk and ring reactions. From Figure 15b, the average collection efficiency (N) is estimated to be 0.40.

The ORR activity of the Pd-HNC samples in acidic media was also assessed in O_2-saturated 0.1 M $HClO_4$ at the sweep rate of 10 mV s^{-1} and the rotation rate of 1600 rpm

(Figure 16). The Pd-HNC$_{10}$ again showed the best activity among the series of samples with an E_{onset} of +0.912 V and an $E_{1/2}$ of +0.792 V.

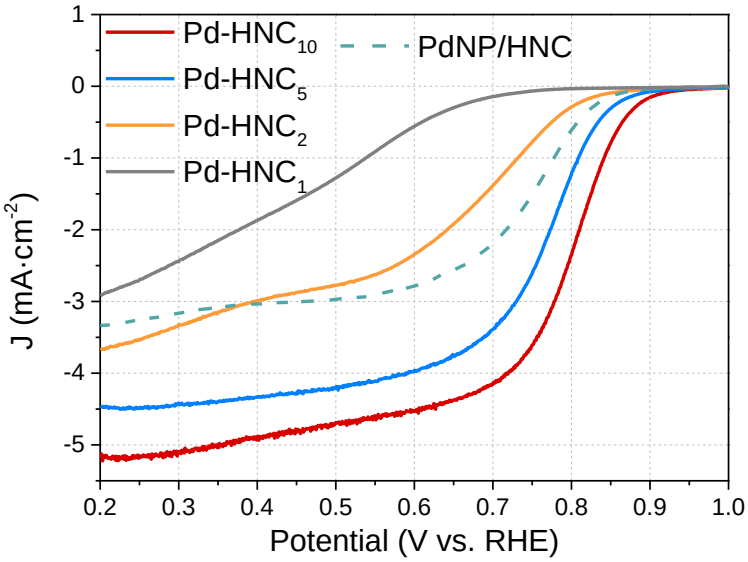

Figure 16. Linear sweep voltammograms (LSVs) of Pd-HNC nanocomposites and PdNP/HNC at the rotation rate of 1600 rpm in 0.1 M $HClO_4$. It should be noted that in acid, Pd-HNC$_2$ exhibits an ORR activity worse than PdNP/HNC, possibly because of the lack of neighboring metal atoms around the atomically dispersed Pd species that are crucial to acidic ORR.[84] In fact, the Pd-HNC$_1$ sample performs even worse in acid than in base.

In order to further distinguish the contributions of Pd nanoparticles and Pd atomic species to the ORR activity, electrochemical tests were carried out in the presence of KSCN and EDTA as the poisoning agents. From Figure 14d, one can see that when the Pd-HNC$_{10}$ sample was treated with 10 mM EDTA in the 0.1 M KOH solution, the $E_{1/2}$ shifted negatively by 20 mV and the limiting current decreased by 8%. Yet upon the addition of 10 mM KSCN into the electrolyte, the $E_{1/2}$ shifted negatively by more than 200 mV and the limiting current diminished by over 1/3, and the overall performance

resembled that of HNC alone. Note that SCN^- readily adsorbed to and blocked both Pd nanoparticles and Pd-N sites, whereas EDTA poisoned predominantly the Pd-N species (Figure 17). The different poisoning effects by KSCN and EDTA suggest that both Pd nanoparticles and Pd-N moieties contributed to the ORR activity, with Pd-N being the dominant contributor.

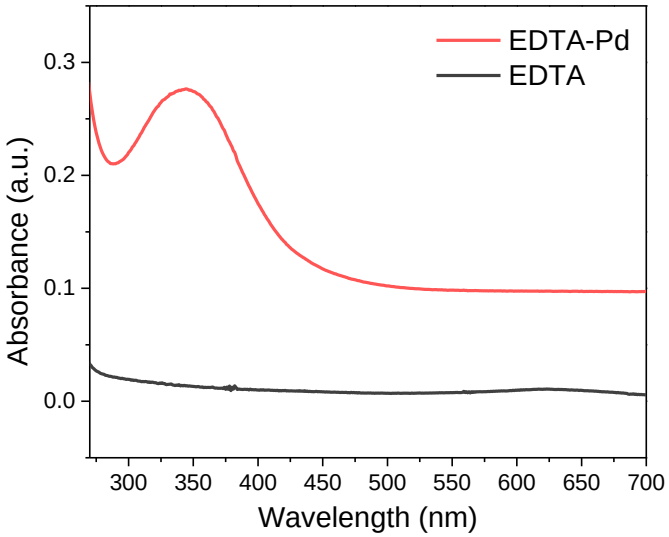

Figure 17. UV-Vis spectra of the supernatant solution collected from the Pd-HNC_{10} sample before and after EDTA treatment.

The long-term durability of the Pd-HNC sample was then evaluated by prolonged potential cycling between +0.65 and +1.05 V at the potential sweep rate of 100 mV s^{-1}. As shown in Figure 14e, after 5000 cycles, the ORR activity of Pd-HNC_{10} remained virtually invariant. Interestingly, from the cyclic voltammograms of Pd-HNC_{10} before and after 5000 potential cycles (inset to Figure 14e), one can see that the cathodic peak of PdO_x reduction became weakened after the stability test, indicating a partial loss of metallic palladium (mostly from the nanoparticles); yet the ORR activity was almost

unaffected, further confirming that indeed the ORR activity was largely due to the Pd-N atomic species.

The contributions of Pd nanoparticles and single atoms to the ORR activity can also be differentiated by correlation of the ORR activity with the concentration of the various Pd species in the Pd-HNC samples. One can see from Figure 18 that if the activity was attributed to the total mass of Pd, the linear fit of the kinetic current density (i.e., specific activity, J_k) at +0.85 V vs. the total mass of Pd (green line) is rather poor with an R^2 coefficient of only 0.777. Since results of XPS measurements showed the formation of both metallic Pd^0 and atomic Pd^{2+}, their contributions to the ORR activity were then analyzed and differentiated. When Pd^0 was assumed as the contributing source of the ORR activity, the correlation of J_k with the Pd^0 mass demonstrated a scatter plot with an even worse correlation coefficient of $R^2 = 0.379$. By contrast, when the ORR activity was correlated to the mass of the Pd^{2+} species (Pd-N active sites), linear regression of the scatter plot showed a better R^2 of 0.826, suggesting that Pd^{2+} is indeed more likely the dominating species responsible for the ORR activity. This is consistent with results from the ORR poisoning test.

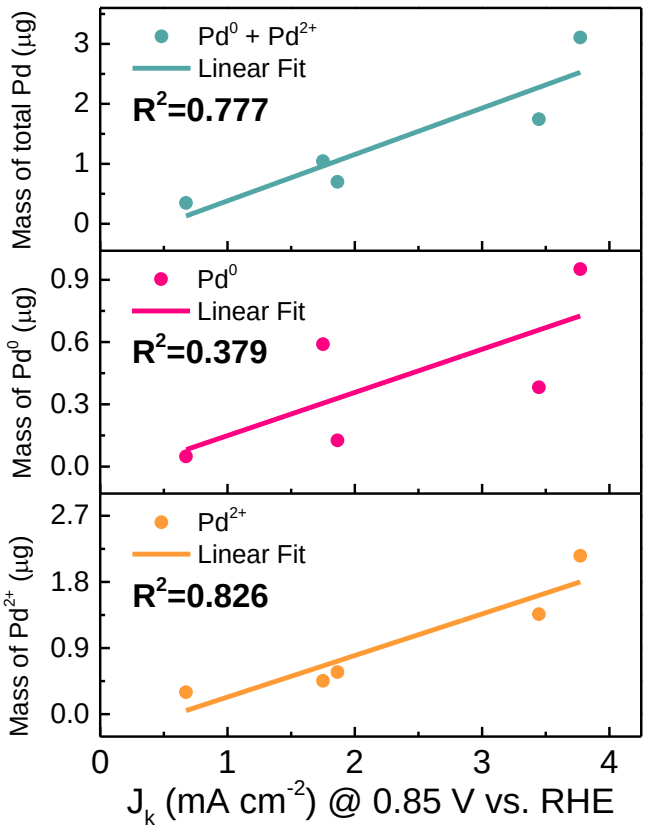

Figure 18. Linear correlation between the ORR kinetic current density (J_k at +0.85 V) and the mass of Pd^0, Pd^{2+}, or Pd^0+Pd^{2+} of Pd-HNC.

2.5 Conclusions

In this study, a facile procedure based on wet impregnation was developed, whereby Pd was atomically dispersed and enriched onto the surface of N-doped porous carbon cages derived from hollow ZIF-8 precursors. This was manifested in high-resolution TEM, XPS and XAS measurements, where Pd was mostly involved in the formation of PdN_x moieties. Electrochemically, the obtained Pd-HNC samples exhibited markedly enhanced ORR activity in alkaline media, as compared to the nanoparticle counterparts and the carbon cages alone, and the Pd-HNC_{10} sample, which

corresponded to a saturated Pd loading, even outperformed Pt/C and leading Pd-based catalysts in the literature. The remarkable ORR performance was ascribed mostly to the atomic Pd species in the samples, which were predominantly enriched on the carbon support surface. Results from this study highlights the significance of metal single atom catalysts and their surface enrichments in ORR electrocatalysis. In addition, such a unique structural scaffold can be exploited for the embedment of a wide range of metal centers for diverse applications.

2.6 Reference

1. M. K. Debe. *Nature* **2012**, *486*, 43-51.

2. Z. W. Seh, J. Kibsgaard, C. F. Dickens, I. B. Chorkendorff, J. K. Norskov, T. F. Jaramillo. *Science* **2017**, *355*, eaad4998.

3. M. H. Shao, Q. W. Chang, J. P. Dodelet, R. Chenitz. *Chem Rev* **2016**, *116*, 3594-3657.

4. D. V. Esposito, J. G. G. Chen. *Energ Environ Sci* **2011**, *4*, 3900-3912.

5. C. Chen, Y. J. Kang, Z. Y. Huo, Z. W. Zhu, W. Y. Huang, H. L. L. Xin, J. D. Snyder, D. G. Li, J. A. Herron, M. Mavrikakis, M. F. Chi, K. L. More, Y. D. Li, N. M. Markovic, G. A. Somorjai, P. D. Yang, V. R. Stamenkovic. *Science* **2014**, *343*, 1339-1343.

6. P. P. Lopes, D. Strmcnik, D. Tripkovic, J. G. Connell, V. Stamenkovic, N. M. Markovic. *Acs Catal* **2016**, *6*, 2536-2544.

7. V. R. Stamenkovic, D. Strmcnik, P. P. Lopes, N. M. Markovic. *Nat Mater* **2017**, *16*, 57-69.

8. J. K. Norskov, J. Rossmeisl, A. Logadottir, L. Lindqvist, J. R. Kitchin, T. Bligaard, H. Jonsson. *Journal of Physical Chemistry B* **2004**, *108*, 17886-17892.

9. D. L. Wang, H. L. L. Xin, R. Hovden, H. S. Wang, Y. C. Yu, D. A. Muller, F. J. DiSalvo, H. D. Abruna. *Nat Mater* **2013**, *12*, 81-87.

10. Z. M. Cui, H. Chen, M. T. Zhao, F. J. DiSalvo. *Nano Lett* **2016**, *16*, 2560-2566.

11. Y. Xiong, Y. Yang, X. R. Feng, F. J. DiSalvo, H. D. Abruna. *J Am Chem Soc* **2019**, *141*, 4412-4421.

12. J. Jiang, W. Ding, W. Li, Z. Wei. *Chem* **2020**, *6*, 431-447.

13. G. M. Jiang, H. Y. Zhu, X. Zhang, B. Shen, L. H. Wu, S. Zhang, G. Lu, Z. B. Wu, S. H. Sun. *Acs Nano* **2015**, *9*, 11014-11022.

14. Y. Wang, Y. Yang, S. F. Jia, X. M. Wang, K. J. Lyu, Y. Q. Peng, H. Zheng, X. Wei, H. Ren, L. Xiao, J. B. Wang, D. A. Muller, H. D. Abruna, B. O. E. Hwang, J. T. Lu, L. Zhuang. *Nat Commun* **2019**, *10*, 1506.

15. Y. Peng, B. Z. Lu, N. Wang, J. E. Lu, C. H. Li, Y. Ping, S. W. Chen. *Acs Appl Mater Inter* **2019**, *11*, 24707-24714.

16. J. Deng, D. H. Deng, X. H. Bao. *Adv Mater* **2017**, *29*, 1606967.

17. G. Q. He, Y. Song, K. Liu, A. Walter, S. Chen, S. W. Chen. *Acs Catal* **2013**, *3*, 831-838.

18. Y. P. Zhu, C. X. Guo, Y. Zheng, S. Z. Qiao. *Accounts Chem Res* **2017**, *50*, 915-923.

19. R. Arrigo, M. E. Schuster, Z. L. Xie, Y. M. Yi, G. Wowsnick, L. L. Sun, K. E. Hermann, M. Friedrich, P. Kast, M. Havecker, A. Knop-Gericke, R. Schlogl. *Acs Catal* **2015**, *5*, 2740-2753.

20. J. Liu, M. G. Jiao, L. L. Lu, H. M. Barkholtz, Y. P. Li, Y. Wang, L. H. Jiang, Z. J. Wu, D. J. Liu, L. Zhuang, C. Ma, J. Zeng, B. S. Zhang, D. S. Su, P. Song, W. Xing, W. L. Xu, Y. Wang, Z. Jiang, G. Q. Sun. *Nat Commun* **2017**, *8*, 15938.

21. H. L. Fei, J. C. Dong, Y. X. Feng, C. S. Allen, C. Z. Wan, B. Volosskiy, M. F. Li, Z. P. Zhao, Y. L. Wang, H. T. Sun, P. F. An, W. X. Chen, Z. Y. Guo, C. Lee, D. L. Chen, I. Shakir, M. J. Liu, T. D. Hu, Y. D. Li, A. I. Kirkland, X. F. Duan, Y. Huang. *Nat Catal* **2018**, *1*, 63-72.

22. X. P. Han, X. F. Ling, D. S. Yu, D. Y. Xie, L. L. Li, S. J. Peng, C. Zhong, N. Q. Zhao, Y. D. Deng, W. B. Hu. *Adv Mater* **2019**, 1905622.

23. S. H. Lee, J. Kim, D. Y. Chung, J. M. Yoo, H. S. Lee, M. J. Kim, B. S. Mun, S. G. Kwon, Y. E. Sung, T. Hyeon. *J Am Chem Soc* **2019**, *141*, 2035-2045.

24. X. Wan, X. F. Liu, Y. C. Li, R. H. Yu, L. R. Zheng, W. S. Yan, H. Wang, M. Xu, J. L. Shui. *Nat Catal* **2019**, *2*, 259-268.

25. T. He, Y. Q. Zhang, Y. Chen, Z. Z. Zhang, H. Y. Wang, Y. F. Hu, M. Liu, C. W. Pao, J. L. Chen, L. Y. Chang, Z. F. Sun, J. Xiang, Y. Zhang, S. W. Chen. *Journal of Materials Chemistry A* **2019**, *7*, 20840-20846.

26. Y. F. Ye, F. Cai, H. B. Li, H. H. Wu, G. X. Wang, Y. S. Li, S. Miao, S. H. Xie, R. Si, J. Wang, X. H. Bao. *Nano Energy* **2017**, *38*, 281-289.

27. P. Q. Yin, T. Yao, Y. Wu, L. R. Zheng, Y. Lin, W. Liu, H. X. Ju, J. F. Zhu, X. Hong, Z. X. Deng, G. Zhou, S. Q. Wei, Y. D. Li. *Angew Chem Int Edit* **2016**, *55*, 10800-10805.

28. H. H. Wu, H. B. Li, X. F. Zhao, Q. F. Liu, J. Wang, J. P. Xiao, S. H. Xie, R. Si, F. Yang, S. Miao, X. G. Guo, G. X. Wang, X. H. Bao. *Energ Environ Sci* **2016**, *9*, 3736-3745.

29. Z. K. Yang, B. X. Chen, W. X. Chen, Y. T. Qu, F. Y. Zhou, C. M. Zhao, Q. Xu, Q. H. Zhang, X. Z. Duan, Y. Wu. *Nat Commun* **2019**, *10*, 3734.

30. B. Z. Lu, T. J. Smart, D. D. Qin, J. E. Lu, N. Wang, L. M. Chen, Y. Peng, Y. Ping, S. W. Chen. *Chem Mater* **2017**, *29*, 5617-5628.

31. C. H. Zhang, J. W. Sha, H. L. Fei, M. J. Liu, S. Yazdi, J. B. Zhang, Q. F. Zhong, X. L. Zou, N. Q. Zhao, H. S. Yu, Z. Jiang, E. Ringe, B. I. Yakobson, J. C. Dong, D. L. Chen, J. M. Tour. *Acs Nano* **2017**, *11*, 6930-6941.

32. S. Q. Zhou, L. Shang, Y. X. Zhao, R. Shi, G. I. N. Waterhouse, Y. C. Huang, L. R. Zheng, T. R. Zhang. *Adv Mater* **2019**, *31*, 1900509.

33. S. J. Wei, A. Li, J. C. Liu, Z. Li, W. X. Chen, Y. Gong, Q. H. Zhang, W. C. Cheong, Y. Wang, L. R. Zheng, H. Xiao, C. Chen, D. S. Wang, Q. Peng, L. Gu, X. D. Han, J. Li, Y. D. Li. *Nature Nanotechnology* **2018**, *13*, 856-861.

34. D. Malko, A. Kucernak, T. Lopes. *Nat Commun* **2016**, *7*, 13285.

35. Y. Peng, B. Z. Lu, S. W. Chen. *Adv Mater* **2018**, *30*, 1801995.

36. O. Y. Podyacheva, D. A. Bulushev, A. N. Suboch, D. A. Svintsitskiy, A. S. Lisitsyn, E. Modin, A. Chuvilin, E. Y. Gerasimov, V. I. Sobolev, V. N. Parmon. *Chemsuschem* **2018**, *11*, 3724-3727.

37. D. A. Bulushev, M. Zacharska, E. V. Shlyakhova, A. L. Chuvilin, Y. N. Guo, S. Beloshapkin, A. V. Okotrub, L. G. Bulusheva. *Acs Catal* **2016**, *6*, 681-691.

38. M. Passaponti, M. Savastano, M. P. Clares, M. Inclan, A. Lavacchi, A. Bianchi, E. Garcia-Espana, M. Innocenti. *Inorg Chem* **2018**, *57*, 14484-14488.

39. W. K. Xiang, Y. H. Zhao, Z. Jiang, X. P. Li, H. Zhang, Y. Sun, Z. J. Ning, F. P. Du, P. Gao, J. Qian, K. Kato, M. Yamauchi, Y. H. Sun. *Journal of Materials Chemistry A* **2018**, *6*, 23366-23377.

40. Y. L. Zhu, W. Zhou, Y. B. Chen, J. Yu, X. M. Xu, C. Su, M. O. Tade, Z. P. Shao. *Chem Mater* **2015**, *27*, 3048-3054.

41. Y. Peng, B. Z. Lu, L. M. Chen, N. Wang, J. E. Lu, Y. Ping, S. W. Chen. *Journal of Materials Chemistry A* **2017**, *5*, 18261-18269.

42. Y. Peng, W. Z. Pan, N. Wang, J. E. Lu, S. W. Chen. *Chemsuschem* **2018**, *11*, 130-136.

43. F. C. Zheng, Y. Yang, Q. W. Chen. *Nat Commun* **2014**, *5*, 5261.

44. Z. Q. Zhang, Y. G. Chen, L. Q. Zhou, C. Chen, Z. Han, B. S. Zhang, Q. Wu, L. J. Yang, L. Y. Du, Y. F. Bu, P. Wang, X. Z. Wang, H. Yang, Z. Hu. *Nat Commun* **2019**, *10*, 1657.

45. J. Yang, Z. Y. Qiu, C. M. Zhao, W. C. Wei, W. X. Chen, Z. J. Li, Y. T. Qu, J. C. Dong, J. Luo, Z. Y. Li, Y. Wu. *Angew Chem Int Edit* **2018**, *57*, 14095-14100.

46. B. Ravel, M. Newville. *J Synchrotron Radiat* **2005**, *12*, 537-541.

47. Q. H. Yang, C. C. Yang, C. H. Lin, H. L. Jiang. *Angew Chem Int Edit* **2019**, *58*, 3511-3515.

48. M. Hu, Y. Ju, K. Liang, T. Suma, J. W. Cui, F. Caruso. *Adv Funct Mater* **2016**, *26*, 5827-5834.

49. T. Liu, W. L. Liu, M. K. Zhang, W. Y. Yu, F. Gao, C. X. Li, S. B. Wang, J. Feng, X. Z. Zhang. *Acs Nano* **2018**, *12*, 12181-12192.

50. W. Zhang, X. F. Jiang, Y. Y. Zhao, A. Carne-Sanchez, V. Malgras, J. Kim, J. H. Kim, S. B. Wang, J. Liu, J. S. Jiang, Y. Yamauchi, M. Hu. *Chem Sci* **2017**, *8*, 3538-3546.

51. S. Choi, M. Oh. *Angew Chem Int Edit* **2019**, *58*, 866-871.

52. F. Zhang, Y. Y. Wei, X. T. Wu, H. Y. Jiang, W. Wang, H. X. Li. *J Am Chem Soc* **2014**, *136*, 13963-13966.

53. C. P. Deming, R. Mercado, J. E. Lu, V. Gadiraju, M. Khan, S. W. Chen. *Acs Sustain Chem Eng* **2016**, *4*, 6580-6589.

54. V. Mazumder, S. Sun. *J Am Chem Soc* **2009**, *131*, 4588-4589.

55. J. Ju, W. Chen. *Anal Chem* **2015**, *87*, 1903-1910.

56. F. Huang, Y. C. Deng, Y. L. Chen, X. B. Cai, M. Peng, Z. M. Jia, P. J. Ren, D. Q. Xiao, X. D. Wen, N. Wang, H. Y. Liu, D. Ma. *J Am Chem Soc* **2018**, *140*, 13142-13146.

57. V. Z. Radkevich, T. L. Senko, K. Wilson, L. M. Grishenko, A. N. Zaderko, V. Y. Diyuk. *Appl Catal a-Gen* **2008**, *335*, 241-251.

58. J. Yang, C. G. Tian, L. Wang, H. G. Fu. *J Mater Chem* **2011**, *21*, 3384-3390.

59. M. Zacharska, L. G. Bulusheva, A. S. Lisitsyn, S. Beloshapkin, Y. N. Guo, A. L. Chuvilin, E. V. Shlyakhova, O. Y. Podyacheva, J. J. Leahy, A. V. Okotrub, D. A. Bulushev. *Chemsuschem* **2017**, *10*, 720-730.

60. F. N. Wang, J. M. Xu, X. Z. Shao, X. Su, Y. Q. Huang, T. Zhang. *Chemsuschem* **2016**, *9*, 246-251.

61. S. Y. Ding, J. Gao, Q. Wang, Y. Zhang, W. G. Song, C. Y. Su, W. Wang. *J Am Chem Soc* **2011**, *133*, 19816-19822.

62. L. Y. Li, H. X. Zhao, J. Y. Wang, R. H. Wang. *Acs Nano* **2014**, *8*, 5352-5364.

63. H. Gabasch, W. Unterberger, K. Hayek, B. Klotzer, G. Kresse, C. Klein, M. Schmid, P. Varga. *Surf Sci* **2006**, *600*, 205-218.

64. D. Zemlyanov, B. Aszalos-Kiss, E. Kleimenov, D. Teschner, S. Zafeiratos, M. Havecker, A. Knop-Gericke, R. Schlogl, H. Gabasch, W. Unterberger, K. Hayek, B. Koltzer. *Surf Sci* **2006**, *600*, 983-994.

65. H. Gabasch, W. Unterberger, K. Hayek, B. Klotzer, E. Kleimenov, D. Teschner, S. Zafeiratos, M. Havecker, A. Knop-Gericke, R. Schlogl, J. Y. Han, F. H. Ribeiro, B. Aszalos-Kiss, T. Curtin, D. Zemlyanov. *Surf Sci* **2006**, *600*, 2980-2989.

66. J. Wang, Z. Q. Huang, W. Liu, C. R. Chang, H. L. Tang, Z. J. Li, W. X. Chen, C. J. Jia, T. Yao, S. Q. Wei, Y. Wu, Y. D. Lie. *J Am Chem Soc* **2017**, *139*, 17281-17284.

67. G. Vile, D. Albani, M. Nachtegaal, Z. P. Chen, D. Dontsova, M. Antonietti, N. Lopez, J. Perez-Ramirez. *Angew Chem Int Edit* **2015**, *54*, 11265-11269.

68. J. B. Xi, H. Y. Sung, D. Wang, Z. Y. Zhang, X. M. Duan, J. W. Xiao, F. Xiao, L. M. Liu, S. Wang. *Appl Catal B-Environ* **2018**, *225*, 291-297.

69. X. N. Zang, C. Y. Jian, T. S. Zhu, Z. Fan, W. L. Wang, M. S. Wei, B. X. Li, M. F. Diaz, P. Ashby, Z. M. Lu, Y. Chu, Z. Z. Wang, X. R. Ding, Y. X. Xie, J. H. Chen, J. N. Hohman, M. Sanghadasa, J. C. Grossman, L. W. Lin. *Nat Commun* **2019**, *10*, 3112.

70. A. Kodre, I. Arcon, J. Batista, A. Pintar. *J Synchrotron Radiat* **1999**, *6*, 458-459.

71. K. Koh, M. Jeon, D. M. Chevrier, P. Zhang, C. W. Yoon, T. Asefa. *Appl Catal B-Environ* **2017**, *203*, 820-828.

72. W. X. Huang, S. R. Zhang, Y. Tang, Y. T. Li, L. Nguyen, Y. Y. Li, J. J. Shan, D. Q. Xiao, R. Gagne, A. I. Frenkel, F. Tao. *Angew Chem Int Edit* **2016**, *55*, 13441-13445.

73. Y. Yang, W. P. Xiao, X. R. Feng, Y. Xiong, M. X. Gong, T. Shen, Y. Lu, H. D. Abruna, D. L. Wang. *Acs Nano* **2019**, *13*, 5968-5974.

74. C. Fan, Z. H. Huang, C. Wang, X. Y. Hu, X. Y. Qiu, P. L. She, D. M. Sun, Y. W. Tang. *Chem-Eur J* **2019**, *25*, 4920-4926.

75. K. Maiti, J. Balamurugan, S. G. Peera, N. H. Kim, J. H. Lee. *Acs Appl Mater Inter* **2018**, *10*, 18734-18745.

76. J. Li, H. Zhou, H. Zhuo, Z. Z. Wei, G. L. Zhuang, X. Zhong, S. W. Deng, X. N. Li, J. G. Wang. *Journal of Materials Chemistry A* **2018**, *6*, 2264-2272.

77. Q. Xue, J. Bai, C. C. Han, P. Chen, J. X. Jiang, Y. Chen. *Acs Catal* **2018**, *8*, 11287-11295.

78. W. Yan, W. Wu, K. Wang, Z. H. Tang, S. W. Chen. *Int J Hydrogen Energ* **2018**, *43*, 17132-17141.

79. S. Kabir, A. Serov, P. Atanassov. *J Power Sources* **2018**, *375*, 255-264.

80. H. Begum, M. S. Ahmed, S. Cho, S. Jeon. *Int J Hydrogen Energ* **2018**, *43*, 229-238.

81. S. Kabir, A. Serov, K. Artyushkova, P. Atanassov. *Acs Catal* **2017**, *7*, 6609-6618.

82. J. Chlistunoff. *J Phys Chem C* **2011**, *115*, 6496-6507.

83. U. A. Paulus, T. J. Schmidt, H. A. Gasteiger, R. J. Behm. *J Electroanal Chem* **2001**, *495*, 134-145.

84. J. C. Dong, X. G. Zhang, V. Briega-Martos, X. Jin, J. Yang, S. Chen, Z. L. Yang, D. Y. Wu, J. M. Feliu, C. T. Williams, Z. Q. Tian, J. F. Li. *Nat Energy* **2019**, *4*, 60-67.

Chapter 3 Oxygen Reduction Reaction Catalyzed by Carbon Composites with Ruthenium-Doped Iron Oxide Nanoparticles

3.1 Abstract

Carbon nanocomposites based on transition-metal oxides have been attracting extensive attention as cost-effective catalysts towards oxygen reduction reaction (ORR). However, the activity remains subpar as compared to state-of-the-art platinum catalysts. One way to enhance the ORR performance is to dope a second metal into the nanocomposite to manipulate the electronic structure and hence the interactions with key reaction intermediates. Herein, dual metals (Ru and Fe) and nitrogen codoped carbon (RuFe-NC) nanocomposites were synthesized by controlled pyrolysis of a Ru-Fe trinuclear complex along with zeolitic imidazolate framework 8. The obtained porous nanocomposites consisted of Ru-doped Fe_2O_3 nanoparticles embedded within a carbon scaffold and exhibited an ORR activity in alkaline media rivaling that of commercial Pt/C, which was also markedly better than those of the monometallic counterparts and nanocomposites prepared with a simple mixture of the individual monometallic compound precursors. Structural characterization suggests that the use of the trinuclear complex facilitated the atomic dispersion of ruthenium within the iron oxide nanoparticles and charge transfer between the metal centers led to a high ORR activity. Results from this study suggest that rational design of heteronuclear complexes may be a unique strategy in the structural engineering of carbon-metal nanocomposites for high-performance electrocatalysis.

3.2 Introduction

Fuel cell technologies have been attracting extensive interest as an integral part of the sustainable economy.[1] In fuel cell operation, small molecule fuels are oxidized at the

anode and oxygen is reduced at the cathode, where both reactions necessitate appropriate catalysts so as to boost the electron-transfer kinetics and produce a sufficiently high current density for practical applications.[2-5] Of these, oxygen reduction reaction (ORR) at the cathode has been recognized as a major bottleneck that limits the fuel cell performance, largely because of the complex reaction pathways and sluggish electron-transfer kinetics. Towards this end, platinum-based nanoparticles have been used extensively as the catalysts of choice for ORR.[4-7] Yet, the high cost and low natural abundance of platinum have significantly hampered the wide-spread application of fuel cell technologies. Thus, in recent studies, a range of strategies have been developed to reduce the metal loadings (and costs) and concurrently retain/enhance the catalytic activity.[8-13] One effective route is to exploit low-cost 3d transition metals (i.e., Fe, Co, Ni, and Cu) and their derivatives (i.e., oxides, carbides, and nitrides) as the catalytic active centers.[14-17]

Among these various candidates, transition metal oxides (TMOs) have been extensively investigated with promising advances.[18-21] Nevertheless, it should be noted that the intrinsic activity of TMOs has remained mostly uncompetitive to that of the commercial Pt/C benchmark. For instance, theoretical studies based on first principles calculations have shown that the FeO_5, CoO_5, and NiO_5 centers are too weak for the adsorption of O* species, while CrO_5 and MnO_5 are too strong rendering the desorption of O* difficult, owning to their different electronic structures.[22] Thus, none of these is ideal for ORR electrocatalysis. To increase their activity towards ORR, a variety of strategies have been utilized to modify TMOs. For example, Wu et al.[23] grew Fe_3O_4

nanoparticles on N-doped graphene aerogel and found that the substrate significantly increased the onset potential and cathodic current density, in contrast to those with (undoped) carbon black. Ma et al.[24] also observed that with N-doped carbon black, ultrafine $FeO_{1.4}$ nanoparticles exhibited an ORR activity competitive to that of Pt/C. Fan et al.[25] showed that the carbon substrate could benefit FeO_x with rapid mass transfer and catalyst stability.

In addition to structural engineering of the substrate, compositional manipulation of the oxide materials is another viable route with dual- or even tri-metal centers, where the metal-to-metal charge transfer can be exploited for enhanced electrical conductivity and improved ORR activity. For instance, Gao et al.[26] atomically dispersed Pt on α-Fe_2O_3 and observed a dramatically enhanced ORR activity with a half-wave potential ($E_{1/2}$) of +1.05 V vs. reversible hydrogen electrode (RHE), owning to the strong electronic coupling of the Pt-Fe atomic pairs. Such a synergistic effect facilitated the adsorption of O_2 and dissociation of the O=O bonds. Wei et al.[27] found that Ru dopants could facilitate O_2 adsorption on Co_3O_4 and significantly improve the ORR activity with $E_{1/2}$ increased from +0.32 to +0.77 V. In fact, Ru has been widely utilized as dopants of TMOs in various oxygen-involved reactions, due to its optimal affinity to oxygen intermediate species.[8,28] Theoretical calculations have shown that Ru can serve as the active sites on SnO_2 for the adsorption of oxygen species owning to the delocalization of electrons.[29] Dong et al.[30] also showed that Ru could regulate the charge transfer among the Cr, Co, and oxygen species. That is, the introduction of Ru

into TMOs may tune their electronic structures and improve the ORR activity due to enhanced interactions with O*.

Herein, nanocomposites based on Ru-doped Fe_2O_3 nanoparticles supported on porous N-doped carbon were prepared by controlled pyrolysis of a Ru-Fe trinuclear complex ($[(DMAP)_4Ru^{II}\{(\mu\text{-}NC)Fe^{III}(CN)_5\}_2](PPh_4)_4$, $Ru(LFe)_2$, with DMAP = 4-(dimethylamino)pyridine and PPh_4 = tetraphenylphosphonium)[31] as the metal sources and zeolitic imidazolate framework-8 (ZIF-8) as the carbon and nitrogen precursor. The resulting RuFe-NC nanocomposites exhibited a hierarchical porous structure, with abundant nitrogen dopants in the carbon scaffold and Ru homogeneously doped into the Fe_2O_3 nanoparticles. By contrast, for the control sample prepared with a physical mixture of ZIF-8 and individual Fe and Ru metal salts at equivalent feeds, partial phase segregation was observed between Fe and Ru. Notably, in alkaline media, RuFe-NC displayed an ORR activity rivalling that of commercial Pt/C and was the best among the metal, nitrogen-codoped carbon composites. Results from this study highlight the significance of pre-designed metal precursors in spatial control of dual metal oxide nanoparticles in carbon nanocomposites for high-performance electrocatalysis.

3.3 Experimental Section

Chemicals

Dichlorotetrakis(dimethylsulfoxide)ruthenium(II) ($cis\text{-}Ru(DMSO)_4Cl_2$), tetraphenylphosphonium ferricyanide ($(PPh_4)_3[Fe(CN)_6]$), $Ru(LFe)_2$, and ZIF-8 were prepared according to methods described in the literature.[31,32] All other chemicals and

reagents were commercially available and used as received without further purification. Water was supplied with a Barnstead Nanopure Water system (18 MΩ cm).

Sample preparation

To prepare the RuFe-NC composites, 0.1 g (0.4 mmol) of ZIF-8 was mixed with 0.01 g (0.004 mmol) of $Ru(LFe)_2$ synthesized above in 10 mL of hexane under sonication for 10 min and then under magnetic stirring for 2 h at room temperature. The solid was then collected by centrifugation at 6000 rpm for 5 min and dried under vacuum at 50 °C for 12 h. The resulting ZIF-8@$Ru(LFe)_2$ precursor was then loaded onto a ceramic boat, which was transferred to a tube furnace and heated at 900 °C for 2 h under a nitrogen atmosphere, producing RuFe-NC.

A series of control samples were prepared in the same fashion: (i) NC by direct pyrolysis of ZIF-8, (ii) Ru-NC by a mixture of 0.1 g (0.4 mmol) of ZIF-8, 0.002 g (0.004 mmol) of cis-$Ru(DMSO)_4Cl_2$, and 0.003 g of DMAP, (iii) Fe-NC by 0.1 g (0.4 mmol) of ZIF-8 and 0.01 g $(PPh_4)_3[Fe(CN)_6]$, and (iv) RuFe-NC_{mix} by 0.1 g (0.4 mmol) of ZIF-8, 0.002 g (0.004 mmol) of cis-$Ru(DMSO)_4Cl_2$, 0.003 g of DMAP and 0.01 g of $(PPh_4)_3[Fe(CN)_6]$.

Characterizations

Transmission electron microscopic (TEM) measurements were carried out on a JEOL JEM-2100F electron microscope. Scanning electron microscopy (SEM) and energy dispersive spectroscopic (EDS) mapping studies were carried out with an Apreo SEM microscope. X-ray diffraction (XRD) patterns were acquired with a Bruker D8 Advance diffractometer with Cu K_α radiation (λ = 0.15418 nm). X-ray photoelectron

spectra (XPS) were obtained with a PHI-5400 XPS instrument with an Al K_α source operated at 350 W and 10^{-9} Torr. X-ray absorption spectroscopy (XAS) measurements were carried out at 10 K on beamline 4-1 at the Stanford Synchrotron Radiation Light source using an Oxford liquid helium cryostat. Nitrogen sorption isotherms were acquired with a Micromeritics ASAP 2020 porosimetry system at 77.3 K. UV−vis absorption spectra were collected on a PerkinElmer Lambda 35 UV−vis spectrometer. Infrared spectroscopic measurements were conducted with a PerkinElmer Spectrum One FTIR spectrometer. Inductively coupled plasma-optical emission spectrometry (ICP-OES) measurements were conducted with an iCap 7400 analyzer.

Electrochemistry

The electrochemical tests were carried out on a CHI 710 electrochemical workstation in a standard three-electrode configuration. A graphite rod was used as the counter electrode, a Ag/AgCl in 0.1 M KCl as the reference electrode, and a polished rotating (gold) ring-(glassy carbon) disk electrode (RRDE, from Pine Instrument Co.) as the working electrode. The Ag/AgCl electrode was calibrated against an RHE and all potentials in the present study were referenced to this RHE. During the ORR tests, the ring potential was set at +1.5 V vs RHE. To prepare the catalyst inks, 2 mg of the samples obtained above was added into 1 mL of an isopropanol/water (3:1 v/v) mixture and 10 μL of a 100 wt% Nafion solution. The suspension was sonicated to form a homogeneous ink. 20 μL of the ink was then dropcast onto the glassy carbon disk electrode (surface area 0.246 cm^2), dried at room temperature, and coated with 5 μL of

a 20 wt % Nafion solution, corresponding to a catalyst loading of 0.162 mg cm^{-2}. A same loading of commercial 20% Pt/C was used in the test.

3.4 Results and discussion

3.4.1 Synthesis and morphological characterization

The synthetic procedure of the RuFe-NC composite consists of three major steps, as shown in Scheme 1. The first step is the synthesis of the $Ru(LFe)_2$ trinuclear complex by simple refluxing of cis-$Ru(DMSO)_4Cl_2$, DMAP, and $(PPh_4)_3[Fe(CN)_6]$ (Figure 1-3),[31] where one Ru atom is bridged by two cyanide (CN) ligands to two Fe centers. Second, rhombic dodecahedral ZIF-8 crystals were synthesized by mixing 2-methylimidazole and zinc nitrate salts,[33,34] onto which was adsorbed the $Ru(LFe)_2$ complex in hexane. Third, controlled pyrolysis of the ZIF-8@$Ru(LFe)_2$ mixture at 900 °C for 2 h in a nitrogen atmosphere led to the production of porous carbons doped with Ru and Fe (RuFe-NC). Control samples of RuFe-NC_{mix}, Ru-NC, Fe-NC, and NC were synthesized in the same fashion.

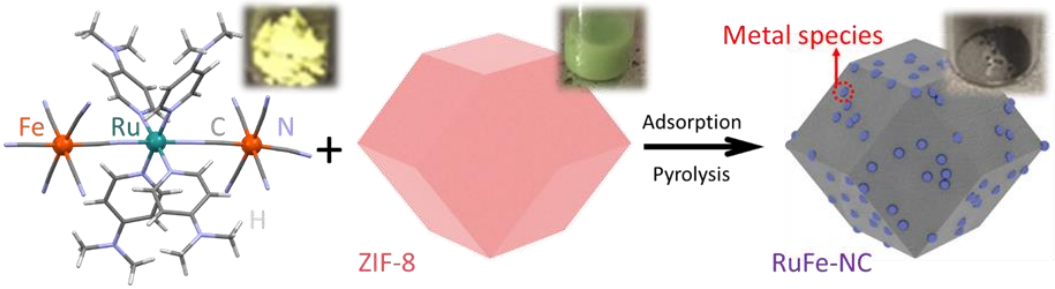

Scheme 1. Molecular structure of the $Ru(LFe)_2$ complex and the synthetic procedure of the RuFe-NC composite. Insets show the photographs of the products at different reaction stages.

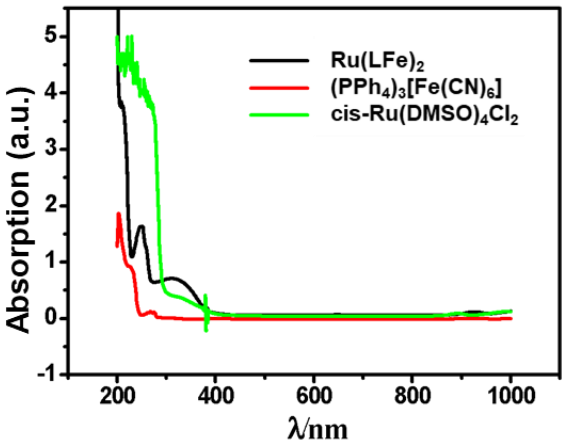

Figure 1. UV-Vis spectra of $Ru(LFe)_2$, $cis\text{-}Ru(DMSO)_4Cl_2$, and $(PPh_4)_3[Fe(CN)_6]$.

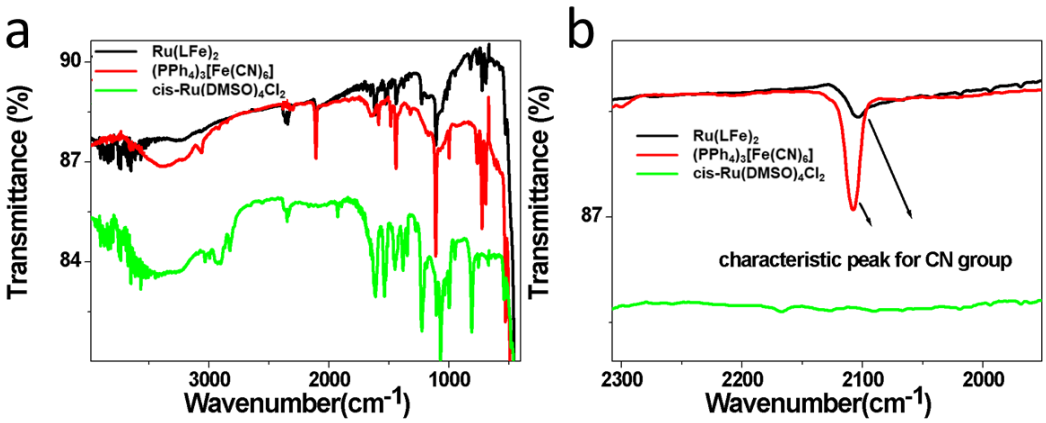

Figure 2. (a) FTIR spectra of $Ru(LFe)_2$, $cis\text{-}Ru(DMSO)_4Cl_2$, and $(PPh_4)_3[Fe(CN)_6]$, and (b) the zoom in of the region between 2300 and 1950 cm^{-1}.

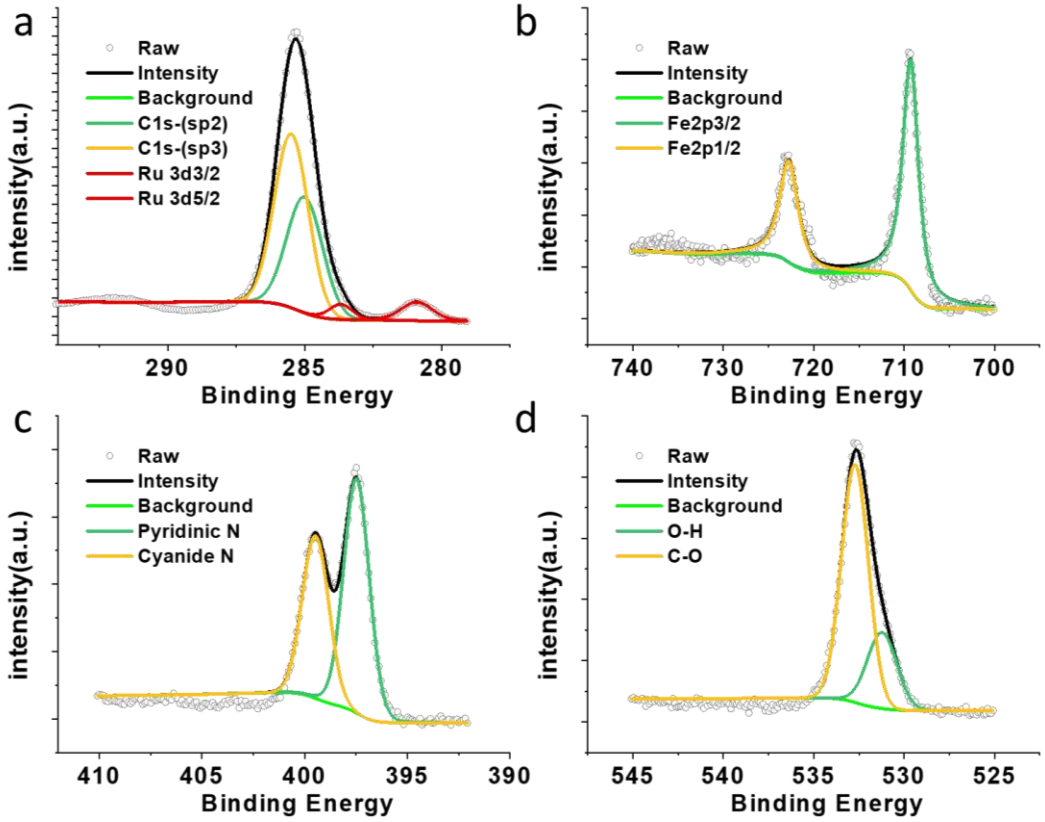

Figure 3. High-resolution XPS scans of the (a) C 1s and Ru 3d, (b) Fe 2p, (c) N 1s and (d) O 1s electrons of the $Ru(LFe)_2$ complex. Black curves are experimental data and colored curves are deconvolution fits.

The porous structure of RuFe-NC was confirmed by Brunauer–Emmett–Teller (BET) measurements. As shown in Figure 4a, the RuFe-NC, RuFe-NC_{mix}, Ru-NC, Fe-NC, and NC samples all exhibited an H_4-type hysteresis loop in the N_2 sorption isotherms, suggesting the formation of a mesoporous structure within the carbon matrices, and RuFe-NC shows an abrupt increase of the adsorbed N_2 quantity at relatively low pressures, indicative of a large number of micropores. Notably, the specific surface area varied markedly among the sample series, 507.6 $m^2 g^{-1}$ for RuFe-NC, 540.2 $m^2 g^{-1}$ for RuFe-NC_{mix}, 452.3 $m^2 g^{-1}$ for Ru-NC, 442.7 $m^2 g^{-1}$ for Fe-NC, and only 163.2 $m^2 g^{-1}$ for

NC, suggesting that the metal precursors actually behaved as effective porogens due to the high thermal volatility.[35] In addition, by the nonlocal density functional theory (NLDFT), the pore size distributions were then derived and depicted in Figure 4b. Both RuFe-NC and NC can be seen to entail mesopores in the range of 1 to 2 nm, while RuFe-NC_{mix} has a large portion of micropores at 0.8 nm. As for both Ru-NC and Fe-NC, the micropore fraction was relatively small, in comparison to the dual-metal counterparts. The RuFe-NC sample also showed a larger fraction of mesopores and lower fraction of micropores than NC, as confirmed from the cumulative pore volume in Figure 5. The enhanced surface area and porosity of the metal-containing nanocomposites is anticipated to facilitate mass transfer and accessibility of the catalytic active sites,[35] as demonstrated below in electrochemical measurements.

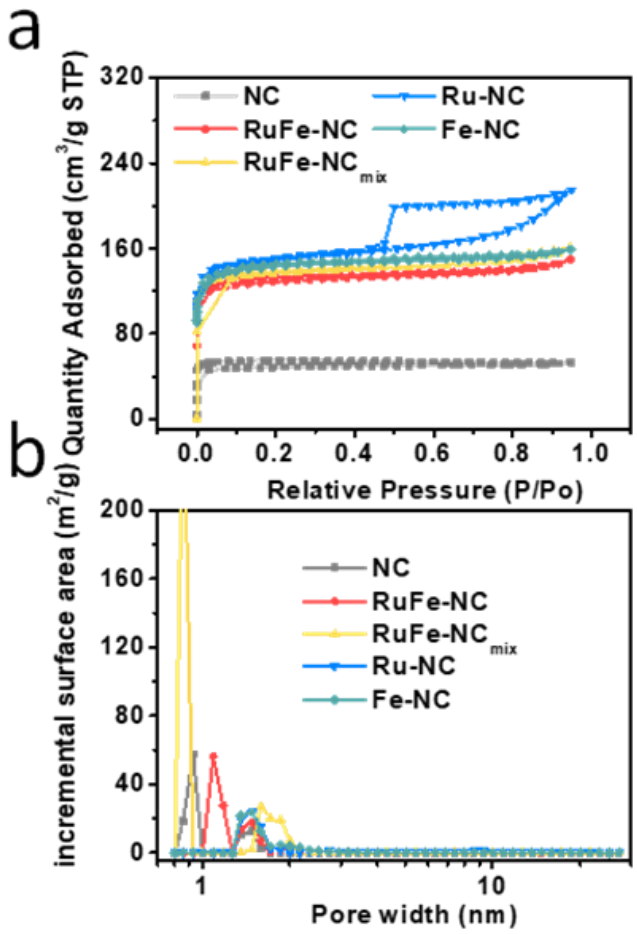

Figure 4. (a) Nitrogen sorption isotherms of RuFe-NC, RuFe-NC$_{mix}$, Ru-NC, Fe-NC, and NC, and (b) the corresponding pore size distribution profiles.

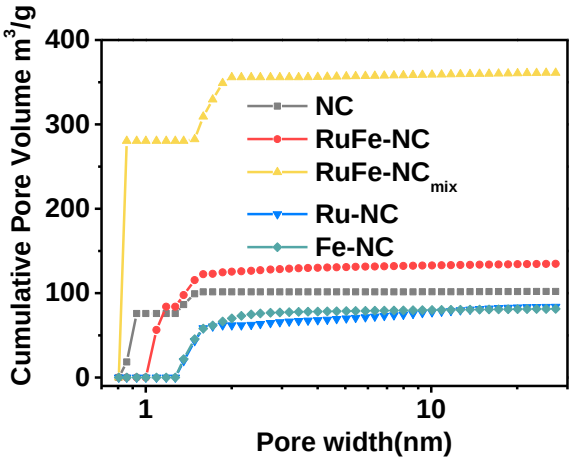

Figure 5. Profiles of cumulative pore volume as the function of pore width of RuFe-NC, RuFe-NC_{mix}, Ru-NC, Fe-NC, and NC.

Further structural insights were obtained from TEM measurements. One can see from Figure 6a and 6b that the RuFe-NC sample partially retained the dodecahedral shape of the ZIF-8 precursor, exhibiting a lateral length of several hundred nm with an apparent porous structure (as highlighted by the pink circles in Figure 6a). At higher magnifications (Figure 6c and 7), one can find nanoparticles of ca. 2 nm in diameter that were encapsulated with a graphitized carbon shell. These nanoparticles exhibited well-defined lattice fringes, with a *d* spacing of ca. 0.220 and 0.235 nm that may be ascribed to the (113) and (400) facets of Fe_2O_3 (PDF#32-0469, red dashed circles),[36] respectively. It should be noted that no apparent RuO_2 or Ru nanoparticles can be found, and both d spacings are slightly larger than those of standard hematite Fe_2O_3, likely due to the doping of Ru into the iron oxide lattices (Figure 7-9). Meanwhile, graphitized carbon can be seen to show a hemispherical shape with a d spacing of 0.338 nm (blue circle), corresponding to the (002) facet of graphitized carbon (JCPDS No. 01-0646).[37,38] Furthermore, in elemental mapping analysis (Figure 6d and 10), it can be seen that Ru was mostly confined within the dark-contrast nanoparticles, consistent with the notion that Ru was doped into Fe_2O_3 nanoparticles. In addition, the RuFe-NC sample was found to consist of ca. 0.9 at% of Fe and 0.3 at% of Ru (Figure 11).

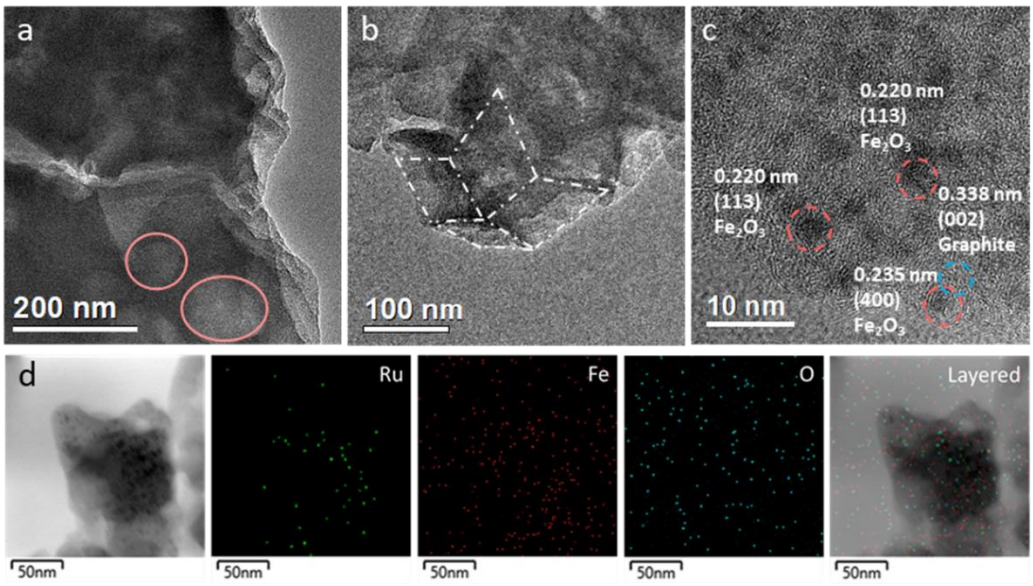

Figure 6. (a-c) Representative TEM images of RuFe-NC at varied magnifications. The pink circles highlight the microporous structure of the carbon matrix. (d) Representative TEM image of RuFe-NC and the corresponding EDS elemental maps of Ru, Fe, and O.

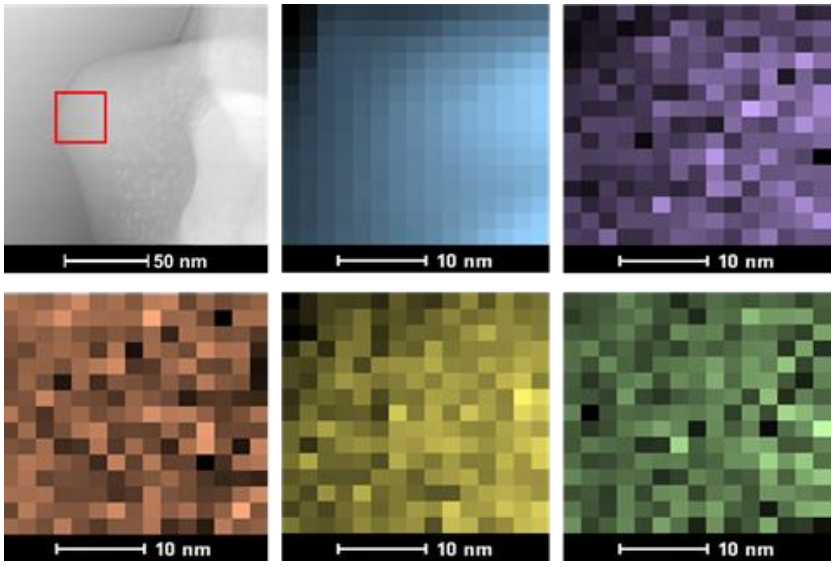

Figure 7. Dark-field TEM image of RuFe-NC and the corresponding EELS elemental maps of the red box region: carbon (blue), nitrogen (purple), iron (orange), ruthenium (yellow), oxygen (green).

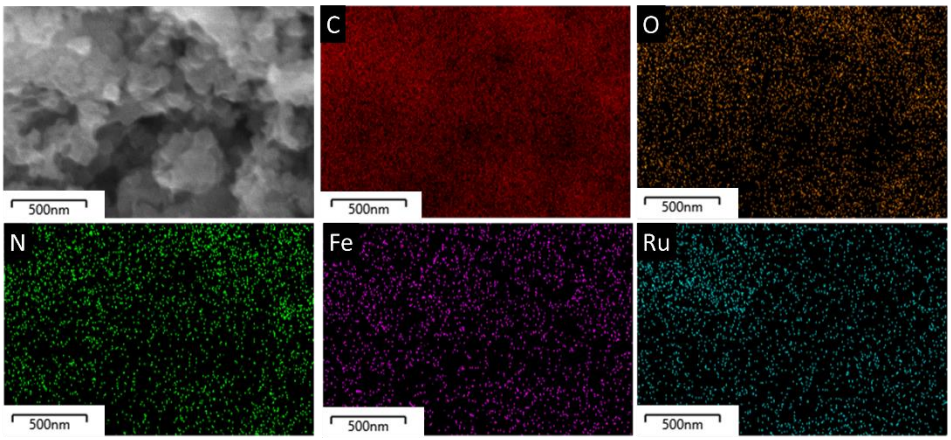

Figure 8. SEM image and the corresponding EDS-based elemental maps of C, O, N, Fe, and Ru of RuFe-NC.

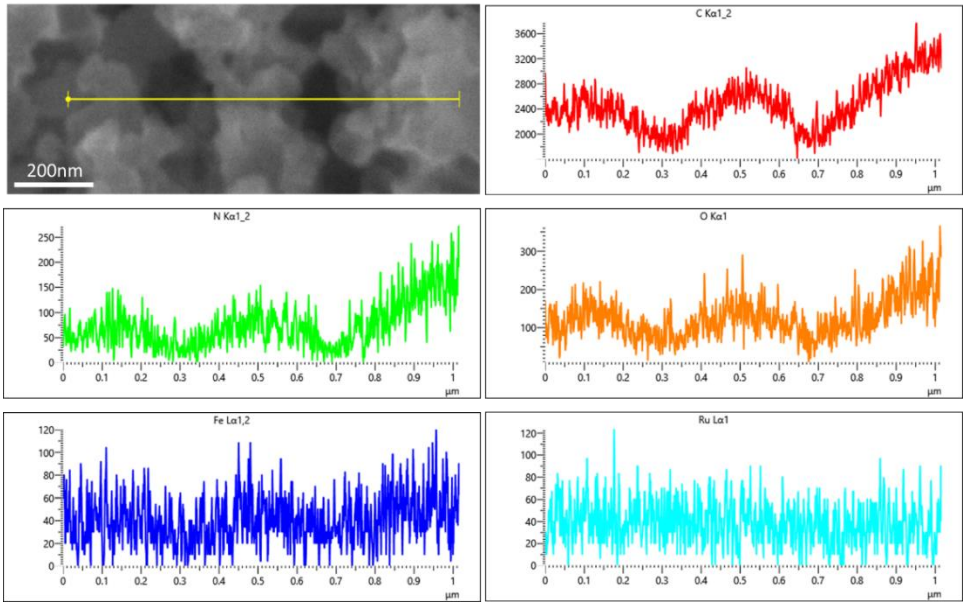

Figure 9. SEM image and EDS line scans of the chemical composition of the RuFe-NC sample.

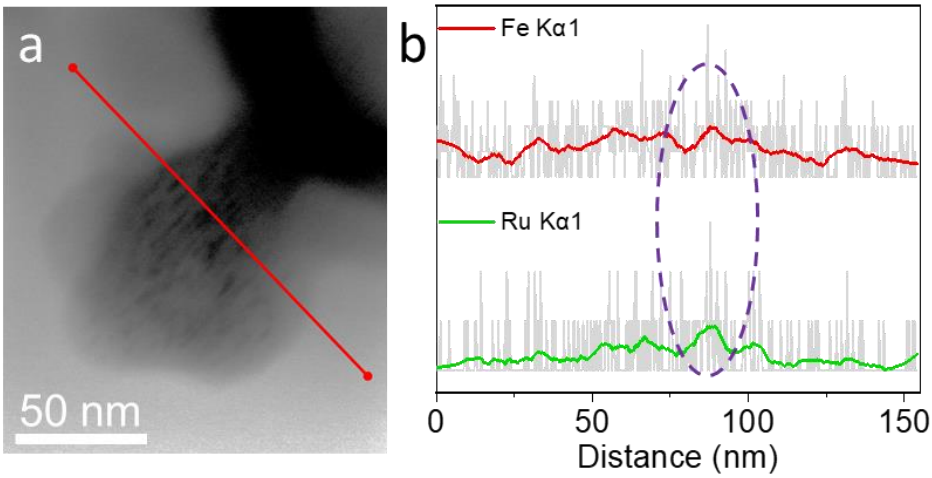

Figure 10. (a) Representative TEM image of RuFe-NC. The red solid line represents the EDS line scan. (b) EDS line scan measurements of Fe and Ru. Note that gray curves are raw data, colored curves are smoothened results. Dashed purple circle highlights the concurrent increase of the Fe and Ru contents.

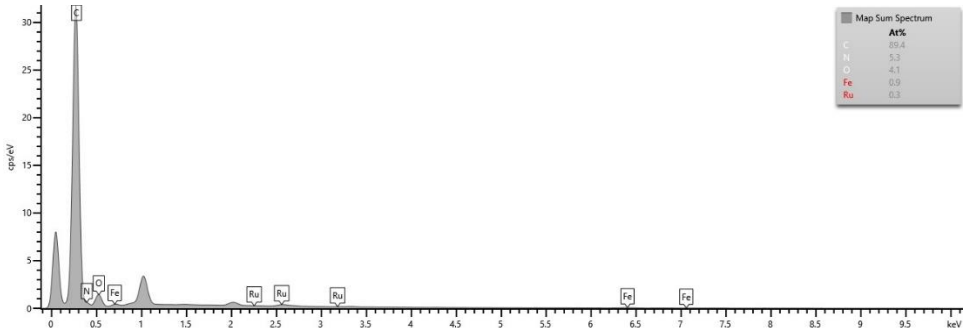

Figure 11. EDS spectrum of RuFe-NC. Inset lists the elemental contents.

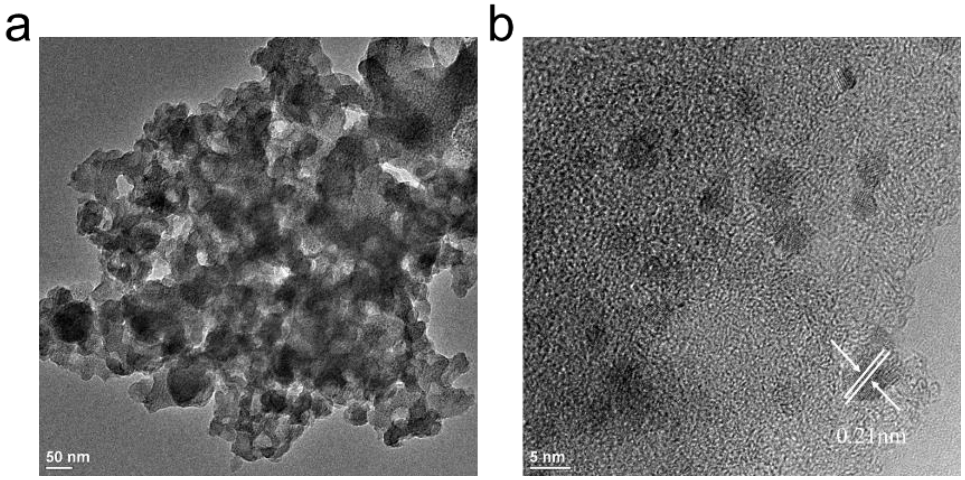

Figure 12. Representative TEM images of Ru-NC at different magnifications. Scale bars are (a) 50 nm and (b) 5 nm.

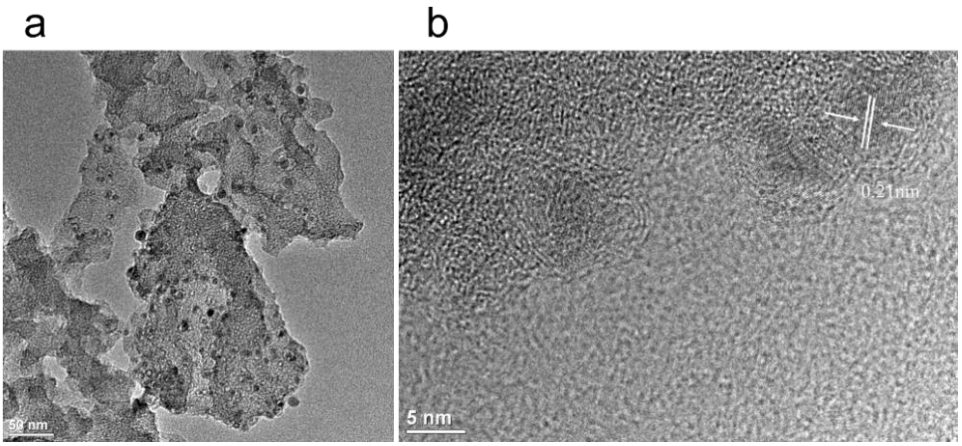

Figure 13. Representative TEM images of Fe-NC at different magnifications. Scale bars are (a) 50 nm and (b) 5 nm.

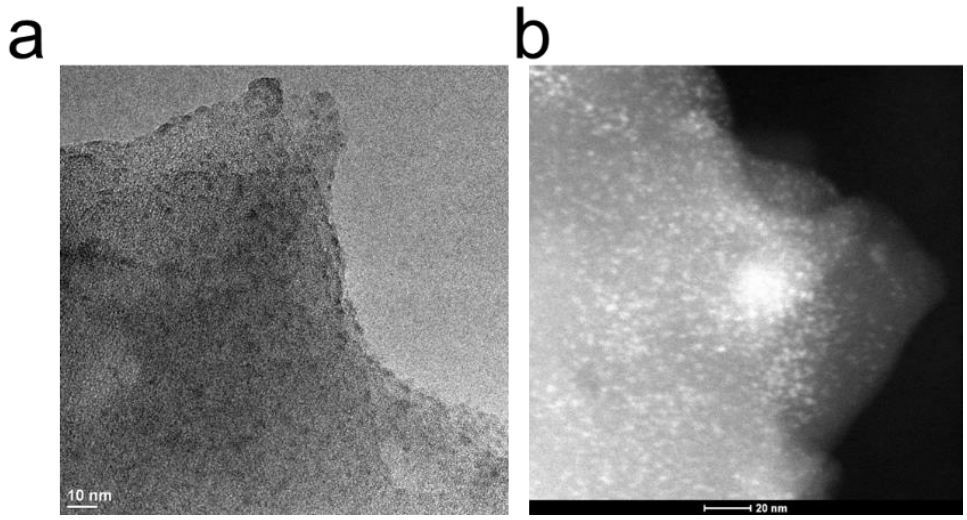

Figure 14. (a) Bright-field and (b) dark-field TEM images of RuFe-NC_{mix}.

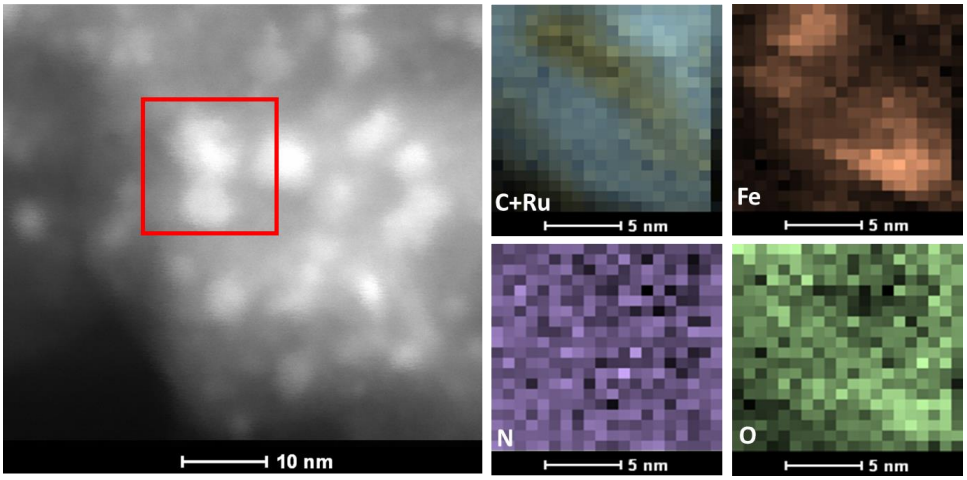

Figure 15. (a) Representative dark-field TEM image of RuFe-NC_{mix} and the corresponding elemental maps of C (blue), Ru (yellow), Fe (orange), N (purple), and O (green) in the red box region in panel (a).

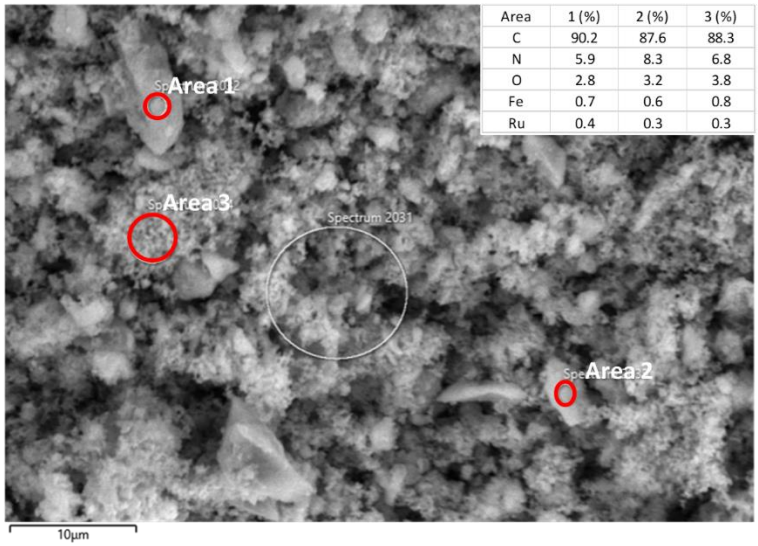

Figure 16. SEM image of RuFe-NC_{mix} and the corresponding EDS survey of the elemental composition (inset table).

A similar structural morphology was observed with the Ru-NC (Figure 11), Fe-NC (Figure 12), and RuFe-NC_{mix} samples (Figure 13). Notably, the RuFe-NC_{mix} composite can be seen to consist of nanoparticles of ca. 4 nm in diameter embedded within the carbon sheets (Figure 14). Elemental mapping analysis of the selected area (Figure 15) showed a homogeneous distribution of C and N, while the elements Fe and O were concentrated at the bright regions in the dark-field image, suggesting the formation of FeO_x nanoparticles. Yet, the distribution pattern of ruthenium was different from that of Fe, suggesting partial segregation between these two elements. Furthermore, EDS measurements (Figure 16) showed that the RuFe-NC_{mix} sample consisted of ca. 0.6 at% of Fe and 0.3 at% of Ru, consistent with the initial feed ratio. A similar sheet-like structure was observed withe both Ru-NC (Figure 12) and Fe-NC (Figure 13), which also featured metal oxide particles with a diameter of around 5 nm on the carbon sheets.

Note that the nanoparticles were all markedly larger in these control samples than those in RuFe-NC, likely because of the bonding constraint in the $Ru(LFe)_2$ complex precursor (Scheme 1) and the geometric confinement by the micropores (Figure 4b) in the pyrolytic preparation of RuFe-NC.

3.4.2 X-ray spectroscopy analysis

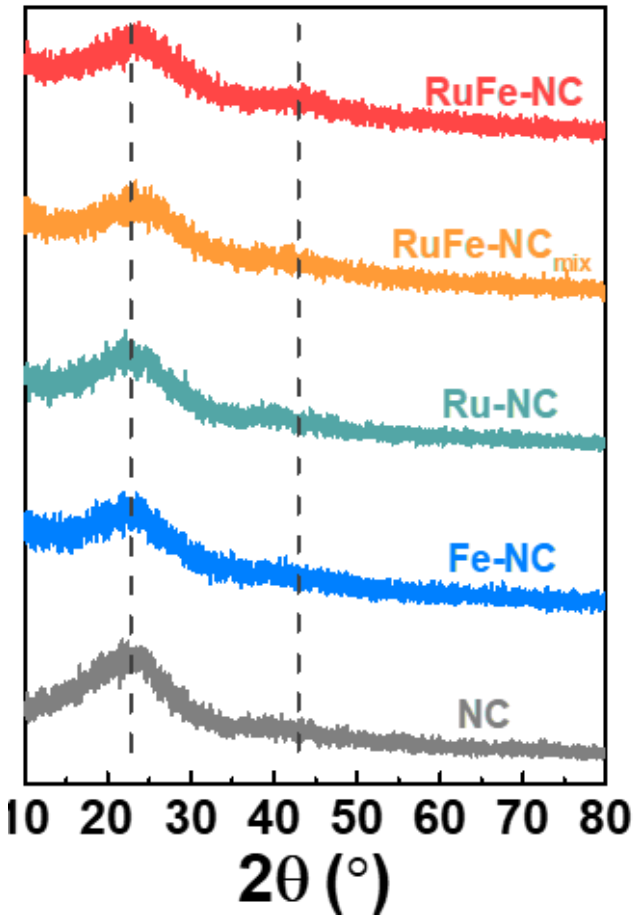

Figure 17. XRD patterns of RuFe-NC, $RuFe\text{-}NC_{mix}$, Ru-NC, Fe-NC, and NC. The dashed lines indicate the expected 2θ position of the (002) and (100) diffractions of graphite (JCPDS No. 01-0646). Units on the y-axis have arbitrary units.

XRD measurements were then carried out to examine the graphitization of the samples prepared by high-temperature pyrolysis. From Figure 17, all samples can be seen to exhibit two broad diffraction peaks at $2\theta \approx 23°$ and 43°, which can be assigned to the (002) and (100) facets of graphite (JCPDS No. 01-0646), in good agreement with results from TEM measurements (Figure 6c). No Additional diffraction peaks of metal or metal oxides can be discerned from the XRD profiles, most likely due to the low contents as detected in EDS measurements (Figure 11 and 16) and the small size of the nanoparticles (Figure 5 and 7).

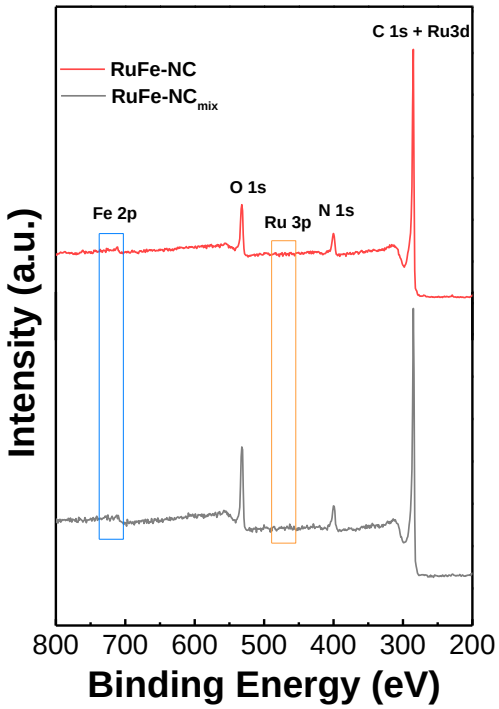

Figure 18. XPS survey spectra of RuFe-NC and RuFe-NC_{mix}.

XPS measurements were further performed to determine the elemental composition and valence states of the samples. From the survey spectra of RuFe-NC and RuFe-NC_{mix} in Figure 18, the C 1s, N 1s, and O 1s electrons can be readily identified at ca. 285 eV, 398 eV, and 531 eV, respectively. Figure 19a depicts the high-resolution Fe 2p spectra of the $Ru(LFe)_2$ complex, RuFe-NC, RuFe-NC_{mix}, and Fe-NC, where the Fe $2p_{3/2}$ peaks of RuFe-NC (711.51 eV), RuFe-NC_{mix} (711.26 eV) and Fe-NC (711.31 eV) can be found to blue-shift by ca. 2 eV in comparison to that of the $Ru(LFe)_2$ complex (709.38 eV), suggesting an increase of the Fe valence state from Fe(II) in the complex to Fe(III) in the pyrolytic products.[39,40]

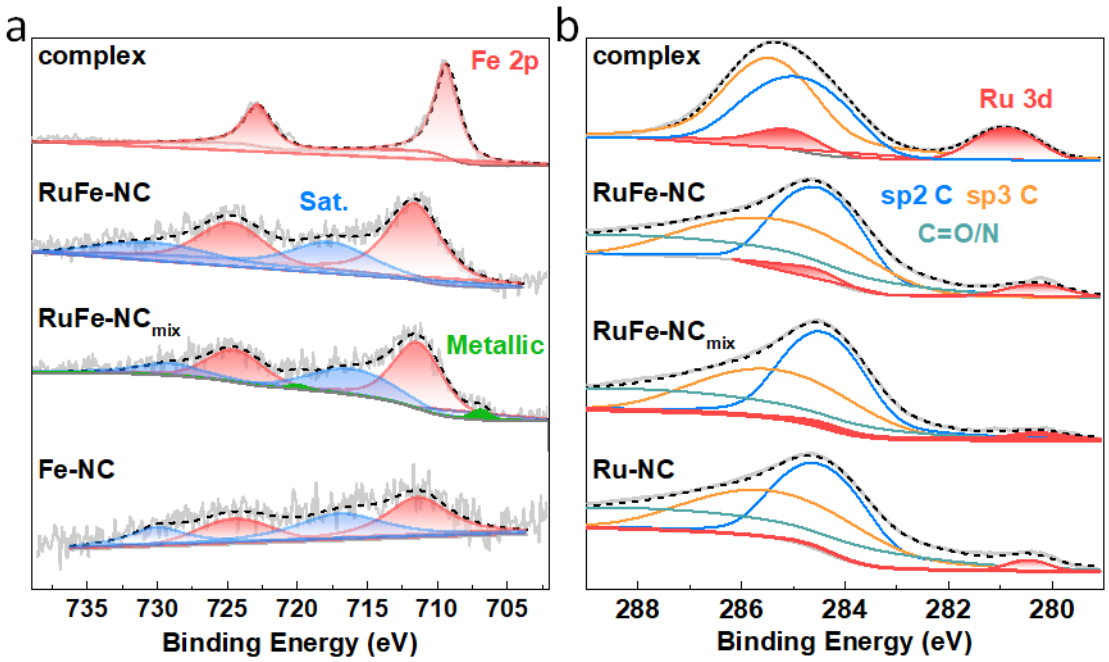

Figure 19. (a) High-resolution XPS spectra of the Fe 2p electrons of the RuFe complex, RuFe-NC, RuFe-NC_{mix}, and Fe-NC. (b) High-resolution XPS spectra of the C 1s and Ru 3d electrons of RuFe complex, RuFe-NC, RuFe-NC_{mix}, and Ru-NC. Note, the y-axis is logarithmic.

As for the Ru 3d spectra in Figure 19b, RuFe-NC, RuFe-NC_{mix} and Ru-NC showed a small shoulder near 280.30 eV, which is ca. 0.6 eV lower than that of the $Ru(LFe)_2$ complex (280.90 eV), suggesting partial reduction (electron enrichment) of ruthenium(II) in the complex precursor after pyrolysis (i.e., the Ru valence state in RuFe-NC was between 0 and +2).[37,41] Notably, the Ru 3d binding energy of RuFe-NC and RuFe-NC_{mix} was ca. 0.15 eV lower than that of Ru-NC (280.45 eV). This observation, in conjunction with the variation of the Fe(III) $2p_{3/2}$ binding energy of RuFe-NC (711.51 eV) > RuFe-NC_{mix} (711.26 eV) > Fe-NC (711.31 eV), suggests charge transfer from Fe to Ru in the Fe_2O_3 nanoparticles of RuFe-NC, which diminished in RuFe-NC_{mix} due to segregated distributions of Fe and Ru (Figure 6 and 13). In fact, metallic Fe was even found in RuFe-NC_{mix} (706.89 eV, 0.068 at%, Figure 19a).

In addition, based on the integrated peak areas, the elemental compositions of the samples were also evaluated. The Fe content was estimated to be ca. 1.97 wt% (0.45 at%) for RuFe-NC and 2.35 wt% (0.54 at%) for RuFe-NC_{mix}, close to the results from ICP-OES (1.69 wt% and 2.64 wt%, respectively) and EDS measurements (vide ante, Figure 11 and 16). The Ru contents, 0.50 wt% for RuFe-NC and 0.33 wt% for RuFe-NC_{mix}, were substantially lower than those from EDS analysis; such a difference suggests Ru enrichment on the surface of RuFe-NC as compared to that of RuFe-NC_{mix}. From the C 1s spectra in Figure 19b, one can see that the samples all consists of a large amount (284.63 eV, 38.9 at%) of sp^2-hybridized C, along with sp^3 C (285.69 eV) and

C=O/N (288.80 eV), suggesting successful graphitization of the ZIF-8 precursors.[34] The N 1s spectrum of RuFe-NC is shown in Figure 20, which can be deconvoluted into four peaks at 398.3 eV for pyridinic N, 399.7 eV for pyrrolic N, 400.8 eV for graphitic N, and 403.4 eV for oxidized N, with an atomic content of 2.0, 1.7, 2.0, and 1.2 at%, respectively (6.9 at% in total). With such abundant pyridinic N and pyrrolic N moieties, it is possible that part of the Fe species was coordinated to those N moieties. In fact, from the O 1s spectra in Figure 21, RuFe-NC can be seen to entail a small metal-O shoulder, which accounted for 0.20 at% of the sample, corresponding to 0.13 at% Fe in Fe_2O_3, which suggests that the rest of about 0.32 at% of Fe was in the form of FeN_x moieties. Such a metal-lattice O component was markedly more pronounced with RuFe-NC_{mix}, which was estimated to be 0.92 at%, ca. 1.75 times that of Fe in FeO_x (0.53 at%), very close to the atomic ratio of 1.5 in Fe_2O_3. This suggests that the Fe species in RuFe-NC_{mix} was mostly in the form of Fe_2O_3 (Figure 15), with a minor component of metallic Fe and no FeN_x moieties.[42] These results are also listed in Table 1-6.

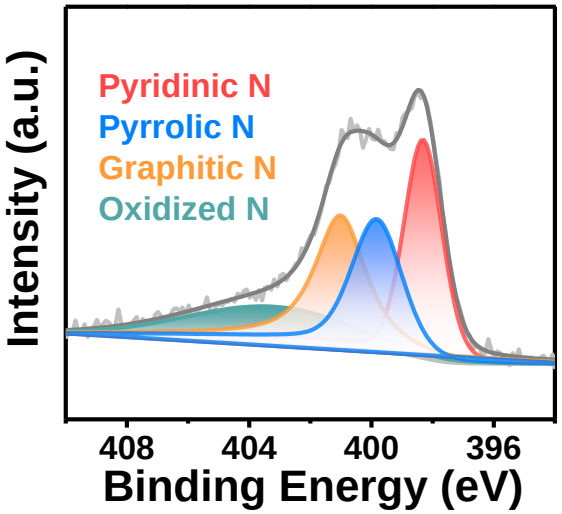

Figure 20. High-resolution XPS spectrum of the N 1s electrons of RuFe-NC. Black curve is the experimental data and colored curves are deconvolution fits.

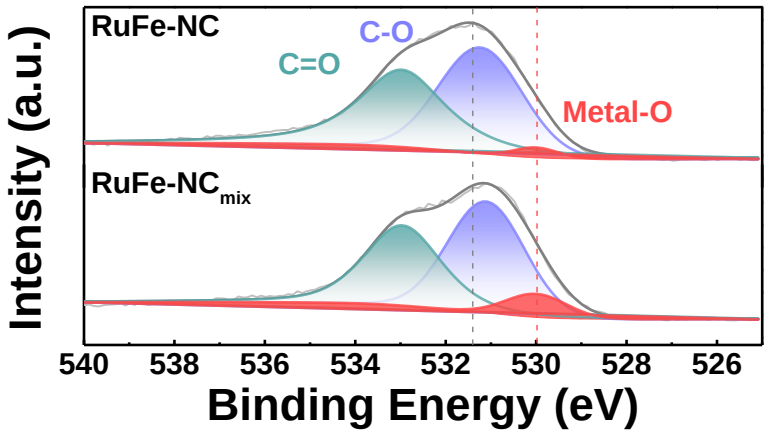

Figure 21. High-resolution XPS spectra of the O 1s electrons of RuFe-NC and RuFe-NC-P. Black curves are the experimental data and colored curves are deconvolution fits.

Table 1. Detailed data of XPS devolution and calculations of RuFe-NC.

Elements	**Types**	**Positions (eV)**	**Percentage (at%)**	**Percentage (at%)**	**Percentage (wt%)**
C 1s	Sp2 C	284.63	38.893	84.241	79.438
	Sp3 C	285.69	24.706		
	C=O/N	288.80	20.682		
N 1s	Pyridinic N	398.30	2.036	6.917	7.610
	Pyrrolic N	399.68	1.672		

	Graphitic N	400.82	2.03		
	Oxidized N	403.36	1.176		
O 1s	C-O	531.23	3.962	8.329	10.473
	C=O	532.97	4.164		
	Metal-O	530.00	0.204		
Fe 2p	2p 3/2	711.51	0.199	0.448	1.973
	Satellite	717.57	0.010		
	2p 1/2	724.61	0.010		
	Satellite	730.67	0.005		
Ru 3d	3d 3/2	280.31	0.038	0.064	0.506
	3d 5/2	284.51	0.025		

Table 2. Detailed data of XPS devolution and calculations of RuFe-NC_{mix}.

Elements	**Types**	**Positions (eV)**	**Percentage (at%)**	**Percentage (at%)**	**Percentage (wt%)**
C 1s	Sp2 C	284.50	37.925	81.168	75.722
	Sp3 C	285.57	23.401		
	C=O/N	288.36	19.842		

N 1s	Pyridinic N	398.17	1.604	7.146	7.778
	Pyrrolic N	399.40	1.427		
	Graphitic N	400.77	2.363		
	Oxidized N	403.74	1.752		
O 1s	C-O	531.10	5.459	11.103	13.811
	C=O	532.96	4.722		
	Metal-O	530.00	0.921		
Fe 2p	Fe^0 2p 3/2	706.89	0.045	0.593	2.351
	Fe^{3+} 2p 3/2	711.26	0.224		
	Satellite	715.94	0.126		
	Fe^0 2p 1/2	719.99	0.023		
	Fe^{3+} 2p1/2	724.36	0.112		
	Satellite	729.04	0.063		
Ru 3d	3d 3/2	280.28	0.026	0.043	0.338
	3d 5/2	284.48	0.017		

Table 3. Detailed data of XPS devolution and calculations of NC.

Elements	Types	Positions (eV)	Percentage (at%)	Percentage (at%)	Percentage (wt%)
C 1s	Sp2 C	284.60	23.884	80.204	76.407
	Sp3 C	285.36	32.189		
	C=O/N	287.65	24.130		
N 1s	Pyridinic N	398.41	4.309	9.776	10.865
	Pyrrolic N	399.57	2.154		
	Graphitic N	400.95	2.548		
	Oxidized N	403.30	0.765		
O 1s	C-O	531.41	3.713	10.020	12.727
	C=O	532.93	6.306		

Table 4. Detailed data of XPS devolution and calculations of Ru-NC.

Elements	Types	Positions (eV)	Percentage (at%)	Percentage (at%)	Percentage (wt%)
C 1s	Sp2 C	284.63	37.712	83.658	80.305
	Sp3 C	285.71	26.381		
	C=O/N	288.44	19.565		

N 1s	Pyridinic N	398.21	2.311	9.050	10.135
	Pyrrolic N	398.91	1.931		
	Graphitic N	400.6	2.816		
	Oxidized N	401.82	1.992		
O 1s	C-O	531.07	3.187	7.258	9.290
	C=O	532.90	4.071		
Ru 3d	3d 3/2	280.45	0.020	0.033	0.271
	3d 5/2	284.65	0.013		

Table 5. Detailed data of XPS devolution and calculations of Fe-NC.

Elements	**Types**	**Positions (eV)**	**Percentage (at%)**	**Percentage (at%)**	**Percentage (wt%)**
C 1s	Sp2 C	284.69	29.500	78.704	73.587
	Sp3 C	285.70	29.162		
	C=O/N	288.99	20.041		
N 1s	Pyridinic N	398.45	4.747	10.007	10.916

	Pyrrolic N	399.88	1.450		
	Graphitic N	401.06	2.420		
	Oxidized N	403.30	1.389		
O 1s	C-O	531.14	32.156	10.833	13.505
	C=O	532.77	66.261		
	Metal-O	530.00	1.583		
Fe 2p	2p 3/2	711.31	0.097	0.457	1.992
	Satellite	716.84	0.069		
	2p 1/2	724.41	0.236		
	Satellite	729.94	0.035		

Table 6. Fe and Ru contents of the sample series

Sample	**Theoretical values (wt%)**		**XPS values (wt%)**		**ICP values (wt%)**	
	Fe	**Ru**	**Fe**	**Ru**	**Fe**	**Ru**
$Ru(LFe)_2$ complex	4.50%	4.00%	4.05%	4.43%		
RuFe-NC	1.30%	1.20%	1.97%	0.50%	1.69%	0.0026%

RuFe-NC(x1/2)	0.70%	0.60%			1.14%	0.0019%
RuFe-NC(x2)	2.60%	2.40%			3.07%	0.0089%
RuFe-NC_{mix}	1.30%	1.20%	2.35%	0.33%	2.64%	0.0059%
Ru-NC		1.20%		0.27%		0.0026%
Fe-NC	1.30%		1.99%		1.91%	

Further structural insights were obtained in XAS measurements. From the Fe K edge spectra in Figure 22a, one can see that RuFe-NC exhibited a similar pre-edge profile and post-edge oscillations to Fe_2O_3, suggesting an analogous chemical environment of the Fe centers. In fact, both RuFe-NC and (hematite) Fe_2O_3 can be seen to display a small pre-edge peak at 7113 eV (magenta arrow) arising from the 1s to 3d forbidden electric dipole transition, consistent with an octahedral coordination shell in the samples,[43,44] in sharp contrast to Fe foil which featured an intense shoulder in the pre-edge region. The Ru K edge spectra are depicted in Figure 22b. One can see that the main edge energy of RuFe-NC was lower than that of RuO_2, but higher than that of Ru foil, suggesting electron enrichment of Ru in RuFe-NC in comparison to RuO_2. These observations are consistent with results from the XPS measurements which suggested Fe to Ru charge transfer in the composites.

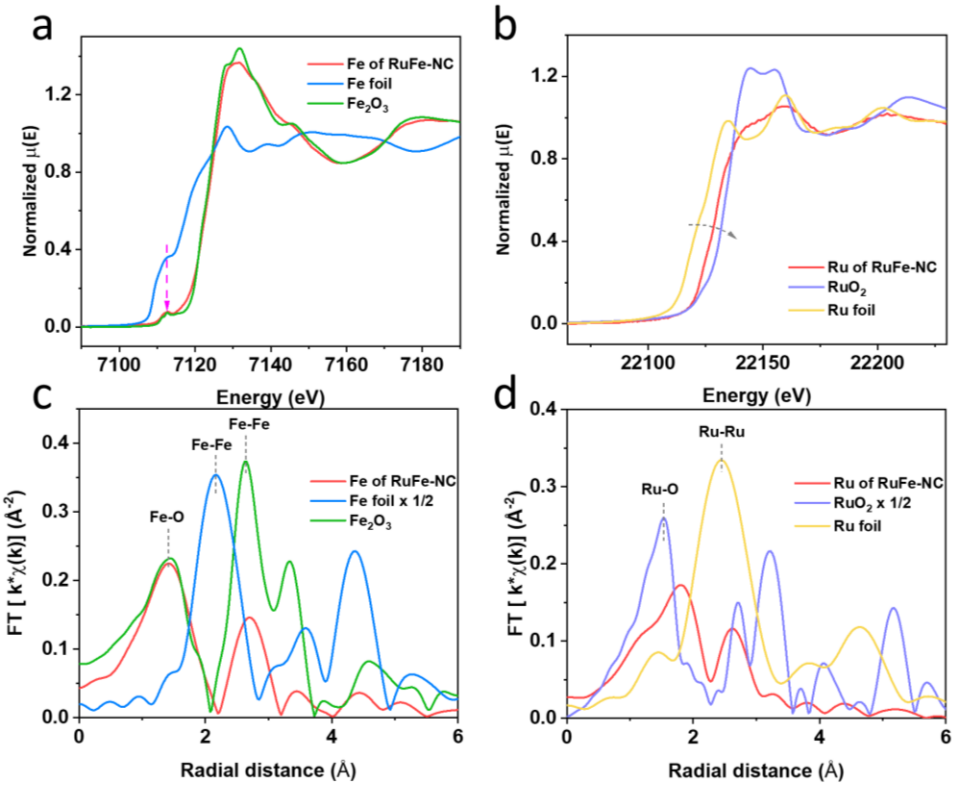

Figure 22. X-ray absorption near-edge spectra (XANES): (a) Fe K edge of RuFe-NC, Fe foil, and Fe_2O_3 (hematite); (b) Ru K edge of RuFe-NC, Ru foil, and RuO_2. Corresponding extended X-ray absorption fine structure (EXAFS) spectra of (c) Fe of RuFe-NC, Fe foil, and Fe_2O_3; (d) Ru of RuFe-NC, Ru foil, and RuO_2.

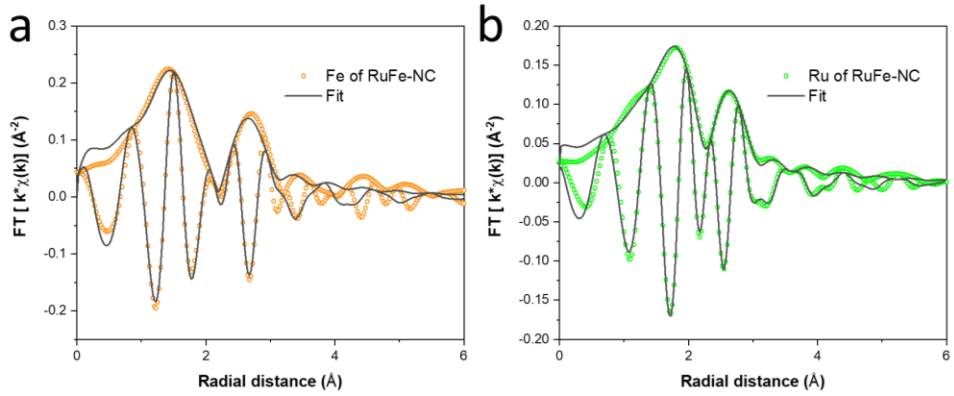

Figure 23. Fitting results of the FT-EXAFS spectra of (a) Fe K edge and (b) Ru K edge of RuFe-NC. FFT range is 3.5 to 11 Å.

Table 7. Fitting results of XAS for RuFe-NC.

Bond	**Bond Length (Å)**	**Coordination Number**	**R^2**
Fe-O	1.999	4.81	0.099
Fe-Fe	2.950	2.00	
Bond	**Bond Length (Å)**	**Coordination number**	**R^2**
Ru-O	2.044	2.50	0.06
Ru-P	2.289	1.85	
Ru-Fe	2.987	1.16	
Ru-Ru	2.742	0.62	
Ru-Fe	3.882	1.74	

The corresponding R-space EXAFS spectra are shown in Figure 22c and 22d. One can see that the peak patterns, again, are very similar between RuFe-NC and Fe_2O_3. In the Fe R space spectrum of RuFe-NC (Figure 22c), two main peaks can be identified at ca. 1.42 and 2.70 Å, which can be assigned to the Fe-O/N bonds and second-shell Fe-Fe/Ru, respectively, in good agreement with the formation of (Ru-doped) Fe_2O_3 nanoparticles and FeN_x moieties, as suggested in XPS measurements (Figure 19). From the fitting results (Figure 23a, Table 7), one can see that that the Fe-O/N bonds in RuFe-NC possessed a coordination number of 4.8 with a bond length of 2.00 Å, while the Fe-Fe/Ru linkage featured a coordination number of 2.0 with a bond length of 2.95 Å. These fitting results are consistent with the small size and poor crystallinity of the Ru-

doped Fe_2O_3 nanoparticles, and the formation of FeN_x moieties as speculated in TEM and XPS measurements (vide ante). In the corresponding Ru EXAFS data (Figure 22d), Ru of RuFe-NC displayed an apparently different pattern from those of Ru foil and RuO_2. Three major species can be resolved in RuFe-NC, i.e., Ru-O (shoulder, ca. 1.3 Å), Ru-P (1.81 Å), and Ru-Ru (2.61 Å). These lengths are approximately 0.3 Å shorter than the realized bond length due to the well-known phase shift in EXAFS. Ru-doped α-Fe_2O_3 was used to calculate the FEFF functions of the Ru-O and Ru-Fe standard paths for EXAFS fitting. Data of the RuFe-NC sample was fitted by using two distinct structures, Ru-doped α-Fe_2O_3 and tetragonal RuP_3, where the former accounted for ca. 80 % in the sample and 20% for the latter.[45] As shown in Figure 23b and Table 4, one can see that the Ru-O bond possessed a coordination number of 2.5 with a bond length of 2.04 Å, which is larger than the typical Ru-O bond length of RuO_2 (1.98 Å)[46,47] and closer to that of M-O bond of hematite. The Ru-Fe path featured a coordination number of 1.16 and a bond length of 2.99 Å, which is smaller than the Ru-Ru bond length in RuO_2 (3.3 Å) but closer to the one in hematite (2.97 Å), suggesting the successful incorporation of Ru into α-Fe_2O_3. Note that the low coordination number of Ru-O (2.51) is strong evidence for significant disorder in α-Fe_2O_3, likely due to the small oxide particle size and presence of amorphous iron oxide within the sample. Also, the fact that the peak at ca. 3.2 Å observed with RuO_2 was absent in RuFe-NC suggests atomic dispersion of Ru into the Fe_2O_3 nanoparticles, as proposed in the above TEM and XPS measurements.

3.4.3 Electrocatalytic activity

The ORR activity of the obtained samples was then examined by electrochemical measurements. All samples displayed a similar cyclic voltammetric (CV) profile in N_2-saturated 0.1 M KOH that is free of redox features, most likely due to the low content of the metal species (Figure 24). From the linear sweep voltammograms (LSV) acquired in rotating ring-disk electrode (RRDE) measurements in O_2-saturated 0.1 M KOH (Figure 25a), all composite samples with metal dopants can be seen to exhibit an apparently better ORR performance than the metal-free NC, and the dual-metal samples, RuFe-NC and RuFe-NC_{mix}, display a further enhanced performance in comparison with the monometal counterparts of Ru-NC and Fe-NC. Remarkably, RuFe-NC stood out as the best ORR catalyst among the series. For instance, Ru-NC exhibited an onset potential (E_{onset}) of +0.90 V, ca. 60 mV more positive than that of NC, but the half-wave potential was slightly inferior ($E_{1/2}$ = +0.62 V vs. +0.64 V). Fe-NC was significantly more active towards ORR, with an E_{onset} of +0.94 V and $E_{1/2}$ of +0.81 V, which were similar to those of RuFe-NC_{mix} (though the latter actually showed a much higher diffusion current density of ca. 4 mA cm^{-2} than other monometal-doped samples). This suggests that iron oxides played a dominant role in these samples in ORR electrocatalysis.[23,25] Notably, an even better ORR activity was observed with RuFe-NC, where the performance (E_{onset} = +0.99 V, $E_{1/2}$ = +0.87 V) was actually highly comparable to commercial Pt/C (E_{onset} = +1.00 V, $E_{1/2}$ = +0.87 V), suggesting the significance of Ru doping in Fe_2O_3 nanoparticles in enhancing the ORR activity of RuFe-NC likely due to the Fe-Ru charge transfer. It should be noted that increasing or

decreasing the $Ru(LFe)_2$ loading in the sample preparation actually led to a diminished ORR performance, suggesting that RuFe-NC represented the optimal composite (Figure 26).

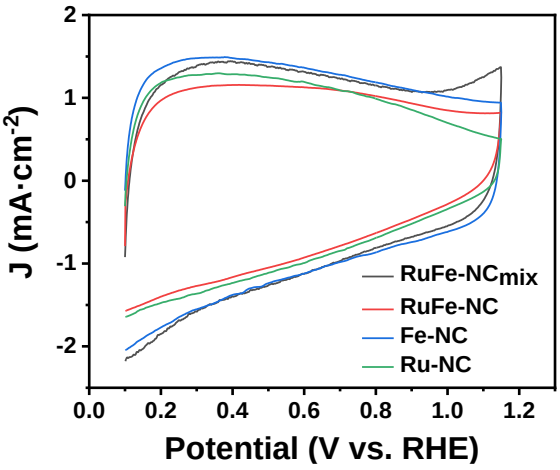

Figure 24. CV measurements of RuFe-NC, $RuFe\text{-}NC_{mix}$, Fe-NC, and Ru-NC in N_2-saturated 0.1 M KOH at a scan rate of 50 mV s^{-1}.

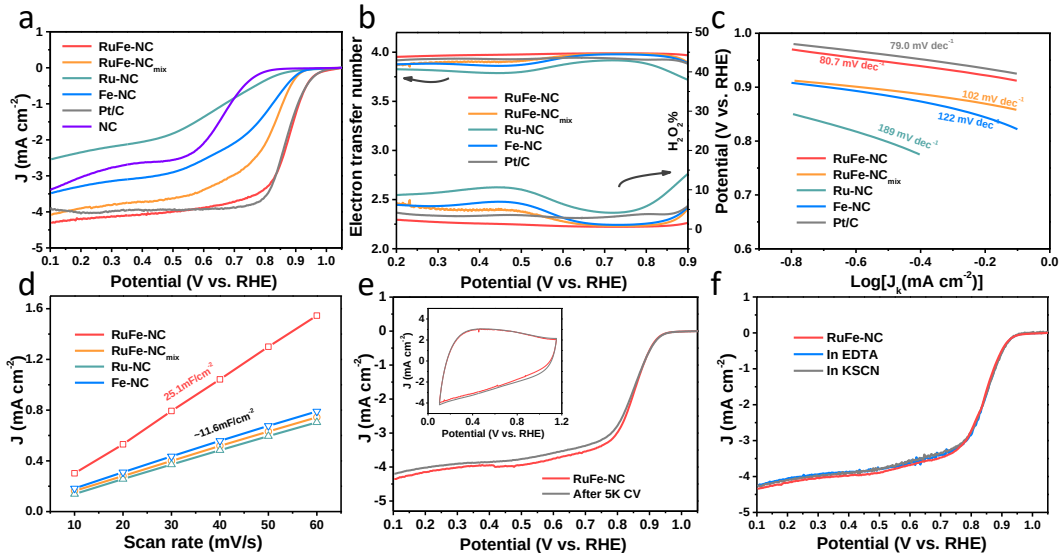

Figure 25. ORR performance of the RuFe-NC and its control samples in oxygen-saturated 0.1 M KOH. (a) linear sweep voltammograms (LSVs) of RuFe-NC and control samples of RuFe-NCmix, Ru-NC, Fe-NC, Pt/C, and NC at the rotation rate of

1600 rpm. (b) The corresponding electron-transfer number (n, left y-axis), the yield of H_2O_2 (%, right y-axis), and (c) Tafel plots with the slopes shown in mV dec^{-1}. (d) Double layer capacitances (C_{dl}s) of selected samples. (e) Stability test of RuFe-NC for 5000 cycles in N_2-saturated 0.1 M KOH. Inset is the corresponding cyclic voltammograms at the scan rate of 50 mV s^{-1} before and after the stability test. (f) Poisoning test of RuFe-NC with EDTA and KSCN treatments.

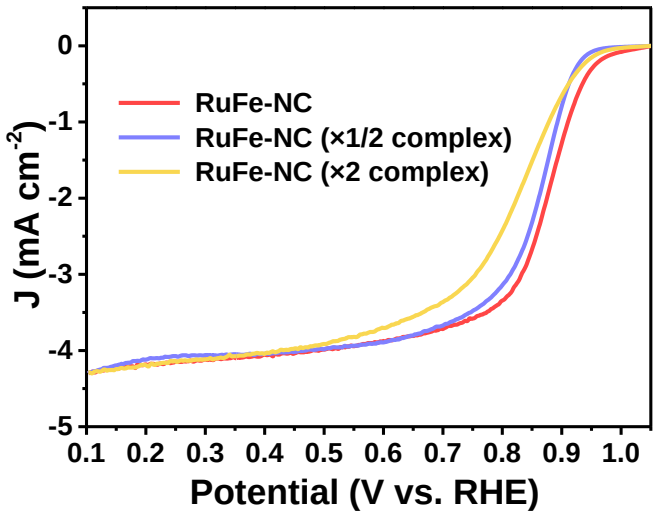

Figure 26. ORR polarization curves of the RuFe-NC samples prepared at different $Ru(LFe)_2$ loadings at the rotation rate of 1600 rpm in O_2 saturated 0.1 M KOH. Two additional RuFe-NC samples were prepared, one with the feeding ratio of RuFe complex to ZIF-8 reduced by half, RuFe-NC (x1/2 complex), and the other doubled, RuFe-NC (x2 complex). From Figure 26, one can see that the LSV curves of both samples actually shifted cathodically as compared to that of RuFe-NC, suggesting that RuFe-NC represented the optimal composition for ORR.

To gain further insights into the ORR electrocatalysis, the number of electron transfer (n) and H_2O_2% yield were evaluated by $n = \frac{4i_D}{i_D + i_R/N}$ and $H_2O_2\% = \frac{200i_R/N}{i_D + i_R/N}$, respectively, where i_R and i_D are the ring current and disk current, and N is the collection efficiency of the ring electrode (0.40). One can see from Figure 25b that at +0.8 V the n value is

ca. 3.98 with an ultralow H_2O_2% of 0.65% for RuFe-NC, suggestive of the four-electron pathway of ORR. The performance of RuFe-NC_{mix} was a close second, with n = 3.98 and a slightly higher H_2O_2% of 0.95%. Note that these are even better than that of commercial Pt/C (n = 3.92, H_2O_2% = 3.82%). In contrast, a substantially lower performance was observed with Fe-NC (n = 3.97 and H_2O_2% = 1.40%) and Ru-NC (n = 3.88, H_2O_2% = 5.81%). In the Tafel plots (Figure 25c), RuFe-NC can be seen to display a Tafel slope of 80.7 mV dec^{-1}, which is close to that of Pt/C (79.0 mV dec^{-1}), indicating highly efficient electron-transfer kinetics where the first electron reduction of oxygen was likely the rate-determining step.[34,40,48] Notably, the Tafel slope was greater for RuFe-NC_{mix} at 102 mV dec^{-1}, and markedly higher for Ru-NC (188 mV dec^{-1}) and Fe-NC (122 mV dec^{-1}), indicating a diminishingly ability to cleave the O-O bonds during the ORR process.[49]

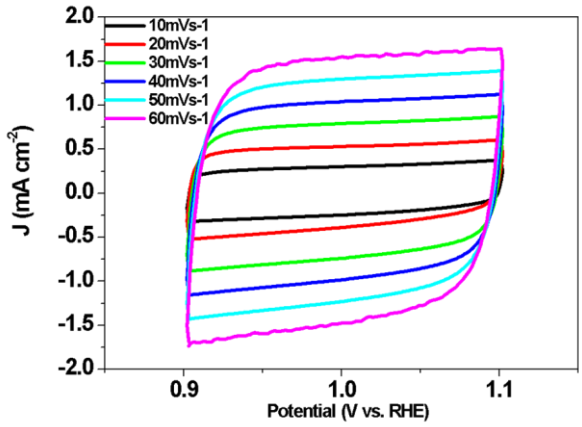

Figure 27. Cyclic voltammograms of RuFe-NC in 0.1 M KOH within the potential range of +0.9 to +1.1V where no faradaic reaction occurs at difference scan rates.

The effective electrochemical surface areas of the samples were then evaluated by the electrode double-layer capacitance (C_{dl}). Within the potential range of +0.9 to +1.1 V

(i.e., a non-faradaic region), CVs were acquired at scan rates varied from 10 to 60 mV s^{-1} (Figure 27), from which the corresponding C_{dl} was derived. One can see from Figure 6d that RuFe-NC possessed the largest C_{dl} of 25.1 mF cm^{-2}, over two times those of other samples (ca. 11.6 mV cm^{-2}). This is consistent with the porous structure as manifested in the above BET and TEM measurements, which is beneficial to increase the accessibility to the catalytically active sites.

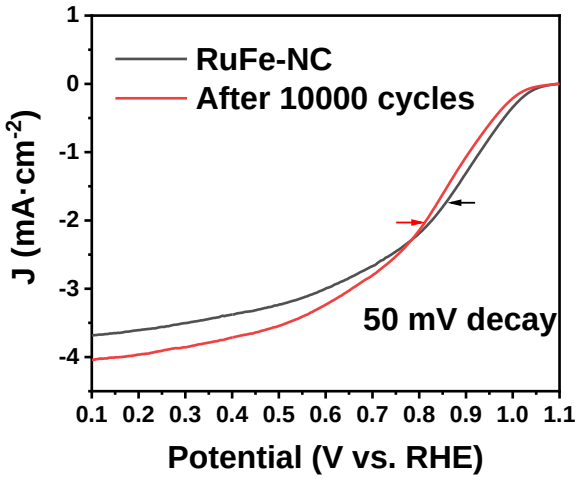

Figure 28. LSV curves of RuFe-NC at a scan rate of 10 mV s^{-1} and a rotation speed of 1600 rpm in O_2 saturated 0.1 M KOH before and after stability tests of 10000 cycles in N_2-saturated 0.1 M KOH.

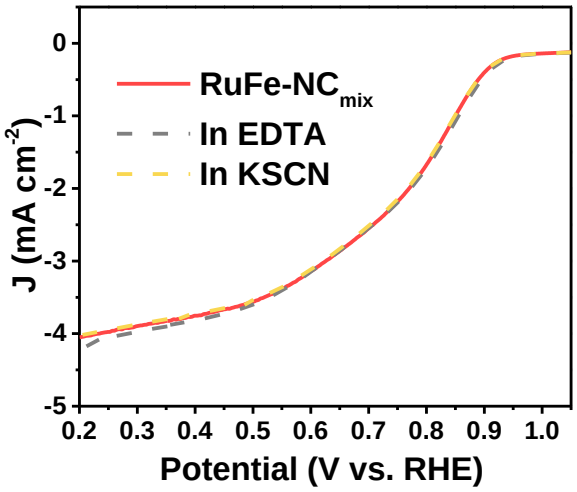

Figure 29. Poisoning test of RuFe-NC$_{mix}$ with EDTA and KSCN treatments.

The robustness of the active sites of RuFe-NC was then tested by repeated potential cycling between +0.6 and +1.0 V. After 5000 cycles, there were only minimal changes of the voltammograms (inset to Figure 6e) and a slight shift of the diffusion-limited current density (less than 5%) in the corresponding LSV curve, manifesting excellent catalyst durability. After 10,000 cycles, the activity of RuFe-NC decayed somewhat with a cathodic shift of $E_{1/2}$ by 50 mV (Figure 28), but remained better than those of a number of relevant catalysts reported recently in the literature (Table 8). Furthermore, the RuFe-NC catalysts exhibited remarkable tolerance against poisoning species like KSCN or EDTA, where negligible changes were discerned upon the addition of such poisoning species into the electrolyte (Figure 25f and 29). Such an anti-poisoning property against SCN^- might be due to the unique structure of the Ru-doped Fe_2O_3 nanoparticles where the O-rich surface rendered the binding of SCN^- ligands difficult. Meanwhile, as a hexadentate ligand, EDTA mostly chelates mononuclear metal centers,

and the minimal impacts on the ORR performance suggests that Fe single atoms (e.g., FeN_x) are unlikely the dominant active sites.[37,50] These results further confirm that the Ru-doped Fe_2O_3 nanoparticles, rather than the FeN_x moieties, were responsible for the ORR activity, within the present experimental context.

Table 8. Comparison of catalyst performance with relevant materials in the literature.

Sample	**Precursors**	**$E_{1/2}$ (V vs. RHE)**	**n**	**Stability**	**Reference**
RuFe-NC	Trinuclear complex/ZIF8	+0.87	3.98 @ +0.8 V vs. RHE	negligible change after 5K CVs, 40 mV after 10K CVs.	This work
Fe_2O_3@NC&bio-C-800	$FeCl_3$ and pyrrole	+0.85	4.0 @ +0.2 V vs. RHE	91% retention of current density after 10000s	J. Energy Chem., 2020, 44, 121-130
Fe_2O_3/KB	$Fe(NO_3)_3$ and Ketjen Black	+0.7	3.7 @ +0.2 V vs. RHE	42 mV decay after 21K CVs	ACS Appl. Mater. Interfaces, 2021, 13, 44195-44206

γ-Fe_2O_3@CNFs-12	$FeSO_4$ and Pt/C	+0.905	3.5-4.0	5 mV after 5K CVs	Chem. Eng. J., 2021, 415, 129033
Fe_2O_3-MoO_3/NG	$FeCl_3$/$(NH_4)_6Mo_7O_{24}$/ GO/Melamine	+0.82	3.8	15 mV after 2K CVs	Chem. Eng. J., 2021, 410, 128358
α- Fe_2O_3/A-C3N4	$FeCl_4$/1-Butyl-3-methylimidazolium chloride	+0.6	3.7	86% retention of current density after 10000s	J. Mater. Sci., 2022, 57, 2012-2020
Fe_2O_3/N-PCs-850/GC	$FeCl_3$/mulberry leaves	+0.8	3.9	76.8% retention after 3000s	Catalysts, 2018, 8, 101
GF+N_2+Fe1_800	$FeCl_3$/GO	+0.84	4 @ +0.65 V vs. RHE	96.2% retention after 20h	ACS Catal., 2016, 6, 3558-3568
$LaMn_xFe_{1-x}O_3$	$La(NO_3)_3$/ $Fe(NO_3)_3$/ Mn(NO3)2	+0.7	3.87 @ +0.3-0.5 V vs .RHE	88.1% retention after 10000s	Front. Mater. Sci., 2020, 14, 459-468
CoNP@bio-C-a	$Co(OH)_2$/$NaH_2PO_2 \cdot H_2O$ /CC powder	+0.85	4 @ +0.4-0.5 V vs. RHE	73% retention after 10000s	RSC Adv., 2022, 12, 207-215
MnO_2/C	$Mn(NO_3)_2$	+0.75	Not provided	~50 mV decay	ACS Catal., 2015, 5,

				after 1K CVs	4825-4832

Mechanistically, the remarkable ORR activity most likely arose from the Fe to Ru charge transfer in Ru-doped Fe_2O_3, owing to their different electronegativity. In fact, electron depletion of Fe within Fe_2O_3 has been demonstrated as an effective strategy to manipulate the spin states of the Fe centers, generate partially occupied e_g orbital and facilitate the adsorption of O_2.[26,51-53] In the present study, the atomic dispersion of Ru within RuFe-NC helped maximize such charge transfer and hence the ORR activity, in contrast to the RuFe-NC_{mix} sample where apparent segregation of Ru and Fe occurred. In fact, when RuFe-NC was subject to acid leaching with 0.5 M H_2SO_4 at 80 °C for 4 h, the ORR activity was markedly diminished, with E_{onset} = +0.93 V and $E_{1/2}$ = +0.74 V (Figure 30), a negative shift of 130 mV as compared to the as-prepared sample. These results demonstrate, again, the dominant contributions of metal oxide nanoparticles in the RuFe-NC composite to the ORR activity, with a minor contribution from the FeN_x moieties (as manifested by the leached sample which contained mainly atomically disperse FeN_x moieties but still outperformed the metal-free NC).

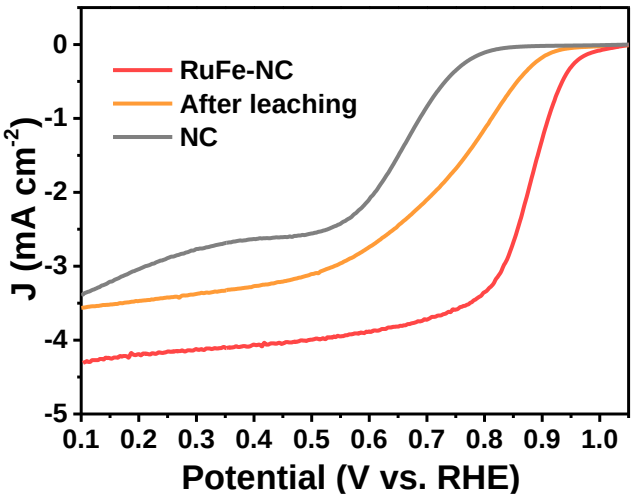

Figure 30. LSV curves of RuFe-NC in 0.1 M KOH before and after acid leaching treatment.

3.5 Conclusions

In this study, a trinuclear $Ru(LFe)_2$ complex was used as the metal precursors to prepare carbon nanocomposites with Ru-doped Fe_2O_3 nanoparticles, as confirmed in a range of microscopic and spectroscopic measurements. The obtained RuFe-NC nanocomposites exhibited an excellent ORR activity, with an E_{onset} of +0.99 V and an $E_{1/2}$ of +0.87 V, which is comparable to that of state-of-the-art Pt/C catalyst. Notably, the ORR activity was also markedly better than those of the monometal counterparts and samples prepared with a simple physical mixture of the relevant metal salts (where partial segregation of the metal species occurred). This was accounted for by the Fe to Ru charge transfer in the RuFe-NC composites that was advantageous for the adsorption of key reaction intermediates and enhanced electrochemical surface area that facilitated the accessibility of the catalytic active sites. Results from this study suggest that rational design of the metal precursors may be exploited as an effective strategy in

manipulating the morphological and electronic structure of the carbon for high-performance electrocatalysis.

3.6 Reference

1. K. I. Ozoemena, S. Chen, Nanomaterials for Fuel Cell Catalysis. In *Nanostructure Science and Technology,*, 1st ed.; Springer International Publishing : Imprint: Springer,: Cham, 2016; pp 1 online resource (VIII, 583 pages 248 illustrations, 177 illustrations in color.

2. M. Shao, Q. Chang, J. P. Dodelet, R. Chenitz. *Chem Rev* **2016**, *116*, 3594-657.

3. Z. Y. Lu, B. F. Wang, Y. F. Hu, W. Liu, Y. F. Zhao, R. O. Yang, Z. P. Li, J. Luo, B. Chi, Z. Jiang, M. S. Li, S. C. Mu, S. J. Liao, J. J. Zhang, X. L. Sun. *Angew Chem Int Edit* **2019**, *58*, 2622-2626.

4. A. Morozan, B. Jousselme, S. Palacin. *Energ Environ Sci* **2011**, *4*, 1238-1254.

5. X. J. Zhou, J. L. Qiao, L. Yang, J. J. Zhang. *Adv Energy Mater* **2014**, *4*, 1301523.

6. C. Du, X. H. Gao, W. Chen. *Chinese J Catal* **2016**, *37*, 1049-1061.

7. J. A. Trindell, Z. Y. Duan, G. Henkelman, R. M. Crooks. *Chem Rev* **2020**, *120*, 814-850.

8. H. S. Wang, Y. Yang, F. J. DiSalvo, H. D. Abruna. *Acs Catal* **2020**, *10*, 4608-4616.

9. V. Stamenkovic, T. J. Schmidt, P. N. Ross, N. M. Markovic. *Journal of Physical Chemistry B* **2002**, *106*, 11970-11979.

10. Y. C. Xing, Y. Cai, M. B. Vukmirovic, W. P. Zhou, H. Karan, J. X. Wang, R. R. Adzic. *J. Phys. Chem. Lett.* **2010**, *1*, 3238-3242.

11. A. U. Nilekar, Y. Xu, J. L. Zhang, M. B. Vukmirovic, K. Sasaki, R. R. Adzic, M. Mavrikakis. *Top Catal* **2007**, *46*, 276-284.

12. Y. Xiong, Y. Yang, H. Joress, E. Padgett, U. Gupta, V. Yarlagadda, D. N. Agyeman-Budu, X. Huang, T. E. Moylan, R. Zeng, A. Kongkanand, F. A. Escobedo, J. D. Brock, F. J. DiSalvo, D. A. Muller, H. D. Abruna. *P Natl Acad Sci USA* **2019**, *116*, 1974-1983.

13. D. L. Wang, H. L. L. Xin, R. Hovden, H. S. Wang, Y. C. Yu, D. A. Muller, F. J. DiSalvo, H. D. Abruna. *Nat Mater* **2013**, *12*, 81-87.

14. E. L. Hu, X. Y. Yu, F. Chen, Y. D. Wu, Y. Hu, X. W. Lou. *Adv Energy Mater* **2018**, *8*, 1702476.

15. X. Han, Z. P. Zheng, J. Y. Chen, Y. K. Xue, H. Q. Li, J. Zheng, Z. X. Xie, Q. Kuang, L. S. Zheng. *Nanoscale* **2019**, *11*, 12610-12618.

16. W. J. Jiang, L. Gu, L. Li, Y. Zhang, X. Zhang, L. J. Zhang, J. Q. Wang, J. S. Hu, Z. D. Wei, L. J. Wan. *J Am Chem Soc* **2016**, *138*, 3570-3578.

17. H. S. Park, S. B. Han, D. H. Kwak, J. H. Han, K. W. Park. *J Catal* **2019**, *370*, 130-137.

18. A. Bonnefont, A. S. Ryabova, T. Schott, G. Kerangueven, S. Y. Istomin, E. V. Antipov, E. R. Savinova. *Curr Opin Electroche* **2019**, *14*, 23-31.

19. Y. J. Wang, H. B. Fan, A. Ignaszak, L. Zhang, S. Q. Shao, D. P. Wilkinson, J. J. Zhang. *Chem Eng J* **2018**, *348*, 416-437.

20. Y. G. Yao, Z. N. Huang, P. F. Xie, S. D. Lacey, R. J. Jacob, H. Xie, F. J. Chen, A. M. Nie, T. C. Pu, M. Rehwoldt, D. W. Yu, M. R. Zachariah, C. Wang, R. Shahbazian-Yassar, J. Li, L. B. Hu. *Science* **2018**, *359*, 1489-1494.

21. R. J. Toh, Z. Sofer, M. Pumera. *Chemphyschem* **2015**, *16*, 3527-3531.

22. J. Hwang, R. R. Rao, L. Giordano, Y. Katayama, Y. Yu, Y. Shao-Horn. *Science* **2017**, *358*, 751-756.

23. Z. S. Wu, S. B. Yang, Y. Sun, K. Parvez, X. L. Feng, K. Mullen. *J Am Chem Soc* **2012**, *134*, 9082-9085.

24. Y. J. Ma, H. Wang, J. Key, V. Linkov, S. Ji, X. F. Mao, Q. Z. Wang, R. F. Wang. *Int J Hydrogen Energ* **2014**, *39*, 14777-14782.

25. Z. Y. Fan, J. Li, W. Yang, Q. Fu, K. Sun, Y. C. Song, Z. D. Wei, Q. Liao, X. Zhu. *Chem Eng J* **2020**, *385*, 123393.

26. R. J. Gao, J. Wang, Z. F. Huang, R. R. Zhang, W. Wang, L. Pan, J. F. Zhang, W. K. Zhu, X. W. Zhang, C. X. Shi, J. Lim, J. J. Zou. *Nat Energy* **2021**, *6*, 614-623.

27. M. R. Wei, S. Huang, Y. Wang, Y. H. Liu, Y. F. He, C. Wang, L. Yang. *J Alloy Compd* **2020**, *827*, 154207.

28. J. Yu, Q. J. He, G. M. Yang, W. Zhou, Z. P. Shao, M. Ni. *Acs Catal* **2019**, *9*, 9973-10011.

29. Z. G. Zhu, R. C. Deka, A. Chutia, R. Sahnoun, H. Tsuboi, M. Koyama, N. Hatakeyama, A. Endou, H. Takaba, C. A. Del Carpio, M. Kubo, A. Miyamoto. *J Phys Chem Solids* **2009**, *70*, 1248-1255.

30. C. L. Dong, X. L. Zhang, J. Xu, R. Si, J. Sheng, J. Luo, S. N. Zhang, W. J. Dong, G. B. Li, W. C. Wang, F. Q. Huang. *Small* **2020**, *16*, 1905328.

31. M. B. Rossi, K. A. Abboud, P. Albores, L. M. Baraldo. *Eur J Inorg Chem* **2010**, 5613-5616.

32. J. Wang, Z. Q. Huang, W. Liu, C. R. Chang, H. L. Tang, Z. J. Li, W. X. Chen, C. J. Jia, T. Yao, S. Q. Wei, Y. Wu, Y. D. Lie. *J Am Chem Soc* **2017**, *139*, 17281-17284.

33. C. Z. Zhu, Q. R. Shi, B. Z. Xu, S. F. Fu, G. Wan, C. Yang, S. Y. Yao, J. H. Song, H. Zhou, D. Du, S. P. Beckman, D. Su, Y. H. Lin. *Adv Energy Mater* **2018**, *8*, 1801956.

34. Q. M. Liu, Y. Peng, Q. X. Li, T. He, D. Morris, F. Nichols, R. Mercado, P. Zhang, S. W. Chen. *Acs Appl Mater Inter* **2020**, *12*, 17641-17650.

35. S. H. Lee, J. Kim, D. Y. Chung, J. M. Yoo, H. S. Lee, M. J. Kim, B. S. Mun, S. G. Kwon, Y. E. Sung, T. Hyeon. *J Am Chem Soc* **2019**, *141*, 2035-2045.

36. B. D. Adams, A. C. Chen. *Materials today* **2011**, *14*, 282-289.

37. B. Z. Lu, L. Guo, F. Wu, Y. Peng, J. E. Lu, T. J. Smart, N. Wang, Y. Z. Finfrock, D. Morris, P. Zhang, N. Li, P. Gao, Y. Ping, S. W. Chen. *Nat Commun* **2019**, *10*, 631.

38. F. Liu, S. Y. Song, D. F. Xue, H. J. Zhang. *Adv Mater* **2012**, *24*, 1089-1094.

39. X. Tian, X. Zhao, Y. Su, L. Wang, H. Wang, D. Dang, B. Chi, H. Liu, E. J. Hensen, X. W. D. Lou. *Science* **2019**, *366*, 850-856.

40. B. Z. Lu, T. J. Smart, D. D. Qin, J. E. Lu, N. Wang, L. M. Chen, Y. Peng, Y. Ping, S. W. Chen. *Chem Mater* **2017**, *29*, 5617-5628.

41. D. J. Morgan. *Surf Interface Anal* **2015**, *47*, 1072-1079.

42. D. Flak, Q. L. Chen, B. S. Mun, Z. Liu, M. Rekas, A. Braun. *Appl Surf Sci* **2018**, *455*, 1019-1028.

43. T. E. Westre, P. Kennepohl, J. G. DeWitt, B. Hedman, K. O. Hodgson, E. I. Solomon. *J Am Chem Soc* **1997**, *119*, 6297-6314.

44. L. X. Chen, T. Liu, M. C. Thurnauer, R. Csencsits, T. Rajh. *Journal of Physical Chemistry B* **2002**, *106*, 8539-8546.

45. B. K. Teo, *EXAFS: basic principles and data analysis*. Springer Science & Business Media: **2012**, Vol. 9.

46. C. H. Zhang, J. W. Sha, H. L. Fei, M. J. Liu, S. Yazdi, J. B. Zhang, Q. F. Zhong, X. L. Zou, N. Q. Zhao, H. S. Yu, Z. Jiang, E. Ringe, B. I. Yakobson, J. C. Dong, D. L. Chen, J. M. Tour. *Acs Nano* **2017**, *11*, 6930-6941.

47. M. A. Hubert, A. M. Patel, A. Gallo, Y. Z. Liu, E. Valle, M. Ben-Naim, J. Sanchez, D. Sokaras, R. Sinclair, J. K. Norskov, L. A. King, M. Bajdich, T. F. Jaramillo. *Acs Catal* **2020**, *10*, 12182-12196.

48. B. Lu, Q. Liu, F. Nichols, R. Mercado, D. Morris, N. Li, P. Zhang, P. Gao, Y. Ping, S. W. Chen. *Research* **2020**, *2020*, 9167829.

49. J. Chlistunoff. *J Phys Chem C* **2011**, *115*, 6496-6507.

50. J. Wang, X. M. Ge, Z. L. Liu, L. Thia, Y. Yan, W. Xiao, X. Wang. *J Am Chem Soc* **2017**, *139*, 1878-1884.

51. S. Y. Chen, Y. Yan, P. P. Hao, M. H. Li, J. Y. Liang, J. Guo, Y. Zhang, S. W. Chen, W. P. Ding, X. F. Guo. *Acs Appl Mater Inter* **2020**, *12*, 12686-12695.

52. R. J. Gao, L. Pan, Z. W. Li, C. X. Shi, Y. D. Yao, X. W. Zhang, J. J. Zou. *Adv Funct Mater* **2020**, *30*, 1910539.

53. G. Q. Shen, R. R. Zhang, L. Pan, F. Hou, Y. J. Zhao, Z. Y. Shen, W. B. Mi, C. X. Shi, Q. F. Wang, X. W. Zhang, J. J. Zou. *Angew Chem Int Edit* **2020**, *59*, 2313-2317.

Chapter 4 Rapid Preparation of Carbon-Supported Ruthenium Nanoparticles by Magnetic Induction Heating for Efficient Hydrogen Evolution Reaction in Both Acidic and Alkaline Media

4.1 Abstract

Ruthenium has been hailed as a competitive alternative for platinum towards hydrogen evolution reaction (HER), a critical process in electrochemical water splitting. In this study, we successfully prepare metallic Ru nanoparticles supported on carbon paper by utilizing a novel magnetic induction heating (MIH) method. The samples are obtained within seconds, featuring a Cl-enriched surface that is unattainable via conventional thermal annealing. The best sample within the series shows a remarkable HER activity in both acidic and alkaline media with an overpotential of only -23 mV and -12 mV to reach the current density of 10 mA cm^{-2}, highly comparable to that of Pt/C benchmark. Theoretical studies based on density functional theory show that the excellent electrocatalytic activity is accounted for by the surface metal-Cl species that facilitate charge transfer and downshift the d-band center. Results from this study highlight the unique advantages of MIH in rapid sample preparation where residual anion ligands play a critical role in manipulating the electronic properties of the metal surfaces and the eventual electrocatalytic activity.

4.2 Introduction

With the ever-increasing need of energy and rapid depletion of traditional fossil fuels, hydrogen gas (H_2) has been considered as one of the most promising green energy resources. However, currently H_2 is produced mostly by steam-methane reforming at high temperatures (700~1000 °C), making it energy- and capital-consuming.[1] Electrochemical water splitting (water electrolyzer) represents an effective alternative, where H_2 is produced at the cathode using electricity produced from a sustainable

source such as wind, sun light, and hydraulics. Yet, an appropriate catalyst is needed to catalyze the hydrogen evolution reaction (HER) so as to decrease the overpotential and increase the current density. Thus far Pt-based nanoparticles have remained the catalysts of choice towards HER; yet the high cost and limited natural abundance has hampered the wide-spread applications.[2,3]

Ruthenium (Ru), which costs about half of Pt, has emerged as a viable substitute, due to its similar bonding strength with hydrogen (~65 kcal mol^{-1}) to that of Pt-H, a critical parameter in dictating the HER activity.[4] Nevertheless, in the well-known volcano plot of the hydrogen adsorption Gibbs free energy (ΔG_{H^*}),[5,6] Ru is actually situated on the left side, suggesting a somewhat strong adsorption of H that is unfavorable for H desorption from the catalyst surface. Computational studies based on density functional theory (DFT) have shown that H adsorption onto the top sites of Ru(0001) facet possesses an almost ideal ΔG_{H^*} of only -0.07 eV, in comparison to the adjacent hollow Ru_3 sites that exhibit a far more negative ΔG_{H^*} of ca. -0.45 eV, suggesting that the latter is actually the most likely dominant binding sites, leading to an nonideal HER performance.[7] In another study, Li et al.[8] investigated the effect of ruthenium crystallinity on the HER activity and observed that the ΔG_{H^*} on the hollow or bridge sites on most facets of *hcp* Ru and *fcc* Ru all ranged from -0.5 to -0.7 eV, markedly greater than that on Pt(111) (ca. 0 eV).[9] This indicates that manipulation of the Ru crystallinity is unlikely to be effective in diminishing ΔG_{H^*} for optimal HER.

Preparation of nanocomposite catalysts with Ru supported on select functional substrates (i.e., carbon, nitride, oxide, etc.) has been adopted as a feasible strategy to

tune the energetics of H adsorption.[10] For instance, Ru nanoparticles supported on graphitic carbon nitride (g-C_3N_4) outperformed Pt in alkaline HER, due to the reduced energy barrier of water dissociation and optimal ΔG_{H^*}.[7] Ru atomically dispersed into g-C_3N_4 or N-doped carbon also showed unprecedented HER performance in both alkaline and acidic media, owning to the unique Ru-N/C atomic coordination for optimal adsorption of H.[11-13] Alloying is another strategy to control the electronic structure of Ru. For example, Cai et al.[14] synthesized ultrathin RuCo alloy nanosheets and observed a low overpotential (η_{10}) of -10 mV to reach the current density of 10 mA cm^{-2} in 1 M KOH, consistent with results from DFT studies that Ni or Co could efficiently downshift the d-band center of Ru and weaken H* adsorption. Non-metal elements have also been integrated into Ru producing RuX hybrids (X = B, Si, P, S, Se, and Te) to tune the electronic structure and the adsorption of H* on Ru.[7,15-19] For instance, interstitial alloying of Si atoms into Ru has been found to render the top adsorption of H* to be dominant, leading to an HER activity that rivals that of commercial Pt.[7] In addition, it has been shown that surface electronic structure of Ru can be manipulated by coordination with P atoms, where electron-transfer from Ru to P dopants reduced ΔG_{H^*} and hence enhanced both HER and HOR.[20]

In these prior studies, the Ru-based catalysts were typically prepared by wet chemical reduction or pyrolysis, and a range of chemicals and solvents are consumed, making the process ungreen and time-consuming. In the present study, we report a novel method based on magnetic induction heating (MIH) to synthesize Ru nanoparticles supported on carbon paper within seconds. Notably, in the ultrafast heating-quench

process, metallic Ru nanoparticles were generated and deposited evenly on carbon paper by thermal decomposition of $RuCl_3$ salt even in the ambient atmosphere. Because of the short heating duration, $RuCl_3$ was incompletely decomposed, leading to residual Cl on the Ru surface with the content readily controlled by the magnetic current and heating time. This turned out to play a critical role in the HER performance of the samples, as confirmed in DFT studies where the surface Cl species influenced the electronic structure of metallic Ru and the adsorption configuration and energetics of H*. Among the series, the best sample was obtained with a magnetic current of 300 A and heating time of 6 s, which demonstrated an HER activity similar to that of commercial Pt/C in both alkaline and acidic media with a respective η_{10} of -12 and -23mV.

4.3 Results and Discussion

4.3.1 Sample preparation

The synthesis of Ru nanoparticles supported on carbon paper consisted of two major steps, as shown in Figure 1a. $RuCl_3$ solution was first dropcast onto a piece of pretreated carbon paper and dried at room temperature for 10 min. The carbon paper was then wrapped with graphite paper and sandwiched between two iron sheets, and the assembly was placed into the middle of the induction coil of a magnetic induction heater and heated at a controlled current for a varied period of time before being dropped into a beaker containing cold ethanol (-78 °C) to quench the sample and to prevent oxidation in the air (Figure 1b). By virtue of the Joule effect, the iron sheets can be heated up to ca. 1500 °C at an ultrafast rate (up to 200 K s^{-1}, Figure 1c) owning

to the Eddy current generated instantly by the magnetic field. As a thermal-radiative material, carbon paper can be heated up simultaneously, converting $RuCl_3$ into Ru nanoparticles supported on carbon paper.

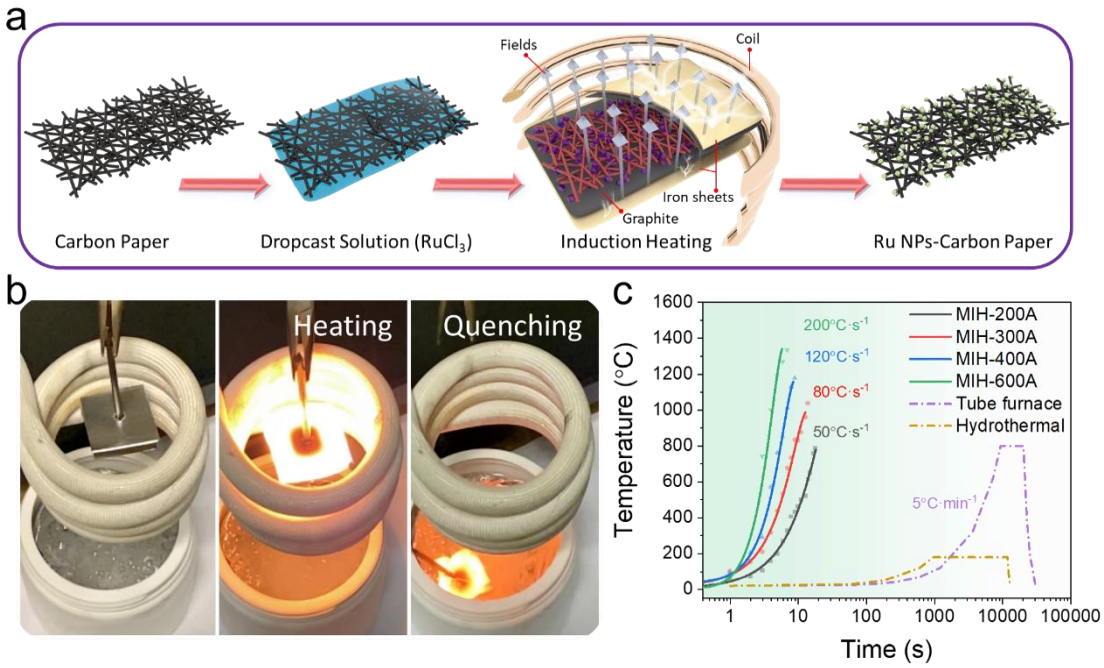

Figure 1. (a) Schematic illustration of the preparation of Ru nanoparticles supported on carbon paper by magnetic induction heating. (b) Photographs of synthetic process. (c) Heating temperature as the function of time by using MIH at different heating currents, as determined with an infrared thermometer (Figure 2).

Figure 2. Temperature measurement setup for MIH. The inset shows the lase points of the thermometer on the iron sheets. A tripod is used to fix the thermometer during the measurements.

4.3.2 Structural characterizations

The structure of the samples was first characterized by transmission electron microscopy (TEM) measurements. From Figure 3-6, one can clearly see a structural evolution of the ruthenium species from an amorphous state to metallic ruthenium nanoparticles with increasing magnetic current. For instance, for Ru-200 that was prepared by MIH treatment at 200 A for 6 s, the sample contained mostly amorphous particles (2 – 5 nm in diameter), as manifested in bright-field TEM measurements (Figure 4). This was likely because the temperature was not sufficiently high for complete decomposition of $RuCl_3$ and for the production of crystalline nanoparticles. When the magnetic current was increased to 300 A, the corresponding sample, Ru-300 (Figure 3a), actually consisted of nanoparticles evenly distributed on the carbon paper,

most of which fell in the size range of 2 to 10 nm in diameter (Figure 3b), with an average size of 6 nm. Additionally, clearly-defined lattice fringes can be resolved from these nanoparticles in high-resolution TEM measurements (Figure 3c), featuring two interplanar spacings of ca. 0.135 and 0.205 nm that can be ascribed to the Ru(11-20) and (10-11) facets (JCPDS-ICDD card No. 06-0663), respectively. The good crystallinity of the nanoparticle can also be evidenced in the bright spots of the fast Fourier transform of the TEM image, as shown in the insets to Figure 3c and 5, suggesting the formation of *hcp* Ru nanoparticles. At even higher magnetic current (e.g., Ru-600, Figure 6), apparent aggregation of crystalline Ru occurred forming large agglomerates.

The sample morphology can also be readily manipulated by the heating time. For instance, when the heating time was reduced to 3 s (Ru-300-S), only amorphous particles were produced on carbon (Figure 7); yet with the heating time prolonged to 12 s (Ru-300-L), the sample consisted mostly of *hcp* Ru agglomerates (Figure 8). Taken together, these results suggest that 300 A and 6 s represent the optimal conditions to produce *hcp* Ru nanoparticles that were well dispersed on the surface of carbon paper, a unique feature conducive for HER electrocatalysis (vide infra).

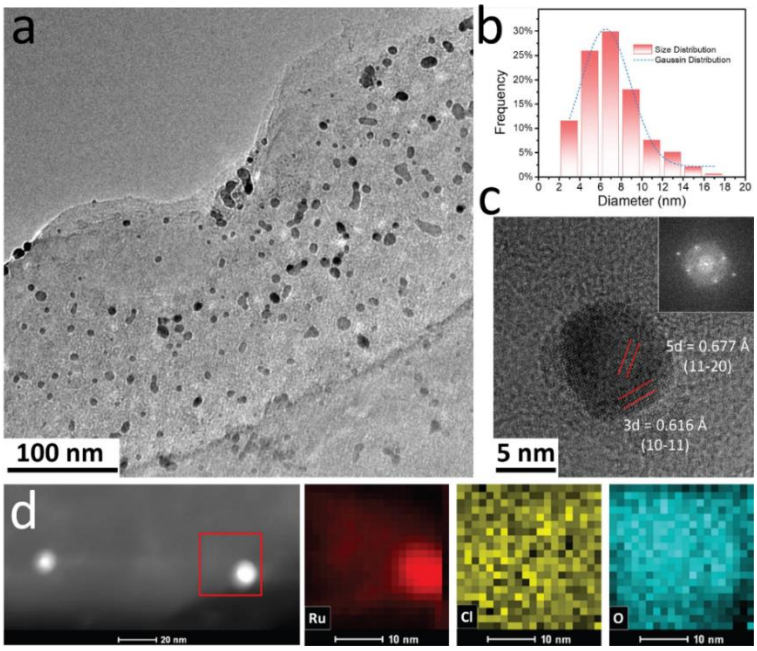

Figure 3. TEM studies of the Ru-300 sample. (a) TEM image of Ru nanoparticles at low magnification and (b) the corresponding core size histogram. (C) HRTEM image of a Ru nanoparticle with the corresponding fast-Fourier transform (FFT) image shown in the inset. (d) ADF-TEM image of Ru nanoparticles and the corresponding elemental maps of the red-circled area.

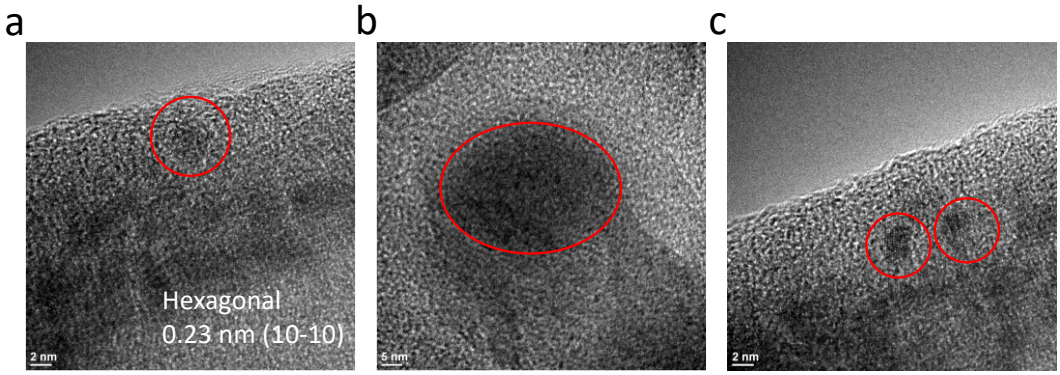

Figure 4. Representative TEM images of Ru-200. Red circles highlight the Ru nanoparticles which feature an interplanar spacing of 0.23, consistent with hexagonal Ru.

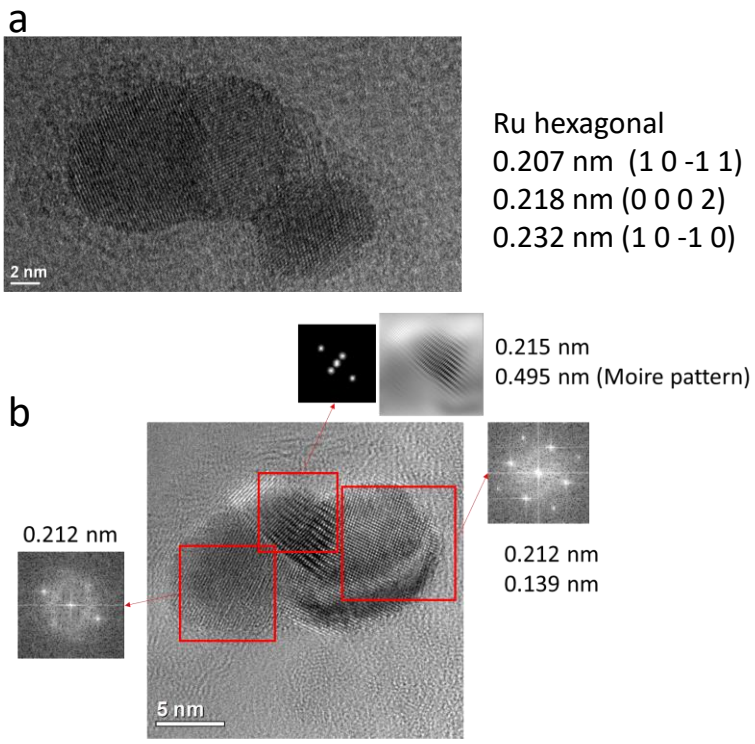

Figure 5. Representative high-resolution TEM images of Ru-300. Insets to panel (b) are the Fourier transforms of the red-box areas.

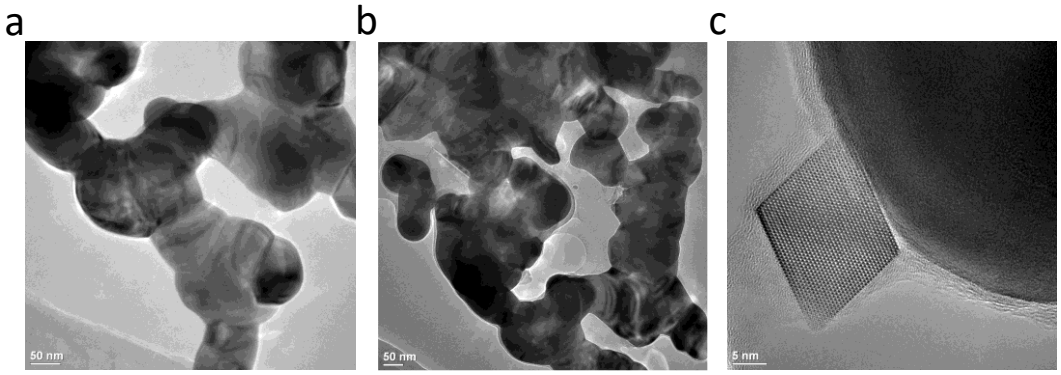

Figure 6. Representative TEM images of Ru-600.

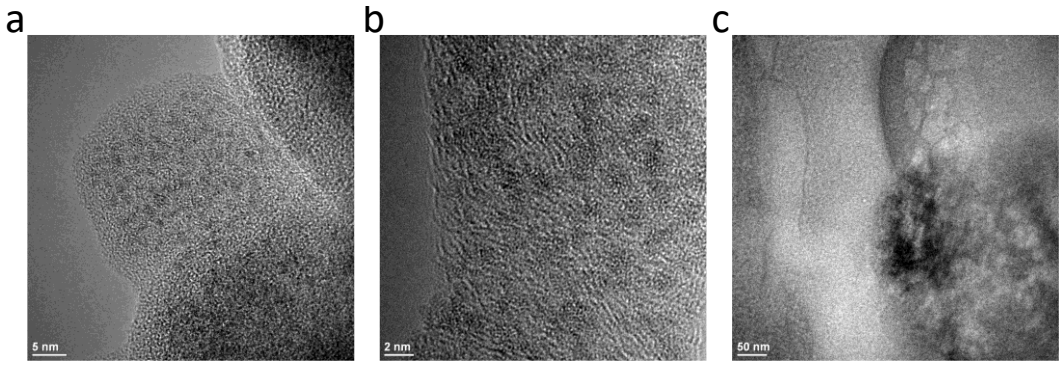

Figure 7. Representative TEM images of Ru-300-S.

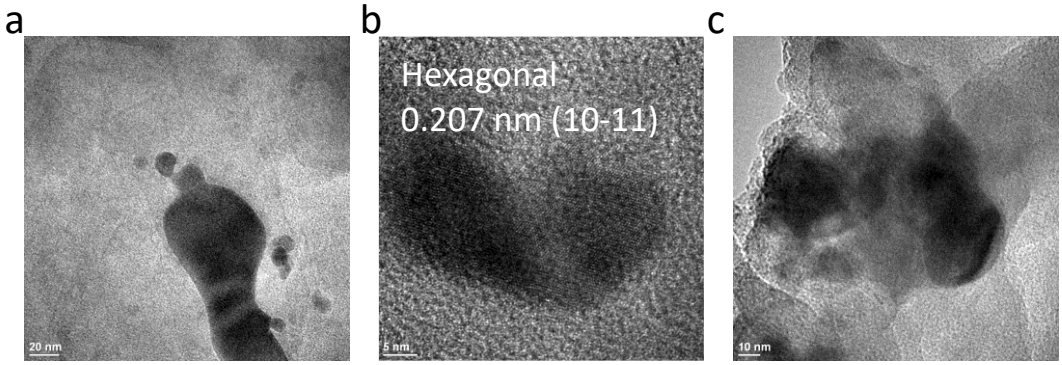

Figure 8. Representative TEM images of Ru-300-L.

Interestingly, elemental mapping analysis based on electron energy loss spectroscopy (EELS) measurements showed that Ru was mostly confined within the nanoparticles, with residual O and Cl (Figure 3d). Indeed, these elements can also be identified in X-ray photoelectron spectroscopy (XPS) measurements. From the XPS survey spectra in Figure 9, the Ru 3d, C 1s, Ru 3p, and O 1s peaks can be clearly resolved at ca. 280, 284, 474, and 530 eV, respectively, in all samples. Notably, the Cl 2p peak (ca. 200 eV) can also be seen in some of the samples that were prepared at relatively low currents for a short heating time, such as Ru-200, Ru-300 and Ru-300-S, suggesting the formation of residual Cl. By sharp contrast, the Cl 2p peak vanished in samples

prepared by prolonged heating at a higher current, such as Ru-400, Ru-600 and Ru-200, implying complete decomposition of $RuCl_3$ into Ru nanoparticles.

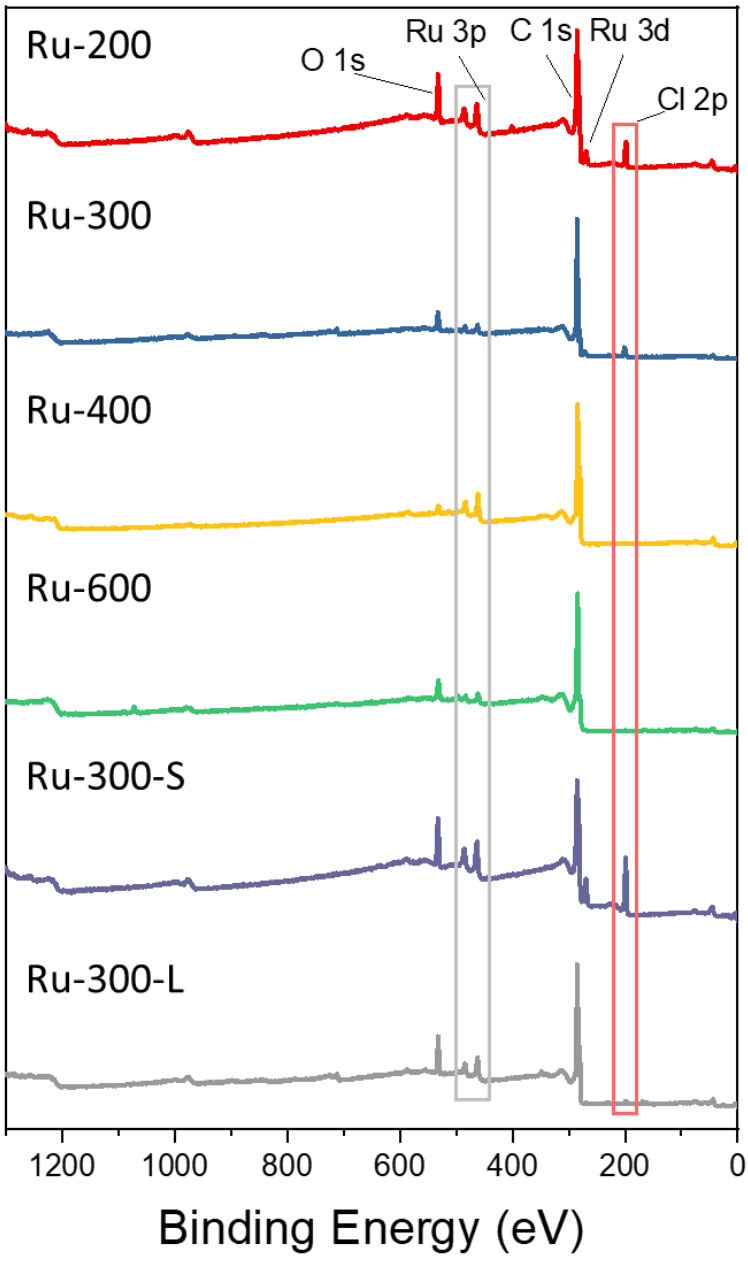

Figure 9. XPS survey spectra of Ru-200, Ru-300, Ru-400, Ru-600, Ru-300-S, and Ru-300-L.

Figure 10a shows the high-resolution scans of the Ru 3p electrons in the series of samples prepared at different magnetic currents (200 to 600 A) but for the same heating time of 6 s. One can see that the Ru-600 sample consisted of a single doublet (red peaks) at 461.1/483.3 eV arising from the $3p_{3/2}/3p_{1/2}$ electrons of metallic ruthenium,[21-23] consistent with results from TEM measurements where large agglomerates of crystalline Ru were found (Figure 6). For Ru-400 that was prepared at a lower magnetic current, in addition to the metallic Ru $3p_{3/2}/3p_{1/2}$ pair at 461.2/483.4 eV, a small, second doublet (blue peaks) can be resolved at 463.9/485.1 eV, signifying the formation of electron-deficient Ru likely in the forms of $RuCl_x/RuO_y$ species.[21,24-26] The latter became more pronounced in Ru-300 (464.1/486.3 eV), with the corresponding metallic peaks at 461.6/483.8 eV. Ru-200 exhibited an even more prominent doublet for the $RuCl_x/RuO_y$ species though at a binding energy about 0.8 eV higher at 465.3/487.5 eV. The other doublet (orange peaks) can be deconvoluted at 462.7/484.9 eV, which were at least 1.1 eV higher than those of the other samples in the series but markedly lower than those of $RuCl_3$ (464.1 eV for Ru $3p_{3/2}$),[21] suggesting only partial decomposition of $RuCl_3$ and the formation of amorphous Ru nanoclusters as observed in TEM measurements (Figure 4). In fact, on the basis of the integrated peak areas, one can see a clear decline of the relative content of the $RuCl_x/RuO_y$ species in total Ru with increasing magnetic current, Ru-200 (49.7%) > Ru-300 (29.3%) > Ru-400 (11.5%) > Ru-600 (0%) (Table 1).[8,27]

A similar trend was observed when the heating duration was increased at a fixed magnetic current. From Figure 11, one can see that the binding energies of the Ru $3p_{3/2}/3p_{1/2}$ peaks decreased by ca. 1.3 eV from Ru-300-S to Ru-300 and Ru-300-L, and the fraction of the $RuCl_x/RuO_x$ species diminished accordingly, Ru-300-S (45.5%) > Ru-300 (29.3%) > Ru-300-L (17.8%). It should be noted that in comparison with Ru-200, the Ru $3p_{3/2}/3p_{1/2}$ binding energies of Ru-300-S were ca. 0.3 eV higher, implying an even lower degree of decomposition of $RuCl_3$ into Ru nanoparticles. That is, prolonged heating facilitates the formation of metallic Ru nanoparticles, consistent with the TEM results (Figure 3-8). The corresponding Ru 3d profiles are also in good agreement (Figure 12).

Consistent results were obtained from the Cl 2p spectra. From Figure 10b, one can clearly see that Ru-200, Ru-300, and Ru-400 all possessed a doublet (green peaks) at 198.0/199.6 eV that can be assigned to Ru-Cl_x.[24,28,29] For Ru-600, this doublet appears at a higher binding energy by (ca. 0.5 eV) suggesting weakened interaction between Cl and Ru, likely because of structural hinderance by a thin carbon shell, as observed in TEM measurements (Figure 6c). For Ru-200 and Ru-300, a second doublet emerged at 200.0/201.6 eV that can be ascribed to organic Cl (orange peaks, C-Cl_x or O-Cl_x species),[28] which vanished altogether in Ru-400 and Ru-600, implying thermal instability of the organic Cl species. Furthermore, the content of Ru-Cl_x diminished appreciably with increasing magnetic current (Table 1),[24] Ru-200 (6.24 at%) > Ru-300 (0.96 at%) > Ru-600 (0.47 at%) > Ru-400 (0.35 at%). This suggests almost complete decomposition of $RuCl_3$ into Ru nanoparticles at a current greater than 400 A for a

heating time of at least 6 s. A similar trend was observed when the magnetic current was fixed at 300 A, with the heating time increased from 3 s (Ru-300-S) to 12 s (Ru-300-L), which led to a clear diminishment of the organic Cl species, and Ru-Cl_x being the increasingly dominant component in the sample (Figure 13).

The C 1s and O 1s spectra of the samples series also provide important insights into the structural change during the ultrafast heating process. One can see from Figure 12 that with increased magnetic current, the main C 1s peak decreased from ca. 284.4 eV for Ru-200 and Ru-300 to ca. 284.1 eV for Ru-400 and Ru-600, implying that the carbon substrate was somewhat electron-deficient at low currents. As for the O 1s spectra (Figure 14a), the major species were C-O (533.5 eV) and C=O (531.5 eV) moieties on carbon paper. With increasing magnetic current (temperature), the C=O peaks diminished in intensity, and the overall O content decreased from 14.5 at% for Ru-200 to ca. 7% for other samples prepared at higher magnetic currents (Table 1). It is likely that the decomposition of these oxygen groups produced CO and/or CO_2,[30] facilitating the carbothermal reduction of $RuCl_x$ to ruthenium nanoparticles and protection against oxidation. Yet, with a prolonged heating duration, the overall content of O increased from 7.3 at% for Ru-300 to 11.3 at% for Ru-300-L (Figure 14b). Notably, for Ru-200, Ru-300, and Ru-400, there is a minor peak at 530.0 eV suggesting the formation of RuO_x species on the nanoparticle surface (it is unlikely to be bulk RuO_2 as no RuO_2 lattice fringes were observed in TEM measurements).

Taken together, these results suggest the successful transformation of $RuCl_3$ into Ru nanoparticles by MIH, which were decorated with $RuCl_x/RuO_y$ species on the surface.

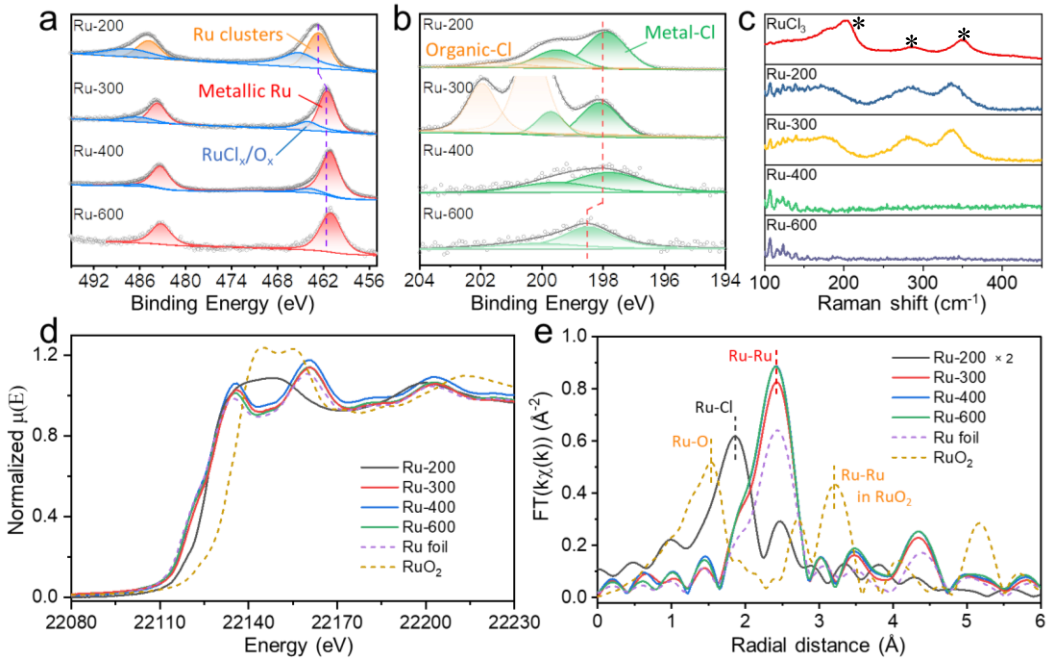

Figure 10. (a) Ru 3p XPS spectra and (b) Cl 2p XPS spectra of Ru-200, Ru-300, Ru-400, and Ru-600. (c) Raman spectra of $RuCl_3$, Ru-200, Ru-300, Ru-400, and Ru-600. (d) X-ray absorption near edge spectra (XANES) and (e) the corresponding Fourier transformed extended X-ray absorption spectra (FT-EXAFS) of Ru-200, Ru-300, Ru-400, and Ru-600. "Ru-Ru" in red represents Ru-Ru bonds in metallic Ru, while orange represents Ru-Ru bonds in RuO_2.

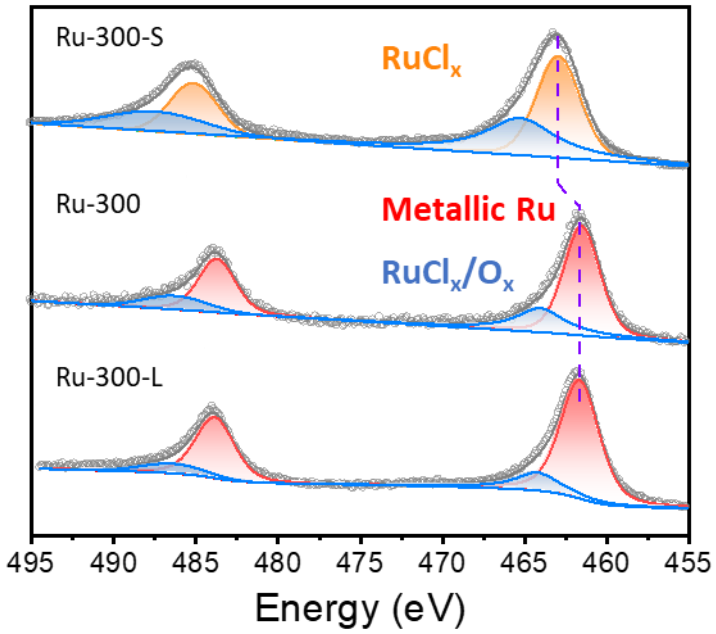

Figure 11. Ru 3p XPS spectra of Ru-300-S, Ru-300, and Ru-300-L. Symbols are experimental data and colored peaks are deconvolution fits.

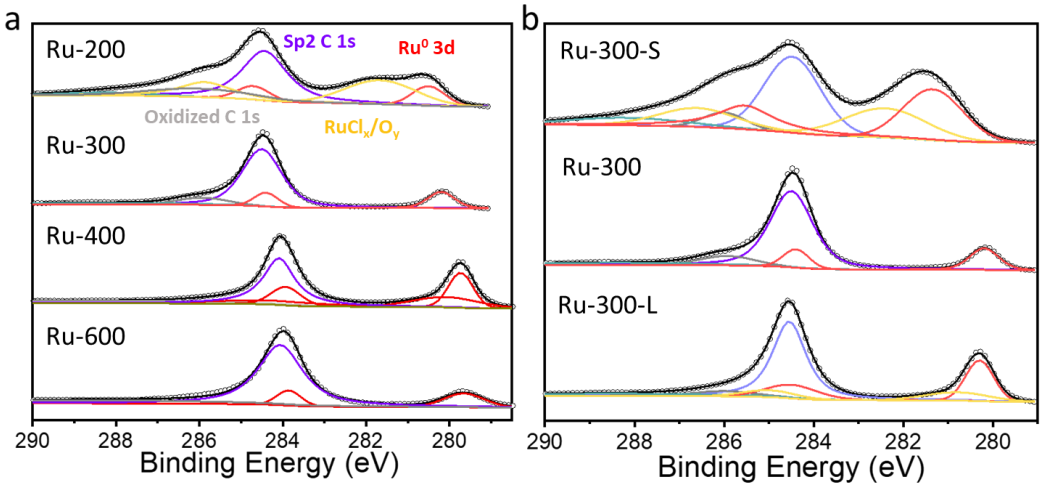

Figure 12. C 1s and Ru 3d spectra of (a) Ru-200, Ru-300, Ru-400, and Ru-600, (b) Ru-300-S, Ru-300, and Ru-300-L. Symbols are experimental data and colored peaks are deconvolution fits.

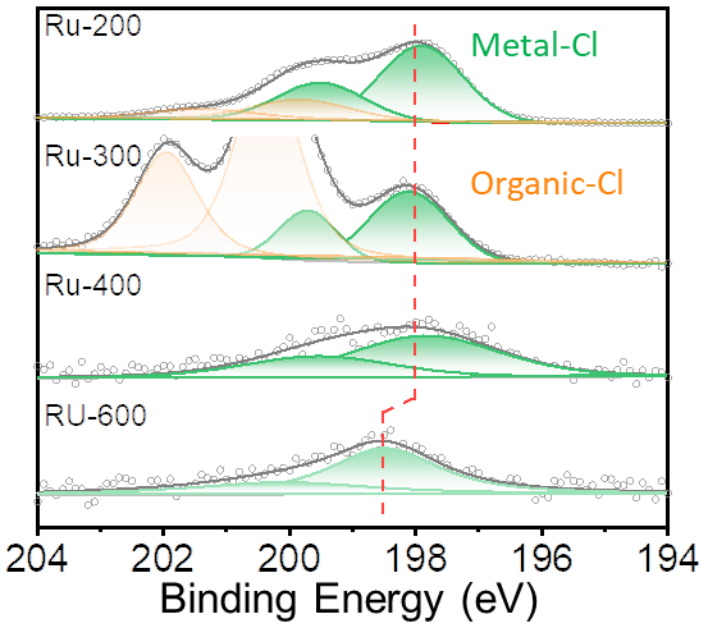

Figure 13. Cl 2p XPS spectra of Ru-300-S, Ru-300, and Ru-300-L. Symbols are experimental data and colored peaks are deconvolution fits.

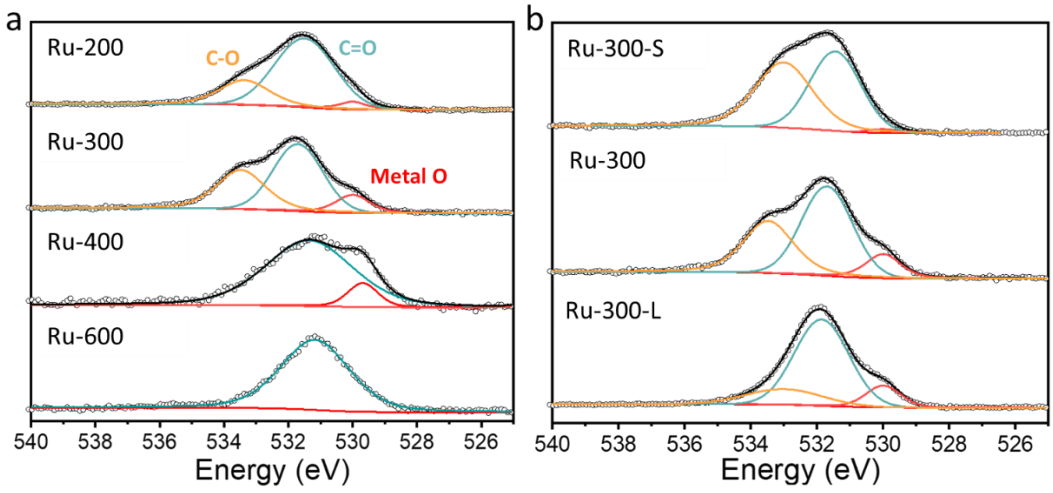

Figure 14. O 1s spectra of (a) Ru-200, Ru-300, Ru-400, and Ru-600, (b) Ru-300-S, Ru-300, and Ru-300-L. Symbols are experimental data and colored peaks are deconvolution fits.

Table 1. Results of XPS analysis.

Samples	**Ru-200**	**Ru-300**	**Ru-400**	**Ru-600**	**Ru-300-S**	**Ru-300-L**	**Ru-300 after tests in acid**	**Ru-300 after tests in alkaline**
C (at%)	72.47	87.93	91.07	91.63	61.83	84.39	75.72	79.67
Ru (at%)	5.04	1.28	4.62	1.39	5.93	3.16	1.47	0.58
Cl (at%)	8.02	3.51	0.35	0.47	17.04	1.15	0.75	0.83
O (at%)	14.47	7.29	3.96	6.51	15.2	11.29	22.07	18.92
Ru-O (at%)	0.77	0.85	0.46	0	0.19	1.39	0	0
Ru-Cl (at%)	6.24	0.96	0.35	0.47	16.39	0.96	0.06	0.72
Metallic Ru (at%)	2.53	0.9	4.09	1.39	3.29	2.59	1.21	0.21
$RuCl_x/O_x$ (at%)	2.5	0.37	0.53	0	2.65	0.57	0.26	0.37
Ru-Cl: total Ru	1.24	0.75	0.08	0.34	2.76	0.3	0.04	0.63

Metallic Ru: $RuCl_y/O_x$	1	2.4	7.7	-	1.2	4.6	4.6	0.56

Raman spectroscopic measurements showed that abundant $RuCl_x$ species were indeed formed in Ru-200 and Ru-300, but not in Ru-400 or Ru-600. From Figure 10c, one can see that $RuCl_3$ (on carbon paper) exhibited three major peaks at 202, 286, and 350 cm^{-1} (marked with asterisks), which can be assigned to the different A_g vibrational modes of Ru-Cl.[31-33] Notably, these three bands red-shifted somewhat for Ru-200 and Ru-300 to 171, 280, and 336 cm^{-1}, respectively. This may be accounted for by the change of the stacking mode and symmetry of the Ru-Cl species in comparison to pristine $RuCl_3$,[32] as a result of the decomposition of $RuCl_3$ during the ultrafast heating process. No apparent signals of Ru-Cl could be discerned from the spectra of Ru-400 or Ru-600, consistent with the complete decomposition of $RuCl_x$ into metallic Ru in these samples, as manifested in XPS measurements.

Further structural details of the samples were obtained from X-ray absorption spectroscopy (XAS) measurements. Figure 10d shows the X-ray absorption near-edge spectra (XANES) of the Ru K edge of the sample series. One can see that the absorption edge of Ru-200 was situated between those of Ru foil and RuO_2, suggesting an average valence state between 0 to +4, consistent with incomplete decomposition of $RuCl_3$ into Ru nanoparticles, as suggested in the above XPS measurements (Figure 10a). For other samples prepared at higher magnetic currents, the absorption edges, as well as the

postedge modulations, were all almost identical to that of Ru foil, confirming that metallic Ru was the dominant species in these samples, in excellent agreement with the TEM and XPS results (Figure 3 and 10). This also implies that the $RuO_x/RuCl_y$ species represent only a trace amount and were mostly residing only on the surface of Ru nanoparticles.

The corresponding Fourier-transformed extended X-ray absorption fine structure (FT-EXAFS) spectra are depicted in Figure 10e. One can see that Ru-200 exhibits a main peak at 1.86 Å, most likely arising from the Ru-Cl path,[26,29] and another at 2.48 Å due to the Ru-Ru bond,[13] which is slightly greater than that of Ru foil (2.42 Å). Fitting of the EXAFS data was then performed for the 6 samples in the series. Ru-200 is fitted by using a hexagonal $RuCl_3$ and hexagonal metallic Ru structure with a dummy variable incorporated to model the fraction of $RuCl_3$ to metallic Ru within the sample. The remaining 5 samples were all fitted to hexagonal metallic Ru. Standard paths for the structures were created using FEFF7 software.[34] The Fourier transform range was 3.5 to 11.75 $Å^{-1}$ and the fit range was 1.7 to 4.8 Å for all samples. Due to this range selection, the first 4 Ru-Ru standard paths and 2 multiscattering paths were used from the hexagonal metallic Ru structure for all fittings except for the Ru-200 sample which only used the first Ru-Ru metallic path due to a limited structure above 3 Å likely arising from disorder in the sample. Coordination number (CN) and distance ratios for all metallic samples were constrained to reflect the theoretical structure while allowing for a complete expansion/contraction. The constraints resulted in 8 degrees of freedom. Figure 15a and Table 2 show that for sample Ru-200 the Ru-Cl path possessed a CN of

5.5 with a bond length of 2.36 Å, while for the Ru-Ru path the distance is 2.70 Å with a CN of 0.95. Again, these suggest incomplete decomposition of $RuCl_3$ into Ru nanoclusters at 200 A for 6 s. For the samples prepared at higher magnetic currents (300 – 600 A), the main peak all appears at ca. 2.4 Å, consistent with the Ru-Ru bond in Ru foil, with a weak shoulder around 1.9 Å for the Ru-Cl bond. In addition, a small peak can be found at ca. 1.5 Å, similar to the Ru-O path of RuO_2. These observations are consistent with results from TEM and XPS measurements, where metallic Ru nanoparticles were the predominant product, and the nanoparticle surface was decorated with $RuO_x/RuCl_y$ species. Indeed, the fitting of the EXAFS data (Figure 15b-d and Table 2) indicates that the sample structure is identical to that of the Ru foil with a Ru-Ru bond length of ca. 2.67 Å and a CN of 12. A similar structural evolution was also observed with samples prepared at 300 A but for a different heating duration (Figure 15e-f and 16).

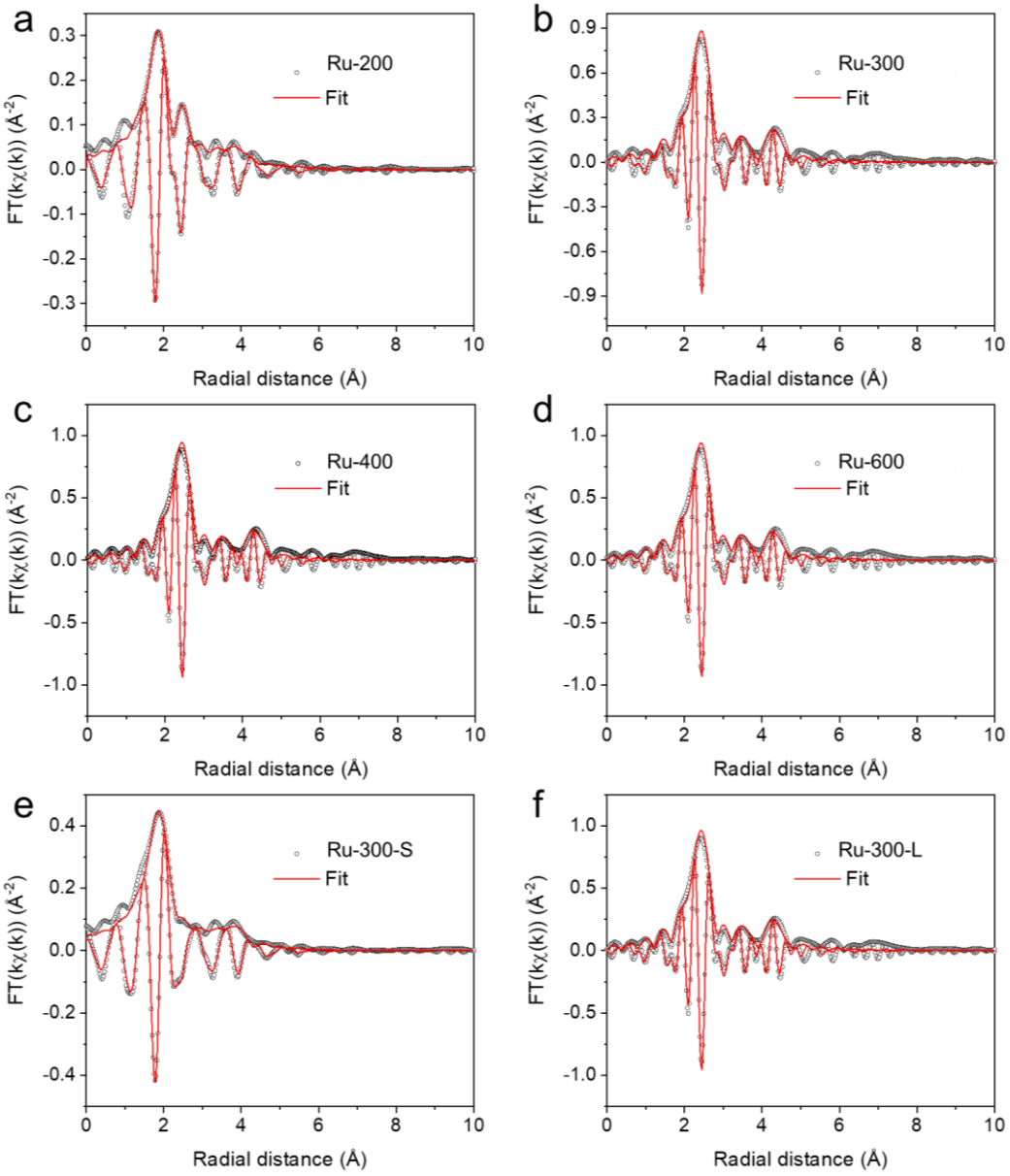

Figure 15. EXAFS fittings of Ru-200, Ru-300, Ru-400, Ru-600, Ru-300-S, and Ru-300-L.

Table 2. Fitting results of XAS spectra for of Ru-200, Ru-300, Ru-400, Ru-600, Ru-300-S, and Ru-300-L.

Sample	Peak	s^2 ($Å^2$)	Distance (Å)	Coordination number	Metallic Ru content
Ru-200	Ru-Cl	0.012	2.4	5.527	8.80%
	Metallic Ru-Ru	0.0020	2.4	0.947	
	Ru-Cl Multi-scattering	0.016	4.8	16.58	
Ru-300	Ru-Ru	0.0025	2.7	12	100%
	Ru-Ru	0.0052	3.8	6	
	Ru-Ru	0.0044	4.7	18	
	Ru-Ru multi-scattering	0.014	4.0	48	
	Ru-Ru multi-scattering	0.04	4.6	48	
	Ru-Ru	0.04	4.3	2	
	Ru-Ru multi-scattering	0.0016	5.0	96	
Ru-400	Ru-Ru	0.0019	2.7	12	100%
	Ru-Ru	0.0038	3.8	6	
	Ru-Ru	0.0037	4.7	18	

	Ru-Ru multi-scattering	0.010	4.0	48	
	Ru-Ru multi-scattering	0.032	4.6	48	
	Ru-Ru	0.023	4.3	2	
	Ru-Ru multi-scattering	0.0016	5.0	96	
Ru-600	Ru-Ru	0.0020	2.7	12	100%
	Ru-Ru	0.0034	3.8	6	
	Ru-Ru	0.0042	4.6	18	
	Ru-Ru multi-scattering	0.010	4.0	48	
	Ru-Ru multi-scattering	0.036	4.6	48	
	Ru-Ru	0.030	4.3	2	
	Ru-Ru multi-scattering	0.0016	5.0	96	
Ru-300-S	Ru-Ru	0.0025	2.7	12	100%
	Ru-Ru	0.0052	3.8	6	
	Ru-Ru	0.0044	4.7	18	

	Ru-Ru multi-scattering	0.014	4.0	48	
	Ru-Ru multi-scattering	0.04	4.6	48	
	Ru-Ru	0.04	4.3	2	
	Ru-Ru multi-scattering	0.0016	5.0	96	
Ru-300-L	Ru-Ru	0.0019	2.7	12	100%
	Ru-Ru	0.0038	3.8	6	
	Ru-Ru	0.37	4.7	18	
	Ru-Ru multi-scattering	0.010	4.0	48	
	Ru-Ru multiscattering	0.032	4.6	48	
	Ru-Ru	0.023	4.3	2	
	Ru-Ru multi-scattering	0.0016	5.0	96	

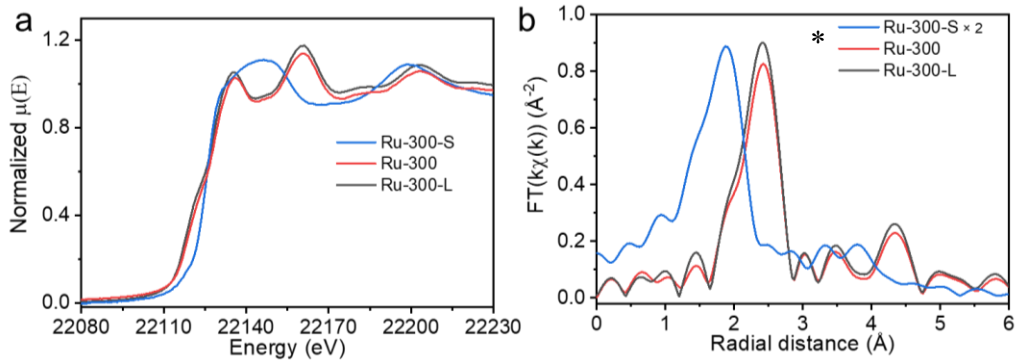

Figure 16. (a) X-ray absorption near edge spectra (XANES) and (b) the corresponding Fourier transformed extended X-ray absorption spectra (FT-EXAFS) of Ru-300-S, Ru-300, Ru-300-L. The blue peak (*, in panel b) for Ru-300-S is for the Ru-Cl path, which disappears in the other two samples. The peak near 2.5 A is the Ru-Ru path for metallic Ru.

4.3.3 Electrocatalytic activity

Significantly, the obtained Ru nanoparticles possessed a remarkable HER activity in both acidic and alkaline media. In cyclic voltammetry (CV) measurements (Figure 17), Ru-300 can be seen to exhibit a strong absorption/ desorption of H around 0 V, consistent with the formation of Ru nanoparticles, in comparison to others in the series. Figure 18a shows the polarization curves of the samples prepared under different conditions in 0.5 M H_2SO_4. One can see that Ru-300 showed a much better activity than other samples with a low η_{10} of -23 mV, as compared to -53 mV for Ru-200, -81 mV for Ru-400, -113 mV for Ru-600, -117 mV for Ru-300-S, and -33 mV for Ru-300-L. Such a performance of Ru-300 actually rivals that of commercial Pt/C (η_{10} = -11 mV). The corresponding Tafel plots are depicted in Figure 18b, where Ru-300 possessed the lowest slope (26 mV dec^{-1}) amongst the series, indicating a Volmer-Tafel

pathway. This pathway was also likely followed on Ru-200 and Ru-300-L which featured a low slope of 35 and 33 mV dec^{-1}, respectively (Figure 19). Nevertheless, the Tafel slope was markedly higher at 66 mV dec^{-1} for Ru-400, 80 mV dec^{-1} for Ru-600 and 74 mV dec^{-1} for Ru-300-S, suggesting a more sluggish Vomer-Heyrovsky pathway instead.[13,35,36]

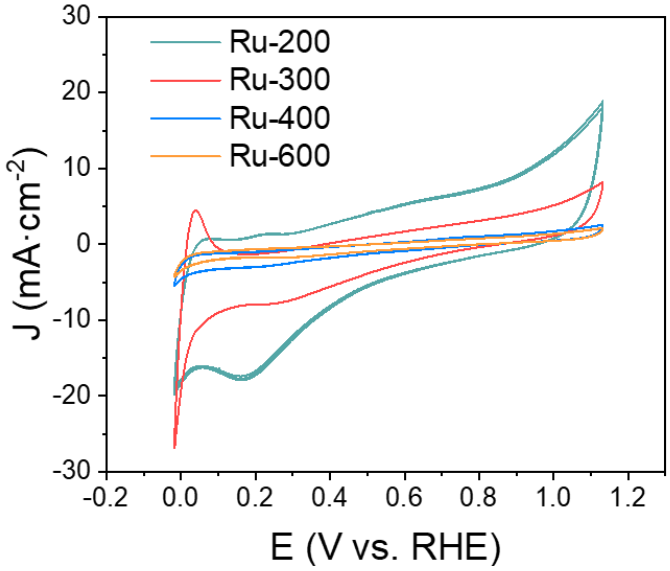

Figure 17. CV scans of Ru-200, Ru-300, Ru-400, and Ru-600 at a scan rate of 50 mV s^{-1} in N_2 saturated 0.5 M H_2SO_4.

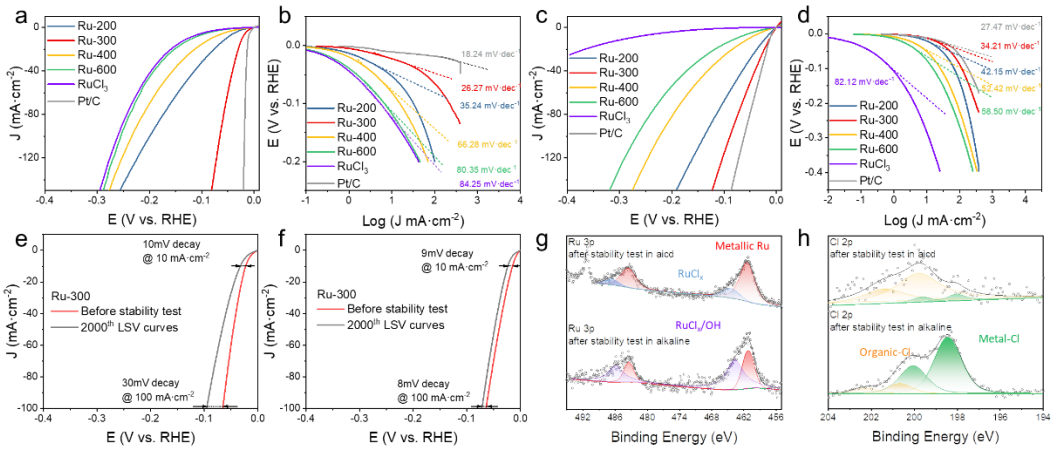

Figure 18. (a) Linear scanning voltammetry (LSV) curves and (b) the corresponding Tafel plots of Ru-200A, Ru-300, Ru-400, Ru-600, and $RuCl_3$ in 0.5 M H_2SO_4. (c) LSV curves of Ru-200, Ru-300, Ru-400, Ru-600, and $RuCl_3$ in 1 M KOH and (d). Stability test of Ru-300 in (e) 0.5 M H_2SO_4 and (f) 1 M KOH. XPS spectra of the (g) Ru 2p and (h) Cl 2p electrons of Ru-300 after stability test in acidic and alkaline media.

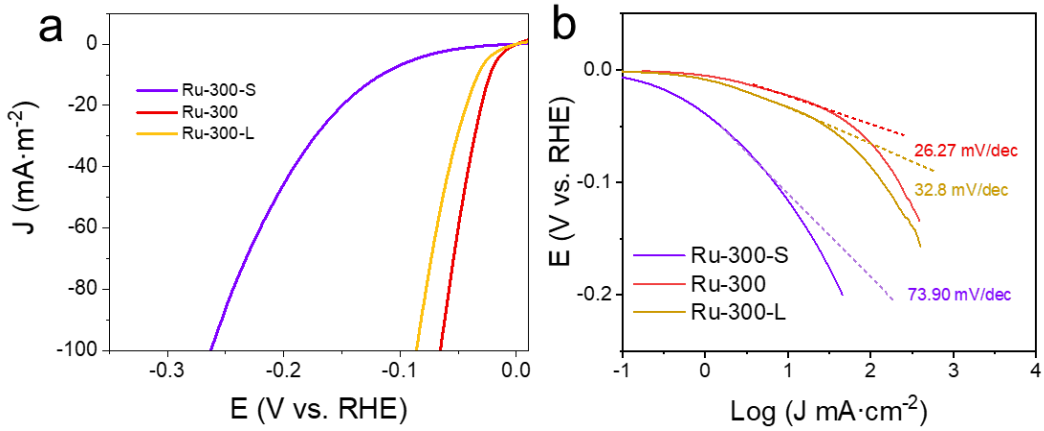

Figure 19. (a) LSV curves of Ru-300-S, Ru-300, and Ru-300-L at the scan rate of 10 mV s^{-1} and (b) the corresponding Tafel plots in 0.5 M H_2SO_4.

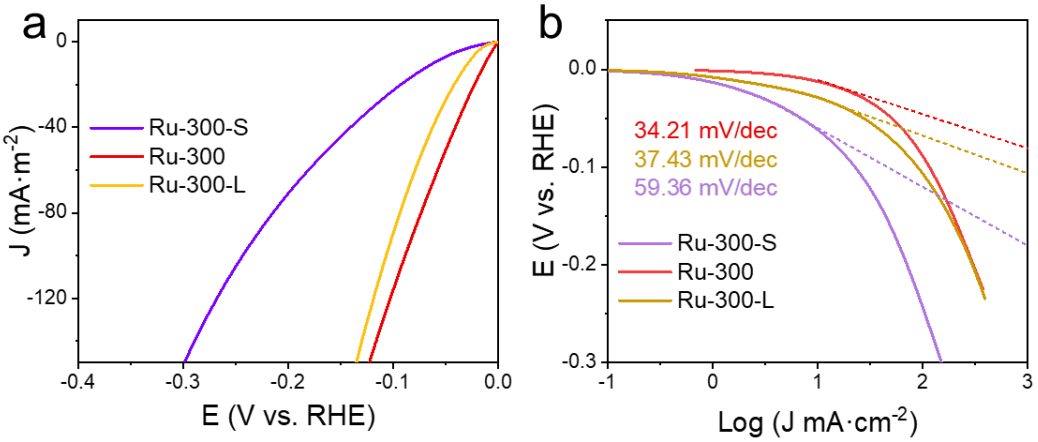

Figure 20. (a) LSV curves of Ru-300-S, Ru-300, and Ru-300-L in 1 M KOH at the scan rate of 10 mV s^{-1} and the (b) corresponding Tafel plots in 1 M KOH.

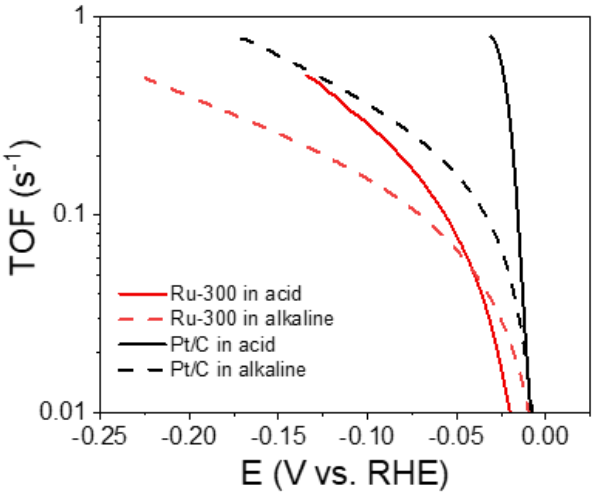

Figure 21. TOF curves of Ru-300 and Pt/C in acid and alkaline.

The Ru samples also exhibited outstanding HER activity in alkaline media. Figure 18c shows the polarization curves in 1 M KOH. The η_{10} can be found to decrease drastically in the order of Ru-600 (η_{10} = -78 mV) > Ru-400 (-52 mV) > Ru-200 (-21 mV) > Ru-300 (-12 mV). Again, Ru-300 stood out as the best among the series. In the Tafel plots (Figure 18d), Ru-300 also showed a low slope of 34 mV dec^{-1}, comparable to that of

Pt/C (η_{10} = 12 mV, 27 mV dec^{-1}), manifesting a Volmer-Tafel pathway.[36] Other samples exhibited relatively slower kinetics, with a Tafel slope of 42, 52, and 59 mV dec^{-1} for Ru-200, Ru-400, and Ru-600, respectively. As for Ru-300-L and Ru-300-S (Figure 20), their η_{10} values are -28 and -64 mV, along with a Tafel slope of 59 and 37 mV dec^{-1}, respectively. Taken together, these results indicate that Ru-300 represents the optimal catalyst within the present experimental context.

Notably, at the overpotential of -100 mV, the turnover frequency (TOF) of Ru-300 was estimated to be 0.30 s^{-1} and 0.15 s^{-1} in the acidic and alkaline media, respectively (Figure 21). One can see that whereas the intrinsic activity in acid remains subpar as compared to that of Pt/C, the performance in alkaline media is actually very close to that of Pt/C (0.36 s^{-1}).

Ru-300 also exhibited excellent stability in both acidic and alkaline media. In accelerated LSV tests for 2,000 cycles (Figure 18e-f), one can see that η_{10} in 0.5 M H_2SO_4 shifted negatively by only 10 mV and η_{100} by 30 mV, whereas in 1 M KOH, the decay of the overpotential was much smaller, with a negative shift of only 9 mV for η_{10} and 8 mV for η_{100}. This is consistent with results from XPS measurements (Figure 18g-h and Table 1) where the Ru-Cl species remained well-defined in Ru-300 after the stability test in both 0.5 M H_2SO_4 (0.06 at%) and in 1 M KOH (0.72 at%), though at a somewhat reduced concentration as compared to that (0.96 at%) of the as-produced sample (Table 1). In contrast, no RuO_x species could be resolved in XPS measurements after the stability tests (Figure 22), suggesting that RuO_x was unlikely to make substantial contributions to the HER performance.

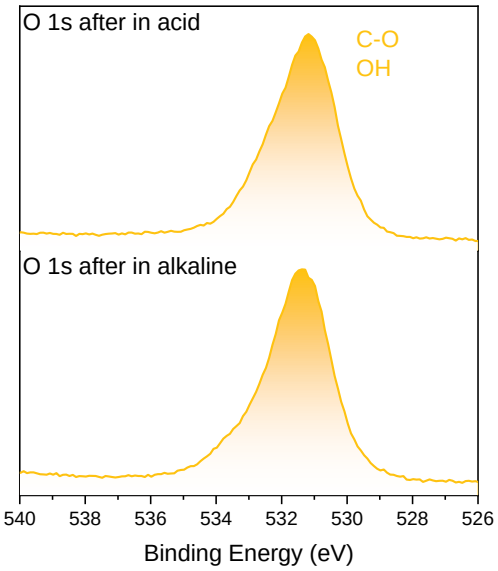

Figure 22. High resolution O 1s spectra of Ru-300 after stability test in acid (upper panel) and in alkaline (lower panel).

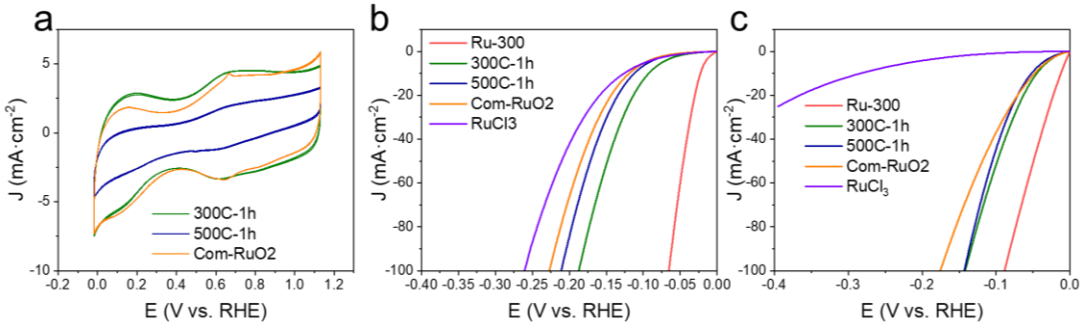

Figure 23. (a) CVs of RuCl3 treated at 300°C, 500°C, and commercial RuO2 after electrochemical activations, at a scan rate of 50 mV s^{-1} in 0.5 M H_2SO_4. HER LSV curves of corresponding samples in (b) 0.5 M H_2SO_4 and (c) 1 M KOH, at a scan rate of 10 mV s^{-1}.

To further highlight the unique advantages of MIH in sample preparation, we also thermally treated $RuCl_3$ in a conventional tube furnace at a comparable temperature (i.e., 300 and 500 °C) under ambient conditions for 1 h. In electrochemical

measurements (Figure 23), the obtained samples behaved analogously to commercial RuO_2, rather than metallic Ru, and the HER activity was markedly lower than that of Ru-300. In fact, Ru-300 ranks among the best in relevant HER catalysts in the literature, but the sample preparation takes only seconds, as compared to hours for others prepared by conventional thermal procedures (Table 3).

Table 3. Comparison of HER activity with relevant samples in the literature.

Samples	**η_{10} (media)**	**Duration of synthesis**	**Reference**
Ru-300	-23 mV (acid) -12 mV (alkaline)	6 s	This work
Ru@C_2N	-13.5 mV (acid) -17 mV (alkaline)	8 h	*Nat. Nanotechnol.* 12 (2017) 441-446.
RuCoP clusters	-11 mV (acid) -23 mV (alkaline)	32.5 h	*Energy Environ. Sci.* 11 (2018) 1819-1827.
Hcp-Ru@NC	-27.5 mV (acid)	9 h	*ACS Catal.* 8 (2018) 5714-5720.

$RuTe_2$ $RuSe_2$	-35.7 mV (acid) -29.5 mV (alkaline)	> 8 h	*Small* 17 (2021) 2007333.
Ru/GLC	-35 mV (acid)	> 24 h	*ACS Appl. Mater. Interfaces* 8 (2016) 35132-35137.
Ru@CQDs	-10 mV (alkaline)	26 h	*Adv. Mater.* 30 (2018) 1800676.
P-Ru/C	-31 mV (alkaline)	> 4 h	*ACS Catal.* 10 (2020) 11751-11757.
RuCo@NC	-28 mV (alkaline)	> 5 h	*Nat. Commun.* 8 (2017) 14969.
NiRu nanoalloys	-50 mV (acid) -32 mV (alkaline)	36 h	*J. Mater. Chem. A* 6 (2018) 1376-1381.
Ru@SC-CDs	-59 mV (acid) -29 mV (alkaline)	24 h	*Nano Energy* 65 (2019) 104023.
RuSi nanoalloy	-19 mV (acid)	4 h	*Angew. Chem. Int. Edit.* 131 (2019) 11531-11535.

4.3.4 Computational study

Based on the above experimental studies, it is likely that Ru-Cl species played an important role in the HER process. To understand the remarkable HER activity of Ru nanoparticles with surface-enriched Cl, DFT calculations were conducted to unravel the fundamental mechanism. As shown in Figure 24a, as (10-11) (i.e., (101)) is the main facet of *hcp* Ru, we used it to build the Cl-related models for H adsorption. We first tested the possibility of on-top adsorption of H on Ru-101 as the input model (Figure 25), but it relaxed into the hollow-site adsorption (Figure 24a, black frame), confirming that the on-top adsorption is subordinate to the hollow-fashion.[7] This was further evidenced by the Gibbs free energy of H adsorption (ΔG_{H^*}), as shown in Figure 24b, which has been widely used as a descriptor of the HER activity. Typically, a ΔG_{H^*} close to 0 eV is the ideal condition for H to adsorb and desorb. In fact, H was favorably adsorbed on the hollow site of Ru-101 with a ΔG_{H^*} of -0.54 eV, indicating that desorption of H from the surface would be energetically difficult. With Cl atom adsorbed on Ru-101 in a tetradentate fashion (Ru-101-tCl), it was found that the ΔG_{H^*} slightly shifted to -0.51 eV. With two neighboring Cl (Figure 26), ΔG_{H^*} decreased further to -0.50 eV, implying that surface-adsorbed Cl indeed could facilitate the desorption of H from the Ru-101 surface. However, the effect remains too trivial. Considering that the interaction distance between Cl and H (3.7 Å) was still too far, a closer situation was then examined, where Cl was located at the hollow site of Ru-101 (Ru-101-hCl, teal colored frame in Figure 24a), with a separation of 3.1 Å to the adsorbed H at the nearby hollow site. It was found that ΔG_{H^*} decreased to -0.47 eV. If

another Cl was added at the hollow site of Ru-101 (Ru-101-2hCl, green frame in Figure 24a), ΔG_{H^*} now diminished to -0.38 eV, much improved for HER as compared to pristine Ru-101. We further considered $RuCl_x$ species including $(RuCl_2)^+$ and $(RuCl)^{2+}$ on the surface of the Ru slab by building models shown in Figure 24a (in purple and red frames) and 27. One can see that with such an adatom mode, the H atom could stably adsorb onto the Ru atom in an on-top fashion, and a significant change was observed with ΔG_{H^*}, i.e., +0.11 eV and +0.26 eV for Ru-101-RuCl and Ru-101-$RuCl_2$, respectively. Taken together, these results indicate that the $RuCl_x$ species could indeed enhance the HER activity by weakening the H adsorption.

To further investigate the mechanism of weakened H adsorption, we calculated the total density of states (DOS) and partial density of states (PDOS) of the d electrons to understand the electronic structure of the bulk and the surface atoms. One can see from Figure 28 that the total DOS of several models with adsorbed Cl or $RuCl_x$ species all have similar profiles, meaning similar bulk electronic properties near the Fermi level, in agreement with the lack of significant difference amongst the Ru K-edge adsorption edges in XANES study (Figure 10). Further analysis of PDOS of the Ru active sites (Figure 24c) showed an apparent change of the Ru d electrons, especially the d band centers (E_d). One can see that in comparison with surface Ru of Ru-101 where E_d is located at -1.33 eV, with the adsorption of even only one Cl, the neighboring Ru on Ru-101-hCl shifts negatively to -1.44 eV; and for Ru-101-2hCl (with the adsorption of two Cl's), the E_d downshifts further to -1.59 eV. Meanwhile, from Figure 29, it can be seen that the E_d of Ru atoms without direct coordination with Cl also shifted slightly to -

1.40 eV, signifying that adsorption of Cl atoms rendered a strong impact on the local electronic structure. Furthermore, both Ru-101-RuCl and Ru-101-$RuCl_2$ can be seen to exhibit a downshift of E_d to -1.52 and -1.50 eV, respectively (Figure 24c), significantly different from the pristine Ru-101.

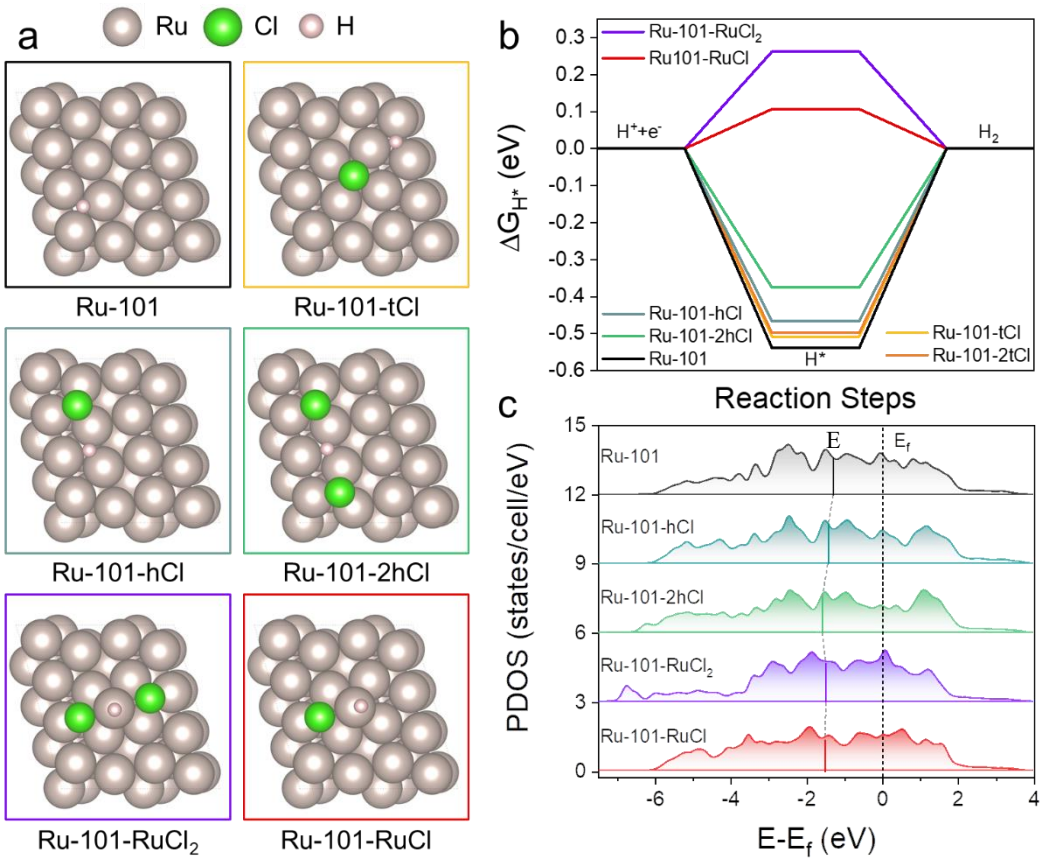

Figure 24. DFT studies of Ru with surface enriched Cl. (a) Models of Ru (10-11) with various $RuCl_x$ species. (b) Gibbs free energy of H* (ΔG_{H*}) adsorption on corresponding models in panel (a). (c) Projected density of states (PDOS) of d-electrons of Ru active sites in panel (a).

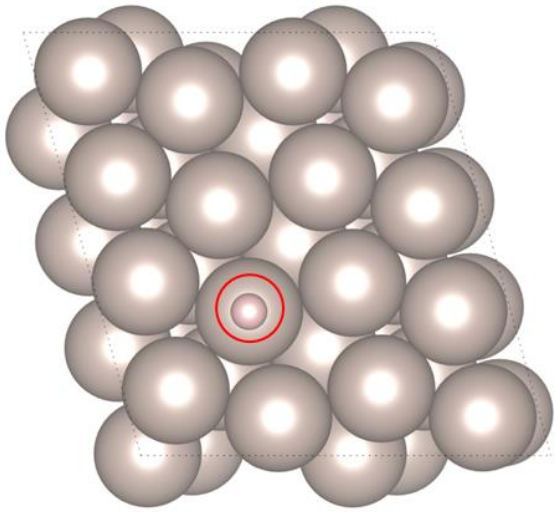

Figure 25. Initial input model of on-top H adsorption (circled in red) on Ru (10-11).

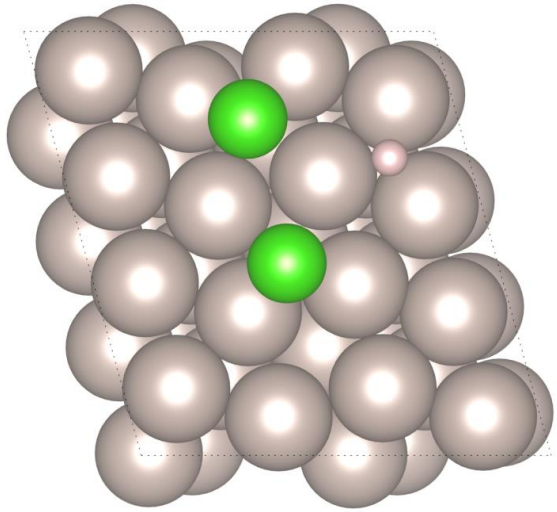

Figure 26. Computational model of Ru-101-2tCl with H atoms adsorbed on the adjacent hollow sites after relaxing.

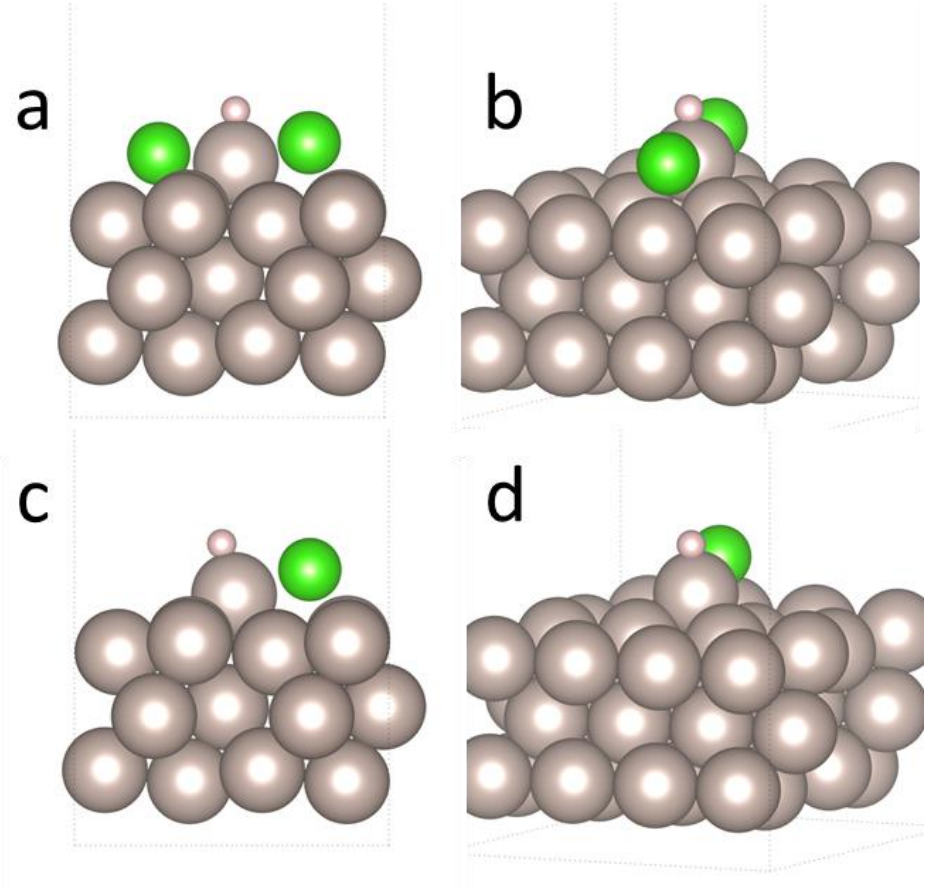

Figure 27. Computational models of (a, b) Ru-101-$RuCl_2$ and (c, d) Ru-101-RuCl with adsorbed H atoms after relaxing.

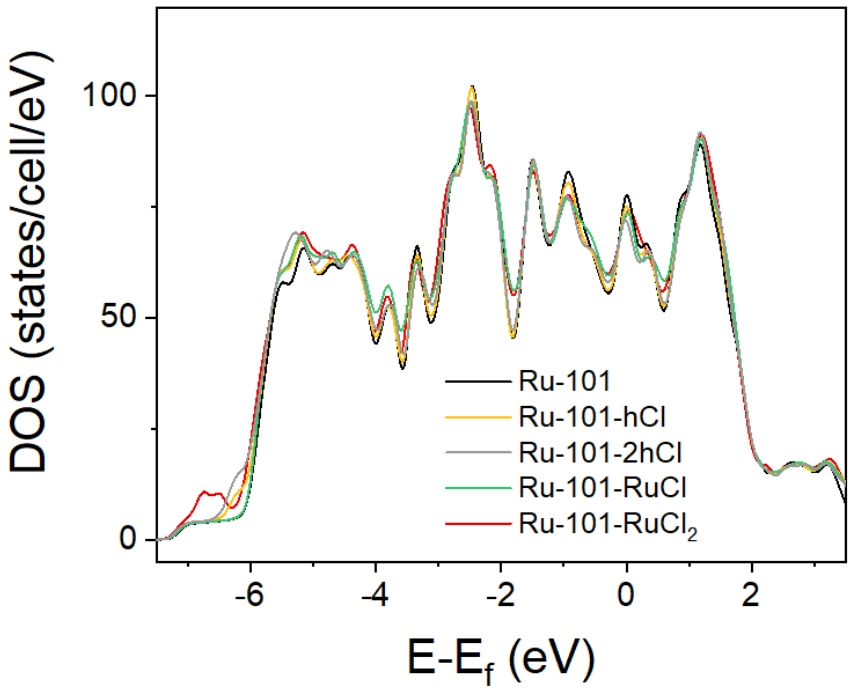

Figure 28. Calculated total DOS of Ru-101, Ru-101-hCl, Ru-101-$RuCl_2$, Ru-101-RuCl.

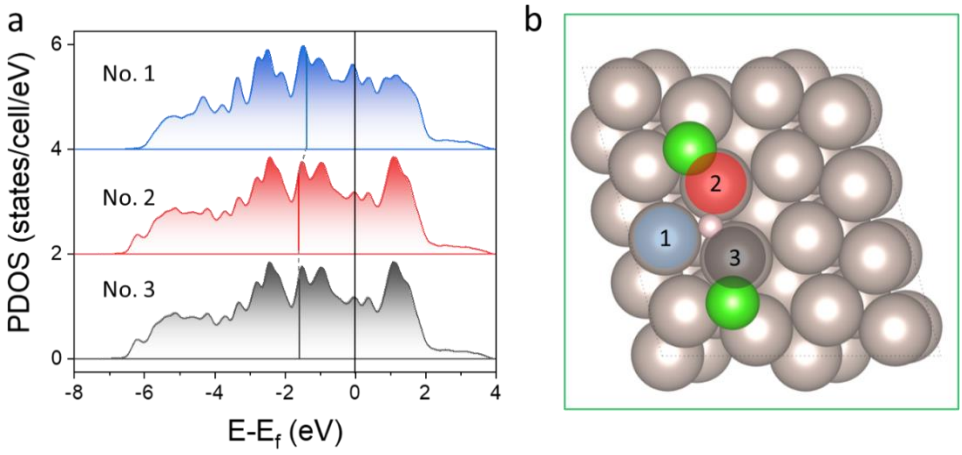

Figure 29. (a) PDOS of d-electrons for different Ru atoms in (b) model Ru-101-2hCl.

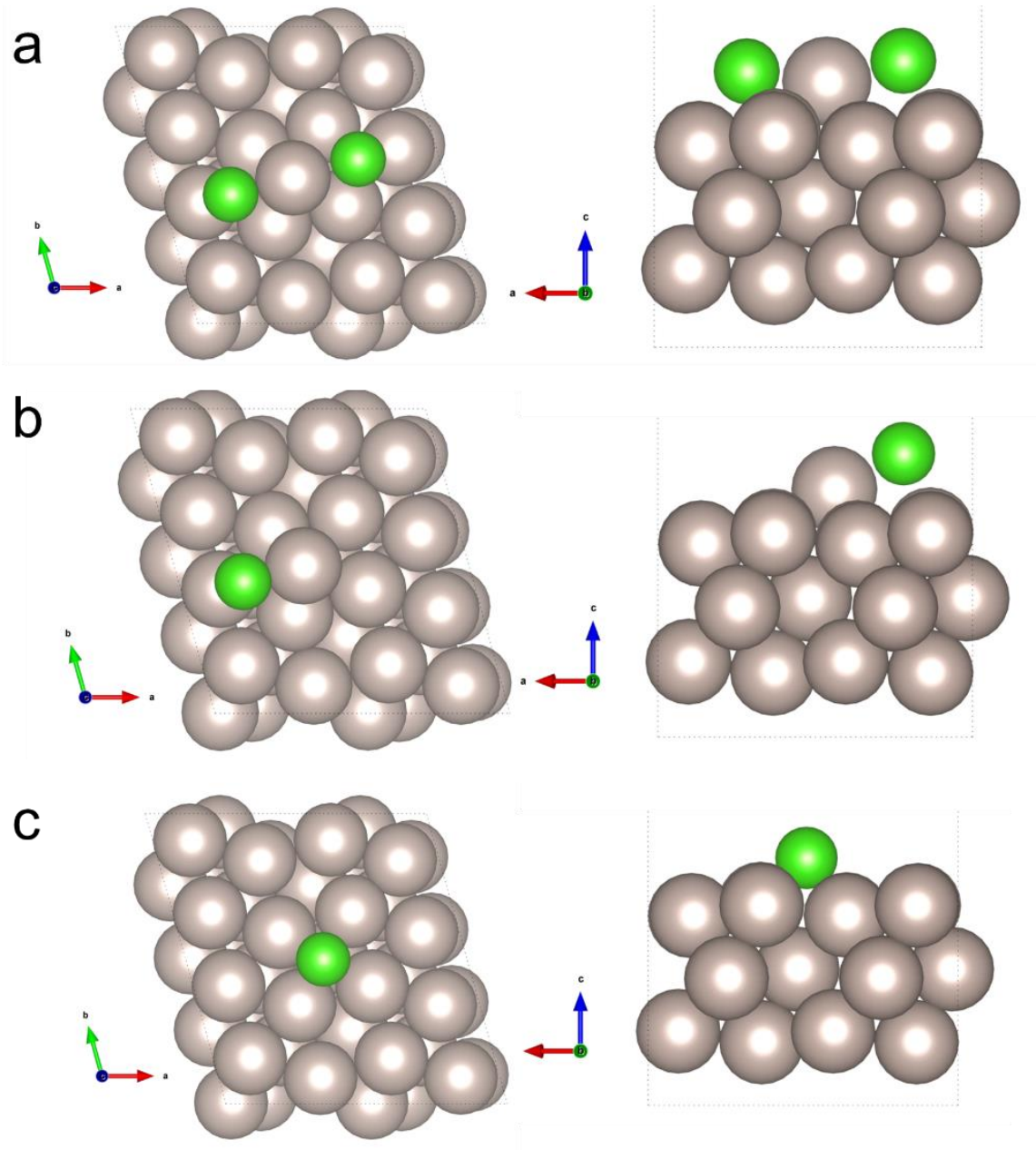

Figure 30. Models for Bader charge analysis. (a) Ru-101-$RuCl_2$, (b) Ru-101-RuCl, and (c) Ru-101-tCl.

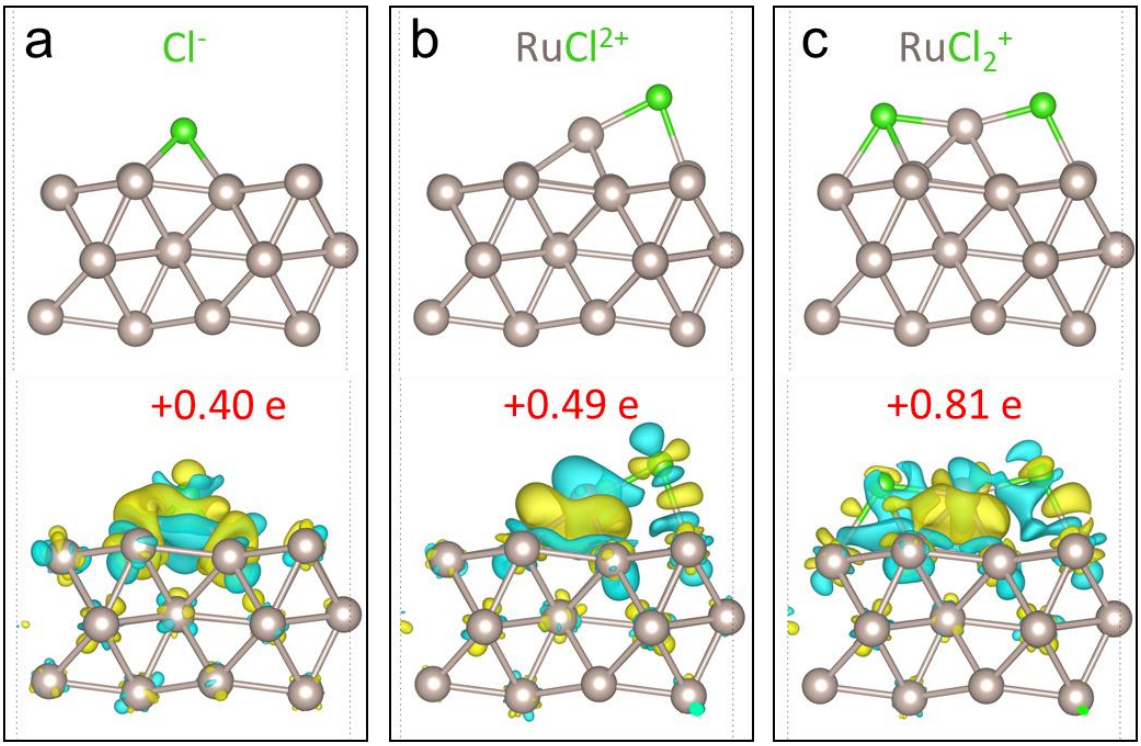

Figure 31. Bader charge analysis of (a) Cl^-, (b) $RuCl^{2+}$, and (c) $RuCl_2^+$ on the surface of Ru (10-11). The cyan and yellow areas signify electron loss and electron gain, respectively. The isovalue of charge density is 0.001 e au^{-3}.

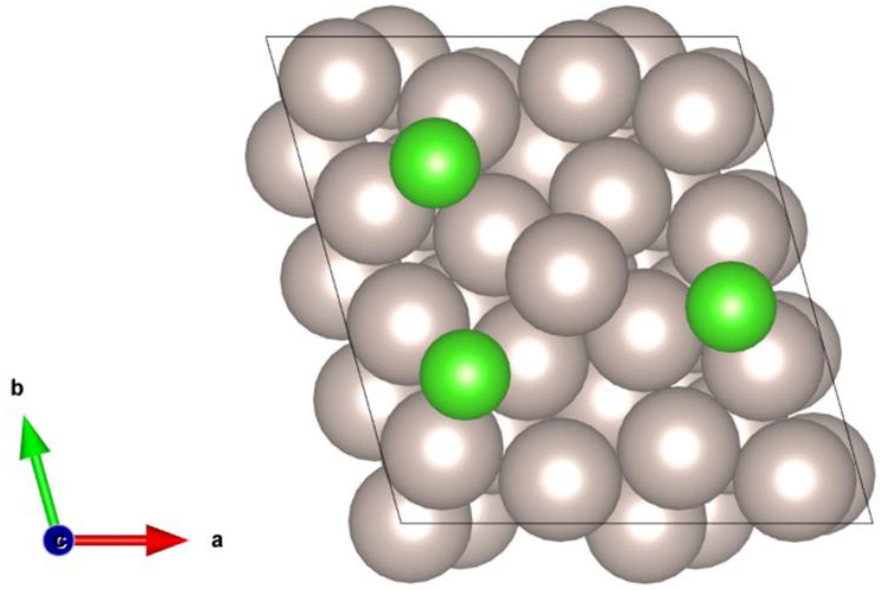

Figure 32. Relaxed model of $RuCl_3$ on Ru (10-11).

Further insights into the interactions between Ru nanoparticles and $RuCl_x$ or Cl ligands were obtained by Bader charge analysis, as shown in Figure 30 and 31. A *hcp* Ru (10-11) slab was built with surface adsorption of Cl^-, $(RuCl)^{2+}$, and $(RuCl_2)^+$ species to represent the incomplete decomposition of $RuCl_3$. It should be noted that $RuCl_3$ would spontaneously decompose into Cl^- and Ru atoms on the Ru slab (Figure 32). Significantly, one can see that efficient charge transfer occurred from the Ru slab to these Cl species (Figure 31). For one adsorbed Cl^-, it could withdraw 0.40 electron from the Ru slab, whereas 0.49 and 0.81 electrons from the Ru slab to $(RuCl)^{2+}$ and $(RuCl_2)^+$, respectively.[37-40] It is therefore likely that such interfacial charge transfer was responsible for the downshift of E_d and weakened adsorption of H on the Ru nanoparticle surface, leading to enhanced HER activity, as observed experimentally.[38,41,42]

4.4 Conclusion

In summary, magnetic induction heating was exploited for the ultrafast and green preparation of Ru nanoparticles supported on carbon paper. The samples could be prepared within seconds, and the rapid synthesis led to the formation of metal-Cl species on the Ru nanoparticle surface. With this unique structural feature, the samples all exhibited apparent electrocatalytic activity towards HER in both acidic and alkaline media, and the best sample, Ru-300, needed an overpotential of only -23 and -12 mV to reach 10 mA cm^{-2}, respectively, rivaling commercial Pt/C benchmark, along with excellent stability. Results from DFT calculations showed that the surface Cl species induced apparent electron transfer from the Ru nanoparticles, leading to a downshift of the Ru E_d and hence weakened H adsorption, a unique feature for enhanced HER activity, as observed experimentally. Results from this study highlight the unique significance of MIH in the structural engineering of metal nanoparticles by heteroanion functionalization for enhancement of their electrocatalytic performance.

4.5 Experimental section

Chemicals

Ruthenium(III) chloride hydrate ($RuCl_3 \cdot xH_2O$, 35-40%, ACROS Organics), acetone (Fisher chemicals), carbon paper (TGP-H-90, Toray), ruthenium(IV) oxide (RuO_2, 99.5%, anhydrous, ACROS Organics) and Pt/C (20 wt %, Alfa Aesar) were used as received. Water was purified with a Barnstead Nanopure Water System (18.2 MW cm).

Sample synthesis

Carbon paper was thermally treated in a Muffle furnace at 500 °C in ambient for 1 h to increase surface wettability, cut into 1 × 2 cm^2 pieces, and rinsed with acetone several times. $RuCl_3$ was dissolved into acetone to form a solution at a concentration of 20 mg mL^{-1}, 100 μL of which was then dropcast onto the carbon paper. After drying in air for 30 min, the carbon paper was wrapped in graphite paper (0.1 mm thick) before being sandwiched between two iron sheets (2.5 cm x 2.5 cm x 0.1 mm) to prevent direct contact of the samples to the iron sheets. The assembly was then placed in the center of a four-turn induction coil with a diameter of 5 cm, and magnetic induction heating was carried out at a controlled current (X = 200-600 A) for a select heating time (Y = 3-12 s), when the sample was dropped into an ethanol-dry ice solution (-78 °C) placed underneath the induction coil for rapid quenching (Caution, the ethanol must be fully cooling down by dry ice, or it will catch fire). Control samples were also prepared in a tube furnace at a comparable temperature (i.e., 300 and 500 °C) for 1 h under ambient conditions.

Characterizations

Transmission electron microscopy (TEM) images were acquired with a Tecni G2 operated at 200 kV. X-ray photoelectron spectroscopy (XPS) measurements were carried out with a Thermo Fisher K-alpha system, where the binding energy was calibrated against the C 1s binding energy. Raman measurements were conducted using a Horiba Jobin Yvon LabRAM ARAMIS automated scanning confocal Raman microscope under 532 nm excitation. X-ray absorption spectroscopy (XAS)

measurements were carried out at 10 K on beamline 4-1 of the Stanford Synchrotron Radiation Lightsource using an Oxford liquid helium cryostat.

Electrochemistry

Electrochemical measurements were carried out with a CHI 700E electrochemical workstation in a three-electrode configuration. The obtained carbon paper was fixed onto a graphite electrode holder, with an exposed surface area of 0.25 cm^2. A graphite rod was used as the counter electrode and a Ag/AgCl in saturated KCl as the reference electrode. The reference electrode was calibrated against a reversible hydrogen electrode (RHE) and all potentials in the present study were referenced to this RHE. To load Pt/C onto the carbon paper, 1 mg of Pt/C (20%) was dispersed under sonication in 190 μL of isopropanol solution and 10 μL of 100% Nafion solution; and 125 μL of the dispersion was dropcast onto part of the carbon paper (with an area of 0.25 cm^2). RuO_2 was deposited onto the carbon paper in the same fashion at the same metal loading.

Theoretical study

First-principles computations were performed using Quantum ESPRESSO, an open-source plane-wave code.[43] A 4 × 4-unit cell with 48 atoms was used to build a hexagonal Ru (10-11) slab supercell, where periodic image interactions were removed by setting a vacuum of 15 Å. Ru atoms of the bottom layer have been fixed during all relax calculations. A cutoff of 50 and 500 Ry for kinetics and charge density was chosen with the GBRV ultrasoft pseudopotential.[44] The total energy of the Monkhorst-Pack 4 × 4 × 1 K-point grid in the supercell was calculated at the convergence level of 1 meV per atom. The smearing parameter was set at 0.01 Ry in the Marzari-Vanderbilt smearing

for all calculations.[45] For geometric relaxation, the convergence was 10^{-8} Ry of the electronic energy and 10^{-4} au for the total force. Density functional perturbation theory was employed to calculate the phonon frequency as inputs for entropy and zero-point energy.[46]

4.6 Reference

1. J. A. Turner. *Science* **2004**, *305*, 972-974.

2. Y. X. Wang, H. Y. Su, Y. H. He, L. G. Li, S. Q. Zhu, H. Shen, P. F. Xie, X. B. Fu, G. Y. Zhou, C. Feng, D. K. Zhao, F. Xiao, X. J. Zhu, Y. C. Zeng, M. H. Shao, S. W. Chen, G. Wu, J. Zeng, C. Wang. *Chem Rev* **2020**, *120*, 12217-12314.

3. W. Song, M. Li, C. Wang, X. Lu. *Carbon Energy* **2021**, *3*, 101-128.

4. W. J. Mitchell, J. Xie, T. A. Jachimowski, W. H. Weinberg. *J Am Chem Soc* **1995**, *117*, 2606-2617.

5. Y. J. Yang, Y. H. Yu, J. Li, Q. R. Chen, Y. L. Du, P. Rao, R. S. Li, C. M. Jia, Z. Y. Kang, P. L. Deng, Y. J. Shen, X. L. Tian. *Nano-Micro Lett* **2021**, *13*, 160.

6. E. Skulason, V. Tripkovic, M. E. Bjorketun, S. Gudmundsdottir, G. Karlberg, J. Rossmeisl, T. Bligaard, H. Jonsson, J. K. Norskov. *J Phys Chem C* **2010**, *114*, 22374-22374.

7. H. Chen, X. Ai, W. Liu, Z. B. Xie, W. Q. Feng, W. Chen, X. X. Zou. *Angew Chem Int Edit* **2019**, *58*, 11409-11413.

8. Y. G. Yao, Z. N. Huang, P. F. Xie, S. D. Lacey, R. J. Jacob, H. Xie, F. J. Chen, A. M. Nie, T. C. Pu, M. Rehwoldt, D. W. Yu, M. R. Zachariah, C. Wang, R. Shahbazian-Yassar, J. Li, L. B. Hu. *Science* **2018**, *359*, 1489-1494.

9. Z. W. Seh, J. Kibsgaard, C. F. Dickens, I. B. Chorkendorff, J. K. Norskov, T. F. Jaramillo. *Science* **2017**, *355*, aad4998.

10. Y. Ding, K.-W. Cao, J.-W. He, F.-M. Li, H. Huang, P. Chen, Y. Chen. *Chinese J Catal* **2022**, *43*, 1535-1543.

11. Y. Peng, W. Z. Pan, N. Wang, J. E. Lu, S. W. Chen. *Chemsuschem* **2018**, *11*, 130-136.

12. Y. Peng, B. Z. Lu, L. M. Chen, N. Wang, J. E. Lu, Y. Ping, S. W. Chen. *Journal of Materials Chemistry A* **2017**, *5*, 18261-18269.

13. B. Z. Lu, L. Guo, F. Wu, Y. Peng, J. E. Lu, T. J. Smart, N. Wang, Y. Z. Finfrock, D. Morris, P. Zhang, N. Li, P. Gao, Y. Ping, S. W. Chen. *Nat Commun* **2019**, *10*, 631.

14. C. Cai, K. Liu, Y. M. Zhu, P. C. Li, Q. Y. Wang, B. Liu, S. Y. Chen, H. J. W. Li, L. Zhu, H. M. Li, J. W. Fu, Y. Chen, E. Pensa, J. H. Hu, Y. R. Lu, T. S. Chan, E. Cortes, M. Liu. *Angew Chem Int Edit* **2022**, *61*, e202113664.

15. D. Chen, T. T. Liu, P. Y. Wang, J. H. Zhao, C. T. Zhang, R. L. Cheng, W. Q. Li, P. X. Ji, Z. H. Pu, S. C. Mu. *Acs Energy Lett* **2020**, *5*, 2909-2915.

16. Y. Y. Qiao, P. F. Yuan, C. W. Pao, Y. Cheng, Z. H. Pu, Q. Xu, S. C. Mu, J. N. Zhang. *Nano Energy* **2020**, *75*, 104881.

17. J. Wang, L. L. Han, B. L. Huang, Q. Shao, H. L. L. Xin, X. Q. Huang. *Nat Commun* **2019**, *10*, 5692.

18. F. Zhou, R. J. Sa, X. Zhang, S. Zhang, Z. H. Wen, R. H. Wang. *Appl Catal B-Environ* **2020**, *274*, 119092.

19. S. Q. Zhu, X. P. Qin, F. Xiao, S. L. Yang, Y. Xu, Z. Tan, J. D. Li, J. W. Yan, Q. Chen, M. S. Chen, M. H. Shao. *Nat Catal* **2021**, *4*, 711-718.

20. Y. M. Zhao, X. W. Wang, G. Z. Cheng, W. Luo. *Acs Catal* **2020**, *10*, 11751-11757.

21. D. J. Morgan. *Surf Interface Anal* **2015**, *47*, 1072-1079.

22. C. Bock, C. Paquet, M. Couillard, G. A. Botton, B. R. MacDougall. *J Am Chem Soc* **2004**, *126*, 8028-8037.

23. X. M. Ren, M. Guo, H. Li, C. B. Li, L. Yu, J. Liu, Q. H. Yang. *Angew Chem Int Edit* **2019**, *58*, 14483-14488.

24. A. M. Ruppert, M. Jedrzejczyk, O. Sneka-Platek, N. Keller, A. S. Dumon, C. Michel, P. Sautet, J. Grams. *Green Chem* **2016**, *18*, 2014-2028.

25. B. C. Man, H. Y. Zhang, C. M. Zhang, X. Li, H. Dai, M. Y. Zhu, B. Dai, J. L. Zhang. *New J Chem* **2017**, *41*, 14675-14682.

26. V. Giulimondi, S. K. Kaiser, M. Agrachev, F. Krumeich, A. H. Clark, S. Mitchell, G. Jeschke, J. Perez-Ramirez. *Journal of Materials Chemistry A* **2021**, 5953-5961.

27. S. Q. Chen, L. L. Ling, S. Zhang, S. F. Jiang, Z. R. Xu, W. J. Liu, H. Jiang. *Adv Sustain Syst* **2017**, *1*.

28. K. Park, S. Padmanaban, S. H. Kim, K. D. Jung, S. Yoon. *Chemcatchem* **2021**, *13*, 695-703.

29. A. Lebedeva, B. L. Albuquerque, J. B. Domingos, J. F. Lamonier, J. M. Giraudon, P. Lecante, A. Denicourt-Nowicki, A. Roucoux. *Inorg Chem* **2019**, *58*, 4141-4151.

30. H. Z. Zhao, M. Lei, X. Yang, J. K. Jian, X. L. Chen. *J Am Chem Soc* **2005**, *127*, 15722-15723.

31. J. H. Lee, Y. Choi, S. H. Do, B. H. Kim, M. J. Seong, K. Y. Choi. *Npj Quantum Mater* **2021**, *6*, 43.

32. G. M. Li, X. B. Chen, Y. Gang, F. L. Li, M. Q. Yan, F. Ye, S. H. Pei, Y. J. Zhang, L. Wang, H. M. Su, J. F. Dai, Y. Z. Chen, Y. G. Shi, X. W. Wang, L. Y. Zhang, S. M. Wang, D. P. Yu, F. Ye, J. W. Mei, M. Y. Huang. *Phys Rev Mater* **2019**, *3*, 023601.

33. T. T. Mai, A. McCreary, P. Lampen-Kelley, N. Butch, J. R. Simpson, J. Q. Yan, S. E. Nagler, D. Mandrus, A. R. H. Walker, R. V. Aguilar. *Phys Rev B* **2019**, *100*, 134419

34. A. L. Ankudinov, J. J. Rehr. *Phys Rev B* **1997**, *56*, R1712-R1715.

35. M. R. G. Dechialvo, A. C. Chialvo. *J Electroanal Chem* **1994**, *372*, 209-223.

36. M. Bhardwaj, R. Balasubramaniam. *Int J Hydrogen Energ* **2008**, *33*, 2178-2188.

37. R. Ciganda, N. Li, C. Deraedt, S. Gatard, P. X. Zhao, L. Salmon, R. Hernandez, J. Ruiz, D. Astruc. *Chem Commun* **2014**, *50*, 10126-10129.

38. Y. Peng, Q. M. Liu, B. Z. Lu, T. He, F. Nichols, X. Hu, T. Huang, G. Huang, L. Guzman, Y. Ping, S. W. Chen. *Acs Catal* **2021**, *11*, 1179-1188.

39. X. W. Kang, N. B. Zuckerman, J. P. Konopelski, S. W. Chen. *Angew Chem Int Edit* **2010**, *49*, 9496-9499.

40. P. G. Hu, L. M. Chen, X. W. Kang, S. W. Chen. *Accounts Chem Res* **2016**, *49*, 2251-2260.

41. H. L. Xin, A. Vojvodic, J. Voss, J. K. Norskov, F. Abild-Pedersen. *Phys Rev B* **2014**, *89*, 115114

42. J. R. Kitchin, J. K. Norskov, M. A. Barteau, J. G. Chen. *Phys Rev Lett* **2004**, *93*, 156801.

43. P. Giannozzi, S. Baroni, N. Bonini, M. Calandra, R. Car, C. Cavazzoni, D. Ceresoli, G. L. Chiarotti, M. Cococcioni, I. Dabo, A. Dal Corso, S. de Gironcoli, S. Fabris, G. Fratesi, R. Gebauer, U. Gerstmann, C. Gougoussis, A. Kokalj, M. Lazzeri, L. Martin-Samos, N. Marzari, F. Mauri, R. Mazzarello, S. Paolini, A. Pasquarello, L. Paulatto, C. Sbraccia, S. Scandolo, G. Sclauzero, A. P. Seitsonen, A. Smogunov, P. Umari, R. M. Wentzcovitch. *J Phys-Condens Mat* **2009**, *21*, 395502.

44. K. F. Garrity, J. W. Bennett, K. M. Rabe, D. Vanderbilt. *Comp Mater Sci* **2014**, *81*, 446-452.

45. N. Marzari, D. Vanderbilt, A. De Vita, M. C. Payne. *Phys Rev Lett* **1999**, *82*, 3296-3299.

46. S. Baroni, S. de Gironcoli, A. Dal Corso, P. Giannozzi. *Rev Mod Phys* **2001**, *73*, 515-562.

Chapter 5 Ultrafast Synthesis of Cobalt/Carbon Nanocomposites by Magnetic Induction Heating for Oxygen Evolution Reaction

5.1 Abstract

Metal/carbon nanocomposites have shown great potential as high-performance, low-cost electrocatalysts owing to the unique metal-support interactions. These nanocomposites are typically prepared by conventional pyrolysis that is tedious and energy-intensive. Herein, we report the ultrafast preparation of cobalt/carbon nanocomposites by magnetic induction heating (MIH) of metal organic frameworks within seconds under an inert atmosphere. The resulting samples consist of cobalt nanoparticles encapsulated within defective carbon shells, and effectively catalyze oxygen evolution reaction (OER) in alkaline media. Among the series, the sample prepared at 400 A for 10 s exhibit the best OER performance, needing a low overpotential of +308 mV to reach the current density of 10 mA cm^{-2}, along with excellent stability, and even outperforms commercial RuO_2 at high overpotentials. This is ascribed to the charge transfer between the carbon scaffold and metal nanoparticles. Operando X-ray absorption spectroscopy measurements show that the electrochemically produced CoOOH species is responsible for the high electrocatalytic performance. The results highlight the unique potential of MIH in the development of effective nanocomposite catalysts for electrochemical energy technologies.

5.2 Introduction

Natural gas reforming accounts for 95% of the hydrogen gas produced in the United States; yet the hydrogen is non-sustainable and “grey”, as it originates from fossil fuels [1]. To obtain sustainable “green” hydrogen gas, electrochemical water splitting by using renewable electricity has emerged as one of the most promising technologies, which

consists of hydrogen evolution reaction (HER) at the cathode and oxygen evolution reaction (OER) at the anode [2]. Yet, due to the sluggish electron-transfer kinetics and complex reaction pathways, OER typically entails a large overpotential and severely hampers the overall efficiency of the water electrolyzers [3]. Iridium and ruthenium-based nanoparticles have been the leading catalysts for OER; yet their natural scarcity and high costs have made widespread applications impractical [4-6]. Thus, extensive research has been carried out to develop efficient alternatives, such as metal alloys [7-9], metal oxides [10-13], hydroxides [14,15], oxyhydroxides [16,17], sulfides [8,18], phosphides [4,19], etc. Recently, metal/carbon nanocomposites have also been attracting intensive attention [20-23], owing to their high electrical conductivity and strong metal-support interactions (e.g., charge transfer between carbon and metal, spatial confinement by encapsulation). For example, Cui et al. [24] prepared a series of nanocomposites with non-noble metal nanoparticles (e.g., Fe, Co, Ni, and their alloys) encapsulated within single-layer graphene, in which FeNi showed the best OER activity with an overpotential (η_{10}) of +280 mV at 10 mA cm^{-2} in alkaline media. Theoretical studies based on density functional theory (DFT) calculations showed that electron transfer occurred from the metal cores to the graphene layer and significantly altered the adsorption energetics of oxygen species on the graphene surface, leading to an enhanced OER performance. Yang et al. [25] prepared FeCoNi ternary nanoalloys encapsulated in N-doped graphene layers by direct annealing of Prussian blue, which showed a low η_{10} of +288 mV towards OER in alkaline media. Similarly, they found that charge transfer from the metals to graphene lowered the energy barrier of OER electrochemistry. In these studies,

the metal/carbon nanocomposites are prepared via a variety of strategies, including pyrolysis of metal-organic frameworks (MOFs) [26], chemical vapor deposition (CVD) [27], electrospun nanofibers [28], wet chemistry [29,30], etc. These procedures, while effective, are in general tedious (of the order of hours) and may need sophisticated instrumentation [31-33].

Such issues can be mitigated by the recent emergence of ultrafast synthesis, e.g., carbothermal shock, flash Joule heating, laser ablation, and magnetic induction heating (MIH) [21,34-38]. These techniques can not only cut down the sample preparation time to (milli)seconds but also create non-equilibrium structures, such as stacking faults, point defects, and high-entropy mixtures, that are unattainable in conventional methods [34]. For instance, Meng et al. [39] utilized a laser to heat a cobalt target in liquid, and produced CoOOH with abundant oxygen vacancies, owing to the ultrafast heating rate. The resulting defective CoOOH exhibited an η_{10} of +330 mV for OER, much better than bulk CoOOH without oxygen vacancies. In another study, Cui et al. [18] prepared high-entropy metal sulfide $(CrMnFeCoNi)S_x$ nanoparticles by using carbothermal shock within just 55 ms, and observed a high OER performance with a low overpotential (η_{100}) of +295 mV to reach a high current density of 100 mA cm^{-2}. Recently, we demonstrated that MIH could also be exploited for the ultrafast synthesis of high-performance electrocatalysts [35,36]. MIH is a traditional metallurgical tool, where upon the application of a high-frequency AC current to the solenoid, a strong magnetic field is generated, which instantly produces a high Eddy current in the conductors within the field and heats the sample rapidly to a high temperature. In one recent study [36], FeNi spinel

nanostructures were produced within seconds featuring a homogenous mixing of the Fe and Ni phases and substantial Cl residuals, both of which were difficult to obtain in conventional methods and contributed collectively to the remarkable OER performance (η_{100} = +260 mV). In another study [35], ruthenium nanoparticles supported on carbon paper were prepared by MIH, where the surface Cl residuals were found to be responsible for the high HER activity (η_{10} = -23 and -12 mV in acidic and alkaline media, respectively) that was highly comparable to that of commercial Pt/C benchmark. Nevertheless, despite the progress, to date, very few studies have focused on the controllable synthesis of metal/carbon nanocomposites by ultrafast synthesis [34,40].

Herein, we prepared a series of cobalt/carbon nanocomposites by MIH treatment for 10 s [35,36] of zeolitic imidazolate frameworks-67 (ZIF-67), where cobalt nanoparticles were encapsulated within defective N-doped carbon shells. Owing to the different degrees of carbonization (by controlling the magnetic induction current), various amounts of Co species were exposed to the electrolytes, which effectively impacted the OER activity. Amongst the series, the sample prepared at the applied current of 400 A showed the best OER performance in alkaline media, with a low η_{10} of +308 mV and η_{200} of +410 mV, a performance even higher than that of commercial RuO_2 in the high overpotential range. Operando X-ray absorption spectroscopy measurements showed that the excellent activity was due to the formation of CoOOH on the carbon shell surface, likely due to electrochemical decomposition of the encapsulated metallic nanoparticles.

5.3 Experimental Section

Synthesis of ZIF-67

In a typical synthesis [30], 1.092 g of $Co(NO_3)_2 \cdot 6H_2O$ was dissolved in 30 mL of methanol in a vial, and 1.232 g of 2-methylimidazole in 30 mL methanol in another vial. These two solutions were mixed under sonication for 10 min to form a purple solution. The solution was then transferred to a 100 mL Teflon-lined stainless-steel autoclave and heated at 120 °C for 2 h, producing a purple precipitate that was collected via centrifugation at 6000 rpm for 5 min, rinsed three times with methanol, and dried under vacuum at 50 °C for 12 h. The obtained product was the ZIF-67 crystals.

MIH synthesis

Carbon paper was thermally treated in a muffle furnace at 500 °C in ambient for 1 h to increase surface wettability, cut into 1 × 2 cm^2 pieces, and rinsed with acetone several times. The ZIF-67 produced above was sonicated and dispersed into ethanol at a concentration of 60 mg mL^{-1}, 100 μL of which was then dropcast onto the carbon paper. After drying in air for 30 min, the carbon paper was put on an iron sheet (2.5 cm x 2.5 cm x 0.2 mm) covered with a piece of graphite paper (0.01 mm thick) to prevent contamination from iron, and the assembly was placed on the center of a firebrick inside a quartz tube that was purged with high-purity Ar gas for 10 min. The quartz tube was then set into a four-turn induction coil with a diameter of 5 cm, and MIH was carried out at a controlled current (X = 200-600 A) for a heating time of 10 s before the sample was naturally cooled down to room temperature. The resulting samples were denoted as Co-NC-X.

Characterizations

Transmission electron microscopy (TEM) images were acquired with a Tecni G2 operated at 200 kV. X-ray photoelectron spectroscopy (XPS) measurements were carried out with a Thermo Fisher K-alpha system, where the binding energy was calibrated against the C 1s binding energy. Raman measurements were conducted using a Horiba Jobin Yvon LabRAM ARAMIS automated scanning confocal Raman microscope under 532 nm excitation. Ex situ X-ray absorption spectroscopy (XAS) measurements were carried out at 10 K at beamline 4-1 of the Stanford Synchrotron Radiation Lightsource using an Oxford liquid helium cryostat. Operando XAS measurements were carried out at room temperature in a homemade cell.

Electrochemistry

Electrochemical measurements were carried out with a CHI 700E electrochemical workstation in a three-electrode configuration. The obtained carbon paper was fixed onto a graphite electrode holder, with an exposed surface area of 1 cm^2. A graphite rod was used as the counter electrode and a Ag/AgCl in saturated KCl as the reference electrode. The reference electrode was calibrated against a reversible hydrogen electrode (RHE) and all potentials in the present study were referenced to this RHE. Commercial RuO_2 was dropcast onto a carbon paper for benchmarking at the same metal loading.

5.4 Results and Discussion

5.4.1 Sample preparation and structural characterizations

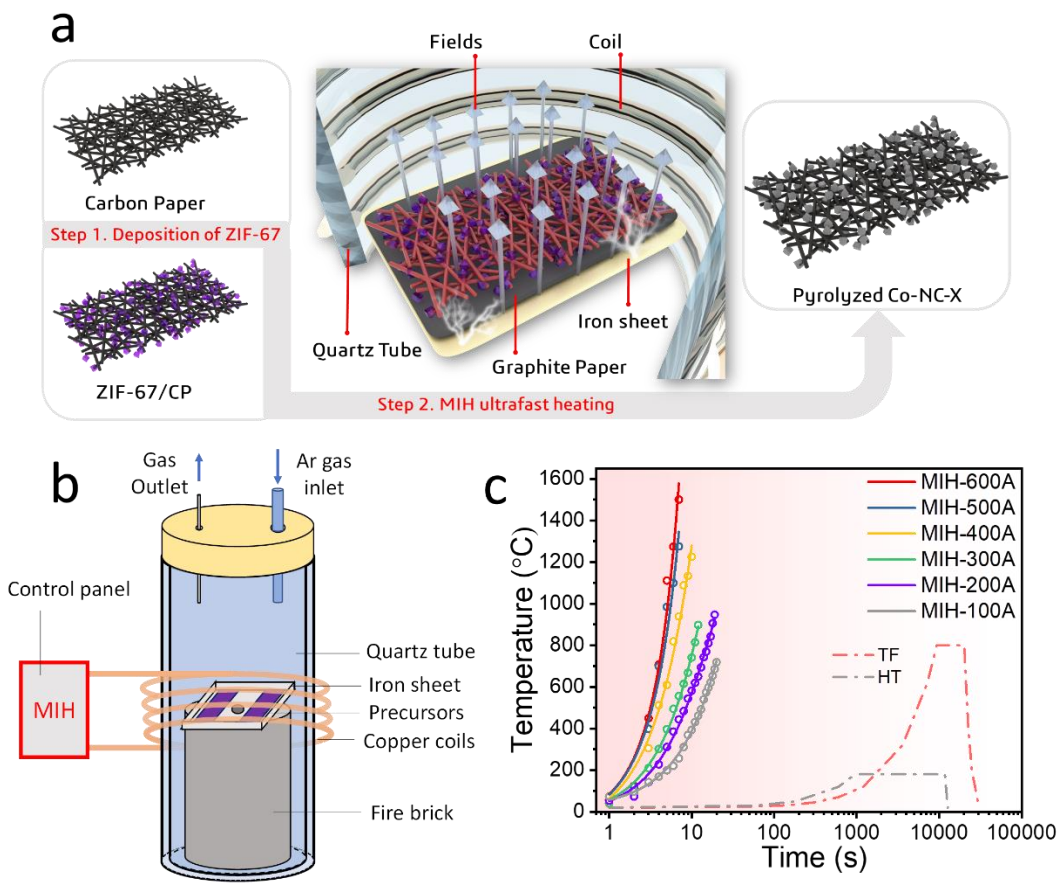

Figure 1. (a, b) Schematic illustration of ultrafast pyrolysis of ZIF-67 by MIH, where CP denotes carbon paper. (c) Heating temperature as the function of time by using MIH at different heating currents, as determined with an infrared thermometer. TF and HT denote conventional tube furnaces and hydrothermal methods, respectively.

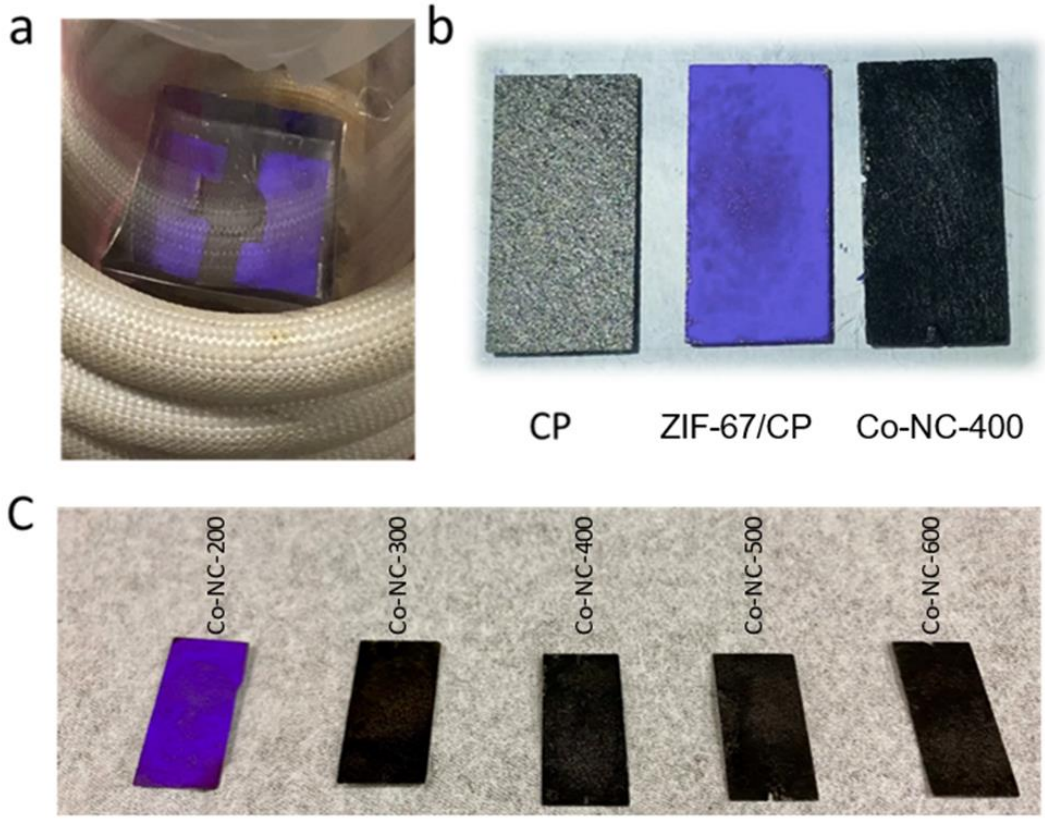

Figure 2. Photographs of (a) ZIF-67 on carbon paper (ZIF-67/CP) on an iron sheet covered with graphite paper, (b) carbon paper (CP), ZIF-67/CP, and Co-NC-400, and (d) Co-NC-200, Co-NC-300, Co-NC-400, Co-NC-500, and Co-NC-600.

As shown in Figure 1a, the preparation of Co-NC nanocomposites by MIH treatment of ZIF-67 consists of two major steps [35,36]. First, ZIF-67 was synthesized and dropcast onto a piece of carbon paper (ZIF-67/CP), which was then put onto an iron sheet covered with a piece of graphite paper (Figure 2a). The assembly was inserted into a quartz tube purged with Ar gas, which was placed into the center of a solenoid (Figure 1b). Upon the application of a high-frequency current, the surface of the iron sheet was heated up quickly to over 1000 °C within seconds (Figure 1c), owing to the Joule's heating effect. At the induction current of 300 A or higher for just 10 s, ZIF-67 was

thermoradiatively converted into Co-NC nanocomposites with Co nanoparticles encapsulated within N-doped carbon, as manifested with a rapid color change from purple to black; whereas at a lower current of only 200 A, the sample retained the purple color, signifying incomplete decomposition of ZIF-67 as the MIH temperature was too low (Figure 2b-c). Five samples were prepared at a controlled induction current (X = 200 to 600 A), and denoted as Co-NC-X (Figure 2c).

The sample structures were first characterized by TEM measurements. From Figure 3a-e and 4-7, it can be seen that upon MIH treatment at 200 to 600 A for 10 s, nanocomposites were produced where dark-contrast nanoparticles (dia. 5 to 10 nm) were embedded within a low-contrast scaffold, and the number of nanoparticles increased with increasing induction current, leading to an increasingly roughened morphology. For Co-NC-200 that retained the cubic shape of ZIF-67 with a size about 500 nm (Figure 3a), the relatively low current (and hence temperature, ca. 500 °C) led to only incomplete decomposition of ZIF-67 (Figure 2c), thus the number of nanoparticles was low [41]. In high-resolution TEM measurements (Figure 3f and 4), crystalline lattice fringes can be found in both the nanoparticles and the low-contrast scaffold, with an interplanar spacing of 0.416 and 0.269 nm, which can be ascribed to the enlarged (002) facet of graphitic carbon (owing to the formation of abundant interplanar sp^3 C) [42] and the (111) facet of cubic CoO (JCPDS #43-1004), respectively. When the induction current was increased to 300 A, a higher temperature was reached at ca. 700 °C, which led to the production of a number of metallic Co and CoO nanoparticles encapsulated within a rather thick amorphous carbon layer (Figure 3b, 3g

and 5). The number of nanoparticles became even higher for the Co-NC-400 (Figure 3c, 3h and 3k-3m), Co-NC-500 (Figure 3d, 3i and 6) and Co-NC-600 (Figure 3e, 3j, and 7) samples that were prepared at even higher induction currents (temperatures). In addition, one can see that the metallic Co domain size increased whereas that of CoO diminished from Co-NC-200 to Co-NC-600, suggesting that CoO was likely the structural intermediate during the thermal conversion of ZIF-67 to cobalt nanoparticles (vide infra).

The lattice spacing of the carbon scaffold also exhibited a dynamic evolution. For the samples prepared at relatively low induction currents (i.e., Co-NC-200, Co-NC-300, and Co-NC-400) (Figure 3f-3h), the carbon scaffold can be seen to exhibit a rather consistent d spacing of 0.412 nm, which is markedly larger than that (0.350 nm) observed with Co-NC-500 (Figure 3i) and Co-NC-600 (Figure 3j). This suggests enhanced graphitization of the latter due to a markedly higher heating temperature (up to 1500 °C) and largely defective carbon layers in the former.

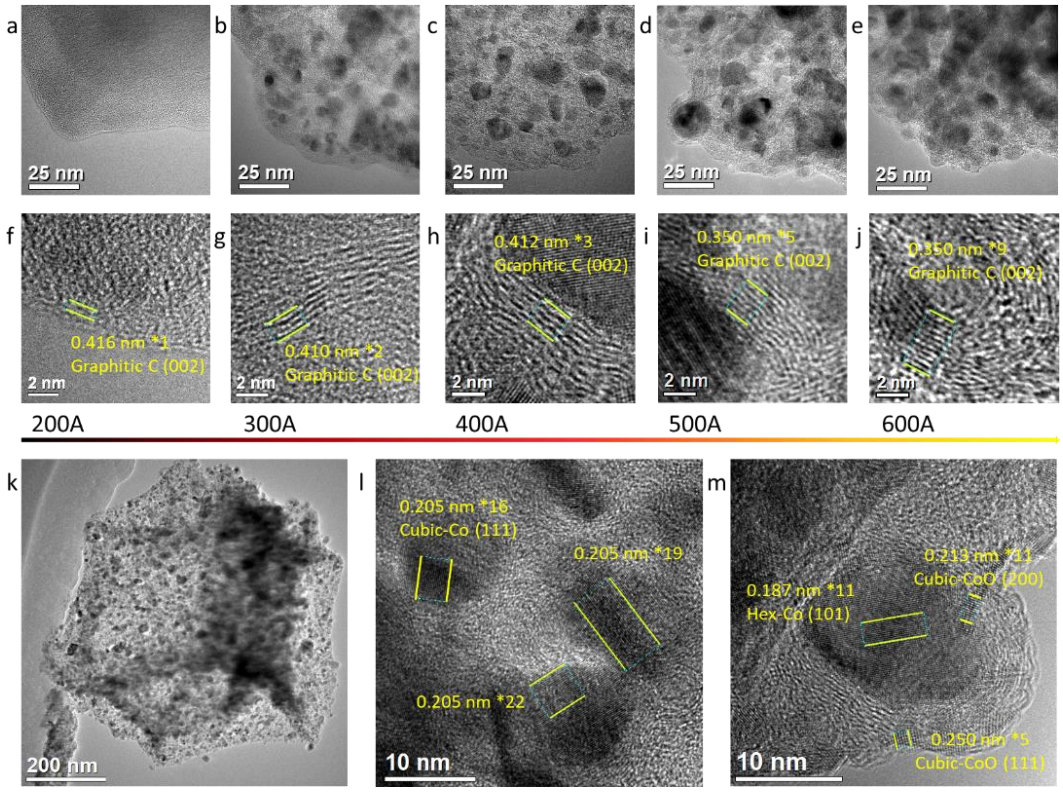

Figure 3. Representative TEM images of (a,f) Co-NC-200, (b,g) Co-NC-300, (c,h) Co-NC-400, (d,i) Co-NC-500, and (e,j) Co-NC-600. (k-m) TEM images of Co-NC-400 at different magnifications where the various lattice fringes are highlighted.

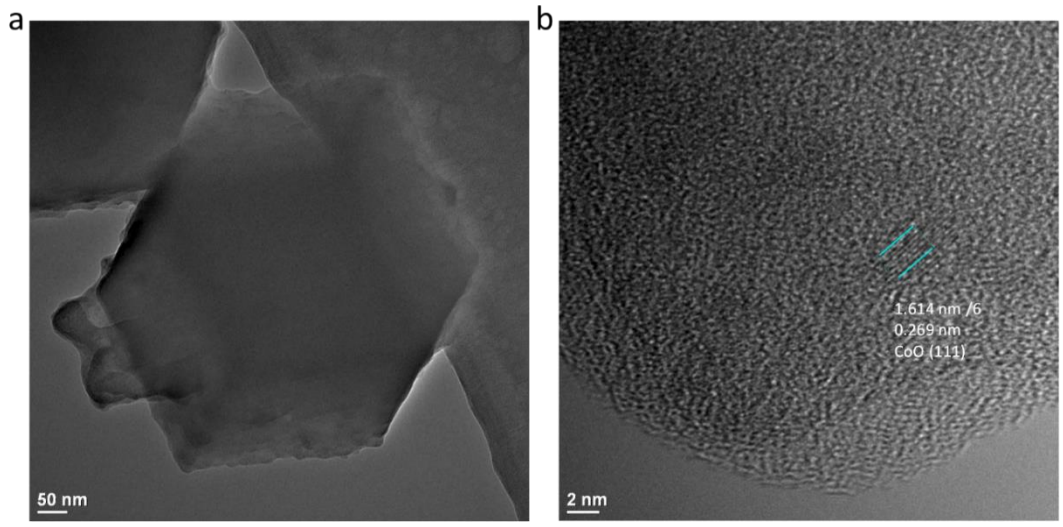

Figure 4. (a, b) Representative TEM images of Co-NC-200. Scale bars are (a) 50 nm and (b) 2 nm.

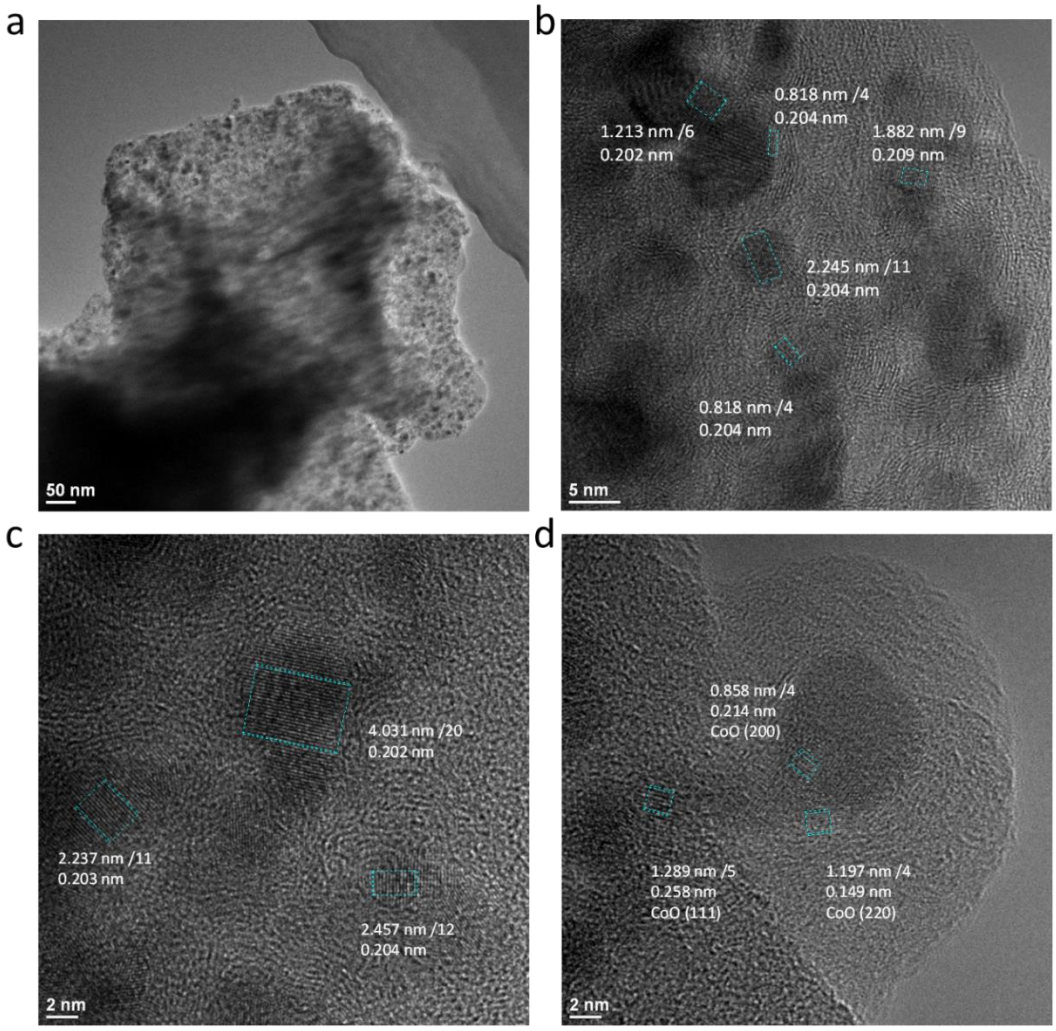

Figure 5. (a-d) Representative TEM images of Co-NC-300. Scale bars are (a) 50 nm, (b) 5 nm, and (c,d) 2 nm.

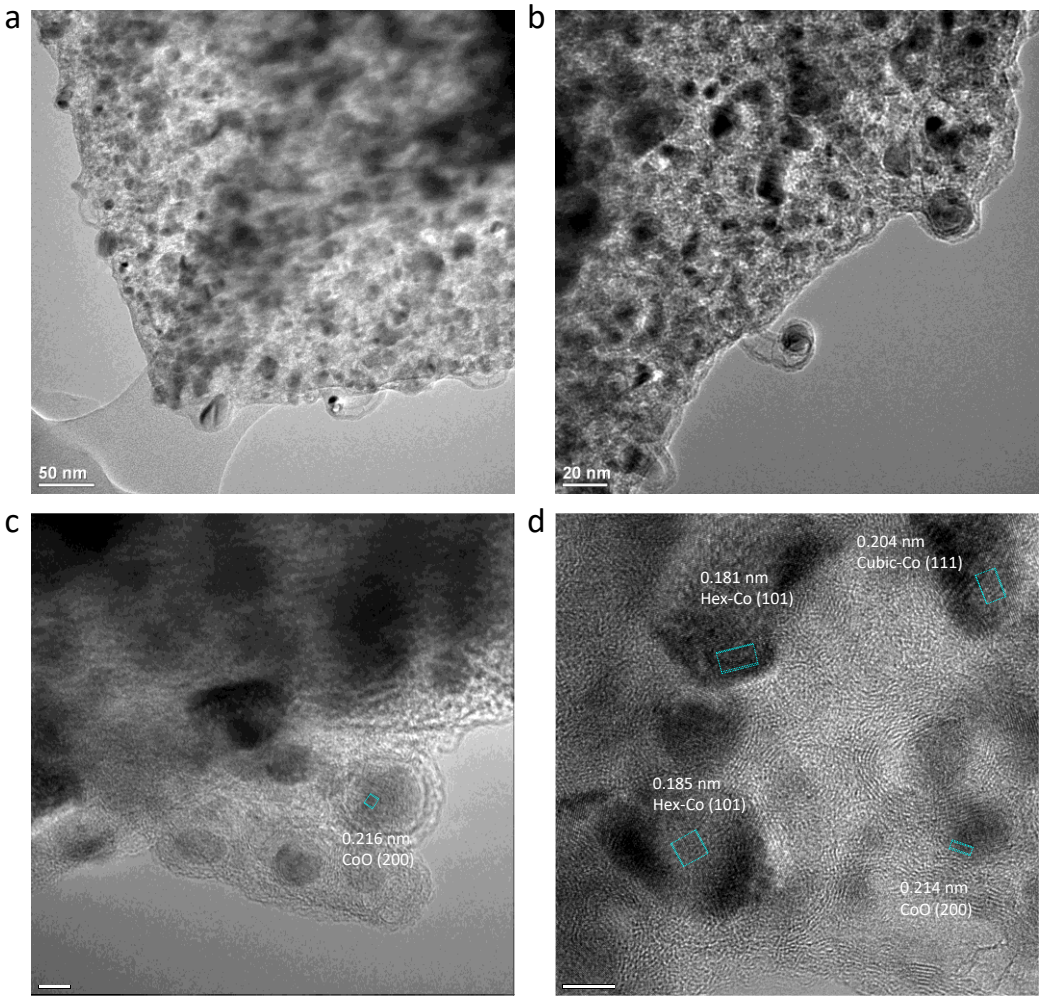

Figure 6. (a-d) Representative TEM images of Co-NC-500. Scale bars are (a) 50 nm, (b) 20 nm, and (c,d) 5 nm.

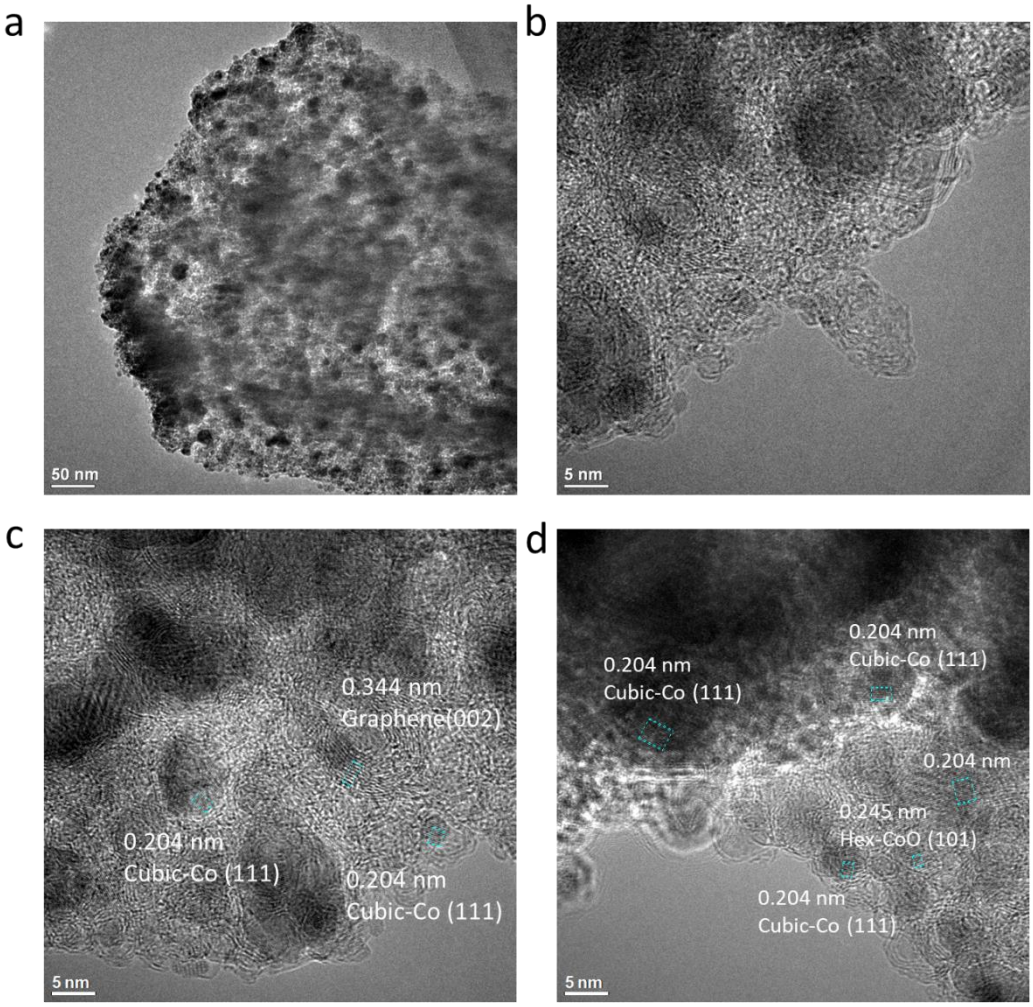

Figure 7. (a-d) Representative TEM images of Co-NC-600. Scale bars are (a) 50 nm and (b-d) 5 nm.

XPS measurements were then performed to examine the chemical compositions and valence states of the samples. From the survey spectra in Figure 8, the samples can be seen to consist of only C, N, and Co (Tables 1-5), suggesting successful conversation of ZIF-67 to Co-NC nanocomposites by MIH treatment. Figure 9a shows the high-resolution scans of the C 1s electrons in the series of samples. One can find that the C 1s spectrum of Co-NC-200 can be deconvoluted into two components, sp^2 C of the

imidazole rings at 284.6 eV and sp^3 C of the methyl groups at 285.8 eV, indeed suggesting incomplete decomposition of the ZIF-67 precursor [43,44]. For samples prepared at higher induction currents, the C 1s spectra can be found to consist of three components, sp^2 C at ca. 284.0 eV, sp^3 C at ca. 284.8 eV, and oxidized C at ca. 288.0 eV. This suggests that 2-methyimidazole in ZIF-67 was gradually decomposed and evolved into sp^2 C of the graphitic carbon layers. This was also manifested by the change of the sp^2 C/sp^3 C ratio (Figure 9e), which increased from 0 for Co-NC-200 to 1.0 for CO-NC-300, and finally to ca. 1.2 for Co-NC-400, Co-NC-500, and Co-NC-600. The increasing graphitization of the carbon shells over Co and CoO nanoparticles was also manifested by the increasing surface content of C from 70.02 at% of Co-NC-200 to 73.91 at% for Co-NC-300, 77.31 at% for Co-NC-400, 81.54 at% for Co-NC-500 and 86.81 at% for Co-NC-600 (Tables 1-5).

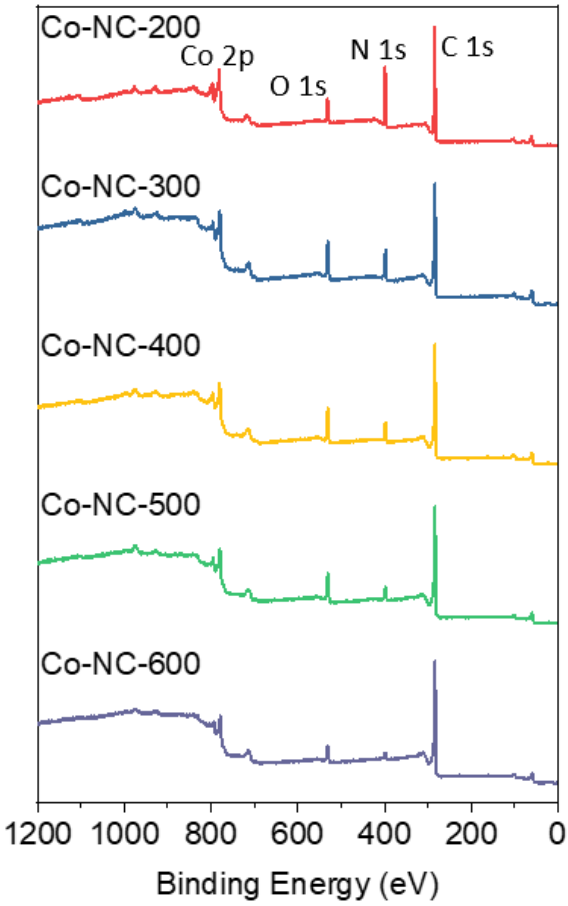

Figure 8. XPS survey spectra of Co-NC-200, Co-NC-300, Co-NC-400, Co-NC-500, and Co-NC-600.

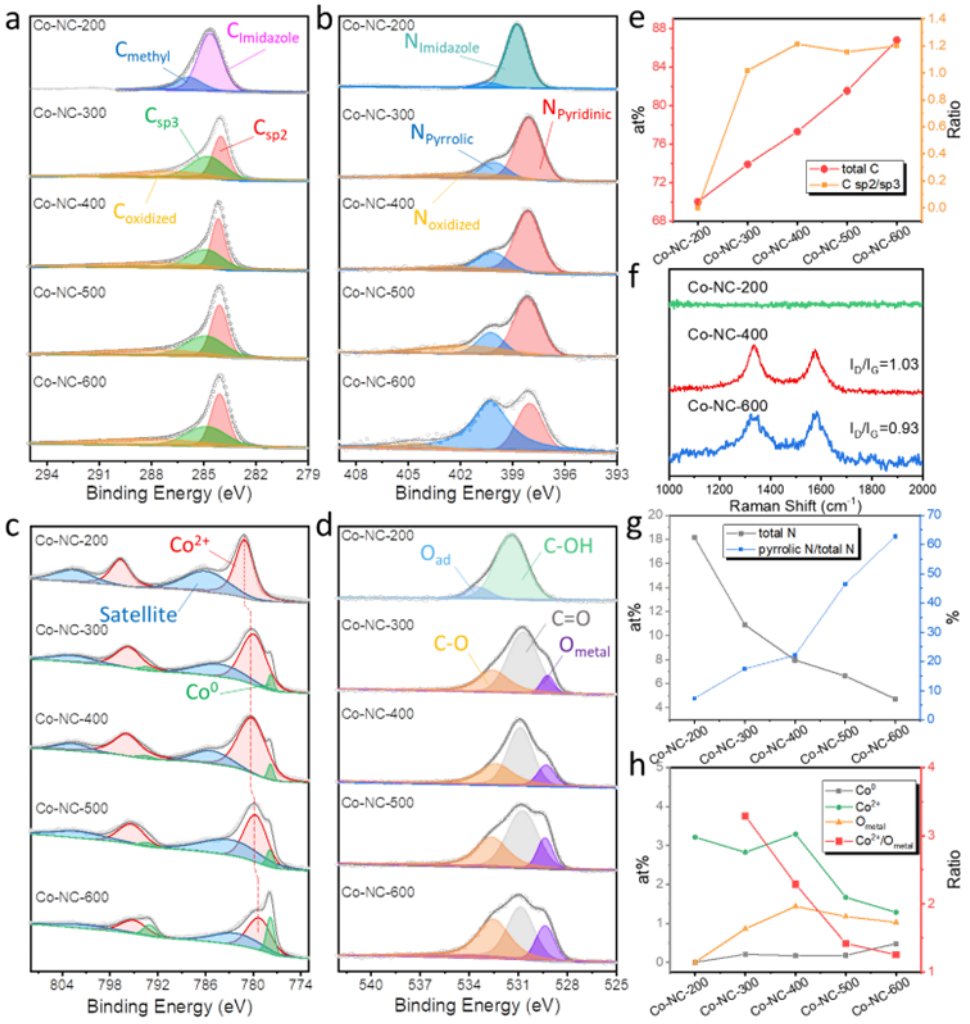

Figure 9. High-resolution scans of the (a) C 1s, (b) N 1s, (c) Co 2p, and (d) O 1s electrons of Co-NC-200, Co-NC-300, Co-NC-400, Co-NC-500, and Co-NC-600. (e) Carbon contents derived from XPS measurements. (f) Raman Spectra of Co-NC-200, Co-NC-400, and Co-NC-600. (g) Contents of total N and pyrrolic N derived from XPS measurements. (h) Variation of the contents of different Co and O species.

Table 1. XPS fitting results of Co-NC-200.

	Species	**BE (eV)**	**Content (at %)**	**Total Content (at %)**
C 1s	sp^2			70.02

	Imidazole	284.60	54.26	
	Methyl	285.83	15.76	
N 1s	Imidazole	398.75	16.82	18.16
	pyrrolic	400.39	1.34	
	oxidized			
O 1s	metal-O			6.28
	C-O	531.41	5.60	
	C=O	533.44	0.68	
Co 2p	metallic			5.53
	Co^{2+}	781.10	2.14	
		796.67	1.07	
	satellite	785.92	1.55	
		802.61	0.77	

Table 2. XPS fitting results of Co-NC-300.

	Species	**BE (eV)**	**Content (at %)**	**Total Content (at %)**
C 1s	sp^2	283.98	28.88	73.91
	sp^3	284.72	28.36	
	oxidized	287.03	16.67	
N 1s	pyridinic	398.05	7.60	10.90

	pyrrolic	400.03	1.90	
	oxidized	401.52	1.40	
O 1s	metal-O	529.17	0.86	10.83
	C-O	530.67	6.70	
	C=O	532.54	3.27	
Co 2p	metallic	777.76	0.14	4.37
		793.37	0.07	
	Co^{2+}	779.94	1.88	
		795.66	0.94	
	satellite	784.22	0.89	
		802.63	0.45	

Table 3. XPS fitting results of Co-NC-400.

	Species	**BE (eV)**	**Content (at %)**	**Total Content (at %)**
C 1s	sp^2	284.03	33.64	77.31
	sp^3	284.76	27.68	
	oxidized	287.82	15.98	
N 1s	pyridinic	398.10	5.78	7.96
	pyrrolic	400.14	1.76	
	oxidized	402.40	0.42	
O 1s	metal-O	529.26	1.44	10.36
	C-O	530.84	5.49	
	C=O	532.34	3.43	
Co 2p	metallic	777.80	0.11	4.37
		793.52	0.06	
	Co^{2+}	780.14	2.19	
		795.90	1.10	
	satellite	785.24	0.61	
		802.68	0.31	

Table 4. XPS fitting results of Co-NC-500.

	Species	**BE (eV)**	**Content (at %)**	**Total Content (at %)**
C 1s	sp^2	284.06	33.88	81.54

	sp^3	284.85	29.29	
	oxidized	288.08	18.37	
N 1s	pyridinic	398.12	3.80	6.64
	pyrrolic	400.23	1.33	
	oxidized	401.85	1.51	
O 1s	metal-O	529.32	1.17	8.45
	C-O	530.70	4.37	
	C=O	532.62	2.90	
Co 2p	metallic	777.87	0.12	3.36
		793.27	0.06	
	Co^{2+}	779.71	1.11	
		795.32	0.56	
	satellite	782.88	1.01	
		802.05	0.51	

Table 5. XPS fitting results of Co-NC-600.

	Species	**BE (eV)**	**Content (at %)**	**Total content (at %)**
C 1s	sp2	284.05	34.67	86.81
	sp3	284.82	28.90	
	oxidized	288.50	23.25	
N 1s	pyridinic	397.99	1.40	4.73
	pyrrolic	400.25	2.97	
	oxidized	404.68	0.37	
O 1s	metal-O	529.31	1.02	5.77
	C-O	530.82	2.33	
	C=O	532.49	2.41	
Co 2p	metallic	777.83	0.32	2.69
		792.99	0.16	
	Co^{2+}	779.25	0.86	
		795.06	0.43	
	satellite	782.12	0.62	
		801.13	0.31	

Consistent results were obtained in Raman measurements. From Figure 9f, Co-NC-200 can be seen to exhibit only a featureless baseline in the range of 1000 to 2000 cm^{-1}, suggesting no well-defined graphitic structure. By contrast, both Co-NC-400 and Co-NC-600 exhibited two prominent peaks at 1333 cm^{-1} (D band) and 1580 cm^{-1} (G band),

due to the out-of-plane (i.e., defects) and in-plane vibrations, respectively [45]. Furthermore, the intensity ratio of these two bands (I_D/I_G) decreased somewhat from 1.03 for Co-NC-400 to 0.93 for Co-NC-600, consistent with increasing graphitization of the samples prepared at increasing induction currents (Figure 9f-j).

The N 1s spectra are depicted in Figure 9b. One can see that Co-NC-200 consists of a main peak at 398.8 eV, due to the N atoms of 2-methylimidazole [43]. For other samples, three N species can be resolved, pyridinic N at ca. 398.1 eV, pyrrolic N at ca. 400.1 eV, and oxidized N (over 401.5 eV), signifying the successful doping of N into the carbon skeletons likely by deamination of the imidazole rings and formation of graphitic C rings during ultrafast heating [46]. Notably, one can see from Figure 9g that with increasing heating currents, the overall content of the N species decreased monotonically from 18.2 at% for Co-NC-200 to 10.9 at% for Co-NC-300, 8.0 at% for Co-NC-400, 6.6 at% for Co-NC-500, and 4.73 at% for Co-NC-600, whereas concurrently the content of pyrrolic N increased from 1.3 at% for Co-NC-200 to 1.9 at% for Co-NC-300, 1.76 at% for Co-NC-400, 1.33 % for Co-NC-500, and 2.97 at% for Co-NC-600 (Table 1-5), signifying that pyrrolic N became the increasingly dominant species in the sample series. Such a trend is contradictory to results in traditional pyrolysis in that pyrrolic N is energetically unstable at high temperatures [47]. This suggests that MIH might be a unique tool to create metastable N-doped carbon structures.

Figure 9c shows the corresponding high-resolution scans of the Co 2p electrons. One can see that Co-NC-200 consisted of a doublet at 781.1/796.7 eV arising from the

$2p_{3/2}/2p_{1/2}$ electrons of Co^{2+} species and a pair of satellite peaks at 785.9/802.6 eV [48,49]. For other samples (i.e., X = 300, 400, 500, and 600 A), an additional doublet appeared at 777.8/793.5 eV, which can be assigned to the $2p_{3/2}/2p_{1/2}$ electrons of metallic Co [50]. This is consistent with the results from TEM measurements where both Co and CoO lattice fringes were observed (Figure 3-7). In fact, the Co^{2+} content can be found to diminish markedly from ca. 3 at% for Co-NC-200, Co-NC-300, and Co-NC-400 to 1.6 at% for Co-NC-500 and 1.3 at% for Co-NC-600, whereas the content of metallic Co was the highest with Co-NC-600 at 0.48 at%, in comparison to ca. 0.2 at% for Co-NC-500, Co-NC-400 and Co-NC-300, and undetectable in Co-NC-200 (Figure 9h). In addition, one can see that the Co^{2+} $2p_{3/2}$ binding energy (red dashed line in Figure 9c) red-shifted from 781.1 eV for Co-NC-200 to 780.1 eV for Co-NC-300 and Co-NC-400, 779.7 eV for Co-NC-500, and further to 779.3 eV for Co-NC-600. This suggests increasing charge transfer from the carbon scaffold to Co^{2+} species (CoO or CoN_x moieties), which facilitated the reduction of Co^{2+} to metallic Co, due to enhanced graphitization at elevated temperatures [51].

High-resolution scans of the O 1s electrons further confirm the formation of CoO species except for Co-NC-200. From Figure 3d, one can see that no peak around 529-530 eV can be discerned in the O 1s spectrum of Co-NC-200, whereas for other samples in the series, the peak (purple color) can be readily deconvoluted due to metal oxide (O_{metal}) [36]. In fact, it can be seen from Figure 9h that the O_{metal} content increased from 0 at% for Co-NC-200 to 0.85 at% for Co-NC-300, 1.44 at% for Co-NC-400, and then decreased to 1.17 at% for Co-NC-500 and 1.03 at% for Co-NC-600. Interestingly, the

atomic ratio between Co^{2+} and O_{metal} decreased from 3.3 for Co-NC-300 to 2.3 for Co-NC-400, 1.4 for Co-NC-500 and 1.3 for Co-NC-600 (Figure 9h). The fact that all are higher than the stoichiometric ratio (1:1) of CoO suggests the formation of CoN_x moieties [49], which likely decomposed at high temperatures, due to the loss of the N dopants (Figure 3g), and aggregated into CoO/Co nanoparticles in the carbon matrix.

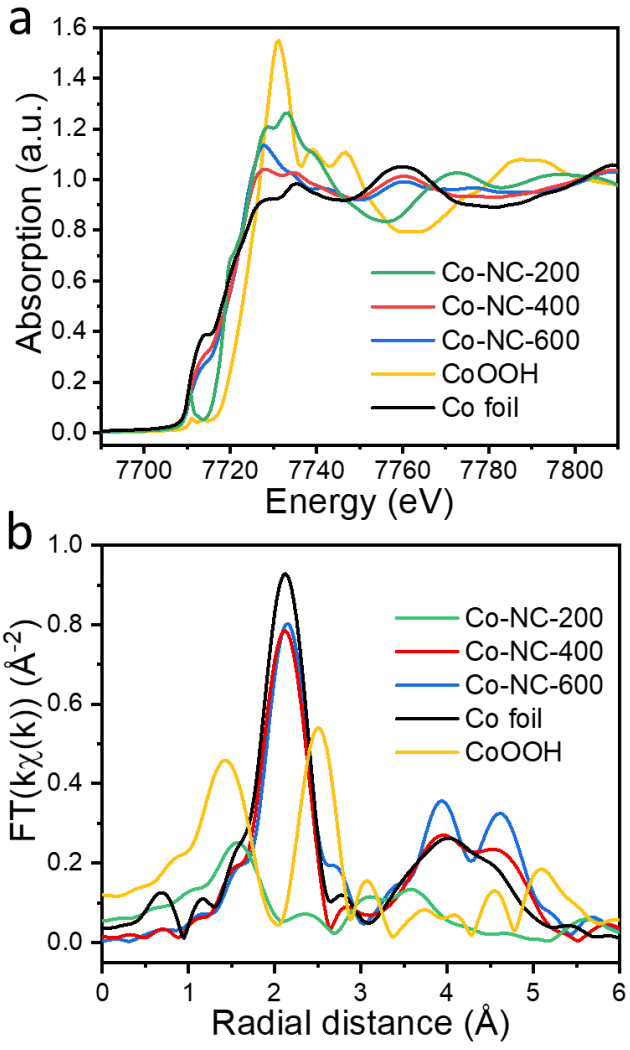

Figure 10. Co K-edge (a) XANES and (b) the corresponding EXAFS of Co-NC-200, Co-NC-400, and Co-NC-600.

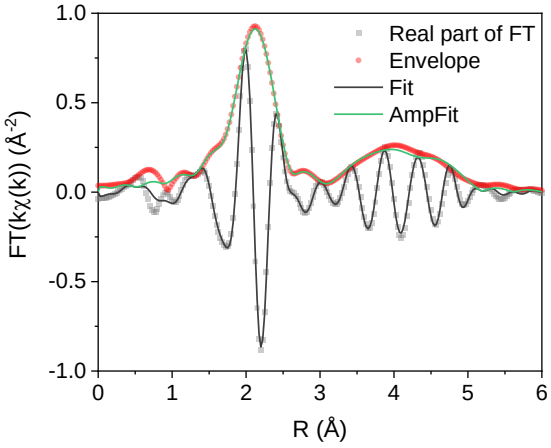

Figure 11. Fitting results of the Fourier transform (FT)-EXAFS of Co foil.

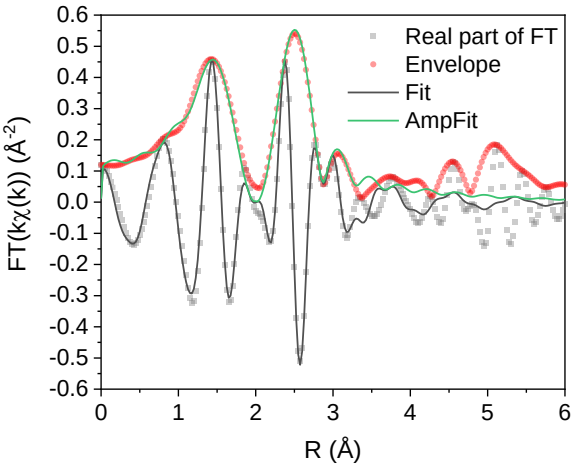

Figure 12. Fitting results of the FT-EXAFS of CoOOH. Amplitude reduction factor (S_0^2) is derived from one peak fitting of CoOOH with a value of 0.76.

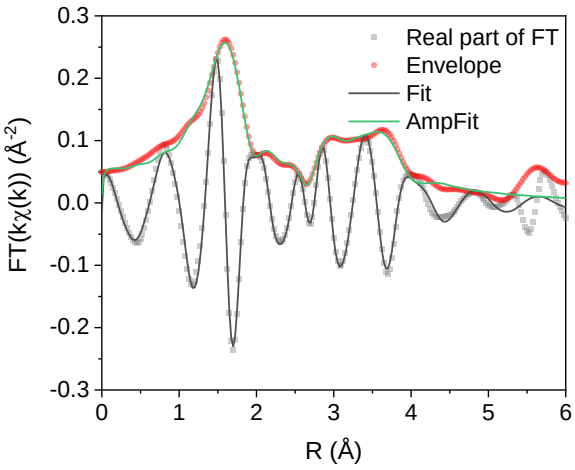

Figure 13. Fitting results of the FT-EXAFS of Co-NC-200.

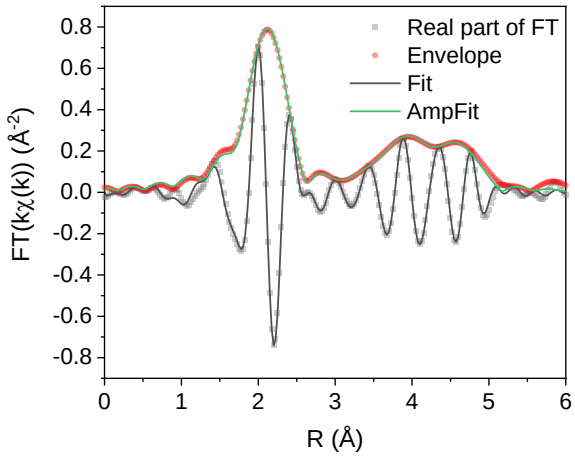

Figure 14. Fitting results of the FT-EXAFS of Co-NC-400.

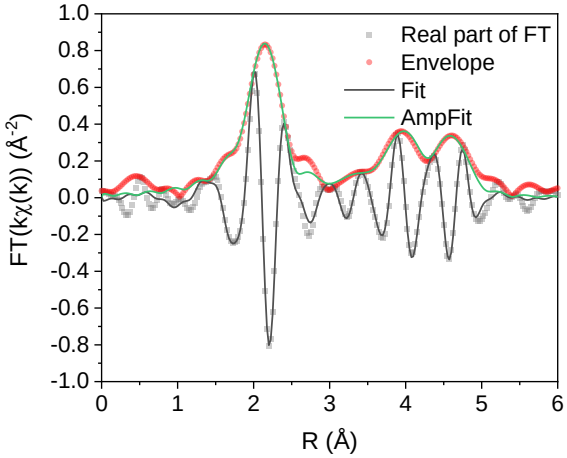

Figure 15. Fitting results of the FT-EXAFS of Co-NC-600.

Table 6. Fitting results of the EXAFS data of the Co foil reference. Note that the coordination numbers are fixed to the theoretical values of bulk Co.

Path	σ^2	Bond Length (Å)	Coordination Number	ΔE_0 (eV)
Co-Co	0.005	2.4958	12	1.16
Co-Co	0.009	3.5295	6	1.16
Co-Co	0.017	3.7436	48	1.16
Co-Co	0.002	4.2606	48	1.16
Co-Co	0.010	4.3228	24	1.16
Co-Co	0.002	4.6573	144	1.16
Co-Co	0.009	4.9916	228	1.16

Table 7. Fitting results of the EXAFS data of the CoOOH reference. Note that the coordination numbers are fixed to the theoretical values of bulk CoOOH.

Path	σ^2	Bond Length (Å)	Coordination Number	ΔE_0 (eV)

Co-O	0.004	1.9208	6	-1.13
Co-Co	0.005	2.8543	6	-1.13
Co-multi-scatters	0.004	3.0602	1	-1.13
Co-O	0.002	3.3549	6	-1.13

Table 8. Fitting results of the EXAFS data of Co-NC-200.

Path	**σ^2**	**Bond Length (Å)**	**Coordination Number**	**ΔE_0 (eV)**
Co-N/O	0.003	1.98	5.24	-3.00
Co-C	0.010	2.92	2.62	-3.00
Co-C	0.002	3.02	7.61	-3.00
Co-multi-scatters	0.002	3.11	0.43	-3.00
Co-C	0.002	3.34	7.36	-3.00
Co-C	0.012	3.56	5.27	-3.00
Co-multi-scatters	0.005	4.21	3.42	-3.00

Table 9. Fitting results of the EXAFS data of Co-NC-400.

Path	**σ^2**	**Bond Length (Å)**	**Coordination Number**	**ΔE_0 (eV)**
Co-Co	0.003	2.4929	7.81	2.20
Co-Co	0.006	3.5174	3.57	2.20
Co-Co	0.013	3.7264	51.67	2.20
Co-Co	0.008	4.3356	29.86	2.20

Co-Co	0.005	4.3360	16.93	2.20
Co-Co	0.002	4.7334	133.56	2.20
Co-Co	0.004	5.0075	132.84	2.20

Table 10. Fitting results of the EXAFS data of Co-NC-600.

Path	**σ^2**	**Bond Length (Å)**	**Coordination Number**	**ΔE_0 (eV)**
Co-Co	0.003	2.4982	8.07	1.82
Co-Co	0.013	3.5393	7.56	1.82
Co-Co	0.002	3.7957	61.03	1.82
Co-Co	0.003	4.2130	42.91	1.82
Co-Co	0.002	4.3351	12.11	1.82
Co-Co	0.004	4.7099	153.42	1.82
Co-Co	0.006	5.0076	226.25	1.82

Further structural insights of the samples were obtained from XAS measurements. Figure 10a depicts the Co K-edge X-ray absorption near edge spectra (XANES) of the sample series, Co foil, and CoOOH. One can see that Co-NC-200, Co-NC-400, and Co-NC-600 all exhibited an absorption edge between those of Co foil and CoOOH, suggesting an average valence state between 0 and +3, which is consistent with the XPS results (Figure 9). Meanwhile, both Co-NC-400 and Co-NC-600 showed a pre-edge feature similar to that of Co foil at 7713 eV, confirming the formation of metallic Co in the samples, while Co-NC-200 possessed a sharp pre-edge peak at 7710 eV, due

to the 1s → 3d transitions of tetrahedral Co^{II}-N_4 [52,53]. Figure 10b shows the corresponding extended X-ray absorption fine structures (EXAFS) of the samples. One can see that none of the Co-NC samples exhibited a profile resembling that of CoOOH (which consisted of two prominent peaks at 1.43 and 2.50 Å due to Co-O and Co-Co, respectively) [54]. Specifically, Co-NC-200 displayed a main peak at 1.55 Å, due to the Co-N/O bonds of the ZIF-67 precursor; and this peak became a shoulder in both Co-NC-400 and Co-NC-600, which actually featured an intense peaks at 2.10 Å, due to the Co-Co bonds of metallic Co, and two minor ones at 3.93 Å and 4.60 Å, all consistent with those of Co foil [55]. From the fitting results (Figure 11-15, Table 6-10), it can be seen that Co-NC-400 and Co-NC-600 exhibited a Co-Co bond length of 2.49 Å and a close coordination number (CN) of 7.81 and 8.07, respectively. These CN values are smaller than that of Co foil (12), possibly due to the much smaller sizes of the nanoparticles (Figure 3). Meanwhile the CN of Co-N/O was ca. 5.24 for Co-NC-200, slightly larger than theoretical value (4) of the Co-N bonds in ZIF-67, likely due to the partial oxidation/decomposition of the precursor. Taken together, these results are consistent with those from the above TEM and XPS measurements.

5.4.2 Electrocatalytic activity

Electrochemical measurements were then carried out to evaluate and compare the electrocatalytic activity. Figure 16 shows the cyclic voltammograms (CVs) of the sample series within the non-Faradaic potential range of -0.1 to +1.1 V. It can be seen that the double-layer charging currents were significantly lower for Co-NC-200 and Co-NC-300 than for Co-NC-400, Co-NC-500, and Co-NC-600 (Co-NC-600 also

shows a small anodic peak at +0.4 V due to the oxidation of surface metallic cobalt [56]). In fact, the electrode double-layer capacitances (C_{dl}) can be estimated to be 3.34 mF cm^{-2} for Co-NC-200 and 2.51 mF cm^{-2} for Co-NC-300, reached the highest at 86.19 mF cm^{-2} for Co-NC-400, and then decreased slightly to 79.92 mF cm^{-2} for Co-NC-500 and 77.25 mF cm^{-2} for Co-NC-600 (Figure 17). This suggests that Co-NC-400 possessed the highest electrochemical surface area (ECSA), a unique feature conducive to accessibility of the catalytic active sites and the eventual electrocatalytic activity.

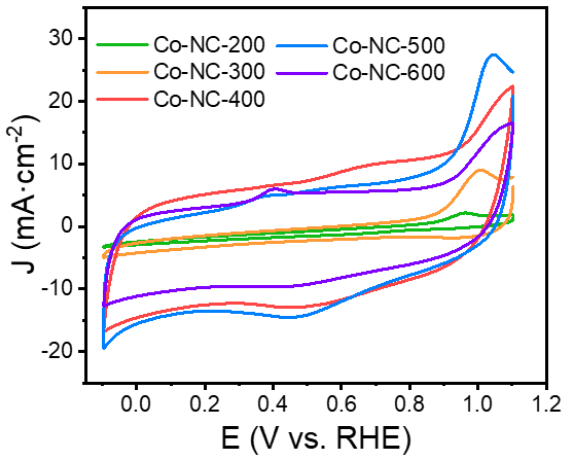

Figure 16. Cyclic voltammetric scans of the sample series in 1 M KOH at a scan rate of 50 mV s^{-1}.

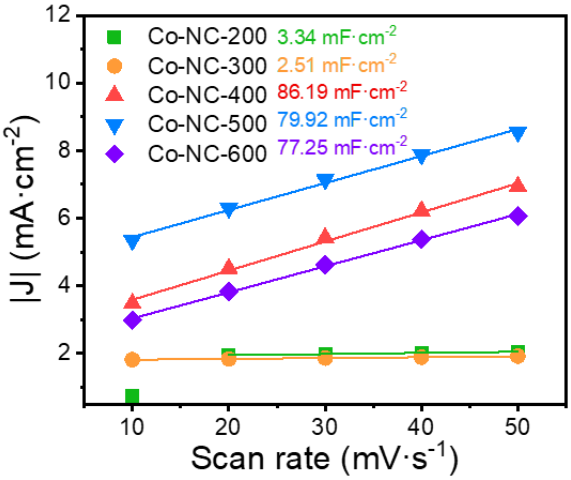

Figure 17. Variation of double-layer charging currents with scan rates for the series of samples. Symbols are data points derived from CV measurements (Figure 16) and lines are linear regressions, from which the double-layer capacitance (C_{dl}) is derived.

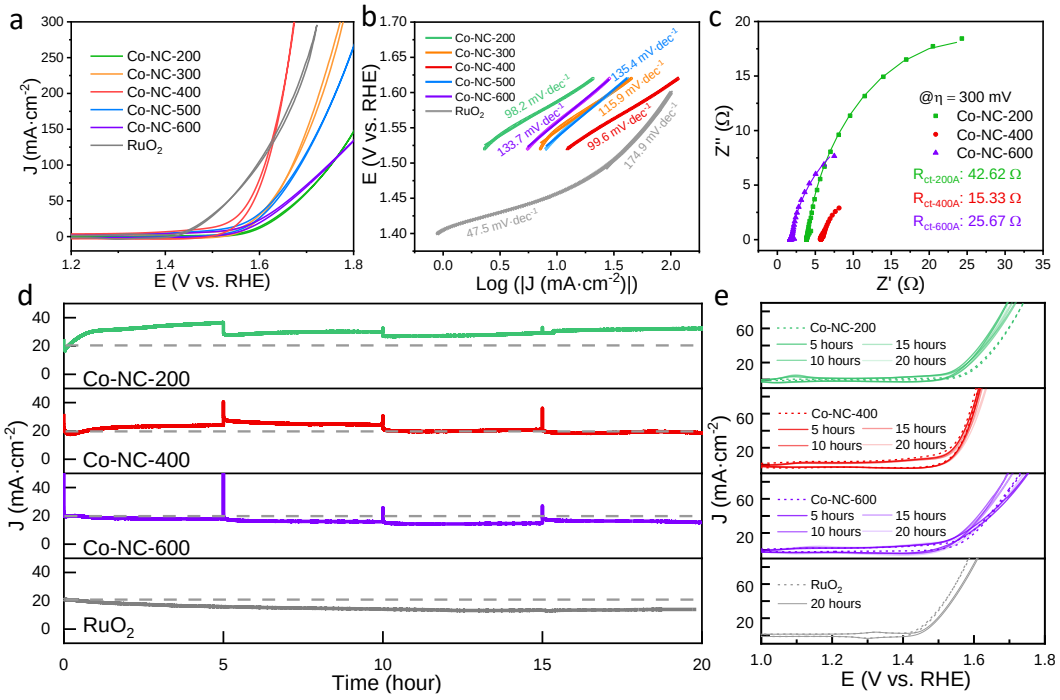

Figure 18. (a) OER Polarization curves of the sample series and commercial RuO_2 in 1 M KOH with a scan rate of 10 mV s^{-1}. (b) Tafel plots of the Co-NC samples and RuO_2. (c) Nyquist plots of Co-NC-200, Co-NC-400, and Co-NC-600 at the overpotential of

+300 mV. (d) Stability tests by i-t measurements of Co-NC-200, Co-NC-400, Co-NC-600, and RuO_2 at their respective η_{20} for 20 h. Note that bubbles were removed from the sample surface every five hours. (e) OER polarization curves of Co-NC-200, Co-NC-400, Co-NC-600, and RuO_2 acquired at different time points during the stability tests.

The OER polarization curves in 1 M KOH are depicted in Figure 18a. One can see that similar to commercial RuO_2, all Co-NC nanocomposites exhibited a sharp increase of the voltametric current with a positive sweep of the electrode potential beyond +1.4 V, suggesting apparent OER activity. Yet, the OER activity varies among the samples. In fact, Co-NC-400 can be seen to stand out as the best OER catalyst amongst the series, with an η_{10} of +308 mV and η_{200} of +410 mV. The overpotentials are much higher for Co-NC-200 (+364 mV and over +600 mV), Co-NC-300 (+340 mV and +500 mV), Co-NC-500 (+330 mV and +530 mV) and Co-NC-600 (+347 mV and over +600 mV), whereas for commercial RuO_2, +230 mV and +450 mV (Figure 19). That is, 400 A turned out to be the optimal heating current for the ultrafast treatment of ZIF-67, and Co-NC-400 even outperformed RuO_2 at high current densities (e.g., over 150 mA cm^{-2}) as well as relevant Co-based nanocomposites reported recently in the literature (Table 11).

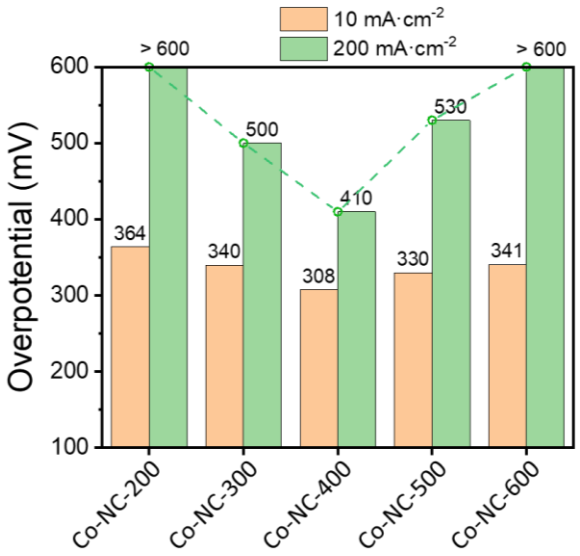

Figure 19. Comparisons of OER overpotentials at 10 and 200 mA cm^{-2} amongst the samples.

Table 11. Comparison of different Co-based nanocomposites toward OER in 1 M KOH.

Sample	**Preparation methods/ time**	**η_{10} (mV)**	**OER Active sites or mechanisms**	**Refence**
Co-NC-400	MIH/ 10 s	+308	CoO_x species formed on surface	This work
CoP/NCNHP	Pyrolysis/ over one day	+320	CoP/CoOOH core−shell structure	J. Am. Chem. Soc. 2018, 140, 2610−2618

$Co(OH)_2$-1	Wet chemistry/ 1.5 h	+354	$Co(OH)_2$	J. Colloid Interface Sci. 2020, 562, 279-286
ZIF-$Co_{0.85}Se$	Solvothermal and calcination/over one day	+360	Co^{3+} species	ACS Appl. Mater. Interfaces 2016, 8, 20534−20539
Co_3O_4/HNCP-40	Pyrolysis/ over 10 h	+333	Oxygen vacancies in Co_3O_4	ACS Catal. 2018, 8, 9, 7879–7888
Co_3O_4/Co-Fe	Wet chemistry/ over 2 h	+297	Co and Fe species	Adv. Mater. 2018, 30, 1801211
NiCo LDH nanoplates	Hydrothermal/ over 2 days	+367	NiCo LDH	Nano Lett. 2015, 15, 1421−1427
CC@$NiCo_2O_4$	Wet chemistry and calcination/ over 8 h	+340	$NiCo_2O_4$	Adv. Energy Mater. 2017, 7, 1602391

F-CoOOH/NF	Calcination and electrochemistry/ over 2 h	+270	F anions	Angew. Chem. Int. Ed. 2018, 57, 15471
$CoCO_3$ PNSs	Wet chemistry/ over one day	+310	$Co(OH)_2$ and CoOOH	Chem. Eng. J. 2021, 417, 128066.
Co_4S_3/Mo_2C-NSC-2	Wet chemistry and calcination/ over one day	+331	Co-S-Mo bonds and Co^{3+} species	Appl. Catal. B, 2020, 260, 118197

The Tafel plots are shown in Figure 18b. One can see that Co-NC-400 featured a Tafel slope of 99.6 mV dec^{-1}, Co-NC-200 displayed a similar one at 98.2 mV dec^{-1}, whereas for Co-NC-300, Co-NC-500, and Co-NC-600, their Tafel slopes are markedly higher at 115.9 mV dec^{-1}, 135.4 mV dec^{-1}, 133.7 mV dec^{-1}, respectively (Figure 18b). This suggests that the Co-NC-400 sample possessed the most facile electron-transfer kinetics in OER as compared to other samples in the series. In addition, RuO_2 can be seen to display a low Tafel slope (47.5 mV dec^{-1}) in the low overpotential region (+1.40 to 1.50 V vs. RHE), but a markedly higher one at 174.9 mV dec^{-1} at high overpotentials, suggesting sluggish kinetics in producing high OER currents [57]. Consistent results were obtained from electrochemical impedance spectroscopy (EIS) measurements. From the Nyquist plots acquired at the overpotential of +300 mV (Figure 18c), one can see that

Co-NC-400 exhibited the lowest charge transfer resistance (R_{ct} = 15.33 Ω), as compared to 25.67 Ω for Co-NC-600, and 42.62 Ω for CO-NC-200.

The nanocomposites also manifested excellent stability towards OER. One can see from Figure 18d that at the overpotential of η_{20}, Co-NC-400 retained its initial current density for 20 h without an apparent decay (the slight fluctuation was due to the accumulation of oxygen bubbles on the electrode surface, and the currents were recovered once the bubbles were shaken off); and the corresponding polarization curves showed a negligible shift over time (Figure 18e). In contrast, Co-NC-200 actually exhibited an increase of the current density in the first 2 h and then maintained it for the next 18 h. The polarization curve also showed a negative shift in the first 5 h and a slightly positive shift after 20 h, implying electrochemical activation likely due to a significant structural rearrangement (recall that the sample involved only incomplete decomposition of ZIF-67). Co-NC-600 also possessed a rather stable i-t profile for 20 h; and the polarization curve remained virtually unchanged in the first 5 h, but showed a significant negative shift after 10 h, denoting drastic structural dynamics. As for commercial RuO_2, both the i-t profile (Figure 18d) and polarization curves (Figure 18e) exhibit a substantial decay (ca. 34% of the initial current was lost at 20 h), signifying structural instability during prolonged operation. These results indicate that the Co-NC samples possessed markedly enhanced stability toward OER, as compared to commercial RuO_2.

Notably, when Co-NC-400 was subject to acid leaching in 0.5 M H_2SO_4 at 80 °C for 8 h, the OER activity diminished significantly (Figure 20), with η_{10} increased to +440

mV and η_{200} to ca. +600 mV. TEM measurements showed that almost all nanoparticles vanished after the acid treatment (Figure 21). Concurrently, the peaks of metallic Co and metal-O disappeared from the Co 2p and O 1s XPS spectra (Figure 22), whereas Co^{2+} and N remained detectable, suggesting the retention of CoN_x moieties in the carbon matrix. This implies that the OER activity was primarily due to the Co/CoO nanoparticles, with only a minimal contribution from the CoN_x moieties.

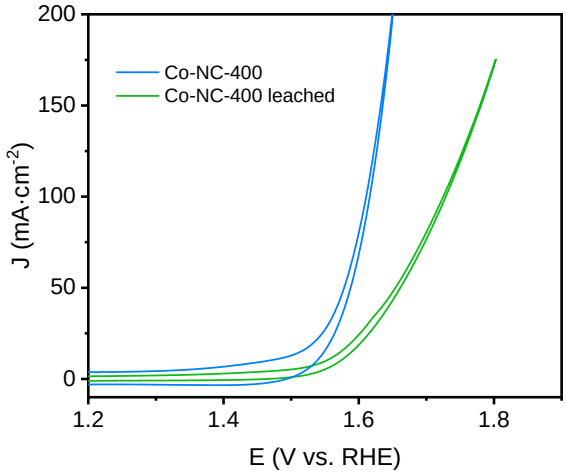

Figure 20. OER Polarization curves of Co-NC-400 before and after acid leaching in 1 M KOH at a scan rate of 10 mV s^{-1}.

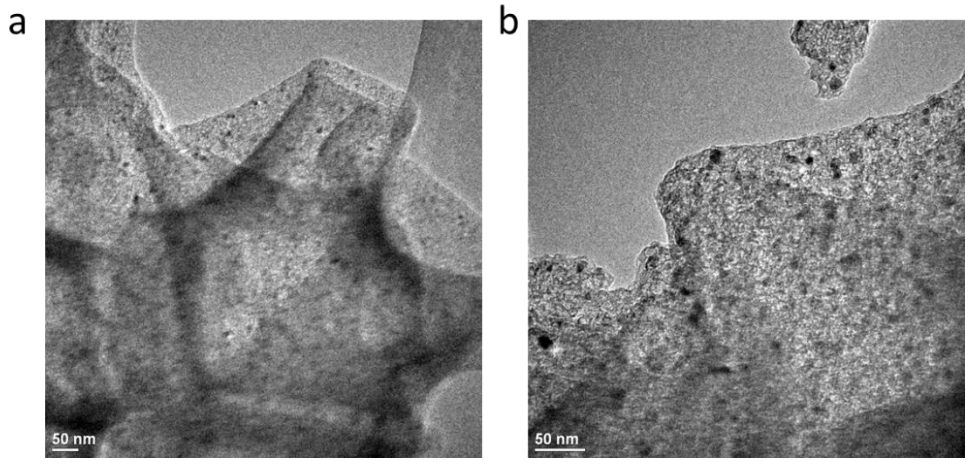

Figure 21. Representative TEM images of Co-NC-400 after leaching in 0.5 M H_2SO_4. Scale bars are both 50 nm.

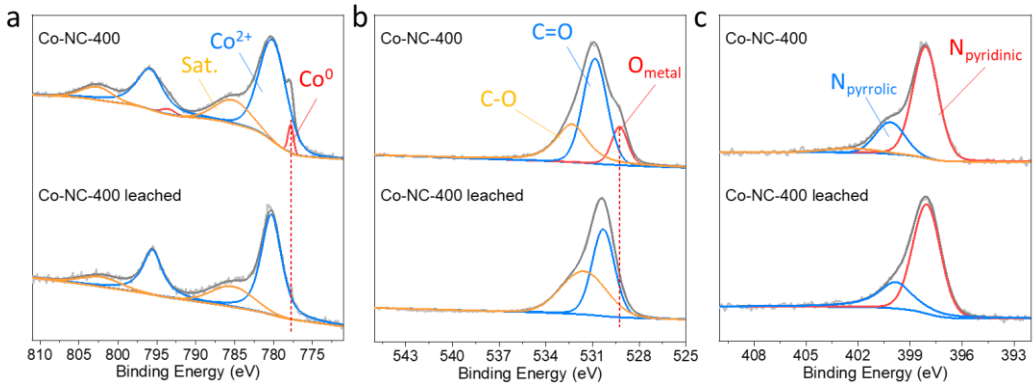

Figure 22. XPS spectra of (a) Co 2p, (b) O 1s, and (c) N 1s spectra for Co-NC-400 before (top curves) and after (bottom curves) acid leaching.

5.4.3 Mechanistic study

To further unravel the mechanistic origin of the OER activity, XPS measurements were carried out with three select Co-NC samples (Co-NC-200, Co-NC-400 and Co-NC-600) after 10 scans of the OER polarization curves. From the Co 2p spectra in Figure 23, all three samples can be seen to exhibit a primary peak at ca. 779 eV, suggesting the formation of Co^{3+} species, most likely due to the oxidation of Co at high electrochemical potentials, and concurrently the disappearance of the 777.8 eV peak indicates the total absence of metallic Co^0 on the sample surface. In addition, the binding energy of the Co^{2+} 2p electrons remained lower in Co-NC-400 and Co-NC-600 than in Co-NC-200. Note that such electron-enriched sites are preferred for OER. This is because in an electron-rich state the d electrons of Co may extend across the Fermi level, creating half-occupancy e_g orbitals for the Co atoms, which facilitates the

coupling of the *OH groups, promotes proton-coupled electron transfer, and enhances the chemisorption of *OOH intermediates and hence O_2 production [46,58]. From the O 1s spectra (Figure 24), a new peak can be seen to emerge at ca. 528.8 eV for all three samples, which can be ascribed to the O atoms in oxyhydroxides (OOH) [43], suggesting the formation of CoOOH species on the catalyst surface. Notably, the total content of the Co species was similar at ca. 10 at% for Co-NC-200 and Co-NC-400 (Figure 25), but drastically lower at 7.4 at% for Co-NC-600, which were all much higher than those of their as-produced counterparts, suggesting that a dissolution-redeposition process likely occurred during OER operation [59]. Furthermore, from the N 1s spectra (Figure 26), one can see that the contents of the N species diminished significantly after OER electrochemistry, from 18.2 to 5.43 at% for Co-NC-200, 8.0 to 1.48 at% for Co-NC-400, and 4.73 to 1.51 at% for Co-NC-600. This implies that the N species (i.e., CoN_x moieties) were unlikely the major contributors to the high and stable OER performance, in accord with results from the acid-etching experiment (Figure 20).

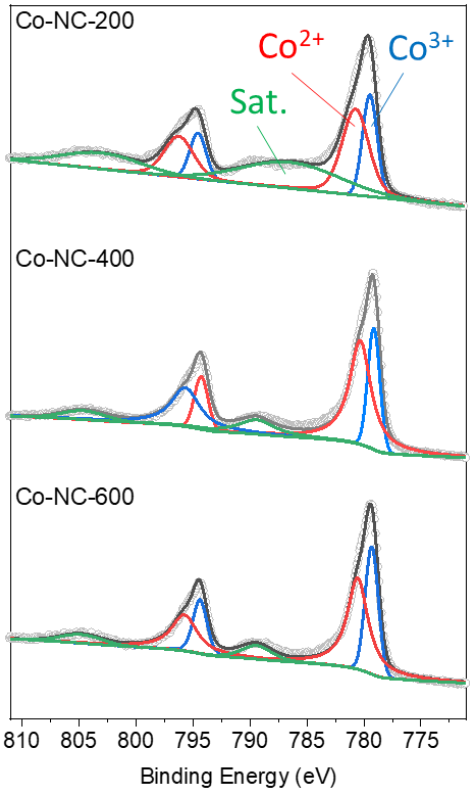

Figure 23. Co 2p spectra of Co-NC-200, Co-NC-300, Co-NC-400, Co-NC-500, and Co-NC-600 after 10 scans of OER polarization curves. Grey symbols are experimental data and colored curves are deconvolution fits.

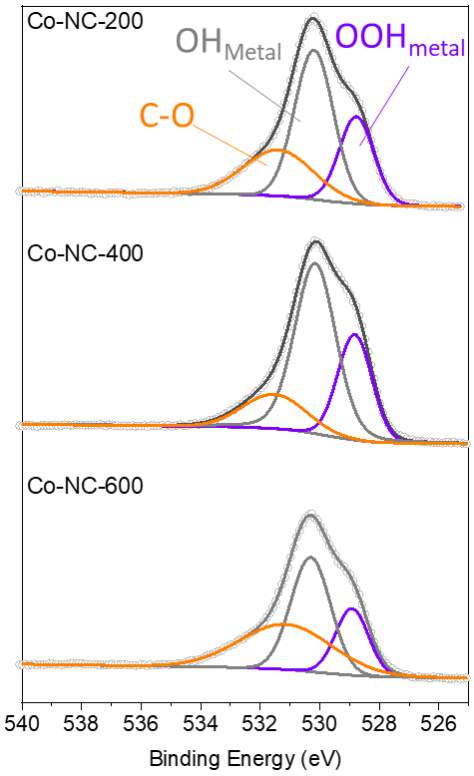

Figure 24. XPS spectra of the O 1s electrons of Co-NC-200, Co-NC-400, and Co-NC-600 after 10 scans of OER polarization curves. Grey symbols are experimental data and colored curves are deconvolution fits.

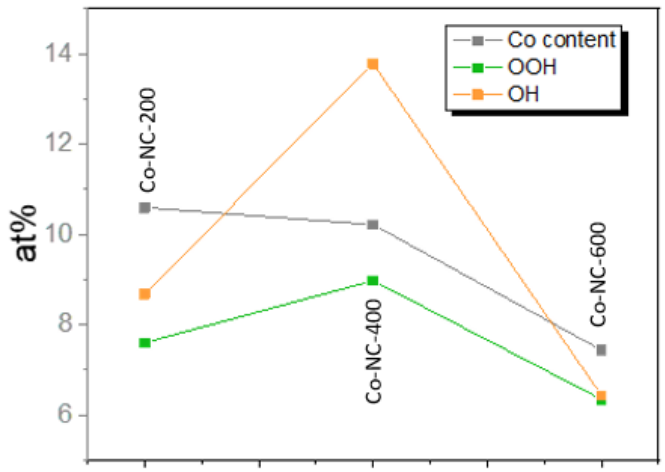

Figure 25. The contents (at%) of Co, OOH, and OH after 10 scans of OER polarization curves for Co-NC-200, Co-NC-400, and Co-NC-600.

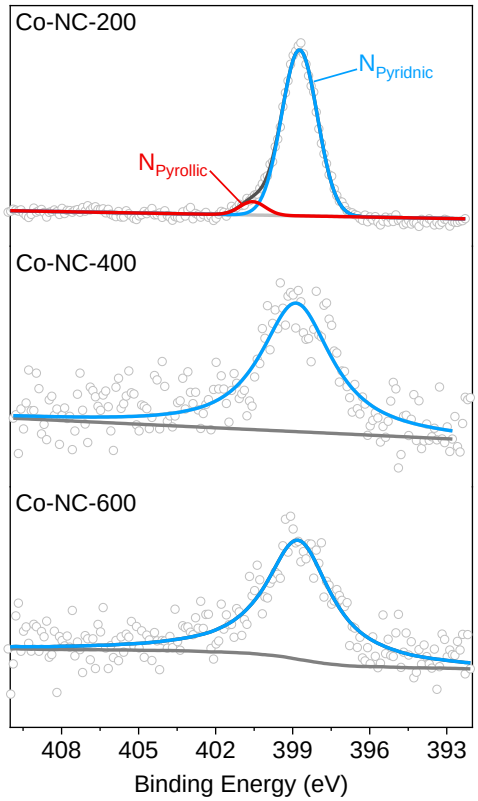

Figure 26. XPS spectra of the N 1s electrons of Co-NC-200, Co-NC-400, and Co-NC-600 after 10 scans of OER polarization curves. Grey symbols are experimental data and colored curves are deconvolution fits.

Consistent results were acquired in TEM measurements. As shown in Figure 27, Co-NC-200 completely collapsed into flaky-like structures after the OER tests, exhibiting clear lattice fringes with a d spacing of 0.198 nm that is consistent with the (104) facets of CoOOH [60]. By contrast, the carbon scaffold of Co-NC-400 retained the original structure and facilitated the formation of abundant CoOOH species on the sample surface (Figure 28). Co-NC-600 exhibited a similar phenomenon with the formation of

CoOOH (Figure 29). Nevertheless, the amount of CoOOH species was apparently lower than that in Co-NC-400, likely because the high degree of graphitization limited the access of the encapsulated Co/CoO nanoparticles to electrolyte solutions and hence the oxidation into CoOOH. This is indeed confirmed in operando XAS measurements (Figure 30), as detailed below.

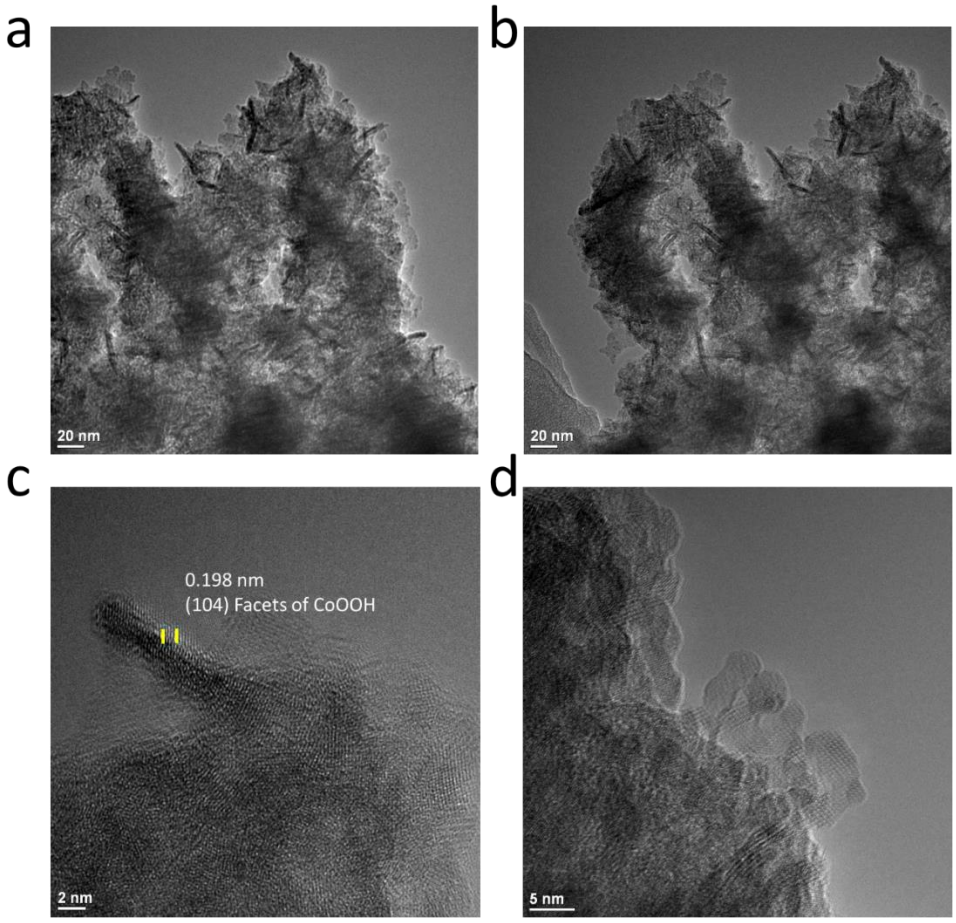

Figure 27. (a-d) Representative TEM images of Co-NC-200 after 10 scans of OER polarization curves. Scale bars are (a,b) 20 nm, (c) 2 nm and (d) 5 nm.

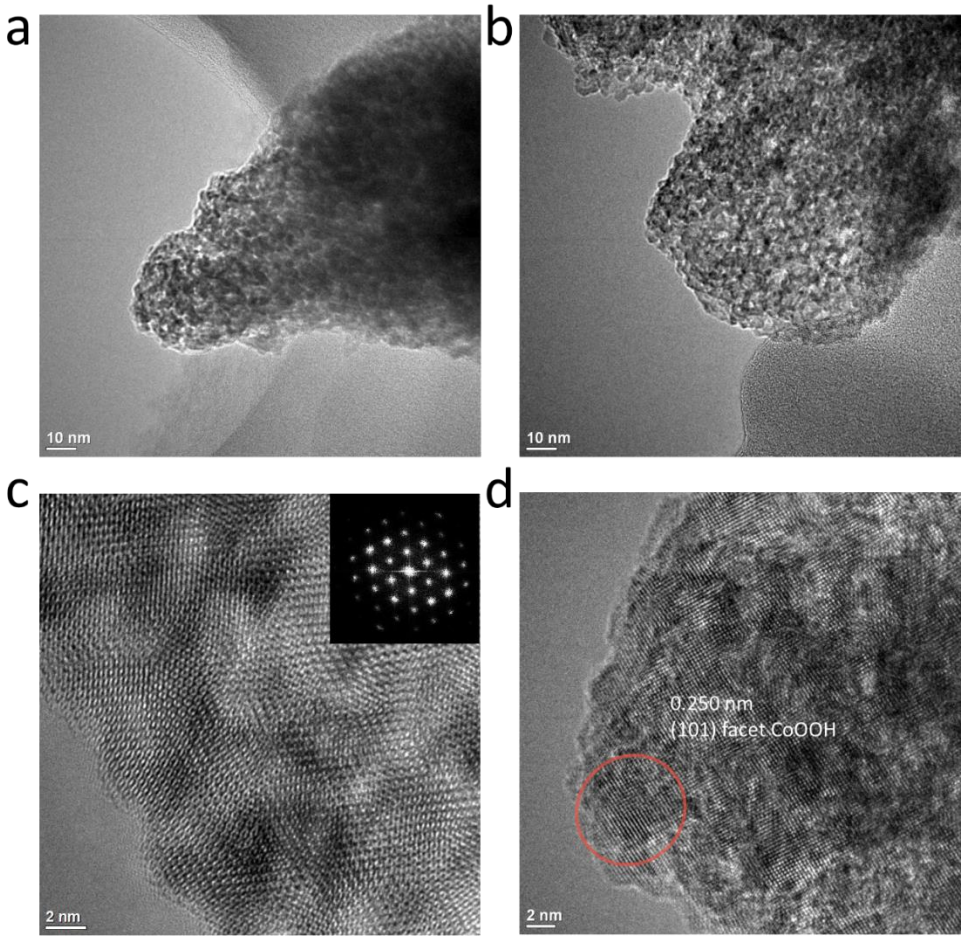

Figure 28. (a-d) Representative TEM images of Co-NC-400 after 10 scans of OER polarization curves. Inset to panel (c) is the FFT patterns. Scale bars are (a,b) 10 nm and (c,d) 2 nm.

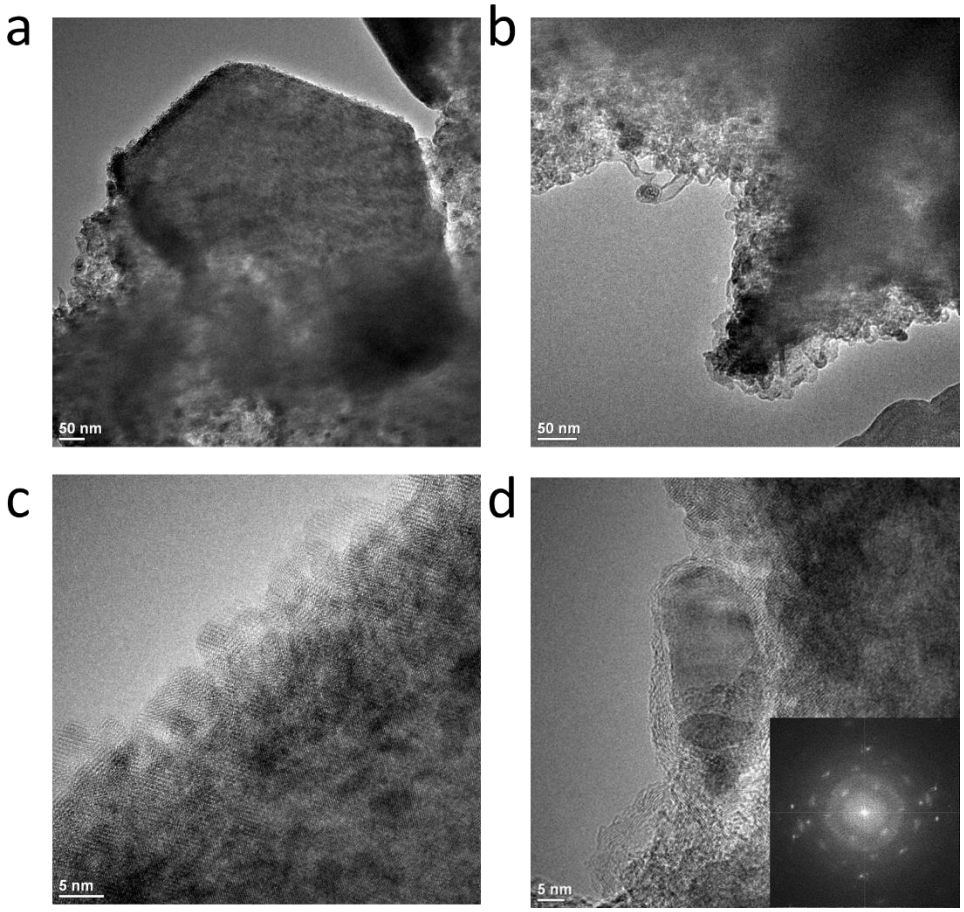

Figure 29. Representative TEM images of Co-NC-600 after 10 scans of OER polarization curves. Inset to panel (d) is the FFT patterns of metallic Co, suggesting many cobalt nanoparticles remain trapped inside the thick carbon shells. Scale bars are (a,b) 50 nm and (c,d) 5 nm.

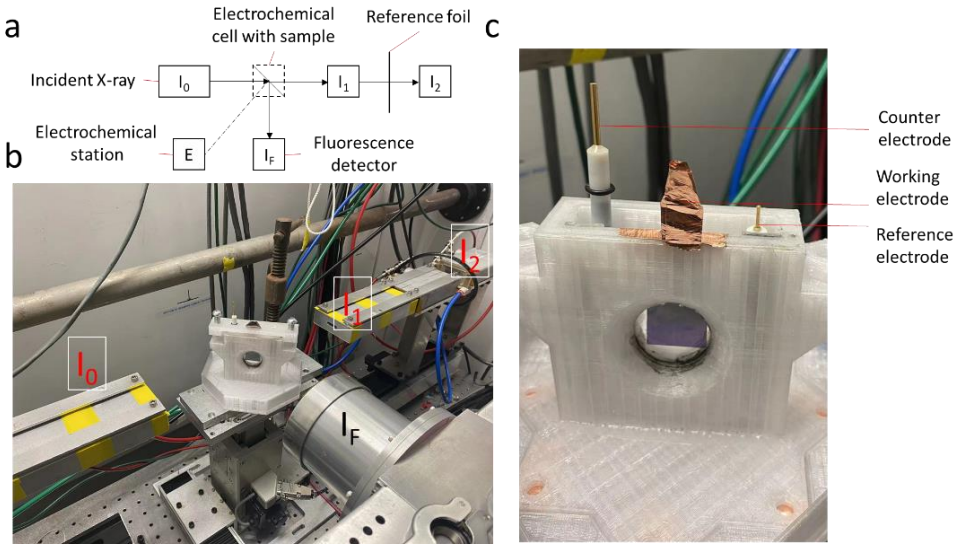

Figure 30. (a) Schematic illustration and (b) photograph of the operando XAS setup. (c) Photograph of the electrochemical cell.

Figure 31a shows the Co K-edge XANES profiles of Co-NC-400 acquired with the electrode potentials varied from open circuit potential (OCP) to +1.6 V. One can see from the figure inset that the absorption edge shifted slightly to a higher energy upon the application of a higher electrode potential, suggesting an increase of the Co valence state. In the corresponding EXAFS profiles in Figure 31b, the peak of the metallic Co-Co bonds (2.1 Å) can be seen to diminish in intensity, and concurrently, that of the Co-O bonds (at ca. 1.4 Å) became intensified, with increasingly positive electrode potentials, suggesting that metallic cobalt was slowly converted into CoOOH species, consistent with results from ex situ XPS and TEM measurements (Figure 23, 24 and 27). The fitting results are shown in Figure 32, 33 and Table 12, where the CN of Co-Co can be seen to decrease from 6.13 to 4.01 while that of Co-O increased from 2.25 to 4.88, consistent with the oxidation of metallic Co into Co-O species under high

electrode potentials. As for Co-NC-200 (Figure 31c), one can see the absorption edge shifted to a significantly higher energy upon the application of a more positive electrode potential, indicating that Co-NC-200 was more susceptible to electrochemical oxidation, most likely due to a low degree of carbonization, as compared to Co-NC-400 and Co-NC-600. Figure 31d shows the corresponding EXAFS curves, which can be seen to evolve into a profile resembling that of CoOOH (Figure 10b) with the application of increasingly positive potentials, indeed confirming a ready transformation into CoOOH by electrochemical oxidation. In fact, one can see that a new peak appeared at 2.55 Å at +1.25 V and migrated to 2.71 at +1.6 V, which can be assigned to the Co-Co path in CoOOH, and the peak became intensified at higher potentials, due to the formation of a larger amount of CoOOH, as observed in TEM measurements (Figure 28-29). Fittings of the EXAFS data (Figure 34, 35, and Table 13) showed that the CN of Co-O/N increased from 4.08 to 6.03, signifying the conversion of the Co-N_4 moieties into the Co-O_6 units in CoOOH.

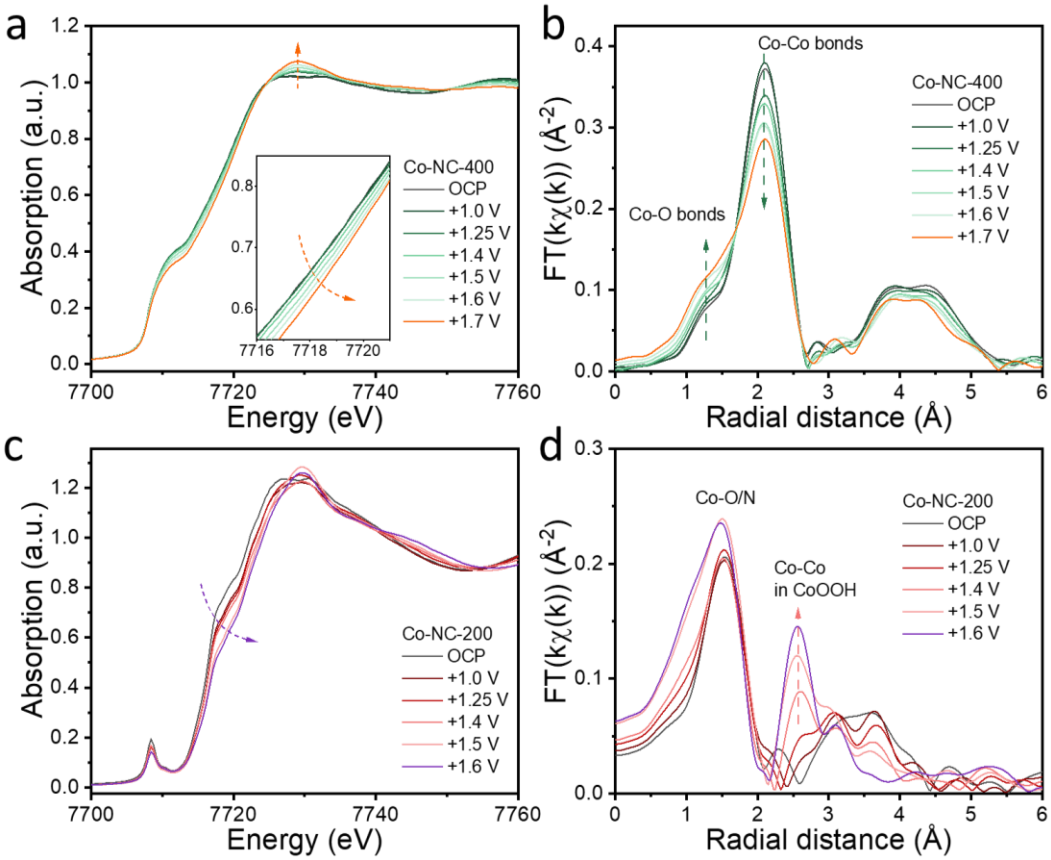

Figure 31. Operando XAS measurements of Co-NC-400 and Co-NC-200. (a) XANES of Co-NC-400 at different electrochemical potentials and (b) their corresponding EXAFS curves. (c) XANES of Co-NC-200 at different electrochemical potentials and (d) their corresponding EXAFS curves.

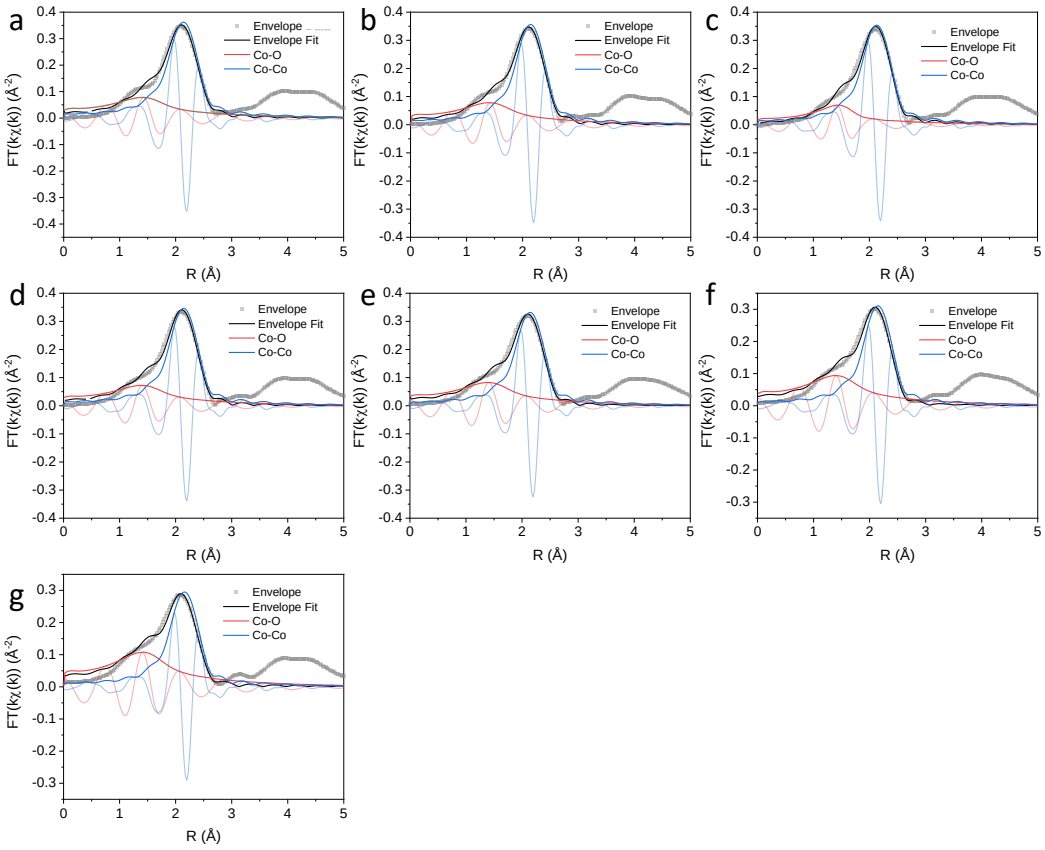

Figure 32. Fitting results of the operando EXAFS of Co-NC-400 at (a) OCP, (b) +1.0 V, (c) +1.25 V, (d) +1.4 V, (e) +1.5 V, (f) +1.6 V, and (g) +1.7 V.

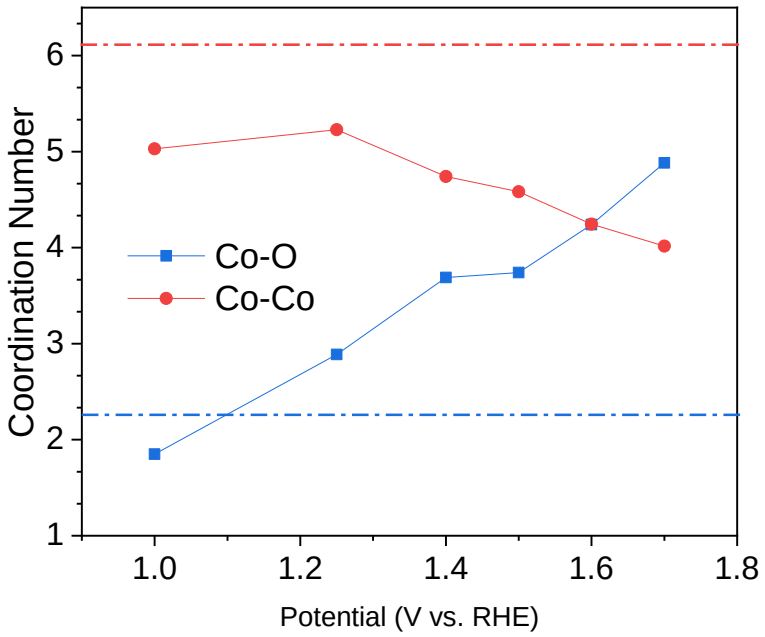

Figure 33. Coordination numbers (CNs) of Co-O (blue) and Co-Co (red) bonds for Co-NC-400 at different electrochemical potentials. Dashed lines are the CNs at open circuit potentials.

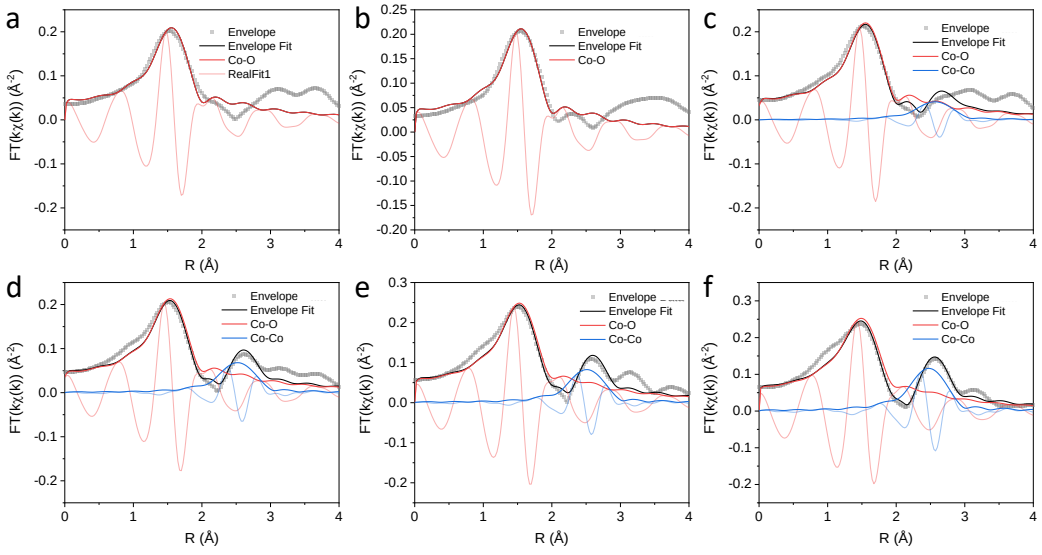

Figure 34. Fitting results of the operando EXAFS of Co-NC-200 at (a) OCP, (b) +1.0 V, (c) +1.25 V, (d) +1.4 V, (e) +1.5 V, and (f) +1.6 V.

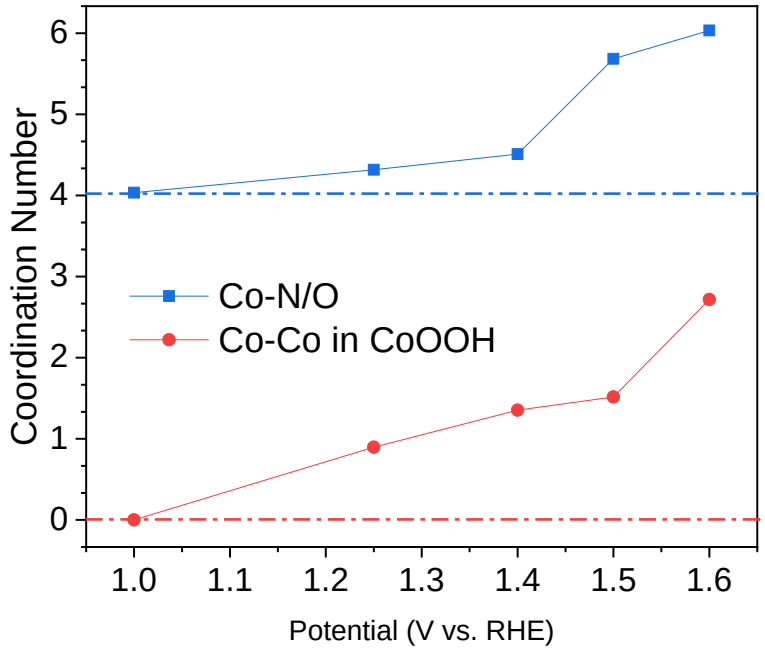

Figure 35. Coordination numbers of the Co-O (blue) and Co-Co (red) bonds for Co-NC-200 at different electrochemical potentials. Dashed lines are values at open circuit potentials.

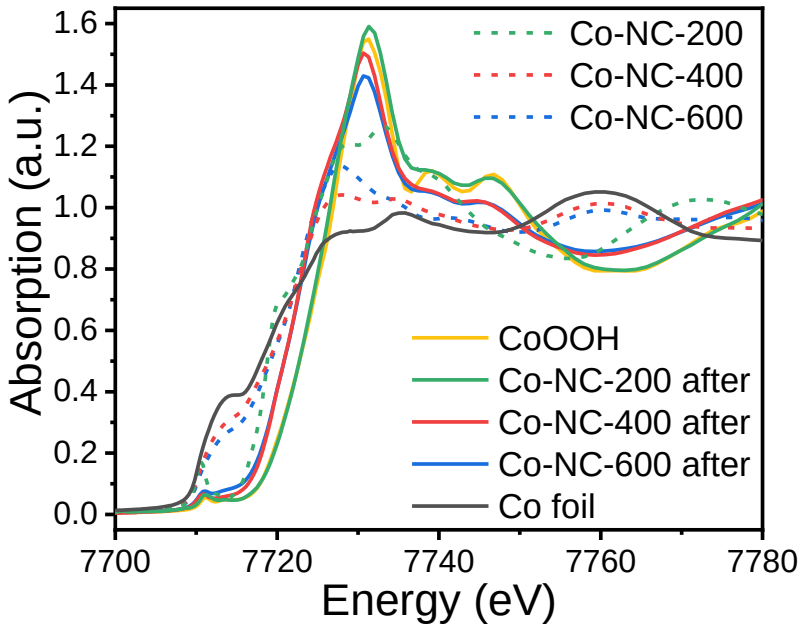

Figure 36. XANES profiles of Co-NC-200, Co-NC-400, and Co-NC-600 before and after 20-h's stability tests.

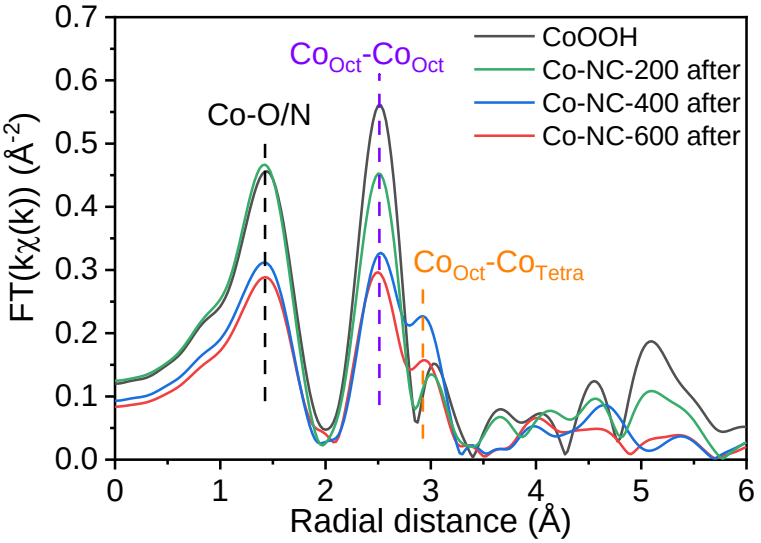

Figure 37. FT-EXAFS profiles of Co-NC-200, Co-NC-400, and Co-NC-600 after 20 h's stability tests, and CoOOH for comparison.

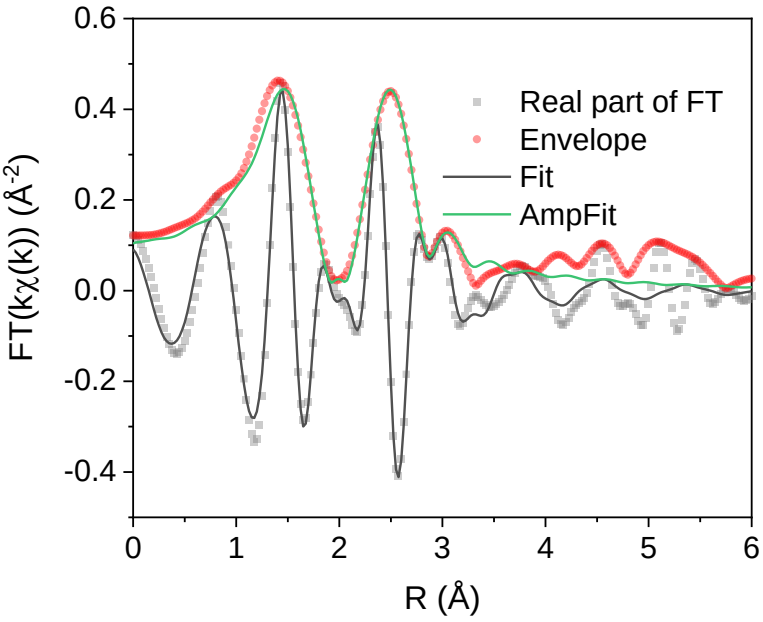

Figure 38. Fitting results of the FT-EXAFS profile of Co-NC-200 after 20 h's stability tests.

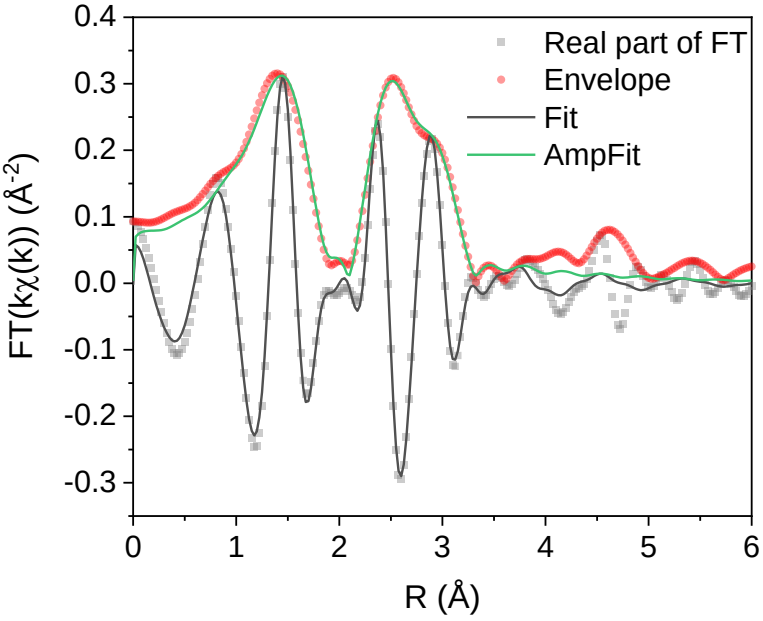

Figure 39. Fitting results of the FT-EXAFS profile of Co-NC-400 after 20 h's stability tests.

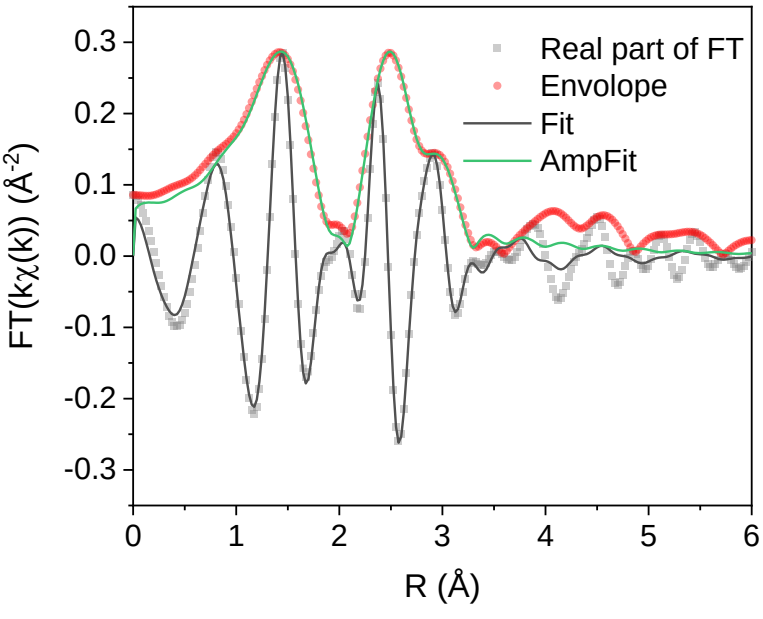

Figure 40. Fitting results of the FT-EXAFS profile of Co-NC-600 after 20 h's stability tests.

Table 12. Fitting results of operando EXAFS of Co-NC-400 at different electrochemical potentials.

Potential (V)	**$CN_{(Co-O)}$**	**$R_{(Co-O)}$ (Å)**	**$\sigma^2_{(Co-O)}$**	**$CN_{(Co-Co)}$**	**$R_{(Co-Co)}$**	**$\sigma^2_{(Co-Co)}$**	**ΔE_0 (eV)**
OCP	2.25	1.927	0.019	6.13	2.494	0.007	-0.24
+1.00	1.85	1.903	0.008	5.03	2.499	0.006	-1.34
+1.25	2.88	1.906	0.019	5.22	2.498	0.006	-1.08
+1.40	3.68	1.900	0.019	4.74	2.501	0.006	-1.65
+1.50	3.74	1.898	0.019	4.58	2.501	0.005	-1.67
+1.60	4.24	1.897	0.019	4.24	2.504	0.005	-1.98
+1.70	4.88	1.907	0.019	4.01	2.509	0.005	-2.8

Table 13. Fitting results of operando EXAFS of Co-NC-200 at different electrochemical potentials.

Potential (V)	**$CN_{(Co-O)}$**	**$R_{(Co-O)}$**	**$\sigma^2_{(Co-O)}$**	**$CN_{(Co-Co)}$**	**$R_{(Co-Co)}$**	**$\sigma^2_{(Co-Co)}$**	**ΔE_0 (eV)**
OCP	4.08	1.988	0.002	0	/	/	-4.42
1.00	4.03	1.990	0.002	0	/	/	-5.08
1.25	4.31	1.983	0.002	0.89	2.935	0	-5.89
1.40	4.51	1.972	0.003	1.35	2.889	0	-5.93

1.50	5.68	1.967	0.004	1.51	2.878	0	-5.6
1.60	6.03	1.953	0.004	2.71	2.873	0	-5.14

Table 14. Fitting results of the EXAFS data of Co-NC-200 after 20 hours' stability tests.

Path	**σ^2**	**Bond Length (Å)**	**CN**	**ΔE_0 (eV)**
Co-O	0.002	1.9561	6.04	1.31
Co-Co	0.004	2.9226	6.67	1.31
Co-multi-scatters	0.002	3.3390	0.96	1.31
Co-O	0.002	3.5504	2.72	1.31

Table 15. Fitting results of the EXAFS data of Co-NC-400 after 20 hours' stability tests.

Path	**σ^2**	**Bond Length (Å)**	**CN**	**ΔE_0 (eV)**
Co-O	0.005	1.9667	5.13	4.03
Co_O-Co_O	0.002	2.9393	2.34	4.03
Co_O-Co_T	0.008	3.5123	6.95	4.03

Table 16. Fitting results of the EXAFS data of Co-NC-600 after 20 hours' stability tests. Note that in Table 15-S16, Co_O and Co_T refer to the Co atoms at the octahedral sites of Co-O_6 and tetrahedral sites of Co-O_4, respectively.

Path	**σ^2**	**Bond Length (Å)**	**CN**	**ΔE_0 (eV)**
Co-O	0.005	1.9671	4.93	3.41

Co_O-Co_O	0.002	2.9384	2.61	3.41
Co_O-Co_T	0.007	3.4937	3.72	3.41

Note that each scan in operando XAS measurements took ca. 20 min, which might be insufficient for the materials to undergo a thorough phase transformation. To further probe the valency and structural changes that occurred at high potentials, ex situ XAS measurements were conducted with Co-NC-200, Co-NC-400, and Co-NC-600 after continuous OER operation for 20 h. As shown in Figure 36, Co-NC-200 can be seen to exhibit an absorption edge similar to that of CoOOH, and Co-NC-400 and Co-NC-600 showed a marked increase of the absorption edge energy towards that of CoOOH, as compared to their as-prepared ones, consistent with the positive shift of the Co 2p binding energy as observed in XPS measurements (Figure 23). Analysis of the EXAFS profiles (Figure 37) and the corresponding fitting results (Figure 38-40, Table 14-16) further elucidated that Co-NC-200 was transformed into CoOOH. Interestingly, Co-NC-400 and Co-NC-600 completely lost their metallic features, with no more Co-Co peaks at around 2.10 Å. This suggests that metallic Co is unlikely to contribute to the OER activity. Meanwhile, both samples exhibited a peak at 2.91 Å, due to the Co at the octahedral site of Co^{III}-O_6 and Co at tetrahedral site of Co^{II}-O_4, which was not found in Co-NC-200. In fact, such a feature normally exists in Co_3O_4 spinels [54,61]. This suggests that the metallic Co was electrochemically transformed into Co^{II}-O_4 during the prolonged operation, and the produced CoOOH species was responsible for the observed OER activity by facilitating the adsorption of oxygen intermediates [62]. This

was most likely aided by the defective carbon shells that encapsulated the Co/CoO nanoparticles such that accessibility by electrolyte species was not completely impeded.

5.5 Conclusions

In summary, MIH was successfully exploited for the ultrafast preparation of Co-NC nanocomposites from ZIF-67 where Co/CoO nanoparticles were encapsulated with defective N-doped carbon layers. The sample prepared at 400 A for 10 s, Co-NC-400, was found to exhibit the best performance towards OER in alkaline media, with a low η_{10} of +308 mV and η_{200} of +410 mV, and even outperformed commercial RuO_2 at high overpotentials and relevant Co-based nanocomposites reported recently in the literature. The combined results from ex situ and operando microscopic and spectroscopic measurements showed that metallic Co species were electrochemically transformed into CoOOH, which acted as the catalytic active sites, and the activity was likely enhanced by charge transfer from the graphitized carbon shells that was also responsible for the excellent stability of the nanocomposite catalysts. Results from this study underline the unique significance of MIH in the engineering of high-performance electrocatalysts from low-cost precursors (Figure 41).

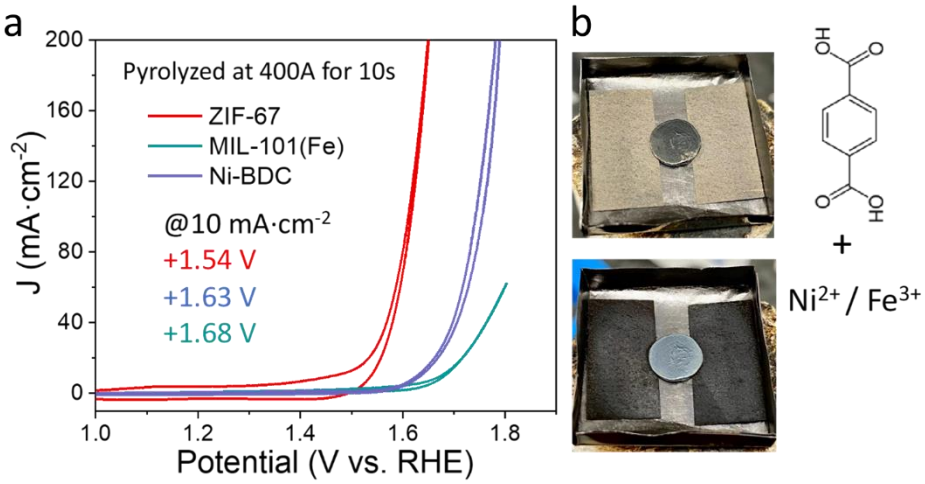

Figure 41. (a) OER polarization curves of nanocomposites prepared by MIH from different MOFs: ZIF-67, MIL-101(Fe) and Ni-BDC. (b) Photographs of MIL-101(Fe) before (top) and after (bottom) MIH treatment.

5.6 Reference

1. A. Haryanto, S. Fernando, N. Murali, S. Adhikari. *Energ Fuel* **2005**, *19*, 2098-2106.

2. J. A. Turner. *Science* **2004**, *305*, 972-974.

3. Z. W. Seh, J. Kibsgaard, C. F. Dickens, I. B. Chorkendorff, J. K. Norskov, T. F. Jaramillo. *Science* **2017**, *355*, eaad4998.

4. P. Z. Chen, X. L. Hu. *Adv Energy Mater* **2020**, *10*, 2002285.

5. T. Reier, M. Oezaslan, P. Strasser. *Acs Catal* **2012**, *2*, 1765-1772.

6. Y. Peng, Q. M. Liu, B. Z. Lu, T. He, F. Nichols, X. Hu, T. Huang, G. Huang, L. Guzman, Y. Ping, S. W. Chen. *Acs Catal* **2021**, *11*, 1179-1188.

7. K. Sheng, Q. F. Yi, A. L. Chen, Y. B. Wang, Y. H. Yan, H. D. Nie, X. L. Zhou. *Acs Appl Mater Inter* **2021**, *13*, 45394-45405.

8. H. Y. Guo, Z. W. Fang, H. Li, D. Fernandez, G. Henkelman, S. M. Humphrey, G. H. Yu. *Acs Nano* **2019**, *13*, 13225-13234.

9. C. H. Wang, H. C. Yang, Y. J. Zhang, Q. B. Wang. *Angew Chem Int Edit* **2019**, *58*, 6099-6103.

10. J. W. D. Ng, M. Garcia-Melchor, M. Bajdich, P. Chakthranont, C. Kirk, A. Vojvodic, T. F. Jaramillo. *Nat Energy* **2016**, *1*, 16053.

11. X. T. Yuan, H. X. Ge, X. Wang, C. L. Dong, W. J. Dong, M. S. Riaz, Z. W. Xu, J. X. Zhang, F. Q. Huang. *Acs Energy Lett* **2017**, *2*, 1208-1213.

12. H. Y. Jin, J. Wang, D. F. Su, Z. Z. Wei, Z. F. Pang, Y. Wang. *J Am Chem Soc* **2015**, *137*, 2688-2694.

13. N. Wang, S. L. Ning, X. L. Yu, D. Chen, Z. L. Li, J. C. Xu, H. Meng, D. K. Zhao, L. G. Li, Q. M. Liu, B. Z. Lu, S. W. Chen. *Appl Catal B-Environ* **2022**, *302*, 120838.

14. C. L. Luan, G. L. Liu, Y. J. Liu, L. Yu, Y. Wang, Y. Xiao, H. Y. Qiao, X. P. Dai, X. Zhang. *Acs Nano* **2018**, *12*, 3875-3885.

15. C. G. Kuai, Z. R. Xu, C. Xi, A. Y. Hu, Z. J. Yang, Y. Zhang, C. J. Sun, L. X. Li, D. Sokaras, C. K. Dong, S. Z. Qiao, X. W. Du, F. Lin. *Nat Catal* **2020**, *3*, 743-753.

16. D. Friebel, M. W. Louie, M. Bajdich, K. E. Sanwald, Y. Cai, A. M. Wise, M. J. Cheng, D. Sokaras, T. C. Weng, R. Alonso-Mori, R. C. Davis, J. R. Bargar, J. K. Norskov, A. Nilsson, A. T. Bell. *J Am Chem Soc* **2015**, *137*, 1305-1313.

17. H. L. Fei, J. C. Dong, C. Z. Wan, Z. P. Zhao, X. Xu, Z. Y. Lin, Y. L. Wang, H. T. Liu, K. T. Zang, J. Luo, S. L. Zhao, W. Hu, W. S. Yan, I. Shakir, Y. Huang, X. F. Duan. *Adv Mater* **2018**, *30*, 1802146.

18. M. J. Cui, C. P. Yang, B. Y. Li, Q. Dong, M. L. Wu, S. Hwang, H. Xie, X. Z. Wang, G. F. Wang, L. B. Hu. *Adv Energy Mater* **2021**, *11*, 2002887.

19. A. Dutta, N. Pradhan. *J. Phys. Chem. Lett.* **2017**, *8*, 144-152.

20. Y. Peng, S. W. Chen. *Green Energy Environ* **2018**, *3*, 335-351.

21. Y. J. Tang, H. Zheng, Y. Wang, W. Zhang, K. Zhou. *Adv Funct Mater* **2021**, *31*, 2102648.

22. D. N. Ding, K. Shen, X. D. Chen, H. R. Chen, J. Y. Chen, T. Fan, R. F. Wu, Y. W. Li. *Acs Catal* **2018**, *8*, 7879-7888.

23. T. Rodenas, S. Beeg, I. Spanos, S. Neugebauer, F. Girgsdies, G. Algara-Siller, P. P. M. Schleker, P. Jakes, N. Pfander, M. Willinger, M. Greiner, G. Prieto, R. Schlogl, S. Heumann. *Adv Energy Mater* **2018**, *8*, 1802404.

24. X. J. Cui, P. J. Ren, D. H. Deng, J. Deng, X. H. Bao. *Energ Environ Sci* **2016**, *9*, 123-129.

25. Y. Yang, Z. Y. Lin, S. Q. Gao, J. W. Su, Z. Y. Lun, G. L. Xia, J. T. Chen, R. R. Zhang, Q. W. Chen. *Acs Catal* **2017**, *7*, 469-479.

26. C. H. Wang, J. Kim, J. Tang, M. Kim, H. Lim, V. Malgras, J. You, Q. Xu, J. S. Li, Y. Yamauchi. *Chem* **2020**, *6*, 19-40.

27. C. Young, J. Wang, J. Kim, Y. Sugahara, J. Henzie, Y. Yamauchi. *Chem Mater* **2018**, *30*, 3379-3386.

28. X. Wang, X. Y. Zhang, G. T. Fu, Y. W. Tang. *Mater Today Energy* **2021**, *22*, 100850.

29. H. Tabassum, A. Mahmood, B. J. Zhu, Z. B. Liang, R. Q. Zhong, S. J. Guo, R. Q. Zou. *Energ Environ Sci* **2019**, *12*, 2924-2956.

30. Q. M. Liu, Y. Peng, Q. X. Li, T. He, D. Morris, F. Nichols, R. Mercado, P. Zhang, S. W. Chen. *Acs Appl Mater Inter* **2020**, *12*, 17641-17650.

31. Q. Hu, G. M. Li, Z. Han, Z. Y. Wang, X. W. Huang, H. P. Yang, Q. L. Zhang, J. H. Liu, C. X. He. *Journal of Materials Chemistry A* **2019**, *7*, 14380-14390.

32. J. W. Zhu, S. C. Mu. *Adv Funct Mater* **2020**, *30*, 2001097.

33. S. H. Lee, J. Kim, D. Y. Chung, J. M. Yoo, H. S. Lee, M. J. Kim, B. S. Mun, S. G. Kwon, Y. E. Sung, T. Hyeon. *J Am Chem Soc* **2019**, *141*, 2035-2045.

34. Q. Liu, S. W. Chen. *Trends in Chemistry* **2022**, *4*, 918-934.

35. Q. Liu, B. Lu, F. Nichols, J. Ko, R. Mercado, F. Bridges, S. Chen. *SusMat* **2022**, *2*, 335-346.

36. B. Lu, Q. Liu, C. Wang, Z. Masood, D. J. Morris, F. Nichols, R. Mercado, P. Zhang, Q. Ge, H. L. Xin, S. Chen. *Research* **2022**, *2022*, 9756983.

37. Y. G. Yao, Z. N. Huang, P. F. Xie, S. D. Lacey, R. J. Jacob, H. Xie, F. J. Chen, A. M. Nie, T. C. Pu, M. Rehwoldt, D. W. Yu, M. R. Zachariah, C. Wang, R. Shahbazian-Yassar, J. Li, L. B. Hu. *Science* **2018**, *359*, 1489-1494.

38. D. X. Luong, K. V. Bets, W. A. Algozeeb, M. G. Stanford, C. Kittrell, W. Chen, R. V. Salvatierra, M. Q. Ren, E. A. McHugh, P. A. Advincula, Z. Wang, M.

Bhatt, H. Guo, V. Mancevski, R. Shahsavari, B. I. Yakobson, J. M. Tour. *Nature* **2020**, *577*, 647-651.

39. C. Meng, M. C. Lin, X. C. Sun, X. D. Chen, X. M. Chen, X. W. Du, Y. Zhou. *Chem Commun* **2019**, *55*, 2904-2907.

40. R. Jiang, Y. M. Da, X. P. Han, Y. A. Chen, Y. D. Deng, W. B. Hu. *Cell Rep Phys Sci* **2021**, *2*, 100302.

41. J. F. Yao, M. He, K. Wang, R. Z. Chen, Z. X. Zhong, H. T. Wang. *Crystengcomm* **2013**, *15*, 3601-3606.

42. X. Miao, D. Qu, D. X. Yang, B. Nie, Y. K. Zhao, H. Y. Fan, Z. C. Sun. *Adv Mater* **2018**, *30*, 1704740.

43. W. R. Zheng, M. J. Liu, L. Y. S. Lee. *Acs Catal* **2020**, *10*, 81-92.

44. W. H. He, R. Ifraemov, A. Raslin, I. Hod. *Adv Funct Mater* **2018**, *28*, 1707244.

45. Y. Jia, L. Z. Zhang, A. J. Du, G. P. Gao, J. Chen, X. C. Yan, C. L. Brown, X. D. Yao. *Adv Mater* **2016**, *28*, 9532-9538.

46. F. M. Tang, W. R. Cheng, Y. Y. Huang, H. Su, T. Yao, Q. H. Liu, J. K. Liu, F. C. Hu, Y. Jiang, Z. H. Sun, S. Q. Wei. *Acs Appl Mater Inter* **2017**, *9*, 26867-26873.

47. T. Sharifi, G. Hu, X. E. Jia, T. Wagberg. *Acs Nano* **2012**, *6*, 8904-8912.

48. Y. Y. Song, T. He, Y. L. Zhang, C. Y. Yin, Y. Chen, Q. M. Liu, Y. Zhang, S. W. Chen. *J Electroanal Chem* **2022**, *906*, 116024.

49. T. He, Y. Peng, Q. X. Jia, J. E. Lu, Q. M. Liu, R. Mercado, Y. Chen, F. Nichols, Y. Zhang, S. W. Chen. *Acs Appl Mater Inter* **2019**, *11*, 46912-46919.

50. B. Z. Lu, Q. M. Liu, F. Nichols, R. Mercado, D. Morris, N. Li, P. Zhang, P. Gao, Y. Ping, S. W. Chen. *Research* **2020**, *2020*, 9167829.

51. X. L. Huang, R. Z. Wang, D. Xu, Z. L. Wang, H. G. Wang, J. J. Xu, Z. Wu, Q. C. Liu, Y. Zhang, X. B. Zhang. *Adv Funct Mater* **2013**, *23*, 4345-4353.

52. S. K. Pandey, A. Kumar, S. Khalid, A. V. Pimpale. *Journal of Physics: Condensed Matter* **2006**, *18*, 7103.

53. D. J. SantaLucia, W. H. Hu, D. N. Wang, J. Huang, J. F. Berry. *Inorg Chem* **2022**, *61*, 6056-6062.

54. B. Seo, Y. J. Sa, J. Woo, K. Kwon, J. Park, T. J. Shin, H. Y. Jeong, S. H. Joo. *Acs Catal* **2016**, *6*, 4347-4355.

55. I. Arcon, A. Tuel, A. Kodre, G. Martin, A. Barbier. *J Synchrotron Radiat* **2001**, *8*, 575-577.

56. A. Holewinski, J. C. Idrobo, S. Linic. *Nature Chemistry* **2014**, *6*, 828-834.

57. K. A. Stoerzinger, L. Qiao, M. D. Biegalski, Y. Shao-Horn. *J. Phys. Chem. Lett.* **2014**, *5*, 1636-1641.

58. Z. Y. Lu, H. T. Wang, D. S. Kong, K. Yan, P. C. Hsu, G. Y. Zheng, H. B. Yao, Z. Liang, X. M. Sun, Y. Cui. *Nat Commun* **2014**, *5*, 4345.

59. C. Stumm, M. Bertram, M. Kastenmeier, F. D. Speck, Z. Z. Sun, J. Rodriguez-Fernandez, J. V. Lauritsen, K. J. J. Mayrhofer, S. Cherevko, O. Brummel, J. Libuda. *Adv Funct Mater* **2021**, *31*, 2009923.

60. B. Zhang, J. W. Shan, W. L. Wang, P. Tsiakaras, Y. Y. Li. *Small* **2022**, *18*, 2106012.

61. F. Reikowski, F. Maroun, I. Pacheco, T. Wiegmann, P. Allongue, J. Stettner, O. M. Magnussen. *Acs Catal* **2019**, *9*, 3811-3821.

62. H. Y. Wang, S. F. Hung, H. Y. Chen, T. S. Chan, H. M. Chen, B. Liu. *J Am Chem Soc* **2016**, *138*, 36-39.

Chapter 6 Ultrafast Preparation of Non-Equilibrium Fe-Ni Spinels by Magnetic Induction Heating for Unprecedented Oxygen Evolution Electrocatalysis

6.1 Abstract

Carbon-supported nanocomposites are attracting particular attention as high-performance, low-cost electrocatalysts for electrochemical water splitting. These are mostly prepared by pyrolysis and hydrothermal procedures that are time-consuming (from hours to days), and typically difficult to produce a non-equilibrium phase. Herein, for the first time ever, we exploit magnetic induction heating-quenching for ultrafast production of carbon-FeNi spinel oxide nanocomposites (within seconds), which exhibit an unprecedentedly high performance towards oxygen evolution reaction (OER), with an ultralow overpotential of only 260 mV to reach the high current density of 100 mA cm^{-2}. Experimental and theoretical studies show that the rapid heating and quenching process (ca. 10^3 K s^{-1}) impedes the Ni and Fe phase segregation and produces a Cl-rich surface, both contributing to the remarkable catalytic activity. Results from this study highlight the unique advantage of ultrafast heating/quenching in the structural engineering of functional nanocomposites to achieve high electrocatalytic performance towards important electrochemical reactions.

6.2 Introduction

Design and engineering of low-cost, high-performance catalysts play an important role in the development and advancement of electrochemical energy technologies, such as fuel cells and water electrolyzers [1]. Up to now, a range of functional nanocomposites have been hailed as viable alternatives to the conventional, noble metal-based catalysts, such as doped carbon, and carbon-supported nanoparticles of metals, metal oxides, sulfides, phosphides, and selenides [2-4]. These materials are typically prepared via the

"traditional" thermal methods based on pyrolysis and hydrothermal procedures [5-12]. While these methods are rather facile and effective in sample synthesis, they are energy and time-consuming [13,14], and the slow heating ramp makes it difficult to produce a non-equilibrium phase within the samples, which might be critical in regulating the electronic structure and hence the electrocatalytic activity [15-18]. In a prior study [19], Holewinski et al. demonstrated that whereas Ag and Co metals were immiscible at equilibrium, AgCo alloy nanoparticles could be obtained by removing the sample from the tube furnace while hot and letting it cool down in ambient instead of following a traditional programmed cooling process, and exhibit a remarkable electrocatalytic activity towards oxygen reduction reaction (ORR) unseen for either Ag or Co metals alone. Du et al. [20,21] showed that the laser ablation method could be exploited for the synthesis of Ag and Ru nanoparticles for high-efficiency water splitting, due to the formation of plenty of stacking faults or grain boundaries that were difficult to produce via conventional methods. Hu et al. [22] developed carbothermal shock synthesis to prepare high-entropy alloy nanoparticles within seconds. Tour et al. [23] adopted flash joule heating to synthesize metastable 1T phase of MoS_2 with S vacancies and observed a high efficiency towards hydrogen evolution reaction (HER). In another study [24], Tour et al. developed a laser scribing method where metal oxide/graphene composites were prepared by simply lasing metal precursors loaded onto a graphene scaffold and exhibited a high performance towards oxygen evolution reaction (OER) likely due to the formation of surface defects. Du et al. [20,25,26] successfully used the laser ablation

method to prepare a series of water splitting electrocatalysts with oxygen vacancies, faults or unique morphologies.

Despite the progress, the toolbox for such sample synthesis has been limited, and the range of materials that can be produced and the extent of structural engineering remain narrow. Thus, further development of effective protocols for the synthesis of materials with unprecedented structures and properties is of both fundamental and technological significance [27,28]. In electrochemical water splitting, OER has been recognized as a major bottleneck that limits the overall performance because of complex reaction pathways and sluggish electron-transfer kinetics [17], and FeNi (oxy)hydroxide and spinel oxides have been extensively studied as a viable alternative to the traditional, noble metal-based commercial catalysts [29-34], where manipulation of the occupation of the e_g orbitals of the octahedral metals and/or metal-oxygen covalency represent the leading strategies for further enhancement of the OER activity [30]. This is generally achieved by engineering the spinel components, heterometal doping, and introduction of oxygen vacancies [25,31,35,36]. Phase segregation of Fe and Ni in the spinels has been believed to be the leading cause of the apparent loss of the electrocatalytic activity [37]. Yet, such segregation is inevitable for samples prepared via a “tedious” conventional thermal procedure as it is energetically favorable. In addition, residual heteroanions (especially Cl) adsorbed on or doped into the surface of Fe, Co and Ni (hydro/oxyhydro)oxides may play a significant role in OER electrocatalysis [38-40]. Yet the impacts of such anion impurities have remained largely ignored, although most pyrolytically prepared spinel oxides are derived from iron and nickel chlorides. These

issues can be addressed with the development of appropriate synthetic methods where non-equilibrium structures can be produced with reduced phase segregation and a remarkable concentration of anion impurities. This is the primary motivation of the present study.

Herein, we report an ultrafast heating/quenching method based on magnetic induction heating/rapid quenching (MIHRQ)[41] to prepare carbon-supported FeNi spinel composites (within seconds), which exhibit a clear mixing of the Ni and Fe phases and a Cl-rich surface, in contrast to the control samples that are prepared by prolonged heating and/or natural cooling to the ambient. In electrochemical measurements, the former displays an outstanding electrocatalytic performance towards OER, with an ultralow overpotential of only 260 mV to reach the high current density of 100 mA cm^{-2}, due to the formation of a non-equilibrium structure that is optimal for the adsorption of key reaction intermediates and eventual production of oxygen. The enhanced performance of the catalyst is also confirmed by results of first principles calculations. These results highlight the unique potential of MIHRQ in the deliberate production of non-equilibrium features in composite electrocatalysts. Notably, such an unprecedented tool can be readily extended to the preparation of a wide range of functional nanocomposites for diverse applications [42-47].

6.3 Results and Discussion

6.3.1 Magnetic induction heating-rapid quenching

The homemade MIHRQ apparatus is shown in Figure 1a. A four-turn induction solenoid was twisted at a diameter of 5 cm, under which was placed a beaker containing

ethanol and dry ice (-78°C) as the quenching agent. Experimentally, a calculated amount of the metal precursors (i.e., $FeCl_3$ and $NiCl_2$) was dropcast onto a piece of carbon paper (1.5 cm × 0.5 cm), which was then sandwiched between two rectangular iron sheets (2.5 cm × 2.5 cm × 0.1 mm). An iron nail was inserted into the center of the iron sheets and clamped to hold the assembly, which was placed in the center of the induction solenoid (Figure 1b). When a high frequency (30 kHz) current was passed to the solenoid, a strong magnetic field was produced, which instantly generated a strong Eddy current in the iron sheets and thus heated the sample rapidly to a high temperature. The induction current and time can be varied to control the heating temperature (Figure 1c). For example, a solenoid current of 200 A for a heating time of 4 s would generate a temperature of 200-300 °C, which barely changed the color of the iron sheets. Yet, when the solenoid current was increased to 400 and 600 A, the temperature could reach ca. 600 and 1000 °C, respectively, inducing a glowing color of the iron sheets from faint red to white (Figure 1b). The fastest instantaneous heating rate can reach an order of 10^3 K/s. Such ultrafast heating can not only drastically enhance the time efficiency of sample preparation but more importantly also be exploited for the kinetic control of the materials structures, in contrast to typical pyrolysis or hydrothermal synthesis, which is usually completed within the time frame of hours to even days. After a select period of heating (of the order of seconds), the sample would be dropped into the quenching solution below (Figure 1a) or removed from the solenoid and cooled down naturally in the ambience. This offers an additional control of the materials structures, especially for the production of non-equilibrium features.

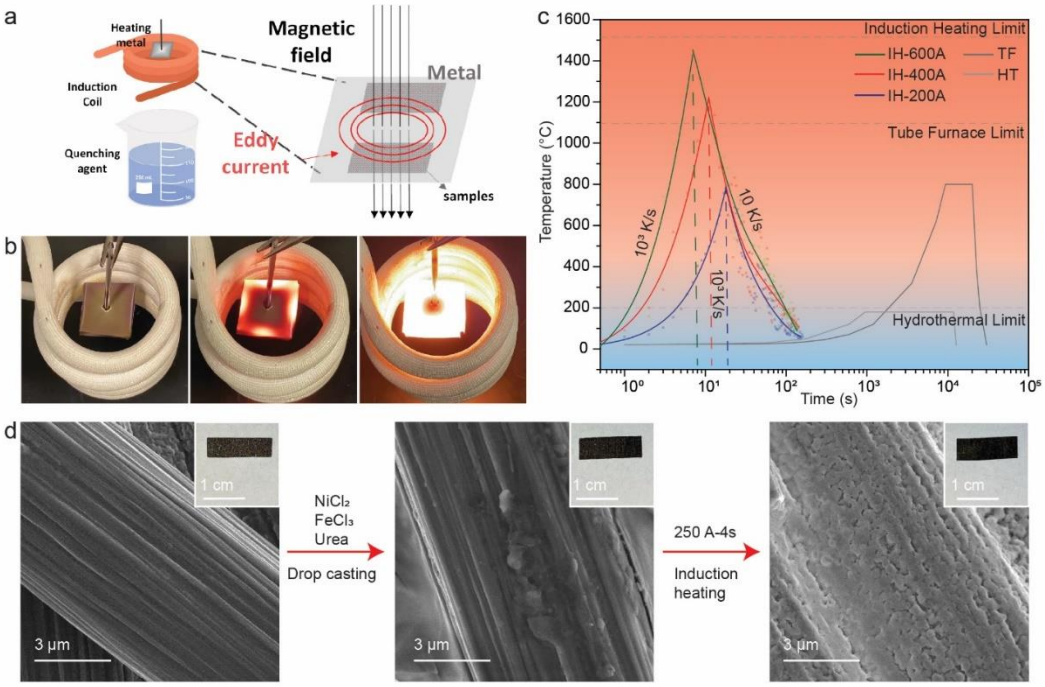

Figure 1. Sample preparation by MIHRQ. (a) Schematic illustration of magnetic induction heating-quenching for material preparation. (b) Photographs of induction heating with a solenoid current at (left) 200 A, (middle) 400 A, and (right) 600 A for 4 s, respectively. (c) Variations of temperature versus time of magnetic induction heating, traditional hydrothermal heating, and pyrolysis. The dash lines indicate the cases with the quenching process. 'IH', 'TF', and 'HT' are short for induction heating, tube furnace, and hydrothermal, respectively. (d) SEM images of the NiFeO-250-4 sample at different preparation stages. The insert images are the corresponding photographs of the electrodes. The carbon paper can be seen to become darkened after the deposition of the metal salt precursors, and subsequent induction heating and rapid quenching leads to a pitch-black appearance of the carbon paper, with particulates formed onto the carbon fibers.

A series of samples were prepared with the MIHRQ setup at a controlled induction current (X) for a select period of time (Y) and denoted as FeNiO-X-Y (Figure 1d). Control samples were prepared in the same manner except for cooling in ambient, and

referred to as $FeNiO_{NC}$-X-Y. Notably, MIHRQ can be extended to the preparation of a wide range of electrocatalysts beyond the Fe-Ni spinel oxides (vide infra).

Structural characterizations

High-angle annular dark field-scanning transmission electron microscopy (HAADF-STEM) measurements of the NiFeO-250-4 sample (Figure 1d) show the formation of a number of nanoparticles (dia. 20 to 100 nm) in irregular shapes (Figure 2a), with the structure consistent with $Fe_{3-x}Ni_xO_4$-type spinel, as observed along the <111> zone axis (Figure 2b and 3). The interatomic distance was estimated to be 0.816-0.824 nm (inset to Figure 2b), close to that of FeNi spinel oxide (0.835 nm) [48]. Additional STEM images acquired along the <112>, <100>, and <103> zone axes also confirmed the spinel lattice structure (Figure 4-6). Furthermore, energy-dispersive X-ray spectroscopy (EDS)-based elemental mapping studies clearly show an even distribution of Fe and Ni within the lattice (Figure 2c), suggesting atomic mixing of the Fe and Ni elements and no phase segregation. Notably, spindle-like FeNi oxide nanocrystals can also be found around these particles (Figure 2d-2f, Figure 7-9), which feature a chlorine-rich surface (Figure 2g), with a Cl concentration of 12% in comparison to under 2% within the particles (Table 1). In fact, the atomic ratio of Fe:Ni:O:Cl in the nanospindles is estimated to be 1.9:1:4.9:1.1, while the overall ratio is close to 4.1:1:5.8:0.22, indicating that the spinel particles were Fe-rich oxide, while the nanospindles likely represent an intermediate phase between the precursors (metal chlorides) and the final spinel crystal (Table 1). Furthermore, it is noticeable that the Fe:Ni ratio is higher than

the feeding ratio. This is likely because part of Ni was not fully converted into Ni oxide and washed away during the rapid quenching process.

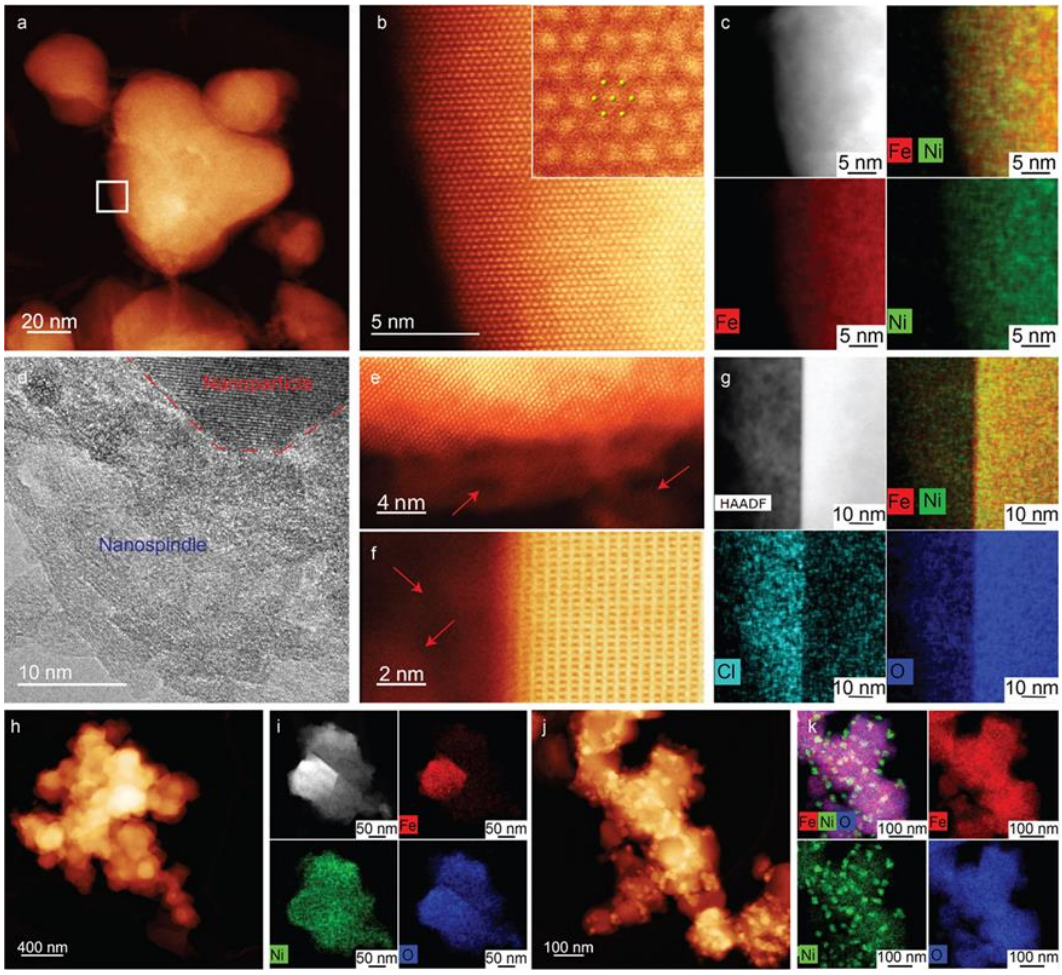

Figure 2. Electron microscopic studies of FeNi spinel oxides. (a) High-angle annular dark-filed scanning transmission electron microscopy (HAADF-STEM) image showing the morphology of FeNiO-250-4. (b) Atomic-resolution HAADF-STEM image and an enlarged image (inset) corresponding to the boxed region in a) acquired along the <111> zone axis. (c) High-resolution energy-dispersive spectroscopy (EDS)-based elemental maps of Fe and Ni in a FeNiO-250-4 particle, which features a Fe-Ni spinel structure with no Fe-Ni phase segregation. (d) High-resolution TEM (HRTEM) image of nanospindles in FeNiO-250-4. (e-f) HAADF-STEM images of nanospindles on the edge of FeNiO-250-4 (low-contrast regions), as highlighted by red arrows. (g)

EDS mapping images of the interface between nanospindles and nanoparticles in FeNiO-250-4, which show a Cl-rich surface of the nanospindles. (h) HAADF-STEM images and (i) EDS mapping images of FeNiONC-250-4, where natural cooling leads to the formation of nanoparticles aggregates and obvious Fe-Ni phase segregation. (j) HAADF-STEM and (k) EDS mapping image of FeNiO-250-16, where prolonged heating (higher temperature) leads to the formation of a significant amount of metallic Ni nanoparticles on the Fe-Ni spinel.

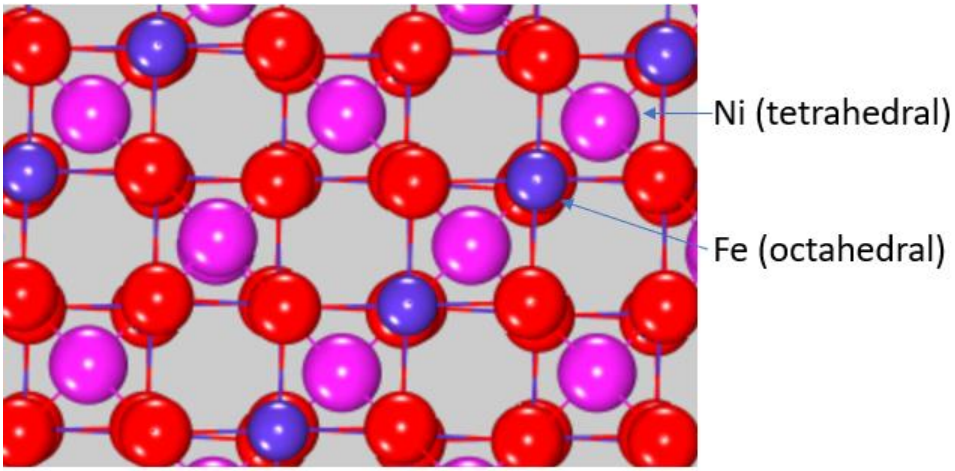

Figure 3. Crystal structure of Fe-Ni oxide spinel, where blue, pink and red indicate Fe, Ni and O atoms, respectively.

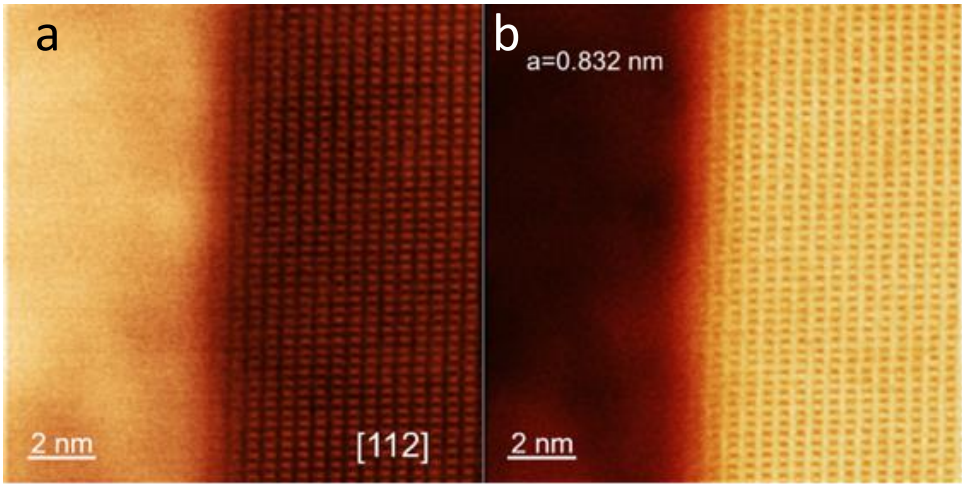

Figure 4. HAADF-STEM images of Fe-Ni oxide spinel in FeNiO-250-4 along the [112] zone axis

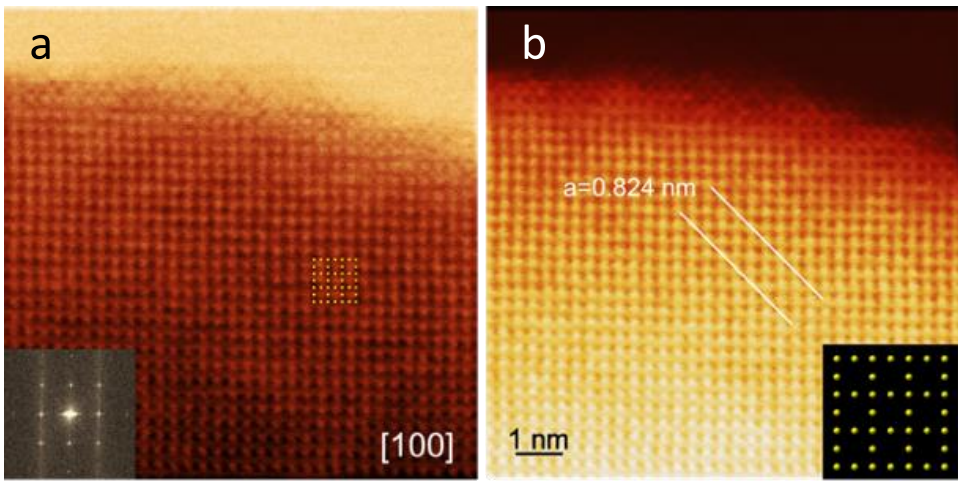

Figure 5. HAADF-STEM images of Fe-Ni oxide spinel in FeNiO-250-4 along the [100] zone axis. Inset to panel (a) is the FFT patterns, whereas inset to panel (b) is a structural model of the atomic arrangement.

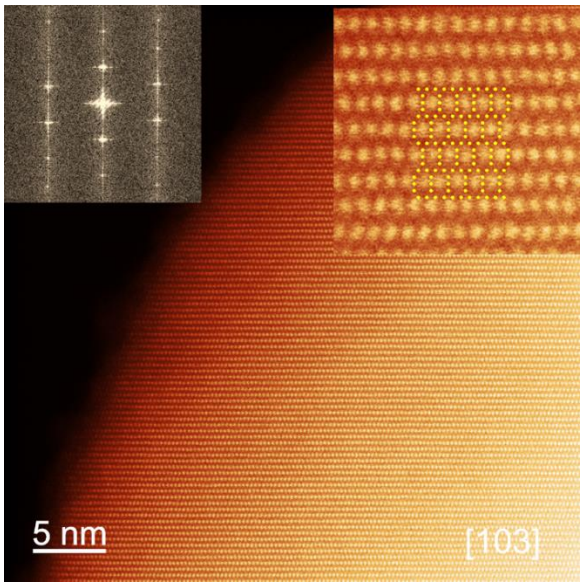

Figure 6. HAADF-STEM images of Fe-Ni oxide spinel in FeNiO-250-4 along the [103] zone axis. Left inset is the FFT patterns, and the right inset is a magnified image highlighting the atomic arrangement.

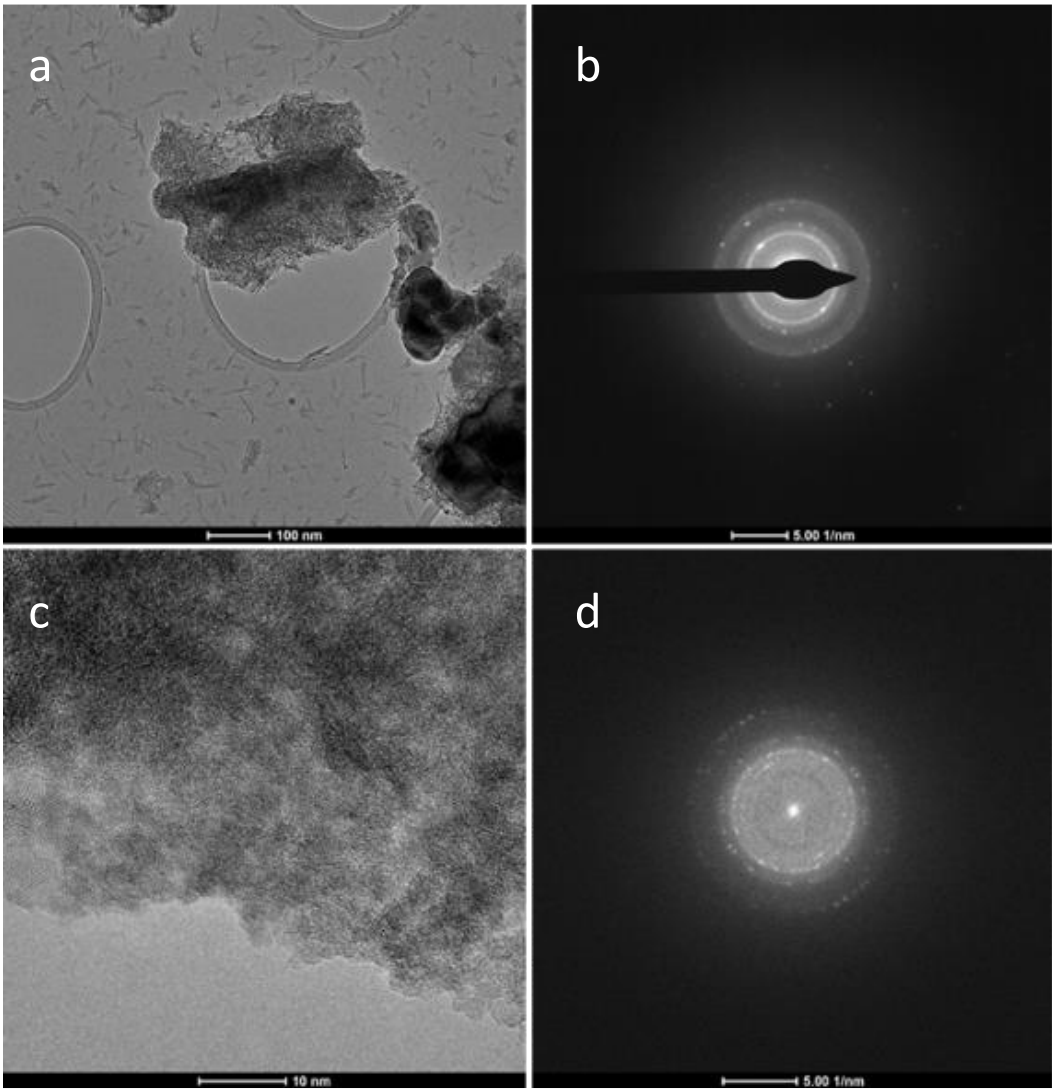

Figure 7. TEM and electron diffraction studies. (a,c) TEM images and (b,d) selected area electron diffraction patterns of nanospindle crystals around the Fe3-xNixO4 particles of FeNiO-250-4. Nanospindles are prevalent on the lacey carbon film of the TEM grid.

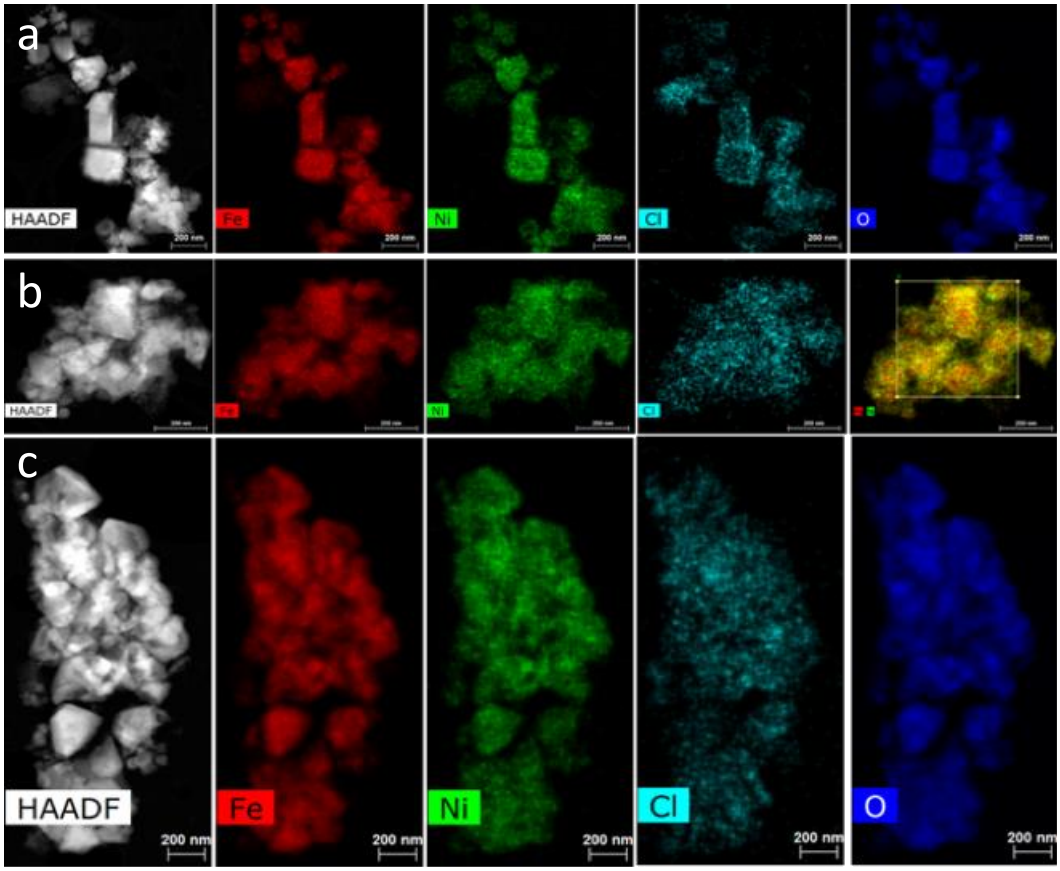

Figure 8. EDS-based elemental mapping analysis. (a-c) EDS mapping studies of FeNiO-250-4. One can see that Cl is rather evenly distributed throughout the samples. Fe and Ni do not show any phase segregation, suggesting a homogeneous distribution within FeNiO-250-4.In the images, The relative larger and uniform crystals are nanoparticles, while the small and uniform structure, with chlorine atoms distribution are nanospindles.

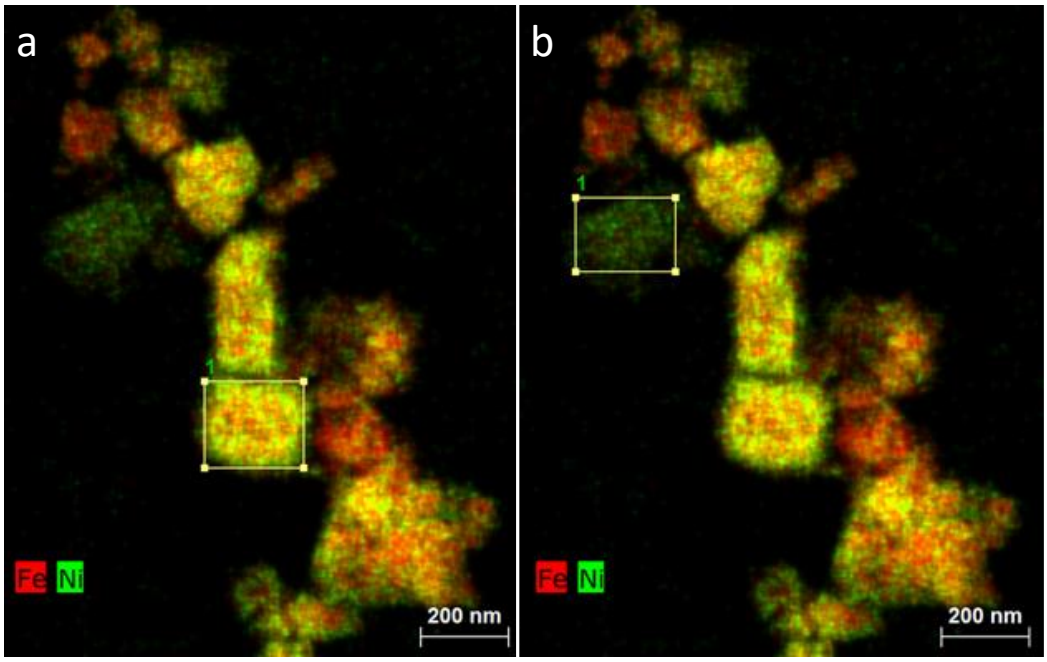

Figure 9. EDS-based elemental mapping analysis. Elemental maps of (a) FeNi oxide spinel nanoparticles and (b) nanospindle area.

Table 1. Elemental contents of the sample series based on EDS measurements.

element	at%			
	FeNiO-250-4	FeNiO-250-4 (spindle)	$FeNiO_{NC}$-250-4	FeNiO-250-16
Fe	37.01	20.99	4.04	40.06
O	51.77	54.89	61.18	52.39
Ni	8.95	11.13	26.22	6.11
Cl	1.96	12.01	0.95	0.17

For FeNiO-250-16 that was prepared via a longer heating time, the Fe:Ni:O:Cl ratio was estimated to be 6.6:1:8.6:0.028 (Table 1), indicative of the formation of a Fe-rich

structure that was almost free of Cl. In fact, the nanospindle features, with the unique chlorine rich surface, can only be produced with a short heating time and rapid quenching process.

The control sample, $FeNiO_{NC}$-250-4 that was produced by similar heating but natural cooling in the ambient, exhibited an obviously different morphology (Figure 2h), consisting of aggregates of nanoparticles into large chunks. In addition, significant phase segregation occurred within the sample (Figure 2i), where the elements of Ni and O appeared to be evenly distributed across the sample, whereas Fe was mostly confined within a small region, suggesting the growth of FeNiO spinel nanocrystals on a nickel oxide scaffold. This is consistent with the sample atomic ratio of Fe:Ni:O:Cl = 0.15:1:2.3:0.036. The fact that the sample was markedly nickel-rich was likely due to higher thermal volatility of the iron compounds [49], where the enhanced loss of Fe was facilitated by the relatively slow cooling (about 10 K s^{-1}). Similar phase segregation was also observed with a prolonged heating time (e.g., FeNiO-250-16), where the temperature could reach ca. 1000 °C (Figure 2j-2k, and Figure 10). Such non-homogeneous segregation is the equilibrium state under high temperatrue on the phase diagram of Fe-Ni-O_2 (FToxid database, FactSage),[50] which can be rationally avoided by rapid heating and quenching process underwent on FeNiO-250-4.

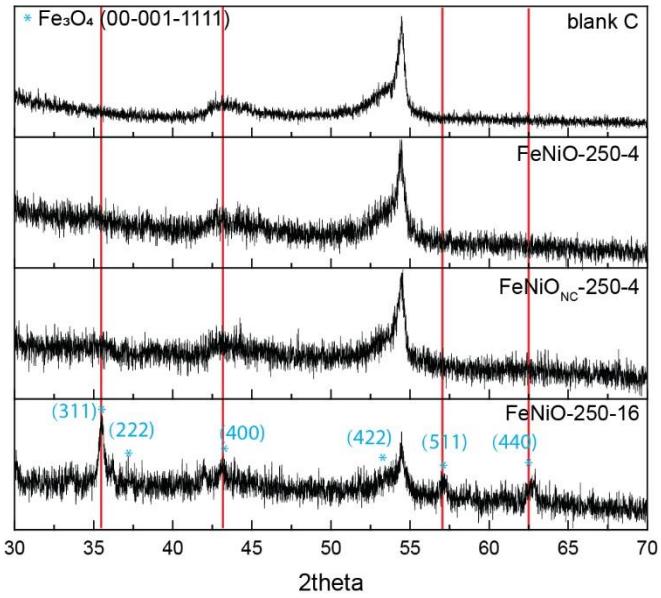

Figure 10. XRD patterns of the sample series. The peak around 2q = 55° is from the carbon background. Notably, no apparent XRD patterns of spinel metal oxide could be resolved with FeNiO-250-4 and $FeNiO_{NC}$-250-4, likely due to the low contents in the samples. By contrast, the FeNiO-250-16 sample exhibited a series of diffraction patterns that matched those of Fe_3O_4 (card 00-001-1111), consistent with the formation of a clear $Fe_{3-x}Ni_xO_4$ spinel structure.

The material structures were further characterized by X-ray photoelectron spectroscopy (XPS) and X-ray absorption spectroscopy (XAS) measurements. Figure 11a depicts the high-resolution XPS scan of the Ni 2p electrons of FeNiO-250-4, where two peaks can be resolved at 855.9 and 856.9 eV for the Ni(II) $3p_{3/2}$ electrons, suggesting the formation of five and six oxygen-coordinated Ni atoms on the surface (i.e., $Ni(OH)_2$), respectively [51], since no NiO species (binding energy around 854.7 eV) was detected [52]. A single peak was resolved at 711.2 eV in the Fe 2p scan (Figure 11b), due to the Fe(III) $3p_{3/2}$ electrons [53], whereas three peaks were deconvoluted in the O 1s spectrum (Figure 3d) at 531.5 eV for hydroxide, 529.9 eV for metal-O, and 533.0 eV for C-O [54].

These observations are consistent with the formation of FeNiO spinel lattices (vide infra). Deconvolution of the Cl 2p spectrum (Figure 12) yields two peaks at 198.3 and 199.9 eV, due to the $2p_{3/2}$ and $2p_{1/2}$ electrons of metal-Cl, respectively [55]. Taken together, these results suggest that the FeNiO-250-4 sample surface was mostly terminated with OH and Cl groups, in good agreement with results from the TEM and EDS measurements.

The XPS spectra of the $FeNiO_{NC}$-250-4 and FeNiO-250-16 samples are shown in Figure 13-15. The Fe 2p spectra showed only a rather insignificant difference among the sample series (Figure 14), likely because of the high thermal activity of $FeCl_3$ and the facile formation of Fe oxide. Additionally, FeNiO-250-4 and $FeNiO_{NC}$-250-4 exhibited a very similar Ni 2p profile with the Ni(II) $2p_{3/2}$ binding energy at 855.9 and 856.9 eV, which was somewhat lower for FeNiO-250-16 (855.6 and 856.75 eV, Figure 13). Furthermore, in the O 1s spectra (Figure 15), the Ni(Fe)-O peaks (ca. 530 eV) of $FeNiO_{NC}$-250-4-NC and FeNiO-250-16 are significantly larger than that of FeNiO-250-4, indicating increasing contributions from bulk oxides.

Further oxidation states and structural insights were obtained by XAS measurements. Figure 3d depicts the Ni K-edge X-ray absorption near edge structure (XANES) spectra of the sample series, where the absorption edge intensity can be seen to vary in the order of Ni foil < FeNiO-250-16 < FeNiO-250-4 < $FeNiO_{NC}$-250-4 < NiO, suggesting that the Ni valence state in the three FeNiO samples was in the intermediate between those of metallic Ni and Ni^{2+}. A similar trend can be observed in the Fe K edge XANES in Figure 11e, where all samples show a clear deviation from that of Fe foil, with the

absorption edge intensity varying in the order of Fe foil < FeNiO-250-16 < FeNiO-250-4 < $FeNiO_{NC}$-250-4 < Fe_2O_3, confirming that the Fe valence state in the three FeNiO samples was in the intermediate between those of metallic Fe and Fe^{3+}. Importantly, the Ni and Fe elements of FeNiO-250-4 can be seen to possess an average oxidation state between those of $FeNiO_{NC}$-250-4 and FeNiO-250-16, likely due to reduced carbothermal effects by the rapid heating and quenching process [22].

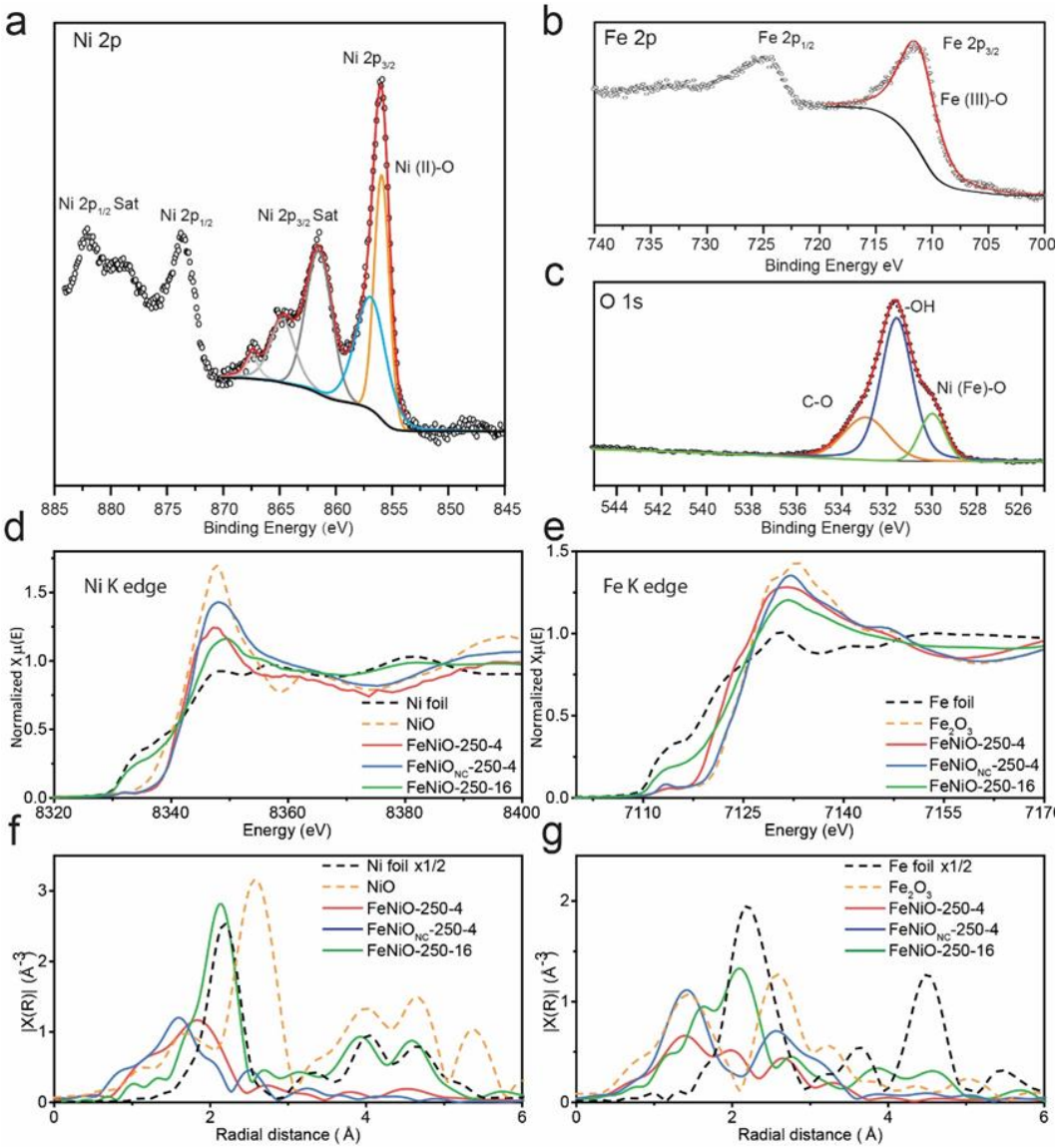

Figure 11. X-ray characterizations of FeNi spinel oxides. High-resolution X-ray photoelectron spectroscopy (XPS) scans of the (a) Ni 2p, (b) Fe 2p, and (c) O 1s electrons of FeNiO-250-4. (d) Ni K-edge and (e) Fe K-edge X-ray absorption near-edge structure spectra (XANES) of FeNiO-250-4, FeNiONC-250-4, FeNiO-250-16, and reference samples (Ni/Fe foil, NiO, and Fe2O3), along with the corresponding Fourier transformed extended X-ray absorption fine structure spectra (FT-EXAFS) of (f) Ni and (g) Fe. Note that the Ni-Ni path (2.57 Å) in NiO is essentially absent in FeNiO-250-4 and FeNiONC-250-4, and FeNiONC-250-4 exhibits a first main peak at 1.58 Å, very close to the Ni-O bonds of the NiO reference (1.64 Å), in comparison to 1.83 Å for FeNiO-250-4, possibly because of strong interactions with Cl atoms.

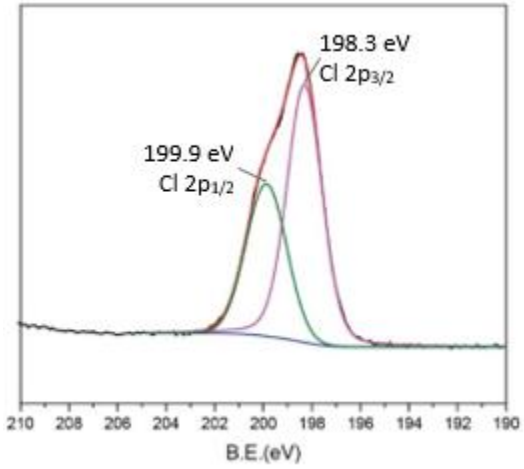

Figure 12. XPS spectrum of the Cl 2p electrons of FeNiO-250-4. The peaks at 198.3 and 199.9 eV are the $2p_{3/2}$ and $2p_{1/2}$ electrons of metal-Cl, respectively. Black curve is experimental data and colored curves are deconvolution fits.

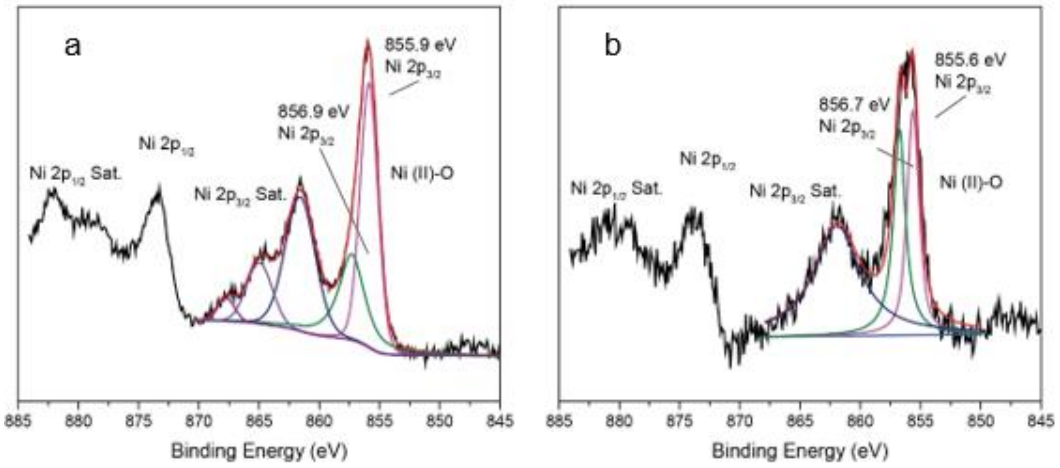

Figure 13. High-resolution XPS spectra of the Ni 2p electrons of (a) $FeNiO_{NC}$-250-4 and (b) FeNiO-250-16. Black curves are experimental data and colored curves are deconvolution fits.

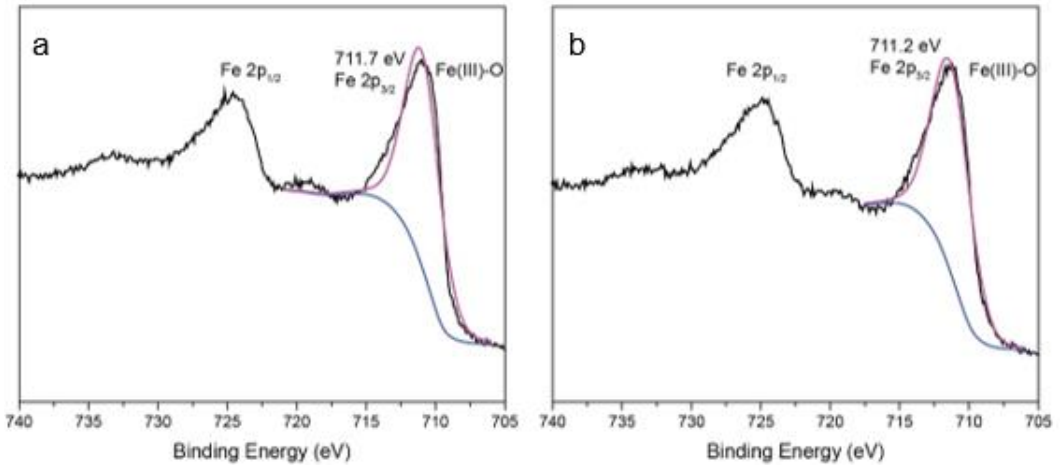

Figure 14. High-resolution XPS spectra of the Fe 2p electrons of (a) $FeNiO_{NC}$-250-4 and (b) FeNiO-250-16. Black curves are experimental data and colored curves are deconvolution fits.

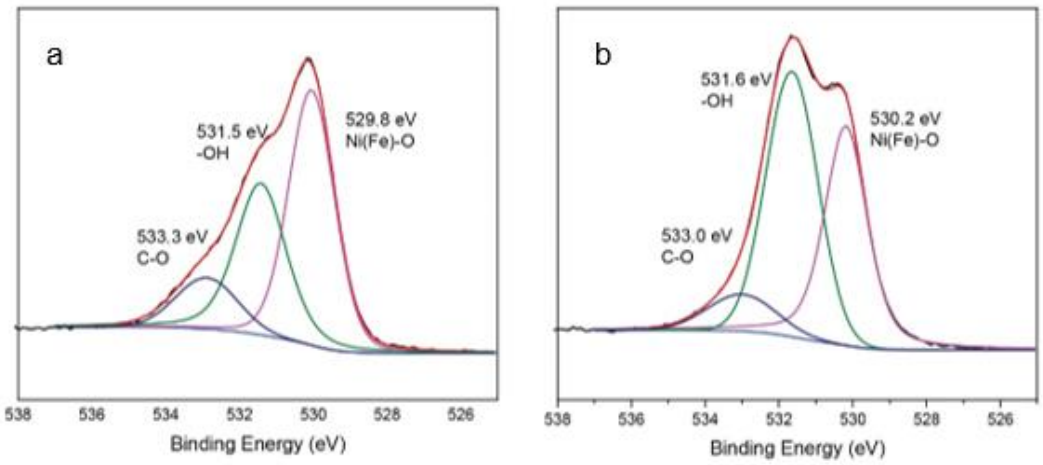

Figure 15. High-resolution XPS scans of the O 1s electrons of a) FeNiO$_{NC}$-250-4 and b) FeNiO-250-16. Black curves are experimental data and colored curves are deconvolution fits.

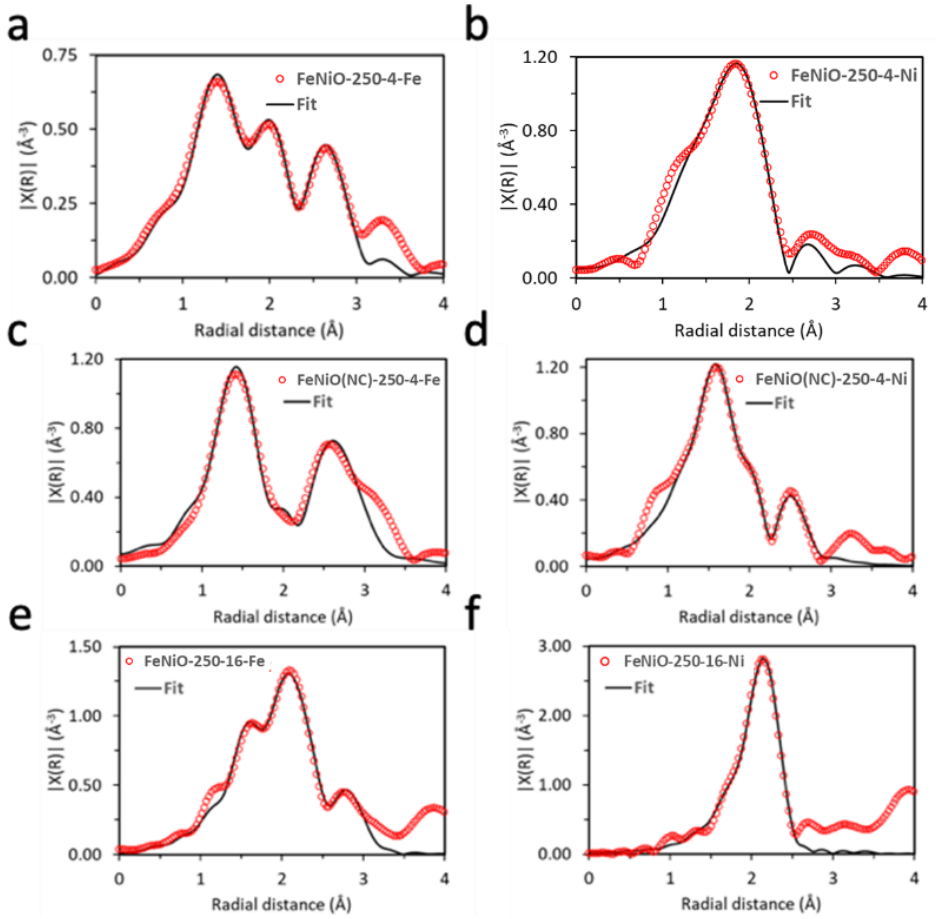

Figure 16. EXAFS fitting results of Fe (left) and Ni (right) for (a, b) FeNiO-250-4, (c, d) $FeNiO_{NC}$-250-4, and (e, f) FeNiO-250-16.

Table 2. Fitting results of the EXAFS data of FeNiO-250-4

bond	CN	R (Å)	σ^2 (Å^2) × 10^{-3}	E_0 (eV)	R factor
Fe-O	3.3(7)	1.98(3)	8(4)	0(2)	0.0266
Fe-Cl	2.1(6)	2.43(3)	8(4)	0(2)	0.0266
Fe-Fe	1.9(7)	3.01(3)	8(4)	0(2)	0.0266
Ni-O	2.7(7)	2.03(5)	3(6)	-3(4)	0.0266
Ni-Cl	3(1)	2.40(4)	3(6)	-3(4)	0.0266

Table 3. Fitting results of the EXAFS data of FeNiONC-250-4

bond	CN	R (Å)	σ^2 (Å^2) × 10^{-3}	E_0 (eV)	R factor
Fe-O	4.2(9)	1.97(3)	7(4)	0(2)	0.0294
Fe-Fe	4(1)	3.04(3)	7(4)	0(2)	0.0294
Fe-Cl	0.7(5)	2.44(4)	7(4)	0(2)	0.0294
Ni-O	4.7(5)	2.05(1)	6(2)	-3(1)	0.0060
Ni-Cl	1.5(3)	2.39(2)	6(2)	-3(1)	0.0060
Ni-Ni	1.6(8)	2.95(2)	9(4)	-3(1)	0.0060

Table 4. Fitting results of the EXAFS data of FeNiO-250-16

bond	CN	R (Å)	σ^2 (Å^2) × 10^{-3}	E_0 (eV)	R factor

Fe-O	2.0(5)	1.98(2)	3(3)	3(2)	0.0113
Fe-Cl	1.2(4)	2.30(3)	3(3)	3(2)	0.0113
Fe-Fe	3(1)	2.57(2)	7(3)	3(2)	0.0113
Fe-Fe	1.9(6)	3.13(3)	7(3)	3(2)	0.0113
Ni-O	2(1)	2.02(3)	6(9)	-7(2)	0.0249
Ni-Ni	8(1)	2.50(1)	6(1)	-7(2)	0.0249

Further insights into the bonding configurations of the metal centers were obtained from the extended X-ray absorption fine structure (EXAFS) results. Fitting of the FT-EXAFS data (Figure 11f, Figure 16 and Table 2-4) show that FeNiO-250-4 actually possessed Ni-O bonds with a bond length of 2.03 Å, somewhat smaller than those of $FeNiO_{NC}$-250-4 (2.05 Å) and rock salt NiO (2.09 Å) [56]. This is consistent with the phase segregation in $FeNiO_{NC}$-250-4 (vide ante). Meanwhile, the Ni-Cl path in FeNiO-250-4 was found to possess a coordination number (CN) of 3 and an average bond length of 2.40 Å, slightly larger than Ni-O (CN = 2.7). Due to the low cooling rate, a severe Cl loss occurred with $FeNiO_{NC}$-250-4 leading to a low CN of 1.5, while its Ni-O showed a CN of 4.7, consistent with the absence of nanospindles in TEM measurements (Figure 1). The profile of FeNiO-250-16 is almost identical to that of Ni foil with a main peak at 2.13 Å for the Ni-Ni path. The Fe EXAFS profile of FeNiO-250-4 (Figure 11g) shows three major peaks at 1.38, 1.96, and 2.63 Å, due to Fe-O, Fe-Cl, and second-shell Fe-Fe/Ni bonds, respectively. Yet, the feature of Fe-Cl diminished in both $FeNiO_{NC}$-250-4 and FeNiO-250-16. FeNiO-250-16 displayed a shorter Fe-Fe/Ni bond

length (2.57 Å) than FeNiO-250-4 (3.01 Å) and $FeNiO_{NC}$-250-4 (3.04 Å), suggesting a possible transition from spinel structure to metallic Fe [57].

In summary, results from these characterization measurements show that prolonged heating and slow cooling facilitated the O and Cl loss for the spinel samples. Prolonged heating also promoted phase segregation of Ni into rock salt NiO or metallic form. With a deliberate control of the heating time and cooling rate, two key non-equilibrium features of the FeNiO spinel nanoparticles can be achieved, minimal Fe-Ni phase segregation, and formation of a Cl-rich surface, both critical in OER electrocatalysis (details below).

6.3.2 Electrocatalytic activity

The FeNiO-250-4 sample that possessed a unique Fe-Ni oxide spinel with Cl-rich surface nanospindles exhibited a remarkably high activity towards OER. From the polarization curves in Figure 17a, FeNiO-250-4 reached the high current density of 100 mA cm^{-2} at an ultralow potential of 1.49 V vs reversible hydrogen electrode (RHE) (corresponding to an overpotential, η_{100}, of only 260 mV), in comparison to 1.54 V for $FeNiO_{NC}$-250-4, 1.60 V for FeNiO-250-16, and 1.55 V for commercial 20% RuO_2. FeNiO-250-4 also displayed a Tafel slope of only 25 mV dec^{-1} markedly lower than the rest of the sample series, 39 mV dec^{-1} for FeNiO-250-16, 48 mV dec^{-1} for $FeNiO_{NC}$-250-4, and 58 mV dec^{-1} for commercial RuO_2 (Figure 17b). In addition, at 100% iR compensation, FeNiO-250-4 can even produce an exceedingly high current density of 1 A cm^{-2} at only 1.64 V (Figure 18), which represents an unprecedentedly high activity

among the leading FeNi oxide-based OER electrocatalysts reported in recent studies (Table 5).

For better comparison of the activity, the LSV curve is further normalized by electrochemical surface area(ECSA) (figure 19, Table 6), the result shows FeNiO-250-4 has largest surface area, at 23.06 cm^2. Moreover, this catalyst exhibits best intrinsic activity. As shown in figure 20a, the current density per surface activity can reach as high as 10 mA cm^{-2} at a potential of +1.64 V vs RHE. In addition, the TOF value can also reach as high as 0.21 s^{-1} (figure 20b). This further confirming the great enhancement caused by Fe-Ni phase mixing and surface Cl.

Notably, the FeNiO-250-4 sample represents the optimal condition (Figure 21). It also shows excellent stability. At the applied potential of 1.53 V, over 80% of the initial current was retained even after 10 h's continuous operation (Figure 17c inset), which is one of the best performances as compared to the state of the art [37]. The corresponding OER polarization curve showed an anodic shift of only 10 mV. When the electrode was subject to additional 1,000 cyclic voltammetric cycles between 1.20 and 1.65 V, the subsequent polarization curve exhibited a further anodic shift of only 10 mV. XPS measurement was further carried out after the stability test (Figure 22). It is discovered that the ratio of Fe and Ni is much less than that of pristine sample (Figure 11a-b), changed to 1:1.8. This indicate part of Fe are leached away during long time OER process, which is commonly observable in similar catalyst [37]. However, Cl is still detectable, and its relative ratio to Fe and Ni (1:3) is consistent with pristine sample. Meanwhile, the EDS mappings in SEM measurements (Figure 23) still showed

homogeneously distributed Fe and Ni, with Cl after the stability test. Consistent with XPS, the ratio of Fe to Ni changed to 1:2. This indicates the activity decrease is due to Fe instead of structural change.

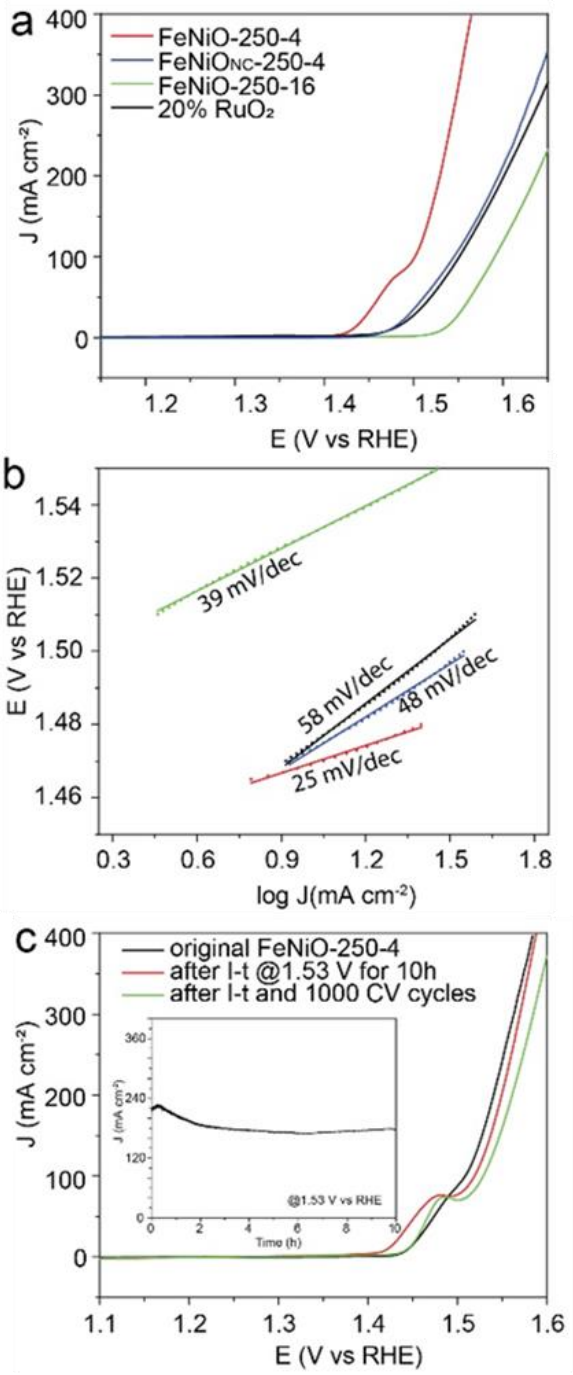

Figure 17. Electrochemical activities. (a) LSV curves and (b) the corresponding Tafel plots of FeNiO-250-4, FeNiO-250-4-NC, FeNiO-250-16 and 20% Ru/C in 1 M KOH. (c) Polarization curves of FeNiO-250-4 in the first scan, after 10 h's stability tests at 1.53 V (the corresponding i-t curve is shown in the figure inset), and after additional 1000 CV cycles within the potential range of 1.20 to 1.65 V at the scan rate of 10 mV s-1.

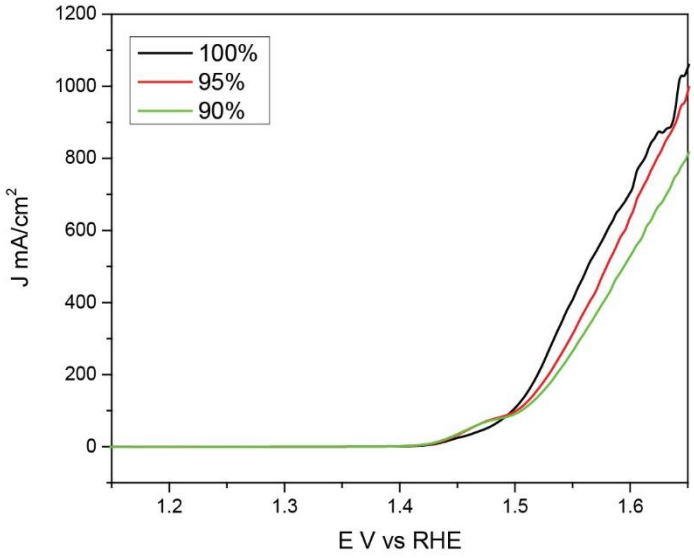

Figure 18. LSV curves of FeNiO-250-4 in 1 M KOH at different levels of iR compensation.

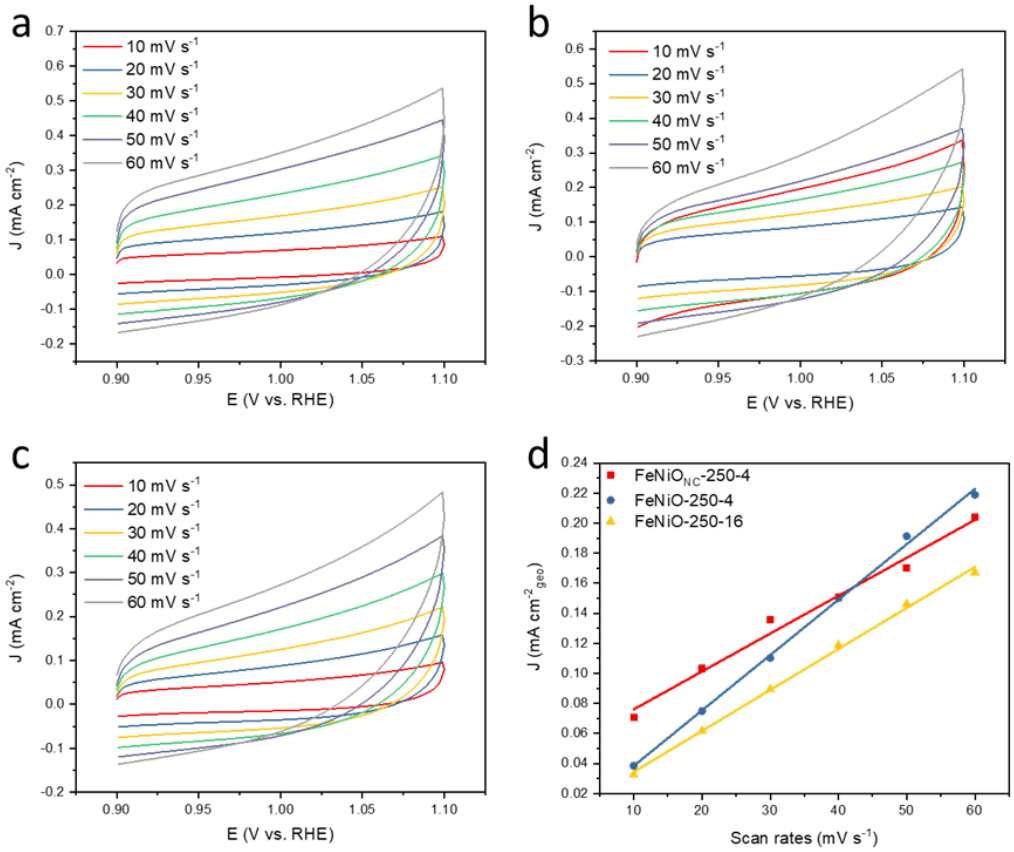

Figure 19. CV curves at difference scan rates for (a) FeNiO-250-4, (b) $FeNiO_{NC}$-250-4, and (c) FeNiO-250-16. (d) Corresponding ECSA calculations. The ECSA was calculated by Cs value of 0.04 mF cm^{-2}, according to the reference[58].

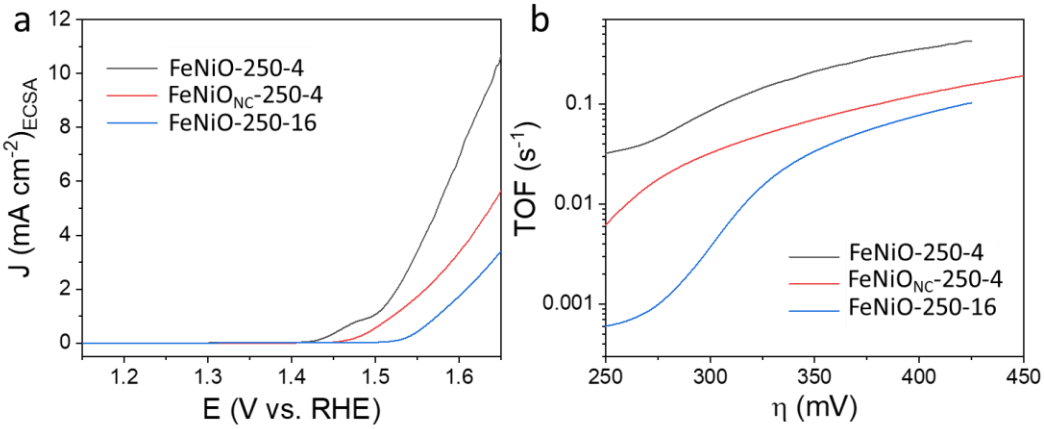

Figure 20. (a) LSV curves normalized by ECSA. (b) TOF curves of FeNiO-250-4, $FeNiO_{NC}$-250-4, and FeNiO-250-16.

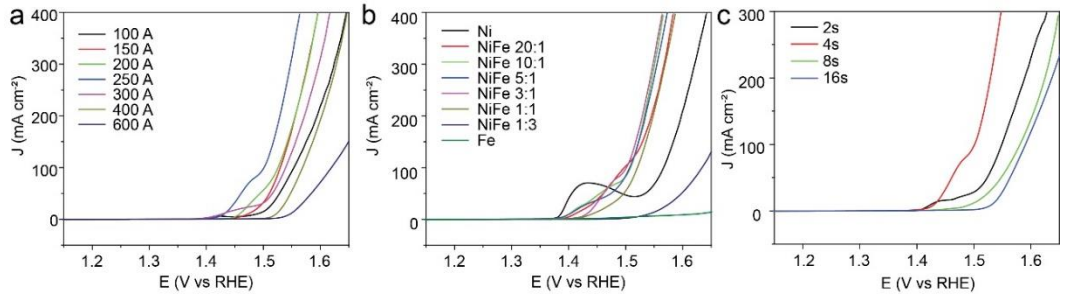

Figure 21. Optimization of OER performance of FeNiO samples. OER polarization curves of (a) FeNiO-X-4 at X = 100, 150, 200, 250, 300, 400, and 600 A, (b) FeNiO-250-4 but at different initial feed ratios of Ni:Fe (1:0, 20:1, 10:1, 5:1, 3:1, 1:1, 1:3, and 0:1), and (c) FeNiO-250-Y at Y = 2, 4, 8, and 16 s. The induction current of 250 A also represents the optimal condition, as the FeNiO-250-4 clearly outperformed others prepared at different currents, with the OER performance decreasing in order of FeNiO-250-4 > FeNiO-200-4 ~ FeNiO-150-4 > FeNiO-300-4 > FeNiO-100-4 > FeNiO-400-4 > FeNiO-600-4 (Figure 21a). This suggests that the resulting heating temperature of 300°C was most favorable for the conversion of the Ni and Fe precursors to metal oxides and minimization of Fe-Ni phase segregation. The impact of the initial feed ratio on the FeNiO OER performance was also examined, and a Ni:Fe feed ratio of 3:1 was found to be the best (Figure 21b). In panel (c), the activity decreases in the order of FeNiO-250-4 > FeNiO-250-2 > FeNiO-250-8 > FeNiO-250-16. This is because too short a heating time (e.g., 2 s) did not produce a high enough temperature for the conversion of $FeCl_3$ and $NiCl_2$ into FeNiO, while too long a heating time (e.g., 8, and 16 s) could induce severe phase segregation of the metal oxides and depleted Cl in the final product; and 4 s represented the optimal heating time.

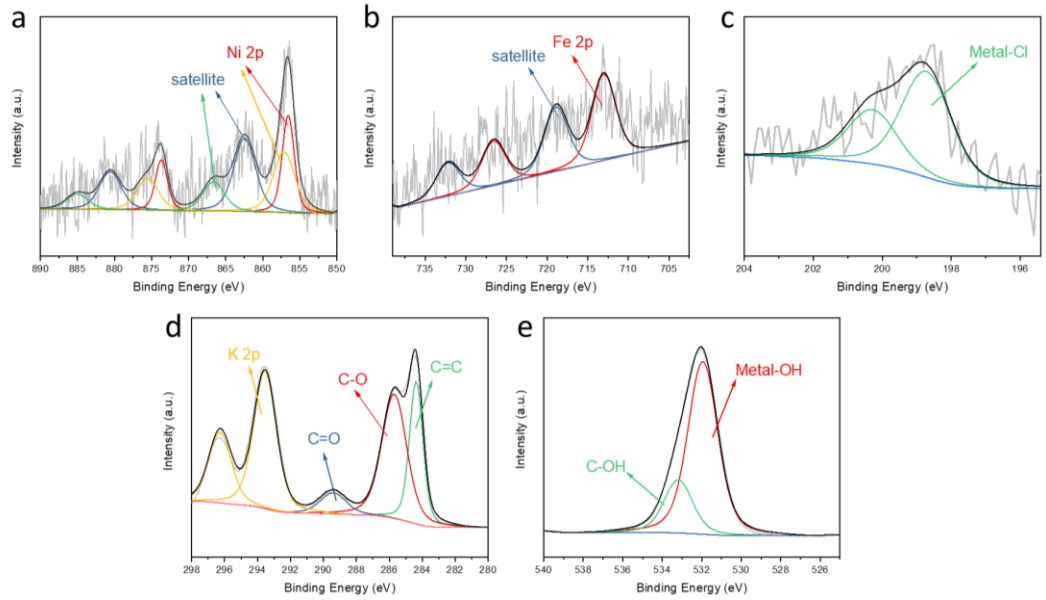

Figure 22. XPS studies of FeNiO-250-4 after stability test.

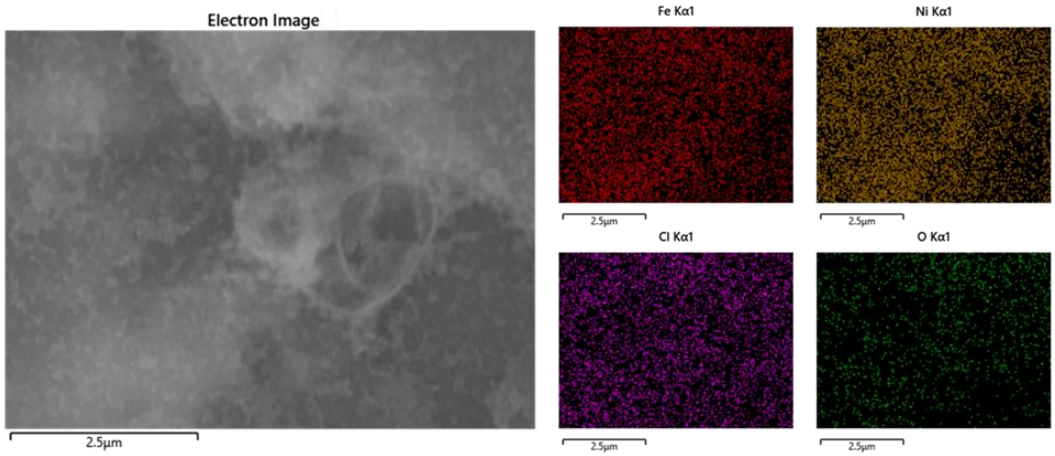

Figure 23. SEM studies of FeNiO-250-4 after stability test.

Table 5. Comparison with relevant Fe-Ni oxide-based OER catalysts reported in the literature.

Initial material	Surface	Catalytic activity	Tafel slope	Current density	η (mV)

			(mV dec^{-1})	(mA cm^{-2})	
Quantum dots $NiFe_2O_4$[59]		Oxygen vacancy	37	10	262
$NiFe_2O_4$[60]	(Ni,Fe)OOH	(Ni)*OH 2.05 eV	40	100	309
$NiFe_2O_4$[61]	Defect's formation	Oxygen vacancy	40	10	350
V-dopped $NiFe_2O_4$[62]			43.9	10	271.3
$NiFe_2O_4$ under layer Ni_3Fe[63]		*O → *OOH RDS	52.3 (TON =0.27/s) ~ 5* NiFe2O4		
$NiFe_2O_4$ NP/NiFe LDH[64]			28	10	300
ɣ-FeOOH on ɣ-NiOOH (support)[65]			34	100 (10)	248 (215)

PA-Gd-$Ni(OH)_2Cl$ (partially alkylated gadolinium-doped nickel oxychloride)[66]			40	10	220
Ruddlesden–Popper-type oxychloride[67]				10	300
FeNi LDH thin film on Fe foam[68]	Layered Double hydroxide		48.3	1000 (500)	340 (300)
$Cu_{1-x}NNi_{3-y}$@FeNiCu (oxy)hydroxide[69]	FeNiCu (oxy)hydroxide		45	10	280
FeCoCrNi alloy film[70]	Metal oxyhydroxides	Ni^{4+} sites	38.7	10	304
Ni-Fe hydroxide[71]	Fe-Ni hydroxides	Fe/NiOOH		100	~340

$NiFe_x$ molecules on Hetero-atom doped graphene[72]	Ni-Fe with OH^- ions	Ni-Fe hydroxides	39	10	310
Ni/NiO-NF[73]	$Ni^{III/IV}$	photogenerated holes	41	100 (20)	380 (260)
MoFe:$Ni(OH)_2$[74]	Mo, Fe, NiOOH		47	100	280
Fe doped NiO_x nanotubes[75]	NiO_x	Ni vacancy	49	10	310

Table 6. Electrochemical surface area measurement

Samples	ECSA/geo area	C_{dl}	ECSA
FeNi-250-4-NC	2.52 mF cm^{-2}	0.63 mF	15.75 cm^2
FeNi-250-4	3.69 mF cm^{-2}	0.92 mF	23.06 cm^2
FeNi-250-16	2.73 mF cm^{-2}	0.68 mF	17.06 cm^{-2}

6.3.3 Theoretical study

To unravel the mechanistic origin of the remarkable OER activity observed above with FeNiO-250-4, slab models were built by chlorine substitution of the surface oxygen atom originally located between Fe_{oct} (octahedral site) and Ni_{td} (tetrahedral site) in $NiFe_2O_4$(100) (Figure 24a), based on the structural features identified in the above

experimental characterization. Free energy calculations indicate that adsorption of OH favors the Ni_{td} sites over the Fe_{oct} sites on the surface, consistent with the XPS results (Figure 11). Consequently, the $NiFe_2O_4(100)$ surface with Cl substituting O and Ni_{td} binding an OH ($Ni(OH)Fe_2O_4(Cl)$ was used as the model catalyst (Figure 24a). Other structures, $Ni(OH)Fe_2O_4$ (Figure 24b), $Fe(OH)Fe_2O_4(Cl)$ (Figure 24c), $Fe(OH)Fe_2O_4$ (Figure 24d), Ni(OH)NiO(Cl) (Figure 24e) Ni(OH)NiO (Figure 24f) were constructed as comparative references.

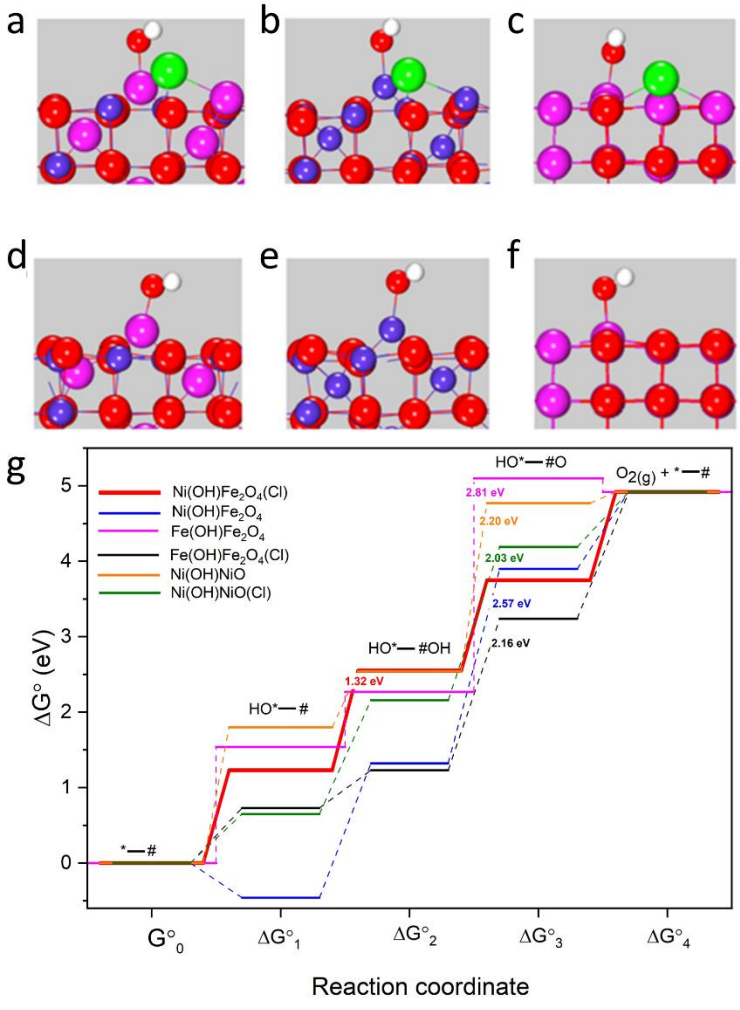

Figure 24. Computational studies of OER energetics. Structural models of (a) $Ni(OH)Fe_2O_4(Cl)$, (b) $Ni(OH)Fe_2O_4$, (c) $Fe(OH)Fe_2O_4(Cl)$, (d) $Fe(OH)Fe_2O_4$, (e) Ni(OH)NiO(Cl), and (f) Ni(OH)NiO. Free energy profile of OER on $Ni(OH)Fe_2O_4$, $Ni(OH)Fe_2O_4(Cl)$, $Fe(OH)Fe_2O_4$, $Fe(OH)Fe_2O_4(Cl)$, Ni(OH)NiO and Ni(OH)NiO(Cl). Color codes: Green, Cl; red, O; dark blue, Fe; magenta, Ni; white, H.

A two-site (*–#) model was adopted to study the OER mechanism (details in the Supporting Information). From the free energy diagram in Figure 24g, $Ni(OH)Fe_2O_4(Cl)$ displays a thermodynamic overpotential of only 90 mV and stands out as the optimal catalyst for OER among all models. The potential-limiting step is the second OH adsorption with a reaction free energy (ΔG_2°) of 1.32 eV, while all other steps, including the first OH binding (ΔG_1°), O–O coupling (ΔG_3°), and O_2 release (ΔG_4°), have a reaction free energy equal to or slightly lower than 1.23 eV. For comparison, $Ni(OH)Fe_2O_4$ with a similar structure but without Cl substitution, shows a very high reaction free energy for the O-O coupling step (ΔG_3°), whereas ΔG_1°, ΔG_2°, and ΔG_4° are all markedly below 1.23 eV. The high reaction free energy of O–O coupling accompanied by proton extraction (ΔG_3°) indicates that this step is the potential limiting step. These results suggest that incorporation of Cl onto the surface of $NiFe_2O_4$ spinel enhances the OER activity by facilitating O–O bond formation.

To confirm that the active site ensemble on $Ni(OH)Fe_2O_4(Cl)$ is unique and responsible for the enhanced activity, we also mapped out the potential energy profiles of OER on the monometal systems of $Fe(OH)Fe_2O_4$, $Fe(OH)Fe_2O_4(Cl)$, Ni(OH)NiO and Ni(OH)NiO(Cl) (Figure 24g), where the O–O coupling step, with a respective reaction free energy of 2.81, 2.16, 2.20 and 2.03 eV, remains to be the potential limiting step.

These results indicate that these monometal systems, even with Cl substitution, exhibited only a limited OER activity. Therefore, the remarkable activity of FeNiO-250-4 is most likely a synergistic effect of the formation of the metastable Fe-Ni spinel phase and the incorporation of Cl in the surface by substituting surface oxygen atom.

To understand the enhanced OER activity in $Ni(OH)Fe_2O_4(Cl)$, we tracked the charge density differences and compared the bond distances of the O*–#OH species on $Fe(OH)Fe_2O_4$, $Fe(OH)Fe_2O_4(Cl)$, $Ni(OH)Fe_2O_4$ and $Ni(OH)Fe_2O_4(Cl)$. For O*–#OH adsorbed on $Fe(OH)Fe_2O_4$ (Figure 25a), there is no observable charge density redistribution at the Fe_1 site (adjacent to Cl) but a significant electron depletion is observed on Fe_2 (away from Cl). With the introduction of Cl (Figure 25b), charge redistribution at Fe_1 is clearly visible whereas the electron density redistribution at Fe_2 is minimal. The electron density redistribution is believed to stabilize the O–O species on $Fe(OH)Fe_2O_4(Cl)$ as a result of losing the proton by O-O--H. Replacing Fe with Ni (Figure 25c) results in a relatively uniform charge density redistribution at both Fe_1 and Fe_2 sites and further stabilized the O–O species on $Ni(OH)Fe_2O_4$. Therefore, the presence of Cl and Ni (Figure 25d) strengthens bonding between the O*–#OH species and lowers the reaction free energy of the O–O coupling step. Charge redistribution at the Fe_1 and Fe_2 sites is also reflected in part in the decrease of Bader charge of the O–O pair, which was -1.2|e|, -1.14|e|, -1.04|e| and -1.0|e| for the O–O pair adsorbed on $Fe(OH)Fe_2O_4$, $Fe(OH)Fe_2O_4(Cl)$, $Ni(OH)Fe_2O_4$ and $Ni(OH)Fe_2O_4(Cl)$, respectively. A decreased negative charge value indicates an increase of acidity of O*–#OH, which benefits the proton transfer from O*–#OH to the OH adsorbed on Ni_{td} or Fe_{td} (Figure

25e–25h). A complete proton transfer from HO*—#O species to the OH facilitates the O–O bond formation, and the O-H distance in HO*—#O increases from 1.074 Å on $Fe(OH)Fe_2O_4$ to 1.307 Å on $Fe(OH)Fe_2O_4(Cl)$, further to 1.399 Å on $Ni(OH)Fe_2O_4$, and finally to 1.579 Å on $Ni(OH)Fe_2O_4(Cl)$ (Figure 25e-25h). Correspondingly, this increasingly detached proton approaches the OH on Ni_{td} or Fe_{td} to form H_2O. The loss of H from HO*—#O also strengthens the O–O bond, as the bond distance decreases from 1.473 Å on $Fe(OH)Fe_2O_4$ to 1.431 Å on $Ni(OH)Fe_2O_4(Cl)$. In summary, the presence of Ni and Cl in the catalyst synergistically stabilizes the O–O species while facilitates proton transfer from HO*—#O to the adjacent OH, resulting in a much reduced free energy barrier for the O–O coupling step.

From the Fe_1 density of states (DOS) plots (Figure 26), it is evident that the presence of Cl in $Fe(OH)Fe_2O_4(Cl)$ and $Ni(OH)Fe_2O_4(Cl)$ shifts the occupied d states closer to the Fermi level. For $Ni(OH)Fe_2O_4(Cl)$, these states remain occupied up to the O–O coupling step (Figure 26m-26p). The upward shift of the occupied d states results in an increased reactivity of the Cl and Ni containing catalysts.

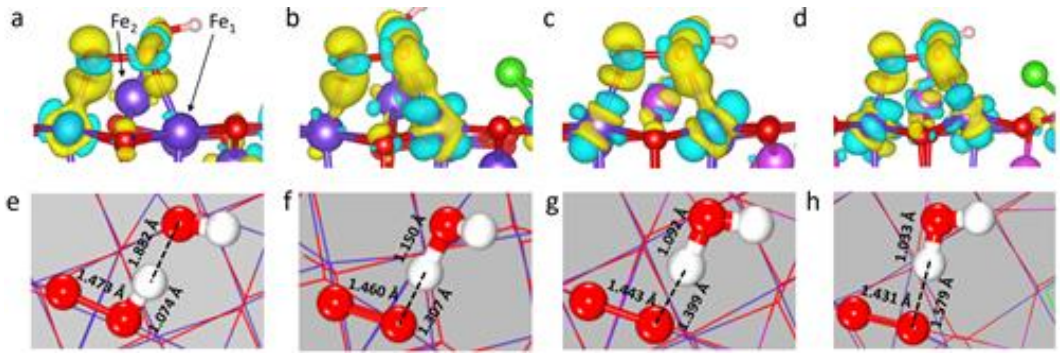

Figure 25. Charge density difference and evolution of bond lengths of two-site models. (a-d) Charge density difference isosurface with a value of 0.01. Light blue corresponds to negative and yellow to positive; (e-h). Evolution of bond distances of HO*—#O species: (a,e) Fe(OH)Fe2O4, (b,f) Fe(OH)Fe2O4(Cl), (c,g) Ni(OH)Fe2O4 and (d,h) Ni(OH)Fe2O4(Cl). Fe1 is next to Cl, and Fe2 is away. Color codes: Green, Cl; red, O; dark blue, Fe; magenta, Ni; white, H.

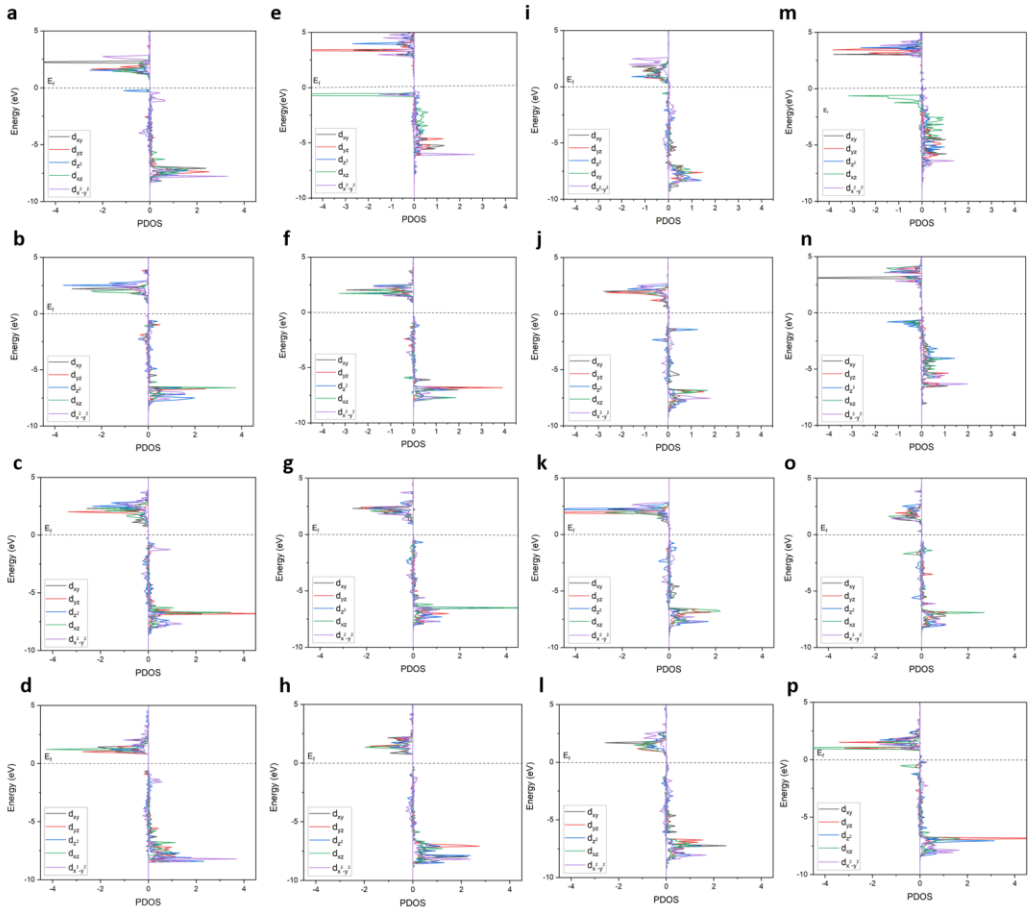

Figure 26. PDOS of the Fe1 atom. (a-d) $Fe(OH)Fe_2O_4$, (e-h) $Fe(OH)Fe_2O_4(Cl)$, (i-l) $Ni(OH)Fe_2O_4$ and (m-p) $Ni(OH)Fe_2O_4$ (Cl). The first row (a, e, I and m) represents PDOS of *–#, the second row (b, f, j, and n) represents PDOS of *–#OH, the third

row (c, g, k, and o) represents PDOS of HO*–# OH, and the fourth row (d, h, l and p) represents PDOS of HO*–# O.

6.4 Conclusions

In summary, the MIHRQ method was successfully developed and exploited for the ultrafast fabrication of metal oxide spinel nanostructures. Using $NiCl_2$ and $FeCl_3$ as the precursors, FeNi oxide spinels were obtained by heating at controlled currents within seconds and exhibited an even mixing of the Ni and Fe elements and a Cl-rich surface, in sharp contrast to samples prepared at prolonged heating and/or natural cooling in the ambient. The best sample, FeNiO-250-4 needed an overpotential of only 260 mV to reach the high current density of 100 mA cm^{-2} and exhibited significant stability in alkaline media. Such a remarkable activity was attributed to the unique metasTable tructure that facilitated the adsorption of key reaction intermediates and O-O coupling, a major limiting step in OER. Results from this study highlight the unique advantages of MIHRQ in the rapid production of unprecedented material structures that are unattainable in conventional thermal processes for enhanced electrocatalytic performance and potential applications in the structural engineering of a diverse range of materials (Figure 27). Moreover, because the fast preparing of material and ease of scale up synthesis, we believe this MIHRQ has great outlook for industrialization.

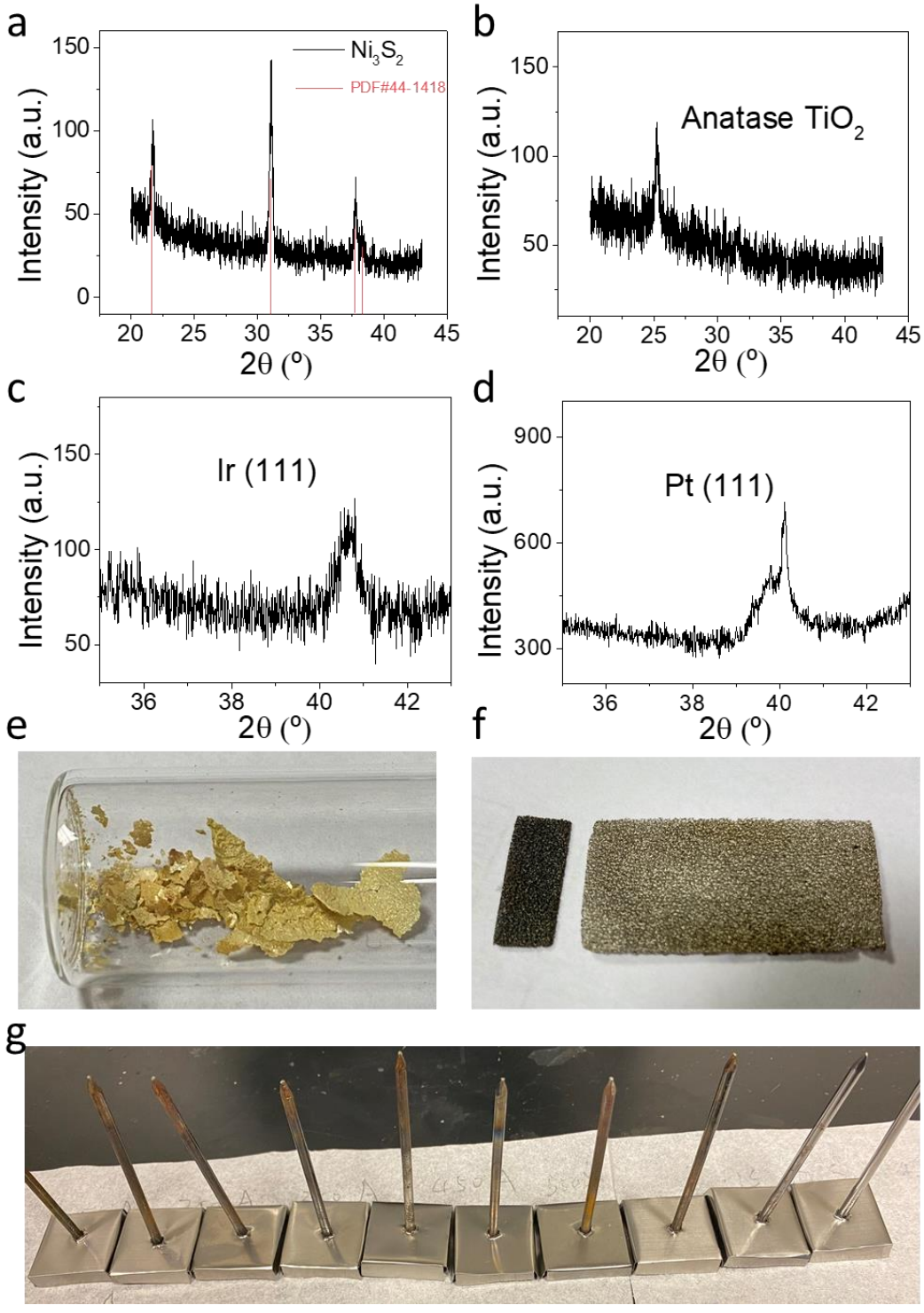

Figure 27. Additional materials prepared by MIHRQ. XRD patterns of (a) Ni_3S_2, (b) TiO_2, (c) Ir, and (d) Pt produced on nickel foam. Photographs of (e) carbon nitride

(C_3N_4), (f) nickel foam before (right piece) and after (left piece) induction heating in air, and (g) 10 heating setups for larger-scale synthesis or for the preparationof a diverse range of materials. The MIHRQ technique can be readily extended to the preparation of a wide range of materials for varied applications (Figure 27), thus offering a new paradigm for materials structural manipulation and engineering. The nickel foam before and after MIH treatment in air is shown in Figure 27f, where the apparent change of the color appearance signifies ready oxidation of the nickel foam. When a calculated amount of a sulfur-toluene solution or tetrabutyl titanate is dropcast onto the nickel foam, MIH treatment leads to facile production of Ni_3S_2 (Figure 27a) or anatase TiO2 (Figure 27b). MIHRQ can also be used to prepare noble metal-based samples. For instance, by dropcasting an ethanolic solution of $Ir(acac)_3$ or $Pt(acac)_2$ onto a piece of carbon paper, we successfully prepared carbon-supported Ir (Figure 27c) or Pt nanoparticles (Figure 27d). This method can also treat free-standing powder materials. For example, with melamine loaded into the heating apparatus, graphitic carbon nitride (C_3N_4) can be produced easily (Figure 27e). Note that the MIHRQ method exhibits a promising outlook for scale-up synthesize. This establishes a solid foundation of industrialization and high-throughput electrode/material synthesis. After attempting the heating elements with different shape, size, thickness, and material, we have successfully normalized the configuration and preparation procedure of the heating element. For instance, with 10 induction heating setups (Figure 27g), we are able to prepare up to 40 samples with different configurations, within just several minutes. We anticipate this method will make significant contributions to material synthesis, structural engineering and applications. Such studies are ongoing and results will be reported in due course.

6.5 Materials and Methods

Sample preparation

Carbon paper (from Toray Industries, Inc.) was cut into 1 cm × 1.5 cm pieces. A solution was prepared by dissolving 40 mg of $NiCl_2•6H_2O$, 10 mg of $FeCl_3$ and 0.8 g of urea

into 10 mL of water (supplied with a Barnstead Nanopure Water System, 18.2 MW cm). 100 mL of the solution was dropcast onto the carbon paper, which was then dried at ambient temperature and sandwiched between two iron sheets of 2.5 cm × 2.5 cm × 0.1 cm. The assembly was then placed in the center of a four-turn induction coil with a diameter of 5 cm, and magnetic induction heating was carried out at a controlled current (X = 100-600 A) for a select heating time (Y = 2-16 s), when the sample was dropped into an ethanol-dry ice solution (-78 °C) placed underneath the induction coil for rapid quenching (caution: the ethanol must be fully cooled down by dry ice, or it will catch fire). The temperature was measured by an industrial infrared laser thermometer (BTMETER, BT-1500). The corresponding sample was denoted as FeNiO-X-Y.

Control samples were also prepared by removing the sample assembly from the heater and being cooled down in ambient to room temperature. These samples were referred to as $FeNiO_{NC}$-X-Y.

Structural characterizations

(Scanning) transmission electron microscopy (S)TEM experiments ware conducted with a transmission electron microscope equipped with an X-FEG field-emission source, operated at 200 keV. To perform the high-angle annular dark-field scanning transmission electron microscopy (HAADF-STEM) imaging and energy-dispersive X-ray spectroscopy (EDS) analysis, the samples were first sonicated, dispersed in ethanol, and then deposited onto copper grids for TEM characterization. Scanning electron microscopy (SEM) studies were carried out on FEI Quanta 3D FEG dual beam instrument. X-ray photoelectron spectroscopy (XPS) measurements were performed

with a Phi 5400/XPS instrument equipped with an Al K_α source operated at 350 W and 10-9 Torr. X-ray diffraction (XRD) patterns were acquired with a Bruker D8 Advance diffractometer with Cu K_α radiation (λ = 0.15418 nm).

X-ray absorption spectroscopy (XAS) studies

Fe and Ni K-edge XAS data was collected from the CLS@APS Sector 20-BM beamline at the Advanced Photon Source (operating at 7.0 GeV) in Argonne National Labs, Chicago, IL, USA. Samples were enclosed within Kapton tape and measured in fluorescence mode simultaneously with each elements foil reference. All measurements were conducted at room temperature and ambient pressure. EXAFS data was transformed and normalized into k- and R-space using the Athena program following conventional procedures. A k weighting of 2 was used to obtain all FT-EXAFS spectra. The k-range used for each sample is as follows for Fe: 3.1–9.2 $Å^{-1}$ for FeNiO-250-4, 2.1–9.1 $Å^{-1}$ for $FeNiO_{NC}$-250-4, 3.3–12.7 $Å^{-1}$ for FeNiO-250-16. For Ni the k-range used was as follows: 3.0–8.9 $Å^{-1}$ for FeNiO-250-4, 2.9–12.2 $Å^{-1}$ for $FeNiO_{NC}$-250-4, 2.6–14.4 $Å^{-1}$ for FeNiO-250-16. The R-range used for Fe is as follows: 1.0-3.7 Å for FeNiO-250-4, 1.0–3.6 Å for $FeNiO_{NC}$-250-4, 1.0–3.4 Å for FeNiO-250-16. The R-range used for Ni is as follows: 1.0-3.5 Å for FeNiO-250-4, 1.0–3.0 Å for $FeNiO_{NC}$-250-4, 1.0–3.0 Å for FeNiO-250-16. Self-consistent multiple-scattering calculations were performed using the FEFF6 program to obtain the scattering amplitudes and phase-shift functions used to fit various scattering paths with the Artemis program. In the fitting of each sample the E_0 values were correlated together to minimize the

number of independent values, allowing reliable fitting results to be obtained. The σ^2 values were also correlated for some samples.

Electrochemistry

Electrochemical measurements were carried out with a CHI 700e electrochemical workstation in a three electrodes configuration. The prepared carbon paper was fixed onto a graphite electrode holder, with an exposed surface area of 1 cm^2. A platinum wire was adopted as the counter electrode and a Ag/AgCl in saturated KCl as the reference electrode. The reference electrode was calibrated against a reversible hydrogen electrode (RHE) and all potentials in the present study were referenced to this RHE.

DFT computation

Spin-polarized density functional theory (DFT) calculations were carried out using the VASP (Vienna Ab-Initio Simulation Package) code.[76] Projector-augmented wave (PAW) method[77] with the Perdew-Burke-Ernzerhof (PBE) exchange-correlation functional[78] was used in all calculations. On-site Coulomb interactions were corrected within the DFT + U framework based on Dudarev's approximation.[79] U_{eff} = 4.20[80] and 6.40[81] for Fe and Ni, respectively, were used.[82] Plane-wave basis set with a 400 eV energy cutoff provides a balance of accuracy and computational cost. Either quasi-Newton scheme or conjugate gradient algorithm implemented in VASP was used to relax structure until forces are converged to less than -0.03 eV $Å^{-1}$ on unconstrained atoms and self-consistent convergence until 10^{-5} eV. The Gaussian smearing with a σ value of 0.05 was used to minimize entropy contribution to free energy. The bulk structure of

$NiFe_2O_4$ was taken from JCPDS (JCPDS Card No. 10-0325) and optimized in (4 x 4 x 1) k-point grid sampling of the surface Brillouin zone. The optimized lattice constant of 8.37 Å was found in close agreement with the experimental value of 8.35 Å.

A supercell consisting of five layers of $NiFe_2O_4$ with an exposed (100) surface was constructed from the optimized bulk structure. A vacuum space of 14 Å in z-direction was inserted between the slabs, and the atoms in the top three layers were allowed to relax while those in the bottom two layers were fixed at the corresponding bulk position during structural optimization.

Additional computational details

Generally, a single active site mechanism, shown in eq. S1-S4, has been widely used in analyzing oxygen evolution reaction (OER) catalyzed by an oxide catalyst, such as Ni, Co, Fe spinels.

$$* + OH \rightarrow *–OH \quad \text{(S1)}$$

$$*–OH + OH \rightarrow *–O + H_2O \quad \text{(S2)}$$

$$*–O + OH \rightarrow *–OOH \quad \text{(S3)}$$

$$*–OOH + OH \rightarrow O_2 + * + H_2O \quad \text{(S4)}$$

On the $NiFe_2O_4$ catalyst, Ni was considered as the active site for OER and the potential limiting step was *-O → *-OOH (eq. S3). This step has a reaction free energy of 2.0 eV, corresponding to a thermodynamic overpotential of ca. 770 mV.[63] Another study reported that *-OH → *-O (eq. S2) was the potential limiting step and had a thermodynamic overpotential of 970 mV.[60] Obviously, the overpotentials from both studies are significantly higher than the present experimental result, i.e., ca. 200 mV at

1 mA cm^{-2} from Figure 4a. Based on the scaling relationship between the binding energies of *OH and *OOH, an overpotential less than 0.4 V cannot be achieved by following the single metal site mechanism.[83] Therefore, the mechanism based on a single metal site was not believed to contribute to the high activity observed in the present study.

We adopted a mechanism involving two adjacent metal sites, i.e., *—#. According to this mechanism, shown in eq. S5–S8, OER starts by OH binding on the first metal site forming HO*—# (ΔG_1°, eq. S5). This is followed by a second OH binding at the neighboring metal site forming HO*—#OH (ΔG_2°, eq. S6). A stepwise reaction of HO*—#OH with OH (ΔG_3°, eq. S7 and ΔG_4°, eq. S8) releases O_2 and H_2O and completes the cycle.

$$*—\# + 4(OH^- + h^+) \rightarrow HO*—\# + 3(OH^- + h^+)^- \qquad \Delta G_1^\circ \qquad (S5)$$

$$HO*—\# + 3(OH^- + h^+) \rightarrow HO*—\#OH + 2(OH^- + h^+) \qquad \Delta G_2^\circ \qquad (S6)$$

$$HO*—\#OH + 2(OH^- + h^+) \rightarrow HO*—\#O + H_2O + (OH^- + h^+) \qquad \Delta G_3^\circ \qquad (S7)$$

$$HO*—\#O + H_2O + (OH^- + h^+) \rightarrow *—\# + O_2 + 2H_2O \qquad \Delta G_4^\circ \qquad (S8)$$

The reaction free energies of these steps were calculated according to eq. S5-S8. Based on the calculated reaction free energies, we constructed the reaction free energy profile shown in Figure 5g and determined the thermodynamic overpotential.

The reaction free energy expressions for the reactions described in eq. S5-S8 are:

$$\Delta G_1^\circ = \mu(HO*—\#) + 3\mu(OH^- + h^+) - \mu(*—\#) - 4\mu(OH^- + h^+) \qquad (S9)$$

$$\Delta G_2^\circ = \mu(HO*—\#OH) + 2\mu(OH^- + h^+) - \mu(HO*—\#) - 3\mu(OH^- + h^+) \qquad (S10)$$

$$\Delta G_3^\circ = \mu(HO*—\#O) + \mu(H_2O) + \mu(OH^- + h^+) - \mu(HO*—\#OH) - 2\mu(OH^- + h^+) \qquad (S11)$$

$\Delta G_4^\circ = 4.92 - (\Delta G_1^\circ + \Delta G_2^\circ + \Delta G_3^\circ)$ (S12)

Since PBE significantly overestimates $\mu(O_{2(g)})$, ΔG_4° in eq. S12 was computed on the basis of the experimental reaction free energy of 4.92 eV for $2H_2O_{(l)} \rightarrow 2H_{2(g)} + O_{2(g)}$. The chemical potential of OH, i.e., $\mu(OH^- + h^+)$ was computed using the approach developed by Tang and Ge[84] based on CHE[85]. Free energies of all intermediates were determined using $G° = E_{elect}^\circ$ - TS + ZPE. E_{elect}° was obtained from DFT calculations, whereas the contributions of TS and ZPE were computed from frequency calculations in which adsorbate together with the atoms in the topmost layer were allowed to move.

6.6 Reference

1. Z. W. Seh, J. Kibsgaard, C. F. Dickens, I. Chorkendorff, J. K. Norskov, T. F. Jaramillo. *Science* **2017**, *355*.

2. M. Shao, Q. Chang, J.-P. Dodelet, R. Chenitz. *Chem Rev* **2016**, *116*, 3594-3657.

3. J. Zhu, L. Hu, P. Zhao, L. Y. S. Lee, K.-Y. Wong. *Chem Rev* **2020**, *120*, 851-918.

4. N.-T. Suen, S.-F. Hung, Q. Quan, N. Zhang, Y.-J. Xu, H. M. Chen. *Chem Soc Rev* **2017**, *46*, 337-365.

5. Y. Peng, B. Lu, S. Chen. *Adv Mater* **2018**, *30*, 1801995.

6. B. Lu, Q. Liu, S. Chen. *Acs Catal* **2020**, *10*, 7584-7618.

7. C. Wang, N. M. Markovic, V. R. Stamenkovic. *Acs Catal* **2012**, *2*, 891-898.

8. S. Anantharaj, S. R. Ede, K. Sakthikumar, K. Karthick, S. Mishra, S. Kundu. *Acs Catal* **2016**, *6*, 8069-8097.

9. Y. L. Zhu, Q. Lin, Y. J. Zhong, H. A. Tahini, Z. P. Shao, H. T. Wang. *Energ Environ Sci* **2020**, *13*, 3361-3392.

10. C. G. Kuai, Y. Zhang, D. Y. Wu, D. Sokaras, L. Q. Mu, S. Spence, D. Nordlund, F. Lin, X. W. Du. *Acs Catal* **2019**, *9*, 6027-6032.

11. M. R. Gao, W. C. Sheng, Z. B. Zhuang, Q. R. Fang, S. Gu, J. Jiang, Y. S. Yan. *J Am Chem Soc* **2014**, *136*, 7077-7084.

12. R. D. L. Smith, M. S. Prevot, R. D. Fagan, S. Trudel, C. P. Berlinguette. *J Am Chem Soc* **2013**, *135*, 11580-11586.

13. B. Lu, Q. Liu, F. Nichols, R. Mercado, D. Morris, N. Li, P. Zhang, P. Gao, Y. Ping, S. Chen. *Research* **2020**, *2020*, 9167829.

14. B. Lu, T. J. Smart, D. Qin, J. E. Lu, N. Wang, L. Chen, Y. Peng, Y. Ping, S. Chen. *Chem Mater* **2017**, *29*, 5617-5628.

15. M. Gong, Y. Li, H. Wang, Y. Liang, J. Z. Wu, J. Zhou, J. Wang, T. Regier, F. Wei, H. Dai. *J Am Chem Soc* **2013**, *135*, 8452-8455.

16. Q. Xiang, F. Li, W. Chen, Y. Ma, Y. Wu, X. Gu, Y. Qin, P. Tao, C. Song, W. Shang, H. Zhu, T. Deng, J. Wu. *Acs Energy Lett* **2018**, *3*, 2357-2365.

17. Q. Zhao, Z. H. Yan, C. C. Chen, J. Chen. *Chem Rev* **2017**, *117*, 10121-10211.

18. R. Jiang, Y. Da, X. Han, Y. Chen, Y. Deng, W. Hu. *Cell Rep Phys Sci* **2021**, *2*, 100302.

19. A. Holewinski, J.-C. Idrobo, S. Linic. *Nature Chemistry* **2014**, *6*, 828-834.

20. Z. Li, J.-Y. Fu, Y. Feng, C.-K. Dong, H. Liu, X.-W. Du. *Nat Catal* **2019**, *2*, 1107-1114.

21. J.-Q. Wang, C. Xi, M. Wang, L. Shang, J. Mao, C.-K. Dong, H. Liu, S. A. Kulinich, X.-W. Du. *Acs Catal* **2020**, *10*, 12575-12581.

22. Y. Yao, Z. Huang, P. Xie, S. D. Lacey, R. J. Jacob, H. Xie, F. Chen, A. Nie, T. Pu, M. Rehwoldt, D. Yu, M. R. Zachariah, C. Wang, R. Shahbazian-Yassar, J. Li, L. Hu. *Science* **2018**, *359*, 1489-1494.

23. W. Chen, Z. Wang, K. V. Bets, D. X. Luong, M. Ren, M. G. Stanford, E. A. McHugh, W. A. Algozeeb, H. Guo, G. Gao, B. Deng, J. Chen, J. T. Li, W. T. Carsten, B. I. Yakobson, J. M. Tour. *ACS Nano* **2021**, *15*, 1282-1290.

24. J. Zhang, M. Ren, Y. Li, J. M. Tour. *Acs Energy Lett* **2018**, *3*, 677-683.

25. X. Yue, X. P. Qin, Y. D. Chen, Y. Peng, C. H. Liang, M. Feng, X. Z. Qiu, M. H. Shao, S. M. Huang. *Adv Sci* **2021**, *8*.

26. C. Meng, M. Lin, X. Sun, X. Chen, X. Chen, X. Du, Y. Zhou. *Chem Commun* **2019**, *55*, 2904-2907.

27. H. Hu, Q. Li, L. Q. Li, X. L. Teng, Z. X. Feng, Y. L. Zhang, M. B. Wu, J. S. Qiu. *Matter-Us* **2020**, *3*, 95-126.

28. G. W. Xiong, Y. K. Chen, Z. Q. Zhou, F. Liu, X. Y. Liu, L. J. Yang, Q. L. Liu, Y. H. Sang, H. Liu, X. L. Zhang, J. Jia, W. J. Zhou. *Adv Funct Mater* **2021**, *31*.

29. F. Ran, S. Chen, *Advanced Nanomaterials for Electrochemical-Based Energy Conversion and Storage*. Elsevier: **2019**.

30. Y. Zhou, S. N. Sun, C. Wei, Y. M. Sun, P. X. Xi, Z. X. Feng, Z. C. J. Xu. *Adv Mater* **2019**, *31*.

31. X. K. Chen, X. H. Zhang, L. Z. Zhuang, W. Zhang, N. C. Zhang, H. W. Liu, T. R. Zhan, X. L. Zhang, X. L. She, D. J. Yang. *Chem-Asian J* **2020**, *15*, 3995-3999.

32. B.-Q. Li, S.-Y. Zhang, C. Tang, X. Cui, Q. Zhang. *Small* **2017**, *13*, 1700610.

33. X.-M. Liu, X. Cui, K. Dastafkan, H.-F. Wang, C. Tang, C. Zhao, A. Chen, C. He, M. Han, Q. Zhang. *Journal of Energy Chemistry* **2021**, *53*, 290-302.

34. C. Tang, H.-S. Wang, H.-F. Wang, Q. Zhang, G.-L. Tian, J.-Q. Nie, F. Wei. *Adv Mater* **2015**, *27*, 4516-4522.

35. B. Lal, P. K. Rastogi. *Orbital* **2020**, *12*, 154-159.

36. D. Lim, H. Kong, N. Kim, C. Lim, W. S. Ahn, S. H. Baeck. *Chemnanomat* **2019**, *5*, 1296-1302.

37. C. Kuai, Z. Xu, C. Xi, A. Hu, Z. Yang, Y. Zhang, C.-J. Sun, L. Li, D. Sokaras, C. Dong, S.-Z. Qiao, X.-W. Du, F. Lin. *Nat Catal* **2020**, *3*, 743-753.

38. Y. Zhu, Q. Lin, Z. Wang, D. Qi, Y. Yin, Y. Liu, X. Zhang, Z. Shao, H. Wang. *Journal of Energy Chemistry* **2021**, *52*, 115-120.

39. J. Zhang, Y. Cui, L. Jia, B. He, K. Zhang, L. Zhao. *Int J Hydrogen Energ* **2019**, *44*, 24077-24085.

40. B. M. Hunter, W. Hieringer, J. R. Winkler, H. B. Gray, A. M. Müller. *Energ Environ Sci* **2016**, *9*, 1734-1743.

41. V. Rudnev, D. Loveless, R. L. Cook, *Handbook of induction heating*. CRC press: **2017**.

42. T. Zhao, C. Xu, W. Ma, Z. Liu, T. Zhou, Z. Liu, S. Feng, M. Zhu, N. Kang, D.-M. Sun, H.-M. Cheng, W. Ren. *Nat Commun* **2019**, *10*, 4854.

43. C. Wu, F. Li, W. Chen, C. P. Veeramalai, P. C. Ooi, T. Guo. *Scientific Reports* **2015**, *5*, 9034.

44. R. Piner, H. Li, X. Kong, L. Tao, I. N. Kholmanov, H. Ji, W. H. Lee, J. W. Suk, J. Ye, Y. Hao, S. Chen, C. W. Magnuson, A. F. Ismach, D. Akinwande, R. S. Ruoff. *ACS Nano* **2013**, *7*, 7495-7499.

45. M. Seifert, S. Drieschner, B. M. Blaschke, L. H. Hess, J. A. Garrido. *Diamond and Related Materials* **2014**, *47*, 46-52.

46. P. Sharma, N. Holliger, P. H. Pfromm, B. Liu, V. Chikan. *ACS Omega* **2020**, *5*, 19853-19860.

47. X.-b. Xiong, J.-y. Zhang, J. Ma, X.-r. Zeng, H. Qian, Y.-y. Li. *Mater Chem Phys* **2016**, *181*, 1-6.

48. R. Tiwari, M. De, H. S. Tewari, S. K. Ghoshal. *Results in Physics* **2020**, *16*, 102916.

49. W. Niu, L. Li, X. Liu, N. Wang, J. Liu, W. Zhou, Z. Tang, S. Chen. *J Am Chem Soc* **2015**, *137*, 5555-5562.

50. C. Bale, P. Chartrand, S. A. Degterov, G. Eriksson, K. Hack, R. Ben Mahfoud, J. Melancon, A. D. Pelton, S. Petersen. *Calphad* **2002**, *26*, 189-228.

51. A. G. Marrani, V. Novelli, S. Sheehan, D. P. Dowling, D. Dini. *Acs Appl Mater Inter* **2014**, *6*, 143-152.

52. A. P. Grosvenor, M. C. Biesinger, R. S. C. Smart, N. S. McIntyre. *Surf Sci* **2006**, *600*, 1771-1779.

53. T. Yamashita, P. Hayes. *Appl Surf Sci* **2008**, *254*, 2441-2449.

54. M. A. Peck, M. A. Langell. *Chem Mater* **2012**, *24*, 4483-4490.

55. L. Liu, F. Tian, X. Wang, Z. Yang, X. Wang. *Ionics* **2013**, *19*, 9-15.

56. C. Lin, Y. H. Zhao, H. J. Zhang, S. H. Xie, Y. F. Li, X. P. Li, Z. Jiang, Z. P. Liu. *Chem Sci* **2018**, *9*, 6803-6812.

57. M. H. Nilsen, C. Nordhei, A. L. Ramstad, D. G. Nicholson, M. Poliakoff, A. Cabanas. *J Phys Chem C* **2007**, *111*, 6252-6262.

58. C. C. L. McCrory, S. Jung, J. C. Peters, T. F. Jaramillo. *J Am Chem Soc* **2013**, *135*, 16977-16987.

59. H. Yang, Y. Liu, S. Luo, Z. Zhao, X. Wang, Y. Luo, Z. Wang, J. Jin, J. Ma. *Acs Catal* **2017**, *7*, 5557-5567.

60. L. Gao, X. Cui, Z. Wang, C. D. Sewell, Z. Li, S. Liang, M. Zhang, J. Li, Y. Hu, Z. Lin. *Proceedings of the National Academy of Sciences* **2021**, *118*.

61. Q. Yue, C. Liu, Y. Wan, X. Wu, X. Zhang, P. Du. *J Catal* **2018**, *358*, 1-7.

62. R. Wei, X. Bu, W. Gao, R. A. B. Villaos, G. Macam, Z.-Q. Huang, C. Lan, F.-C. Chuang, Y. Qu, J. C. Ho. *Acs Appl Mater Inter* **2019**, *11*, 33012-33021.

63. M. Alharthy, M. H. Suliman, A.-R. Al-Betar, Y. Wang, Z. Tian, Q. A. Drmosh, Z. H. Yamani, M. Qamar. *Sustainable Energy & Fuels* **2021**, *5*, 2704-2714.

64. Z. Wu, Z. Zou, J. Huang, F. Gao. *Acs Appl Mater Inter* **2018**, *10*, 26283-26292.

65. F. Song, M. M. Busch, B. Lassalle-Kaiser, C.-S. Hsu, E. Petkucheva, M. Bensimon, H. M. Chen, C. Corminboeuf, X. Hu. *ACS Central Science* **2019**, *5*, 558-568.

66. T. u. Haq, Y. Haik, I. Hussain, H. u. Rehman, T. A. Al-Ansari. *Acs Appl Mater Inter* **2021**, *13*, 468-479.

67. Y. Miyahara, T. Fukutsuka, T. Abe, K. Miyazaki. *Chem Mater* **2020**, *32*, 8195-8202.

68. Y. P. Liu, X. Liang, L. Gu, Y. Zhang, G. D. Li, X. X. Zou, J. S. Chen. *Nat Commun* **2018**, *9*.

69. Y. P. Zhu, G. Chen, Y. J. Zhong, Y. B. Chen, N. N. Ma, W. Zhou, Z. P. Shao. *Nat Commun* **2018**, *9*.

70. X. Wang, Y. W. Zhang, H. N. Si, Q. H. Zhang, J. Wu, L. Gao, X. F. Wei, Y. Sun, Q. L. Liao, Z. Zhang, K. Ammarah, L. Gu, Z. Kang, Y. Zhang. *J Am Chem Soc* **2020**, *142*, 4298-4308.

71. C. G. Kuai, Z. R. Xu, C. Xi, A. Y. Hu, Z. J. Yang, Y. Zhang, C. J. Sun, L. X. Li, D. Sokaras, C. K. Dong, S. Z. Qiao, X. W. Du, F. Lin. *Nat Catal* **2020**, *3*, 743-753.

72. J. Wang, L. Y. Gan, W. Y. Zhang, Y. C. Peng, H. Yu, Q. Y. Yan, X. H. Xia, X. Wang. *Sci Adv* **2018**, *4*.

73. X. L. Han, Y. F. Yu, Y. Huang, D. L. Liu, B. Zhang. *Acs Catal* **2017**, *7*, 6464-6470.

74. Y. S. Jin, S. L. Huang, X. Yue, H. Y. Du, P. K. Shen. *Acs Catal* **2018**, *8*, 2359-2363.

75. G. Wu, W. X. Chen, X. S. Zheng, D. P. He, Y. Q. Luo, X. Q. Wang, J. Yang, Y. Wu, W. S. Yan, Z. B. Zhuang, X. Hong, Y. D. Li. *Nano Energy* **2017**, *38*, 167-174.

76. G. Kresse, J. Furthmüller. *Phys Rev B* **1996**, *54*, 11169-11186.

77. G. Kresse, D. Joubert. *Phys Rev B* **1999**, *59*, 1758-1775.

78. J. P. Perdew, K. Burke, M. Ernzerhof. *Phys Rev Lett* **1996**, *77*, 3865-3868.

79. S. Dudarev, G. Botton, S. Savrasov, C. Humphreys, A. Sutton. *Phys Rev B* **1998**, *57*, 1505.

80. G. Hautier, S. P. Ong, A. Jain, C. J. Moore, G. Ceder. *Phys Rev B* **2012**, *85*, 155208.

81. L. Wang, T. Maxisch, G. Ceder. *Phys Rev B* **2006**, *73*, 195107.

82. L. Gao, X. Cui, Z. Wang, C. D. Sewell, Z. Li, S. Liang, M. Zhang, J. Li, Y. Hu, Z. Lin. *Proc. Natl. Acad. Sci. U.S.A* **2021**, *118*, e2023421118.

83. I. C. Man, H. Y. Su, F. Calle-Vallejo, H. A. Hansen, J. I. Martínez, N. G. Inoglu, J. Kitchin, T. F. Jaramillo, J. K. Nørskov, J. Rossmeisl. *Chemcatchem* **2011**, *3*, 1159-1165.

84. M. Tang, Q. Ge. *Chinese J Catal* **2017**, *38*, 1621-1628.

85. J. K. Nørskov, J. Rossmeisl, A. Logadottir, L. Lindqvist, J. R. Kitchin, T. Bligaard, H. Jonsson. *The Journal of Physical Chemistry B* **2004**, *108*, 17886-17892.

Chapter 7 Organically Capped Iridium Nanoparticles as High-Performance Bifunctional Electrocatalysts for Full Water Splitting in Both Acidic and Alkaline Media: Impacts of Metal-Ligand Interfacial Interactions

7.1 Abstract

Design and engineering of bifunctional catalysts is critical in the development of electrochemical full water splitting. In this study, 4-ethylphenylacetylene-functionalized iridium (Ir-C≡, 1.7 ± 0.3 nm in diameter) nanoparticles are found to exhibit markedly enhanced electrocatalytic activity towards both hydrogen and oxygen evolution reactions (HER and OER) in acidic and alkaline media, in comparison to the nanoparticles capped with mercapto and nitrene derivatives. Remarkably, the HER and OER performances in alkaline media are even better than those of commercial Ir/C and Pt/C benchmarks. This is accounted for by the formation of Ir-C≡C- conjugated interfacial linkage that leads to significant intraparticle charge delocalization and hence manipulation of the electron density of the Ir nanoparticles and interactions with key reaction intermediates. This is indeed confirmed by results from both spectroscopic measurements and density functional theory calculations. With Ir-C≡ nanoparticles as both the cathode and anode catalysts for electrochemical water splitting, a low cell voltage of 1.495 and 1.473 V is needed to reach the current density of 10 mA cm-2 in alkaline and acidic media, respectively. Such a performance is markedly better than that of commercial Ir/C (1.548 and 1.561 V) and relevant catalysts reported in recent literature, highlighting the significance of interfacial engineering in the development of high-performance bifunctional electrocatalysts.

7.2 Introduction

Electrochemical water splitting represents a unique technology for the sustainable production of hydrogen and oxygen by the hydrogen evolution reaction (HER) at the cathode and oxygen evolution reaction (OER) at the anode under mild conditions.[1,2] Yet, both HER and OER necessitate the employment of appropriate catalysts, so as to achieve a sufficiently high current density for practical applications. Currently, Pt/C is the benchmark electrocatalyst for HER, whereas RuO_2 and IrO_2 for OER.[3] It would be of fundamental and technological significance to develop bifunctional electrocatalysts that are active towards both HER and OER, so as to significantly reduce the costs of catalyst synthesis and electrode fabrication, a critical aspect in practical commercialization.[4] Indeed, a range of nanomaterials, such as non-noble metals, metal oxides/carbide/sulfides, and carbon-based composites, have been examined as bifunctional electrocatalysts.[5-9] However, their performances have mostly remained subpar, as compared to those of the benchmark electrocatalysts and do not meet the requirement for practical applications.[10-23]

Fundamentally, it has been demonstrated that the strength of hydrogen and oxygen binding to the respective electrocatalytic active site is a critical parameter for HER and OER. In fact, the H binding energy ($\square G_{H^*}$) has been used as a unique descriptor to evaluate the HER performance within the framework of a so-call "volcano plot".[24,25] For Ir, the $\square G_{H^*}$ is situated on the left side of the volcano plot, suggesting that the binding of H to Ir is slightly too strong, and thus the surface electron density of Ir needs to be lowered somewhat so as to reach the optimal peak. As for OER, prior research

has shown that metallic Ir is prone to be oxidized at high electrode potentials, and low-valence IrO_x actually exhibits a higher electrocatalytic activity than the high-valence counterparts,[21,26] suggesting that a reduced oxidation state of Ir is desired for enhanced OER performance. This can be achieved by structural engineering that leads to a decreased O binding energy,[27] typically within the context of nanoparticle size, shape, morphology, and alloying.[3,28-34] For instance, Zhu et al.[35] prepared Pd@Ir-nL core-shell nanocubes (n = 1-4, the number of atomic Ir layers) and observed a maximal OER performance at n = 3, with an overpotential ($\eta_{10,OER}$) of only +245 mV to reach the current density of 10 mA·cm^{-2} and a mass activity of 3.33 $A \cdot mg_{Ir}^{-1}$ at η = +300 mV, which was markedly better than that of commercial Ir/C, due to Pd−Ir intermixing, and possible ligand and/or strain effect. In another study,[36] by alloying with tungsten (W), a 5d metal, IrW nanobranches were prepared and used as bifunctional electrocatalysts for full water splitting, where a cell voltage (E_{10}) of 1.58 and 1.60 V was needed to reach 10 mA·cm^{-2} in 0.1 M $HClO_4$ and 0.1 M KOH, respectively, which was 120 mV and 130 mV lower than that with commercial Ir, due to a changed electronic structure of Ir by W. In addition, the electrocatalytic activity can also be manipulated by strong interactions with the supporting substrates, such as carbon-based materials.[37,38] For instance, Wu et al.[21] prepared ultrasmall Ir nanoparticles supported on N-doped graphene (Ir@N-G-750) and observed a cell voltage of 1.6 V for overall water splitting at 20 mA·cm^{-2} in 0.1 M $HClO_4$, due to the formation of abundant Ir-N coordination sites. Cao and coworkers[22] prepared cucurbit[6]uril stabilized Ir nanoparticles, which showed an E_{10} of 1.56 V in full water splitting in 0.1 M $HClO_4$ and long-term stability,

due to the coordination interaction between Ir and cucurbit[6]uril that facilitated the formation and stabilization of surface active species.

In a series of earlier studies,[39,40] we demonstrated that deliberate functionalization of metal nanoparticles with select organic ligands can be exploited as an additional, powerful variable in manipulating the surface electron density and hence electrocatalytic activity towards a range of important reactions, such as the oxygen reduction reaction and formic acid oxidation. For example, it has been shown that the electron withdrawing/donating property of the *para*-substituent groups of phenyl ligands can manipulate nanoparticle's surface electronic structure and hence the electrocatalytic activity, due to effective metal-ligand interfacial charge transfer.[41,42] In the present study, we demonstrate that by surface functionalization of Ir nanoparticles with acetylene derivatives, the resulting Ir nanoparticles can be used as high-performance electrocatalysts towards both HER and OER in both acidic and alkaline media (with the alkaline HER and OER activity significantly better than those of commercial Pt/C and Ir/C). This is ascribed to the formation of conjugated Ir-C≡ metal-ligand interfacial bonding interaction that reduces the electron density of the Ir nanoparticles and the interactions with critical reaction intermediates, in comparison to the mercapto- (Ir-S) and nitrene-capped (Ir=N) counterparts. In fact, the Ir-C≡ nanoparticles can be used as both the anode and cathode catalysts for full water splitting, which displays a low E_{10} of only 1.495 and 1.473 V in alkaline and acidic media, respectively. Such a performance is markedly better than that of commercial Ir/C (1.548 V and 1.561 V).

7.3 Results and Discussion

Organically capped Ir nanoparticles were synthesized by adopting a procedure used previously based on controlled thermolysis and subsequent ligand exchange (details in the Experimental Section).[43,44] It involves two major steps (Scheme 1). "Bare" Ir nanoparticles were first prepared by thermolytic reduction of $IrCl_3$ in 1,2-propanediol in the presence of sodium acetate, and then were functionalized with 4-ethylphenylacetylene (EPA), 4-ethylphenylthiol (EPT), or 4-dodecylbenzenesulfonyl azide (DBSA) by ligand exchange. The resulting nanoparticles were denoted as Ir-C≡, Ir-S and Ir=N, respectively, reflecting the formation of such metal-ligand interfacial bonds. The structures of the nanoparticles were first studied by transmission electron microscopic (TEM) measurements. From the TEM image in Figure 1a, one can see that the Ir nanoparticles were well dispersed on the TEM grid without apparent agglomeration, and in high-resolution measurements (Figure 1b), well-defined lattice fringes can be readily identified, with an interplanar spacing of ca. 0.225 nm that is consistent with the Ir(111) facets (JCPDS card No. 46-1044).[45] Statistical analysis based on more than 100 nanoparticles showed that the nanoparticles were mostly in the narrow range of 1.4 to 2.0 nm in diameter, averaging 1.7 ± 0.3 nm, as depicted in the core size histogram in Figure 1c.

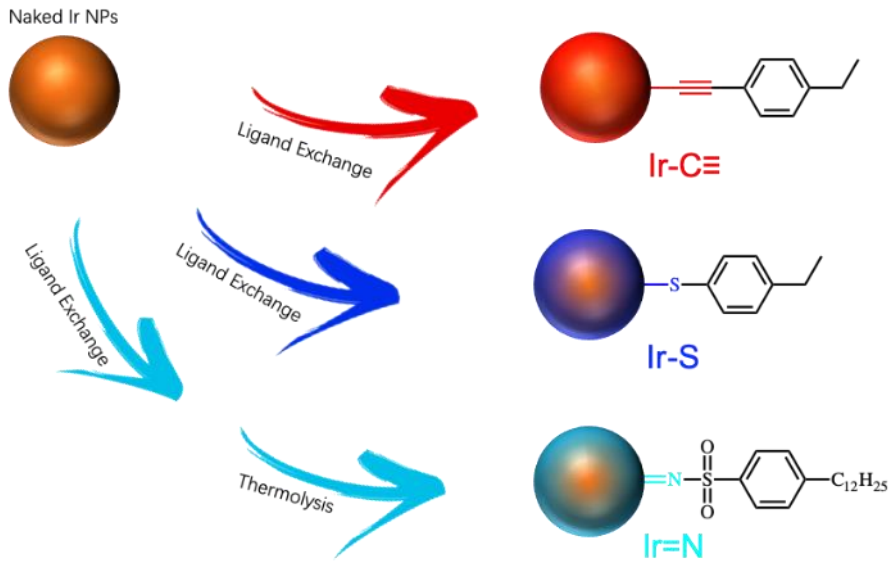

Scheme 1. Schematic illustration of the synthetic procedure of Ir nanoparticles capped with varied organic ligands.

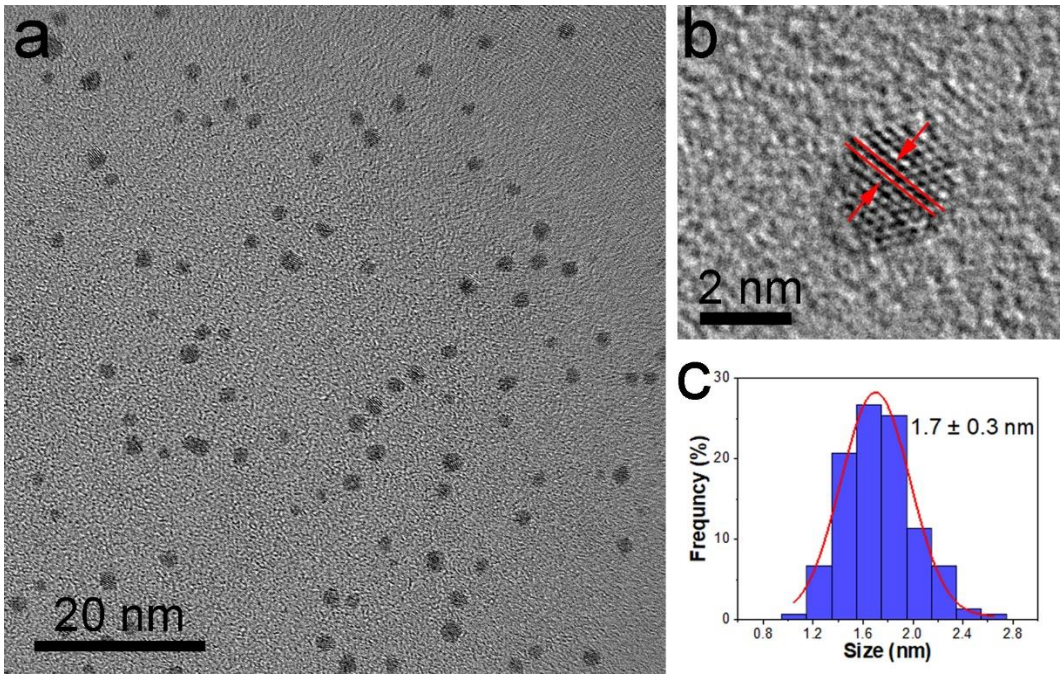

Figure 1. TEM images of (a,b) Ir nanoparticles and (c) the corresponding core size histogram.

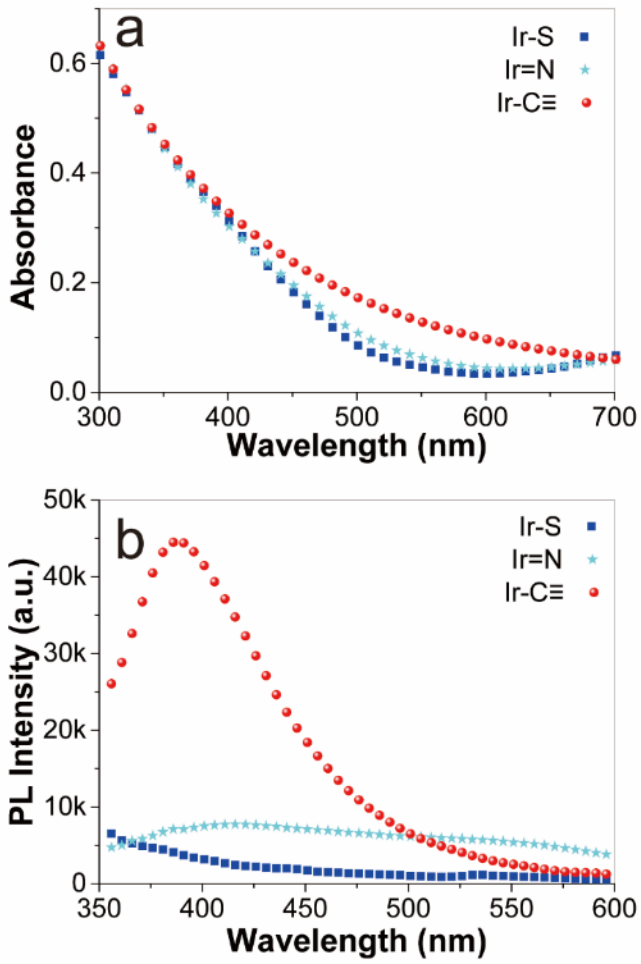

Figure 2. (a) UV-vis absorption and (b) photoluminescence emission spectra of the varied organically capped Ir nanoparticles.

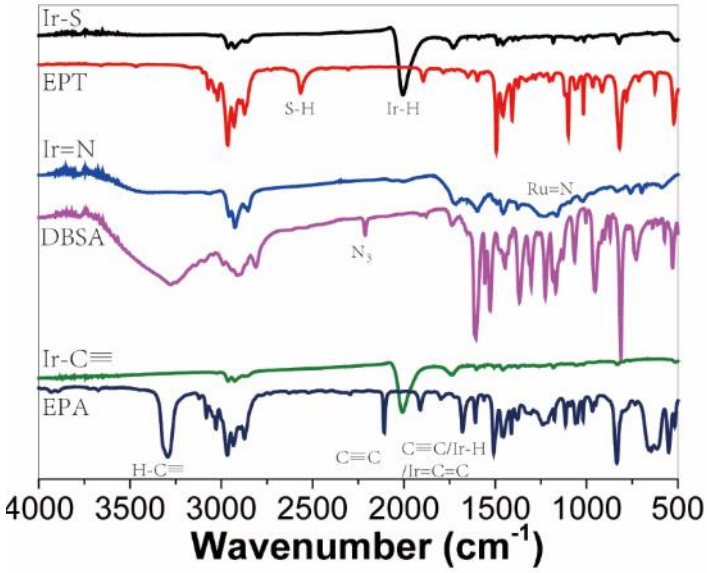

Figure 3. FTIR spectra of EPA, DBSA and EPT monomeric ligands and the corresponding organically capped Ir nanoparticles.

The optical properties of the nanoparticles were then examined by spectroscopic measurements. From Figure 2a, the Ir-C≡, Ir-S and Ir=N nanoparticles can be seen to exhibit a similar exponential decay profile in UV-vis absorption measurements, consistent with the nanosized structure,[46] but markedly different photoluminescence emissions (Figure 2b). Specifically, when excited by 335 nm irradiation, Ir-C≡ exhibited an apparent emission centered at 388 nm. This is attributed to the intraparticle charge delocalization arising from the conjugated Ir-C≡C- interfacial bonds.[44,47] Ir=N displayed a broad, weak emission centered at 425 nm because of the formation of conjugated Ir=N interfacial linkages.[48,49] By contrast, only a featureless profile was observed with the Ir-S sample, due to the formation of only non-conjugated interfacial bonds and lack of intraparticle charge delocalization. Consistent results were obtained in FTIR measurements (Figure 3).[39]

The valence states of the nanoparticles were then studied by X-ray photoelectron spectroscopy (XPS) measurements. Figure 4a depicts the high-resolution scans of the Ir 4f electrons of the three nanoparticle samples, which all entail a doublet with a spin-orbit coupling of 2.90 eV that is consistent with that of Ir(0).[50] Yet the exact binding energies of the $4f_{7/2}/4f_{5/2}$ doublet vary among the samples, at 60.84/83.74 eV for Ir-S, 61.76/83.66 eV for Ir=N, and 61.51/84.41 eV for Ir-C≡. That is, in comparison to Ir-S, the Ir=N and Ir-C≡ nanoparticles exhibited a positive shift of 0.92 and 0.67 eV, respectively, of the Ir 4f binding energy, suggesting charge transfer from the metal core to the respective ligands, most likely due to the formation of conjugated metal-ligand interfacial bonds, as observed previously.[39] Consistent results were obtained in the evaluation of the valence band maximum (VBM) of the respective nanoparticles (Figure 4b), where the Ir-S sample can be seen to exhibit the lowest VBM at about -0.81 eV, in comparison to +0.07 eV for Ir=N and -0.15 eV for Ir-C≡. This suggests that the d-band centers of the latter two samples shift markedly towards the Fermi level, as compared to the former.[51-53]

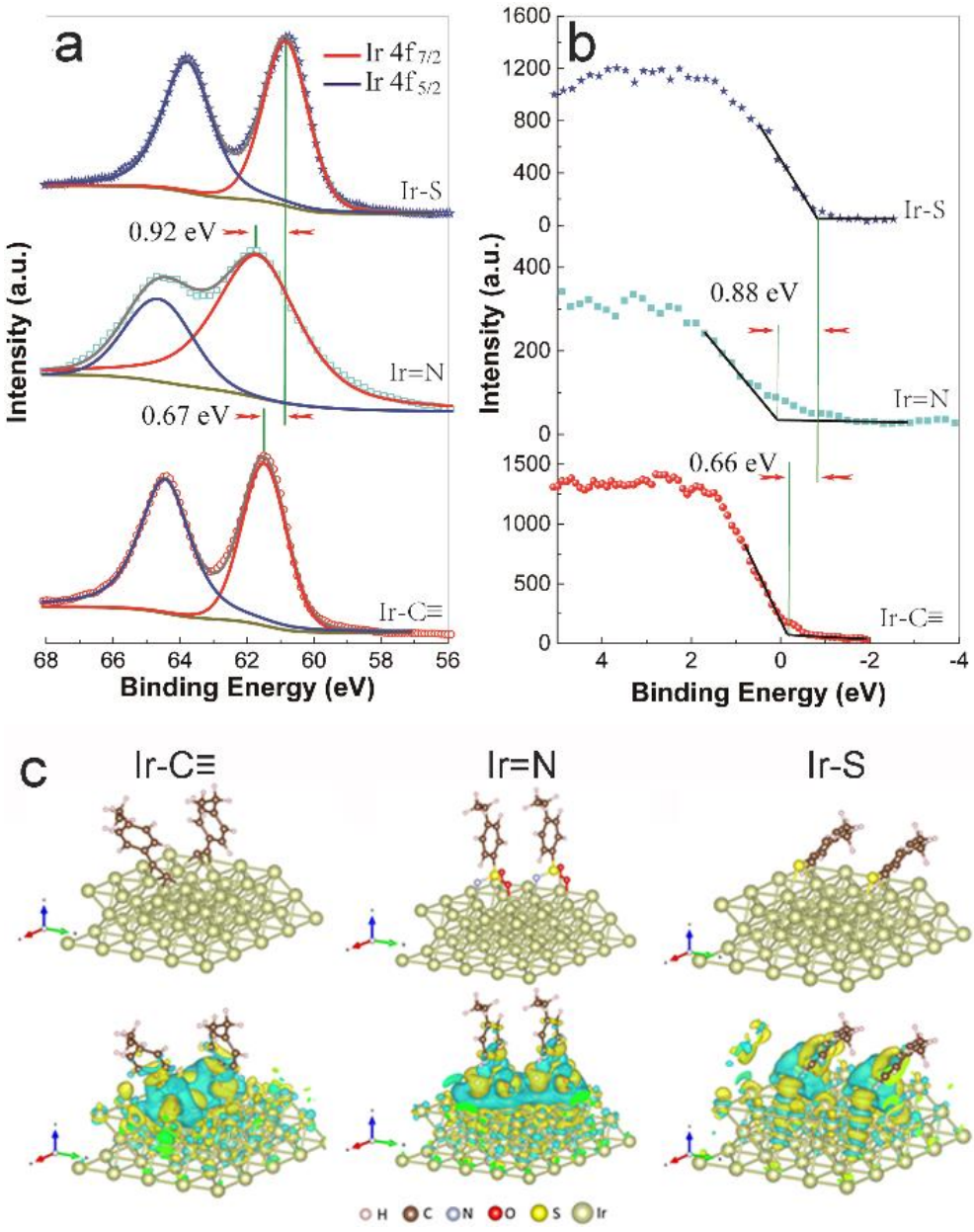

Figure 4. Interfacial charge transfer characterizations. (a) High-resolution XPS profiles of the Ir 4f electrons of Ir-C≡, Ir=N, and Ir-S nanoparticles, and (b) the corresponding spectra of valence band maximum (VBM). (c) (top panels) Optimized structures of Ir-C≡, Ir=N, and Ir-S slabs and (bottom panels) the corresponding interfacial charge density distributions. The cyan and yellow areas signify electron loss and electron gain, respectively. The isovalue of charge density is 0.001 e/au^3.

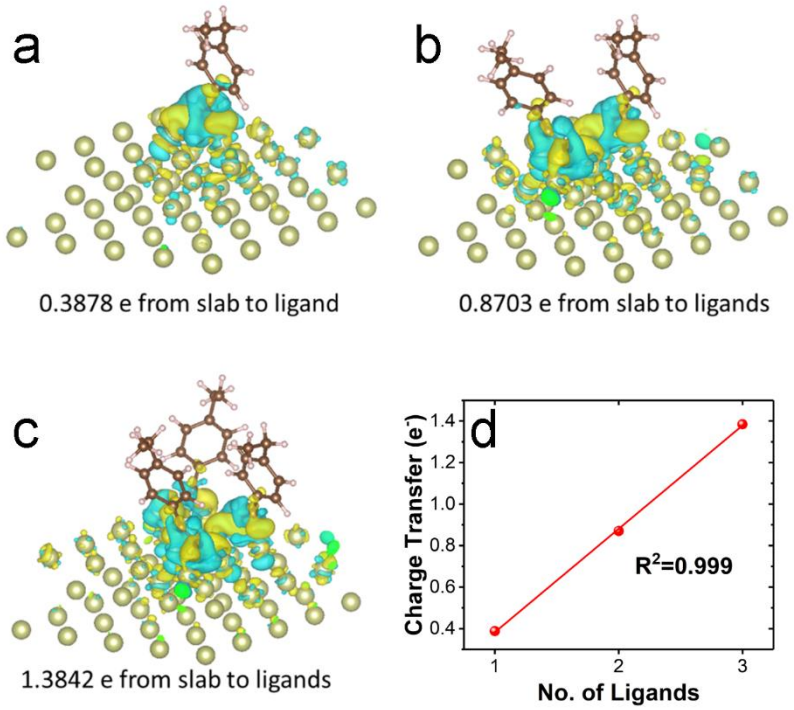

Figure 5. Optimized structures of Ir-C≡ with (a) one, (b) two, or three ligands per slab and the corresponding interfacial charge density distribution. The cyan and yellow areas signify electron loss and electron gain, respectively. The isovalue of charge density is 0.001 e/au^3. (d) The linear correlation between charge transfer and the number of ligands on the slab. The interfacial charge transfer is estimated to be 0.3878 e for one ligand, 0.8703 e for two ligands, and 1.3842 e for three ligands. That is, the interfacial charge transfer is linearly proportional to the number of surface capping ligands.

Consistent results were obtained from density functional theory (DFT) calculations. An Ir(111) slab was adopted based on the TEM results (Figure 1b), and two ligands of -C≡C-, =N-SO_2-, and -S- substituted ethylbenzene were anchored onto the slab and relaxed to the optimal structure. The respective models are shown in the top panels of

Figure 4c. It should be noted that in Ir=N-, two O atoms (red) of the sulfonyl group also participated in the interfacial anchoring. Notably, analysis of the charge density distributions (bottom panels) shows that interfacial charge transfer occurred in all three structures from the Ir slab to the organic capping ligands; yet the extent of charge transfer varied. Specifically, a gain of 0.87, 1.75, and 0.36 electrons for ligands based on Bader charge analysis was observed for the Ir-C≡, Ir=N, and Ir-S structure, respectively, highlighting the significance of conjugated interfacial bonding interactions in facilitating metal-ligand change transfer (Figure 5), as observed above in XPS measurements.

With such apparent manipulation of the electronic properties of the Ir nanoparticles by the organic capping ligands (Figure 4), significant enhancement was indeed observed of the electrocatalytic activities towards both HER and OER. Figure 6a shows the HER polarization curves in 1.0 M KOH of the Ir-S, Ir=N and Ir-C≡ nanoparticles, along with commercial 20 wt% Ir/C as the benchmark. One can see that all samples exhibited non-zero currents as the electrode potential was swept negatively. Yet the activity varied significantly among the samples. For instance, the overpotential ($\eta_{10,HER}$) needed to reach the current density of 10 mA cm^{-2} is markedly different, at -237, -74, -38 and only -7 mV for Ir-S, Ir=N, Ir/C, and Ir-C≡, respectively. That is, the Ir-C≡ sample stood out as the best among the series and even outperformed commercial Ir/C by a large margin (Figure 7a). Of particular note is that the $\eta_{10,HER}$ of Ir-C≡ (-7 mV in 1.0 M KOH) was even significantly lower than leading results in recent literature, such as Ir@N-G-750 (-43 mV),[21] Co@Ir/NC (-121 mV),[37] RuC_xN_y single atom catalysts (-12 mV),[54] and

commercial Pt/C (-49 mV).[54] The corresponding Tafel plots are shown in Figure 6b, and the slope was found to decrease in the order of Ir-S (182 mV dec^{-1}) > Ir=N (91 mV dec^{-1}) > Ir/C (71 mV dec^{-1}) > Ir-C≡ (62 mV dec^{-1}). This indicates that the kinetics of HER on Ir-C≡ was the fastest among the series of catalysts, following mostly the Volmer-Heyrovsky pathway.[55,56] Consistent results were obtained in electrochemical impedance spectroscopy (EIS) measurements. From the Nyquist plots in Figure 8a, the Ir-C≡ sample was found to exhibit the lowest charge-transfer resistance (R_{ct} = 6.6 Ω) among the series (10.8 Ω for Ir/C, 24.1 Ω for Ir=N, and 173.6 Ω for Ir-S).

The OER performance of the samples was also analyzed and compared in a similar manner. From the polarization curves in Figure 6c, one can see that all samples were apparently active towards OER, but $\eta_{10,OER}$ differed substantially, at +300, +316, +333 and +322 mV for Ir-C≡, Ir/C, Ir=N and Ir-S, respectively, with a corresponding Tafel slope of 37, 42, 38 and 48 mV dec^{-1}. This indicates that the Ir-C≡ nanoparticles also exhibited the best OER performance among the series (Figure 7b). Note that the Tafel slope of Ir-C≡ is even markedly lower than those of relevant Ir-based catalysts reported in earlier studies (mostly greater than 50 mV dec^{-1}) in alkaline media,[21,36,37] indicating the unique advantage of surface functionalization of Ir nanoparticles by acetylene derivatives in enhancing the OER kinetics. Consistent results were obtained in EIS measurements, where the Ir-C≡ sample also exhibited the lowest R_{ct} (11.0 Ω) among the series (13.3, 23.5, and 44.8 Ω for Ir/C, Ir-S and Ir=N, respectively, Figure 8b). Notably, the OER performance is actually comparable or superior to results of leading

catalysts reported in the literature, such as IrW,[36] Co@Ir/NC,[37] IrO_x,[57-59] and noble-metal-free catalysts.[60,61]

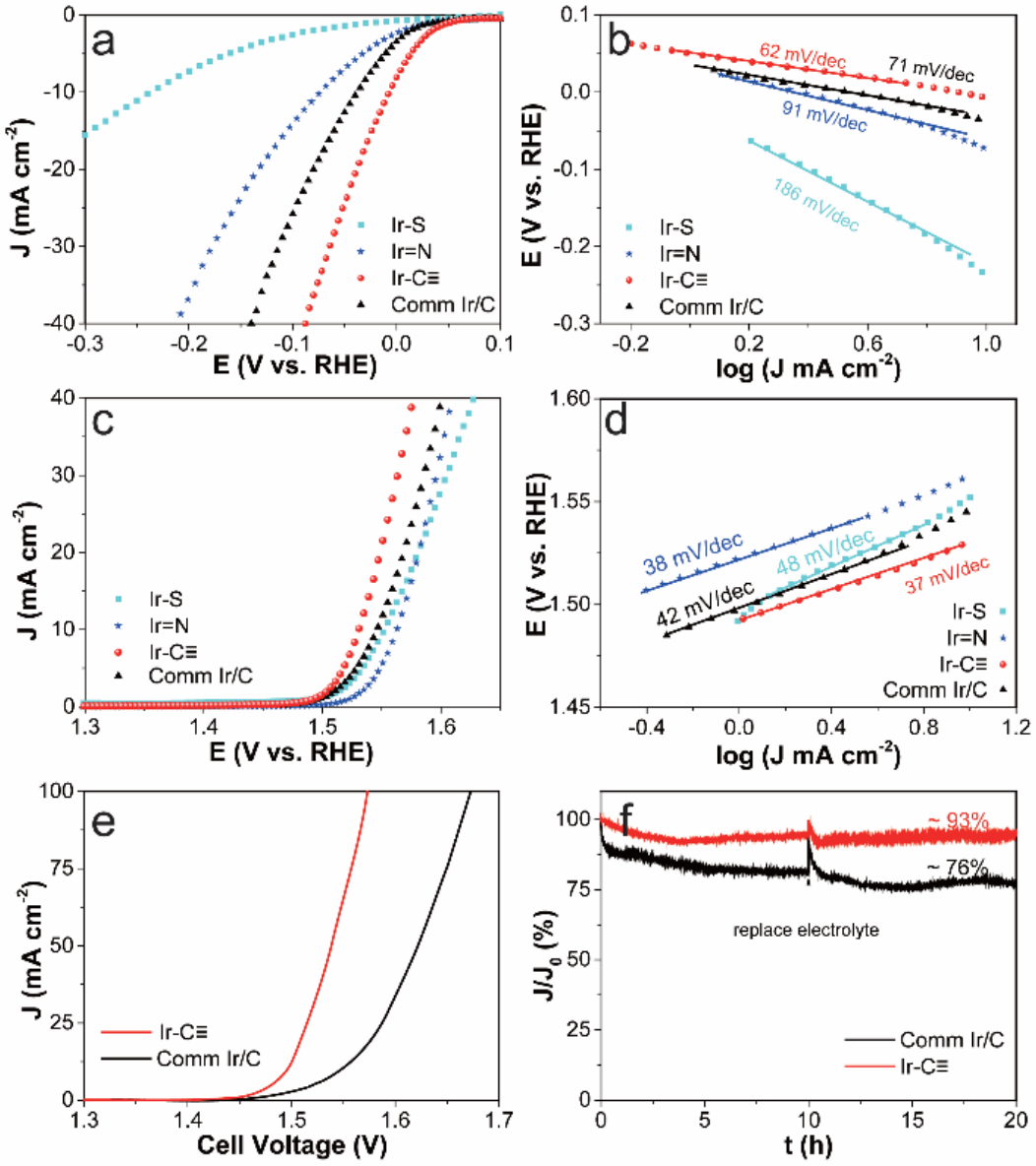

Figure 6. Bifunctional electrocatalytic performance towards HER and OER in 1.0 M KOH. (a) HER polarization curves of the series of electrocatalysts, and (b) the corresponding Tafel plots. (c) OER polarization curves of the series of electrocatalysts, and (d) the corresponding Tafel plots. (e) Current-voltage profiles of overall water

splitting with Ir-C≡ and commercial Ir/C as bifunctional electrocatalysts in 1.0 M KOH, and (f) the corresponding activity retention tests by chronoamperometric measurements at the respective initial E_{10}.

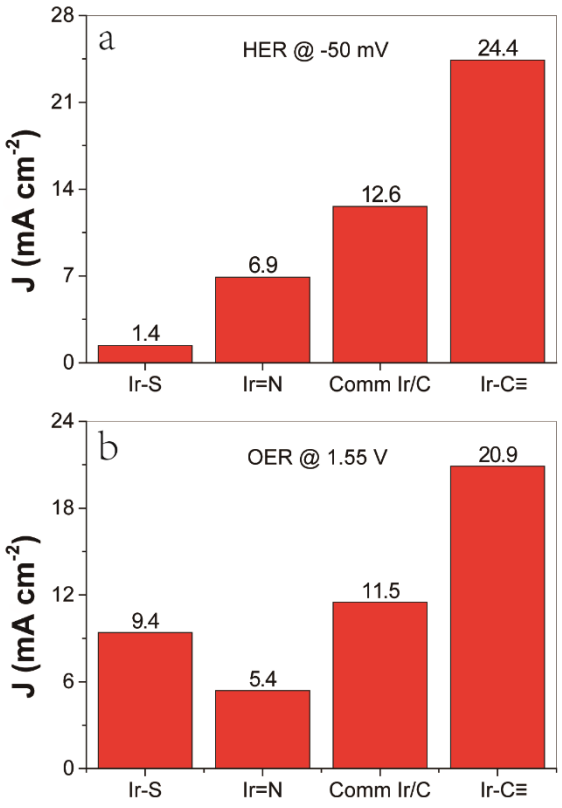

Figure 7. Comparison of the bifunctional catalytic performance in alkaline media. (a) HER current densities of the varied Ir nanoparticles at the potential of -50 mV in 1.0 M KOH. (b) OER current densities of the varied Ir nanoparticles at the potential of +1.55 V in 1.0 M KOH.

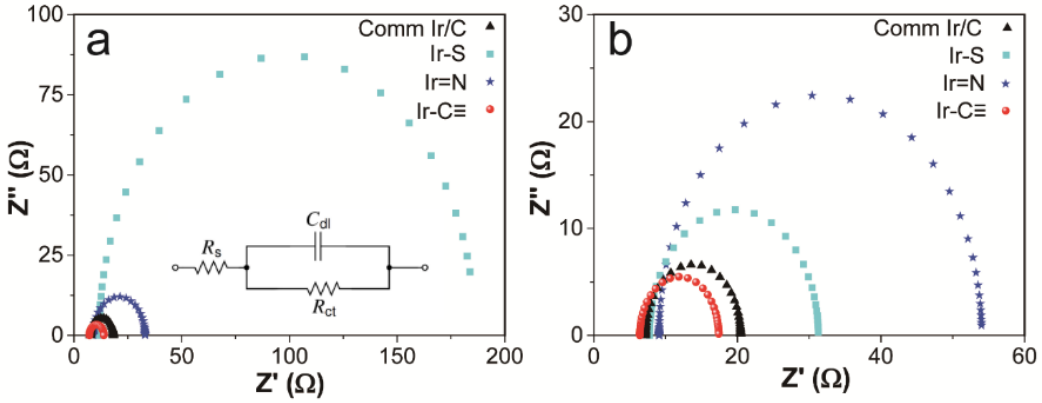

Figure 8. Nyquist plots at the potential of (a) -50 mV (HER) and (b) 1.55 V (OER) in 1 M KOH. Inset is the Randle equivalent circuit: R_{ct} is the charge transfer resistance, C_{dl} is the double layer capacitance, and R_s is the series resistance. One can see that the R_s increases in the order of Ir-C≡ < Ir=N < Ir-S (i.e., electrical conductivity increases in the reverse order), consistent with the variation of interfacial charge transfer from the Ir nanoparticle core to the capping ligands.

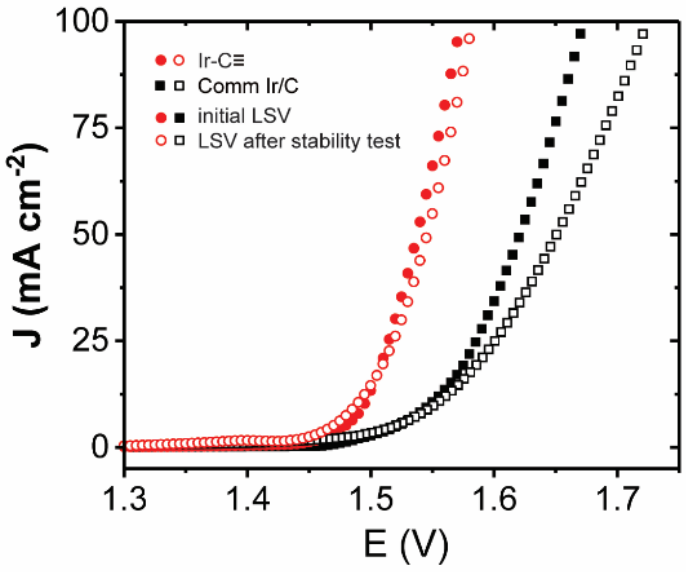

Figure 9. Current-voltage profiles of overall water splitting with Ir-C≡ and commercial Ir/C as bifunctional electrocatalysts in 1.0 M KOH before and after the constant-potential stability test.

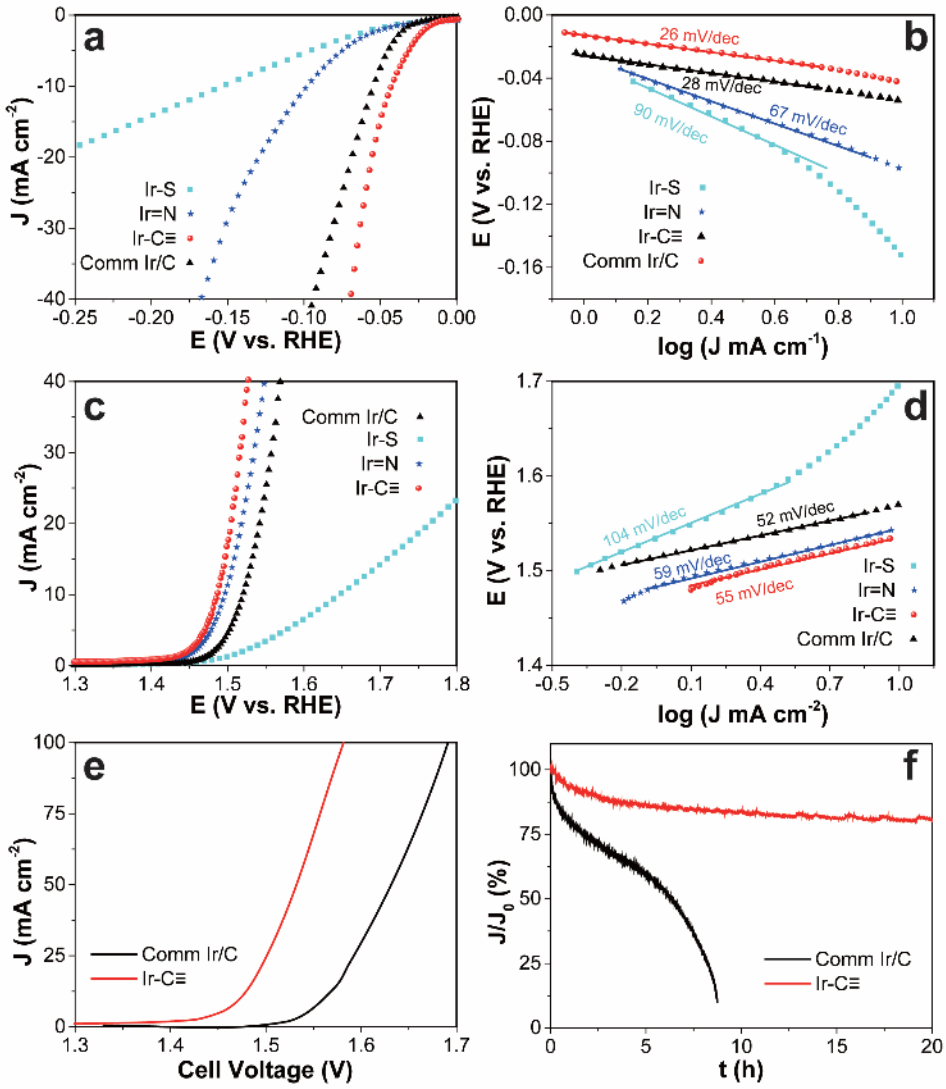

Figure 10. Bifunctional electrocatalytic performance towards HER and OER in 0.5 M H_2SO_4. (a) HER polarization curves of the series of electrocatalysts, and (b) the corresponding Tafel plots. (c) OER polarization curves of the series of electrocatalysts, and (d) the corresponding Tafel plots. (e) Current-voltage curves of overall water splitting using Ir-C≡ and commercial Ir/C as the bifunctional catalysts in 0.5 M H_2SO_4, and (f) the corresponding activity retention test by chronoamperometric measurements at the respective initial E_{10}.

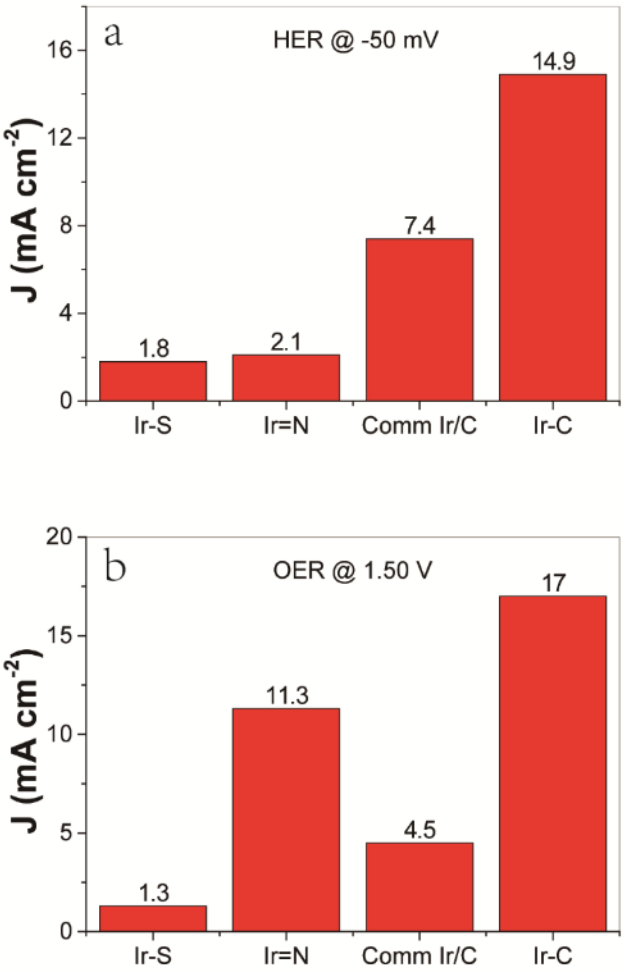

Figure 11. Comparison of the bifunctional catalytic performance in acidic media. (a) HER current densities of the various Ir nanoparticles at the potential of -50 mV in 0.5 M H_2SO_4. (b) OER current densities of the various Ir nanoparticles at the potential of +1.55 V in 0.5 M H_2SO_4.

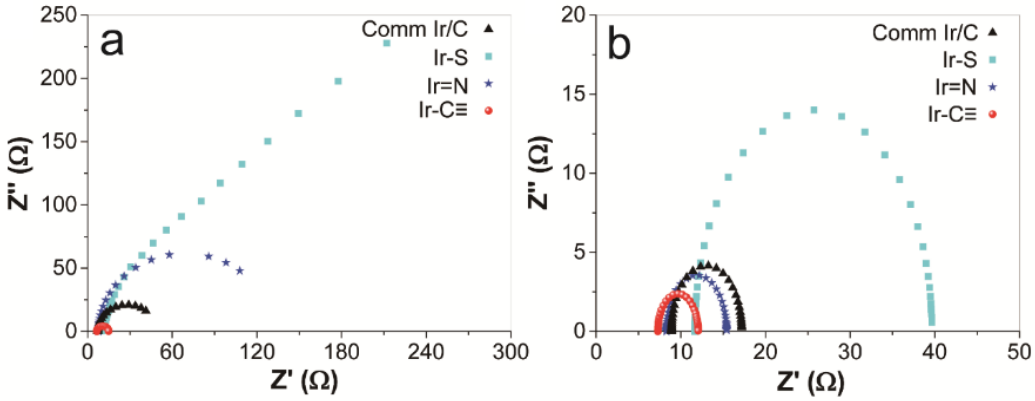

Figure 12. Nyquist plots at the potential of (a) -100 mV (HER) and (b) 1.50 V (OER) in 0.5 M H_2SO_4. One can see that the R_s increases in the order of Ir-C≡ < Ir=N < Ir-S (i.e., electrical conductivity increases in the reverse order), consistent with the variation of interfacial charge transfer from the Ir nanoparticle core to the capping ligands.

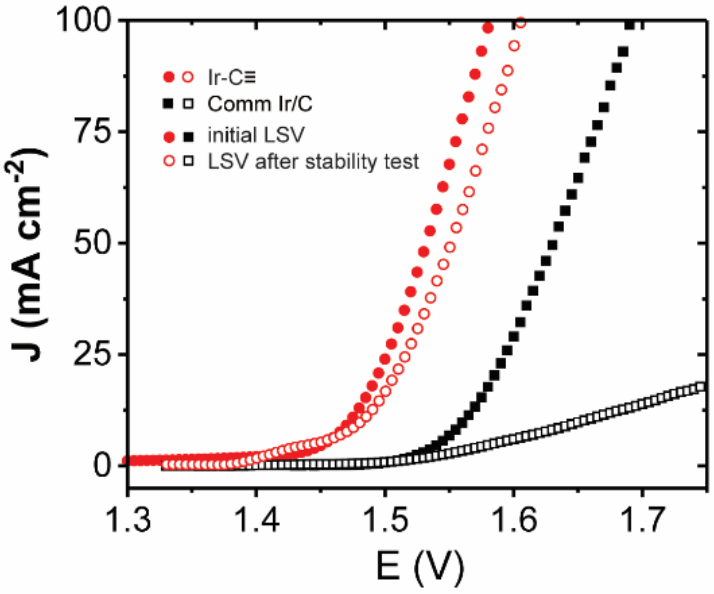

Figure 13. Current-voltage profiles of overall water splitting with Ir-C≡ and commercial Ir/C as bifunctional electrocatalysts in 1.0 M KOH before and after the constant-potential durability test.

Table 1. Comparison of the HER and OER electrocatalytic performances of the Ir nanoparticles in the present study with relevant catalysts in the literature.

catalysts	electrolyte	$\eta_{10,HER}$ (mV)	$\eta_{10,OER}$ (mV)	E_{10} (V)	Mass loading (□g cm^{-2})	references
Ir-C≡	1.0 M KOH	-7	300	1.495	~40	This work
	0.5 M H_2SO_4	-43	256	1.473		
Ir@NG-750	0.5 M H_2SO_4	-19	303	1.54	11.5	21
	1.0 M KOH	-43	270	1.51		
Co@Ir/NC	0.5 M H_2SO_4	-29.4	n/a	n/a	357	37
	1.0 M KOH	-121	280	1.631		
IrNi	0.1 M KOH	-30	270		12.5	3
	0.1 M $HClO_4$	-30	280	n/a		

	0.5 M H_2SO_4	n/a	n/a	1.58		
CB(6)-Ir	0.5 M H_2SO_4	-54	270	1.56	20	22
CuIr nanocages	0.05 M H_2SO_4	n/a	286	n/a	n/a	34
Co-doped IrCu	0.1 M $HClO_4$	n/a	293	n/a	20	28
3D Ir	1 M KOH	n/a	245	n/a	11.5	31
	0.1 M KOH		296			
	0.1 M $HClO_4$		276			
$IrO_x/SrIrO_3$	0.5 M H_2SO_4	n/a	290	n/a	n/a	62
Ir/Au	0.1 M H_2SO_4	n/a	410	n/a	n/a	29
IrNiCu	0.1 M $HClO_4$	n/a	300	n/a	20	18
IrCo NPs	0.5 M H_2SO_4	-24	270	1.55	18.9	33

IrW	0.1 M H_2SO_4	-16	271	1.58	60	36
	0.1 M KOH	-29	281	1.6		
	1 M PBS	-35	326	1.73		
AuCu@IrNi	0.5 M H_2SO_4	n/a	n/a	1.585	100	63
	0.1 M $HClO_4$	-12.7	308	n/a		
3D IrNiCo	0.1 M $HClO_4$	n/a	220	n/a	250	23
	0.1 M KOH	n/a	190	n/a		
	PBS	n/a	290	n/a		
IrP_2@NC	0.5 M H_2SO_4	-8	n/a	n/a	n/a	38
	1.0 M KOH	-28	n/a	n/a		
IrP	0.1 M $HClO_4$		-260		230	32

Ir/GF	0.5 M H_2SO_4	-7	290	1.55		19
IrNSs	0.5 M H_2SO_4	n/a	240	n/a	137	30
IrO_2	0.5 M H_2SO_4	n/a	313	n/a	250	64

With such remarkable activities towards both HER and OER, the Ir-C≡ nanoparticles can be used as effective bifunctional catalysts for full water splitting, as demonstrated by the production of a large number of bubbles on both the cathode and anode. From Figure 6e, the E_{10} can be estimated to be merely 1.495 V, which is 54 mV lower than that of commercial Ir/C. In fact, Ir-C≡ outperformed a large number of Ir-based bifunctional catalysts for full water splitting in alkaline media that were reported recently in the literature (Table 1). Notably, the Ir-C≡ catalysts also exhibited excellent stability. Figure 6f depicts the current profiles of full water splitting during continuous operation for 20 h. One can see that about 93% of the initial current density was retained with Ir-C≡, markedly higher than that (76%) for commercial Ir/C, suggesting enhanced long-term stability of the former. Indeed, the Ir-C≡ sample exhibited virtually no change of the current-voltage profiles before and after the stability test, whereas a drastic anodic shift was observed for Ir/C (Figure 9).

Remarkably, the Ir-C≡ nanoparticles also exhibited a markedly better performance towards both HER and OER in acidic media than others in the series (Figure 10-12).

For HER in 0.5 M H_2SO_4, the $\eta_{10,HER}$, Tafel slope, and R_{ct} were the lowest for Ir-C≡ at -33 mV, 26 mV dec^{-1}, and 8.3 Ω, in comparison to -55 mV, 28 mV dec^{-1}, and 39.3 Ω for commercial Ir/C, -98 mV, 67 mV dec^{-1}, and 122.0 Ω for Ir=N, and -154 mV, 90 mV dec^{-1}, and 278.1 Ω for Ir-S. Similarly, for OER in 0.5 M H_2SO_4, Ir-C≡ exhibited an $\eta_{10,OER}$ of +256 mV, a Tafel slope of 55 mV dec^{-1} and an R_{ct} of 4.8 Ω, a performance much better than those of commercial Ir/C (+291 mV, 55 mV dec^{-1} and 7.1 Ω), Ir=N (+268 mV, 52 mV dec^{-1} and 8.3 Ω), and Ir-S (+417 mV, 104 mV dec^{-1} and 28.0 Ω). In addition, using Ir-C≡ as bifunctional catalysts for acidic electrochemical water splitting, the E_{10} was only 1.473 V, 88 mV lower than that of commercial Ir/C (1.561 V), and more than 80% of the initial current density was retained after 8 h's continuous operation, in comparison to an almost 90% loss with commercial Ir/C. The enhanced stability of Ir-C≡ over Ir/C is also clearly manifested by comparing the polarization curves before and after the stability tests (Figure 13). From these results, one can see that Ir-C≡ can indeed serve as a high-performance bifunctional catalyst towards electrochemical water splitting in both acidic and alkaline media (Table 1).

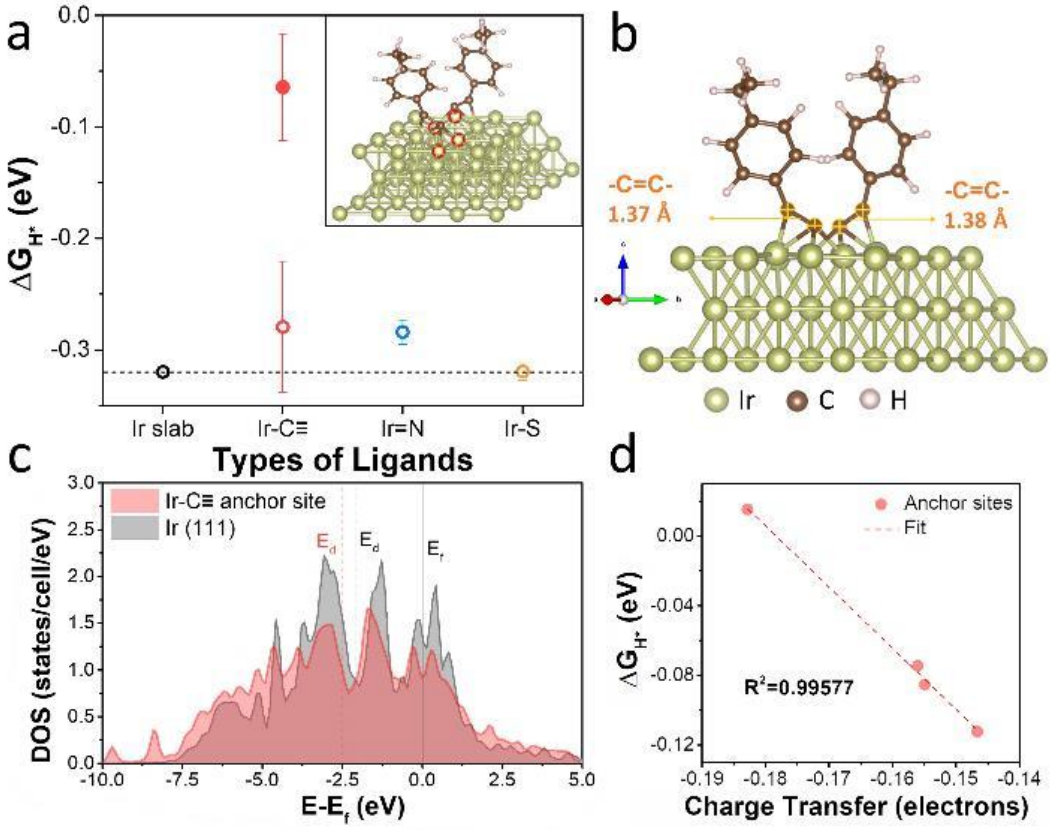

Figure 14. DFT calculation results of HER. (a) Averaged Gibbs free energy of H* adsorption (ΔG_{H^*}) on ligand-anchoring Ir atoms (solid spheres) and the neighboring Ir atoms (hollow spheres) in different organically modified Ir(111) slabs and bare Ir(111) slab. Error bars reflect variations among similar sites. Inset shows the relaxed Ir-C≡ structure and the ligand-anchoring Ir atoms circled in red. (b) Structural configuration of the relaxed Ir-C≡ model. (c) PDOS and d band center (E_d) of ligand-anchoring Ir and bare Ir(111). (d) Linear correlation between the charge transfer from ligand-anchoring Ir atoms to the ligand and their ΔG_{H^*}. The four data points are for the adsorption sites highlighted in panel (a).

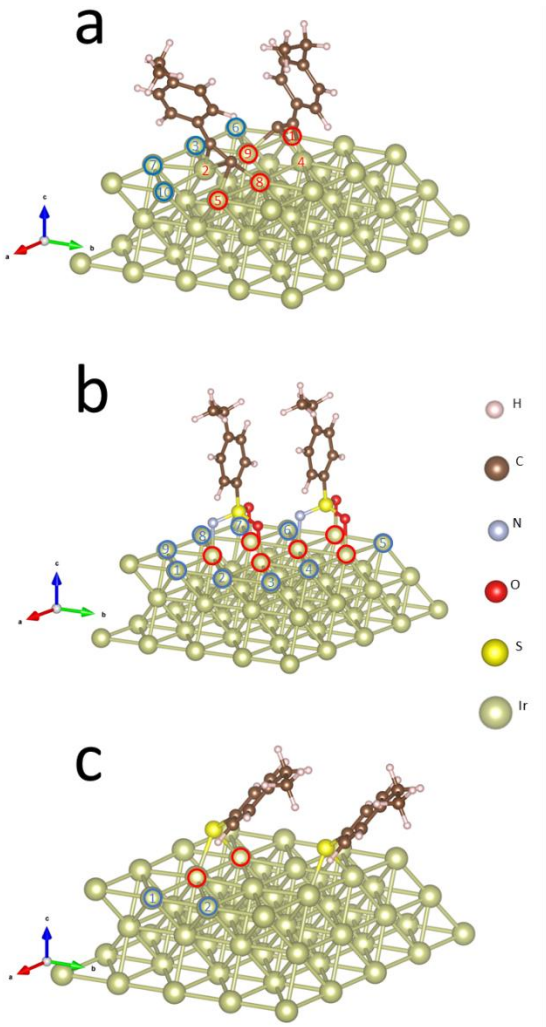

Figure 15. H adsorption sites (ligand-anchoring Ir sites, red circles; neighboring Ir sites, blue circles) in (a) Ir-C≡, (b) Ir=N, and (c) Ir-S. Note that in H* adsorption calculations, to benchmark the three models, non-monodentate adsorption sites are excluded; and for Ir-S, the sites under the phenyl ring are not considered because of steric effect. The atom numbers here correspond to those in the parentheses of Table 2.

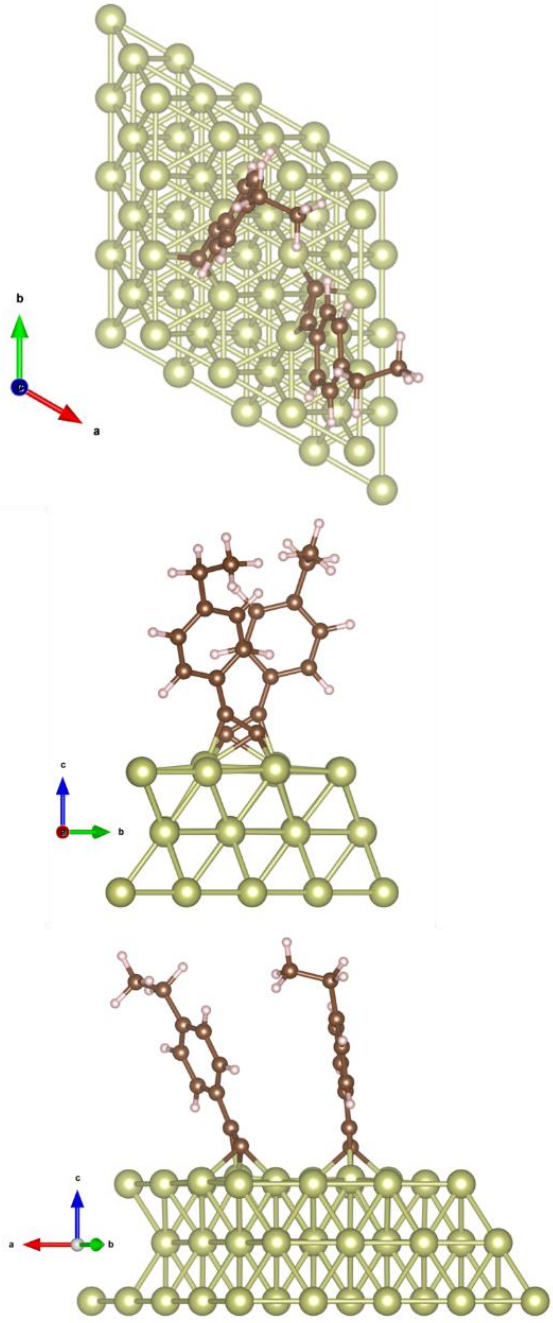

Figure 16. Top and side views of the Ir-C≡ slab.

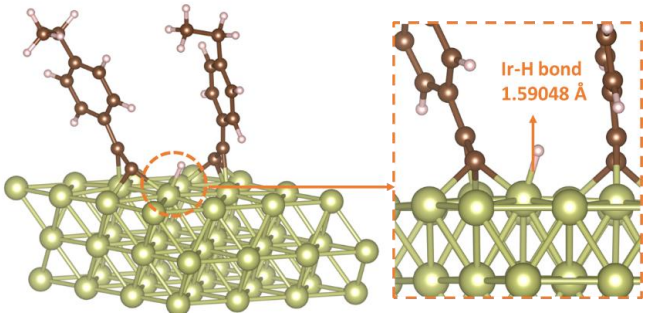

Figure 17. Optimal site in the Ir-C≡ slab for H adsorption, corresponding to site 8 in Figure 15.

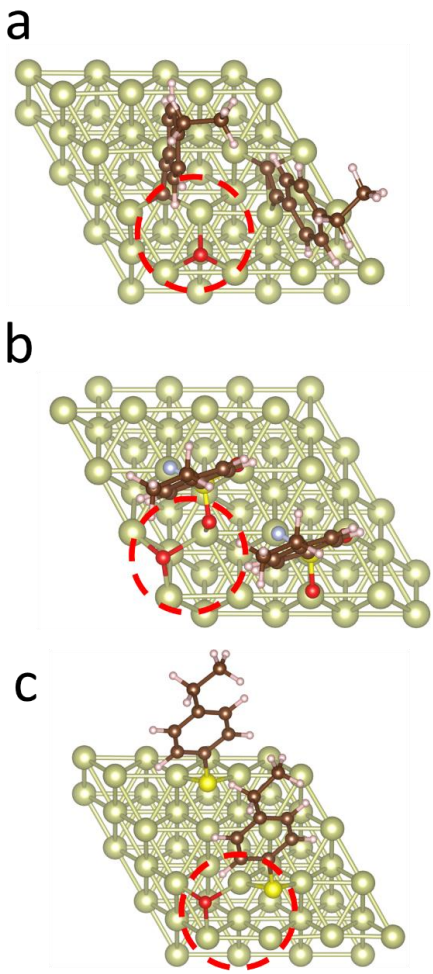

Figure 18. Tridentate adsorption of O* (circled in red) on (a) Ir-C≡, (b) Ir=N, (c) and Ir-S slabs.

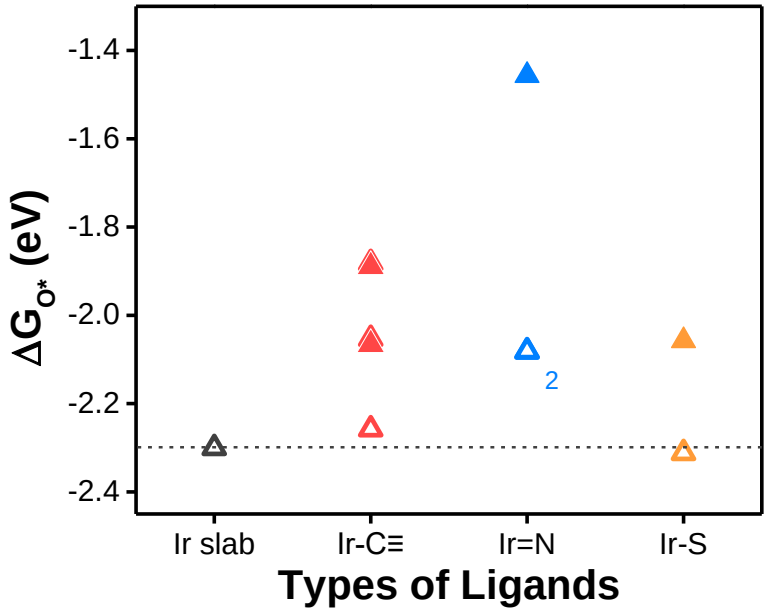

Figure 19. Gibbs free energy of O* adsorption (ΔG_{O^*}) for each model. Note that in O* adsorption calculation, to benchmark the three models, non-tridentate adsorption sites are excluded; and for Ir-S, the sites under the phenyl ring are not considered because of steric hindrance.

Table 2. Gibbs free energy of H* adsorption (ΔG_{H^*}) on bare Ir(111) slab and on ligand-anchoring Ir atoms (blue data points) and their neighboring Ir atoms in different organically capped slabs (the numbers in the red parentheses are the corresponding atoms shown in Figure 15).

	ΔG_{H^*} (eV)					average ΔG_{H^*} (eV)
bare slab	-0.31989					-0.31989

Ir-C≡	-0.34515(10)	-0.18519(7)	-0.30398(3)	-0.28365(6)		-0.27949 ± 0.05878
	-0.08569(9)	-0.07487(5)	-0.11278(1)	0.01513(8)		-0.06455 ± 0.04803
Ir=N	-0.26059(5)	-0.28896(6)	-0.29722(7)	-0.2753(8)	-0.28383(9)	-0.28404 ± 0.01093
	-0.28392(1)	-0.27886(2)	-0.2978(3)	-0.28989(4)		
Ir-S	-0.31166(1)	-0.32711(2)				-0.31939 ± 0.00773

Table 3. Bader charge calculations of ligand-anchoring Ir sites (bold fonts) and neighboring Ir sites (not bold) on Ir-C≡, as specified in Figure 15.

Ir atom number	Charge with ligands (e)	Charge without ligand (e)	Charge transfer (e)
1	**14.89466**	**15.0411**	**-0.14644**
2	**14.85723**	**15.04027**	**-0.18304**

3	15.05838	15.04811	0.010272
4	**14.85255**	**15.0555**	**-0.20296**
5	**14.8955**	**15.05135**	**-0.15585**
6	15.01694	15.02026	-0.00332
7	15.08258	15.04198	0.040595
8	**14.87658**	**15.05934**	**-0.18276**
9	**14.92141**	**15.07618**	**-0.15477**
10	15.05699	15.05161	0.005381

To unravel the mechanistic insights into the remarkably enhanced electrocatalytic performance by organic capping ligands, ΔG_{H^*}, a commonly used descriptor of HER activity, was calculated using the models consisting of an Ir(111) slab capped with varied organic ligands (Figure 4c). As the interfacial charge transfer was mostly confined between the organic ligands and the ligand-anchoring and neighboring Ir sites, only these sites were considered for H adsorption (which are marked in Figure 15), and the corresponding ΔG_{H^*} calculated. Meanwhile, monodentate adsorption of H* was adopted in this study, due to the high H* coverage, as manifested in Tafel analysis (Figure 6b).[65] From Figure 14a, one can see that $|\Delta G_{H^*}|$ is very large at ca. 0.320 eV on the bare Ir(111) slab, consistent with the limited HER activity of Ir/C, and becomes slightly lower (0.279 ± 0.059 eV) for the Ir sites neighboring ligand anchoring, whereas for the ligand-anchoring Ir sites, the $|\Delta G_{H^*}|$ is drastically diminished to only 0.064 ± 0.048 eV (Table 2), suggesting that the latter sites (inset to Figure 14a) are most likely

responsible for the remarkable HER activity observed above (Figure 6 and 10). It should be noted that, upon the binding of the acetylene ligand onto the Ir slab, the -C≡C- bond length increased from ca. 1.2 Å to 1.38 Å (Figure 14b and 16). Such a decrease of the bond order is consistent with the intraparticle charge delocalization arising from the conjugated interfacial bonds.[39,44,66,67] By contrast, a very consistent ΔG_{H^*} was observed at the neighboring Ir sites when the Ir slab was capped with either mercapto or nitrene ligands (Table 2), which was estimated to be -0.319 ± 0.007 eV for Ir-S, and decreased slightly to -0.284 ± 0.010 eV for Ir=N (note that no stable adsorption of H can be observed on the ligand-anchoring Ir sites of Ir=N or Ir-S, data not shown). Overall, the fact that $|\Delta G_{H^*}|$ varies in the order of Ir-C≡ < Ir=N < Ir-S is in excellent agreement with the variation of the HER activity observed experimentally in both acidic and alkaline media (Figure 6 and 10).

The weakened H* adsorption (i.e., diminished $|\Delta G_{H^*}|$) observed with the Ir-C≡ ligand anchoring sites is also manifested in the shift of the d band center (E_d) to -2.59 eV from -2.08 eV of the bare Ir(111) slab, as shown in Figure 4c. Additionally, an apparent electron loss occurs from these ligand anchoring Ir sites to the acetylene moieties (> 0.14 electrons), while the charge density of neighboring Ir sites remains mostly unchanged (Table 3). Notably, such a trend of electron loss is consistent with their ΔG_{H^*} variation. Figure 14d shows the ΔG_{H^*} and interfacial charge transfer of the four different Ir anchoring sites in Ir-C≡ that are highlighted in the inset to Figure 14a, where the excellent linear relationship ($R^2 = 0.996$) suggests a strong correlation between the intrinsic HER activity and change of local charge density. One of these ligand-

anchoring Ir sites is highlighted in Figure 17 and exhibits an extremely low $|\Delta G_{H^*}|$ of only 0.015 eV. Taken together, these results suggest that the ligand-anchoring Ir atoms in Ir-C≡ were most likely responsible for the remarkable HER performance.

To understand the mechanistic origin of the enhanced OER performance, the Gibbs free energy of O* adsorption (ΔG_{O^*}) were calculated to examine the interaction between Ir and O species. Interestingly, O* tends to adsorb onto the various Ir slabs in a tridentate mode with one of the Ir sites also bonded to the organic ligand (Figure 18), and the corresponding ΔG_{O^*} on the ligand-anchoring Ir atoms shows an apparent difference, as compared to that on the bare Ir(111) slab (Figure 19), -1.457 eV for Ir=N, -1.881 eV for Ir-C≡, -2.058 eV for Ir-S, and -2.300 eV for Ir(111). This implies that the capping ligands effectively stabilize the Ir nanoparticles against oxidation, and the stabilization varies in the order of Ir=N > Ir-C≡ > Ir-S > Ir(111).[27] This is consistent with the metal-to-ligand charge transfer observed in both XPS and DFT measurements (Figure 4).[22] As mentioned earlier, low-valence Ir is preferred for OER.[26,68] Thus, Ir=N and Ir-C≡ are expected to have a better OER performance than Ir-S and Ir/C, in good agreement with results from experimental measurements (Figure 6 and 10).

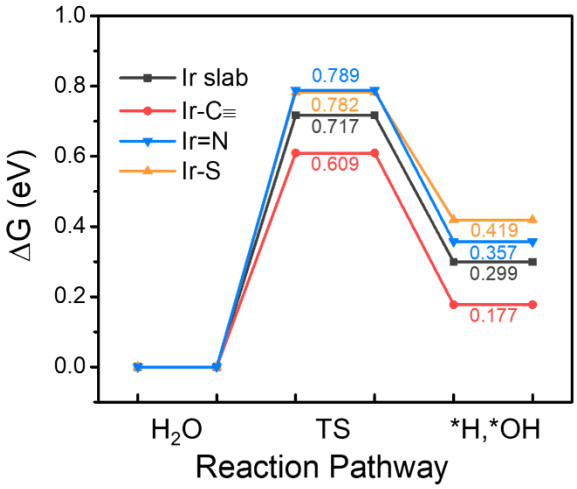

Figure 20. Free energy diagram of water dissociation on Ir(111), Ir-C≡, Ir=N, and Ir-S (Figure 19). TS denotes transition state. The initial states (H_2O) of all samples are set to zero for comparison of their reaction energy barriers.

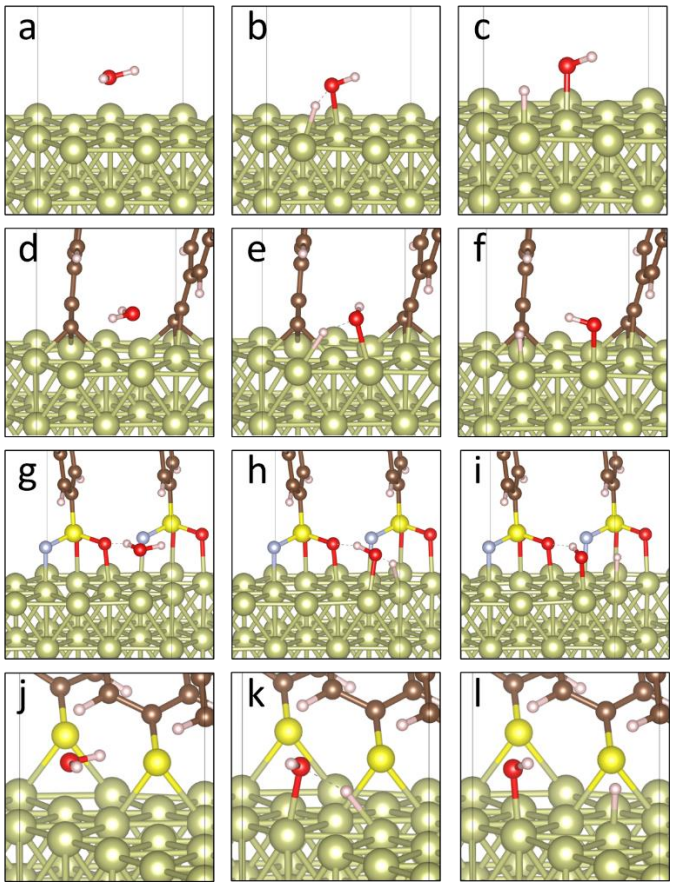

Figure 21. Reaction pathway of water dissociation on (a-c) Ir(111), (d-f) Ir-C≡, (g-i) Ir=N, and (j-l) Ir-S. Water molecules first approach to Ir atoms (a, d, g, j) and become dissociated into *H and *OH intermediates (b, e, h, k), which are then adsorbed vertically onto two neighboring Ir atoms (c, f, i, l).

To gain further mechanistic insights, the reaction barrier of water dissociation, which has been recognized as a critical rate-determining step in OER,[69] was calculated by using the nudged elastic band (NEB) method.[70,71] From Figure 21, one can see that the reaction pathway is similar on Ir-C≡, Ir=N, Ir-S, and Ir(111), where water molecules approach the Ir surface and become dissociated into *H and *OH, and the intermediates are adsorbed onto two neighboring Ir atoms in a vertical configuration. The corresponding reaction free energy diagrams of water dissociation are shown in Figure 20, where Ir-C≡ can be seen to exhibit an energy barrier of only 0.609 eV, markedly lower than those of Ir=N (0.789 eV), Ir-S (0.782 eV) and Ir(111) slab (0.717 eV). This suggests that Ir-C≡ is the most efficient in water dissociation among the series of samples, in excellent agreement with experimental findings (Figure 6 and 10).

7.4 Conclusion

In summary, when Ir nanoparticles were functionalized with acetylene derivatives, the conjugated metal-ligand interfacial bonding interactions were found to lead to effective charge transfer from the Ir core to the acetylene moieties, which significantly enhanced the HER and OER activity in both acidic and alkaline media, due to weakened binding of H and O intermediates, in comparison to leading results of relevant catalysts reported recently in the literature. Of particular note is that the alkaline HER and OER activity

was even better than those of commercial Ir/C and Pt/C benchmarks. Indeed the acetylene-functionalized Ir nanoparticles could be used as effective bifunctional catalysts for full water splitting and significantly outperformed commercial benchmarks. Note that the enhancement was lesser with Ir nanoparticles capped with other ligands such as mercapto and nitrene derivatives, due to limited interfacial charge transfer. Consistent results were obtained in DFT calculations. Results from this study highlight the significance of deliberate interfacial engineering in the manipulation of the electronic properties of metal nanoparticles and hence their electrocatalytic activity towards important reaction in electrochemical energy technologies.

7.5 Experimental Section

Chemicals

Iridium(III) chloride ($IrCl_3$, 53-56%, Arcos), 1,2-propanediol (>99.5%, Acros), sodium acetate trihydrate ($NaOAc \cdot 3H_2O$, MC&B), 4-ethylphenylacetylene (EPA, 97%, Arcos), 4-ethylphenylthiol (EPT, >97%, TCI America), and 4-dodecylbenzenesulfonyl azide (DBSA, >88%, Aldrich) were used as received. Solvents were purchased from typical commercial sources and used without further purification. Water was purified by a Barnstead Nanopure water system (18.3 MΩ·cm).

Nanoparticle synthesis

Organically capped iridium nanoparticles were synthesized by adopting a procedure reported previously.[43,44] Briefly, 0.15 mmol of $IrCl_3$ and 86 mg of $NaOAc \cdot 3H_2O$ were dissolved in 100 mL of 1,2-propanediol under sonication. After refluxing at 165 °C under vigorous stirring for 2 h, the solution color was found to become dark brown,

signifying the formation of Ir nanoparticles. After the solution was cooled down to 60 °C, select organic ligands were added for surface functionalization. Specifically, for EPA and EPT surface functionalization, 4.5 mmol of EPA or EPT in 25 mL of toluene was added into the above Ir nanoparticle solution under refluxing overnight. The Ir nanoparticles were found to transfer to the toluene phase, which was collected with a separatory funnel and washed by methanol for 5 times, affording purified nanoparticles that were denoted as Ir-C≡ and Ir-S for EPA and EPT functionalized Ir nanoparticles, respectively.

To prepare nitrene-functionalized Ir (Ir=N) nanoparticles,[48] 0.56 mmol of DBSA and 20 mL of *sec*-butylbenzene were added into the Ir nanoparticles solution at 60 °C under magnetic stirring for 1 h. The azide ligands were adsorbed on the nanoparticle surface resulting in the transfer of the nanoparticles to the *sec*-butylbenzene phase. The *sec*-butylbenzene phase was then collected and refluxed for 24 h at 165 °C, where nitrene radicals were generated by thermolysis of the azide moiety and attached onto the Ir nanoparticle surface forming Ir=N interfacial bonds. The nanoparticles were then collected and rinsed with acetonitrile for 5 times.

Characterizations

TEM images were acquired with a Philips CM 300 operated at 300 kV. FTIR spectra were collected with a Perkin Elmer FTIR spectrometer (Spectrum One), where the samples were prepared by drop-casting the nanoparticle solutions in DCM onto a NaCl disk. UV-vis absorption measurements were carried out with a Perkin Elmer Lambda 35 UV-vis spectrometer, and the photoluminescence studies were performed with a PTI

fluorospectrometer. XPS measurements were carried out with a Phi X-tool XPS instrument, where the binding energy was calibrated against that of C 1s.

Electrochemistry

The electrocatalytic performance of the organically capped Ir nanoparticles towards HER and OER was examined in a three-electrode system with a CHI 760E Electrochemical Workstation, where a Ag/AgCl (1 M KCl) was used as the reference electrode and a graphite rod as the counter electrode. The Ag/AgCl electrode were calibrated against a reversible hydrogen electrode (RHE) and all potentials in the present study were referenced to this RHE. Catalyst inks were prepared by adding 1 mg of the Ir nanoparticles prepared above and 4 mg of carbon black (Vulcan XC-72R) into a mixture of toluene (500 μL), isopropanol (490 μL), and 100 % Nafion (10 μL). 10 μL of the catalyst ink was then dropcast onto the surface of a clean glassy carbon electrode (geometric surface area 0.246 cm^2) at a catalyst loading of ~40 μg_{IrNPs} cm^{-2}. Commercial 20% Ir/C was used as the benchmark catalyst and loaded on the glassy carbon electrode in the same fashion at the mass loading of 40 μg_{Ir} cm^{-2}.

Linear sweep voltammograms (LSV) were collected in both 1 M KOH and 0.5 M H_2SO_4 at the potential scanning rate of 10 mV s^{-1} and 90% iR compensation. EIS studies were performed within the frequency range of 0.1 Hz to 100 kHz, at the potential of -50 mV for HER and +1.55 V for OER in 0.5 M H_2SO_4, and -100 mV for HER and +1.55 V for OER in 1 M KOH.

Full water splitting was performed in a two-electrode system, where the Ir nanoparticles prepared above were used as both the anode and cathode catalysts at the mass loading

of ~0.7 mg_{IrNPs} cm^{-2}. As a comparison, commercial Ir/C electrodes at the same mass loading were prepared. The current-voltage curves were collected at the potential scanning rate of 10 mV s^{-1}. Durability tests were carried out by chronoamperometric (CA) measurements for 20 h at the respective E_{10}, where the electrolytes were replaced after 10 h.

Theoretical study

First-principles computations were performed using Quantum ESPRESSO, an open-source plane-wave code.[72] A 4 × 4 unit cell with 48 atoms was used to build an Ir(111) slab supercell, where periodic image interactions were removed by setting a vacuum of 14 Å. A cutoff of 40 and 240 Ry for kinetics and charge density was chosen with the ultrasoft pseudopotential.[73] The total energy of the Monkhorst−Pack 3 × 3 × 1 K-point grid in the supercell was calculated at the convergence level of 1 meV per atom. The smearing parameter was set at 0.01 Ry in the Marzari Vanderbilt smearing for all calculations.[74] For geometric relaxation, the convergence was 10^{-8} Ry of the electronic energy and 10^{-4} au for the total force. The dipole correction was added by applying a finite field to the bare ionic potential for all calculations involving ligand modification. Density functional perturbation theory[75] was employed to calculate the phonon frequency as inputs for entropy and zero-point energy. The implicit solvation energy correction was applied with the solvation model CANDLE[76] that has been shown to be suitable for various surfaces, with the open source code JDFTx.[77,78] The energy barrier calculation was carried out by using the NEB method.[70,71]

7.6 Reference

1. S. Chen, S.-Z. Qiao. *ACS Nano* **2013**, *7*, 10190-10196.

2. Z. Wu, Z. Wang, F. Geng. *ACS Appl Mater Interface* **2018**, *10*, 8585-8593.

3. Y. C. Pi, Q. Shao, P. T. Wang, J. Guo, X. Q. Huang. *Adv Funct Mater* **2017**, *27*, 1700886.

4. H.-X. Zhong, J. Wang, Q. Zhang, F. Meng, D. Bao, T. Liu, X.-Y. Yang, Z.-W. Chang, J.-M. Yan, X.-B. Zhang. *Adv Sustain Syst* **2017**, *1*, 1700020.

5. Y. Peng, E. Y. Hirata, W. Z. Pan, L. M. Chen, J. E. Lu, S. W. Chen. *Chin J Chem Phys* **2018**, *31*, 433-438.

6. B. You, Y. J. Sun. *Acc Chem Res* **2018**, *51*, 1571-1580.

7. P. Z. Chen, Y. Tong, C. Z. Wu, Y. Xie. *Acc Chem Res* **2018**, *51*, 2857-2866.

8. J. Zhang, Q. Y. Zhang, X. L. Feng. *Adv Mater* **2019**, *31*, 1808167.

9. Z. Li, W. Niu, Z. Yang, A. Kara, Q. Wang, M. Wang, M. Gu, Z. Feng, Y. Du, Y. Yang. *Energ Environ Sci* **2020**, *13*, 3110-3118.

10. Q. Yao, B. L. Huang, N. Zhang, M. Z. Sun, Q. Shao, X. Q. Huang. *Angew Chem Int Ed* **2019**, *58*, 13983-13988.

11. N. Mamaca, E. Mayousse, S. Arrii-Clacens, T. W. Napporn, K. Servat, N. Guillet, K. B. Kokoh. *Appl Catal B-Environ* **2012**, *111*, 376-380.

12. N. M. AlYami, A. P. LaGrow, K. S. Joya, J. Hwang, K. Katsiev, D. H. Anjum, Y. Losovyj, L. Sinatra, J. Y. Kim, O. M. Bakr. *Phys Chem Chem Phys* **2016**, *18*, 16169-16178.

13. N. C. Cheng, S. Stambula, D. Wang, M. N. Banis, J. Liu, A. Riese, B. W. Xiao, R. Y. Li, T. K. Sham, L. M. Liu, G. A. Botton, X. L. Sun. *Nat Commun* **2016**, *7*, 13638.

14. Y. Zheng, Y. Jiao, Y. H. Zhu, L. H. Li, Y. Han, Y. Chen, M. Jaroniec, S. Z. Qiao. *J Am Chem Soc* **2016**, *138*, 16174-16181.

15. J. Mahmood, F. Li, S. M. Jung, M. S. Okyay, I. Ahmad, S. J. Kim, N. Park, H. Y. Jeong, J. B. Baek. *Nat Nanotechnol* **2017**, *12*, 441-446.

16. Y. H. Han, Y. G. Wang, W. X. Chen, R. R. Xu, L. R. Zheng, J. Zhang, J. Luo, R. A. Shen, Y. Q. Zhu, W. C. Cheong, C. Chen, Q. Peng, D. S. Wang, Y. D. Li. *J Am Chem Soc* **2017**, *139*, 17269-17272.

17. T. J. Qiu, Z. B. Liang, W. H. Guo, S. Gao, C. Qu, H. Tabassum, H. Zhang, B. J. Zhu, R. Q. Zou, Y. Shao-Horn. *Nano Energy* **2019**, *58*, 1-10.

18. J. Park, Y. J. Sa, H. Baik, T. Kwon, S. H. Joo, K. Lee. *ACS Nano* **2017**, *11*, 5500-5509.

19. J. Zhang, G. Wang, Z. Q. Liao, P. P. Zhang, F. X. Wang, X. D. Zhuang, E. Zschech, X. L. Feng. *Nano Energy* **2017**, *40*, 27-33.

20. Q. Xue, W. Gao, J. Y. Zhu, R. L. Peng, Q. Z. Xu, P. Chen, Y. Chen. *J Colloid Interf Sci* **2018**, *529*, 325-331.

21. X. J. Wu, B. M. Feng, W. Li, Y. L. Niu, Y. A. Yu, S. Y. Lu, C. Y. Zhong, P. Y. Liu, Z. Q. Tian, L. Chen, W. H. Hu, C. M. Li. *Nano Energy* **2019**, *62*, 117-126.

22. H. H. You, D. S. Wu, Z. N. Chen, F. F. Sun, H. Zhang, Z. H. Chen, M. N. Cao, W. Zhuang, R. Cao. *Acs Energy Lett* **2019**, *4*, 1301-1307.

23. Y. Zhao, M. Luo, S. F. Chu, M. Peng, B. Y. Liu, Q. L. Wu, P. Liu, F. M. F. de Groot, Y. W. Tan. *Nano Energy* **2019**, *59*, 146-153.

24. J. K. Norskov, T. Bligaard, A. Logadottir, J. R. Kitchin, J. G. Chen, S. Pandelov, J. K. Norskov. *J Electrochem Soc* **2005**, *152*, J23-J26.

25. Y. Jiao, Y. Zheng, M. T. Jaroniec, S. Z. Qiao. *Chem Soc Rev* **2015**, *44*, 2060-2086.

26. T. Li, O. Kasian, S. Cherevko, S. Zhang, S. Geiger, C. Scheu, P. Felfer, D. Raabe, B. Gault, K. J. J. Mayrhofer. *Nat Catal* **2018**, *1*, 300-305.

27. M. M. Montemore, M. A. van Spronsen, R. J. Madix, C. M. Friend. *Chem Rev* **2018**, *118*, 2816-2862.

28. T. Kwon, H. Hwang, Y. J. Sa, J. Park, H. Baik, S. H. Joo, K. Lee. *Adv Funct Mater* **2017**, *27*, 1604688.

29. S. H. Ahn, H. Y. Tan, M. Haensch, Y. H. Liu, L. A. Bendersky, T. P. Moffat. *Energ Environ Sci* **2015**, *8*, 3557-3562.

30. B. Jiang, Y. N. Guo, J. Kim, A. E. Whitten, K. Wood, K. Kani, A. E. Rowan, J. Henzie, Y. Yamauchi. *J Am Chem Soc* **2018**, *140*, 12434-12441.

31. Y. C. Pi, N. Zhang, S. J. Guo, J. Guo, X. Q. Huang. *Nano Lett* **2016**, *16*, 4424-4430.

32. L. S. Yin, T. Yang, X. R. Ding, M. S. He, W. X. Wei, T. T. Yua, H. Zhaoa. *Electrochem Commun* **2018**, *94*, 59-63.

33. X. C. Sun, F. Liu, X. Chen, C. C. Li, J. Yu, M. Pan. *Electrochim Acta* **2019**, *307*, 206-213.

34. C. Wang, Y. M. Sui, G. J. Xiao, X. Y. Yang, Y. J. Wei, G. T. Zou, B. Zou. *J Mater Chem A* **2015**, *3*, 19669-19673.

35. J. W. Zhu, Z. H. Lyu, Z. T. Chen, M. H. Xie, M. F. Chi, W. Q. Jin, Y. N. Xia. *Chem Mater* **2019**, *31*, 5867-5875.

36. L. H. Fu, X. Hu, Y. B. Li, G. Z. Cheng, W. Luo. *Nanoscale* **2019**, *11*, 8898-8905.

37. D. L. Li, Z. Zong, Z. H. Tang, Z. Liu, S. W. Chen, Y. Tian, X. F. Wang. *Acs Sustain Chem Eng* **2018**, *6*, 5105-5114.

38. Z. H. Pu, J. H. Zhao, I. S. Amiinu, W. Q. Li, M. Wang, D. P. He, S. C. Mu. *Energ Environ Sci* **2019**, *12*, 952-957.

39. P. G. Hu, L. M. Chen, X. W. Kang, S. W. Chen. *Acc Chem Res* **2016**, *49*, 2251-2260.

40. Q. Tang, D. E. Jiang. *Chem Mater* **2017**, *29*, 6908-6915.

41. Z. Y. Zhou, X. W. Kang, Y. Song, S. W. Chen. *J Phys Chem C* **2012**, *116*, 10592-10598.

42. P. Hu, L. Chen, C. P. Deming, J. E. Lu, L. W. Bonny, S. Chen. *Nanoscale* **2016**, *8*, 12013-21.

43. P. G. Hu, L. M. Chen, C. P. Deming, X. W. Kang, S. W. Chen. *Angew Chem Int Ed* **2016**, *55*, 1455-1459.

44. X. W. Kang, N. B. Zuckerman, J. P. Konopelski, S. W. Chen. *J Am Chem Soc* **2012**, *134*, 1412-1415.

45. X. Wang, J. Zhuang, Q. Peng, Y. D. Li. *Nature* **2005**, *437*, 121-124.

46. J. A. Creighton, D. G. Eadon. *J Chem Soc-Faraday Trans* **1991**, *87*, 3881-3891.

47. P. G. Hu, L. M. Chen, C. P. Deming, L. W. Bonny, H. W. Lee, S. W. Chen. *Chem Commun* **2016**, *52*, 11631-11633.

48. X. W. Kang, Y. Song, S. W. Chen. *J Mater Chem* **2012**, *22*, 19250-19257.

49. C. P. Deming, X. W. Kang, K. Liu, S. W. Chen. *Sensor Actuat B-Chem* **2014**, *194*, 319-324.

50. T. S. Marinova, K. L. Kostov. *Surf Sci* **1987**, *181*, 573-585.

51. F. H. B. Lima, J. Zhang, M. H. Shao, K. Sasaki, M. B. Vukmirovic, E. A. Ticianelli, R. R. Adzic. *J Phys Chem C* **2007**, *111*, 404-410.

52. V. R. Stamenkovic, B. Fowler, B. S. Mun, G. F. Wang, P. N. Ross, C. A. Lucas, N. M. Markovic. *Science* **2007**, *315*, 493-497.

53. E. Toyoda, R. Jinnouchi, T. Hatanaka, Y. Morimoto, K. Mitsuhara, A. Visikovskiy, Y. Kido. *J Phys Chem C* **2011**, *115*, 21236-21240.

54. B. Z. Lu, L. Guo, F. Wu, Y. Peng, J. E. Lu, T. J. Smart, N. Wang, Y. Z. Finfrock, D. Morris, P. Zhang, N. Li, P. Gao, Y. Ping, S. W. Chen. *Nat Commun* **2019**, *10*, 631

55. M. Bhardwaj, R. Balasubramaniam. *Int J Hydrog Energy* **2008**, *33*, 2178-2188.

56. M. R. G. de Chialvo, A. C. Chialvo. *J Electroanal Chem* **1994**, *372*, 209-223.

57. J. Suntivich, K. J. May, H. A. Gasteiger, J. B. Goodenough, Y. Shao-Horn. *Science* **2011**, *334*, 1383-1385.

58. C. C. L. McCrory, S. H. Jung, J. C. Peters, T. F. Jaramillo. *J Am Chem Soc* **2013**, *135*, 16977-16987.

59. T. Nakagawa, C. A. Beasley, R. W. Murray. *J Phys Chem C* **2009**, *113*, 12958-12961.

60. J. H. Wang, W. Cui, Q. Liu, Z. C. Xing, A. M. Asiri, X. P. Sun. *Adv Mater* **2016**, *28*, 215-230.

61. S. Anantharaj, S. R. Ede, K. Sakthikumar, K. Karthick, S. Mishra, S. Kundu. *Acs Catal* **2016**, *6*, 8069-8097.

62. L. C. Seitz, C. F. Dickens, K. Nishio, Y. Hikita, J. Montoya, A. Doyle, C. Kirk, A. Vojvodic, H. Y. Hwang, J. K. Norskov, T. F. Jaramillo. *Science* **2016**, *353*, 1011-1014.

63. J. Park, S. Choi, A. Oh, H. Jin, J. Joo, H. Baik, K. Lee. *Nanoscale Horiz* **2019**, *4*, 727-734.

64. J. Lim, D. Park, S. S. Jeon, C. W. Roh, J. Choi, D. Yoon, M. Park, H. Jung, H. Lee. *Adv Funct Mater* **2018**, *28*.

65. C. J. Hagedorn, M. J. Weiss, W. H. Weinberg. *Phys Rev B* **1999**, *60*, 14016-14018.

66. F. Q. Zhang, J. J. Fang, L. Huang, W. M. Sun, Z. Lin, Z. Q. Shi, X. W. Kang, S. W. Chen. *Acs Catal* **2019**, *9*, 98-104.

67. J. Gao, H. Ma, X. Lv, T. Yan, N. Li, W. Cao, Q. Wei. *Anal. Chim. Acta* **2015**, *893*, 49-56.

68. X. Wu, B. Feng, W. Li, Y. Niu, Y. Yu, S. Lu, C. Zhong, P. Liu, Z. Tian, L. Chen, W. Hu, C. M. Li. *Nano Energy* **2019**, *62*, 117-126.

69. Y. Ping, R. J. Nielsen, W. A. Goddard Iii. *J Am Chem Soc* **2017**, *139*, 149-155.

70. P. Giannozzi, O. Andreussi, T. Brumme, O. Bunau, M. B. Nardelli, M. Calandra, R. Car, C. Cavazzoni, D. Ceresoli, M. Cococcioni. *J Phys Condens Matter* **2017**, *29*, 465901.

71. G. Henkelman, H. Jónsson. *J Chem Phys* **1999**, *111*, 7010-7022.

72. P. Giannozzi, S. Baroni, N. Bonini, M. Calandra, R. Car, C. Cavazzoni, D. Ceresoli, G. L. Chiarotti, M. Cococcioni, I. Dabo, A. Dal Corso, S. de Gironcoli, S. Fabris, G. Fratesi, R. Gebauer, U. Gerstmann, C. Gougoussis, A. Kokalj, M. Lazzeri, L. Martin-Samos, N. Marzari, F. Mauri, R. Mazzarello, S. Paolini, A. Pasquarello, L. Paulatto, C. Sbraccia, S. Scandolo, G. Sclauzero, A. P. Seitsonen, A. Smogunov, P. Umari, R. M. Wentzcovitch. *J Phys Condens Matter* **2009**, *21*, 395502.

73. K. F. Garrity, J. W. Bennett, K. M. Rabe, D. Vanderbilt. *Comput Mater Sci* **2014**, *81*, 446-452.

74. N. Marzari, D. Vanderbilt, A. De Vita, M. C. Payne. *Phys Rev Lett* **1999**, *82*, 3296-3299.

75. S. Baroni, S. De Gironcoli, A. Dal Corso, P. Giannozzi. *Rev Mod Phys* **2001**, *73*, 515.

76. R. Sundararaman, W. A. Goddard Iii. *J Chem Phys* **2015**, *142*, 064107.

77. S. A. Petrosyan, J.-F. Briere, D. Roundy, T. A. Arias. *Phys Rev B* **2007**, *75*, 205105.

78. Y. Ping, R. Sundararaman, W. A. Goddard Iii. *Phys Chem Chem Phys* **2015**, *17*, 30499-30509.

Chapter 8 Stable Cuprous Hydroxide Nanostructures by Organic Ligand Functionalization

8.1 Abstract

Copper compounds have been extensively investigated for diverse applications. However, studies of cuprous hydroxide (CuOH) have been scarce, due to structural metastability. Herein, a facile, wet-chemistry procedure is reported for the preparation of stable CuOH nanostructures via deliberate functionalization with select organic ligands, such as acetylene and mercapto derivatives. The resulting nanostructures are found to exhibit a nanoribbon morphology consisting of small nanocrystals embedded within a largely amorphous nanosheet-like scaffold. The acetylene derivatives are found to anchor onto the CuOH forming Cu-C≡ linkages, whereas Cu-S- interfacial bonds are formed with the mercapto ligands. Effective electronic coupling occurs at the ligand-core interface in the former, in contrast to mostly non-conjugated interfacial bonds in the latter, as manifested in spectroscopic measurements and confirmed in theoretical studies based on first principles calculations. Notably, the acetylene-capped CuOH nanostructures exhibit markedly enhanced photodynamic activity in the inhibition of bacteria growth, as compared to the mercapto-capped counterparts, due to a reduced material bandgap and effective photocatalytic generation of reactive oxygen species. Results from this study demonstrate that deliberate structural engineering with select organic ligands is an effective strategy in the stabilization and functionalization of CuOH nanostructures, a critical first step in exploring their diverse applications.

8.2 Introduction

Copper, as a multi-valence element, can form a wide range of compounds, including oxides,[1,2] hydroxides,[3,4] chalcogenides,[5,6] halides,[7,8] and some complicated salts (e.g.,

Chevreul's salt),[9] which have found diverse applications, such as catalysis,[10,11] sensing,[12,13] energy conversion,[14,15] and optics.[16] Amongst these, cuprous oxide (CuOH) has long been attracting extensive interest.[17,18] Back in the early 1900s, Miller and Gillett observed that when a NaCl solution was electrolyzed with copper working electrodes at low temperatures (below 60 °C), yellow CuOH precipitates were produced.[19,20] Subsequently, several studies were conducted to investigate the characteristic structure and properties of CuOH synthesized via various methods.[21-23] Nevertheless, in these early studies, CuOH was mostly in the bulk solid form and structurally metastable, where the yellowish precipitates would rapidly change the color appearance to dark red, signifying the formation of Cu_2O, upon exposure to the ambient or thermal treatment, due to the lack of proper protection from oxidation and/or dehydration. Such structural instability makes it difficult to study the properties and applications of the obtained CuOH. In 2012, Korzhavyi et al.[24] carried out theoretical studies and demonstrated that CuOH could exist in a solid form; yet the metastability led to the formation of a random mixture of various configurations in the crystal structure, such as Cu_2O and ice VII H_2O. Soroka et al.[25] found that solid-state CuOH could indeed be produced, most likely in the hydrated form of $CuOH \times H_2O$ as an intermediate product of Cu_2O. In a combined theoretical and experimental study,[26] Korzhavyi's group showed that the ground-state structure of CuOH(s) consisted of both one-dimensional polymeric $(CuOH)_n$ chains and two-dimensional trilayer units, suggesting the possibility of nanosheet production. In addition, density functional theory (DFT) calculations have showed that CuOH is a semiconductor with a wide

bandgap of 3.03 eV (or 2.73 eV in a cation-disorder form), suggestive of its potential optical/photocatalytic applications. However, it should be recognized that, to the best of our knowledge, thus far there has been no success in the experimental preparation of stable CuOH nanostructures.

Organic ligands have been widely used in the surface functionalization and stabilization of metals and metal oxides,[27,28] hydroxides,[29] and chalcogenides.[30,31] For their nanoparticles, select organic ligands can be exploited for the manipulation of the shape,[32,33] size distribution,[34-36] and crystalline facets.[37] Significantly, with the protection of such an organic shell, not only the structural stability can be markedly enhanced,[38] new optical, electronic, and catalytic properties may also emerge, due to the unique interfacial interactions.[28,39,40] Thus, one immediate question arises: Can stable CuOH nanostructures be obtained by deliberate functionalization with select organic ligands? This is the primary motivation of the present study, where we demonstrate an effective strategy to synthesize stable CuOH nanostructures by surface functionalization with acetylene and mercapto derivatives.[28,39,40]

Specifically, for the first time ever, stable CuOH nanostructures were prepared by a facile wet-chemistry method. Experimentally, sulfite ions (SO_3^{2-}) were exploited as the reducing agent and added into a Cu^{2+} solution in a mixture of organic solvents in the presence of select acetylene and mercapto derivatives, with 4-ethylphenyacetylene (EPA), 1-hexadecyne (HC16) and 4-ethylphenylthiol (EPT) as the illustrating examples. The two acetylene derivatives were chosen as prior studies have shown that alkyne ligands may impart unique electrical and optical properties to metal/metal oxide

nanoparticles owing to the conjugated interfacial linkage that leads to intraparticle charge delocalization, which varies with the specific molecular structure of the aliphatic fragments, in contrast to mercapto derivatives like EPT that were involved in non-conjugated interfacial interactions.[28,39,41] Meanwhile, acetylene derivatives were reported to be able to bind to Cu atoms and form into polymeric nanostructures, which may be conducive to stabilize CuOH units. Notably, it was found that the resulting organically capped CuOH nanostructures were readily dispersible in organic media, and stable in both solution and solid forms. Microscopic and spectroscopic studies showed that the obtained CuOH-ligands (i.e., EPA, HC16, EPT) nanostructures exhibited a ribbon nanostructure and were functionalized with Cu-C≡ and Cu-S- interfacial linkages, respectively, and the photoluminescence properties varied with the surface capping ligands, due to a discrepancy of the core-ligand charge transfer at the ligand-CuOH interface and hence the materials bandgap. Consistent results were obtained in first principles calculations. Notably, the EPA-capped CuOH nanostructures manifested drastically enhanced photodynamic antibacterial activity, owing to the conjugated core-ligand linkages that facilitated interfacial charge transfer and generation of reactive oxygen species (ROS) under UV and blue-light photoirradiation, in comparison to the EPT-capped counterparts.

8.3 Results and Discussion

Note that direct mixing of Cu^{+} and OH^{-} led to the uncontrollable formation of yellow CuOH precipitates, which decayed rapidly within a day (Figure 1). Thus, to prepare stable CuOH nanostructures, a unique synthetic procedure was developed in the present

study by using Cu^{2+} and SO_3^{2-} as the precursors. Briefly, a mixture of HSO_3^- and OH^- was injected into a Cu^{2+} solution in a mixed solvent of dichloromethane (DCM), N,N-dimethylformamide (DMF), and ethanol at the volumetric ratio of 1:1:1 in the presence of select organic capping ligands, producing a yellow solution that is consistent with CuOH (Figure 2).[21-23] The experimental details are included in the Supporting information. The mixture of solvents was deliberately chosen to optimize the polarity of the solvents for good dispersion of both the copper salts and organic ligands. The production of organically capped CuOH nanostructures most likely involved the following reactions,

$$HSO_3^- + OH^- \rightleftharpoons SO_3^{2-} + H_2O \quad (1)$$

$$2Cu^{2+} + SO_3^{2-} + 2OH^- \rightarrow 2Cu^+ + SO_4^{2-} + H_2O \quad (2)$$

$$Cu^+ + OH^- \rightarrow CuOH \quad (3)$$

$$Cu^+ + HC{\equiv}CR + 2OH^- \rightarrow CuOH(-C{\equiv}CR) + H_2O \quad (4)$$

$$Cu^+ + HSR + 2OH^- \rightarrow CuOH(-SR) + H_2O \quad (5)$$

First, bisulfite ions were neutralized into sulfite upon the addition of KOH (eq. 1), which then reduced Cu^{2+} into Cu^+, as the formal potential of the SO_4^{2-}/SO_3^{2-} couple ($E° = -0.936$ V) is far more negative than that of Cu^{2+}/Cu^+ (+0.159 V) (eq. 2).[42] The resulting Cu^+ subsequently reacted with OH^- to produce cuprous hydroxide (CuOH) (eq. 3); and in the presence of select organic ligands, such as acetylene (HC≡CR) and mercapto (HSR) derivatives, stable CuOH nanostructures were produced, due to the formation of CuOH-C≡C- and CuOH-S- interfacial bonds (eq. 4 and 5),[43] as manifested by the apparent color change from blue to bright yellow (Figure 2). Three

samples were prepared using EPA, HC16 and EPT as the protecting ligands, and denoted as CuOH-EPA, CuOH-HC16, and CuOH-EPT, respectively. Note that in the synthesis of CuOH-EPT, the solution turned yellow upon the addition of EPT into Cu^{2+} before the addition of sulfite, likely due to the reduction of Cu^{2+} to Cu^{+} by the thiol moieties.[44] Remarkably, all final products (CuOH) can be readily dispersed, and remain stable, in a range of organic media, such as DCM, tetrahydrofuran (THF), toluene, etc., suggesting sufficient protection by the hydrophobic organic ligands.[39] By contrast, without the addition of any organic ligands, greenish yellow precipitates (CuOH) were formed at the bottom of the flask (Figure 3); and X-ray photoelectron spectroscopy (XPS) measurements showed the formation of CuO, which likely arose from the facile decomposition of CuOH upon exposure to the ambient, suggesting that the organic ligands played a critical role in stabilizing the formation of CuOH (Figure 1). In another control experiment without the addition of the sulfite ions, only brownish precipitates were produced (Figure 4), which was identified as CuO by XPS measurements, indicative of the critical role of sulfite ions in the reduction of Cu^{2+} into Cu^{+} (eq. 2). The solution pH was also important in the formation of stable CuOH. When the solution became too acidic (Figure 5 and 6) or too alkaline (Figure 7), other Cu compounds, such as CuO, Cu_2O, or cupric sulfates, would be produced instead. That is, a mildly alkaline condition is conducive to the stabilization of the ligand-capped CuOH nanostructures (Figure 8). In fact, the obtained CuOH samples could be gradually decomposed in strong acid (2 M H_2SO_4) to a colorless solution (Figure 8), consistent with the Cu(I) valence state and the formation of a hydroxide compound. In sharp

contrast, the structural stability of the CuOH samples was significantly enhanced in neutral and mildly alkaline conditions, where the oxidation into Cu(II) was markedly impeded, in comparison to bare CuOH (Figure 1), as manifested in XPS measurements (Figure 9-12).

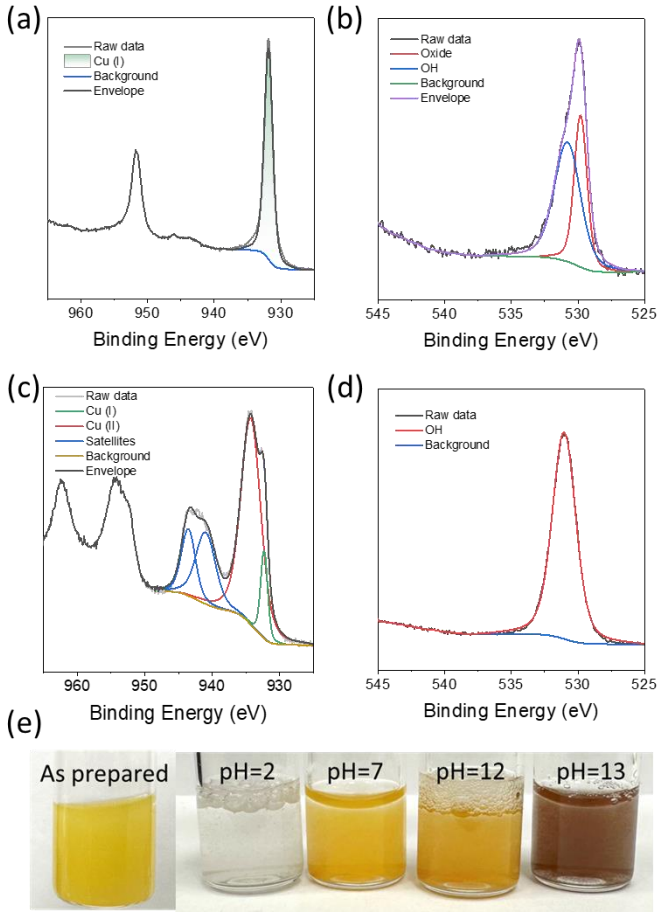

Figure 1. High-resolution scans of the (a,c) Cu 2p, and (b,d) O 1s electrons of (a,b) freshly prepared CuOH by mixing CuI and KOH and (c,d) CuOH stored in water (pH = 7) after one day. (e) Photographs of freshly prepared CuOH and the solutions at different pH.

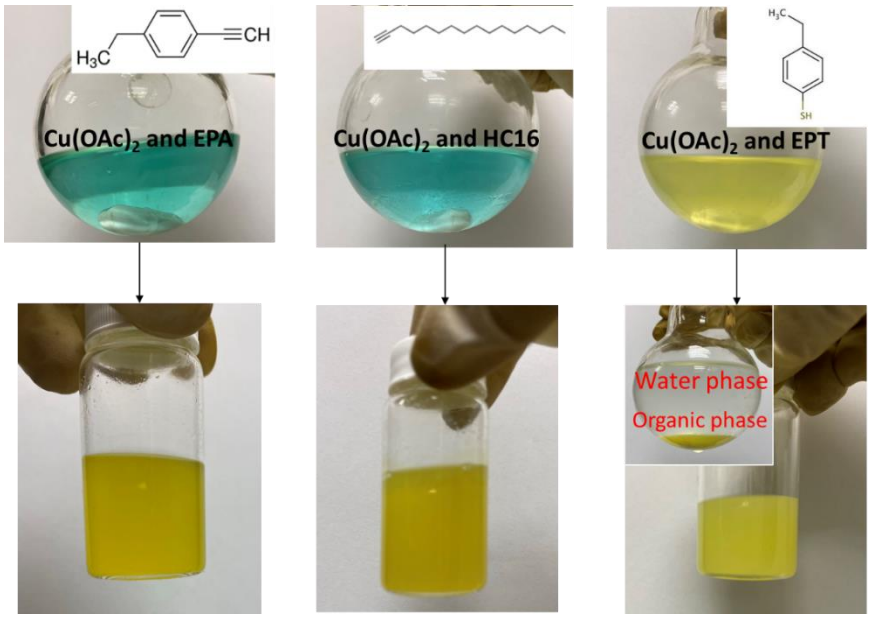

Figure 2. Photographs of the synthesis of the CuOH-EPA, CuOH-HC16, CuOH-EPT samples.

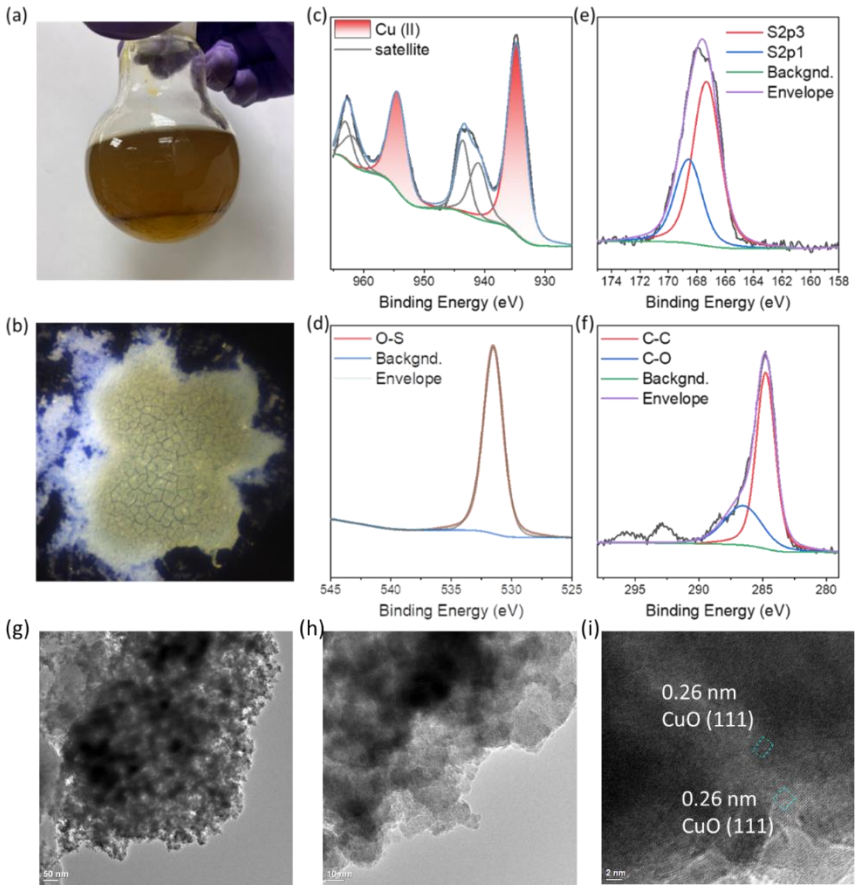

Figure 3. Control sample that is prepared in the same manner except for the addition of any organic ligands. Photographs of the final product (a) in solution and (b) on a silicon wafer. The product shows a greenish color. High-resolution XPS scans of the (c) Cu 2p, (d) O 1s, (e) S 2p, and (f) C 1s electrons of the final product. One can see that the Cu species shows mostly a 2+ valence state with a doublet of 934.74/954.42 eV, with two pairs of strong satellite peaks at 943.63/962.98 eV and 941.05/964.80 eV. S is in the form of SO_x, with an atomic ratio of about 1:5 to O, suggesting that the final product is cupric sulfates. In the TEM images (g-i), the sample can be seen to consist of big chunks of cupric sulfates. Some nanoparticles show well-defined lattice fringes with a spacing of 0.26 nm, corresponding to the (111) facets of CuO.[45]

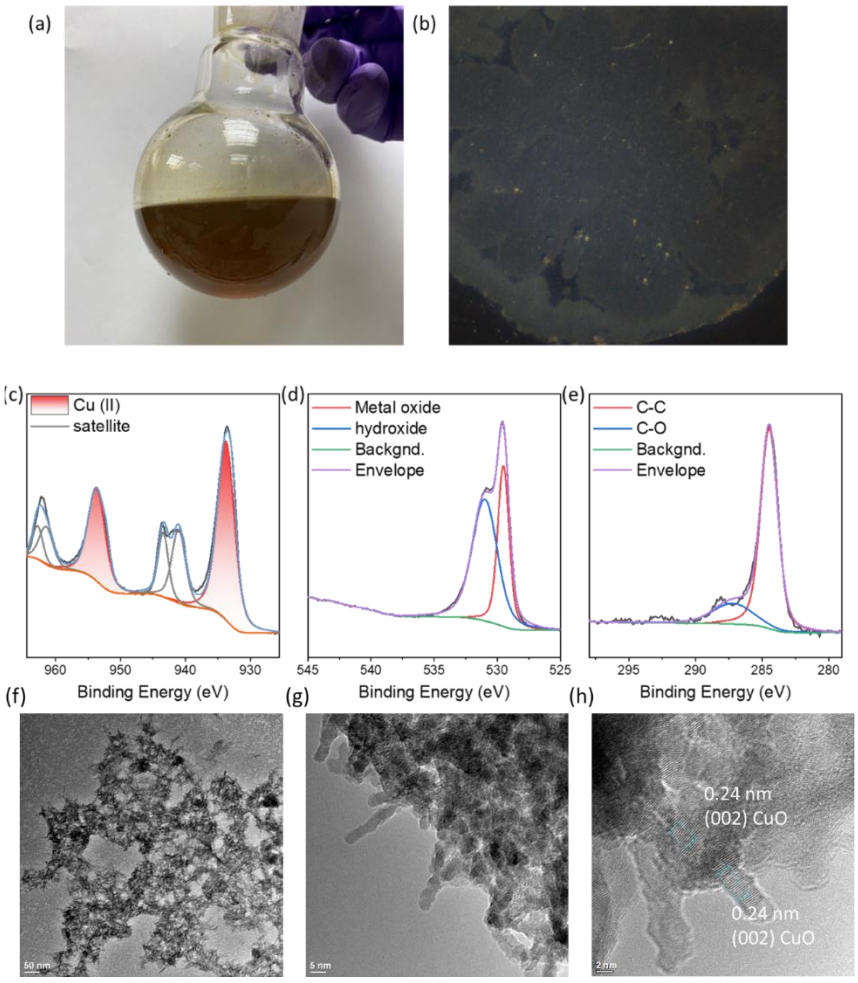

Figure 4. Control sample that is prepared in the same manner but without the addition of $NaHSO_3$. Photographs of the final product (a) in solution and (b) on a silicon wafer. The sample shows a dark brown color. High-resolution XPS scans of the (c) Cu 2p, (d) O 1s, and (e) C 1s electrons of the final product. Cu is in the 2+ valence state with a doublet at 933.71/953.51 eV and two pairs of strong satellite peaks at 940.97/961.44 eV, 943.36/962.71 eV. In the O 1s spectrum, the strong peak at 529.5 eV can be assigned to Cu-O, which is not found in the series of CuOH samples. (f-h) Representative TEM images showed many needle-like particles, with a d-spacing of 0.24 nm, which can be ascribed as (002) facets of CuO.[46]

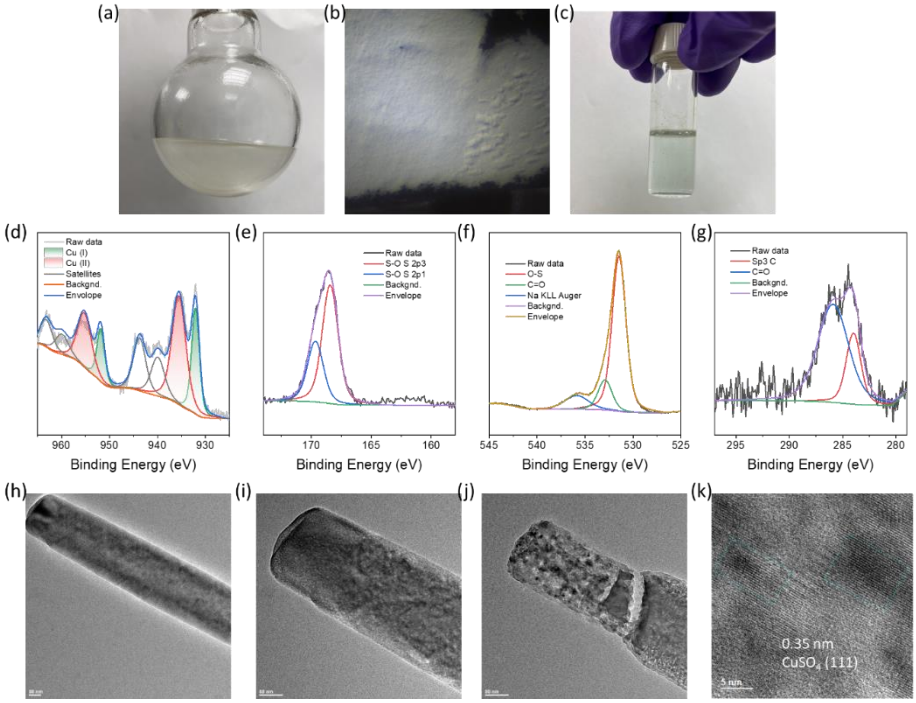

Figure 5. Control sample that is prepared in the same manner but with the addition of 0.5 M H_2SO_4 instead of 0.5 M KOH. Photographs of the final product (a) in organic solution, (b) on a silicon wafer, and (c) in water. One can see that precipitates are formed after the reaction as a white powder in water, with a slight blue color (existence of Cu(II)). This suggests that acidic condition is not good for the reduction of $Cu(OAc)_2$ or the formation of CuOH. High-resolution XPS scans of the (d) Cu 2p, (e) S 2p, (f) O 1s, and (g) C 1s electrons of the final product. One can see that the Cu 2p spectrum consists of two pair of peaks at 932.10/951.80 eV and 935.50/955.40 eV, due to Cu(I) and Cu(II), respectively. As for the S 2p spectrum, one pair of peaks at 168.46/169.65 eV can be resolved and assigned to SO_x, which is further confirmed by the O-S peak at 531.46 eV in the O 1s spectrum. From the representative TEM images (h-k), one can see that the product exhibits a ribbon-like morphology, similar to CuOH-EPA. The product manifests a d-spacing of 0.35 nm, which can be assigned to the (111) facets of $CuSO_4$. Meanwhile, it can be observed that the ribbon will decompose under an electron beam, as shown in (j), suggesting structural instability of the product, which is a typical phenomenon of metal salts under an electron beam.[47] These combined

results show that an acidic condition is not conducive to the formation of CuOH. Meanwhile, the shape of CuOH-EPA is probably templated from the sulfate salt, while the long chain of HC16 may break the shape owing to the steric effects. As for CuOH-EPT, the formation of the EPT-Cu complex may already destroy the ribbon shape.

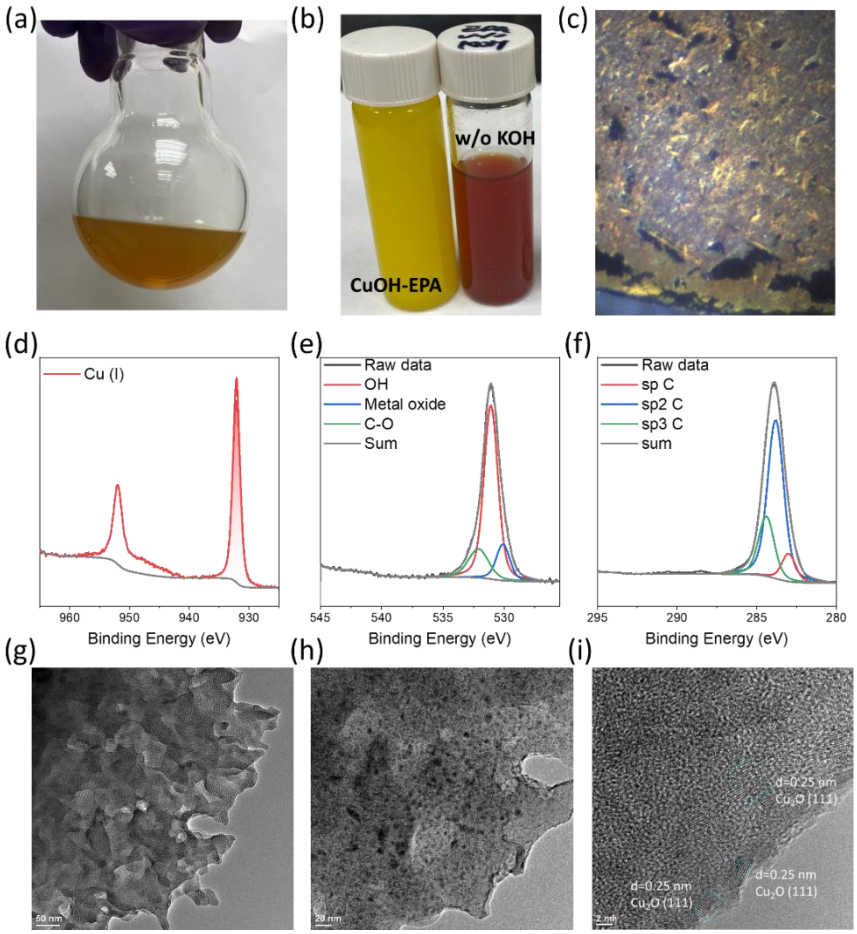

Figure 6. Control sample that is prepared in the same manner but without the addition of 0.5 M KOH. Photographs of the final product (a) in the organic solution, (b) in dichloromethane (comparison with CuOH-EPA), and (c) on a silicon wafer. The product shows a red color, significantly different from CuOH-EPA. High-resolution XPS scans of the (d) Cu 2p, (e) O 1s, and (f) C 1s electrons of the final product. The Cu 2p spectrum consists of a single pair of peaks at 932.05/951.97 eV, due to Cu(I). A metal-oxide peak can be deconvoluted from the (e) O 1s spectrum at 530.10 eV,

suggesting the formation of Cu_2O. (g-i) Representative TEM images confirm the formation of Cu_2O nanoparticles. The sample shows a completely different morphology, not nanoribbons but flaky structures. The product exhibits apparently good crystallinity, with an interplanar spacing of 0.25 nm in the well-defined lattice fringes, due to the (111) facets of Cu_2O.[48] In summary, an alkaline condition is critical to produce the ribbon structure of CuOH.

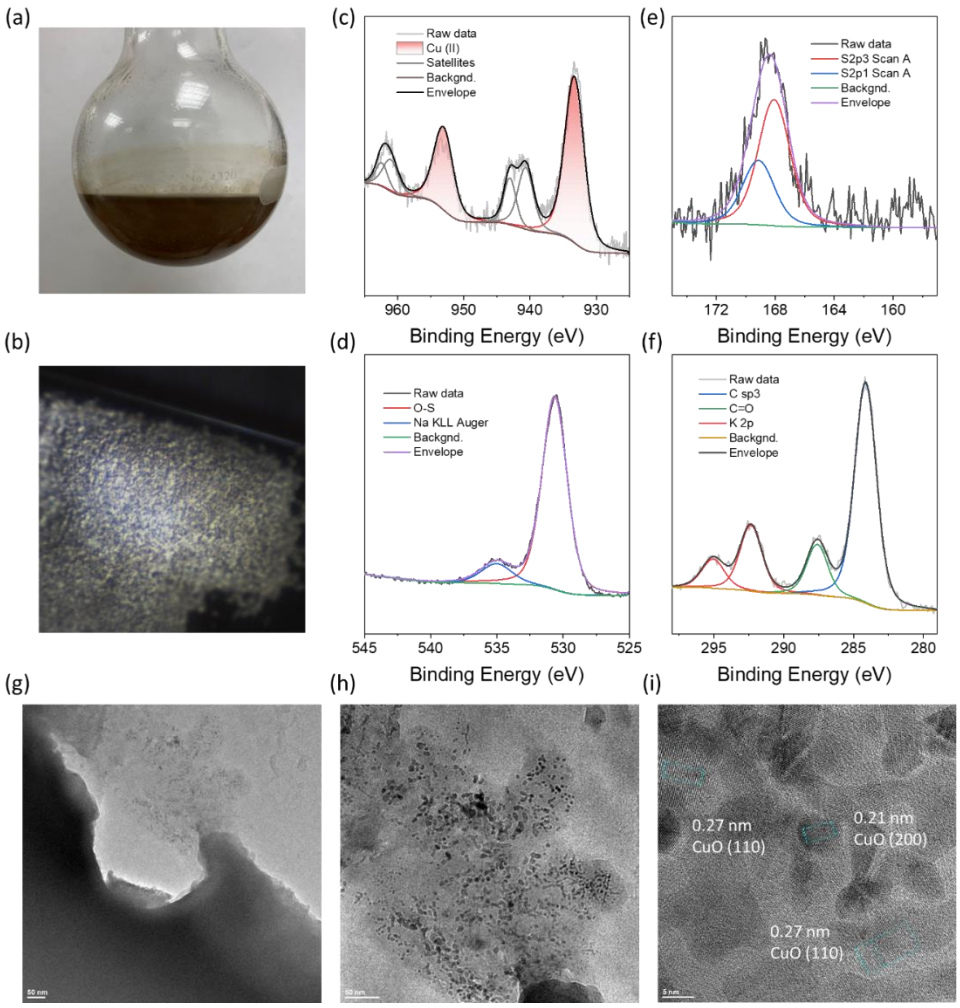

Figure 7. Control sample that is prepared in the same manner but with the addition of 5 M KOH. Photographs of the final product (a) in solution and (b) on a silicon wafer. The product shows a mixture of black spots and white powder. High-resolution XPS scans of the (c) Cu 2p, (d) O 1s, (e) S 2p, and (f) C 1s electrons of the final product. In

panel (c), one can see a pair of peaks at 933.15/953.12 eV with strong satellite peaks at ca. 940/960 eV, corresponding to Cu(II) species. Abundant O-S species are confirmed in the S 2p and O 1s spectra. In the representative TEM images (g-i), one can find a big chunk in dark contrast, which was the Cu sulfate salts. On its periphery, many nanoparticles can be identified with d-spacings of 0.27 nm and 0.21 nm, corresponding to the (110) and (200) facets of CuO,[49] respectively. This suggests that the product is likely a mixture of Cu sulfates and CuO, consistent with the color appearance (black in solution but off-white in solid with black spots). The results also suggest that extra amounts of KOH will render the formation of CuO, and SO_3^{2-} anions are no longer able to reduce Cu^{2+} to Cu^{+}.

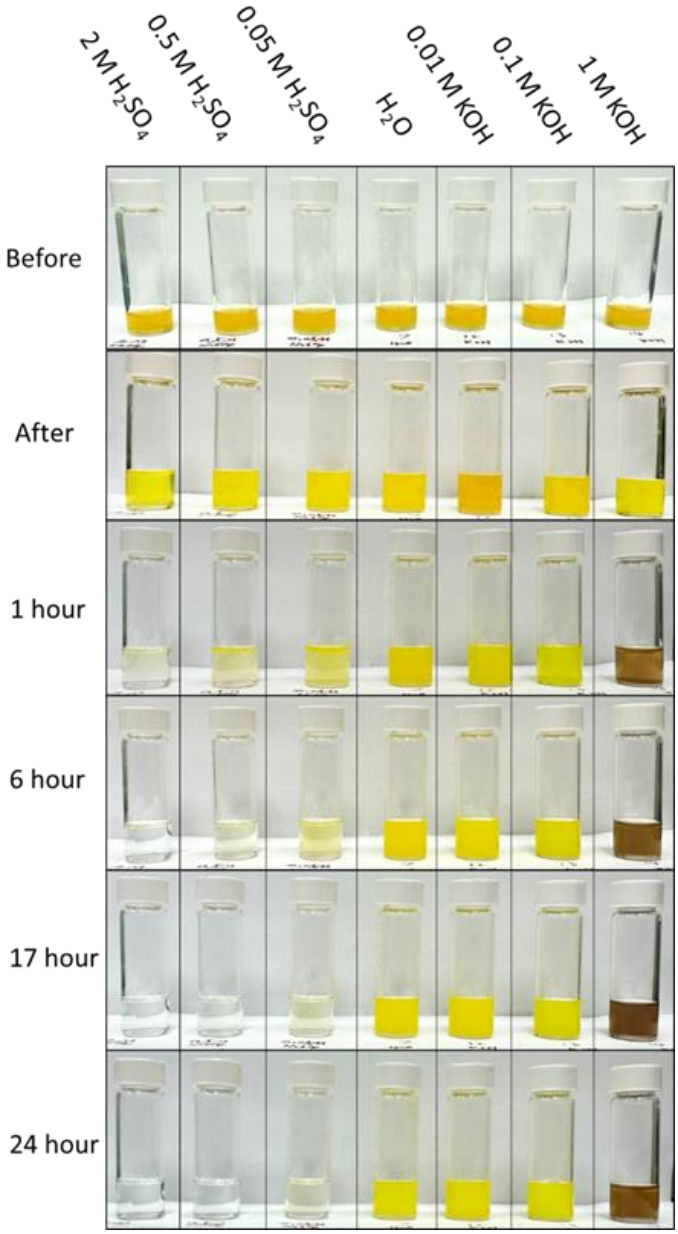

Figure 8. Stability of CuOH-EPA dispersed in ethanol for up to 24 hours with the addition of different concentrations of H_2SO_4 or KOH. Because of their strong hydrophobicity, the as-prepared CuOH-EPA is first dispersed in ethanol (1 mg mL^{-1}). Then, 1 mL of 2 M H_2SO_4, 0.5 M H_2SO_4, 0.05 M H_2SO_4, deionized water, 0.01 M KOH, 0.1 M KOH, and 1 M KOH is added into the vials. One can see that with the addition of 2 M H_2SO_4, the CuOH-EPA solution gradually fades from bright yellow to colorless,

indicating readily decomposition of CuOH-EPA by acid (Cu^+ is colorless). The decomposition is slower with 0.05 M H_2SO_4, where the solution color does not vanish completely even after 24 hours. With the addition of only water or 0.01M KOH, or 0.1 M KOH, the solution color remains bright yellow after 24 hours, suggesting high stability of CuOH-EPA in these two conditions. In contrast, with the addition of 1 M KOH, the solution color becomes intensified to dark brown quickly, indicating the decomposition of CuOH. These results suggest that a mildly alkaline condition is conducive to the formation of stable CuOH nanoparticles. Nevertheless, one should notice that CuOH-EPA does not change color immediately upon the addition of an alkaline or acidic solution, likely because of the good protection by the organic ligands. In fact, ICP-OES measurements showed that the concentration of free copper species was the highests at 175.07 ppm in 0.5 M H_2SO_4, and decreased to 152.89 ppm in 0.05 M H_2SO_4, and only 21.46 ppm in pure water, whereas no copper species was detectable in 0.01, 0.1, or 1.0 M KOH.

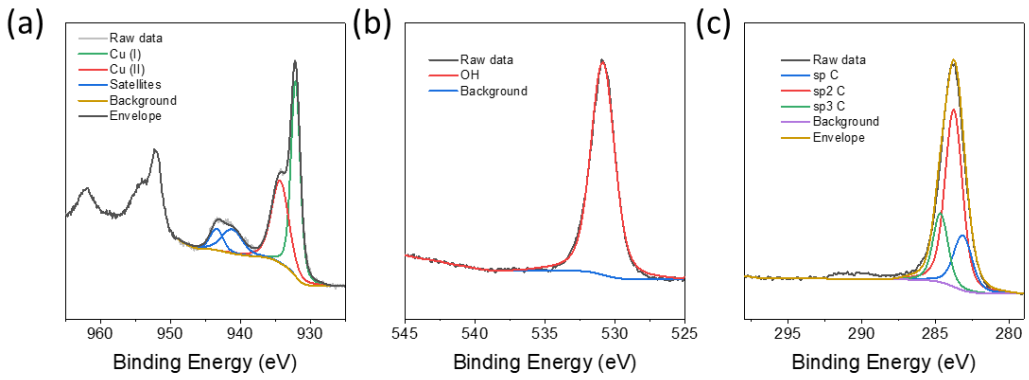

Figure 9. XPS results of CuOH-EPA in water after 24 hours. High-resolution scans of (a) Cu 2p, (b) O 1s, and (c) C 1s spectra.

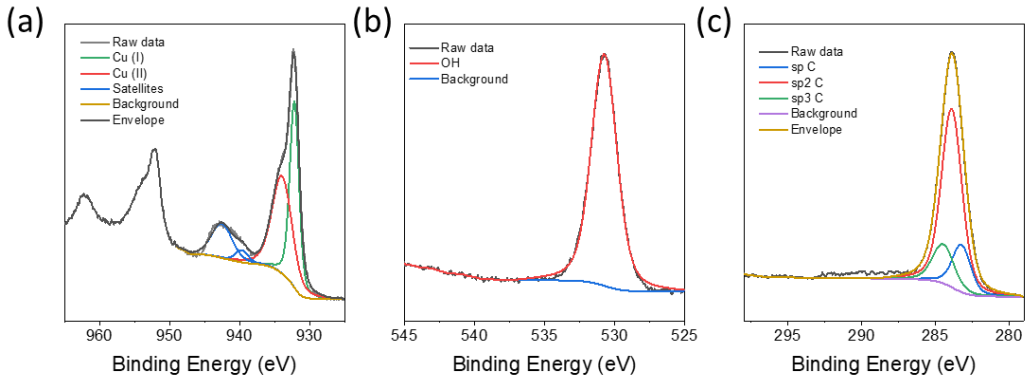

Figure 10. XPS results of CuOH-EPA in 0.01 M KOH after 24 hours. High-resolution scans of (a) Cu 2p, (b) O 1s, and (c) C 1s spectra.

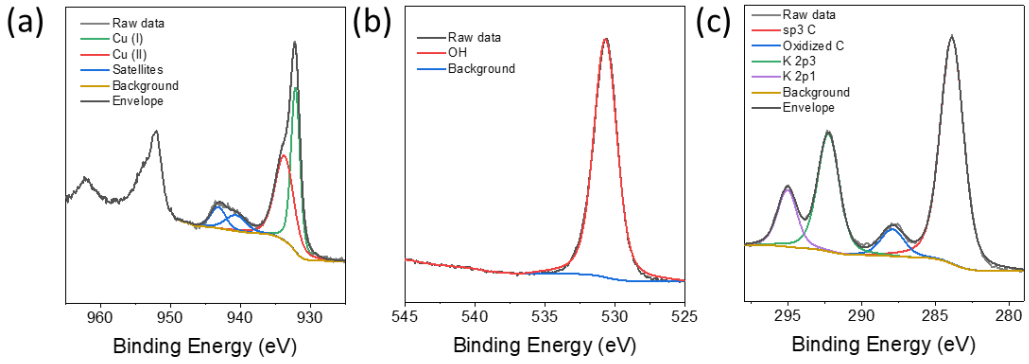

Figure 11. XPS results of CuOH-EPA in 0.1 M KOH after 24 hours. High-resolution scans of (a) Cu 2p, (b) O 1s, and (c) C 1s spectra.

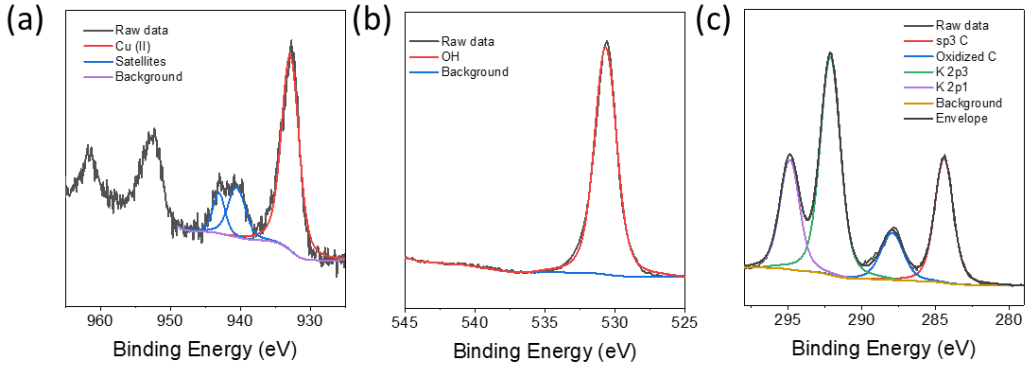

Figure 12. XPS results of CuOH-EPA in 1 M KOH after 24 hours. High-resolution scans of (a) Cu 2p, (b) O 1s, and (c) C 1s spectra.

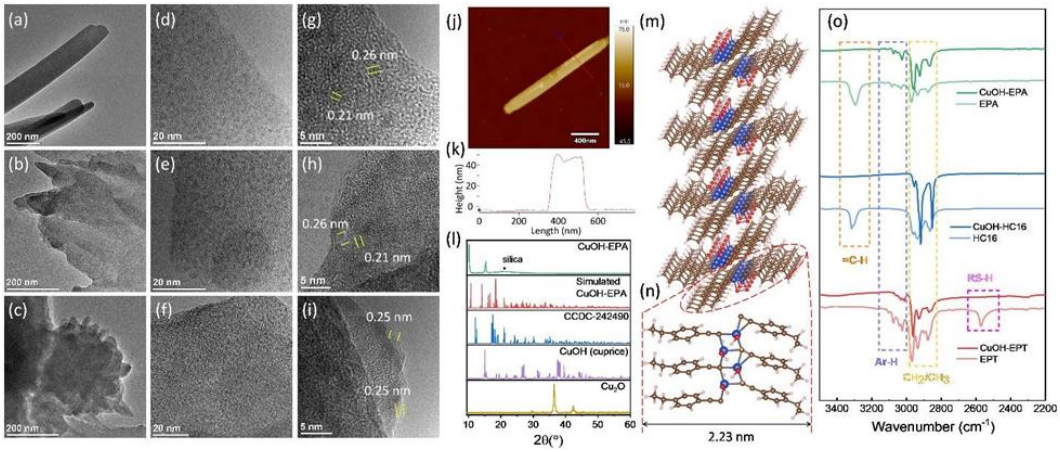

Figure 13. Representative TEM images of the organically capped CuOH samples: (a, d, g) CuOH-EPA, (b, e, h) CuOH-HC16, (c, f, i) CuOH-EPT. Scale bars are (a-c) 200 nm, (d-f) 20 nm, and (g-i) 5 nm. (j) AFM topograph of CuOH-EPA and (k) the corresponding height profile along the red line in panel (j). (l) XRD patterns of CuOH-EPA, simulated CuOH-EPA, traditional Cu-alkyne polymer (CCDC-242490), CuOH (cuprice), and Cu_2O. (m and n) Simulated CuOH-EPA structure. (o) FTIR spectra of CuOH-EPA, CuOH-HC16, and CuOH-EPT nanostructures, and the corresponding ligand monomers (light-colored curves).

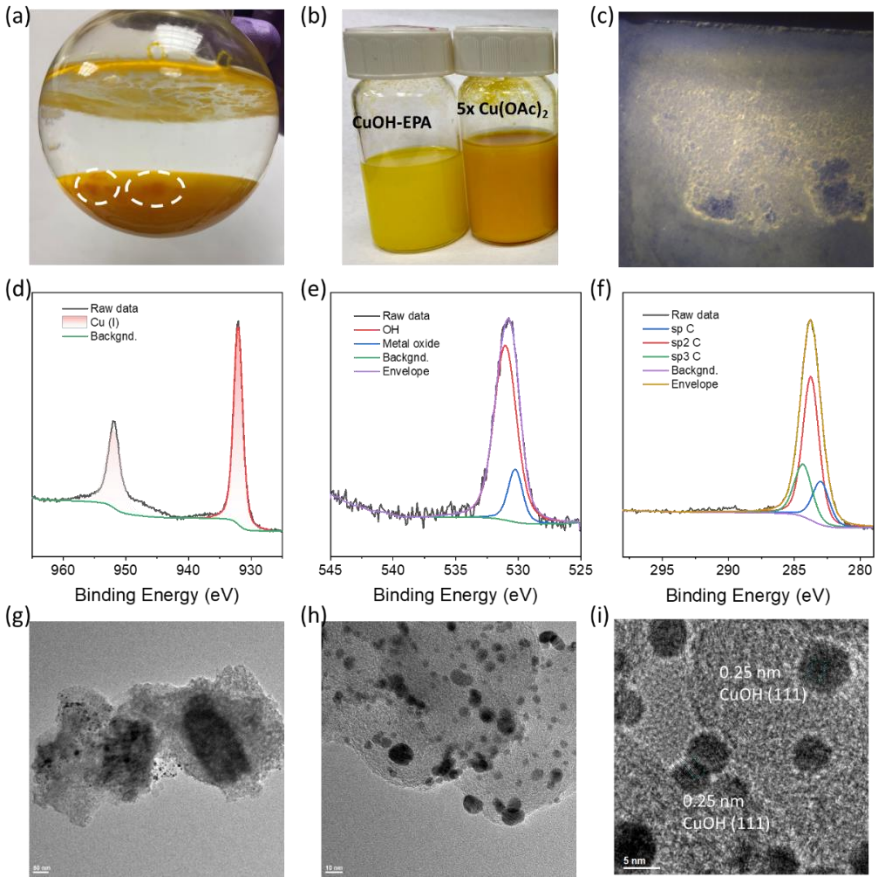

Figure 14. Control sample that is prepared in the same manner but with the addition of a 5× initial feed of Cu(OAc) salts. Photographs of the final product (a) in solution, (b) comparison with CuOH-EPA, and (c) on a silicon wafer. The product shows an orange color, which is possibly the mixture of red Cu_2O and yellow CuOH, as confirmed by the heterogenous red part circled in (a). High-resolution XPS scans of the (d) Cu 2p, (e) O 1s, and (f) C 1s electrons of the final product. One can see a pair of peaks at 931.88/951.98 eV due to Cu(I), without any satellite peaks from Cu(II). In addition, the M-O peak at 530.10 eV can be deconvoluted from the O 1s spectrum, suggesting the formation of metal oxide. The C 1s spectrum shows a Csp peak at 283.00 eV from C≡C bonds, suggesting functionalization by the EPA ligands. (g-i) Representative TEM images of the final product show many dark-contrast nanoparticles, with well-defined lattice fringes of 0.25 nm, which can be identified as the (111) facets of CuOH particles. The amorphous substrates are most likely CuOH-EPA sheets, similar to CuOH-EPA.

One can see that the sample no longer shows a ribbon-like morphology, possibly due to the formation of CuOH nanoparticles, which deviates from CuOH-EPA. The results suggest that excessive Cu salts may lead to the formation of CuOH nanoparticles with poor protection from ligands.

The morphologies of the CuOH samples were first examined by transmission electron microscopic (TEM) measurements. One can see from Figure 13a that CuOH-EPA manifests a ribbon-like shape with a width in the range of 130 to 200 nm and micron-scale length. The CuOH-HC16 (Figure 13b) and CuOH-EPT (Figure 13c) samples also exhibit a flaky structure, but bundled into an irregular shape. High-resolution TEM measurements (Figure 13d-13f) show that the samples actually consisted of ultra-small nanoclusters of less than 2 nm in diameter with well-defined lattice fringes embedded within a largely amorphous scaffold (Figure 13g-13i). The interplanar spacing was estimated to be ca. 0.21 and 0.26 nm for both CuOH-EPA (Figure 13g) and CuOH-HC16 (Figure 13h) and 0.25 nm for CuOH-EPT (Figure 13i), corresponding to the (220), (210) and $(0\bar{2}2)$ facets of CuOH, respectively.[26] Note that with an increasing initial feed of Cu^{2+}, larger CuOH nanoparticles were produced (dia. 5 – 10 nm, Figure 14).

Consistent results were obtained in atomic force microscopy (AFM) measurements. From the topographic images in Figure 13d and Figure 15-17, the three CuOH samples can all be seen to exhibit a one-dimensional nanowire-like morphology. Line scans across the nanowire actually revealed a nanoribbon structure with a width of ca. 200 nm and a thickness of ca. 45 nm (Figure 13e), in good agreement with results from TEM measurements (Figure 13a).

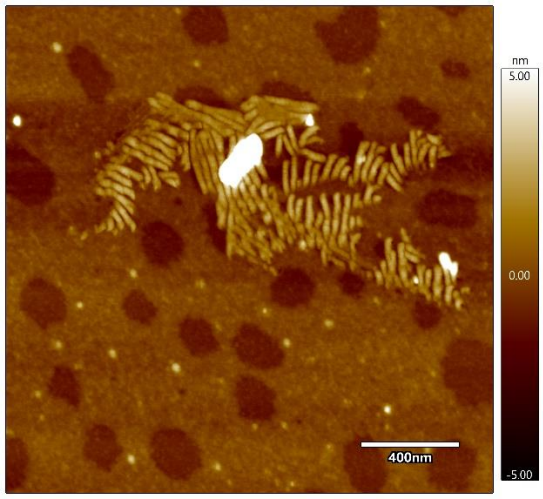

Figure 15. Representative AFM topograph of CuOH-EPA.

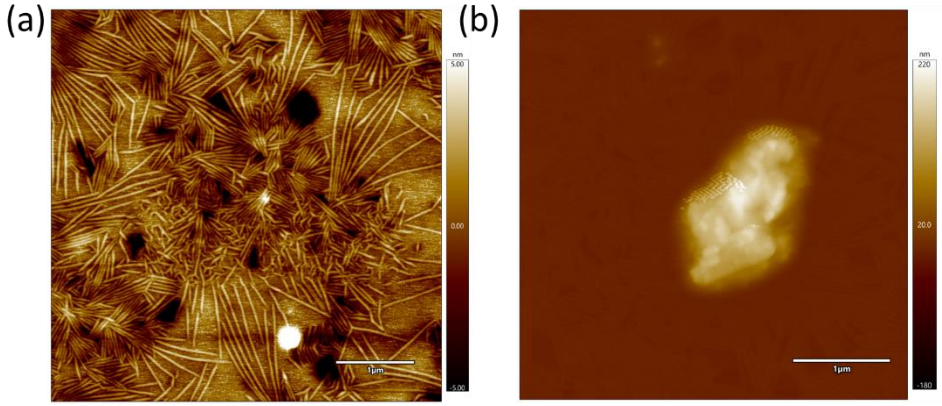

Figure 16. (a, b) Representative AFM topographs of CuOH-HC16.

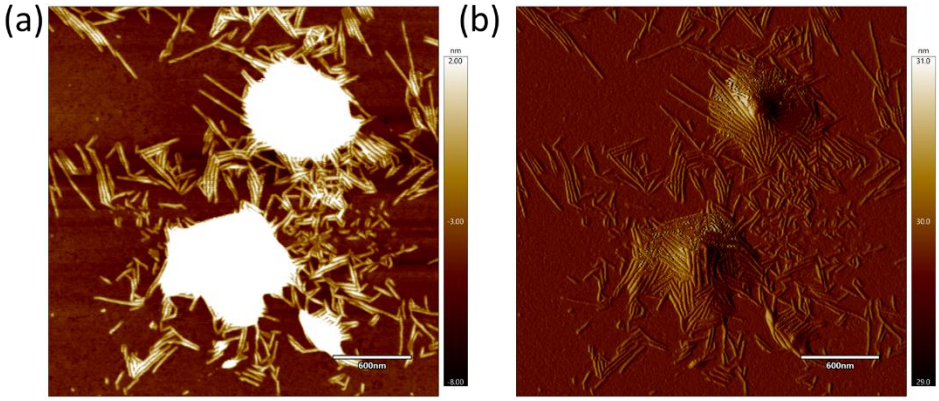

Figure 17. Representative AFM topographs of CuOH-EPT.

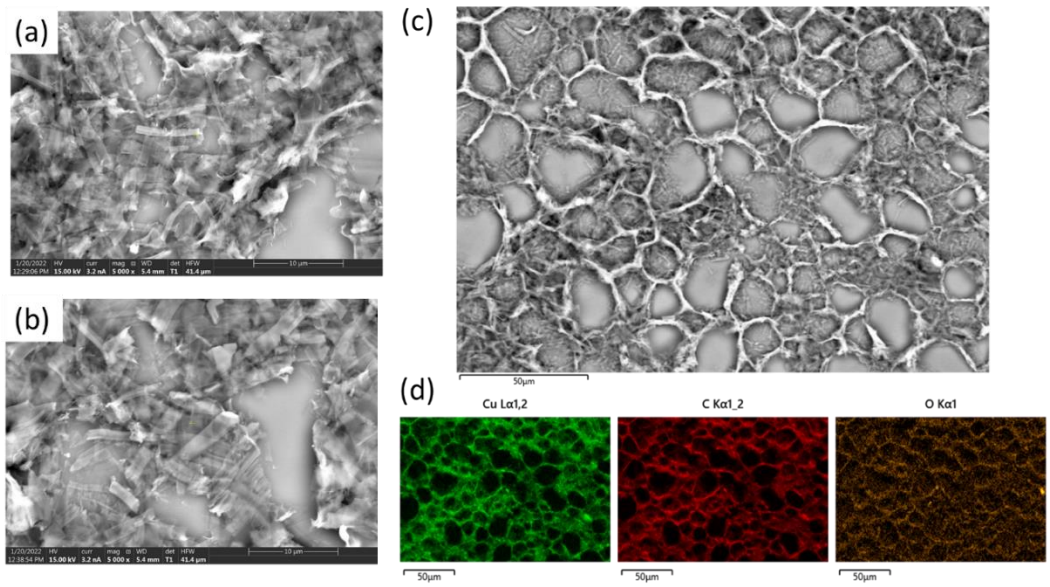

Figure 18. (a-c) SEM images of CuOH-EPA and (d) the corresponding EDX-based elemental maps of Cu, C, and O.

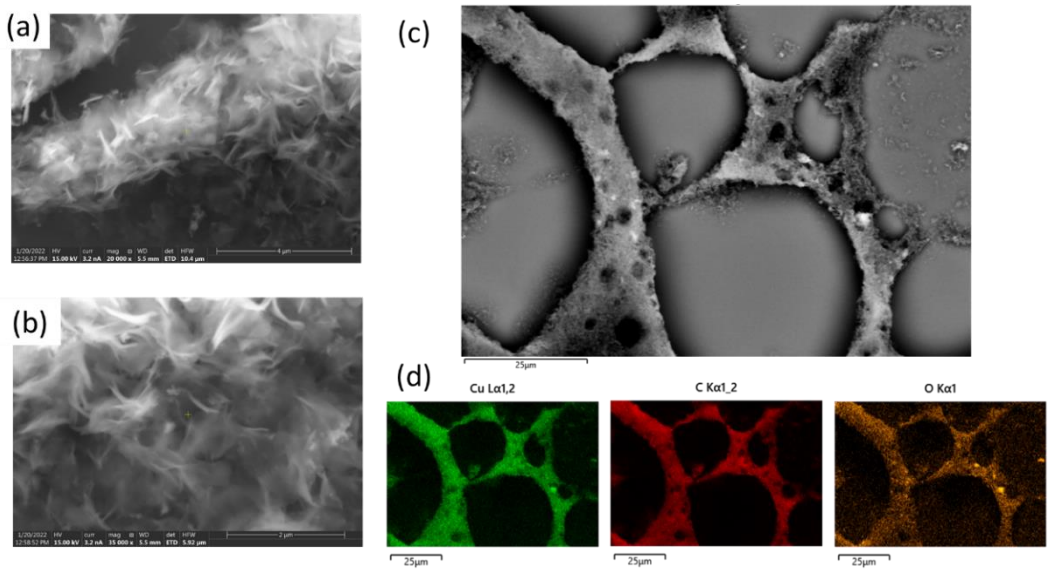

Figure 19. (a-c) SEM images of CuOH-HC16 and (d) the corresponding EDX-based elemental maps of Cu, C, and O.

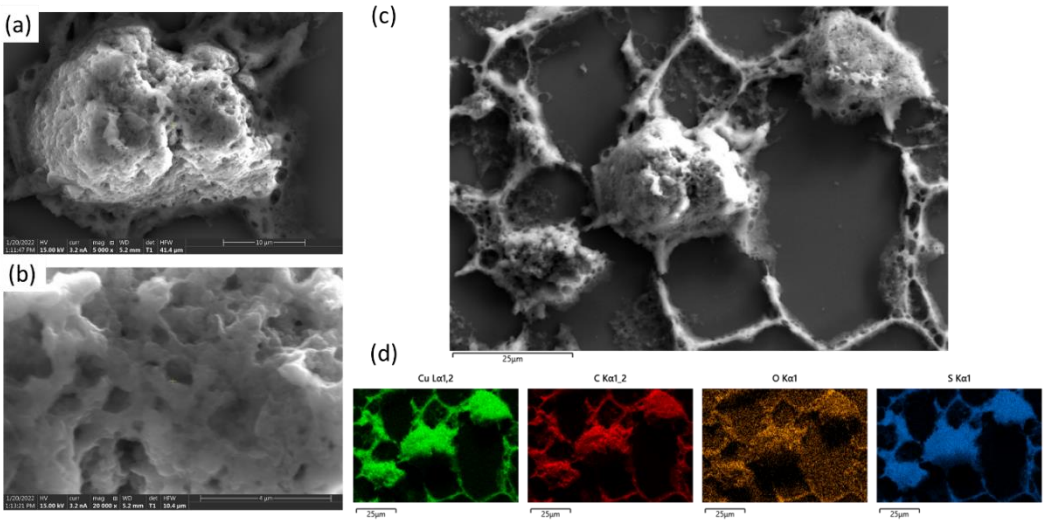

Figure 20. (a-c) SEM images of CuOH-EPA and (d) the corresponding EDX-based elemental maps of Cu, C, O, and S.

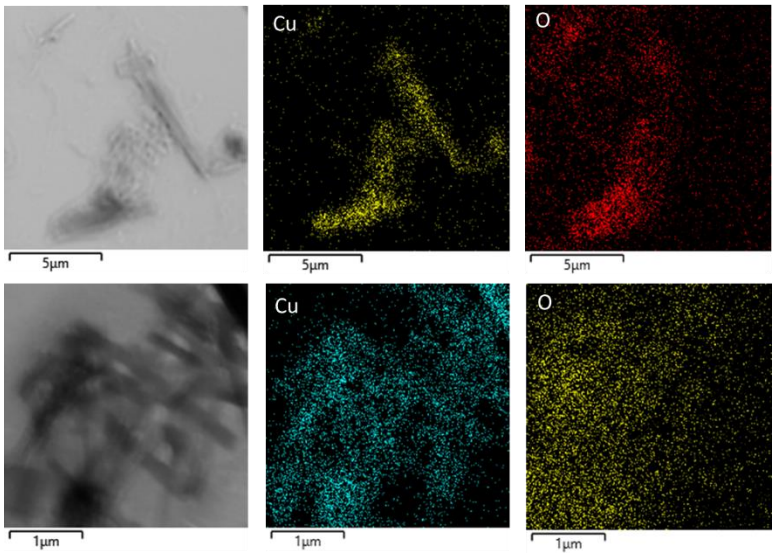

Figure 21. Electron images and corresponding EDS mappings of Cu, O of CuOH-EPA.

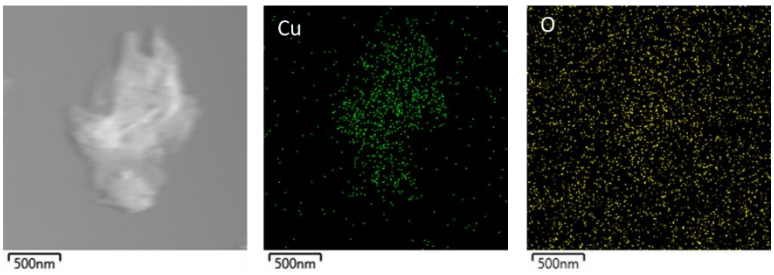

Figure 22. Electron images and corresponding EDS mappings of Cu, O of CuOH-HC16.

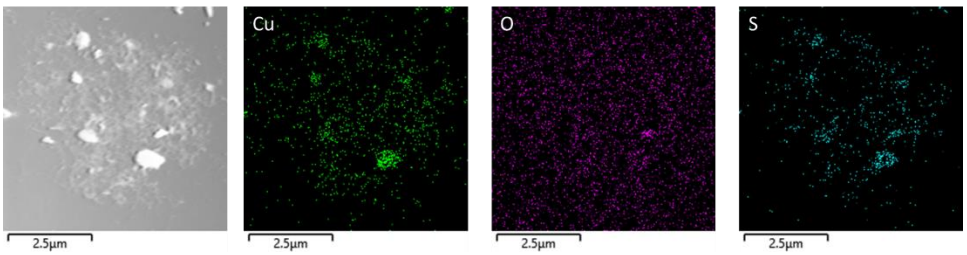

Figure 23. Electron images and corresponding EDS mappings of Cu, O, S of CuOH-EPT.

The nanoribbon structures can also be resolved In scanning electron microscopy (SEM) measurements, where CuOH-EPA can be seen to contain nanoribbons of 5 to 7 mm in length (Figure 18), whereas CuOH-HC16 (Figure 19) and CuOH-EPT (Figure 20) exhibit a mostly irregular flaky structure. Meanwhile, elemental mapping analysis based on energy dispersive X-ray (EDS) spectroscopy showed that all three CuOH samples featured a homogeneous distribution of Cu, O, and C, with S found also in CuOH-EPT, consistent with the formation of the respective ligand-capped nanoparticles. TEM-based EDS scans in higher magnifications showed consistent results (Figure 21-23).

Further structural insights were obtained in X-ray diffraction (XRD) measurements. Figure 13f depicts the XRD patterns of CuOH-EPA, which consists of only two sharp diffraction peaks at 2θ = 10.18° and 15.34°, corresponding to a d value of 0.87 and 0.58 nm, respectively. Note that such patterns are markedly different from those of "cuprice" CuOH,[26] Cu_2O (RRUFF ID: R050374.1), and Cu^I-alkyne coordination polymers reported previously (CCDC-24290, Figure 24).[50,51] Yet, the results are in excellent agreement with a layered structure where each layer consists of one-dimensional assembly of the CuOH-EPA moieties that is facilitated by hydrogen bonding interactions between the OH groups and π-π stacking between the phenyl rings of the EPA ligands (Figure 13g and 13h). In fact, the simulated XRD patterns exhibit two peaks at 2θ = 10.69° and 14.16° (the CIF files are included in the Supporting Information), very close to those of the CuOH-EPA sample.

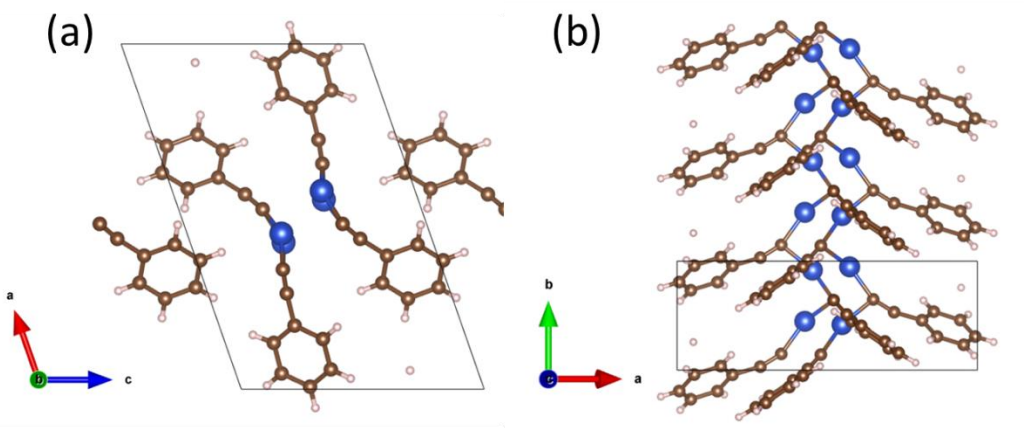

Figure 24. Structural model of Cu^I-alkyne coordination polymer (CCDC-24290).[50,51]

Taken together, results from these characterizations suggest that the obtained samples consist of CuOH nanoclusters embedded within a CuOH-ligand nanoribbon

nanostructures. Such a structure calls for a 1:1 molar ratio between CuOH and the organic ligands, which was indeed observed in XPS measurements (vide infra). Indeed, the expected metal contents were also in excellent agreement with results from inductively coupled plasma-optical emission spectrometry (ICP-OES) measurements (Table 1).

Table 1. Copper contents in the three CuOH samples from ICP-OES measurements, in comparison to the theoretical expectations (by assuming a 1:1:1 molar ratio of Cu:OH:ligands).

Sample	**Cu Molar Mass**	**OH Molar Mass**	**Ligands Molar Mass**	**Total Molar Mass**	**Theoretical Cu content (wt.%)**	**Cu content from ICP-OES (wt.%)**
CuOH-EPA	63.5	17	129	209.5	30.31	30.72
CuOH-HC16	63.5	17	221	301.5	21.06	19.09
CuOH-EPT	63.5	17	137	217.5	29.19	28.33

The surface structure of the obtained CuOH nanostructures was then characterized by Fourier transform infrared (FTIR) spectroscopic measurements. From Figure 1j, one can see that all three CuOH samples exhibited a broad peak around 3400 cm^{-1} (Figure 26), due to the O-H stretch.[25] In addition, in comparison to the spectra of the monomeric

ligands, the organically capped CuOH samples all exhibited vibrational peaks in the range of 2800 to 3000 cm^{-1}, as highlighted by the yellow box, due to the CH_2/CH_3 stretches of the organic ligands. For both the CuOH-EPA and CuOH-EPT, additional vibrational features can be seen in the range of 3000 to 3100 cm^{-1} (purple box), due to the aromatic C-H stretches of the aryl ligands. Consistent profiles can be found in the fingerprint region of 810 to 830 cm^{-1} (Figure 25). Meanwhile, as highlighted in the orange box, unlike their corresponding monomers, the terminal ≡C-H vibration at 3293 – 3313 cm^{-1} vanished with CuOH-EPA and CuOH-HC16, indicating effective cleavage of the ≡C-H bond and their anchorage onto the surface of CuOH, as observed previously.[28,39,40] A similar behavior can be seen with the CuOH-EPT sample, where the S-H vibration was well-defined at 2568 cm^{-1} for the EPT monomers, but disappeared altogether in CuOH-EPT (magenta box). Since no S-O vibration could be identified around 950-800 or 550 cm^{-1},[52] the EPT ligands were most likely bound onto the CuOH surface via the Cu-S- interfacial bonds, rather than Cu-O-S-. Notably, consistent results were obtained from density functional theory (DFT) calculations (Table 2). Of particular notice is the contributions of the OH moiety to the vibrational bands at ca. 821.7, 1119, and 3583.1 cm^{-1}, further confirming the formation of CuOH-EPA nanostructures. In addition, the peak at 547 cm^{-1} is most likely due to the Cu-C≡ vibration, suggesting that the alkyne ligands are bound to the Cu atomic site in CuOH (Figure 13g-13h).

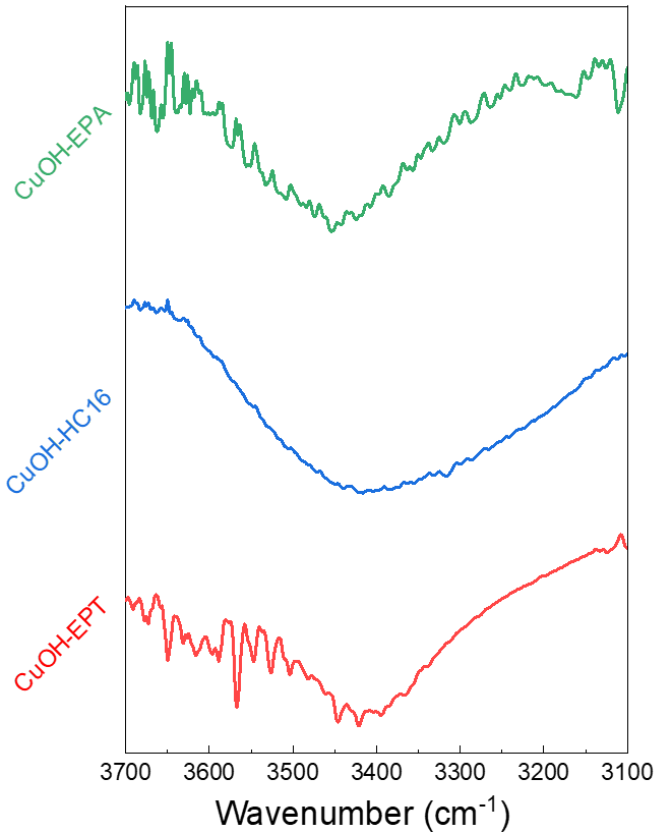

Figure 25. FTIR spectra of EPT-, EPA- and HC16-functionalized CuOH nanoparticles in the range of 3100-3700 cm^{-1}.

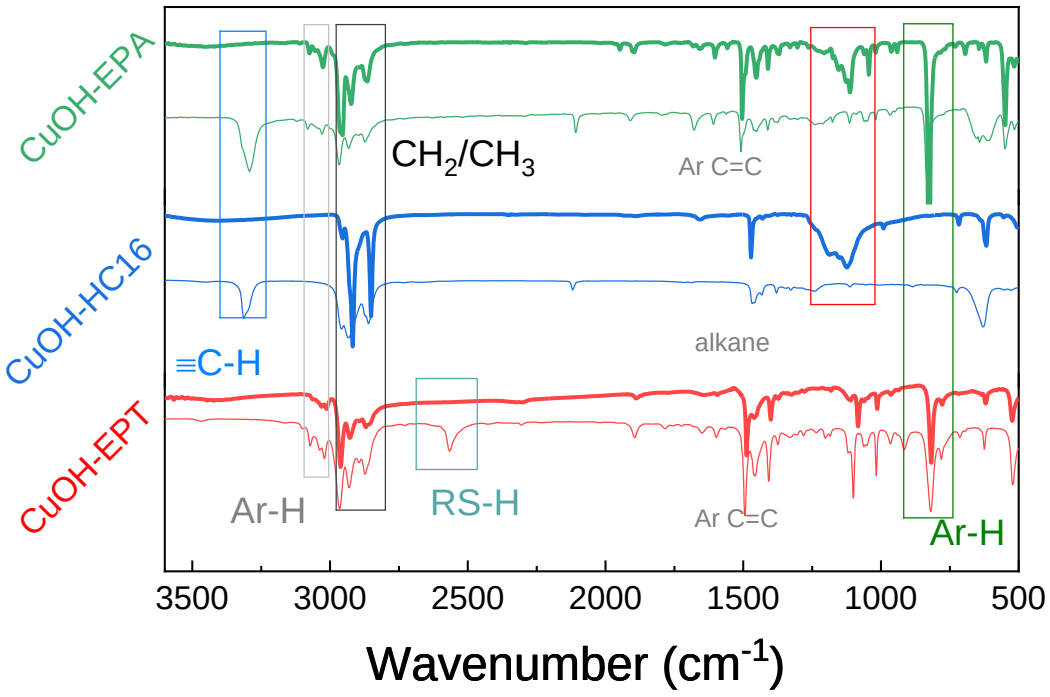

Figure 26. FTIR spectra of EPT-, EPA- and HC16-functionalized CuOH nanoparticles (thick curves) and the corresponding ligand monomers (thin curves).

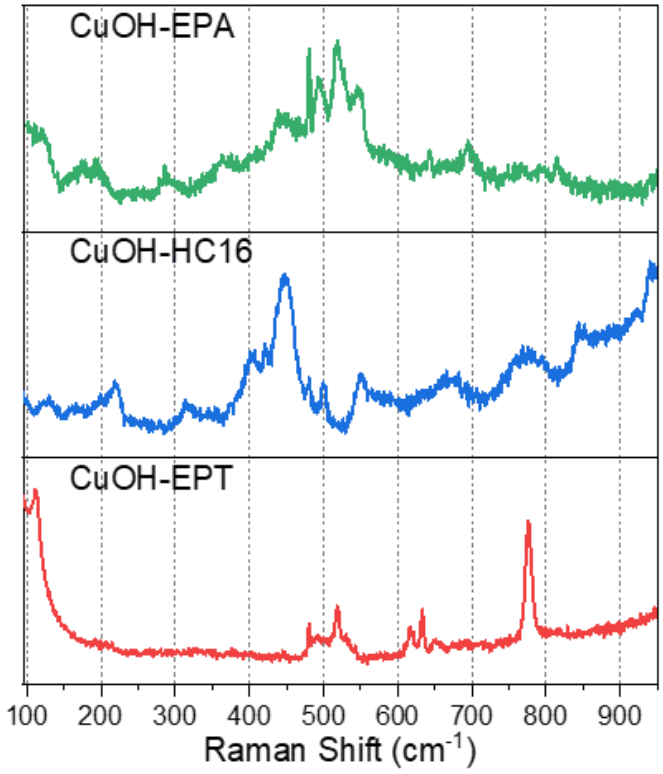

Figure 27. Raman spectroscopy of CuOH samples. Note that peaks at 480 cm^{-1} are spikes but not due to the vibrations.

Table 2. Comparison of vibrational bands of CuOH-EPA from experimental and theoretical measurements.

Vibrations	**DFT calculations (cm^{-1})**	**Experimental values (cm^{-1})**
Cu-C	551	547
OH, phenyl rings	821, 830	826
C-C	1044	1046
C-C, OH	1119	1118
Alkane C-H	1411	1407
Alkane C-H	1455	1454

phenyl ring	1508	1502
phenyl ring	1622	1606
C≡C	1876	1896
C≡C	1975	1948
OH	2853	2865
Alkane C-H	2917	2922
Alkane C-H	2958	2953
Aromatic C-H	3030	3030
Aromatic C-H	3071	3075
OH, C-H	3110~3589	3100~3700

Table 3. Raman vibration peaks from experimental and theoretical calculations of CuOH-EPA.

Vibration	**Experimental data (cm^{-1})**	**DFT calculation (cm^{-1})**
Cu-O	120	125
Cu-C	174	173
Cu-C	196	195
Cu-C	287	284
Cu-O	365	369
Cu-O, O-H	442	436, 446
C≡C	493	497

Phenyl ring	520	525
C≡C, Phenyl ring	549	551
Phenyl ring	642	640
Phenyl ring	693	695
Phenyl ring, O-H	817	816

The interfacial bonding structure is further supported in Raman measurements. From Figure S26, both CuOH-EPA and CuOH-HC16 can be seen to exhibit multiple peaks in the range of 100 to 500 cm^{-1}, which can be attributed to Cu-C or Cu-OH vibrations. For instance, in CuOH-EPA the peaks at 120, 365, and 442 cm^{-1} may be attributed to the Cu-OH vibrations, and those at 174, 196, 287 cm^{-1} due to the Cu-C≡ vibrations,[53] which further confirms that the EPA ligands are indeed directly bonded to Cu instead of O. In fact, these assignments are consistent with results from DFT calculations (Table 3). For CuOH-HC16, the Cu-OH vibrations can be found at 125, 357, and 446 cm^{-1}, with the rest of the peaks arising from Cu-C≡, and C-C vibrations.[53] Meanwhile, the C≡C vibration can be readily resolved in both CuOH-EPA (493 cm^{-1}) and CuOH-HC16 (497 cm^{-1}), but absent in CuOH-EPT. In contrast, CuOH-EPT showed an intense peak at 110 cm^{-1}, due to Cu-S vibrations.[54] In addition, no peak can be identified at ca. 470 cm^{-1} (S-S vibrations) for CuOH-EPT, ruling out the formation of crystalline copper sulfides.[54]

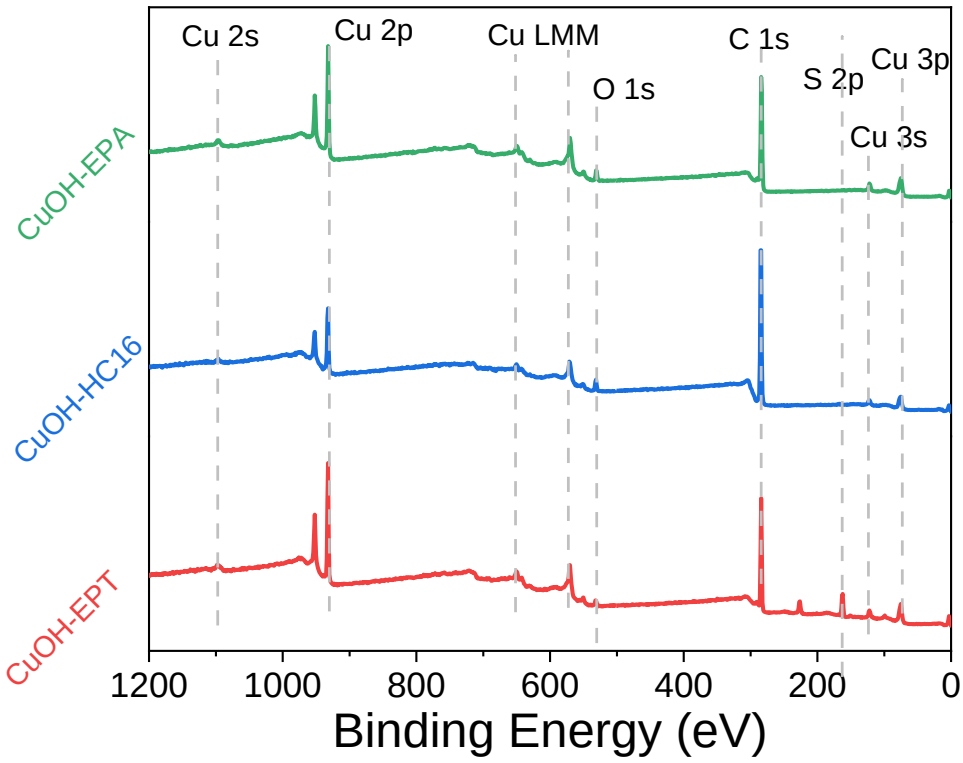

Figure 28. Full XPS survey of the three CuOH samples.

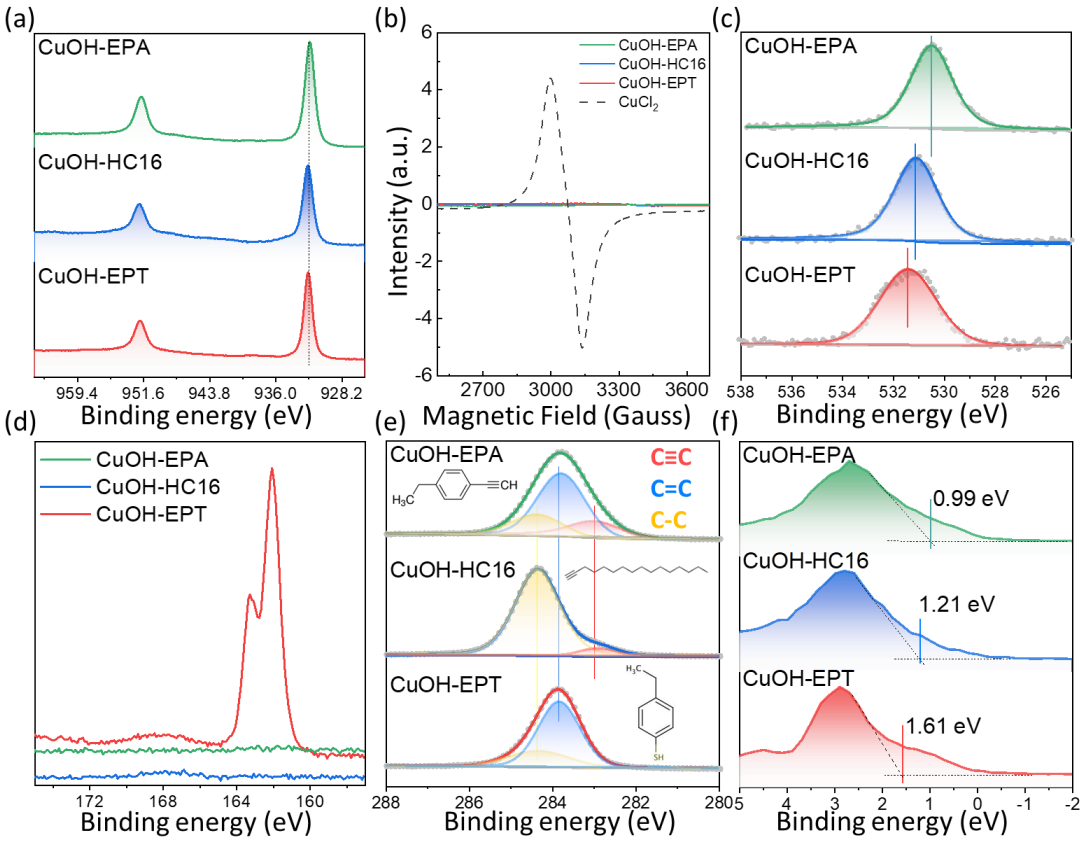

Figure 29. High-resolution XPS spectra of the (a) Cu 2p, (c) O 1s, (d) S 2p, and (e) C 1s electrons of the CuOH-EPT, CuOH-EPA, and CuOH-HC16 samples (bottom to top). The corresponding (b) EPR and (f) VBM spectra.

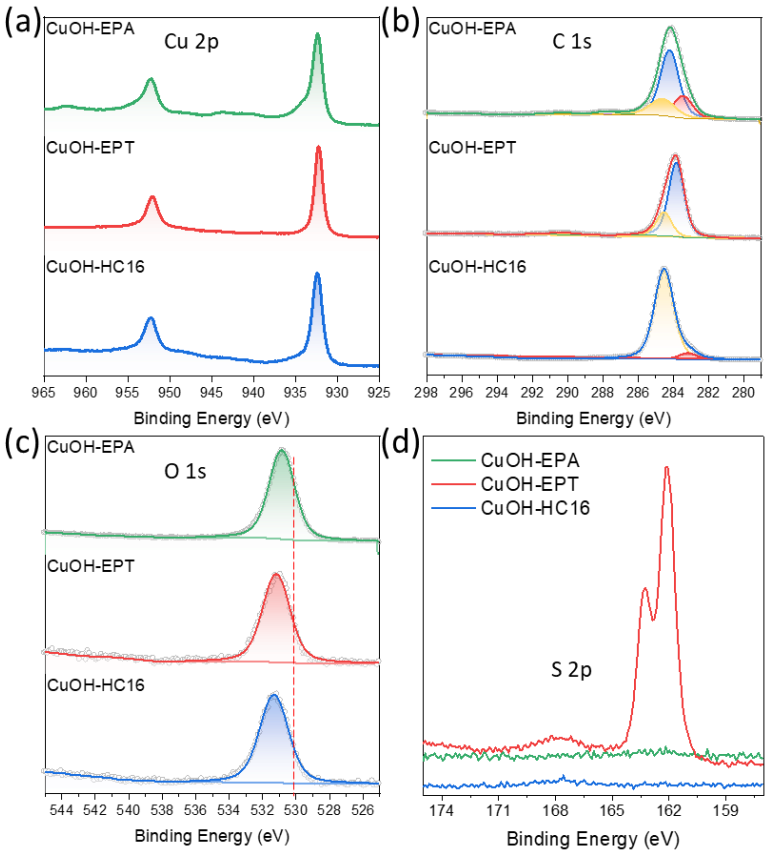

Figure 30. XPS spectra of the three CuOH samples after storage in ambient conditions for 3 months: (a) Cu 2p, (b) C 1s, (c) O 1s, and (d) S 2p.

Table 4. XPS fitting results for CuOH-EPA, CuOH-HC16, and CuOH-EPT.

CuOH-EPA	Species	Binding Energy (eV)	Content (at%)
C	sp	282.99	89.83
	sp^2	283.78	
	sp^3	284.35	
Cu	$2p_{3/2}$	932.04	6.19
	$2p_{1/2}$	951.79	
O	hydroxide	530.50	3.98

CuOH-EPT	**Species**	**Binding Energy (eV)**	**Content (at%)**
C	sp^2	283.83	79.98
	sp^3	284.34	
Cu	$2p_{3/2}$	932.22	6.81
	$2p_{1/2}$	951.97	
O	hydroxide	531.42	2.60
S	$2p_{3/2}$	162.06	10.61
	$2p_{1/2}$	163.27	
CuOH-HC16	**Species**	**Binding Energy (eV)**	**Content (at%)**
C	sp	282.91	94.11
	sp^3	284.36	
Cu	$2p_{3/2}$	932.28	2.72
	$2p_{1/2}$	952.03	
O	hydroxide	531.10	3.17

XPS measurements were then carried out to analyze the elemental compositions and valance states of the samples (Figure 28). Figure 29a depicts the high-resolution scans of the Cu 2p electrons, where the Cu $2p_{3/2}$/$2p_{1/2}$ peaks of all samples can be found around 932.0/951.8 eV for CuOH-EPA, 932.2/952.0 eV for CuOH-EPT, and 932.3/952.0 eV for CuOH-HC16. Note that no apparent satellite peaks that are characteristic of Cu^{2+} can be discerned from the Cu 2p spectra, indicating that Cu^{2+} was

indeed effectively reduced by SO_3^{2-} to Cu^+ (eq. 2).[55,56] This is in sharp contrast to the control experiments where samples were prepared in the same manner but without the addition of $NaHSO_3$ (Figure 4). In fact, electron paramagnetic resonance (EPR) measurements (Figure 29b) show that all CuOH samples displayed only a featureless profile within the magnetic field strength of 2500 to 3500 G, in sharp contrast to $CuCl_2$ that exhibits a clearly-defined signal with a *g* value of 2.188. This is consistent with the diamagnetic nature of Cu^+ and paramagnetic Cu^{2+}.[56] The corresponding high-resolution XPS spectra of the O 1s electrons were exhibited in Figure 29c. One can see that a single component was resolved in all three CuOH samples, 530.5 eV for CuOH-EPA, 531.4 eV for CuOH-EPT, and 531.2 eV CuOH-HC16, that can be ascribed to metal hydroxide.[57] Notably, the red-shift of 0.9 eV with CuOH-EPA and 0.2 eV with CuOH-HC16, as compared to CuOH-EPT, likely arose from different charge transfer from CuOH to the ligands, as a result of the extensive electronic coupling at the interface. This is indeed consistent with the results of DFT calculations, where charge transfer was found to occur from the ligands to CuOH in the case of CuOH-EPA and CuOH-HC16, whereas the direction of charge transfer was reversed for CuOH-EPT (vide infra). The results are also consistent with the variation of the valence band maximum (VBM) of the three samples. From the VBM spectra in Figure 29f, CuOH-EPA can be seen to possess the lowest VBM at 0.99 eV, in comparison to 1.31 eV for CuOH-HC16 and 1.61 eV for CuOH-EPT.

As for CuOH-EPT, the S 2p spectrum shows a well-defined doublet at 162.0/163.3 eV, which can be assigned to the $2p_{3/2}/2p_{1/2}$ electrons of Cu-S,[58,59] consistent with the

stabilization of CuOH by Cu-S interfacial bonds (Figure 29d). Notably, this species was totally absent in both CuOH-HC16 and CuOH-EPA, indicating that these samples were free of metal sulfide impurities.

The C 1s spectra of the three CuOH samples are depicted in Figure 29e, which are completely consistent with their respective ligand structure.[41] For CuOH-EPA, deconvolution yields three peaks at 283.0 eV for sp-hybridized C, 283.8 eV for sp^2 C (aromatic rings), and 284.4 eV for sp^3 C. For CuOH-HC16, only the sp and sp^3 carbon can be resolved, and only the sp^2 and sp^3 species for CuOH-EPT. These results are also listed in Table 4, where the Cu:ligand molar ratio was indeed close to 1:1 for all samples. Notably, the XPS profiles of the three CuOH samples remained virtually invariant even after storage in ambient condition for three months (Figure 30), suggesting remarkable structural stability of the materials that was most likely endowed by the organic functionalization, a drastic deviation from the metastable characteristics observed with bare CuOH (Figure 1) or bulk CuOH.[24,25]

Further structural insights of CuOH-EPA were obtained from X-ray absorption spectroscopic (XAS) measurements. From the X-ray absorption near edge spectra (XANES) in Figure 31a, one can see that all three organically capped CuOH samples possessed an oxidation state close to that of Cu_2O, with the absorption edges situated between those of the Cu foil and CuO references. In fact, from the first-order derivatives of XANES (inset to Figure 31a), it can be seen that the three CuOH samples all exhibit an extremum (pre-edge peak) around 8980 eV, very close to that of Cu_2O, but apparently different from those of Cu foil (8978 eV) and CuO (8982 eV).

Specifically, CuOH-EPA and CuOH-HC16 can be seen to exhibit a pre-edge peak at 8982 eV and 8981 eV, respectively, due to the 1s → $4p_x/p_y$ transitions, and such transitions occurred at 8981 eV for bulk Cu_2O. By contrast, CuOH-EPT exhibited only a shoulder at 8981 eV, suggesting a different chemical environment due to the formation of Cu-S interfacial bonds (vs. Cu-C≡ for CuOH-EPA and CuOH-HC16), whereas bulk CuO showed an even less sharp shoulder at 8984 eV, due to the 1s to $4p_z$ transition.[60] From the Fourier-transform extended X-ray absorption fine spectra (FT-EXAFS) in Figure 31b, one can see that the first main peak, which arose from the Cu-O/C path, appeared at 1.72 Å for CuOH-EPA, and increased to 1.82 Å for CuOH-HC16 and CuOH-EPT. These are all larger than those of bulk CuO (1.57 Å) and bulk Cu_2O (1.47 Å). Fitting of the EXAFS data (Figure 32-33 and Table 5-7) shows that the bond length of Cu-O/C was rather consistent for CuOH-EPA and CuOH-HC16 at ca. 2.01 and 2.05 Å, respectively, yet longer than those of the control samples of Cu_2O (1.85 Å) and CuO (1.95 Å), indicating the absence of copper oxides in the obtained sample. Additionally, the Cu-O/C coordination numbers (5.3 for CuOH-EPA and 5.8 for CuOH-HC16) were larger than that of Cu_2O (2) but consistent with the structure shown in Figure 13g-13h,[61,62] suggestive of an imperfect layered structure of the CuOH-EPA and CuOH-HC16 samples. The second main peak at 2.4 Å of CuOH-EPA and CuOH-HC16 most likely arose from the second shell interaction of Cu-C with the organic capping ligands. By contrast, the first main peak of CuOH-EPT arose from the combined contributions of Cu-O/C and Cu-S bonds (Figure 34 and Table 7), indicating successful formation of the CuOH nanostructures by the EPT ligands, which is significantly

different from CuOH-EPA and CuOH-HC16. Taken together, these results confirm the successful production of a Cu-O/C environment around Cu with no observable Cu-Cu interactions, suggesting an amorphous structure with little to no long-range crystallinity (vide ante).

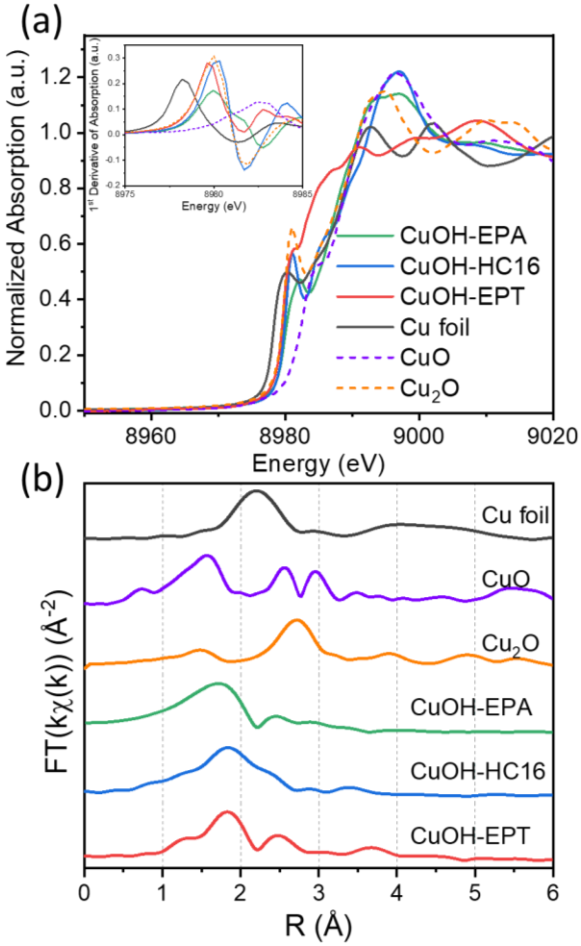

Figure 31. (a) Cu K-edge normalized XANES profiles of CuOH-EPA, CuOH-HC16, CuOH-EPT, Cu foil, Cu_2O, and CuO, and (b) their corresponding FT-EXAFS spectra. Inset to panel (a) is the corresponding first-order derivative of the pre-edge region.

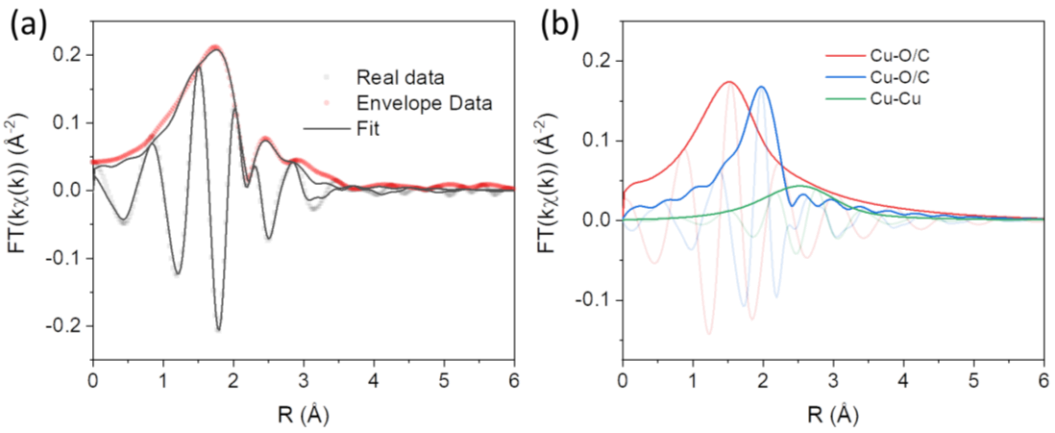

Figure 32. (a) Fittings and (b) deconvolution of the fitting results of the EXAFS spectrum of CuOH-EPA.

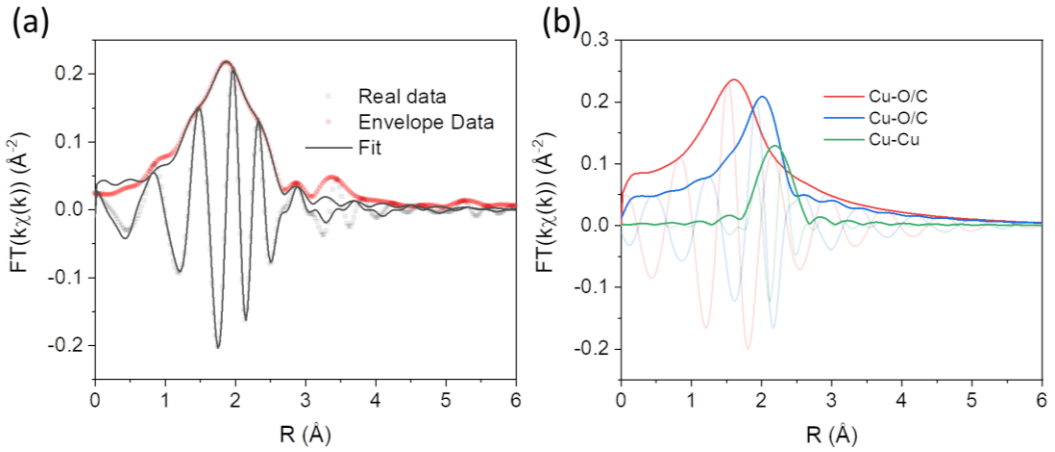

Figure 33. (a) Fittings and (b) deconvolution of the fitting results of the EXAFS spectrum of CuOH-HC16.

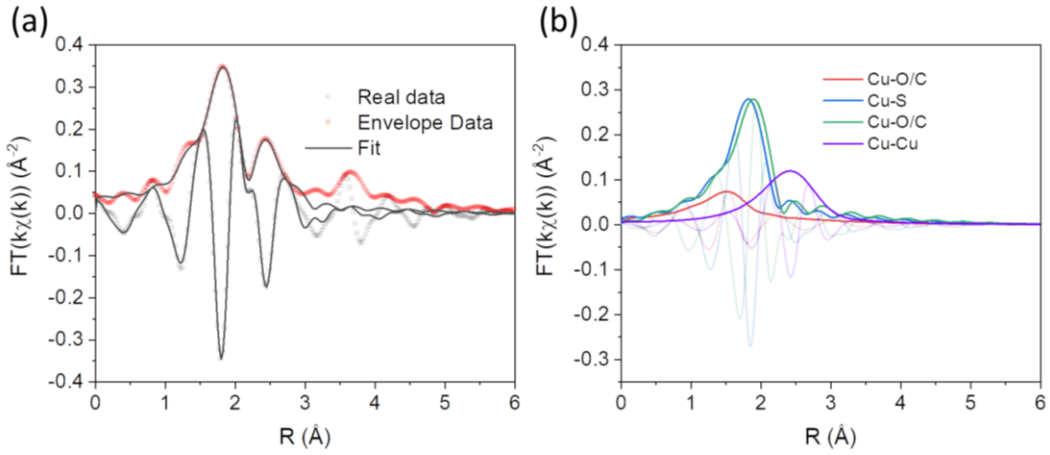

Figure 34. (a) Fittings and (b) deconvolution of the fitting results of the EXAFS spectrum of CuOH-EPT.

Table 5. Fitting results of the EXAFS data of CuOH-EPA.

Path	**σ^2**	**Bond Length (Å)**	**Coordination Number**
Cu-O/C	0.0177	2.0073	5.328
Cu-O/C	0.0017	2.4466	4.617
Cu-Cu	0.0367	2.8647	13.683

Table 6. Fitting results of the EXAFS data of CuOH-HC16.

Path	**σ^2**	**Bond Length (Å)**	**Coordination Number**
Cu-O/C	0.0148	2.0551	5.882
Cu-O/C	0.0050	2.4679	7.282
Cu-Cu	0.0016	2.4530	0.808

Table 7. Fitting results of the EXAFS data of CuOH-EPT.

Path	σ^2	Bond Length (Å)	Coordination Number
Cu-O/C	0.0082	1.9784	1.213
Cu-S	0.0016	2.2693	2.030
Cu-O/C	0.0016	2.3804	8.070
Cu-Cu	0.0188	2.7442	10.250

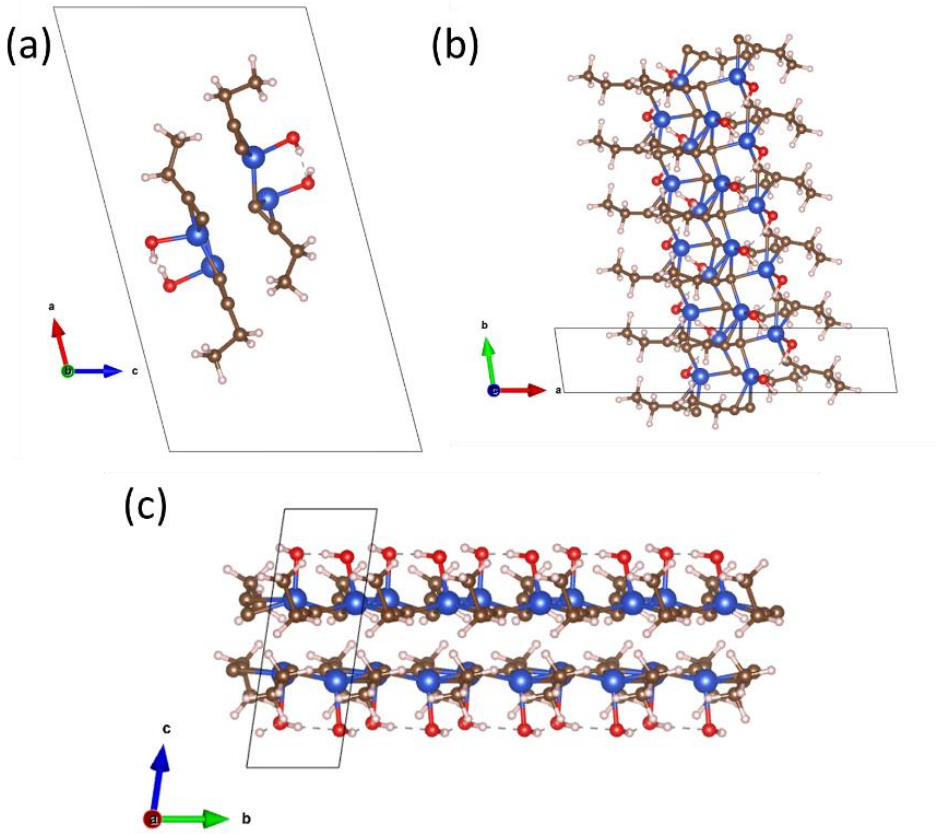

Figure 35. (a) Bulk CuOH-HC4 showing the layered structure, H-bonding between layers. (b) PBE calculated band structure and DOS of CuOH.

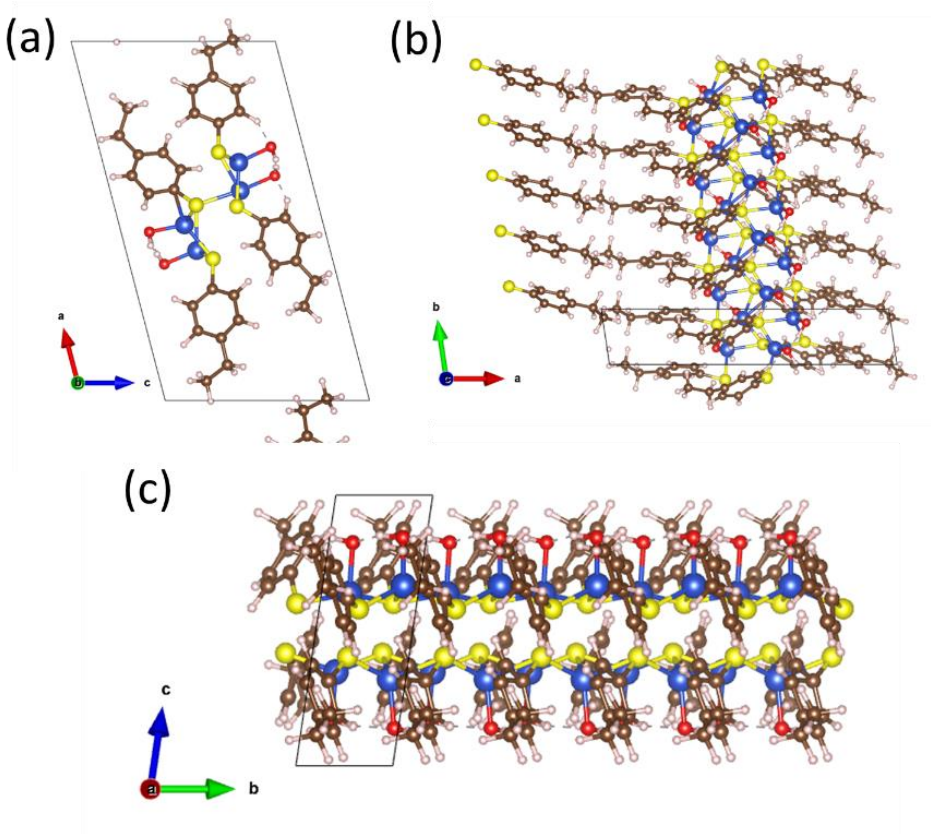

Figure 36. (a) Bulk CuOH-EPT showing the layered structure, H-bonding between layers. (b) PBE calculated band structure and DOS of CuOH.

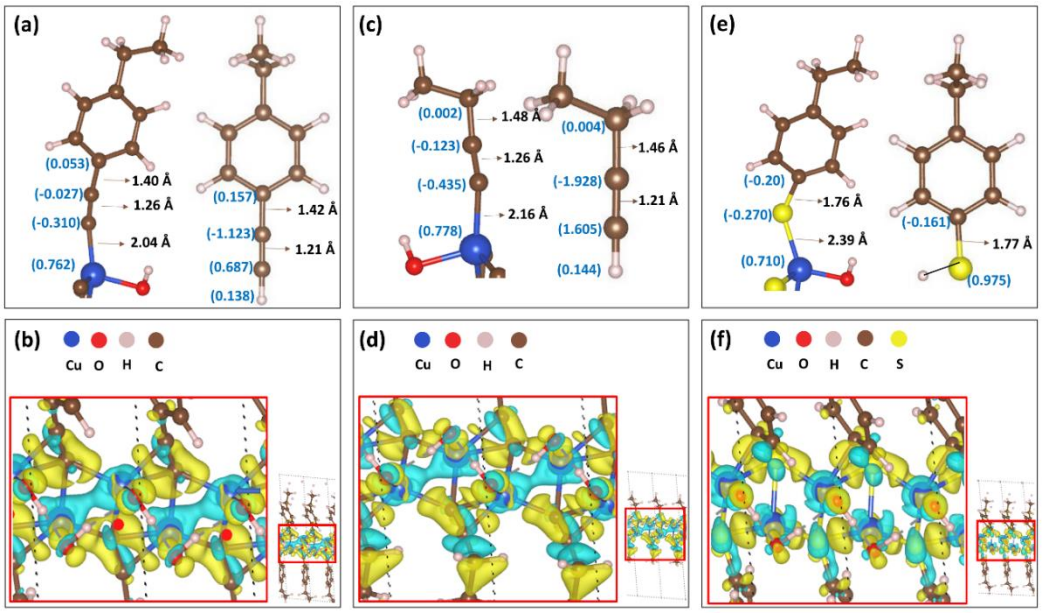

Figure 37. Optimized structure of (a) CuOH-EPA and EPA ligand, (c) CuOH-HC4 and HC4, (e) CuOH-EPT and EPT with corresponding bond distances (black) and Bader charges in |e| (blue). Charge density difference isosurfaces of (b) CuOH-EPA, (d) CuOH-HC4, and (f) CuOH-EPT (±0.0016|e|). Yellow, positive representing electron gains; cyan, negative for electron loss.

To understand the interfacial structure and properties of the organically capped CuOH nanostructures, theoretical studies were performed by using the structural models proposed above (Figure 13g, 35, and 36) anchored with EPA, butyne (HC4, as a simplified representation of HC16), and EPT. Figure 4a depicts the stable configuration of CuOH-EPA after relaxing, from which one can see that the acetylene moiety formed a Cu-C≡C- interfacial structure, which is consistent with the results from FTIR, Raman, and XPS measurements (Figure 13, 29, and 27). Furthermore, one can see that the C≡C bond length increased slightly from 1.21 Å for the EPA monomer to 1.26 Å for CuOH-EPA (Figure 37a). These observations suggest effective electronic coupling at the

CuOH-ligand interface, leading to elongation of the acetylene moiety.[28] In fact, from the Bader charge profile in Figure 37a, one can see a charge transfer of ca. 0.14 |e|, relative to the pristine EPA monomer, from CuOH to the EPA ligands. Charge accumulation in the -C≡C- interfacial bond and phenyl rings in CuOH-EPA is clearly visible in the charge density isosurfaces shown in Figure 37b. CuOH-HC4 shows a similar elongation of the -C≡C- moiety and similar charge accumulation, where ca. 0.38 |e| was transferred from CuOH to primarily -C≡C- (Figure 37c and 37d). Notably, the contribution of the ethyl group to interfacial charge transfer is minimal. This observation is consistent with results of our prior study of alkyne-functionalized Iridium nanoparticles and alkyne-functionalized TiO_2 nanoparticles.[28,63] In contrast, when EPT ligands were bound onto the CuOH cores, the interfacial linkage actually consisted of non-conjugated Cu-S- bonds (Figure 37e and 37f). In this case, there are obvious charge depletions in the S-H and S-Cu interfacial bonds and accumulations in the S-C bond, with a net charge transfer from CuOH to the ligand being 1.38 |e|. Considering that the Cu atoms exhibit similar valence states from XPS, XAS, and charge analysis in Figure 37a-c, the depletion of electrons in Cu-OH units will render a positive shift of the O 1s binding energies, which is in excellent agreement with results from XPS measurements (Figure 29).

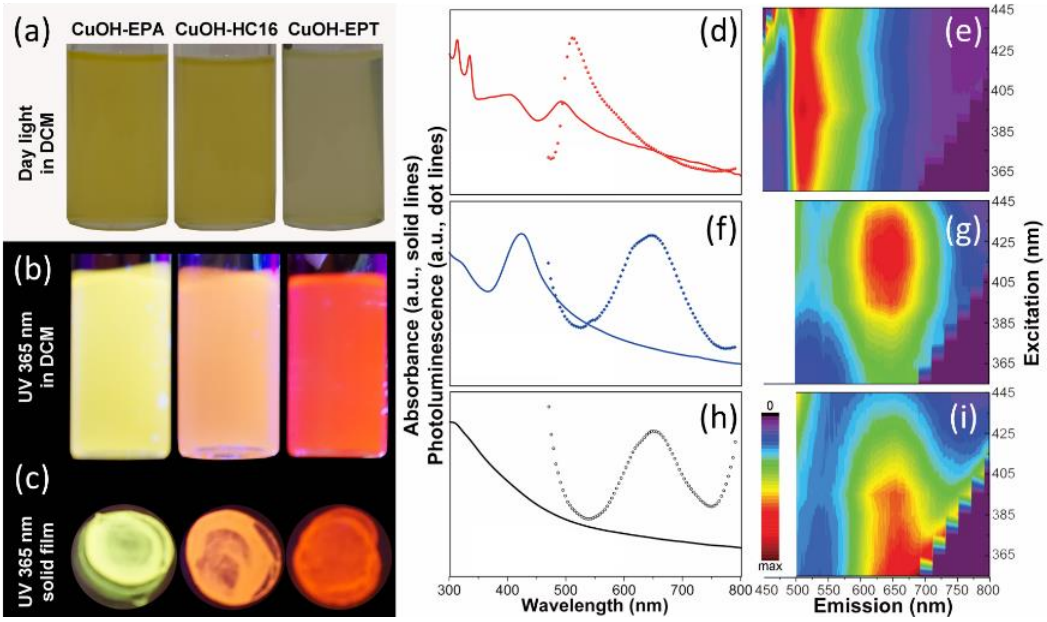

Figure 38. Photographs of different organically capped CuOH nanostructures (a) in ambient light (dispersed in DCM) and under 365 nm photoirradiation (b) when dispersed in DCM and (c) as solid films). The colors of the CuOH-EPA, CuOH-HC16 and CuOH-EPT dispersions in DCM are all yellowish, while the photoluminescence is red, yellow, and orange, respectively when dispersed in DCM or solid films. (d, f, h) UV-vis and photoluminescence spectra of the ligands-functionalized CuOH nanostructures at the excitation at 395 nm and (e, g, i) the excitation-dependent PL profiles: (d,e) CuOH-EPA, (f,g) CuOH-HC16, and (h,i) CuOH-EPT.

Notably, such different interfacial linkages resulted in a marked variation of the optical and electronic properties of the CuOH nanostructures. As mentioned earlier, the samples can all be readily dispersed in typical organic solvents (e.g., DCM, THF, etc) and remain stable without obvious precipitation. The photographs of the suspensions are shown in Figure 38a, where the color was grey-yellow for CuOH-EPT, and dark-yellow for CuOH-EPA and CuOH-HC16. Under photoirradiation with a UV lamp (ca. 365 nm), the samples can be seen to emit orange-red, yellow, and orange photons for

the CuOH-EPT, CuOH-EPA and CuOH-HC16 samples, respectively (Figure 38b). Notably, the color appearance of the DCM solutions was the same as that when they were dropcast onto a glass slide forming a solid film (Figure 38c). These observations indicated that the optical (and hence electronic) properties are different when CuOH were passivated by different organic ligands, as manifested in UV-vis and photoluminescence (PL) spectroscopic measurements (Figure 38d-i). One can see that CuOH-EPT exhibited an exponential decay profile in UV-vis measurements, without any apparent absorption features (Figure 38d),[64] whereas two main peaks can be resolved at 492 and 406 nm for CuOH-EPA (Figure 38f), and one peak at 424 nm for CuOH-HC16 (Figure 38h). At the same excitation wavelength (λ_{ex}) of 405 nm, both CuOH-EPT and CuOH-HC16 showed a PL emission peak (λ_{em}) at 650 nm (Figure 38d and 38h), whereas the emission peak of CuOH-EPA blue-shifted to 512 nm (Figure 38f). Interestingly, for this CuOH sample series, whereas λ_{em} remains virtually unchanged when λ_{ex} was varied within the range of 360 to 445 nm, the emission intensity diminished markedly at $\lambda_{ex} > 400$ nm for CuOH-EPT (Figure 38e) and at $\lambda_{ex} < 385$ nm for CuOH-HC16 (Figure 38i), but exhibited no clear diminishment with CuOH-EPA (Figure 38g).

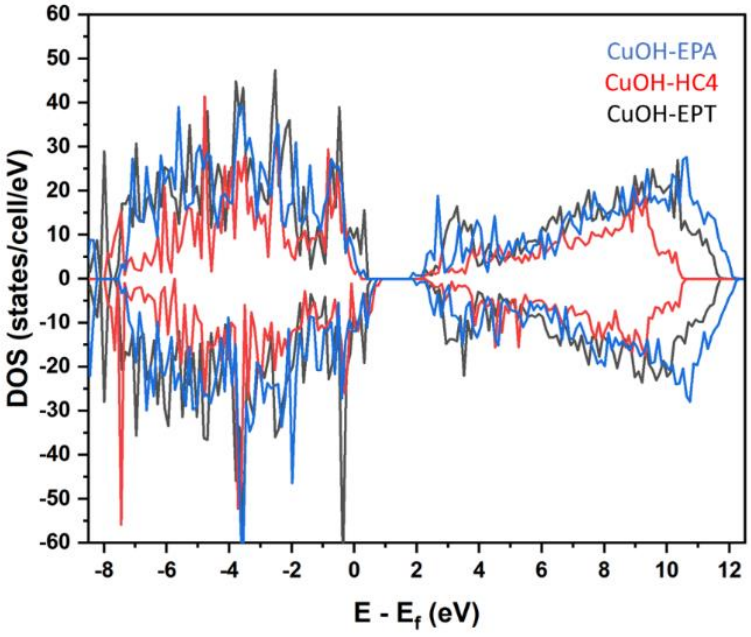

Figure 39. Calculated density of states (DOS) for CuOH-EPA, CuOH-HC4, and CuOH-EPT.

To understand the origins of the different optical properties amongst the samples, we calculated the density of states (DOS) of CuOH-EPA, CuOH-HC4, and CuOH-EPT. From Figure 39, one can clearly see that both CuOH-EPA and CuOH-HC4 exhibited a higher VBM position than CuOH-EPT, consistent with the experimental results shown in Figure 29c. To further discern the difference between CuOH-EPA and CuOH-HC4, projected local DOS (PDOS) were deconvoluted and shown in Figure 40a. It can be seen that whereas both structures showed extensive interfacial charge delocalization, the phenyl ring of EPA anchored on CuOH (CuOH-EPA) made a significant contribution to the states near the Fermi level (E_f) at the both VB and the conduction band (CB), in comparison to CuOH-HC4. A schematic illustration of PL emission is depicted in Figure 40b. For all samples, electrons are excited from the VB (contributed

mainly by Cu-C≡C- interfacial bonds) to the CB (contributed mainly by the p electrons of the capping ligands) under appropriate photoexcitation. For the HC_x (x = 16 for experimental and x = 4 for theory) capped CuOH nanostructures, the excitons relax to the CB edge and then return to the holes to emit light at around 650 nm. The situation for CuOH-EPA is different. In the recombination process, the excitons relax to the dominating states from the phenyl ring rather than the CB edge before combining with the hole states in the ring. As a result, it emits light with a higher energy (shorter wavelength at ca. 512 nm).

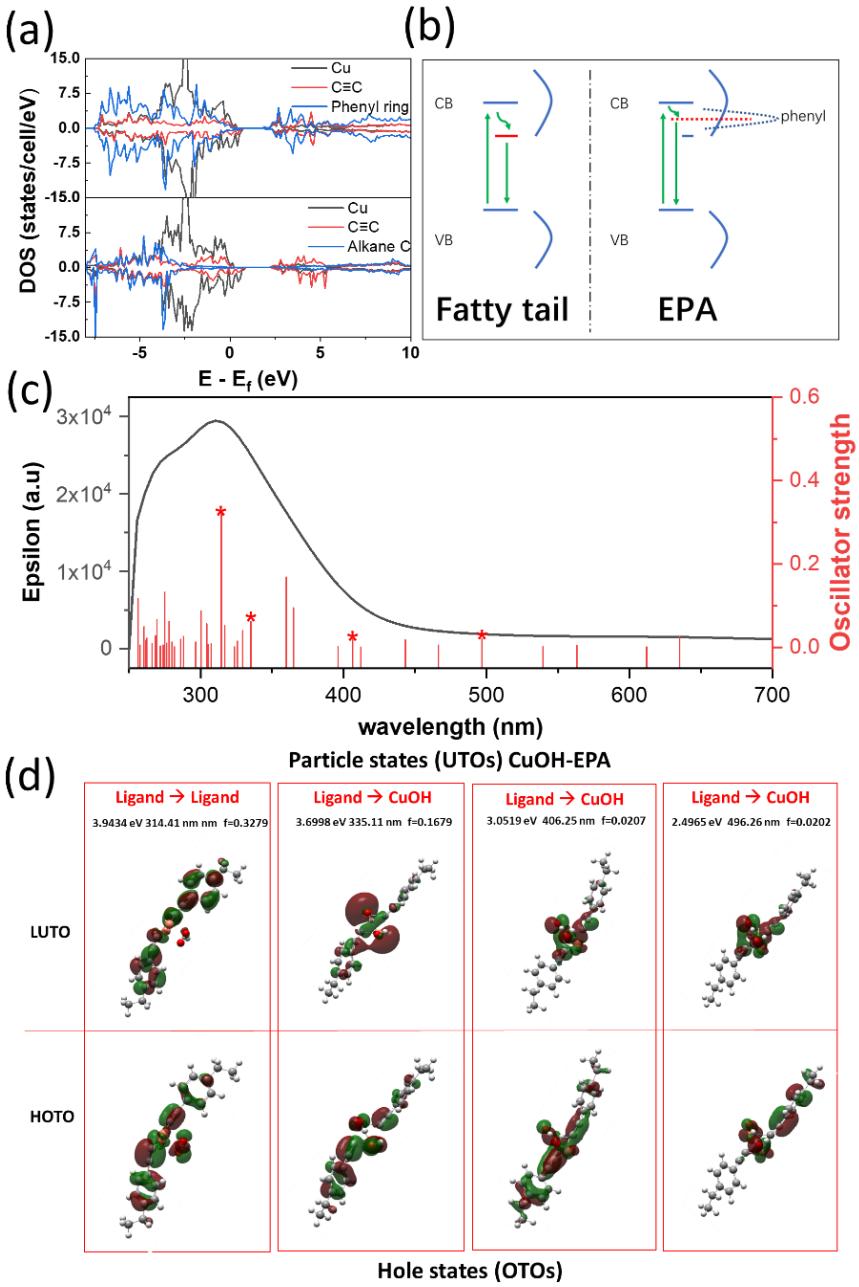

Figure 40. (a) Projected local density of states of CuOH-EPA (top) and CuOH-HC4 (bottom). (b) Proposed PL mechanism. (c) TDDFT-based UV-vis spectrum of CuOH-EPA, "*" means the experimental values. (d) Natural transition orbitals (NTO) analysis of CuOH-EPA.

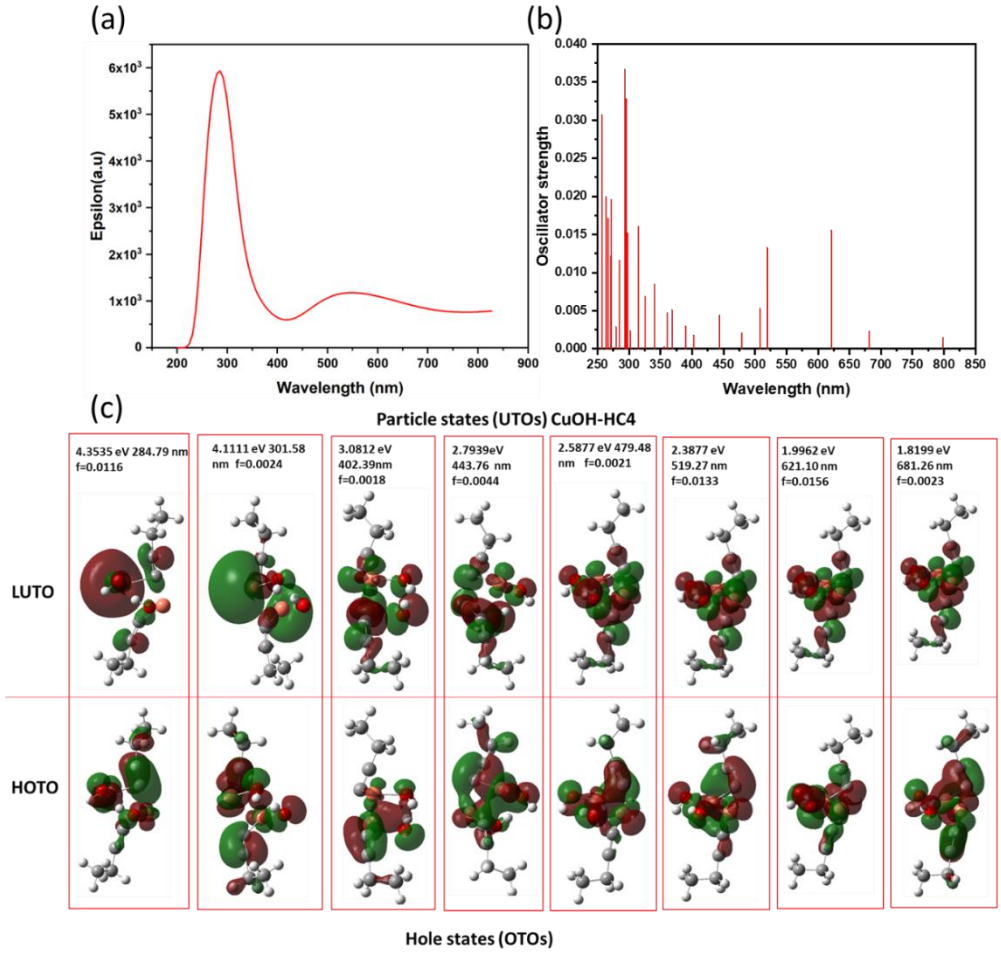

Figure 41. (a) Calculated UV-vis spectra for CuOH-HC4, (b) absorption wavelengths and c) and the corresponding natural transition orbitals.

This emission mechanism is supported by the calculated UV-vis spectra based on time-dependent DFT (TDDFT), as depicted in Figure 40c, where the four absorption peaks of CuOH-EPA observed experimentally in Figure 38f (314, 335, 406 and 492 nm) can be clearly identified (marked with asterisks). Figure 40d presents the natural transition orbitals (NTOs) for CuOH-EPA. NTOs are unitary transformation of the ordinary molecular orbitals to enable an intuitive qualitative description of electronic excitations.

The NTOs are more compact and express the excitation as pairs of NTO orbitals, with transition occurring from excited particle (OTOs) to the empty hole (UTOs). As shown in Figure 40d, the hole states are largely localized on the ligands whereas the particle states concentrate to the CuOH units except for 314 nm. These characteristics are manifestations of the strong interactions between the ligand and the CuOH core, which enable charge transfer excitation from the ligands to the particle, which is likely the origin of the intense emissions across a wide range of excitation wavelength, as shown in Figure 37f, indicating that the optical property of CuOH-EPA was dominated by the EPA ligands, consistent with the results from PDOS analysis. In contrast, for the CuPH-HC4 sample (Figure 41), one can see that most OTOs and UTOs are localized on CuOH instead of the HC4 ligands, suggesting a diminished ligand-core interaction due to the lack of phenyl rings. Therefore, the emissions of CuOH-EPT and CuOH-HC16 are most likely dominated by the semiconducting CuOH cores.

Notably, with such unique optoelectronic properties, the ligand-capped CuOH nanostructures exhibited apparent photodynamic activity towards the inhibition of bacterial growth by using *Escherichia coli* (*E. coli*) as the illustrating example, and the antibacterial activity varied markedly among the sample series. Note that in the dark, none of the CuOH samples exhibited any antimicrobial activity (Figure 42). Yet, under UV photoirradiation for up to 40 min (Figure 43a), the bacterial growth was significantly inhibited by CuOH-EPA and CuOH-EPT, where it took only 12 min to remove 50% of the bacterial cells with the former and 16 min for the latter, whereas virtually no inhibition was observed with CuOH-HC16, as compared to the *E. coli*

control. The overall activity was diminished somewhat under blue light irradiation (465 nm). From Figure 43b, one can see that the growth of *E. coli* was significantly inhibited by CuOH-EPA only, with no survival of bacterial cells after two hours' exposure, and the antibacterial activity was minimal with CuOH-HC16 and CuOH-EPT. Taken together, these results indicate that CuOH-EPA stood out as the best antibacterial agent among the series.

Notably, no copper species were detected by ICP-OES measurements in the bacterial culture medium with CuOH-EPA (after 120 min), in comparison to 1.935 ppm with Cu_2O, signifying no leaching of Cu ions in the former. In Ellman's assay (Figure 43d), where the loss of GSH is an effective representation of oxidative stress,[65] it can be seen that under blue light irradiation for up to 2 h, CuOH-EPA led to the most significant degradation of GSH among the series, suggesting that the high antibacterial activity of CuOH-EPA was most likely due to the substantial oxidative stress produced under photoexcitation. This was indeed confirmed in EPR measurements. From Figure 43e, one can see that after blue light photoirradiation for 10 min, the CuOH-EPA and CuOH-HC16 samples manifested a clear 1:2:2:1 hyperfine structure within the magnetic field strength of 3275-3350 G, with a g value of 2.005 ($a_H = a_N = 14.9$ G), which is characteristic of the DMPO−OH adducts,[66] suggesting the formation of hydroxyl (HO•) radicals. By contrast, for CuOH-EPT and blank water, only a much weaker sextet hyperfine structure was observed within the same magnetic field range ($g = 2.006$, $a_N = 15.625$ G, and $a_H = 6.64$ G), which can be ascribed to the DMPO-OOH adduct stemming from superoxide radicals ($O_2^{\bullet-}$).[66,67] These observations are consistent with

the significantly higher bactericidal activity of CuOH-EPA and CuOH-HC16, as compared to CuOH-EPT (Figure 43a-b), as hydroxyl radicals are far more active in antibacterial action than superoxide radicals.[68] Additionally, CuOH-EPA can be seen to exhibit the highest peak to peak intensity among the series, in excellent agreement with the greatest oxidative stress observed in Ellman's assay and the best antibacterial activity among the series.

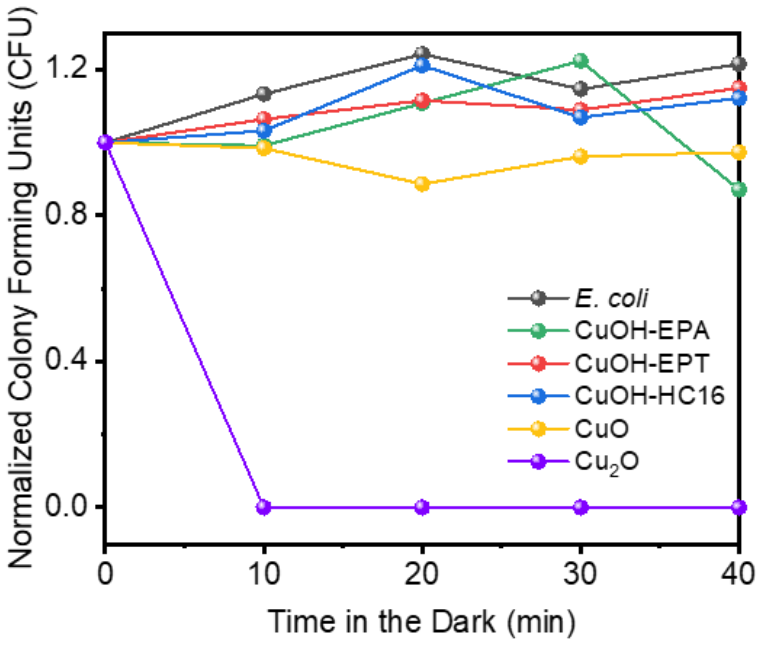

Figure 42. Colony formation units of *E. coli* in the presence of CuOH-EPA, CuOH-HC16, CuOH-EPT, Cu_2O and CuO in the dark for 40 min. *E. coli* in PBS 1X serves as the control. It can be seen that the CuOH samples exhibit no antimicrobial activity in the dark. No activity is observed with CuO, either, whereas apparent inhibition can be seen with Cu_2O, which has been known to be as active as metallic copper in contact killing of bacteria.[69]

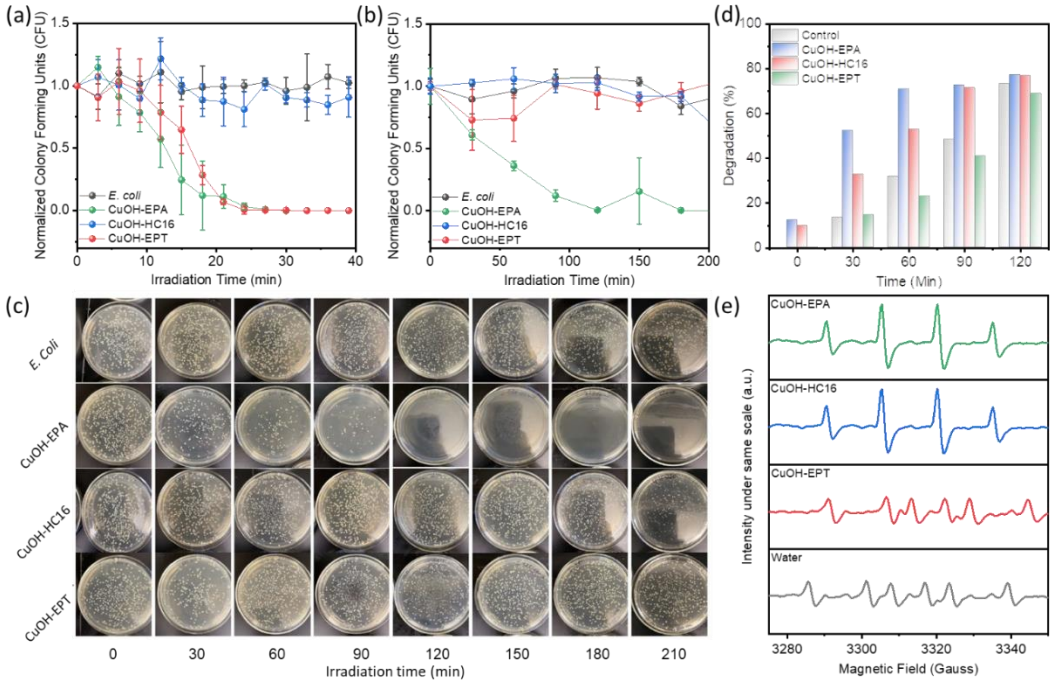

Figure 43. Antibacterial study of CuOH samples series. (a) Study under UV photoirradiation for 40min. Gram negative bacteria E. coli is a control for comparison with CuOH containing samples. (b) Study under blue Light (465 nm) for 200min. Antibacterial studies under blue light photoirradiation. E. coli in PBS 1X (black line) is a control. Error bars are included as the study was done in triplicate. (c) Photographs depicting *E. coli* grown on LB agar plates at different photoirradiation time points (i.e., 0, 30, 60, 90, 120, 150, 180 and 210 min) under blue light (465 nm) in the absence of CuOH and the presence of CuOH-EPA, CuOH-HC16, and CuOH-EPT. (d) Loss of GSH after treatment by materials at different time points. (e) EPR hyperfine splitting patterns in the presence of DMPO after 10 minutes of photoirradiation at 465 nm.

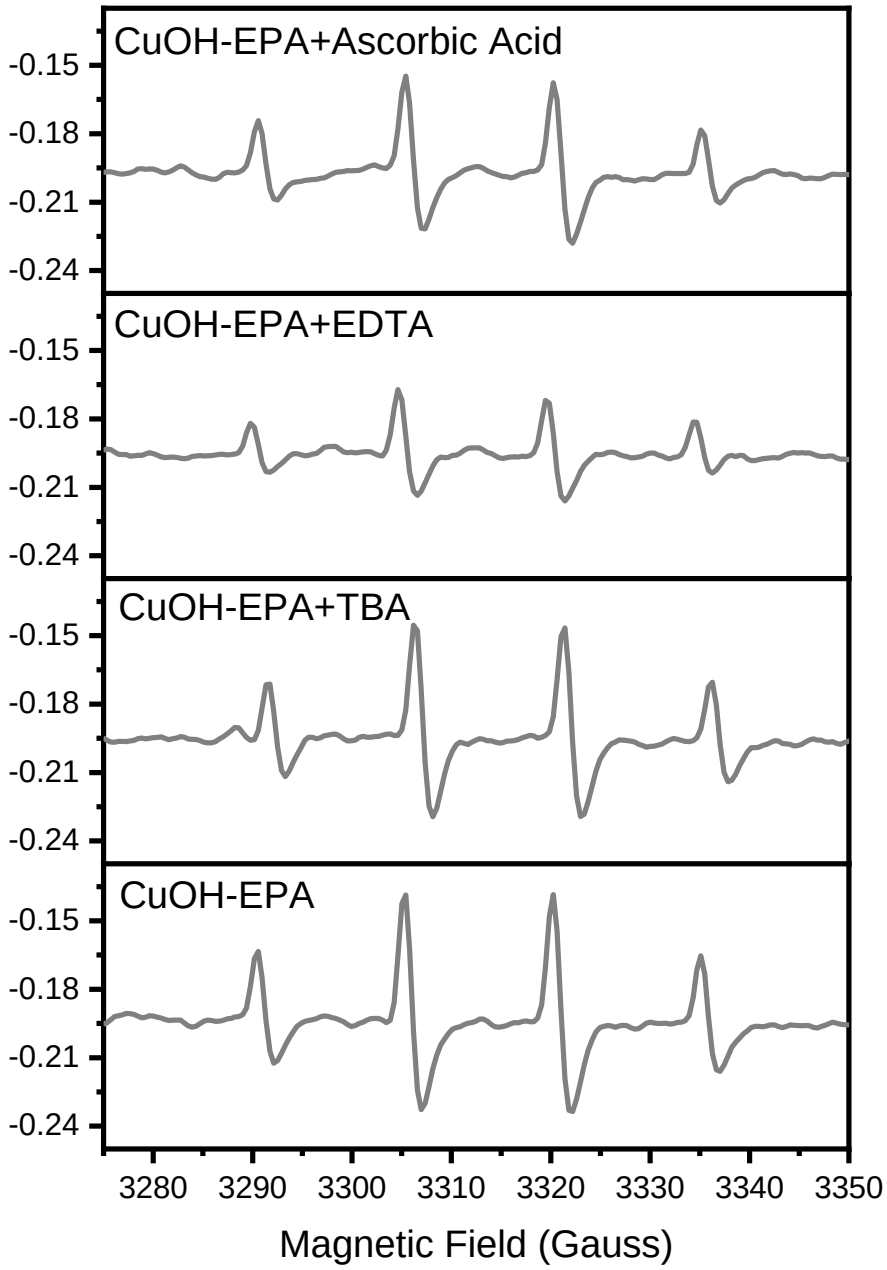

Figure 44. EPR hyperfine splitting patterns of CuOH-EPA in the presence of DMPO and various radical scavengers after 10 min's UV photoirradiation.

In fact, the EPR signal intensity of CuOH-EPA exhibited a noticeable diminishment upon the addition of ethylenediaminetetraacetic acid (EDTA) and much less so with

ascorbic acid (Figure 44), which are the effective scavengers for photogenerated holes and superoxide radicals, respectively.[66] This suggests that the HO• radicals were produced mainly by the hole oxidation of water, $H_2O + h^+ \rightarrow HO\bullet + H^+$, with a minor contribution from the disproportionation reaction of $O_2^{\bullet-}$.[68]

The markedly enhanced antibacterial activity of CuOH-EPA, as compared to others in the series, can be ascribed to its low bandgap (E_g) of 2.52 eV, as compared to CuOH-HC16 (2.94 eV) and CuOH-EPT (2.96 eV) (Figure 45). This is consistent with results from DFT calculations (Figure 39), CuOH-EPA (1.02 eV) < CuOH-EPT (1.46 eV) < CuOH-HC4 (1.64 eV) — note that DFT (PBE) typically underestimates the bandgap of solids.[70] Experimentally, the energy of the blue light photons (465 nm, 2.66 eV) is sufficiently high to excite the valence electrons of CuOH-EPA to the conduction band facilitating the generation of ROS and the eventual antimicrobial activity, but not high enough for CuOH-HC16 and CuOH-EPT.[65,71]

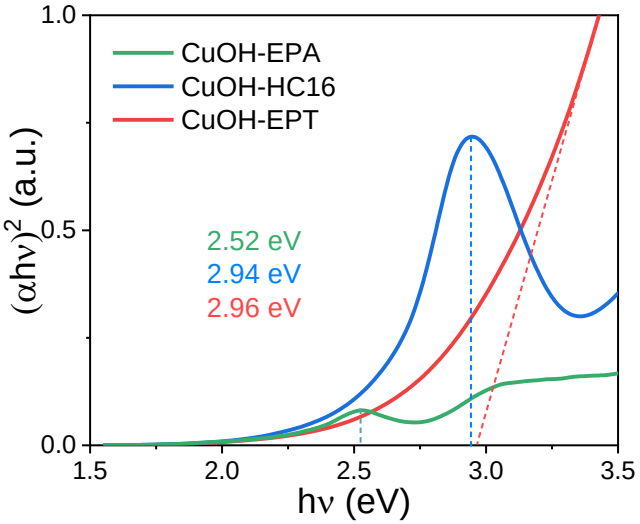

Figure 45. Tauc plots of the three CuOH samples derived from UV-vis measurements.

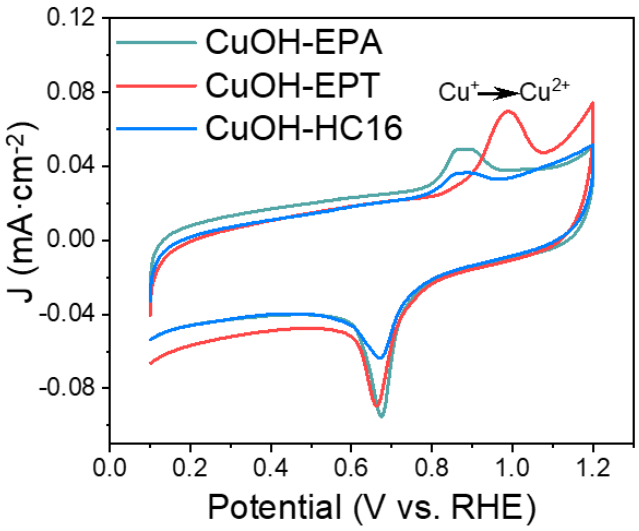

Figure 46. Cyclic voltammograms of different organically capped CuOH nanoparticles 0.1 M KOH. Cyclic voltammograms (CVs) at the scan rate of 10 mV s^{-1} under N_2 saturation.

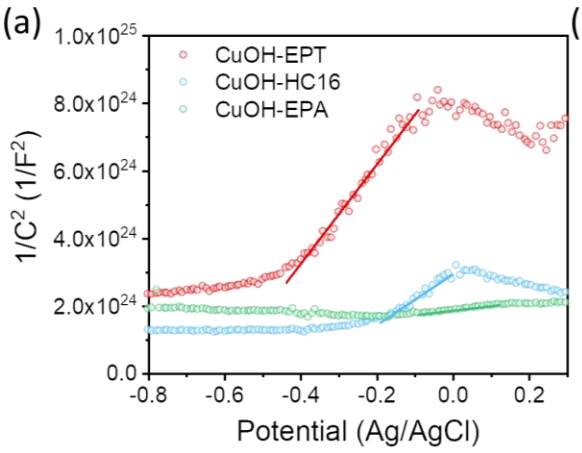

(b)

Name	Slope	Charge carrier density (cm^{-3})	Flat-band potential (V vs. Ag/AgCl)
CuOH-EPT	1.47E+25	9.58E+03	-0.62
CuOH-HC16	2.95E+24	4.78E+04	-0.39
CuOH-EPA	1.87E+24	7.54E+04	-1.41

Figure 47. (a) Mott–Schottky plots of the three CuOH samples. (b) Table of the fitting results including slope, charge carrier density, and flat-band potential.

The discrepancy of interfacial charge transfer between the organic capping ligands and CuOH cores was further evidenced in cyclic voltammetry (CV) and electrochemical impedance measurements. From the CV profiles in Figure 46, both CuOH-EPA and CuOH-HC16 can be seen to exhibit an anodic peak at ca. +0.85 V, due to the oxidation of Cu^{+} to Cu^{2+},[72,73] and the peak potential was substantially more positive at ca. +1.0 V with CuOH-EPT, consistent with the variation of the VBM observed in XPS measurements (Figure 29f). From the Mott–Schottky plots (Figure 47), one can see that all CuOH samples exhibited a positive slope (m), suggestive of an n-type semiconductor.[74] The corresponding charge carrier densities (N_d) were then derived from the plots by using $N_d = \frac{2}{e\epsilon\epsilon_0 m}$, with e being the elementary charge of an electron, ε the dielectric constant, and ε_0 the vacuum permittivity, which decreased markedly in the order of CuOH-EPA (7.54×10^4 cm^{-3}) > CuOH-HC16 (4.78×10^4 cm^{-3}) > CuOH-EPT (9.58×10^3). The markedly higher charge carrier density of CuOH-EPA and CuOH-HC16 can be ascribed to the conjugated CuOH-ligand interfacial linkages that facilitated intraparticle charge delocalization and hence interfacial charge transfer, a critical step in the photocatalytic generation of ROS, in comparison to the CuOH-EPT sample that involved nonconjugated interfacial bonds instead.[75,76]

8.4 Conclusions

In summary, for the first time ever, a facile wet-chemistry procedure was developed for the preparation of stable CuOH nanostructures in the presence of select organic ligands, such as acetylene and mercapto derivatives, where sulfite ions were exploited as the

reducing agent. Electron microscopic study showed that the resulting CuOH nanostructures exhibited a nanoribbon morphology, and spectroscopic measurements confirmed the anchoring of the acetylene moieties onto the CuOH surface forming Cu-C≡ interfacial linkage, whereas for the mercapto ligands, Cu-S- bonds. The former was found to lead to effective electronic coupling between the ligand p electrons and CuOH cores, in contrast to the latter which entailed mostly non-conjugated interfacial bonding interactions, as manifested in optical measurements and confirmed in theoretical studies based on DFT calculations. Significantly, with such unique optoelectronic properties, the CuOH-EPA stood out as the best antibacterial agent among the sample series under both UV and blue light irradiation, due to the effective production of hydroxyl radicals. This was largely ascribed to hole oxidation of water that was facilitated by the conjugated core-ligand linkages and a narrowed bandgap. Results from this study suggest that functionalization by select organic ligands may be an effective strategy in the stabilization and functionalization of CuOH nanostructures, a key step towards their practical applications.

8.5 Experimental Section

Chemicals

Copper(II) acetate monohydrate ($Cu(OAc)_2 \cdot H_2O$, 99.99%, Sigma Aldrich), sodium bisulfite ($NaHSO_3$, Sigma Aldrich), potassium hydroxide (KOH, 99.98%, Fisher Scientific), 4-ethylphenylacetylene (EPA, 97%, Arcos), 4-ethylphenylthiol (EPT, >97%, TCI America), 1-hexadecyne (HC16, >90%, TCI America), hydrogen peroxide (H_2O_2, 30% (w/w), Sigma Aldrich), methylene blue (MB, Sigma Aldrich),

5,5'-dithio-bis-(2-nitrobenzoic acid) (DTNB, ≥98%, Sigma Aldrich), and glutathione (GSH, ≥98 %, Fisher Scientific) were used as received without any further purification. All solvents were obtained from leading suppliers with the highest purity available and used as received, too. Water was supplied by a Barnstead Nanopure Water System (18.3 MΩ cm).

Sample synthesis

Briefly, 1.0 mL of a 0.1 M $Cu(OAc)_2$ aqueous solution and 150 μL of a specific ligand (EPA, EPT or HC16) were added into a mixture of solvents consisting of 10 mL each of dichloromethane, N,N-dimethylformamide, and ethanol under magnetic stirring for ca. 5 min to produce a light-blue quasi-homogenous solution. The solution was then heated in a 100 °C oil bath for 1 min, into which was quickly injected 1 mL of a solution containing 0.5 M $NaHSO_3$ and 0.5 M KOH. The solution was then refluxed for 1 h under vigorous stirring. When the solution was cooled down to room temperature, the addition of 50 mL of Nanopure H_2O yielded a yellowish precipitate in the bottom organic phase, which was separated from the top aqueous phase by centrifugation, rinsed extensively with Nanopure water and methanol to remove excess reactants and impurities, and dried in a vacuum oven. The products were found to be readily dispersed in dichloromethane and other organic solvents, and denoted as CuOH-EPA, CuOH-HC16, and CuOH-EPT, respectively.

Characterization

Transmission electron microscopy (TEM) images were acquired with a Tecnai G2 electron microscope operated at 200 kV. Scanning electron microscopy (SEM) and

energy dispersive spectroscopic (EDS) mapping studies were carried out with an Apreo SEM microscope. TEM elemental mapping analyses based on EDS were carried out with a Talos F200C G2 TEM. FTIR measurements were conducted with a PerkinElmer Spectrum One FTIR spectrometer (with a spectral resolution of 4 cm^{-1}), with the nanoparticle samples deposited onto a NaCl disk. X-ray photoelectron spectroscopy (XPS) measurements were performed with a Phi 5400/XPS instrument equipped with an Al K_α source operated at 350 W and 10^{-9} Torr. X-ray diffraction (XRD) patterns were collected with a Rigaku Americas Miniflex Plus Diffractometer from $2\theta = 10°$ to 80° at a rate of 2° min-1 and 0.04° step size with Cu Ka radiation ($\lambda = 1.5418$ Å). Electron paramagnetic resonance (EPR) measurements were carried out with a Bruker EMX EPR spectrometer at the X-band frequency (~9.4 GHz) using an ER 4122SHQE resonator. All EPR spectra were recorded using a power of 1 mW, a modulation amplitude of 1 G, and a modulation frequency of 100 KHz. UV–vis absorption spectra were collected with a PerkinElmer Lambda 35 UV–vis spectrometer, and photoluminescence measurements were performed with a PTI fluorospectrometer. X-ray absorption (XAS) measurements were carried out at 10 K on beamline 4-1 at the Stanford Synchrotron Radiation Light source using an Oxford liquid helium cryostat. Atomic force microscopy (AFM) measurements were performed using an Asylum Jupiter XR AFM. Inductively coupled plasma-optical emission spectrometry (ICPOES) measurements were conducted with an iCap 7400 analyzer.

Electrochemical Mott-Schottky measurements

The electrochemical tests were performed with a CHI 710 electrochemical workstation in a conventional three-electrode cell, using an Ag/AgCl (3 M KCl) electrode as the reference electrode, a graphite rod as the counter electrode, and a polished glassy carbon disk (surface area 0.196 cm^2) as the working electrode. 2 mg of the CuOH samples obtained above were added into 1 mL of an isopropanol/water (3:1 v/v) mixture and 10 μL of a 100 wt% Nafion solution. The suspension was sonicated to form a homogeneous ink. 5 μL of the ink was then dropcast onto the glassy carbon electrode, dried at room temperature, and coated with 5 μL of a 20 wt % Nafion solution, corresponding to a sample loading of 40.65 μg cm^{-2}. The tests were then performed in 0.1 M KOH (CV) and 0.1 M Na_2SO_4 (EIS) Solution.

Photodynamic bactericidal experiments

The procedure has been detailed previously.[77] Experimentally, *E. coli* cells were grown in Luria−Bertani (LB) agar in a 37 °C incubator for 18 h. A single colony was selected and used to inoculate in 3 mL of LB broth and allowed to shake at 37 °C for 18 h. The sample was then centrifuged at 5000 rpm for 5 min and resuspended in a phosphate buffer saline (PBS, 0.05 M, pH = 8.7) 2 times and set to an optical density (OD) of 0.1 at 600 nm. In photodynamic antibacterial assessments, 10 μL of *E. coli* (OD = 0.1) was transferred to a plastic scintillation vial, into which of the CuOH samples prepared above (5 mg) was added along with 9 mL of PBS creating a total concentration of 0.5 mg mL^{-1}. The scintillation vials containing the bacterial cells and ligand samples were irradiated with a blue light (465 nm) for various timepoints. From the diluted solution, 10 μL was plated and spread on LB agar plates using sterile glass beads and were

incubated at 37 °C for 16 h. Then, the number of bacterial colonies forming units (CFU) was counted by a plate reader (Acolyte Colony Counter). Percent bacterial cell survival was determined by normalizing the CFUs to that prior to light exposure.

Intracellular glutathione activity

The Ellman method based on GSH oxidation was used to evaluate the oxidative stress induced by the materials.[78] In brief, 5 mL solutions of each sample (160 μg mL^{-1}) and glutathione (1 mM) were prepared in PBS. The solutions were then mixed, shaken, and exposed to 465 nm blue light for 2 h. At 30-min intervals, an aliquot of 450 μL was removed and mixed with 785 μL of a Tris−HCl buffer (0.05 M, pH = 8.8) and 15 μL of the Ellman's reagent DTNB (100 mM) and shaken for 1 min. The supernatant was collected by centrifugation, and 200 μL of the supernatant was added to the 96-well plate, which was placed into the Molecular Devices SpectraMax Plus reader. The wavelength of the enzyme marker was set to 410 nm to assess GSH loss.

EPR Measurements

As detailed previously,[79] 63 μL of the CuOH samples (1 mg mL^{-1}) was mixed with 7 μL of DMPO (1 M), with a mixture of Nanopure H_2O and DMPO as a control. The solution was added to a capillary tube which was inserted into a quartz EPR tube (Wilmad, 4 mm outer diameter). The tube was centered in the cavity resonator for data collection. Spectra were recorded at room temperature with a Bruker EMX EPR spectrometer operating at the X-band frequency (~9.3 GHz) using an ER 4122SHQE resonator (Bruker). The samples were irradiated for 10 min with 465 nm blue light before collecting EPR spectra.

Computational methods and models

(a) VASP calculations: The density functional theory (DFT) calculations are performed using the VASP (Vienne Ab-Initio Simulation Package) code[80,81] with the Projector-Augmented Wave potentials[82,83] and the Perdew-Burke-Ernzerhof (PBE) functional[84] with Grimme's G3 dispersion corrections[85]. Model structures of CuOH-EPA (Figure 13g), CuOH-HC4 (Figure 35) and CuOH-EPT (Figure 36) were constructed based on the XRD data. An energy cutoff of 600 eV was chosen based on the previous study of CuOH[86].

CuOH-EPA, CuOH-HC4 and CuOH-EPT were modelled in a supercell of 19.5281 Å × 2.6730 Å × 7.9875 Å. A K-point grid of 1×7×2 was used to sample the Brillion zone of the supercell. All atoms were allowed to relax during geometry optimization and frequency calculations. To speed up calculations, 1-butynyl was chosen to replace HC16.

(b) Gaussian calculations: All electron time-dependent DFT (TDDFT) calculations were carried out using Gaussian 16[87] with the B3LYP hybrid functional and a 6-311g++(2d, p) basis set on models of CuOH with different ligands to better understand the effect of ligand-CuOH interaction on the optical properties. UV-vis spectra were calculated using TDDFT calculations on a monomer of the optimized structures of CuOH-EPA, CuOH-HC4 and CuOH-EPT from VASP calculations. The HC model included a longer C chain based on the C4 structure of the slab model. Natural transition orbital analysis[88] was performed based on the TDDFT wavefunctions.

Statistical analysis

Data included in the present study are the most typical in each measurement (under 5% variation). The error bars in the photodynamic study are based on results of triplicate measurements.

8.6 Reference

1. M. Yin, C. K. Wu, Y. B. Lou, C. Burda, J. T. Koberstein, Y. M. Zhu, S. O'Brien. *J Am Chem Soc* **2005**, *127*, 9506-9511.

2. T. D. Golden, M. G. Shumsky, Y. C. Zhou, R. A. VanderWerf, R. A. VanLeeuwen, J. A. Switzer. *Chem Mater* **1996**, *8*, 2499-2504.

3. X. F. Wu, H. Bai, J. X. Zhang, F. E. Chen, G. Q. Shi. *Journal of Physical Chemistry B* **2005**, *109*, 22836-22842.

4. X. S. Peng, J. Jin, I. Ichinose. *Adv Funct Mater* **2007**, *17*, 1849-1855.

5. P. L. Saldanha, R. Brescia, M. Prato, H. B. Li, M. Povia, L. Manna, V. Lesnyak. *Chem Mater* **2014**, *26*, 1442-1449.

6. S. H. Wang, A. Riedinger, H. B. Li, C. H. Fu, H. Y. Liu, L. L. Li, T. L. Liu, L. F. Tan, M. J. Barthel, G. Pugliese, F. De Donato, M. S. D'Abbusco, X. W. Meng, L. Manna, H. Meng, T. Pellegrino. *Acs Nano* **2015**, *9*, 1788-1800.

7. X. Zhao, G. D. Niu, J. S. Zhu, B. Yang, J. H. Yuan, S. R. Li, W. R. Gao, Q. S. Hu, L. X. Yin, K. H. Xue, E. Lifshitz, X. S. Miao, J. Tang. *J. Phys. Chem. Lett.* **2020**, *11*, 1873-1880.

8. R. Peng, M. Li, D. Li. *Coordin Chem Rev* **2010**, *254*, 1-18.

9. M. Y. Guan, Y. Jian, J. H. Sun, T. M. Shang, Q. Liu, Z. Xu. *Crystengcomm* **2015**, *17*, 7372-7380.

10. J. Singh, V. Kumar, K. H. Kim, M. Rawat. *Environ Res* **2019**, *177*.

11. L. Isac, C. Cazan, A. Enesca, L. Andronic. *Front Chem* **2019**, *7*.

12. P. Samarasekara, N. T. R. N. Kumara, N. U. S. Yapa. *J Phys-Condens Mat* **2006**, *18*, 2417-2420.

13. S. Goel, F. Chen, W. B. Cai. *Small* **2014**, *10*, 631-645.

14. J. C. Li, Y. Kuang, Y. T. Meng, X. Tian, W. H. Hung, X. Zhang, A. W. Li, M. Q. Xu, W. Zhou, C. S. Ku, C. Y. Chiang, G. Z. Zhu, J. Y. Guo, X. M. Sun, H. J. Dai. *J Am Chem Soc* **2020**, *142*, 7276-7282.

15. S. Nitopi, E. Bertheussen, S. B. Scott, X. Y. Liu, A. K. Engstfeld, S. Horch, B. Seger, I. E. L. Stephens, K. Chan, C. Hahn, J. K. Norskov, T. F. Jaramillo, I. Chorkendorff. *Chem Rev* **2019**, *119*, 7610-7672.

16. M. Porta, M. T. Nguyen, T. Tokunaga, Y. Ishida, W. R. Liu, T. Yonezawa. *Langmuir* **2016**, *32*, 12159-12165.

17. M. Tariq, M. D. Koch, J. W. Andrews, K. E. Knowles. *J Phys Chem C* **2020**, *124*, 4810-4819.

18. K. Sekar, C. Chuaicham, U. Balijapalli, W. Li, K. Wilson, A. F. Lee, K. Sasaki. *Appl Catal B-Environ* **2021**, *284*.

19. D. Miller. *J Phys Chem* **1909**, *13*, 256-261.

20. H. W. Gillett. *J Phys Chem* **1909**, *13*, 332-335.

21. K. L. Cheng. *Anal Chem* **1955**, *27*, 1165-1166.

22. T. P. Nevell, O. P. Singh. *Text Res J* **1986**, *56*, 270-280.

23. C. J. Whitham, H. Ozeki, S. Saito. *Journal of Chemical Physics* **2000**, *112*, 641-646.

24. P. A. Korzhavyi, I. L. Soroka, E. I. Isaev, C. Lilja, B. Johansson. *P Natl Acad Sci USA* **2012**, *109*, 686-689.

25. I. L. Soroka, A. Shchukarev, M. Jonsson, N. V. Tarakina, P. A. Korzhavyi. *Dalton T* **2013**, *42*, 9585-9594.

26. Y. G. Li, C. M. Lousada, I. L. Soroka, P. A. Korzhavyi. *Inorg Chem* **2015**, *54*, 8969-8977.

27. T. Rajh, L. X. Chen, K. Lukas, T. Liu, M. C. Thurnauer, D. M. Tiede. *Journal of Physical Chemistry B* **2002**, *106*, 10543-10552.

28. Y. Peng, B. Z. Lu, F. Wu, F. Q. Zhang, J. E. Lu, X. W. Kang, Y. Ping, S. W. Chen. *J Am Chem Soc* **2018**, *140*, 15290-15299.

29. W. Y. Chen, H. L. Zuo, E. Q. Zhang, L. Li, P. Henrich-Noack, H. Cooper, Y. J. Qian, Z. P. Xu. *Acs Appl Mater Inter* **2018**, *10*, 20326-20333.

30. M. P. Hendricks, M. P. Campos, G. T. Cleveland, I. Jen-La Plante, J. S. Owen. *Science* **2015**, *348*, 1226-1230.

31. M. V. Kovalenko, M. Scheele, D. V. Talapin. *Science* **2009**, *324*, 1417-1420.

32. Y. G. Sun, Y. N. Xia. *Science* **2002**, *298*, 2176-2179.

33. Y. N. Xia, Y. J. Xiong, B. Lim, S. E. Skrabalak. *Angew Chem Int Edit* **2009**, *48*, 60-103.

34. V. P. Ananikov, N. V. Orlov, I. P. Beletskaya, V. N. Khrustalev, M. Y. Antipin, T. V. Timofeeva. *J Am Chem Soc* **2007**, *129*, 7252-7253.

35. Y. J. Xiong, I. Washio, J. Y. Chen, H. G. Cai, Z. Y. Li, Y. N. Xia. *Langmuir* **2006**, *22*, 8563-8570.

36. M. Dasog, G. B. De los Reyes, L. V. Titova, F. A. Hegmann, J. G. C. Veinot. *Acs Nano* **2014**, *8*, 9636-9648.

37. M. H. Jao, C. F. Lu, P. Y. Tai, W. F. Su. *Cryst Growth Des* **2017**, *17*, 5945-5952.

38. R. B. Grubbs. *Polym Rev* **2007**, *47*, 197-215.

39. P. G. Hu, L. M. Chen, X. W. Kang, S. W. Chen. *Accounts Chem Res* **2016**, *49*, 2251-2260.

40. Y. Peng, Q. M. Liu, S. W. Chen. *Chem Rec* **2020**, *20*, 41-50.

41. Y. Peng, J. E. Lu, C. P. Deming, L. M. Chen, N. Wang, E. Y. Hirata, S. W. Chen. *Electrochimica Acta* **2016**, *211*, 704-710.

42. A. Bard, *Standard potentials in aqueous solution*. Routledge: **2017**.

43. N. J. Long, C. K. Williams. *Angew Chem Int Edit* **2003**, *42*, 2586-2617.

44. S. W. Chen, A. C. Templeton, R. W. Murray. *Langmuir* **2000**, *16*, 3543-3548.

45. H. N. Bai, H. Guo, C. Feng, J. Wang, B. Liu, Z. L. Xie, F. Q. Guo, D. J. Chen, R. Zhang, Y. D. Zheng. *J Mater Chem C* **2022**, *10*, 3756-3769.

46. M. K. Ge, W. J. Yuan, L. L. Zhou, Z. L. Deng, M. Hu, X. Li, J. He, W. Xi, J. Luo. *Adv Mater Interfaces* **2020**, *7*.

47. H. C. Allen, M. L. Mecartney, J. C. Hemminger. *Microsc Microanal* **1998**, *4*, 23-33.

48. M. Z. Wei, J. Z. Huo. *Mater Chem Phys* **2010**, *121*, 291-294.

49. M. Vaseem, A. Umar, S. H. Kim, Y. B. Hahn. *J Phys Chem C* **2008**, *112*, 5729-5735.

50. J. Li, M. Tian, W. Zhang, J. Qian, S. Zhao, W. Q. Dang, H. Y. Jiang, C. B. Li. *Appl Organomet Chem* **2021**, *35*.

51. Z. Wei, J. S. Hu, K. J. Zhu, W. Q. Wei, X. G. Ma, Y. F. Zhu. *Appl Catal B-Environ* **2018**, *226*, 616-623.

52. B. P. Vinayan, Z. Zhao-Karger, T. Diemant, V. S. K. Chakravadhanula, N. I. Schwarzburger, M. A. Cambaz, R. J. Behm, C. Kubel, M. Fichtner. *Nanoscale* **2016**, *8*, 3296-3306.

53. H. Y. Jiang, P. Zhou, Y. Y. Wang, R. Duan, C. C. Chen, W. J. Song, J. C. Zhao. *Adv Mater* **2016**, *28*, 9776-+.

54. S. Wang, S. Q. Jiao, J. X. Wang, H. S. Chen, D. H. Tian, H. P. Lei, D. N. Fang. *Acs Nano* **2017**, *11*, 469-477.

55. C. Q. Zhu, A. Osherov, M. J. Panzer. *Electrochim Acta* **2013**, *111*, 771-778.

56. T. T. Sun, M. Wu, X. W. He, W. Y. Li, X. Z. Feng. *J Mater Chem B* **2015**, *3*, 6971-6978.

57. B. B. Jia, R. Hao, Z. N. Huang, P. F. Hu, L. D. Li, Y. Zhang, L. Guo. *Journal of Materials Chemistry A* **2019**, *7*, 4383-4388.

58. Y. Y. Huai, Y. P. Qian, Y. J. Peng. *Appl Surf Sci* **2020**, *531*.

59. N. Wang, L. G. Li, D. K. Zhao, X. W. Kang, Z. H. Tang, S. W. Chen. *Small* **2017**, *13*.

60. J. D. Yi, R. K. Xie, Z. L. Xie, G. L. Chai, T. F. Liu, R. P. Chen, Y. B. Huang, R. Cao. *Angew Chem Int Edit* **2020**, *59*, 23641-23648.

61. A. Herzog, A. Bergmann, H. S. Jeon, J. Timoshenko, S. Kuhl, C. Rettenmaier, M. L. Luna, F. T. Haase, B. Roldan Cuenya. *Angew Chem Int Edit* **2021**, *60*, 7426-7435.

62. G. Silversmit, H. Poelman, V. Balcaen, P. M. Heynderickx, M. Olea, S. Nikitenko, W. Bras, P. F. Smet, D. Poelman, R. De Gryse, M. F. Reniers, G. B. Marin. *J Phys Chem Solids* **2009**, *70*, 1274-1284.

63. Y. Peng, Q. M. Liu, B. Z. Lu, T. He, F. Nichols, X. Hu, T. Huang, G. Huang, L. Guzman, Y. Ping, S. W. Chen. *Acs Catal* **2021**, *11*, 1179-1188.

64. H. Weller. *Angew Chem Int Edit* **1993**, *32*, 41-53.

65. J. L. Liu, W. X. Cheng, Y. H. Wang, X. Y. Fan, J. H. Shen, H. Liu, A. Q. Wang, A. P. Hui, F. Nichols, S. W. Chen. *Acs Appl Nano Mater* **2021**, *4*, 4361-4370.

66. G. Chata, F. Nichols, R. Mercado, T. Assafa, G. L. Millhauser, C. Saltikov, S. W. Chen. *Acs Appl Bio Mater* **2021**, *4*, 7025-7033.

67. J. L. Clement, N. Ferre, D. Siri, H. Karoui, A. Rockenbauer, P. Tordo. *J Org Chem* **2005**, *70*, 1198-1203.

68. F. Nichols, K. I. Ozoemena, S. Chen. *Chinese J Catal* **2022**, *43*, 1399-1416.

69. M. Hans, A. Erbe, S. Mathews, Y. Chen, M. Solioz, F. Mucklich. *Langmuir* **2013**, *29*, 16160-16166.

70. E. M. Flores, M. L. Moreira, M. J. Piotrowski. *J Phys Chem A* **2020**, *124*, 3778-3785.

71. J. N. Guo, J. M. Zhou, Z. Sun, M. Y. Wang, X. Y. Zou, H. L. Mao, F. Yan. *Acta Biomater* **2022**, *146*, 370-384.

72. K. Liu, Y. Song, S. W. Chen. *J Power Sources* **2014**, *268*, 469-475.

73. K. Liu, Y. Song, S. W. Chen. *Int J Hydrogen Energ* **2016**, *41*, 1559-1567.

74. Y. Peng, W. Z. Pan, N. Wang, J. E. Lu, S. W. Chen. *Chemsuschem* **2018**, *11*, 130-136.

75. X. M. Jiang, W. W. He, X. W. Zhang, Y. Wu, Q. Zhang, G. J. Cao, H. Zhang, J. W. Zheng, T. R. Croley, J. J. Yin. *J Phys Chem C* **2018**, *122*, 29414-29425.

76. H. Guo, C. G. Niu, C. Y. Feng, C. Liang, L. Zhang, X. J. Wen, Y. Yang, H. Y. Liu, L. Li, L. S. Lin. *Chem Eng J* **2020**, *385*.

77. F. Nichols, J. E. Lu, R. Mercado, M. D. Rojas-Andrade, S. L. Ning, Z. Azhar, J. Sandhu, R. Cazares, C. Saltikov, S. W. Chen. *Langmuir* **2020**, *36*, 11629-11636.

78. J. Liu, W. Cheng, K. Zhang, H. Liu, J. Li, J. Tressel, S. Chen. *Acs Appl Bio Mater* **2022**, *5*, 3912-3922.

79. G. Chata, F. Nichols, R. Mercado, T. Assafa, G. L. Millhauser, C. Saltikov, S. Chen. *Acs Appl Bio Mater* **2021**, *4*, 7025-7033.

80. G. Kresse, J. Hafner. *Phys. Rev. B* **1993**, *48*, 13115-13118.

81. G. Kresse, J. Hafner. *Phys. Rev. B* **1993**, *47*, 558-561.

82. P. E. Blochl. *Phys. Rev. B* **1994**, *50*, 17953-17979.

83. G. Kresse, D. Joubert. *Phys. Rev. B* **1999**, *59*, 1758-1775.

84. J. P. Perdew, K. Burke, M. Ernzerhof. *Phys. Rev. Lett.* **1996**, *77*, 3865-3868.

85. S. Grimme, J. Antony, S. Ehrlich, H. Krieg. *The Journal of Chemical Physics* **2010**, *132*, 154104-154123.

86. Y. Li, C. M. Lousada, I. L. Soroka, P. A. Korzhavyi. *Inorg Chem* **2015**, *54*, 8969-8977.

87. M. J. Frisch, G. W. Trucks, H. B. Schlegel, G. E. Scuseria, M. A. Robb, J. R. Cheeseman, G. Scalmani, V. Barone, G. A. Petersson, H. Nakatsuji, X. Li, M. Caricato, A. V. Marenich, J. Bloino, B. G. Janesko, R. Gomperts, B. Mennucci, H. P. Hratchian, J. V. Ortiz, A. F. Izmaylov, J. L. Sonnenberg, Williams, F. Ding, F. Lipparini, F. Egidi, J. Goings, B. Peng, A. Petrone, T. Henderson, D. Ranasinghe, V. G. Zakrzewski, J. Gao, N. Rega, G. Zheng, W. Liang, M. Hada, M. Ehara, K. Toyota, R. Fukuda, J. Hasegawa, M. Ishida, T. Nakajima, Y. Honda, O. Kitao, H. Nakai, T. Vreven, K. Throssell, J. A. Montgomery Jr., J. E. Peralta, F. Ogliaro, M. J. Bearpark, J. J. Heyd, E. N. Brothers, K. N. Kudin, V. N. Staroverov, T. A. Keith, R. Kobayashi, J. Normand, K. Raghavachari, A. P. Rendell, J. C. Burant, S. S. Iyengar, J. Tomasi, M. Cossi, J. M. Millam, M. Klene, C. Adamo, R. Cammi, J. W. Ochterski, R. L. Martin, K. Morokuma, O. Farkas, J. B. Foresman, D. J. Fox *Gaussian 16 Rev. C.01*, Wallingford, CT, 2016.

88. R. L. Martin. *The Journal of Chemical Physics* **2003**, *118*, 4775-4777.

Chapter 9 Summary and Perspectives

In summary, my dissertation is focused on the design and structural engineering of nanostructured catalysts for efficient energy conversion. The valuable findings in each chapter help advance our understanding of the catalytic systems and their potential applications.

In **Chapter 2**, a novel wet impregnation procedure was developed to create Pd atomically dispersed and enriched on N-doped porous carbon cages derived from hollow ZIF-8 precursors. These Pd-HNC samples exhibited remarkable ORR activity in alkaline media, outperforming traditional Pt-based counterparts and even leading Pd-based catalysts reported in the literature. The key to the enhanced performance lay in the formation of atomic Pd-N species predominantly enriched on the carbon support surface. This result highlighted the significance of metal single-atom catalysts and their surface enrichments in ORR electrocatalysis. Moreover, the unique structural scaffold offered potential for a diverse range of metal centers, promising applications in various fields.

Chapter 3 explored the use of a trinuclear $RuFe_2$ complex as a metal precursor to create carbon nanocomposites with Ru-doped Fe_2O_3 nanoparticles. The resulting RuFe-NC nanocomposites displayed exceptional ORR activity, comparable to state-of-the-art Pt/C catalysts. The superior performance of RuFe-NC was attributed to the favorable Fe to Ru charge transfer within the composites, facilitating the adsorption of key reaction intermediates and increasing the electrochemical surface area. The rational

design of metal precursors demonstrated its effectiveness in manipulating the morphological and electronic structure of carbon for high-performance electrocatalysis.

Chapter 4 introduced the innovative use of magnetic induction heating (MIH) to rapidly prepare Ru nanoparticles supported on carbon paper. These Ru-Cl functionalized samples exhibited significant electrocatalytic activity towards HER in both acidic and alkaline media, outperforming commercial Pt/C benchmarks. DFT calculations revealed that the surface Cl species induced electron transfer from the Ru nanoparticles, leading to a downshift of the d band center of Ru and weakened H adsorption, a unique feature responsible for the enhanced HER activity. This study revealed the importance of MIH in structural engineering of metal nanoparticles by heteroanion functionalization, enhancing their electrocatalytic performance.

Similarly, in **Chapter 5**, MIH was successfully employed to synthesize Co-NC nanocomposites from ZIF-67, where Co/CoO nanoparticles were encapsulated with defective N-doped carbon layers. The resulting Co-NC-400 exhibited outstanding OER performance in alkaline media, outperforming commercial RuO_2 and other Co-based nanocomposites. CoOOH species resulting from the transformation of metallic Co nanoparticles acted as the catalytic active sites, while the graphitized carbon shells enhanced stability, as confirmed by operando XAS measurements. The results further highlighted the unique significance of MIH in engineering high-performance electrocatalysts from cost-effective precursors.

In **Chapter 6**, MIH was used for rapid production of FeNi spinel nanostructures which showed a remarkable OER activity due to their unique metastable structure, with

homogeneous Fe-Ni elemental distribution and abundant Cl residues on the surface. The effective herteroanion functionalization allows for unprecedented material structures that led to an enhanced OER performance and showed potential for industrial-scale synthesis.

In **Chapter 7**, Ir nanoparticles functionalized with acetylene derivatives exhibited enhanced HER and OER activity, surpassing commercial benchmarks. The effective charge transfer from the Ir core to acetylene moieties weakened the binding of H and O intermediates, contributing to improved electrocatalytic activity. Deliberate interfacial engineering emerged as a significant factor in manipulating the electronic properties of metal nanoparticles for electrochemical energy technologies.

Finally, **Chapter 8** developed a facile wet-chemistry procedure for the preparation of unprecedentedly stable CuOH nanostructures with select organic ligands, showing enhanced antibacterial activity under UV and blue light irradiation, due to effective production of hydroxyl radicals which was facilitated by the conjugated core-ligand linkages and narrowed bandgap. Functionalization with organic ligands proved effective in stabilizing and functionalizing CuOH nanostructures for practical applications.

In these studies, a range of nanostructured catalysts were found to exhibit a remarkable performance for electrochemical energy conversion. Further studies are desired to optimize the electrocatalytic performance by more deliberate engineering of the materials structures and morphologies. For single-atom catalysts, fine-tuning of the local atomic coordination of the metal centers is anticipated to replace the hodgepodge-

like pyrolysis approach through careful metal precursor selection and novel synthetic chemistry. Furthermore, ultrafast synthesis can be used as a powerful tool for discovering novel catalysts with non-equilibrium and metastable structures, which can maximize the density of catalytic sites and break the linear scaling relationships in catalysis. Integrating conjugated ligands, such as acetylene derivatives, onto various semiconductor surfaces like metal oxides and chalcogenides, offers another opportunity for interfacial charge transfer, allowing for the unprecedented tuning of the electronic structures and physical/chemical properties. Furthermore, by incorporating theoretical studies (such as DFT) and employing in-situ/operando characterizations, we anticipate a significant advance of the understanding of the underlying mechanisms behind the catalytic processes. This can provide a precise guidance for catalyst design through reasonable structural engineering.

It is envisaged that the continuous development of advanced catalysts may promisingly address global energy and environmental challenges. Moreover, it offers potential applications across diverse fields, including energy conversion, environmental protection, and biomedicine. Hence, through structural engineering, we can create sustainable energy solutions toward a future with enhanced efficiency and sustainable energy sources. To make a positive and transformative impact on global green energy, it is imperative to continue the exploration of novel catalysts.